UNIVERSITÉ DU LUXEMBOURG

PhD-FSTM-2022-145
The Faculty of Science, Technology and Medicine

DISSERTATION

Defence held on 21/11/2022 in Esch-Sur-Alzette, Luxembourg
to obtain the degree of

DOCTEUR DE L'UNIVERSITÉ DU LUXEMBOURG

EN BIOLOGIE

by

Leticia SORIANO BAGUET
Born on 22nd March 1994 in Brussels (Belgium)

PYRUVATE DEHYDROGENASE FUELS A CRITICAL CITRATE POOL THAT IS ESSENTIAL FOR TH17 CELL EFFECTOR FUNCTION

Dissertation defence committee

Dr. Dirk Brenner, dissertation supervisor
Professor, Université du Luxembourg
Experimental & Molecular Immunology, Luxembourg Institute of Health

Dr. Christoph Hess
Professor, University of Cambridge and University Hospital of Basel

Dr. Serge Haan, Chairman
Professor, Université du Luxembourg

Dr. Stefano Angiari
Assistant Professor, Medical University of Graz

Dr. Paul Coffer, Vice Chairman
Professor, University Medical Center Utrecht

UNIVERSITÉ DU LUXEMBOURG

PhD-FSTM-2022-145
The Faculty of Science, Technology and Medicine

DISSERTATION

Presented on 21/11/2022 in Esch-Sur-Alzette, Luxembourg

to obtain the degree of

DOCTEUR DE L'UNIVERSITÉ DU LUXEMBOURG

EN BIOLOGIE

by

Leticia SORIANO BAGUET

Born on 22nd March 1994 in Brussels (Belgium)

PYRUVATE DEHYDROGENASE FUELS A CRITICAL CITRATE POOL THAT IS ESSENTIAL FOR TH17 CELL EFFECTOR FUNCTION

The work presented in this thesis was conducted at the:

Experimental & Molecular Immunology Group

Department of Infection and Immunity

Luxembourg Institute of Health

In association with:

Cancer Metabolism Group, Department of Cancer Research, **Luxembourg Institute of Health**

Luxembourg Centre for Systems and Biomedicine, University of Luxembourg

Department of Life Sciences and Medicine, University of Luxembourg

National Center of Pathology (NCP), Laboratoire national de santé (LNS)

Braunschweig Integrated Center of Systems Biology, Technische Universität Braunschweig

Funded by:

Ministère de l'Enseignement supérieur et de la Recherche (MESR)

Luxembourg National Research Fund (FNR) :

NextImmune – Next Generation Immunoscience, under:

PRIDE – Programme for Research-intensive Doctoral Education

AFFIDAVIT

I hereby confirm that the PhD thesis entitled “Pyruvate dehydrogenase fuels a critical citrate pool that is essential for the Th17 cell effector function” has been written independently and without any other sources than cited. All necessary ethical approvals have been obtained in accordance with the law, following the EU Directive **2010/63/EU** of care and use of laboratory animals.

Luxembourg, 21st October 2022,

Leticia Soriano Baguet

ACKNOWLEDGEMENTS

I would first like to thank my supervisor, Prof. Dr. Dirk Brenner for allowing me to join the team when I was only a “silly” bachelor’s student and still wanting to keep me for four more years as a PhD student. Thank you for everything you taught me during all these years and your support through it all.

Then, I want to thank THE team. I have to start with the original team and the people that made me want to do a PhD in this group in the first place. Henry, thank you for your patience and tolerance to my blabbering during all these years. I am so glad we managed to get you talking at some point, even if it was just to say that you were hungry. Luana, thank you for being the big sister I didn’t know I wanted nor needed, all the encouragements you have given me throughout the years (which have been A LOT) and dealing with my constant drama. Davide, thank you for the bad jokes that always made me laugh, the cakes and funny T-shirts that made my day. Especially, thank you for the hugs. Lynn, thank you for being one of the most entertaining people on Earth, while still being one of the kindest. Thank you for sharing all the stories you have to tell that always got me bursting out laughing. Melanie, thank you for your support even when I was at my lowest and still finding ways to make me laugh and feel loved. Also, thank you for teaching me how to work in the lab while still having fun, despite all the Michael Bublé I have had to endure each Christmas season. Carole B., thank you for your kindness, your optimism and the many many WB you did for me in the last few years, but mostly, thank you for all your help and patience to all my nonsense and disorganization, I know it was not always easy. Catherine, thank you for allowing me to vent when I was about to burst and especially for all the times you improved my writing, we both know that was not the most pleasant times for you and I apologize for making you go through it over and over again. Now, to the people that have been joining the EMI team later. Anouk, thank you for all your constant support and always finding the right words to get me going. Thank you for being there since our “student” times and allowing me to be silly and childish without shame. I know I leave the title of senior PhD student in great hands, especially if seahorse assays are needed. Takumi, thank you for your input, kind words and support. You always find a way of making me feel better. Also, thank you for all the Japanese goodies, I still wake up dreaming of those rice cookies. Charlène, thank you for your optimism and always having a smile on your face even in those tough days. Sophie, thank you for your support and the patience to help me deal with my mouse drama. Nika, thank you for the help of this last year and showing me how to keep sane while doing 10 things at once. Joseph, thank you for dealing with all the computational thingies while enriching my Musicals’ culture. Thank you Janika for always being up for anything and filling the office with plants. Thank

you Carole W. for the gossip and excitement for free drinks as well as your help in all bureaucratic messes.

Now, I would like to thank the people who have always believed in me, my family back home: mum, dad, David, and Eric, as well as my Belgian family: Mamy, Etienne, Tisiana, Françoise, Jean-Luc, François, Nicolas, Maxime and Julie. Thank you for your constant support, even from a distance, and asking how my mice are doing every time we see each other. I wouldn't have been able to get anything done in my life without your help, so thank you very very much, merci and gracias.

To my Luxembourgish family, the Lokians, Nils, Luana, Anna, Sinan, Tatiana, Evy and Vasco. Thank you for making me feel at home and filling my evenings and weekends of very good food, movies, popcorn, love, hugs, laughter and happiness. The idea of coming home carried me through those very long days at work.

To Nathan, for always having my back from every "good morning" to "good night" text. Thank you for making me see things in a different way and bringing out my Belgian side eh! Thank you for taking care of me when I was down and for cooking and cleaning much better than me. I can't wait to continue our adventures.

Finally, I would also like to thank the people at LIH that made my days at work lighter. Special thanks goes to Alessandro and François for all your Marvelousness.

TABLE OF CONTENT

LIST OF ILLUSTRATIONS

LIST OF FIGURES

LIST OF TABLES

LIST OF PUBLICATIONS AND MANUSCRIPTS

I. Appendix 1: submitted research manuscript from thesis project (*first author*)

SORIANO-BAGUET, L., GRUSDAT, M., KURNIAWAN, H., BENZARTI, M., BONETTI, L., EWEN, A., GUERRA, L., FRANCHINA, D.G., KOBAYASHI, T., LONGWORTH, J., BINSFELD, C., VERSCHUEREN, C., HELGUETA-ROMERO, S., GERARD, D., MORE, T., HENNE, A., DOSTERT, C., FARINELLE, S., JÄGER, C., MITTELBRONN, M., SINKKONEN, L., HILLER, K., MEISER, J., BRENNER, D. **Pyruvate dehydrogenase fuels a critical citrate pool that is essential for Th17 cell effector functions.**

II. Appendix 2: Review publication (*shared first author*)

KURNIAWAN, H., SORIANO-BAGUET, L., BRENNER, D., 2020. **Regulatory T cell metabolism at the intersection between autoimmune diseases and cancer.** *Eur. J. Immunol.* 50, 1626–1642.

III. Appendix 3: Research publication (*co-author*)

FRANCHINA, D.G., KURNIAWAN, H., GRUSDAT, M., BINSFELD, C., GUERRA, L., BONETTI, L., SORIANO-BAGUET, L., EWEN, A., KOBAYASHI, T., FARINELLE, S., MINAFRA, A.R., VANDAMME, N., CARPENTIER, A., BORGMANN, F.K., JÄGER, C., CHEN, Y., KLEINEWIETFELD, M., VASILIOU, V., MITTELBRONN, M., HILLER, K., LANG, P.A., BRENNER, D., 2022. **Glutathione-dependent redox balance characterizes the distinct metabolic properties of follicular and marginal zone B cells.** *Nat Commun* 13, 1789.

IV. Appendix 4: Research publication (*co-author*)

KURNIAWAN, H., FRANCHINA, D. G., GUERRA, L., BONETTI, L., BAGUET, L. S., GRUSDAT, M., SCHLICKER, L., HUNEWALD, O., DOSTERT, C., MERZ, M. P., BINSFELD, C., DUNCAN, G. S., FARINELLE, S., NONNENMACHER, Y., HAIGHT, J., DAS GUPTA, D., EWEN, A., TASKESEN, R., HALDER, R., CHEN, Y., JÄGER, C., OLLERT, M., WILMES, P., VASILIOU, V., HARRIS, I. S., KNOBBETHOMSEN, C. B., TURNER, J. D., MAK, T. W., LOHOFF, M., MEISER, J., HILLER, K. & BRENNER, D. 2020. **Glutathione Restricts Serine Metabolism to Preserve Regulatory T Cell Function.** *Cell Metab*, 31, 920-936.e7.

V. Appendix 5: Research publication (*co-author*)

KIWELER, N., DELBROUCK, C., POZDEEV, V.I., NEISES, L., SORIANO-BAGUET, L., EIDEN, K., XIAN, F., BENZARTI, M., HAASE, L., KONCINA, E., SCHMOETTEN, M., JAEGER, C., NOMAN, M.Z., VAZQUEZ, A., JANJI, B., DITTMAR, G., BRENNER, D., LETELLIER, E., MEISER, J., 2022. **Mitochondria preserve an autarkic one-carbon cycle to confer growth-independent cancer cell migration and metastasis.** *Nat Commun* 13, 2699.

VI. Appendix 6: Research publication (*co-author*)

YANG, W., DENGER, A., DIENER, C., KÜPPERS, F., SORIANO-BAGUET, L., SCHÄFER, G., YANAMANDRA, A.K., ZHAO, R., KNÖRCK, A., SCHWARZ, E.C., HART, M., LAMMERT, F., ROMA, L.P., BRENNER, D., CHRISTIDIS, G., HELMS, V., MEESE, E., HOTH, M., QU, B., 2022. **Unspecific CTL Killing Is Enhanced by High Glucose via TNF-Related Apoptosis-Inducing Ligand.** *Front. Immunol.* 13, 831680.

VII. Appendix 7: Research publication (*co-author*)

ZHU, J., YANG, W., ZHOU, X., ZÖPHEL, D., SORIANO-BAGUET, L., DOLGENER, D., CARLEIN, C., HOF, C., ZHAO, R., YE, S., SCHWARZ, E.C., BRENNER, D., PRATES ROMA, L., QU, B., 2021. **High Glucose Enhances Cytotoxic T Lymphocyte-Mediated Cytotoxicity.** *Front. Immunol*. 12, 689337.

LIST OF ABBREVIATIONS

1C	One-carbon
2-DG	2-deoxy-D-glucose
2-HG	2-hydroxyglutarate
2-NBDG	2-(N-(7-Nitrobenz-2-oxa-1,3-diazol-4-yl)Amino)-2-Deoxyglucose
3-PG	Glyceraldehyde 3-phosphate
4E-BP	4E-binding protein
5 mC	5-methylcytosine
AA	Amino acid
ACAD	Acyl-CoA dehydrogenase
ACC1	Acetyl-CoA carboxylase
ACLY	Acetyl-CoA citrate lyase
ACS	Acyl-CoA synthetases
AMPK	Adenosine monophosphate-activated protein kinase
APCs	Antigen presenting cells
ATAC	Assay for transposase-accessible chromatin
ATP	Adenosine triphosphate
BBB	Blood-brain barrier
BCR	B-cell receptor
C. rodentium	*Citrobacter rodentium*
cDCs	Conventional dendritic cells
CFA	Complete Freund's adjuvant
CNS	Central nervous system
CoA	Coenzyme A
CoQ	Ubiquinone
CPT1	Carnitine palmitoyltransferase-1
Cre	Cre recombinase
CTLs	Cytotoxic T lymphocytes
CTV	Cell-trace violet
Cys	Cysteine
Cyt c	Cytochrome c
DCA	Dichloroacetate
DCs	Dendritic cells
DNMT	DNA methyltransferases
EAE	Experimental autoimmune encephalomyelitis
ECAR	Extracellular acidification rate
ECH	Enoyl-CoA hydratase
ETC	Electron transport chain
F6P	Fructose-6-phosphate
FA	Fatty acid
FABP	Fatty acid binding protein
FADH2	Flavin adenine dinucleotide
FAO	Fatty acid oxidation
FAS	Fatty acid synthesis
FASN	Fatty acid synthase
FATP	Fatty acid transport protein
FCCP	Carbonyl cyanide 4-(trifluoromethoxy)phenylhydrazone
FoxP3	Forkhead box P3
G6P	Glucose-6-phosphate
GF	Growth factor
GLS	Glutaminase
Glu	Glutamate
Glut	Glucose transporters
GzmB	Granzyme B
H	Histone
H^+	Protons
H2O	Water
HAD	Beta-hydroxyl acyl-CoA dehydrogenase
HAT	Histone acetyltransferases
HDAC	Histone deacetylases
HDM	Histone demethylases
HIF1α	Hypoxia inducible factor 1α
HLA	Human leukocyte antigen
HMT	Histone methyltransferases
IFNγ	Interferon γ
Ig	Immunoglobulins
ILCs	Innate lymphoid cells

Ionomycin/Iono	Calcium ionophore A23187
ITAMs	Immunoreceptor tyrosine-based activation motifs
K	Lysine
Kyn	Kynurenine
LCFA	Long-chain fatty acid
LDH	Lactate dehydrogenase
LoxP	Locus of crossover in P1
LTi	Lymphoid-tissue inducer
MBP	Myelin basic protein
MCFA	Medium-chain fatty acid
MCT	Acetate
Met	Methionine
MHC	Major histocompatibility complex
mIg	Membrane-bound immunoglobulins
MOG	Myelin oligodendrocyte glycoprotein
MPC	Mitochondrial pyruvate carrier
MS	Multiple sclerosis
Mspec	Mass spectrometry
MTHFD2	Methylenetetrahydrofolate dehydrogenase 2
mTOR	Mechanistic target of rapamycin
Myc	Myelocytomatosis oncogene
NADPH	Nicotinamide adenine dinucleotide phosphate
NK	Natural killer
O2	Oxygen
OAA	Oxaloacetate
OCR	Oxygen consumption rate
OXPHOS	Oxidative phosphorylation
PAMPs	Pathogen-associated molecular patterns
PC	Pyruvate carboxylase
pDCs	Plasmacytoid dendritic cells
PDH	Pyruvate dehydrogenase
PDHc	PDH complex
PDK	Pyruvate dehydrogenase kinase
PDP	Pyruvate dehydrogenase phosphatase
PEP	Phosphoenolpyruvate
PFN	Perforin
PK	Pyruvate kinase
PKM2	Pyruvate kinase M2 isoform
PLP	Proteolipid protein
PMA	Phorbol 12-myristate 13-acetate
PMNs	Polymorphonuclear
PPMS	Primary progressive multiple sclerosis
PPP	Pentose-phosphate pathway
PRRs	Pattern recognition receptors
PTM	Post-translational modifications
PTx	Pertussis toxin
RORγT	Retinoic acid receptor-related orphan receptor-γT
RRMS	Relapsing-remitting multiple sclerosis
S6K	S6 kinases
SAM	S-adenosylmethionine
SCFA	Short-chain fatty acid
Seq	Sequencing
SGLTs	Sodium-glucose linked transporters
sIg	Secreted immunoglobulins
SLE	Systemic lupus erythematosus
SPF	Specific pathogen-free
SPMS	Secondary progressive multiple sclerosis
SREBP1	Sterol regulatory element-binding protein 1
STAT	Signal transducer and activator of transcription
SUCNR1	Succinate receptor 1
TAM	Tamoxifen
T-bet	T-box transcription factor
TCA	Tricarboxylic acid
TCR	T-cell receptor
Teff	Effector T cells
TET	Ten-eleven translocation
TF	Transcription factors
Th	T helper

THIO	Beta-keto thiolase
TME	Tumor microenvironment
Treg	Regulatory T cells
Trp	Tryptophan
VLCFA	Very-long-chain fatty acid
WT	Wild-type
αKG	α-ketoglutarate
βox	Beta-oxidation

SUMMARY

Th17 cells are a subset of effector $CD4^+$ T cells essential for the protection against extracellular bacteria and fungi. At the same time, Th17 cells have been implicated in the progression of autoimmune diseases, including multiple sclerosis, rheumatoid arthritis and psoriasis. Effector T cells require energy and building blocks for their proliferation and effector function. To that end, these cells switch from oxidative and mitochondrial metabolism to fast and short pathways such as glycolysis and glutaminolysis. Pyruvate dehydrogenase (PDH) is the central enzyme connecting cytoplasmic glycolysis to the mitochondrial tricarboxylic acid (TCA) cycle. The specific role of PDH in inflammatory Th17 cells is unknown.

To unravel the role of this pivotal enzyme, a mutant mouse line where T cells do not express the catalytic subunit of the PDH complex was generated, using the Cre-Lox recombination system. In this study, PDH was shown to be essential for the generation of an exclusive glucose-derived citrate pool needed for the proliferation, survival, and effector functions of Th17 cells. *In vivo*, mice harboring a T cell-specific deletion of PDH were less susceptible to experimental autoimmune encephalomyelitis (EAE), a mouse model of multiple sclerosis, showing lower disease burden and increased survival. *In vitro*, the absence of PDH in Th17 cells increased glutamine and glucose uptake, as well as glycolysis and glutaminolysis. Similarly, lipid uptake was increased through CD36 in a glutamine-mTOR axis-dependent manner. On the contrary, the TCA cycle was impaired, interfering with oxidative phosphorylation (OXPHOS) and causing levels of cellular citrate to remain critically low in mutant Th17 cells. Citrate is the substrate of ATP citrate synthase (ACLY), an enzyme responsible for the generation of acetyl-CoA, which is essential for lipid synthesis and histone acetylation, crucial for the transcription process. In line, PDH-deficient Th17 cells showed a reduced expression of Th17 signature genes. Notably, increasing cellular citrate by the addition of acetate in PDH-deficient Th17 cells restored their metabolism and function. PDH was identified as a pivotal enzyme for the maintenance of a metabolic feedback loop within central carbon metabolism that can be of relevance for therapeutically targeting Th17 cell-driven autoimmunity.

INTRODUCTION

1. THE IMMUNE SYSTEM

The immune system has evolved as a response to life-threatening pathogens and diseases. It operates in a four-phase coordinated response: recognition (detection of the infection), effector function (elimination of the infection), regulation (adjustment of the effector response) and memory (protection against recurrent infection).

During an immune response to a pathogen, there are several stages of coordinated action. First, the innate immune system is activated in a range of minutes to hours upon the detection of the infection. This is followed by the adaptive immune response, which can persist several weeks. Only after eradication of the pathogen, the immunological memory is formed, which allows the rapid elimination of recurrent pathogens. The immunological memory can be lifelong (Murphy et al., 2017).

The main players of the innate and adaptive immune responses are leukocytes, which develop from hematopoietic stem cells in the bone marrow, giving rise to common lymphoid and myeloid progenitors (Murphy et al., 2017).

1.1. The innate immune system

The innate immunity is the first line of defense against pathogens. It is comprised of several barriers: anatomic (skin and mucosal membranes), physiologic (temperature, pH and chemical mediators), phagocytic (innate immune cells) and inflammatory (humoral and phagocytic responses to tissue damage). The cells involved in the innate response are mostly derived from the common myeloid progenitor and respond to common and evolutionary conserved structures known as pathogen-associated molecular patterns (PAMPs) through pattern recognition receptors (PRRs) (Kindt et al., 2007).

1.1.1. Granulocytes

Granulocytes are a group of innate cells containing small granules in their cytoplasm. This group includes neutrophils, eosinophils, basophils and mast cells. Neutrophils (or polymorphonuclear neutrophilic leukocytes, PMNs) are phagocytic cells and the first ones involved in the response to most bacterial and fungal pathogens. Eosinophils are bi-lobed nuclear and phagocytic cells involved in the defense against parasites. Basophils are non-phagocytic cells involved in inflammation and

allergic responses. Mast cells are involved in mucosal protection, allergic reactions and response to parasitic worms (Kindt et al., 2007; Murphy et al., 2017).

1.1.2. Innate lymphoid cells

One of the most recent discoveries on the components of the innate immune system are the innate lymphoid cells (ILCs). Unlike most innate cells, ILCs derive from common lymphoid progenitors in the bone marrow, in opposition to the myeloid compartment. They are structurally and functionally similar to lymphocytes of the lymphoid lineage, however, they lack antigen-specific receptors (Abbas et al., 2015; Vivier et al., 2018). According to their functional characteristics, ILCs are subdivided in three groups: type 1 ILCs, type 2 ILCs and type 3 ILCs, mirroring the categories of effector T helper cells (Th) (confer (cf.) to section 1.2.2.2) (Spits et al., 2013).

Group 1 ILCs are characterized by their ability to produce the pro-inflammatory cytokine interferon-γ (IFNγ) and the main actor in this subset are natural killer (NK) cells. NK cells possess cytotoxic granules containing granzymes and perforin, giving them the ability to induce programmed cell death in their target cells. As NK cells possess invariant receptors, they are considered innate-like cells and the innate equivalent of CD8 cytotoxic T cells of the adaptive immune system. In addition to NK cells, the group 1 ILCs is also comprised of ILC1 cells, which are IFNγ-producing non-cytotoxic cells, the innate counterpart to Th1 cells (Murphy et al., 2017; Spits et al., 2013).

Cells from the group 2 of ILCs (ILC2) produce Th2-like cytokines such as IL-5 and IL-13, moreover, they are involved in the repair of respiratory tissue after infection. However, it is worth noting that these cells have also been implicated in the pathology of allergic asthma (Spits et al., 2013).

Finally, group 3 ILCs produce type 3 cytokines such as IL-17A and IL-22; similarly to the adaptive Th17 cells. The main example of this cell subtype are lymphoid-tissue inducer (LTi) cells, essential for the formation of secondary lymphoid organs (Spits et al., 2013).

1.1.3. Monocytes and macrophages

Macrophages are mature monocytes that leave the blood circulation to differentiate in all tissues and become resident cells. Upon activation, their functions comprise phagocytosis, activation of bactericidal mechanisms, as well as antigen processing and presentation for the induction of the adaptive arm of the immune system (cf. to sections 1.1.4.1 and 1.1.4.2) (Kindt et al., 2007).

1.1.4. Dendritic cells

Dendritic cells (DCs) comprise functionally distinct groups of cells that have an important phagocytic function: plasmacytoid (pDCs) and conventional (cDCs) dendritic cells. pDCs produce high levels of type I interferons and have been proven crucial for antiviral responses. However, cDCs are considered as the interface between the innate and the adaptive branches of the immune system. Their major role is to screen the body for potential pathogens, phagocyte them and present foreign antigens to T cells in order to induce adaptive immunity, similarly to macrophages (Murphy et al., 2017).

1.1.4.1. Antigen processing

Antigens are peptide fragments of foreign objects such as pathogens, or "self" molecules (autoantigens) and can be recognized by antigen receptors of B or T cells (Male, 2013).

Antigen processing can be divided in six steps: (1) acquisition of antigen, where antigen presenting cells, such as macrophages and DCs, uptake the antigen from the extracellular milieu through phagocytosis or endocytosis; (2) antigen tagging for proteolysis, where antigens are marked by physicochemical means for degradation such as ubiquitination or changes in pH altering the structure of the protein; (3) proteolysis, resulting in the degradation of the protein; (4) delivery of antigens to the major histocompatibility complex (MHC); (5) loading of peptides onto MHC via accessory proteins; and (6) display of antigen-MHC complexes at the cell surface (Pishesha et al., 2022).

1.1.4.2. Antigen presentation

There are two classes of antigen-presenting molecules: MHC class I (MHC-I) and class II (MHC-II). The major differences between both classes is the cellular compartment from which the antigen is generated and the cells that express them. MHC-I molecules carry to the surface antigens recognized in the cytosol such as viral proteins. Importantly, MHC-I molecules are expressed on virtually all the cells of the body. On the other hand, MHC-II molecules present antigens from the vesicular compartment, namely proteins derived from pathogens engulfed by macrophages, DCs and B cells (professional antigen presenting cells, APCs). The structural differences found in MHC class molecules determine the T cell type that will bind to it. While CD8 T cells selectively recognize peptides on MHC-I molecules, CD4 T cells recognize peptides loaded on MHC-II molecules (Murphy

et al., 2017). The interaction between an APC and a T cell is called the “immunological synapse” (cf. to section 1.2.2) (Male, 2013).

The outcome of the interaction between CD4 T cells and different types of APCs varies. For instance, DCs induce naïve CD4 T cell activation, expansion and differentiation into effector T cells. Alternatively, an activated CD4 T cell induces the activation of macrophages. Finally, the result of the interaction between effector CD4 T cells and a B cell is the production of antibodies (Abbas et al., 2015).

1.2. The adaptive immune system

Despite a coordinated innate function of the immune system, many microbes have developed a way to evade this early response. Therefore, a powerful adaptive immune response evolved for their eradication. The cells responsible for this arm of the immune response are antigen-specific lymphocytes, called B or T cells (also known as B or T lymphocytes, respectively) and are derived from the common lymphoid progenitor (Abbas et al., 2015; Murphy et al., 2017).

B or T cells have on their surface an antigen-specific receptor that recognizes a single antigen, allowing them to mount pathogen-specific and specialized immune responses. The adaptive immune system is also able to generate immunologic memory, which in case of reoccurrence of infection/encounter of an auto-antigen, would induce a faster and more efficient response to the antigen.

Upon recognition of an antigen by the cognate receptor, the specific lymphocyte proliferates, generating a high number of cells expressing that single clone’s receptor, in a process denominated “clonal expansion”. Finally, once the threat has been eliminated, most of the effector cells are eliminated by apoptosis and the immune system contracts to its basal state, although a significant number of antigen-specific B and T cells remain to form the immunological memory (Abbas et al., 2015).

1.2.1. B cells

B cells express the B-cell receptor (BCR) on their surface and, upon binding to the antigen in secondary lymphoid tissues such as the spleen, lymph nodes and Peyer's patches, these B-lymphocytes proliferate and differentiate into plasma cells. Plasma cells are mature B cells that produce antibodies with the exact same specificity as the BCR. They are responsible for the humoral response to the pathogen (Cyster and Allen, 2019; Murphy et al., 2017).

Antibody molecules belong to the class of immunoglobulins (Ig) and can be either secreted (sIg) or membrane-bound (mIg), such as the BCR. Their structure is based on a symmetrical form of two identical heavy and light chains bound covalently by disulfide bonds. Each of the chains contains a variable region, which forms the antigen-binding site, and a constant region, which is not involved in antigen recognition but mediates the function of antibodies (cf. to illustration 1). Antibody molecules can be separated into isotypes according to the structure of the constant part of the heavy chain: IgA, IgD, IgE, IgG and IgM, which have different functions. IgA's main effect is in the intestinal immune protection, while IgD and IgM are antigen receptors of naïve B cells. IgEs are involved in allergy and induce mast cell degranulation and IgGs mark antigens for opsonization by phagocytosis, activate the complement (as well as IgM) and NK cells (Abbas et al., 2015). Naïve B cells express IgD and IgM, however cytokines produced by T cells and other cells can induce the class switch recombination to generate IgG, IgA or IgE, thus changing the effector function of the antibody and specializing to the elimination of the specific pathogen (Stavnezer and Schrader, 2014).

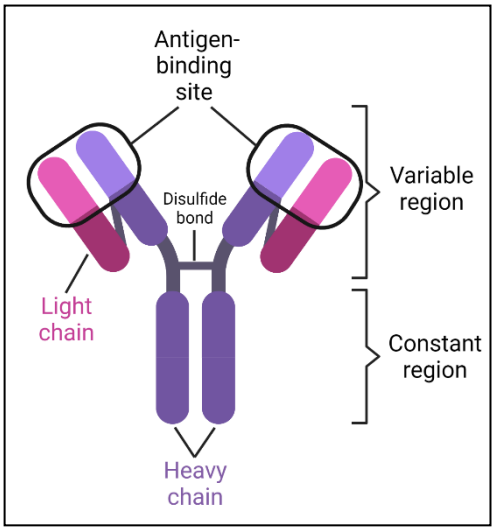

Illustration 1 : Antibody molecules are constituted of different parts.

Antibodies consist of two heavy- and two light-chains connected through disulfide bonds. Each chain possesses a variable region that forms the antigen-binding site and a constant region that determines the antibody isotype. (Created in BioRender)

1.2.2. T cells

Similar to B cells, T cells express an antigen-specific T-cell receptor (TCR) on their surface and are activated following an interaction with APCs through an immunological synapse. The TCR is a heterodimer of αβ chains. However, for intracellular signal transduction, the TCR relies on its constitutively associated CD3 complex. This complex is composed of heterodimers of CD3εδ and CD3γδ and homodimer CD3ζζ, that contain the immunoreceptor tyrosine-based activation motifs (ITAMs) (cf. to illustration 2) (Bettini et al., 2017; Birnbaum et al., 2014).

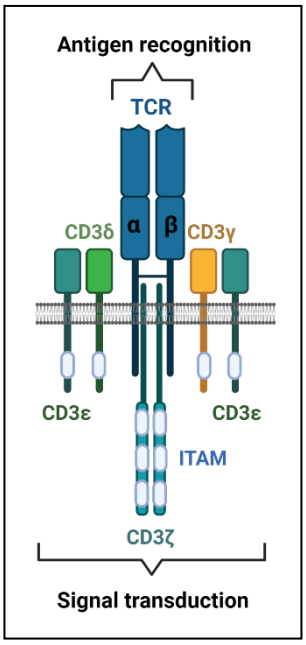

Illustration 2 : T cells express the TCR-CD3 complex for antigen recognition and intracellular signaling.

The T-cell receptor (TCR) is formed by the αβ heterodimer, which is in charge of the antigen recognition. It is associated to the CD3 complex, essential for the intracellular signal transduction through the immunoreceptor tyrosine-based activation motifs (ITAMs). The CD3 complex is constituted of the heterodimers of CD3εδ and CD3γδ and homodimer CD3ζζ. (Created in BioRender).

The activation of T cells by APCs is mediated by three signals: (1) interaction between the TCR and peptide-MHC (class I or II) complex, stabilized by interaction with CD8 or CD4 co-receptor, respectively, (2) co-stimulatory signals such as the interaction of CD28 with CD80/86, CD2 to CD48 or CD40L to CD40, and (3) secretion of cytokines by the APC (cf. to illustrations 3 and 4) (Male, 2013; Moser and Leo, 2010).

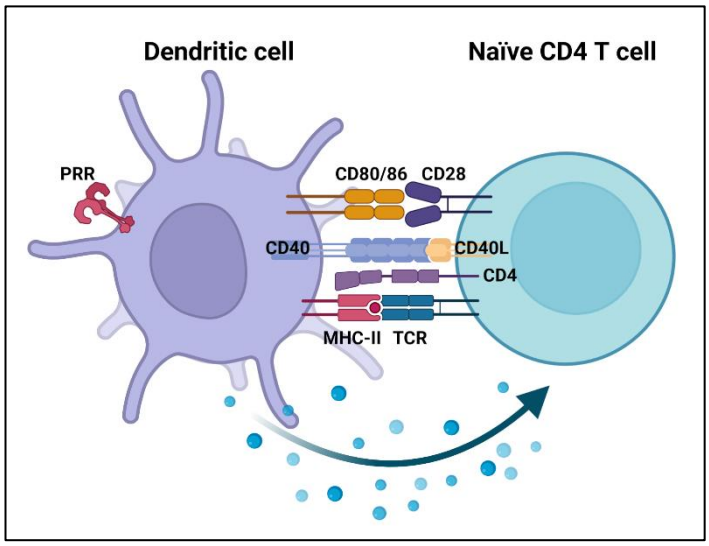

Illustration 3 : The interaction of a dendritic cell and naïve CD4 T cells in the immunological synapse.

Upon encounter with an antigen, dendritic cells present the antigen-derived peptides to naïve CD4 T cells through interaction of their MHC-II with TCR-CD4. However other signals are required for the activation of naïve T cells such as co-stimulatory signals (CD80/86 binding to CD28 or CD40 binding to CD40L) and cytokine secretion. (Created in BioRender)

Importantly, it is crucial to maintain a large repertoire of antigen-receptor interactions in T cells, while avoiding exacerbated immune reactions to self-antigens, which could lead to severe autoimmune diseases. Therefore, during their development in the thymus, T cells undergo two selection processes: the positive and negative selection. In the positive selection, immature thymocytes that interact with intermediate affinity to self-peptides are selected for further maturation. On the other hand, cells that bind with too high affinity to self-antigens are eliminated through the process of negative selection (Klein et al., 2014; Moser and Leo, 2010).

1.2.2.1 CD8 T cells

CD8 T cells are also known as cytotoxic T lymphocytes (CTLs). These cells recognize antigens presented by MHC-I molecules and are capable of killing aberrant cells such as viral infected or cancer cells by secreting the pore-forming molecule perforin. These pores allow the entry of CD8-produced proteases (e.g. granzyme B) into target cells, which finally induce apoptosis of the latter (cf. to illustration 4) (Moser and Leo, 2010).

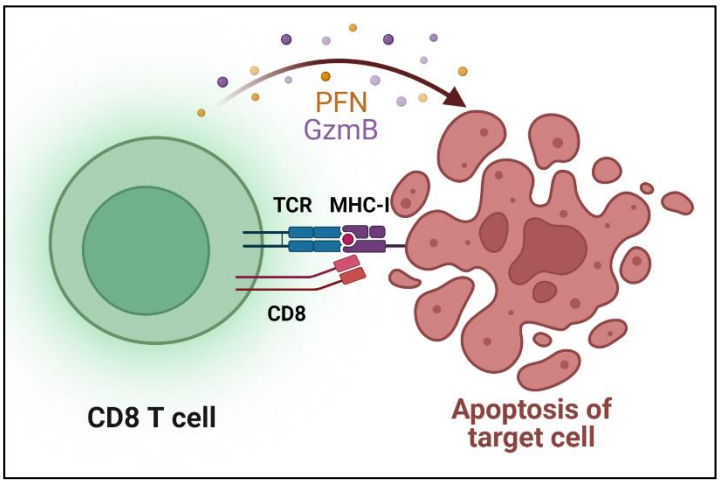

Illustration 4 : CD8 T cell effector function.

CD8 T cells recognize MHC-I bound antigens through interaction with their T-cell receptor (TCR) and CD8 co-receptor. To induce apoptosis of the target cell, CD8 T cells produce pore-forming molecule perforin (PFN), which allows the entry of protease granzyme B (GzmB) causing apoptosis. (Created in BioRender)

1.2.2.2 CD4 T cells

Unlike CD8 T cells, CD4 expressing T cells, also referred to as T helper (Th) cells, eliminate pathogens by orchestrating the recruitment and activation of other leukocytes.

There are several subsets of Th cells with different roles in the immune system. The differentiation into each subset depends on the cytokine milieu during activation (cf. to illustration 5). For example, IL-12 promotes the differentiation of naïve Th cells into Th1 cells, while IL-4 induces Th2 cell differentiation and IL-1β, IL-6, IL-21, IL-23 and TGFβ promote Th17 cell generation. Th1, Th2 and Th17 are considered as the effector CD4 T cells (Teff). Notably, IL-2 and TGFβ induce the differentiation of naïve Th cells into regulatory T cells (Treg) which are responsible of suppressing the CD4 and CD8 effector responses (Saravia et al., 2019).

Each Th subset can also be categorized by the expression of signature transcription factors (TF) and cytokines and have different functions (cf. to illustration 5).

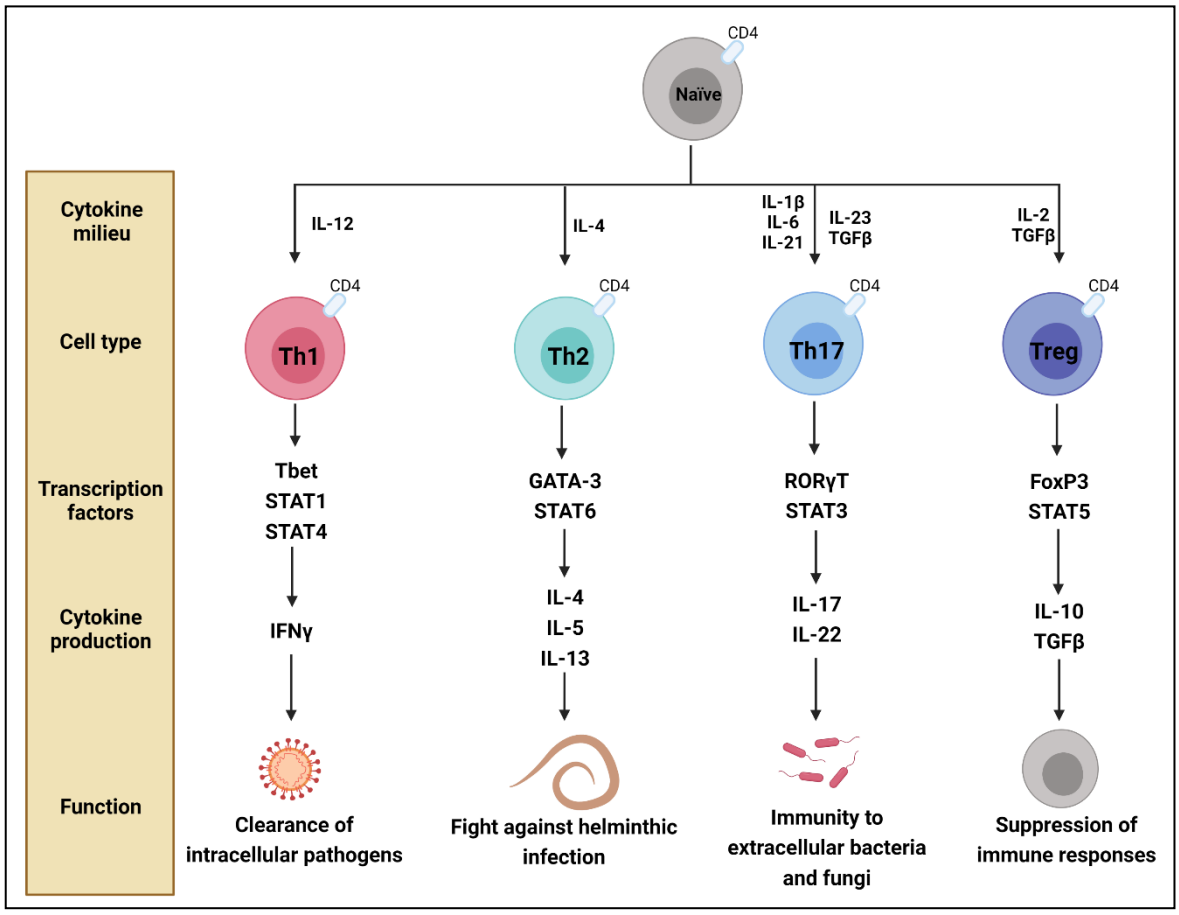

Illustration 5 : T helper subsets differentiation and function.

Upon activation by APCs, naïve CD4 T cells differentiate into different T helper subsets according to the cytokine milieu. T helper (Th) 1 cells differentiate in an IL-12 context, express transcription factors (TF) Tbet, STAT1 and STAT4, produce IFNγ and are involved in the clearance of intracellular pathogens. Th2 cells are generated by IL-4, express GATA-3 and STAT6, and yield IL-4, IL-5 and IL-13 to fight against helminthic infections. Naïve CD4 T cells differentiate to Th17 cells when IL-1β, IL-6, IL-21, IL-23 and TGFβ are present in the milieu. Th17 express RORγT and STAT3 and produce IL-17 and IL-22 to defend the host against extracellular bacteria and fungi. Tregs are generated by IL-2 and TGFβ to express FoxP3 and STAT5, produce IL-10 and TGFβ and suppress effector immune responses. (Created in BioRender)

Th1 cells express the T-box transcription factor (T-bet) and signal transducer and activator of transcription 1 (STAT1) and STAT4, while producing IFNγ in response to intracellular pathogens. Th1-produced IFNγ also blocks the differentiation into the Th2 and Th17 subsets (Abbas et al., 2015; Luckheeram et al., 2012).

Th2 cells express as master TFs GATA-3 and STAT6, and produce IL-4, IL-5 and IL-13. IL-4 and IL-13 induce B cells to produce IgE. IgE bind to mast cells and induce an allergic reaction and are involved

in mucosal immunity. Finally, Th2-produced IL-5 activates eosinophils to fight helminthic infections. The expression GATA-3 in this T cell subset strongly inhibits Tbet-associated genes (Abbas et al., 2015; Luckheeram et al., 2012; Murphy et al., 2017).

Th17 cells' master regulators are retinoic acid receptor-related orphan receptor-γt (RORγT) and STAT3. RORγT regulates the expression of Th17 cell-signature genes, such as *Il17a* and *Il17f*, encoding for IL-17A and IL-17F respectively, the main cytokines produced by this subset. They induce the recruitment of neutrophils to the site of inflammation, contributing to the elimination of extracellular bacteria and fungi. Th17 cells are also able to produce IL-22, which has an important role in maintaining epithelial integrity (Abbas et al., 2015; Luckheeram et al., 2012; Murphy et al., 2017).

Finally, Treg cells express forkhead box P3 (FoxP3) as master TF. Their differentiation is also regulated by the expression of STAT5 and CD25. Treg produce anti-inflammatory cytokines IL-10 and TGFβ to limit and suppress the immune response by Teff cells (Luckheeram et al., 2012; Moser and Leo, 2010; Murphy et al., 2017).

Importantly, it has been extensively described that Th cells maintain a certain plasticity concerning the acquisition of subset features, which would allow the differentiated cells to adapt to the microenvironment and respond to molecular signals. For instance, Th17 in culture with IL-12 can express IFNγ (Luckheeram et al., 2012; Male, 2013). On the other hand, other specific subpopulations have been reported in the inflamed central nervous system (CNS) and the gut, such as CD4 T cells co-expressing Tbet and RORγT. These cells are able to produce both, IFNγ and IL-17 cytokines (Luckheeram et al., 2012).

2. AUTOIMMUNITY AND AUTOIMMUNE DISEASES

Immunologic tolerance is an essential mechanism to maintain a functioning organism. This requires reactivity against pathogens while limiting tissue-destructive inflammatory immune responses and attacks against self-antigens. As previously mentioned, T cells responding strongly to self-antigens are eliminated during the process of thymic selection (Abbas et al., 2015; Male, 2013; Moser and Leo, 2010). However, some auto-reactive lymphocytes escape this central tolerance mechanism. Nevertheless, different layers of peripheral tolerance act in a coordinated way, namely by driving the differentiation of suppressive Treg cells instead of Teff cells, and elimination from the lymphocytic repertoire of over-activated cells by a mechanism of activation-induced cell death. Nonetheless, some cells manage to escape all the layers of self-tolerance, which can lead to autoimmune diseases. Although uncommon individually, collectively, these disorders affect up to 5% of the western population (Murphy et al., 2017).

Autoimmune diseases can be grouped according to the location and distribution of the autoantigen into organ-specific autoimmune diseases or systemic autoimmune diseases. For instance, Hashimoto's thyroiditis is an organ-specific autoimmune disease as the antigen targeted is only expressed in the thyroid. On the contrary, systemic lupus erythematosus (SLE) is a systemic autoimmune disease, as patients generate autoantibodies and autoreactive T cells against DNA, chromatin proteins and small nuclear ribonucleoprotein antigens, which are expressed ubiquitously throughout the body (Kindt et al., 2007; Male, 2013; Murphy et al., 2017).

2.1. Mechanisms of autoimmunity

The exact causes of autoimmune diseases are not yet clear. However, certain factors have been shown to correlate with autoimmunity. For example, it has been reported that genetic factors play an important role in the development of certain autoimmune diseases, particularly the human leukocyte antigen (HLA) allele (human equivalent to the MHC molecules). Namely, people expressing the HLA-B27 allele are 100 to 200 times more predisposed to suffer from ankylosing spondylitis, a type of arthritis with inflammation in the joints and ligaments of the spine. There are nonetheless other genetic factors associated with autoimmune diseases other than the HLA-allele. One of those examples are polymorphisms on the insulin gene affecting the level of expression of the antigen in the thymus, which have been associated with type 1 diabetes (Abbas et al., 2015; Sieper and Poddubnyy, 2017). Other studies have shown that viral and bacterial infections can

contribute to the development of autoimmunity, such as an invading pathogen that presents antigens that cross-react with self-antigens, a phenomenon known as molecular mimicry, the response to that pathogen can lead to uncontrolled parallel activation of the immune response against the "self". Finally, it has also been seen that injuries to certain tissues, releasing sequestered self-antigens that have never been presented to the immune system, can lead to autoimmunity (Abbas et al., 2015).

2.2. Multiple sclerosis

What all the autoimmune diseases have in common is that the body's own structures are attacked by an uncontrolled immune reaction, sometimes with devastating consequences for the whole organism. Multiple sclerosis (MS) is a chronic inflammatory autoimmune disease in which autoreactive CD4 T cells recognize myelin and attack the central nervous system (CNS), causing lesions or plaques in the white matter of the CNS (Aranami and Yamamura, 2008). MS affects more than one million people worldwide and the symptoms usually manifest between the ages of 30 and 40 years old and strikes more women than men (approximatively to a ratio of 3:1) (Constantinescu et al., 2011; Kindt et al., 2007).

2.2.1. Clinical symptoms and progression

MS symptoms can evolve from mild (slight numbness of the limbs) to severe (paralysis or loss of vision) (Kindt et al., 2007).

The clinical course varies according to the subtype of MS. The most common subtype is the relapsing-remitting MS (RRMS) affecting 87% of MS patients. These patients suffer from flare-ups of disease in between periods without symptomatic progression. Another subtype is the secondary progressive MS (SPMS), where after each flare-up there is neurological deterioration. In addition, there are primary progressive MS (PPMS) patients that suffer from visible neurological deterioration since onset of the disease. Finally, some patients experience one episode of demyelination without a second one, those are described as clinically isolated MS syndrome patients (Constantinescu et al., 2011; Ghasemi et al., 2017).

2.2.2. MS pathogenesis

MS is a disease where autoreactive T cells that recognize myelin basic protein (MBP), proteolipid protein (PLP) and/or myelin oligodendrocyte glycoprotein (MOG), migrate from the blood vessels into brain tissue crossing the blood-brain barrier (BBB). Once the T cells infiltrate the CNS, the microglia (macrophage-like cells from the CNS) present the autoantigen through their MHC-II inducing the production of cytokines. This, in turn, recruits more immune cells to the site of inflammation, aggravating the damage and leading to demyelination of neurons, thus impairing their function (Murphy et al., 2017).

2.2.3. Experimental autoimmune encephalomyelitis

Experimental autoimmune encephalomyelitis (EAE) is a model developed almost 90 years ago to mimic MS symptoms in mice. EAE is a disease model mediated by T cells and is induced by immunization with myelin oligodendrocyte glycoprotein (MOG) in combination with complete Freund's adjuvant and pertussis toxin injections. After 9 days, mice start to develop MS-like motor symptoms (cf. to illustration 6) (Constantinescu et al., 2011; Kindt et al., 2007; Rangachari and Kuchroo, 2013; Rivers et al., 1933; Rivers and Schwentker, 1935).

Studies have shown that Th17 cells and signaling directing Th17 differentiation are the main drivers of EAE, as the development of symptoms is impaired when IL-17, IL-17 receptor or IL-23 are blocked (Hu et al., 2010; Komiyama et al., 2006; Langrish et al., 2005; Park et al., 2005; Sarma et al., 2009). In the same line, the disease symptoms become more severe in the mice upon T-cell specific RORγT overexpression, while Tbet expression was deemed not necessary for the development of the disease (Martinez et al., 2014; O'Connor et al., 2013). Taken together, these studies show that EAE is a valuable model to analyze the function of Th17 cells *in vivo* and may give us further insights on the origin and development of MS.

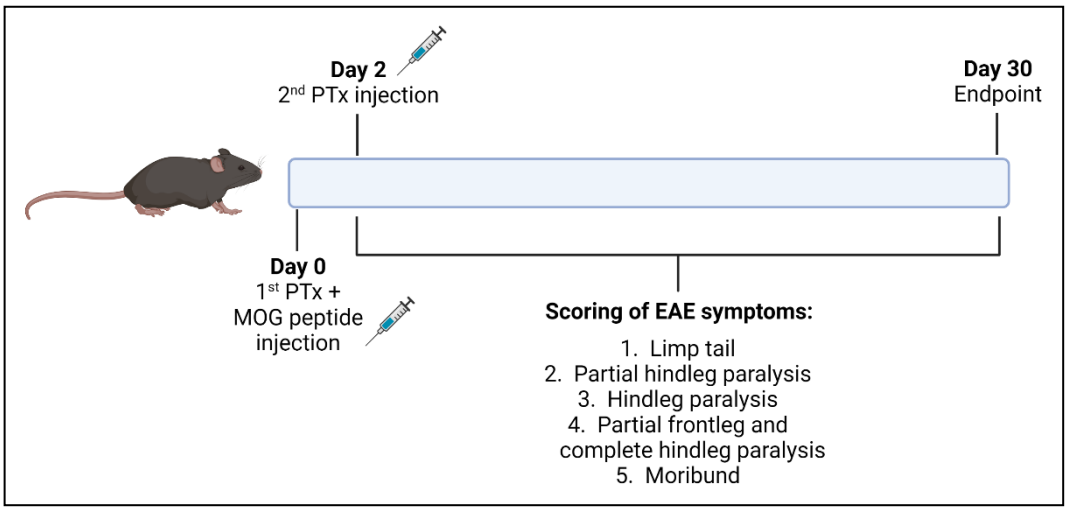

Illustration 6 : Induction of EAE, a mouse model of multiple sclerosis.

To induce EAE, an intraperitoneal (ip) injection of pertussis toxin (PTx) and subcutaneous injection of the MOG peptide is performed at day 0. At day 2, a second ip injection of PTx is administered. The mice are scored daily according to their EAE motor symptoms. A score of 1 is given once the tail goes limp, a 2 when the hind legs are partially paralyzed, a 3 when the hind legs are completely paralyzed, a 4 when the front legs become partially paralyzed and a 5 when the mouse is moribund. (Created in BioRender)

3. T CELL METABOLISM

Nutrients and metabolites are essential for the functioning of T cells. Moreover, there has been ample evidence that cells adapt their metabolism depending on their energy requirements (Buck et al., 2015; Franchina et al., 2018; Guerra et al., 2020; Kurniawan et al., 2020b; Rangel Rivera et al., 2021). The main sources of energy in T cells are glucose, amino acids and fatty acids. There are different metabolic pathways that can follow the uptake of these nutrients to support the T cell function and survival. Their common goal is to produce energy in the form of adenosine triphosphate (ATP) as well as building-blocks for biomass, such as proteins and nucleotides (Buck et al., 2015).

3.1. Glucose metabolism

Glucose is the primary source of energy for all T cells, however, it is also an important carbon source for the generation of other macromolecules. Glucose metabolism can generate cofactors such as nicotinamide adenine dinucleotide phosphate (NADPH), important for the generation of lipids (MacIver et al., 2008; Yang et al., 2015).

Glucose uses two types of transporters to enter the cells: sodium-glucose linked transporters (SGLTs), which transport glucose together with sodium depending on the sodium concentration gradient, and glucose transporters (Gluts), which transport glucose by facilitated diffusion (Navale and Paranjape, 2016). Glucose is taken up by T cells mainly through Gluts, especially the most ubiquitously expressed glucose transporter 1 (Glut1). Glut1 has been shown to be essential for Teff cell differentiation and activation, although not in Treg cells (Macintyre et al., 2014; MacIver et al., 2008; Palmer et al., 2015; Yang et al., 2015). A recent study showed that Glut3 is also essential for Th17 effector function, despite the fact that it is not crucial for the generation of ATP in these cells (Hochrein et al., 2022). Another study shows that overexpression of Glut3 in CD8 T cells induced more efficient memory effector function (Cribioli et al., 2022).

3.1.1. Glycolysis

As soon as glucose enters the cytoplasm of the cell, the glycolytic pathway is engaged (cf. to illustration 7). Once inside of the cell, a rate-limiting reaction performed by the hexokinase (HK)

enzyme transforms glucose into glucose-6-phosphate (G6P) to initiate glycolysis, which occurs in the cytosol (Palmer et al., 2015). Following this step, there is a cascade of enzymatic reactions, including the generation of one molecule of fructose-6-phosphate (F6P), two molecules of glyceraldehyde 3-phosphate (3-PG), two molecules of phosphoenolpyruvate (PEP) and finally two molecules of pyruvate per glucose molecule (Chaudhry and Varacallo, 2022). The generation of pyruvate is mediated by the pyruvate kinase (PK) of which its M2 isoform (PKM2) has been shown to be essential for the development of Th1 and Th17 cells (Angiari et al., 2020).

The entire process of glycolysis provides 2 molecules of ATP per molecule of glucose without the need for oxygen, which is why this pathway is also known as anaerobic glycolysis, making this pathway a fast way to generate metabolic intermediates for the synthesis of biomolecules and energy (O'Neill et al., 2016).

Importantly, certain glycolytic intermediates allow T cells to branch out into other pathways such as the lactic fermentation, pentose phosphate pathway (PPP), serine metabolism and one-carbon (1C) metabolism that are essential for T cell survival, proliferation and biosynthetic abilities (cf. to illustration 7) (Sugiura et al., 2022).

3.1.1.1. Lactic fermentation

At the end of glycolysis, pyruvate can be transformed into lactate by the lactate dehydrogenase (LDH) enzyme in a process known as lactic fermentation (cf. to illustration 7) (Jones and Bianchi, 2015). Xu et al. have seen that LDH-dependent ATP production was essential for the activation of the PI3K-Akt-Foxo1 axis, which regulates the Th17 effector function program (K. Xu et al., 2021).

3.1.1.2. Pentose phosphate pathway

The pentose phosphate pathway (PPP) diverges from the glycolysis at the level of G6P. It is essential to generate pentoses (5-carbon sugars), needed for the generation of nucleotides and amino acid (AA) precursors, and NADPH to maintain the redox balance in the cells and allow fatty acid synthesis (cf. to illustration 7) (Domínguez-Amorocho et al., 2019; O'Neill et al., 2016).

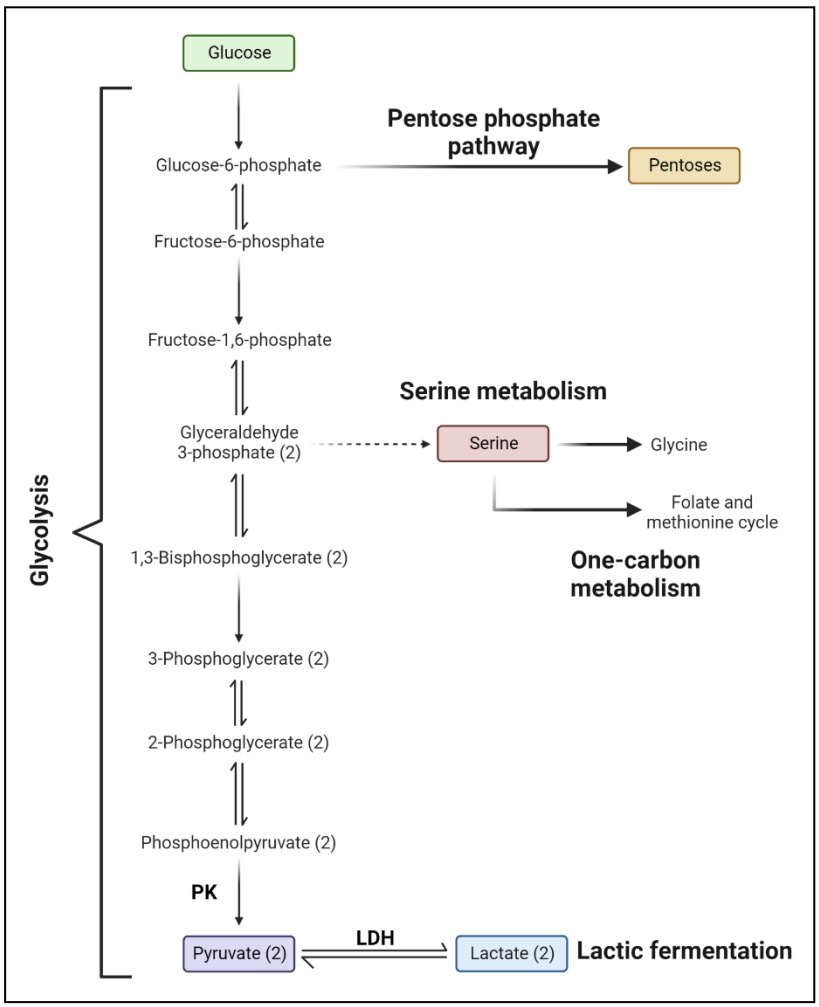

Illustration 7 : Glycolysis and branching pathways for energy generation in T cells.

Once glucose is taken up, the glycolytic enzymes begin to metabolize it to generate pyruvate. Pyruvate can be transformed into lactate through lactic fermentation driven by lactate dehydrogenase (LDH). However some intermediate metabolites of the glycolysis pathway can divert the carbons to other pathways such as the pentose-phosphate pathway or serine and one-carbon metabolism. (Created in BioRender)

3.1.1.3. Serine metabolism and one-carbon metabolism

Serine, as a non-essential AA, can be synthesized *de novo* by the cells using glycolytic 3PG as a substrate, however it can also be taken up by cells through neutral AA transporters (Yang and Vousden, 2016). Serine is crucial for the generation of glycine, which is a component of glutathione (GSH), an important antioxidant for redox balance in lymphocytes (cf. to illustration 7) (Franchina et al., 2022; Kurniawan et al., 2020a; Mak et al., 2017). On another note, serine is an essential part of the folate-driven one-carbon (1C) metabolism, a pathway that occurs in two cellular compartments, cytosol and mitochondria, and generates substrates for epigenetic modifications (S-adenosylmethionine, SAM), NADPH and ATP (cf. to illustration 7) (Ducker and Rabinowitz, 2017;

Kurniawan et al., 2020a). It has also been shown that the 1C-metabolism is essential for proliferation of mammalian cells, notably CD4 and CD8 T cells, *in vitro* and *in vivo* (Ma et al., 2017; Meiser et al., 2016).

3.1.2. Tricarboxylic acid cycle

Pyruvate can also translocate into the mitochondria through the mitochondrial pyruvate carrier (MPC) to pursue its oxidation in the tricarboxylic acid (TCA) cycle (cf. to illustration 8) (Bricker et al., 2012; Herzig et al., 2012). The first step in the TCA cycle is the transformation of pyruvate into acetyl-coenzyme A (acetyl-CoA) by the pyruvate dehydrogenase (PDH; cf. to section 3.1.2.1). In turn, acetyl-CoA condenses with oxaloacetate (OAA) to generate citrate (O'Neill et al., 2016; Pearce et al., 2013). Through several enzymatic reactions, the TCA cycle generates intermediate metabolites such as α-ketoglutarate (αKG), succinate, fumarate and malate (cf. to illustration 8).

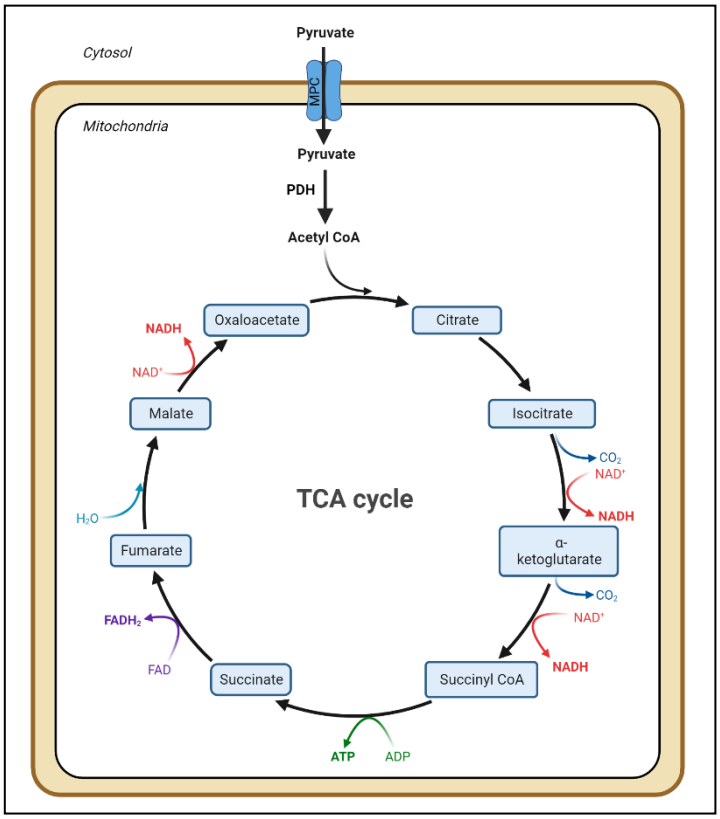

Illustration 8 : The TCA cycle.

Glycolysis-derived pyruvate can enter the mitochondria through the mitochondrial pyruvate carrier (MPC). There, it is metabolized by PDH to generate acetyl-CoA, which with OAA will generate citrate and thus the cycle begins. Other TCA metabolites are isocitrate, α-ketoglutarate, succinyl-CoA, succinate, fumarate and malate. Each cycle produces three molecules of NADH, one molecule of $FADH_2$ and one molecule of ATP. (Created in BioRender)

These intermediate metabolites are essential for the generation of AAs, lipids and reductive equivalents such as NADH and flavin adenine dinucleotide ($FADH_2$), crucial for the function of the electron transport chain (ETC) and oxidative phosphorylation (OXPHOS) leading to ATP synthesis (cf. to section 3.1.3) (O'Neill et al., 2016; Pearce and Pearce, 2013).

Of note, other carbon sources can feed into the TCA cycle in a process called anaplerosis. For instance, glutamine can be metabolized to generate αKG, while lipid oxidation can generate acetyl-CoA (O'Neill et al., 2016).

3.1.2.1. Pyruvate dehydrogenase

PDH, the enzyme converting pyruvate into acetyl-CoA, is a complex of three enzymes that work sequentially to decarboxylate pyruvate and generate acetyl-CoA, CO_2 and NADH: pyruvate dehydrogenase (E1), dihydrolipoamide acetyltransferase (E2) and dehydrolipoamide dehydrogenase (E3). The E1 subunit is a tetramer constituted of two α subunits, where the catalytic site resides, and two β subunits. The E1 catalyzes the decarboxylation of pyruvate and generates the acetyl molecule, while E2 ligates the CoA to the acetyl molecule and E3 generates the NADH (cf. to illustration 9) (Patel et al., 2014).

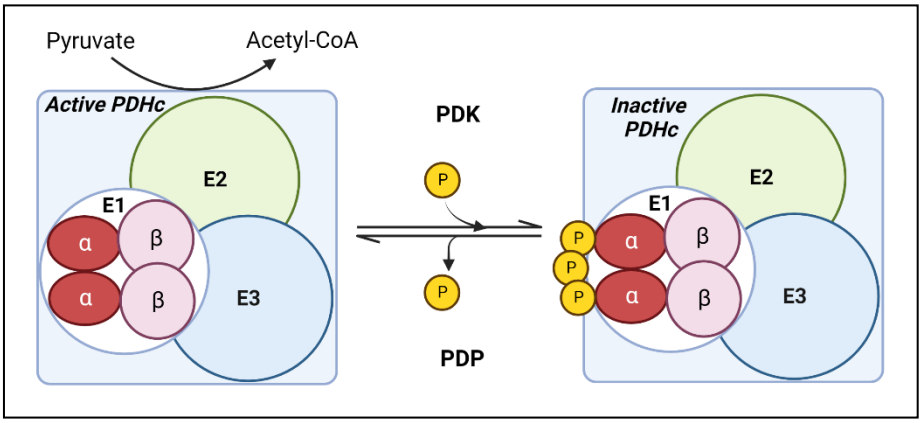

Illustration 9 : The PDH complex.

The PDH complex (PDHc) is constituted of three subunits: E1 that performs the pyruvate decarboxylation generating an acetyl molecule, E2 that adds the CoA to the acetyl and E3 that produces the NADH. PDHc is regulated through phosphorylation by PDH kinases (PDK) and PDH phosphatases (PDP). PDHc is inactive when phosphorylated.

The PDH complex regulates the cytoplasmic glucose flux into the mitochondrial TCA cycle (DeBrosse and Kerr, 2016). Given its central role, PDH activity is strictly controlled by phosphorylation through pyruvate dehydrogenase kinases (PDKs) and de-phosphorylation by pyruvate dehydrogenase

phosphatases (PDPs) of the E1α catalytic site (cf. to illustration 9) (Hitosugi et al., 2011; Kaplon et al., 2013; Korotchkina and Patel, 2001). The PDKs inhibit PDH function through phosphorylating three sites of the E1α subunit: (1) serine-264-α (Ser-264-α), (2) Ser-271-α and (3) Ser-203-α, whereas PDPs activate PDH by dephosphorylating those sites (Patel et al., 2014). PDKs can be inhibited by dichloroacetate (DCA), which has been shown to suppress Th17 differentiation while promoting Treg differentiation (Gerriets et al., 2015).

In humans, the E1α subunit is encoded by the X-linked gene *PDHA1* and mutations of that gene cause PDH deficiency which gives rise to lactic acidosis, progressive neuromuscular, neurological degeneration and, often leading to childhood mortality (DeBrosse and Kerr, 2016; Patel et al., 2012).

3.1.3. Electron transport chain and oxidative phosphorylation

As mentioned in the previous section, the TCA cycle generates reductive equivalents NADH and $FADH_2$ for the ETC and OXPHOS. ETC is a series of molecules composed of five complexes that are located in the inner membrane of the mitochondrion and perform the OXPHOS process. Complex I takes the electrons from NADH and transfers them to ubiquinone (CoQ), inducing the pumping of protons into the intermembrane space by Complex I. The electrons from $FADH_2$ are donated to Complex II, which in turn transfers them to CoQ to promote proton pumping by Complex I. CoQ transfers the electrons to Complex III and cytochrome c, causing the former to pump protons into the intermembrane space and reducing the latter. Once reduced, cytochrome c transfers electrons to Complex IV inducing its pumping of protons into the intermembrane mitochondrial space and the reduction of O_2 into H_2O. This final step is known as the mitochondrial respiration. Through Complex I, III and IV, a proton gradient, known as the mitochondrial membrane potential, is created. This gradient is dissipated by the Complex V or ATP synthase, pumping the protons back into the matrix from the intermembrane space, while generating an ATP molecule. The processes carried out by Complex IV and V are also known as OXPHOS (cf. to illustration 10) (Nolfi-Donegan et al., 2020).

Although the whole process is more complex, the combination of TCA cycle and OXPHOS generates up to 36 molecules of ATP per glucose, making the mitochondrial oxidation of glucose the most efficient pathway for the generation of energy (Klein Geltink et al., 2018).

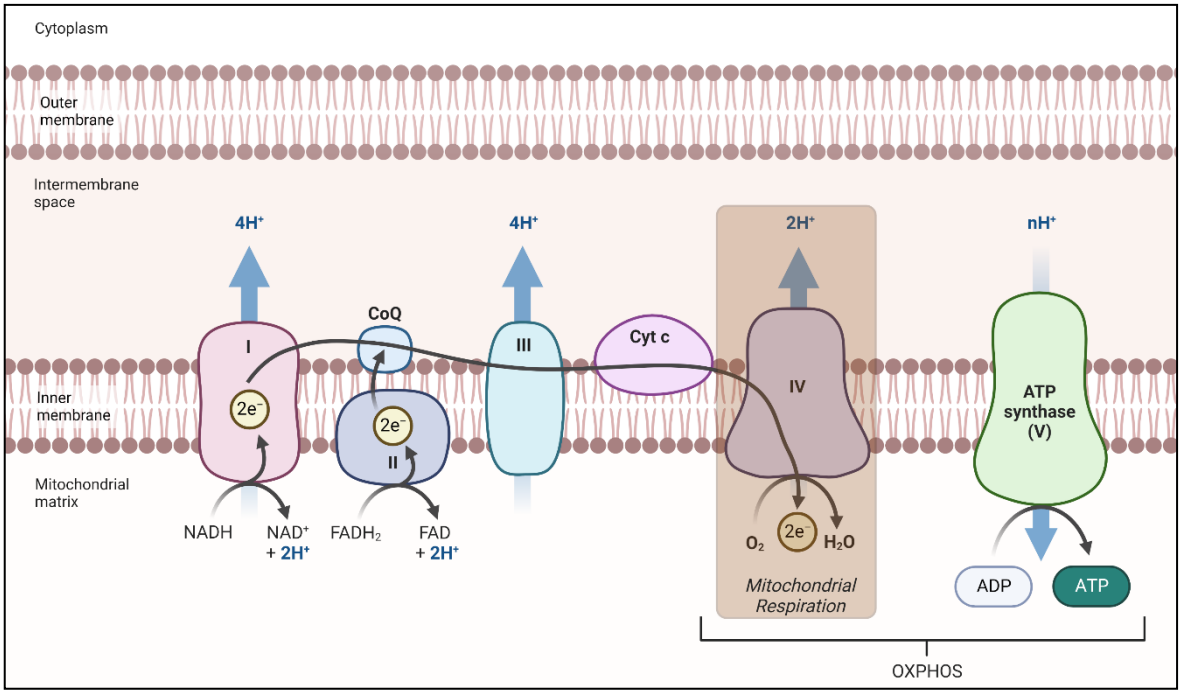

Illustration 10 : The electron transport chain and OXPHOS.

The electron transport chain (ETC) is composed of five complexes, ubiquinone (CoQ) and cytochrome c (Cyt c). Complex I pump protons (H^+) into the intermembrane space of the mitochondria while transferring electrons (e^-) to CoQ and consuming NADH. Complex II donates e^- to CoQ derived from $FADH_2$. CoQ transfers the e^- to Complex III, which further donates them to Cyt c and pumps more H^+ in the intermembrane space. Finally, Cyt c transfers the e^- to Complex IV that carries out the mitochondrial respiration, turning oxygen (O_2) into water (H_2O), simultaneously pumping H^+ in the intermembrane space. Complex V dissipates the proton gradient by bringing H^+ back into the mitochondrial matrix and generating ATP in a process called oxidative phosphorylation (OXPHOS). (Created in BioRender)

3.2. Amino acid metabolism

Amino acids (AA) are sources of energy and substrates for the generation of proteins and nucleic acids. They can be divided into essential AA, obtained only from the diet, and non-essential AA, that can be produced by mammals (Kurniawan et al., 2020b).

3.2.1. Glutamine

Glutamine is a non-essential AA that has been shown to be crucial for proliferation of T cells, as it is used as a precursor for nucleotides and protein synthesis (Yoo et al., 2020). As previously mentioned, glutamine can generate TCA cycle intermediates after being metabolized by

glutaminases (GLS) into glutamate that will be transformed into αKG. GLS has been shown to be essential for Th17 differentiation (Johnson et al., 2018).

There are two ways of metabolizing glutamine in the TCA cycle. In the oxidative path, αKG is oxidized to succinate, while in the reductive way, αKG is converted into citrate (cf. to illustration 11) (Fendt et al., 2013).

Importantly, the intermediate metabolite glutamate is also an essential component of antioxidant glutathione and thus, crucial to maintain redox balance (Tomé, 2021).

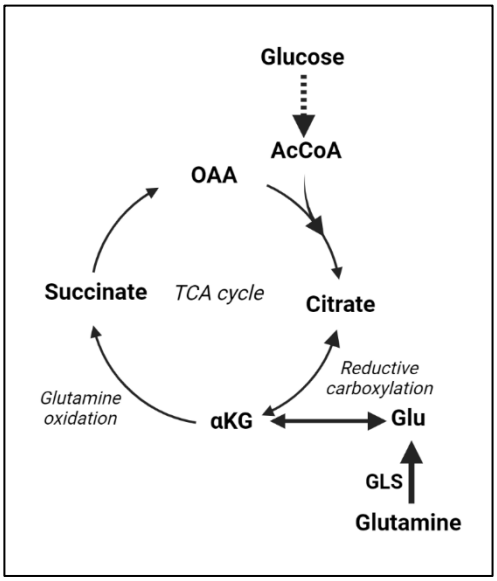

Illustration 11 : Glutamine metabolism.

After entering the cytosol, glutamine can also enter the mitochondria where the glutaminase enzyme (GLS) will transform it into glutamate (Glu). The latter will be further converted into α-ketoglutarate (αKG) and thus enter the TCA cycle. There are two pathways to metabolize αKG either the oxidative pathway (glutamine oxidation) in which αKG is transformed into succinyl-CoA, or the reductive carboxylation, generating citrate directly. (Created in BioRender)

3.2.2. Other amino acids

Tryptophan (Trp) is an essential AA, precursor of kynurenine (Kyn), NAD, serotonin and melatonin. Kyn and Kyn-derivates have been shown to block Teff proliferation (Tomé, 2021).

Arginine is a non-essential AA that participates in the urea cycle and is a precursor of glutamate (Ligthart-Melis et al., 2008). It has been shown that arginine is a regulator of T cell metabolism by inducing a shift from glycolysis to OXPHOS and thus promoting memory-like cell generation (Geiger et al., 2016).

Serine is important for cell proliferation and, as mentioned previously, can be taken up by the cells or generated *de novo*. Serine is a crucial element for the production of antioxidant glutathione (Kurniawan et al., 2020a). In the case of Treg cells, our group has shown the importance of glutathione in the strict control of the serine and 1C-metabolism, which is crucial for the expression of the transcription factor FoxP3 and consequently, their suppressive capacity (Kurniawan et al., 2020a).

Methionine (Met) is an essential AA, precursor of cysteine (Cys). However, as T cells do not possess the enzyme converting Met to Cys, the uptake of Cys is required, which is why Cys is considered a semi-essential AA. Met is also critical for epigenetic modifications such as histone methylation (Tomé, 2021).

3.3. Fatty acid metabolism

It has been extensively described how glucose and AA, especially glutamine, are easily metabolized and available to promote T cell function. On the other hand, fatty acids (FAs), despite being more complex biomolecules, have also been deemed essential for T cell function, proliferation and survival (Yang et al., 2015).

There are several groups of FAs according to the number of carbon atoms in their carbon chain: short-chain (SCFA), medium-chain (MCFA), long-chain (LCFA) and very-long-chain FA (VLCFA). SCFA are the product of microbiota's fermentation of dietary fiber (Lim et al., 2022).

FA metabolism has two major branches: the fatty acid oxidation (FAO), also known as the catabolism of FA, taking place in the mitochondria of T cells, and the cytosolic fatty acid synthesis (FAS) or FA anabolism (cf. to illustration 12) (Lim et al., 2022).

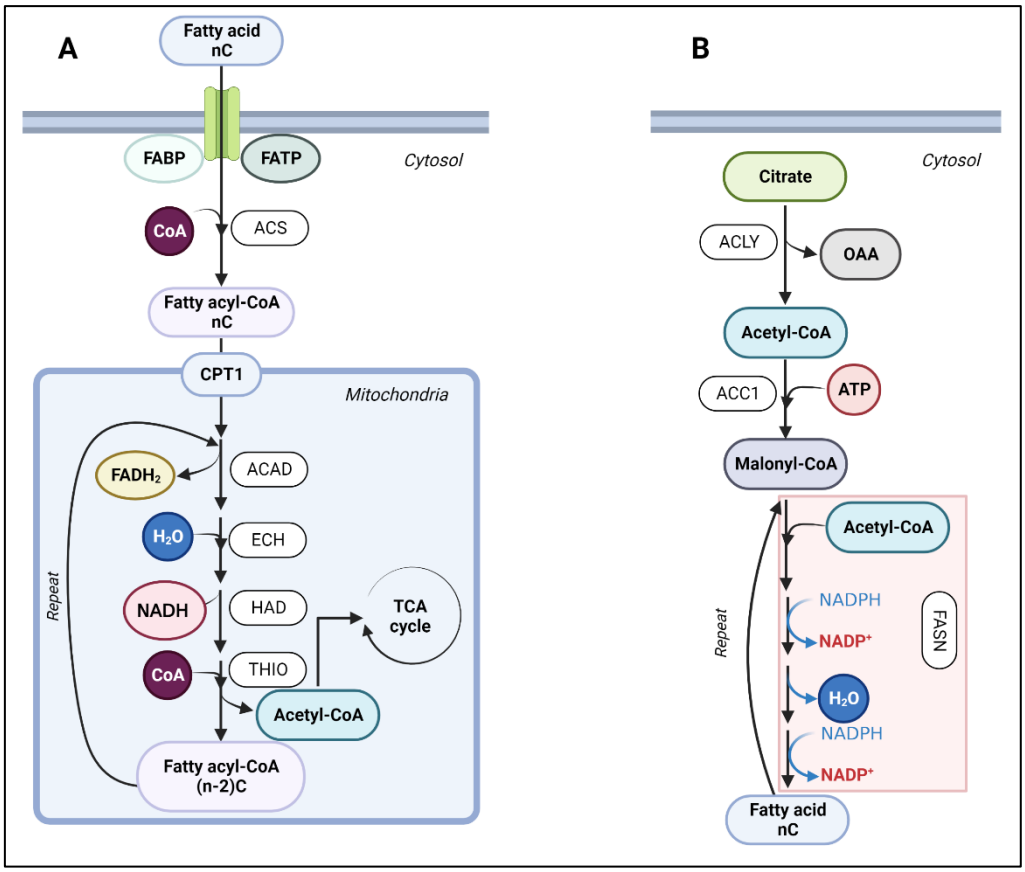

Illustration 12 : Fatty acid oxidation and fatty acid synthesis pathways.

(A) Fatty acid oxidation. Fatty acids are taken up by transporters in the cell membrane and transported in the cytosol by fatty acid binding proteins (FABP) and transport proteins (FATP). Before entering the mitochondria, fatty acids are activated by adding a coenzyme A (CoA) molecule via acyl-CoA synthetases (ACS), generating a fatty acyl-CoA that can translocate into the mitochondria through carnitine palmitoyltransferase-1 (CPT1). In the mitochondria, the beta-oxidation takes place through four consecutive enzymes: acyl-CoA dehydrogenase (ACAD), enoyl-CoA hydratase (ECH), beta-hydroxyl acyl-CoA dehydrogenase (HAD) and beta-keto thiolase (THIO). In this process, one molecule of $FADH_2$, NADH, acetyl-CoA and a fatty acyl-CoA molecule with two carbons less are produced. The resulting fatty acyl-CoA repeats the steps of beta-oxidation until in the last cycle two molecules of acetyl-CoA are produced. Acetyl-CoA then can be used as a substrate for the TCA cycle. **(B)** Fatty acid synthesis. For the generation of fatty acids, citrate is transformed into acetyl-CoA through the acetyl-CoA citrate lyase (ACLY) which is further converted into malonyl-CoA by acetyl-CoA carboxylase (ACC1). Malonyl-CoA is then extended by the fatty acid synthase complex (FASN) into a long-chain fatty acid. This process requires ATP and NADPH for its completion. (Created in BioRender)

3.3.1. Fatty acid oxidation

To take FAs up from the extracellular milieu, T cells express SCFA receptors and the scavenger receptor CD36 on their cell surface, then proceed to their transport and oxidation in the mitochondria (cf. to illustration 12A) (Chen et al., 2022; Lim et al., 2022). T cells require FA-binding proteins (FABPs) and FA-transport protein (FATPs) to transport FA from the cytosol to the mitochondria. More specifically, to translocate into the mitochondria, LCFA require carnitine palmitoyltranferase-1 (CPT1) (Kurniawan et al., 2020b). It is noteworthy that the membrane mitochondrial translocation by CPT1, requires the previous activation of FA by binding to Coenzyme A (CoA). This process is carried out by acyl-CoA synthetases in an ATP-dependent manner. The resulting molecules, known as fatty acyl-CoAs, enter the mitochondria (Talley and Mohiuddin, 2022).

Once acyl-CoAs are in the mitochondria, the four steps of beta-oxidation (β-ox) take place. First, acyl-CoA dehydrogenase forms a double bond between the alpha and beta carbon of the fatty acyl-CoA molecule while producing $FADH_2$. Second, enoyl-CoA hydratase hydrates the double bond generated in the first step resulting in a hydroxyl group on the beta carbon. Third, beta-hydroxyl acyl-CoA dehydrogenase oxidizes the beta carbon to produce NADH. Finally, beta-keto thiolase cleaves the bond between alpha and beta carbons with CoA, producing a molecule of acetyl-CoA and a new molecule of fatty acyl-CoA with two carbons less. The procedure of β-ox is repeated until the acyl-CoA is completely converted into acetyl-CoA. Per β-ox loop, the cell generates one molecule of FADH2, one molecule of NADH, both used to generate energy in the ETC and OXPHOS, and one molecule of acetyl-CoA, which can merge with OAA and enter the TCA cycle, connecting FAO with the mitochondrial oxidation of glucose (Talley and Mohiuddin, 2022).

3.3.2. Fatty acid synthesis

While FAO generates energy, FAS requires it in the form of NADPH (cf. to illustration 12B). However, FAS is essential for the generation of membranes (cytoplasm, nucleus, etc.) and thus, cell proliferation (O'Neill et al., 2016; van der Windt and Pearce, 2012; Yang et al., 2015).

Three main enzymes direct FAS: acetyl-CoA citrate lyase (ACLY), acetyl-CoA carboxylase (ACC1) and fatty acid synthase complex (FASN). ACLY converts citrate into acetyl-CoA, which in turn will be converted into malonyl-CoA by ACC1. Then, the carbon chain of malonyl-CoA is extended by FASN. The FASN reaction is divided in four steps: first, a molecule of acetyl-CoA and one of malonyl-CoA are converted into an acetoacyl molecule, which is then reduced, dehydrated and reduced again.

The activity of FASN is repeated in cycle until the expected chain length is reached (Lim et al., 2022; O'Neill et al., 2016; Riezman, 2007; van der Windt and Pearce, 2012).

3.4. Regulators of metabolism

All metabolic pathways have to be coordinated for the proper functioning of T cells. There are two major metabolic regulators in T cells responsible for the metabolic rewiring upon activation, mechanistic target of rapamycin (mTOR) and adenosine monophosphate-activated protein kinase (AMPK) (cf. to illustration 13) (Chapman and Chi, 2022).

3.4.1. mTOR

mTOR is often described as the key metabolic regulator and sensor of changes in the levels of nutrients, energy and stress cues. mTOR regulates functions through two complexes mTORC1 and mTORC2 (Buck et al., 2015).

mTORC1 is activated upon TCR-CD28 engagement via the PI3K-AKT pathway as well as growth factors and AA signaling (cf. to illustration 13) (Kurniawan et al., 2020b; Salmond, 2018). mTORC1's key downstream targets are sterol regulatory element-binding protein 1 (SREBP1), ribosomal protein S6 kinases (S6Ks), 4E-binding proteins (4E-BPs), myelocytomatosis oncogene (Myc) and hypoxia inducible factor 1α (HIF1α) (Salmond, 2018). SREBP1 induces FAS, while S6Ks and 4E-BPs promote protein translation, and Myc and HIF1α promote glycolysis (Palmer et al., 2015).

mTORC2 is induced by cellular stress and growth factors and its most described downstream target is AKT, which is involved in the early thymocyte development (Ouyang et al., 2019).

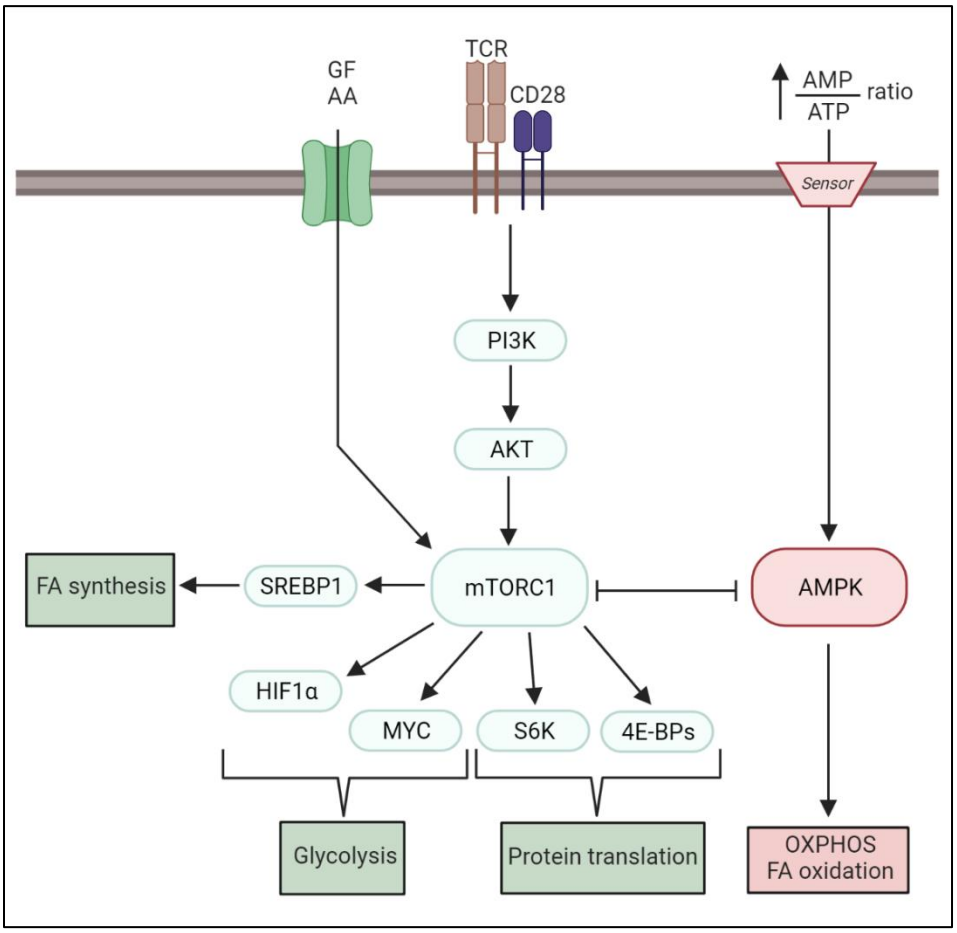

Illustration 13 : Metabolic regulators in T cells: mTOR and AMPK.

mTOR and AMPK are regulators of the metabolic pathways in T cells, ensuring proper coordination. Part of the mTOR function is carried out through mTOR complex 1 (mTORC1). mTORC1 is activated through TCR-CD8 stimulation and PI3K-AKT pathway as well as growth factors (GF) and amino acid (AA) signaling. Downstream targets of mTORC1 are sterol regulatory element-binding protein 1 (SREBP1) that induces fatty acid (FA) synthesis, hypoxia inducible factor 1α (HIF1α) and myelocytomatosis oncogene (MYC), which both prompt glycolysis, and ribosomal protein S6 kinases (S6K) and 4E-binding proteins (4E-BPs) that promote protein translation. AMPK senses low levels of energy in the cell through the AMP/ATP ratio and induces oxidative phosphorylation (OXPHOS) and FA oxidation. (Created in BioRender)

3.4.2. AMPK

AMPK is an energy stress sensor detecting changes in intracellular AMP/ATP concentrations and is activated once energy levels are low (cf. to illustration 13) (Buck et al., 2015; Kurniawan et al., 2020b). AMPK is a negative regulator of mTORC1 and induces opposing metabolic pathways such as FAO and OXPHOS (Palmer et al., 2015; Salmond, 2018).

3.5. Metabolic adaptations to energy status

As previously mentioned, T cells adapt their metabolism according to their energy demands in order to execute their functions (Franchina et al., 2018; Guerra et al., 2020).

Naïve T cells rely on TCA cycle and OXPHOS for the metabolism of glucose, as well as FAO. These pathways do not require high uptake of nutrients and are mainly used for the maintenance of naïve cells while waiting for the antigen encounter and activation (Rangel Rivera et al., 2021).

Upon activation, naïve T cells differentiate into effector T cells. During this process, there is a metabolic reprogramming, induced by mTORC1, characterized by the switch from mitochondrial-driven pathways to glycolysis and glutaminolysis to generate ATP and biosynthetic precursors in a rapid manner. This phenomenon also known as the Warburg effect, has originally been described by Otto Warburg in cancer cells. This metabolic rewiring is needed to support T cell growth, proliferation, and expression of signaling molecules important for effector functions (Buck et al., 2015; Kurniawan et al., 2020b; Pearce and Pearce, 2013; Rangel Rivera et al., 2021; Otto Warburg, 1956; O. Warburg, 1956).

However, there are differences between the metabolism of Teff and Treg cells. Unlike Teff cells, such as Th1, Th2 and Th17 cells, that become more glycolytic upon activation, Treg cells rely intensely on FAO for their function while maintaining their glycolysis at a lower rate (Kurniawan et al., 2020b; Michalek et al., 2011).

Once the pathogen is cleared, the effector response contracts and the generation of memory T cells takes place (Abbas et al., 2015). The metabolism of memory T cells is similar to the one of naïve and quiescent cells, relying on mitochondrial pathways such as the TCA cycle, FAO and OXPHOS (Corrado and Pearce, 2022; Franchina et al., 2018).

4. EPIGENETICS AND METABOLISM REGULATE EFFECTOR T CELL FUNCTIONS

Epigenetic modifications are characterized by reversible processes affecting gene expression without alteration of the DNA sequence. There are four types of modifications that alter gene expression, such as DNA methylation, histone changes (acetylation and methylation), non-coding RNAs and higher-order structure of the chromatin (Liotti et al., 2022; Rhodes and Lin, 2023).

T cell differentiation and function are dependent on epigenetic modifications mainly involved in histone modifications and/or DNA methylation that are often stabilized through the binding of TF, thus the proper regulation of these modifications is essential for the correct function of the adaptive immune system (Dutta et al., 2021).

Recent studies have connected T cell metabolism with epigenetics. Namely, it was shown that some enzymes and substrates of different metabolic pathways play a role in chromatin accessibility and/or gene expression (Hochrein et al., 2022; Kurniawan et al., 2020a; Qiu et al., 2019; Sugiura et al., 2022).

4.1 Histone modifications in T cells

A complex of eight histones, two of each histone proteins (H2A, H2B, H3 and H4), form the core of the nucleosome in the chromatin. Each core has a globular C-terminal domain and an N-terminal tail that is the site of numerous post-translational modifications (PTMs) such as acetylation and methylation of its lysine (K) residues (cf. to illustration 14) (Rhodes and Lin, 2023).

Different PTMs on the histone cores alter the chromatin accessibility allowing or blocking gene expression (cf. to table 1).

Table 1 : Effects of histone modifications on gene expression.

PTM	Histone modification		Gene expression
Acetylation	H3K9, K14, K18 and K27	Mono- or di-acetylation	Active
	H4K5, K8, K12 and K16		
Methylation	H3K4	Tri-methylation	Active
	H3K9 and K27	Tri-methylation	Inactive
	H4K20		

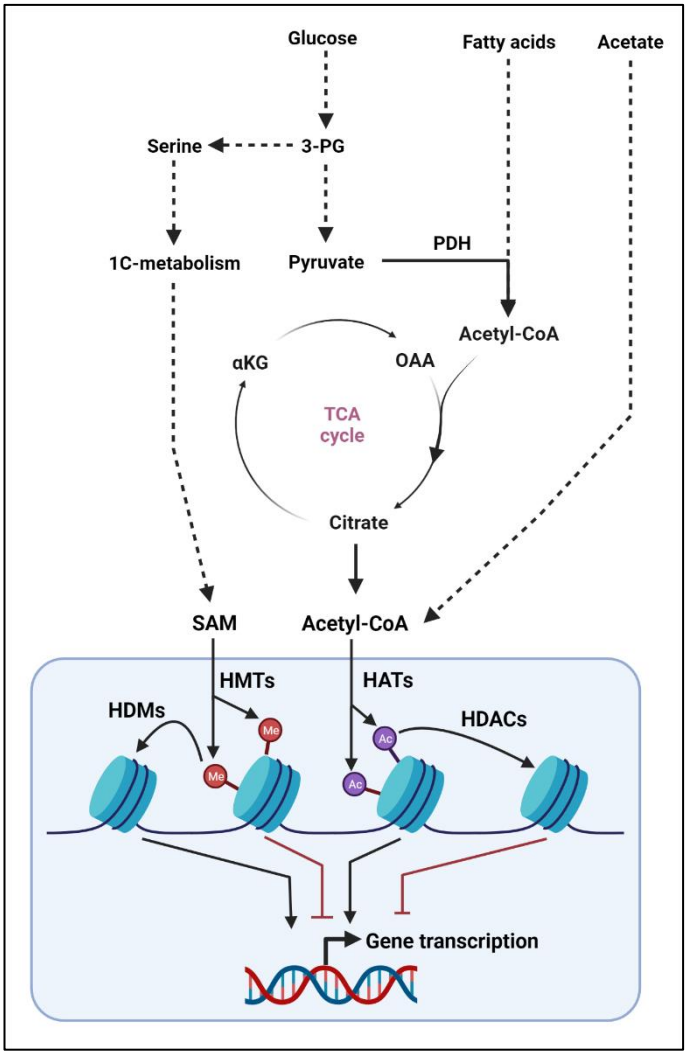

Illustration 14 : Histone methylation and acetylation.

Histone methyltransferases (HMTs) use S-adenosylmethionine (SAM), a product of the one-carbon (1C) metabolism, as a substrate for histone methylation, which in general blocks gene transcription. Histone demethylases (HDMs) eliminate the methyl groups from the histones allowing for gene transcription. Acetyl-CoA, generated through the metabolism of glucose, fatty acids or acetate, is the substrate of histone acetyltransferases (HATs) to generate acetylated histones, which promote gene transcription. Histone deacetylases (HDACs) remove the acetyl groups impairing gene transcription. (Created in BioRender)

4.1.1. Histone acetylation

The status of histone acetylation is dependent on the function of the modifiers histone acetyltransferases (HATs) and histone deacetylases (HDACs) (Dutta et al., 2021).

On one hand, histones are acetylated by HATs, which transfer the acetyl group from acetyl-CoA to specific lysine residues of H3 or H4. Histone acetylation is a dynamic modification and shows high turnover and, as previously mentioned, allows chromatin to de-condense, increasing DNA accessibility and thus, gene transcription (Dutta et al., 2021; Ellmeier and Seiser, 2018). On the other hand, this markers can be removed by HDACs, causing chromatin re-condensation (Sun et al., 2015). HATs and HDACs are also referred to as activators and inhibitors of transcription, respectively (cf. to illustration 14) (Ellmeier and Seiser, 2018; Liotti et al., 2022).

Acetyl-CoA is a substrate of HATs that can be produced by several metabolic pathways such as the TCA cycle, FAO and acetate metabolism, thus connecting metabolism to epigenetic modifications (Møller et al., 2022). Recently, Hochrein et al. connected the GLUT3-dependent glycolysis to effector functions of T helper (Th) 17 cells through acetyl-CoA production and epigenetic alterations in these cells (Hochrein et al., 2022). Also, Qiu et al. have demonstrated that in glucose limiting environments, such as the tumor niche, CD8 T cells' effector functions could be activated through the uptake of acetate, which induced histone acetylation and chromatin accessibility (Qiu et al., 2019). On a similar note, Peng et al. showed that LDH in Th1 cells is necessary to maintain the acetyl-CoA pool for histone acetylation and thus the production of IFNγ (Peng et al., 2016).

On the contrary, it is known that NAD^+ is a co-factor for the HDAC family of sirtuins and is generated through multiple metabolic pathways such as ETC and tryptophan metabolism, thus inducing histone deacetylation (Møller et al., 2022).

4.1.2. Histone methylation

Histone methylation is the product of transferring up to three methyl groups onto lysine or arginine residues at the N-terminal of core histones. The process is carried out by histone methyltransferases (HMTs). HMTs are divided into lysine- or arginine-specific HMTs depending on the residue these enzymes transfer the methyl group onto. However, a majority of HMTs are lysine-specific. The methyl residues on lysines are removed by histone demethylases (HDMs) (cf. to illustration 14) (Rhodes and Lin, 2023).

The main donor of methyl groups for HMTs is S-adenosylmethionine (SAM), which is produced in the 1C-metabolism (Ducker and Rabinowitz, 2017). It has been shown that the 1C-metabolism

enzyme methylenetetrahydrofolate dehydrogenase 2 (MTHFD2) is essential for histone methylation in Th17 cells and their function (Sugiura et al., 2022).

On the other hand, α-KG (metabolite of the glutaminolysis and TCA cycle) is a co-factor for several members of the HDMs family, for instance KDM6B (Tran et al., 2019). Recent studies showed that KDM6B is essential for the differentiation and proliferation of effector CD8 T cells (Li et al., 2021; T. Xu et al., 2021).

Conversely, 2-hydroxyglutarate (2-HG) is a metabolite produced by mutant isocitrate dehydrogenase in hypoxic environments and inhibits HDM KDM4A (Carbonneau et al., 2016). It has been shown that the treatment of CD8 T cells with 2-HG enhances proliferation, persistence and anti-tumor capacity in CD8 T cells (Tyrakis et al., 2016).

4.2. DNA methylation in T cells

DNA methylation is required for the maintenance of stability in the genome. DNA methyltransferases (DNMTs) add methyl groups to cytosines, generating 5-methylcytosines (5 mC), which repress gene expression, using SAM as a methyl-donor. On the contrary, the ten-eleven translocation (TET) protein family perform DNA demethylation to activate gene expression (cf. to illustration 15) (Dutta et al., 2021).

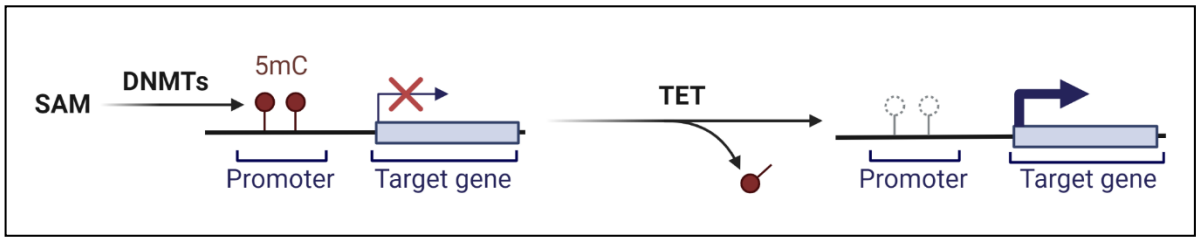

Illustration 15 : DNA methylation.

S-adenosylmethionine (SAM) is the substrate for DNA methyltransferases (DNMTs) to generate 5-methylcytosine (5mC) in the promoter of the target gene, which blocks its transcription. Ten-eleven translocation (TET) proteins remove the methyl groups from gene promoters to allow for its expression. (Created in BioRender)

During CD8 and CD4 T cell differentiation into effector cells, the status of DNA methylation around promoters of effector genes is altered and declines progressively. Nevertheless, upon prolonged

antigen exposure, CD8 T cells can become exhausted and lose their ability to eradicate aberrant cells by inducing *de novo* DNA methylation (Ghoneim et al., 2017; Møller et al., 2022).

Studies have shown that blocking *de novo* DNA methylation in CD8 T cells, in combination with immune-checkpoint blockade treatment, limit the "exhaustion" phenotype allowing for better control of tumor growth (Ghoneim et al., 2017; Møller et al., 2022). In a similar concept, Carty et al. have shown that TET2-deficient CD8 T cells acquire the memory phenotype earlier than wild-type CD8 T cells, thus becoming more efficient in case of reinfection by the same pathogen (Carty et al., 2018).

In another study, 2-HG has been shown to promote Th17 differentiation by inducing hypermethylation of the *Foxp3* gene locus and thus blocking its transcription. This effect could be reversed upon inhibition of the conversion of glutamate into α-KG, reducing the accumulation of 2-HG and allowing for the transcription of the *Foxp3* gene (Xu et al., 2017).

SCOPE AND AIMS

T cells are an essential part of the adaptive immune system. Th17 cells are a subset of the $CD4^+$ T cells that have a major role in the protection of the host against extracellular bacteria and fungi. The expression of the transcription factor (TF) RORγT and their ability to produce IL-17 to exert their function are the characteristic features of this subset (Basu et al., 2013; Wu and Wan, 2020). However, Th17 cells have been linked to several autoimmune diseases such as multiple sclerosis and rheumatoid arthritis (Aranami and Yamamura, 2008; Basu et al., 2013).

To execute their function, T cells adapt their metabolism according to their energy demands (Franchina et al., 2018; Guerra et al., 2020). Upon activation, T cells undergo a process known as metabolic reprogramming, CD4 T cells switch from oxidative metabolism (i.e. tricarboxylic citric acid cycle (TCA), oxidative phosphorylation (OXPHOS), and fatty acid beta-oxidation) to glycolysis and glutaminolysis. This energetic rewiring enables the rapid generation of ATP and biosynthetic precursors and is essential for the growth, proliferation, and generation of the signaling molecules for the functions of effector T cells (Buck et al., 2015; Kurniawan et al., 2020b; Pearce and Pearce, 2013; Rangel Rivera et al., 2021).

The pyruvate dehydrogenase (PDH) complex harbors a key role in mammalian metabolism by regulating the cytoplasmic glucose flux into the mitochondrial TCA cycle (DeBrosse and Kerr, 2016). PDH is a mitochondrial enzyme catalyzing the conversion of glucose-derived pyruvate into acetyl-coenzyme A (CoA) (Hitosugi et al., 2011; Kaplon et al., 2013; Korotchkina and Patel, 2001). Once produced, acetyl-CoA is linked with oxaloacetate (OAA) to generate citrate in the mitochondria (O'Neill et al., 2016; Pearce et al., 2013).

The cellular citrate pool is utilized for several pathways that are essential for energy metabolism and transcriptional activity. Citrate can be processed through the TCA cycle to produce reductive equivalents necessary for ATP production via electron transport chain and OXPHOS. In addition, citrate can exit the mitochondria through citrate transporters into the cytoplasm and even enter the nucleus (Chapman and Chi, 2022; Wang and Green, 2012). In the cytoplasm or the nucleus, citrate can be converted into acetyl-CoA and OAA by the ATP-citrate lyase (ACLY) (Koundouros and Poulogiannis, 2020; Wellen et al., 2009; Zhao et al., 2016). Cytoplasmic acetyl-CoA can be used for lipids synthesis, whilst nuclear acetyl-CoA contributes to protein acetylation such as histone acetylation. Histone acetylation allows for the de-condensation of chromatin, essential for cell type-specific gene expression (Li et al., 2007; Pietrocola et al., 2015; Sivanand et al., 2018).

In this study, we aim to decipher the role of PDH in Th17 cells function both *in vivo* and *in vitro*.

The specific objectives of this study are:

- Identify the importance of PDH in distinct T helper subsets
- Generate a T cell-specific PDH-deficient mouse line
- Determine whether PDH has a role in the Th17 cell-driven mouse model of experimental autoimmune encephalomyelitis (EAE)
- Investigate if PDH ablation has an effect on Th17 cell differentiation *in vitro*
- Evaluate the metabolic adaptations of Th17 cells upon PDH ablation
- Decipher the molecular alterations caused by PDH ablation
- Analyze the consequences of PDH-deficiency in Th17 cells' proliferation
- Investigate the role of PDH in Th17 cells signature gene transcription
- Determine a compensatory mechanism that could restore the effects of *Pdhα1* ablation in Th17 cells.

MATERIALS AND METHODS

1. MICE AND *IN VIVO* MODEL

1.1. Mice

PDH$^{fl/fl}$ mice [B6.129P2-Pdha1tm1Ptl/J] were purchased from The Jackson Laboratory and crossed with CD4 Cre-expressing mice also obtained from The Jackson Laboratory. All experiments used age- and gender-matched mice (8-12 weeks old) with respective littermate controls. All animal experimentation protocols were approved and conducted according to the LIH Animal Welfare Structure (AWS) and Luxembourgish Ministry of Agriculture, Viticulture and Rural Development guidelines. Maintenance of the lines and all *in vivo* experiments were performed under specific pathogen-free (SPF) conditions.

1.2. Genotyping of PDH$^{fl/fl}$ CD4 Cre+ mice

To determine the genotype of the mice, tail tips from each mouse were obtained. Then, DNA was extracted using the NucleoSpin® 96 Tissue Core Kit (Macherey Nagel) following the manufacturer's instructions. Following the extraction, a polymerase chain reaction (PCR) was performed to amplify the relevant DNA fragment with the appropriate DNA primers (cf. table 2) using the DreamTaq Green PCR Mastermix (Thermo Scientific). Finally, electrophoresis was done to separate the fragments according to size on a gel containing 1,5% agarose (Lonza) and 0,01% Sybr™ Safe DNA gel stain (Invitrogen). The program GenSnap (Syngene) was used to take images of the gel with UV light, and Smart Ladder (Kaneka Eurogentec) were used to analyze the results.

Table 2: Primers and band sizes for genotyping of WT and PDH$^{fl/fl}$ CD4 Cre + mice

Gene	Primer	Result and band size
PDH reaction	Primer 1: CGTCTGTTGAGAGAGCAGCA	Wild-type: 303 bp
	Primer 2: CGCACAAGATATCCATTCCA	PDH$^{fl/fl}$: 380 bp
CD4-Cre reaction	Primer 1: CTAGGCCACAGAATTGAAAGATCT	CD4 Cre +: 500 bp
	Primer 2: GTAGGTGGAAATTCTAGCATCATCC	
	Primer 3: CATGTCCATCAGGTTCTTGC	
	Primer 4: CCA GGG TCG GAG ACA ATA AC	

1.3. Experimental autoimmune encephalomyelitis (EAE) mouse model

Induction of EAE was performed as previously described (Brüstle et al., 2012) in 10 week-old male mice. The animals were injected subcutaneously with MOG_{35-55}/CFA emulsion at day 0 and two intraperitoneal injections of 200 ng of pertussis toxin at days 0 and 2 (Hooke labs). Daily scoring was done according to the neurological signs (cf. table 3).

Table 3 : EAE scoring based on neurological signs

Score	Neurological signs
0	No neurological signs
1	Loss of tail tonicity
2	Abnormal gait and hind limb weakness
3	Hind limb paralysis
3,5	Hind limb paralysis and falling over
4	Hind limb paralysis and forelimb involvement
5	Moribund or dead

2. CELL ISOLATION AND CULTURE

2.1. Naïve T cell isolation

Naïve $CD4^+$ T cells were isolated from mouse spleen and lymph nodes by negative magnetic bead sorting (MACS) following the manufacturer's protocol using the Naïve $CD4^+$ T cell isolation kit (Miltenyi Biotec) and sorting was performed by autoMACS® pro Separator (Miltenyi Biotec). CASY cell counter (Omni Life Science) was used to perform cell number calculations.

2.2. *In vitro* Th subsets differentiation

For *in vitro* differentiation, isolated naïve T cells were counted by CASY and seeded at a concentration of $2x10^6$ cells/mL during 3 days in IMDM (Westburg) supplemented with 10% FBS (Biochrom GmbH), 55µM 2-mercaptoethanol (Gibco) and 1% penicillin/streptomycin (Gibco) (complete medium), and in the presence of Th-specific cytokine mix (cf. table 4).

Table 4 : Cytokine mix cocktails Th-subset specific for naïve differentiation *in vitro*.

Th subset	Cytokine	Concentration	Source
Th0	anti-CD3 (plate-bound)	5 µg/mL	BioLegend
	anti-CD28	1 µg/mL	BioLegend
	anti-IFNγ	5 µg/mL	BD Biosciences
	IL-2	50 U/mL	Miltenyi Biotec
Th1	anti-CD3 (plate-bound)	5 µg/mL	BioLegend
	anti-CD28	1 µg/mL	BioLegend
	IL-12	2 ng/mL	Miltenyi Biotec
	IL-2	50 U/mL	Miltenyi Biotec
Th17	anti-CD3 (plate-bound)	5 µg/mL	BioLegend
	anti-CD28	1 µg/mL	BioLegend
	IL-6	30 ng/mL	Miltenyi Biotec
	anti-IFNγ	5 µg/mL	BD Biosciences
	TGFβ	2 ng/mL	Bio-Techne
Treg	anti-CD3 (plate-bound)	5 µg/mL	BioLegend
	anti-CD28	1 µg/mL	BioLegend
	IL-2	50 U/mL	Miltenyi Biotec
	anti-IFNγ	5 µg/mL	BD Biosciences
	TGFβ	4 ng/mL	Bio-Techne

All results were obtained from *in vitro* differentiated cells generated from naïve T cells isolated from $PDH^{fl/fl}$ and $PDH^{fl/fl}$ CD4 Cre+ mice, unless mentioned otherwise in the figure legends.
For acetate-treated cells, the differentiation was performed adding 10 mM sodium acetate (Sigma-Aldrich) diluted in culture medium.

2.3. Isolation of lymphocytes from brain of EAE mice

Isolation of lymphocytes from the brains of EAE mice at day 14 post-induction was performed as previously described (Brüstle et al., 2012). Briefly, mice were sacrificied and brain was perfused with 20 mL of cold PBS through the left ventricle. Digestion of brain was done in RPMI supplemented with 50 ug/mL collagenase D (Roche) and 10 ug/mL DNAseI (Sigma-Aldrich) for 1 hour at 37°C in a mixer (Labortechnik). Lymphocyte enrichment was obtained by centrifugation using a two-layer Percoll gradient (40% and 70%) and then washed twice in RPMI.

3. PROTEOME ANALYSIS

3.1. Flow cytometry

3.1.1. Extracellular staining

For the detection of surface markers, cells were stained in fluorescence-activated single cell sorting (FACS) buffer (PBS supplemented with 1% FBS and 5 mM EDTA, pH=8.0) with fluorescent labelled antibodies (cf. Key Resources Table; 1:200 dilution) and live/dead dye (DAPI (Thermo Fisher Scientific), LIVE/DEAD® Fixable Near-IR or Green dye (BioLegend) or 7-AAD (Thermo Fisher Scientific) diluted between 1:1000-1:3000) for 30 minutes at 4°C. Before flow cytometry measurement, cells were washed in FACS buffer.

3.1.2. Intracellular stainings

3.1.2.1. Transcription factors

For intracellular staining of transcription factors, cells were fixed at 4°C for 1 hour in the eBioscience™ FoxP3/Transcription Factor Fixation kit (Thermo Fisher Scientific) and permeabilization was done in the buffer provided by the kit. Intracellular antibodies were diluted 1:200 in 1X eBioscience™ Permeabilization Buffer and incubated for 30 minutes at 4°C.

3.1.2.2. Cytokines

To measure intracellular cytokine expression, cells were restimulated for 5 hours *in vitro* with phorbol 12-myristate 13-acetate (PMA; Sigma, 50 ng/mL), calcium ionophore A23187 (Ionomycin, Sigma, 750 ng/mL) and cytokine release was blocked using BD GolgiPlug™ Protein Transport Inhibitor (BD, 1:1000 dilution). After stimulation, cells were washed once with FACS buffer before extracellular staining, then fixed 20 min at 4°C with BD Cytofix/Cytoperm and permeabilized in BD Perm/Wash™ buffer (BD Biosciences). Intracellular antibodies were diluted 1:200 in the BD Perm/Wash™ buffer and incubated for 30 minutes at 4°C.

3.1.2.3. Hexokinase-1

To stain hexokinase-1, cells were fixed in 4% formaldehyde (Sigma-Aldrich) diluted in PBS (Westburg) for 10 minutes at room temperature (RT), then permeabilized and stained with intracellular antibodies (diluted 1:200) in PBS 0.1% Tween-20 and incubated for 30 minutes at 4°C.

3.1.2.4. p-mTOR and p-S6

For p-mTOR and p-S6 detection, cells were fixed in 2% formaldehyde (Sigma-Aldrich) diluted in PBS (Westburg) for 10 minutes at RT, then permeabilized in 0.01% saponin (Sigma-Aldrich) diluted in FACS buffer. Intracellular antibodies were diluted 1:200 in 0,01% saponin and incubated for 30 minutes at 4°C.

3.1.3. Metabolic activity stainings

3.1.3.1. Glucose uptake measurement

For glucose uptake measurements, cells were incubated in glucose-free RPMI for 2h at 37°C in the presence of 50 µM 2-NBDG (Thermo Fisher Scientific).

3.1.3.2. Lipid uptake measurement

To measure lipid uptake, cells were incubated in IMDM with 1 µM Bodipy™ FL C16 (Invitrogen) for 30 minutes at 37°C. Cells were washed once with PBS prior to flow cytometric measurement.

3.1.4. Proliferation measurement

To determine proliferation indexes, naïve cells were labeled with 5µM cell-trace violet (CVT; Thermo Fisher Scientific) on the day of isolation and analyzed by flow cytometry three days later. Proliferating cells are gated on $CVT^{med\text{-}low}$ cells.

3.1.5. Flow cytometry measurements and analysis

Flow cytometric measurements were performed on a BD Fortessa instrument (BD Biosciences) and analysis was done using FlowJo v10.6.2 software (Tree Star).

3.2. Immunoblotting

Samples were lysed in lysis buffer (CST, 9803S) with protein/phosphatases inhibitors (Bioké) following manufacturer's instructions and blotting was performed as previously described (Kurniawan et al., 2020a). The antibodies used for detection were anti-Pdha1 (Abcam, ab168379), anti-actin (Sigma Aldrich), anti-acetyl-histone H3 Lys27 (Cell Signaling Technology, 8173S), anti-histone H3 (Cell Signaling Technology, 9715S) and anti-acetyl-histone H3 (Millipore, 06-599) all diluted 1:1000 in TBS-T.

3.3. IL-17 cytokine quantification

IL-17 quantification was performed on supernatants of *in vitro* differentiated Th17 cells using the Mouse IL-17 DuoSet ELISA kit (Bio-Techne) and following the manufacturer's instructions. Briefly, 96-well plates were coated overnight at RT with the capture antibody provided by the kit. After three washes with the wash buffer, each well was blocked by 300 µL of reagent diluent for 1 hour, also at RT. Following three more washes, 100 µL of samples and standards diluted in reagent diluent were added in the appropriate well and incubated for 2 hours at RT. After incubation, the plate was washed as described above and 100 µL of detection antibody were added and the plate was kept 2 hours at RT. After washing, 100 µL of Streptavidin-HRP was added to each well and the plate was left in the dark at RT for 20 minutes. Finally, after the last washing step, 100 µL of substrate solution was added in each well and before saturation of the standard curve, 50 µL of stop solution was added to stop the reaction. Measurement of the optical density was performed with SpectraMax ELISA plate reader instrument (Molecular Devices). Results were analyzed using Excel and normalized by cell number.

4. METABOLIC STUDIES

4.1. Metabolic flux measurements

In vitro-differentiated Th17 cells were seeded on a XFe96 cell culture plate (Agilent Technologies) pre-coated with Corning™ Cell-Tak Cell and Tissue Adhesive (Thermo Fisher Scientific) with 0.1M sodium bicarbonate (Sigma-Aldrich), at a density of $3x10^5$ cells/well. Experiments were performed on an XFe96 Extracellular Flux Analyzer (Agilent).

4.1.1. Oxygen consumption rate (OCR) measurement

For OCR measurements, cells were cultured in XF Seahorse DMEM medium (Agilent Technologies) containing 2 mM of glutamine (Westburg), 1 mM sodium pyruvate (Gibco) and 25 mM glucose (Sigma-Aldrich). OCR was measured using the XF Cell Mito Stress Test (Agilent Technologies) following the manufacturer's protocol during sequential injections of oligomycin A (1 µM), carbonyl cyanide 4-(trifluoromethoxy)phenylhydrazone (FCCP; 3 µM) and antimycin A/rotenone (1 µM) (all from Sigma-Aldrich). Three measurements were performed before and after each injection in 7 min intervals.

4.1.2. Extracellular acidification rate (ECAR) measurement

For ECAR measurements, cells were cultured in XF Seahorse DMEM medium (Agilent Technologies) containing 2 mM of glutamine (Westburg) and ECAR was determined by the XF Glycolysis Stress Test Kit (Agilent Technologies). As for OCR, the measurement was taken during sequential injections of glucose (10 mM), oligomycin (1 µM) and 2-deoxy-D-glucose (2-DG; 50 mM) (all from Sigma-Aldrich). Three measurements were performed before and after each injection in 7 min intervals.

4.2. Metabolic flux analysis

Results were analyzed using the Wave 2.6.1 software (Agilent Technologies) and all measurements were calculated from raw OCR or ECAR data as described in the table below (cf. table 5).

Table 5 : Calculations of OCR and ECAR measurements.

Parameter	Raw data source	Calculations
Basal OCR	OCR	3rd minus 12th measurement
Maximal respiration	OCR	9th minus 12th measurement
OCR-dependent ATP production	OCR	3rd minus 6th measurement
Spare respiratory capacity	OCR	9th minus 3rd measurement
Glycolytic capacity	ECAR	9th minus 12th measurement
ECAR glycolysis	ECAR	6th minus 3rd measurement

5. MASS SPECTROMETRY SAMPLE PREPARATION AND ANALYSIS

5.1. Isotopic labelling

For glucose and glutamine tracing, naïve T cells were differentiated for 3 days into Th17 cells in complete medium. At day 3, cells were counted, washed and seeded for 24h with tracing media consisting of SILAC RPMI 1640 (Fisher Scientific) supplemented with 10% FBS (Biochrom GmbH), 55µM 2-mercaptoethanol (Gibco), 1% penicillin/streptomycin (Gibco), L-Arginine (Sigma Aldrich) and L-Lysine (Sigma Aldrich) and containing [U-$^{13}C_6$]-glucose (11.1 mmol/L; Cambridge Isotope Laboratories) or [U-$^{13}C_5$]-glutamine (2 mmol/L; Cambridge Isotope Laboratories). Extraction of intracellular metabolites, multiple ion detection (MID) and carbon contribution determinations, gas chromatography- (GC-) and liquid chromatography-mass spectrometry (LC-MS) measurements and substractions of natural isotope abundance of the polar fraction were done as previously described (Battello et al., 2016) using the MetaboliteDetector software.

5.2. Uptake and release rate measurement

Glucose, lactate and glutamine concentrations in medium were measured by YSI 2950D Biochemistry Analyzer (YSI Incorpoated). After normalization with control samples, uptake and release rates were determined.

5.3. GC-MS of the non-polar fraction

5.3.1. GC-MS measurement of the non-polar fraction

Measurements of the non-polar fraction via GC-MS were done as previously described (Modamio et al., 2021). Derivatization was performed by using a multi-purpose sample preparation robot (Gerstel). Dried non-polar extracts were dissolved in 30 µl of MTBSTFA with 1% TBDMCS and incubated for 60 minutes at 55°C under continuous shaking.

GC-MS analysis was performed by using an Agilent 7890A GC coupled to an Agilent Mass Selective Detector (MSD; Agilent Technologies). A sample volume of 1 µl was injected into a Split/Splitless inlet, operating in splitless mode at 280 °C. The gas chromatograph was equipped with a 30 m (I.D.

0.25 mm, film 0.25 µm) ZB-5MSplus capillary column (Phenomenex) with 5 m guard column in front of the analytical column. Helium was used as carrier gas with a constant flow rate of 1.4 ml/min. GC temperature program was as follows, 100 °C for 1 minute then increased to 325 °C at 7.5 °C/min and held for 4 minutes. The total run time was 35 minutes.

The transfer line temperature was set to 280 °C. The MSD was operating under electron ionization at 70 eV. The MS source was held at 230 °C and the quadrupole at 150 °C. GC-MS measurements were performed in selected ion monitoring mode for precise determination of the MIDs.

5.3.2. GC-MS data of the non-polar fraction processing and normalization

Processing and normalization of the non-polar fraction measurements via GC-MS were done as previously described (Modamio et al., 2021). MetaboliteDetector (v3.2.20190704) was used to process all GC-MS chromatograms (Hiller et al., 2009). Compounds were annotated by retention time and mass spectrum using an in-house mass spectral library (overall similarity: >0.85). The following deconvolution settings were applied: Peak threshold: 2; Minimum peak height: 2; Bins per scan: 10; Deconvolution width: 8 scans; No baseline adjustment; Minimum 1 peaks per spectrum; No minimum required base peak intensity. MIDs for the following fragments were calculated (cf. table 6).

Table 6 : Fragments calculated for MIDs of the non-polar fraction.

Derivative	Metabolite	*m/z* - *R*ange	Sum Formula (Fragment)	MID size
Dodecanoic acid 1TBDMS	C12:0	257-272	C14H29O2Si	13
Tetradecanoic acid 1TBDMS	C14:0	285-302	C16H33O2Si	15
Hexadecanoic acid 1TBDMS	C16:0	313-332	C18H37O2Si	17
Hexadecenoic acid 1TBDMS	C16:1	311-330	C18H35O2Si	17
Octadecanoic acid 1TBDMS	C18:0	341-362	C20H41O2Si	19
Octadecenoic acid 1TBDMS	C18:1	339-360	C20H39O2Si	19
Octadecadienoic acid 1TBDMS	C18:2	337-358	C20H37O2Si	19
Cholesterol 1TBDMS	Cholesterol	443-473	C29H51OSi	28

5.4. LC-MS analysis of histone

Sample preparation for analysis of histones with LC-MS was performed as described previously (Lauterbach et al., 2019). Briefly, histones were extracted using acid extraction and separated on 16% polyacrylamide gel. In-gel acylation of histones was performed using propionic anhydride to

mimic the situation of the light histone peptides. Subsequently, in-gel digestion of histone proteins was performed to obtain tryptic-digested peptides. Peptides were desalted using C18-Omix tips (Agilent Technologies), vacuum dried, and reconstituted in 0.1 % formic acid in water. 10 µl of the peptide digest was injected into Vanquish UHPLC Systems (Thermo Scientific) equipped with Hypersil GOLD™ coupled to Orbitrap ID-X Tribrid Mass Spectrometer (Thermo Scientific). The peptides were separated on Vanquish™ C18 UHPLC Columns (150*2.1 mm, 1.9 µm) at a flow rate of 300 µL/min using a 50 minutes gradient program starting from 5 % to 50% of mobile phase B, where mobile phase A was water with 0.1% formic acid and mobile phase B was acetonitrile with 0.1% formic acid. The MS instrument was operated in full scan mode (m/z 350 -1600) with resolution R = 60,000 at m/z 400. Peptide fragmentation was performed using data-dependent acquisition (DDA). The peptide ions (top 10) for DDA-based ms/ms fragmentation were selected based on peptide ions' intensity. Typical mass spectrometric conditions were as follows: AGC target, standard; spray voltage, 4000 V; sheath and, 45; auxiliary gas flow, 10; ion transfer tube temperature, 325°C; vaporizer temperature, 325; DDA cycle time, 3; collision energy, 30%. Tracefinder software was used for manual inspection of chromatograms and integration of peak areas. Peptide identification and confirmation were performed using Skyline software.

6. SEQUENCING SAMPLES PREPARATION AND ANALYSIS

6.1. RNA extraction and quantitative RT-PCR

RNA was extracted following the protocol from NucleoSpin RNA Kit (Macherey-Nagel). RNA concentrations were measured by NanoDrop 2000c Spectrophotometer (Thermo Fisher Scientific). Quantitative RT-PCR (RT-qPCR) was carried out by mixing 2µL RNA (30 ng) with 5µL Master Mix (Luna Universal One-Step RT-qPCR Kits; Bioké), 2pmol of forward primer and 2pmol of reverse primer, 0.3µL reverse transcriptase and filled up to 10 µL with RNAse-free water per sample (cf. Key Resources Table). Reactions were run on a CFX384 instrument (Bio-Rad). Data were normalized to *Tbp* and analyzed using the ΔΔCt method as previously described (Mak et al., 2017).

6.2. RNA-seq samples preparation and analysis

6.2.1. RNA-seq sample preparation

RNA extraction was performed as described above. The mRNA sequencing of Th17 cells differentiated *in vitro* for 72 h from naïve T cells of $PDH^{fl/fl}$ and $PDH^{fl/fl}$ CD4 Cre+ mice was done with the same pool of cells that were used for ATAC-seq. The sequencing was done at the sequencing platform in the Luxembourg Centre for Systems Biomedicine (LCSB) of the University of Luxembourg. The single-end, stranded sequencing was applied by the Illumina NextSeq 500 machine with read length of 75 bp. The TruSeq Stranded mRNA Library Prep kit (Illumina) was used for library preparation.

6.2.2. RNA-seq data analysis

FastQC (v0.11.5) was used for the quality control of the raw reads (Andrews, S., 2010). Adapter removal was done using PALEOMIX pipeline (v1.2.12) (Schubert et al., 2014), with a minimum length of the remaining reads set to 25 bp. SortMeRNA (v2.1) was used to remove rRNA reads (Kopylova et al., 2012) and afterwards the mapping was done by STAR (v.2.5.2b) (Dobin et al., 2013). RNA-seq transcript alignment was performed with Salmon (Patro et al., 2017) against the Mouse transcriptome from Genecode v.M27 (Frankish et al., 2019). Subsequent analysis were being conducted in R. Tximeta (Love et al., 2020) was used to assign transcripts to gene before performing differential analysis with DESeq2 (Love et al., 2014). Gene set enrichment analysis (GSEA) was

performed with cluseterProfiler (Yu et al., 2012). Decorated KEGG view pathways were prepared using Pathview (Luo and Brouwer, 2013).

6.3. ATAC-SEQ samples preparation and analysis

6.3.1. ATAC-seq sample preparation

Tagmentation of Th17 cells differentiated *in vitro* for 72 h from naïve T cells of $PDH^{fl/fl}$ and $PDH^{fl/fl}$ CD4 Cre+ mice was done with the same pool of cells that were used for RNA-seq. ATAC-seq was performed as described in OMNI-ATAC supplementary protocol 1 (Corces et al., 2017) with some changes. 100 000 viable cells were resuspend in 50 µL cold ATAC-Resuspension Buffer (RSB) containing 0.1% Tween-20, adding 0.1% NP40 and 0.01% Digitonin, and lysed for 3 min on ice. After 3 minutes incubation, lysates were washed with 1 mL cold ATAC-RSB containing 0.1% Tween-20 but no NP40 or digitonin. Samples are centrifuged for 10 minutes at 500g and 4 °C, supernatant was removed, while pellets were resuspended in 50 µL transposition mix: Tagment DNA buffer (Illumina) containing 2.5 µL Tagment DNA TDE1 Enzyme (Illumina). After 45 minutes incubation at 37 °C and 1000 rpm in Eppendorf ThermoMixer, chromatin fragments were isolated using Zymo Research DNA Clean & Concentrator kit (ZymoResearch). For the pre-amplification of transposed fragments, 5 PCR cycles were run using primers Ad1 and Ad2.x (Buenrostro et al., 2015). The rest of the additional cycles of library amplification were determined by qPCR (Adams et al., 2000). Another cleanup was done using Zymo Research DNA Clean & Concentrator kit with 21 ul elution volume, followed by AMPure XP bead (Beckman Coulter) size selection with samples adjusted to 100 µL and 55 µL of beads to remove large fragments. Incubation of 5 minutes followed by separation of beads on magnetic stand was done before transferring supernatants to a new tube, where 225 µL of beads were added, followed by an incubation for 10 minutes and a separation on magnetic stand. After washing with 80% ethanol, beads are resuspended in 20 µL elution buffer and incubate during 5 minutes. After separation on magnetic stand eluate was transferred to a new tube. Library quality control was performed using Agilent DNA High sensitivity Bioanalyzer chip (Agilent). The sequencing of ATAC-seq libraries was done at the sequencing platform in the Luxembourg Centre for Systems Biomedicine (LCSB) of the University of Luxembourg. The paired-end, unstranded library sequencing was performed using Illumina NextSeq 500/550 75 cycles High Output Kit.

6.3.2. ATAC-seq data analysis

FastQC (v0.11.5) was used for the quality control of the raw reads (Andrews, S., 2010). Alignment and mapping to generate BAM files were done with BWA (v.0.7.16a) (Li et al., 2009). The mouse reference genome used for the mapping was GRCm38 release 102 downloaded from GENCODE (https://www.gencodegenes.org/). Picard tool (v2.10.9) was used to validate the BAM files (Adams et al., 2000). After obtaining the BAM files, Genrich (https://github.com/jsh58/Genrich) was used for peak calling with parameters "-r -m 30 -j -a 200 -g 15 -l 15 -d 50" to remove PCR duplicates and include only reads with mapping quality of at least 30. Also, to get a minimum AUC for a peak of 200 bp, a maximum distance between significant sites of 15 bp, a minimum length of a peak of 15 bp, and for defining expand cut sites to 50 bp.
Differentially accessible regions were detected using DiffBind (3.4.3) (10.18129/B9.bioc.DiffBind) in R (4.1.2) (Ross-Innes et al., 2012). Briefly, peaks from all samples have been overlapped, resulting in 119 671 unique regions. 103 563 of 119 671 peaks were identified in at least two samples and constituted the peakset. Then, the number of mapped reads was calculated for each peak included in the peakset and background normalization was performed. Finally, differential analysis was performed using DESeq2. The differentially accessible regions were annotated using the ChIPseeker R package (1.30.3) (Yu et al., 2015).

For the metagene plots the BAMs from ATAC-seq analysis, filtered for a minimal mapping quality of 30, were processed by bamCoverage (Ramírez et al., 2018) (deepTools v3.5.0) using the CountsPerMillion (CPM) normalization to generate bigwigs. These bigwigs were further used as input for ComputeMatrix (Ramírez et al., 2018) (deepTools v3.5.0) using the command "scale-regions -m 450 -b 50 -a 50 -bs 10" for all peaks with significantly differential accessibility according to DiffBind. Meaning that the CPM signal was binned per 10 bp and each peak was scaled to 450 bp (the median peak width across the samples) with additional flanking regions of 50 bp included.

7. QUANTIFICATION AND STATISTICAL ANALYSIS

Data are represented in means ± SEM with a minimum of n=3 per group (for more information confer to Figure Legends). P values were calculated using unpaired Student's t test, one or two-way ANOVA plus multiple comparisons with Bonferroni correction by Prism 9.3.1 (GraphPad). P value for statistical significance were determined as ≤ 0.05 and indicated by asterisks accordingly (* p≤ 0.05; ** p≤ 0.01; *** p≤ 0.001; **** p≤ 0.0001 and ns: not significant).

8. KEY RESOURCES TABLE

REAGENT or RESOURCE	SOURCE	IDENTIFIER
Antibodies		
CD4-APC Clone GK1.5 (1:200)	BioLegend	#100412
CD3ε-PE-Cy7 Clone 145-2C11 (1:200)	BioLegend	#100320
CD4-PE Clone GK1.5 (1:200)	BioLegend	#100408
CD4-BV785 Clone GK1.5 (1:200)	BioLegend	#100453
CD4-BUV737 Clone GK1.5 (RUO) (1:200)	BD Biosciences	#612761
IL17A-BV605 Clone TC11-18H10 (1 :200)	BD Biosciences	#564169
IFN-γ-APC Clone XMG1.2 (1:200)	BioLegend	#505810
RORγT-BV421 Clone Q31-378 (1:200)	BD Biosciences	#562894
Tbet-PE/Cy7 Clone 4B10 (1:200)	BioLegend	#644824
FoxP3-APC Clone FJK-16 s (1:200)	Thermo Fisher	#17-5773-82
CD25-PE Clone PC61 (1:200)	BioLegend	#102008
pmTOR-PE Clone MRRBY (1:200)	Thermo Fisher	#12-9718-42
pS6-APC Clone cupk43k (1:200)	Thermo Fisher	#17-9007-42
CD45-PerCP/Cyanine5.5 Clone 30-F11 (1:200)	BioLegend	#103132
Glut-1 – Alexa Fluor® 647 Clone EPR3915 (1:200)	Abcam	#ab195020
Hexokinase-1 - Alexa Fluor® 488 Clone EPR10134(B) (1:200)	Abcam	#ab184818
CD36-PerCP/Cyanine5.5 Clone HM36 (1:200)	BioLegend	#102620
Ultra-LEAF™ Purified anti-mouse CD3ε Clone 145-2C11	BioLegend	# 100340
Ultra-LEAF™ Purified anti-mouse CD28 Clone 37.51	BioLegend	# 102116
Purified NA/LE Rat Anti-Mouse IFN-γ Clone XMG1.2	BD Biosciences	#554408
Anti-Pyruvate Dehydrogenase E1-alpha subunit antibody	Abcam	#ab168379
anti-acetyl-histone H3	Millipore	#06-599
Anti-Actin antibody produced in rabbit	Sigma-Aldrich	# A2066-.2ML
Mouse anti-rabbit IgG-HRP	Santa Cruz Biotechnology	#sc-2357
Chemicals, Peptides and Recombinant Proteins		
PBS (1X) without Ca++, Mg++, 500ml	Westburg	#BE17-516F
FBS Superior Lot: 0193F	Biochrom GmbH	#S0615
Penicillin-Streptomycin (10,000 U/mL)	Gibco	#11548876
L-Glutamine	Westburg	#BE17-605E
2-Mercaptoethanol	Gibco	#11508916
Methanol	Sigma-Aldrich	#1060351000
Chloroform	Sigma-Aldrich	#34854-1L-M
Ethanol absolute	VWR	#20821.330
Ethanol eurodenatured	VWR	#85823.440
Sodium Acetate trihydrate	Sigma-Aldrich	#71188-250MG
HEPES	Sigma-Aldrich	#H4034-100G
EDTA	Sigma-Aldrich	#EDS-100G

DL-Dithiothreitol solution (DTT)	Sigma-Aldrich	#43816-10ML
Bovine Serum Albumin (BSA)	Sigma-Aldrich	#A9647-500G
RPMI 1640 (without L-Glutamine)	Westburg	#BE12-167F
IMDM with HEPES and L-Glutamine	Westburg	#BE12-722F
Collagenase D from Clostridium histolyticum	Roche	#11088866001
DNAseI	Sigma-Aldrich	#D4513-1VL
Percoll®	Sigma-Aldrich	#GE17-0891-01
Recombinant human TGF-β	Bio-Techne	#240-B-002
Mouse IL-6, research grade	Miltenyi Biotec	#130-094-065
Mouse IL-2, research grade	Miltenyi Biotec	#130-098-221
Mouse IL-12, research grade	Miltenyi Biotec	#130-096-707
Cell Trace Violet	Thermo Fisher	#C34557
Molecular Probes™ 2-NBDG	Thermo Fisher Scientific	#11569116
SYBR™ Fast Green Master Mix	Thermo Fisher Scientific	#4385612
Luna Universal One-Step RT-qPCR Kit	Bioké	#E3005E
Formaldehyde	Sigma-Aldrich	#252549-1L
Saponin	Sigma-Aldrich	#S4521-25G
DAPI (1:2000)	Thermo Fisher Scientific	#D1306
Zombie NIR™ Fixable Viability Kit	BioLegend	#423106
Zombie Green™ Fixable Viability Kit	BioLegend	#423112
7-AAD	Thermo Fisher Scientific	#A1310
Bodipy™ FL C16	Thermo Fisher Scientific	#10654623
Corning™ Cell-Tak Cell and Tissue Adhesive	Thermo Fisher Scientific	#10317081
Oligomycin A	Sigma-Aldrich	#75351-5MG
FCCP	Sigma-Aldrich	#C2920-10MG
Antimycin A	Sigma-Aldrich	#A8674-25MG
Rotenone	Sigma-Aldrich	#R8875-1G
2-Deoxy-D-Glucose	Sigma-Aldrich	#D6134-1G
Sodium pyruvate	Gibco	#12539059
Phorbol 12-myristate 13-acetate (PMA)	Sigma-Aldrich	#P8139-1MG
Calcium Ionophore A23187	Sigma-Aldrich	#C7522-1MG
Rapamycin	Invivogen	#tlrl-rap
Torin 1	Sigma-Aldrich	#475991-10MG
SILAC RPMI 1640 Flex Media	Gibco	#15347143
$^{13}C_6$-glucose	Cambridge Isotope Lab	#CLM-1396
$^{13}C_5$-L-Glutamine	Cambridge Isotope Lab	#CLM-1822-H
$^{13}C_2$-Acetate	Sigma-Aldrich	#282014-250MG
D-(+)-Glucose solution	Sigma-Aldrich	#G8769-100ML
GolgiPlug™ (Protein Transport Inhibitor)	BD Biosciences	#555029

Tween 20	Sigma-Aldrich	#P7949-500ML
NaCl	Sigma-Aldrich	# S9888-5KG
Sodium bicarbonate solution	Sigma-Aldrich	#S8761-100ML
Protease/Phosphatase Inhibitor Cocktail (100x)	Bioké	#5872
Powdered milk	Carl Roth	#T145.2
Luminata™ Crescendo Western HRP substrate	Thermo Fisher Scientific	#10776189
Seahorse XF DMEM medium	Agilent Technologies	#103575-100
Critical Commercial Assays and Kits		
CD4+ T Cell Isolation Kit	Miltenyi Biotec	#130-104-454
Naive CD4+ T Cell Isolation Kit, mouse	Miltenyi Biotec	#130-104-453
NucleoSpin RNA 250	Macherey-Nagel	#740955.250
Foxp3/Transcription Factor Staining Buffer Set	Thermo Fisher Scientific	#15151976
BD Cytofix/Cytoperm Fixation/Permeabilization kit	BD Biosciences	#554714
Mouse IL17 DuoSet ELISA	BIO-TECHNE	#DY421
Seahorse XFe96 Fluxpak	Agilent Technologies	#102416-100
EAE induction kit: MOG35-55/CFA Emulsion PTX	Hooke Laboratories, Inc	#EK-2110
Experimental Models: Organisms/Strains		
$PDH^{fl/fl}$:B6	The Jackson laboratory	#17443
CD4 Cre+:B6	The Jackson laboratory	#022071
Deposited Data		
RNA-Seq	This paper	N/A
ATAC-Seq	This paper	N/A
Oligonucleotides		
Tbp F : GAAGAACAATCCAGACTAGCAGCA R : CCTTATAGGGAACTTCACATCACAG	(Kurniawan et al., 2020)	
Pdha1 F : CGT CTG TTG AGA GAG CAG CA R : CGC ACA AGA TAT CCA TTC CA	This paper	
Pdhb F : AGGAGGGAATTGAATGTGAGGT R : ACTGGCTTCTATGGCTTCGAT	This paper	
Software and Algorithms		
FlowJo Software 10.6.2	Tree Star	N/A
Graphpad Prism 9.3.1	GraphPad Software, Inc	N/A
Wave Software 2.6.1	Agilent	N/A
Inkscape 1.1	Inkscape	N/A

RESULTS

PART I

1.1. Generation of T-cell specific pyruvate dehydrogenase (PDH) knockout mice

PDH is the enzyme linking the cytoplasmic glycolysis with the mitochondrial tricarboxylic acid (TCA) cycle. It transforms the glucose-derived pyruvate into acetyl-CoA for condensation with oxaloacetate (OAA) in the mitochondria to generate citrate in the first step of the TCA cycle (cf. to illustration 8) (DeBrosse and Kerr, 2016; O'Neill et al., 2016; Pearce et al., 2013). This critically rewires the metabolism of T cells upon activation (Marelli-Berg et al., 2012; Pearce and Pearce, 2013; Wang and Green, 2012). Therefore, it is pivotal to unravel whether and how PDH influences the physiology and the function of $CD4^+$ T cells.

The initial step was the analysis of the expression of *Pdha1* in *in vitro*-differentiated $CD4^+$ Th subsets. Naïve $CD4^+$ T cells from wild-type mice's spleen and lymph nodes were isolated, and then activated by anti-CD3 and anti-CD8 under appropriate cytokine conditions according to the Th subset. Th0 cells were differentiated in an IL-2 and anti-IFNγ cytokine mix, Th1 cells were generated with IL-12 and IL-2 stimulation, a combination of IL-6, anti-IFNγ and TGFβ was used to skew Th17 cells, and a cocktail containing IL-2, TGFβ and anti-IFNγ was used to induce Treg differentiation, as previously described (Baricza et al., 2018; Ivanov et al., 2006). After three days of incubation, RNA was isolated and *Pdha1* expression was measured by qPCR. Interestingly, Th17 cells showed the highest *Pdha1* expression compared with control Th0, Th1 and Treg cells implying that PDH might be of particular importance for Th17 cells (Figure 1A).

To determine the importance of PDH in T cells, a mutant mouse strain ($PDH^{fl/fl}$ CD4 Cre+) was generated by crossing CD4 Cre+ expressing mice with $Pdha1^{flox8}$ mice (cf. to Illustration 16). In these mice, T cells did not express a crucial part of the PDH-E1α subunit, encoded by the exon 8 of the *Pdha1* gene (Figure 1B and 1C). PDH-E1α is the subunit of the E1 complex of PDH that catalyzes the rate-limiting step of the conversion of pyruvate into acetyl-CoA (cf. to illustration 9) (Yang et al., 2021). It is important to note that T cells of these mutant mice still express *Pdhb* gene encoding for the other PDH-E1 subunit (PDH-E1β), which is a regulatory subunit and does not harbor a catalytic activity without PDH-E1α (Figure 1D) (Yang et al., 2021).

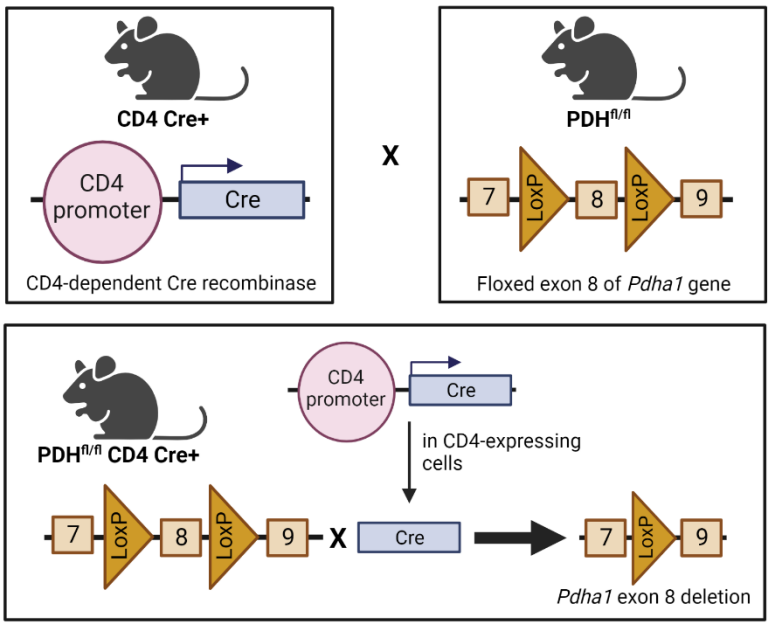

Illustration 16: T cell-specific PDH-deficient mice are generated by the crossing CD4 Cre+ with PDH$^{fl/fl}$ mice.

T cell specific genetic pyruvate dehydrogenase alpha 1 subunit (*Pdha1*) deletion is achieved by using the Cre-Lox recombination system. Mice expressing the Cre recombinase (Cre) enzyme under the CD4 promoter (CD4 Cre+) are crossed with mice carrying two flanking locus of crossover in P1 (LoxP) sites in the same direction around the exon 8 of the *Pdha1* gene (PDH$^{fl/fl}$). CD4-expressing cells in these mice have a deletion of the *Pdha1* exon 8 due to the action of the Cre recombinase, followed by a recombination of LoxP sites (PDH$^{fl/fl}$ CD4 Cre+). (Created in BioRender)

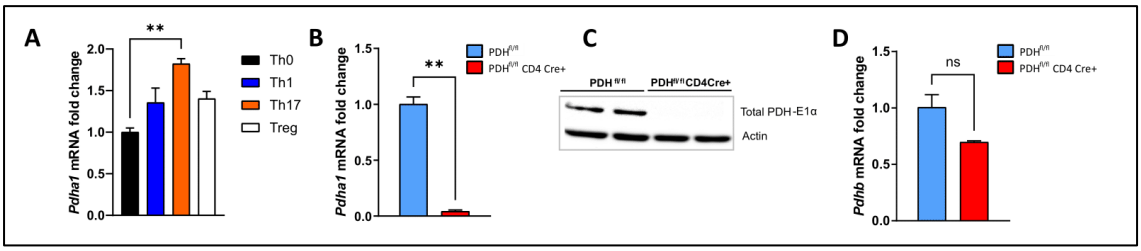

Figure 1: PDH-deficient T cells do not express *Pdhα1* mRNA nor PDH-E1α protein.

(A, B and D) mRNA levels of *Pdhα1* (A,B) or *Pdhb* (D) genes were determined by RT-qPCR in indicated cell types. ΔΔCt values were normalized to Tbp expression. **(A)** Naïve T cells were isolated from spleen and lymph nodes of wild-type (WT) mice and differentiated *in vitro* into T helper (Th) 0, Th1, Th17, and regulatory (Treg) T cells for 3 days. For each subset differentiation, different cytokine cocktails were added to the media: Th0 with anti-CD3, anti-CD28, anti-IFNγ, and IL-2; Th1 with anti-CD3, anti-CD28, IL-12 and IL-2; Th17 with anti-CD3, anti-CD28, IL-6, anti-IFNγ, and TGFβ; Treg with anti-CD3, anti-CD28, IL-2, anti-IFNγ, and TGFβ. Data are means±SEM (n=3) and representative of 2 trials. **(B)** Total CD4 T cells were isolated from spleen and lymph nodes of control ($PDH^{fl/fl}$) and PDH-deficient ($PDH^{fl/fl}$ CD4 Cre+) mice and activated for 24h with anti-CD3 and anti-CD28. Data are means±SEM (n=3) and representative of 2 trials. **(C)** Representative immunoblot detecting total PDH-E1α protein in 24h activated total CD4 T cells from two control ($PDH^{fl/fl}$) and two PDH deficient ($PDH^{fl/fl}$ CD4 Cre+) mice. Actin detection as a loading control. Data are representative of 4 mice per genotype in 2 independent experiments. **(D)** Total CD4 T cells were isolated from spleen and lymph nodes of $PDH^{fl/fl}$ and $PDH^{fl/fl}$ CD4 Cre+ mice and activated for 24h with anti-CD3 and anti-CD28. Data are means±SEM (n=3) and representative of 2 trials. **p≤0.01; ns: non-significant.

1.2. Interfering with PDH expression in T cells reduces the experimental autoimmune encephalomyelitis (EAE) disease burden

Th17 cells have been implicated in multiple sclerosis (MS), a chronic inflammatory autoimmune disease in which autoreactive CD4 T cells recognizing myelin antigens are activated and attack the central nervous system (CNS) (Aranami and Yamamura, 2008). A mouse model of MS symptoms is experimental autoimmune encephalomyelitis (EAE) which was established almost 90 years ago (Rivers et al., 1933; Rivers and Schwentker, 1935). In this model, mice develop MS-like symptoms after approximately 9 days post-immunization with MOG protein in combination with CFA and pertussis toxin injections. The immune reaction is mainly driven by inflammatory Th17 cells migrating to the CNS, making it a commonly used model to study Th17 cells' immune response *in vivo* (Constantinescu et al., 2011; Rangachari and Kuchroo, 2013).

The data shown in the previous section would suggest that PDH is crucial for Th17 cell function, and hence that PDH-deficiency in $CD4^+$ T cells would alter the severity of autoimmune pathologies in EAE. Indeed, upon induction of EAE, mice harboring PDH-deficient T cells ($PDH^{fl/fl}$ CD4 Cre+) showed significantly lower disease burden, as observed by the reduced EAE score, and increased survival compared to wild-type (WT) littermate control ($PDH^{fl/fl}$) mice (Figure 2A and 2B).

As the symptoms of EAE are caused by neurodegeneration which is triggered by inflammatory Th17 cells activated in secondary lymphoid organs that migrated to the CNS, T cells from the brain and spleen of these mice 14 days post-EAE induction were examined via flow cytometry. First, similar percentages and numbers of infiltrating $CD45^+$ cells in the brain and spleens of control and $PDH^{fl/fl}$ CD4 Cre+ mice were observed, which suggests that the migration of total leukocytes is not affected by the CD4-specific PDH deletion (Figure 2C and 2D). However, reduced infiltration of Th17 ($ROR\gamma T^+$) and Treg ($CD25^+FoxP3^+$) cells in $PDH^{fl/fl}$ CD4 Cre+ mice's brains was discerned (Figure 2E and 2F), whilst the percentages of Th1 ($Tbet^+$) cells in the brain were similar between WT and $PDH^{fl/fl}$ CD4 Cre+ mice (Figure 2G). In the spleen, no differences in the percentage of Th subsets were detected (Figure 2E, 2F and 2G). This indicates that, in accordance with the reduction in EAE severity, the $PDH^{fl/fl}$ CD4 Cre+ mice have reduced relative frequencies of Th17 cells in the brain. Given the crucial role of Th17 in the pathology of EAE, pathogenic Th17 effector functions were analyzed by measuring the production of effector cytokines IFNγ and IL-17A in the CNS. In accordance with a less severe disease burden, a reduced percentage of $CD4^+$ T cells producing both IFNγ and IL-17A in

PDH$^{fl/fl}$ CD4 Cre+ mice in the brain was detected, whereas the frequencies of CD4^{+} T cells producing either of the cytokines did not show significant differences between genotypes (Figure 2H, 2I and 2J).

These results indicate that PDH has an important role in the effector function of Th17 cells *in vivo*.

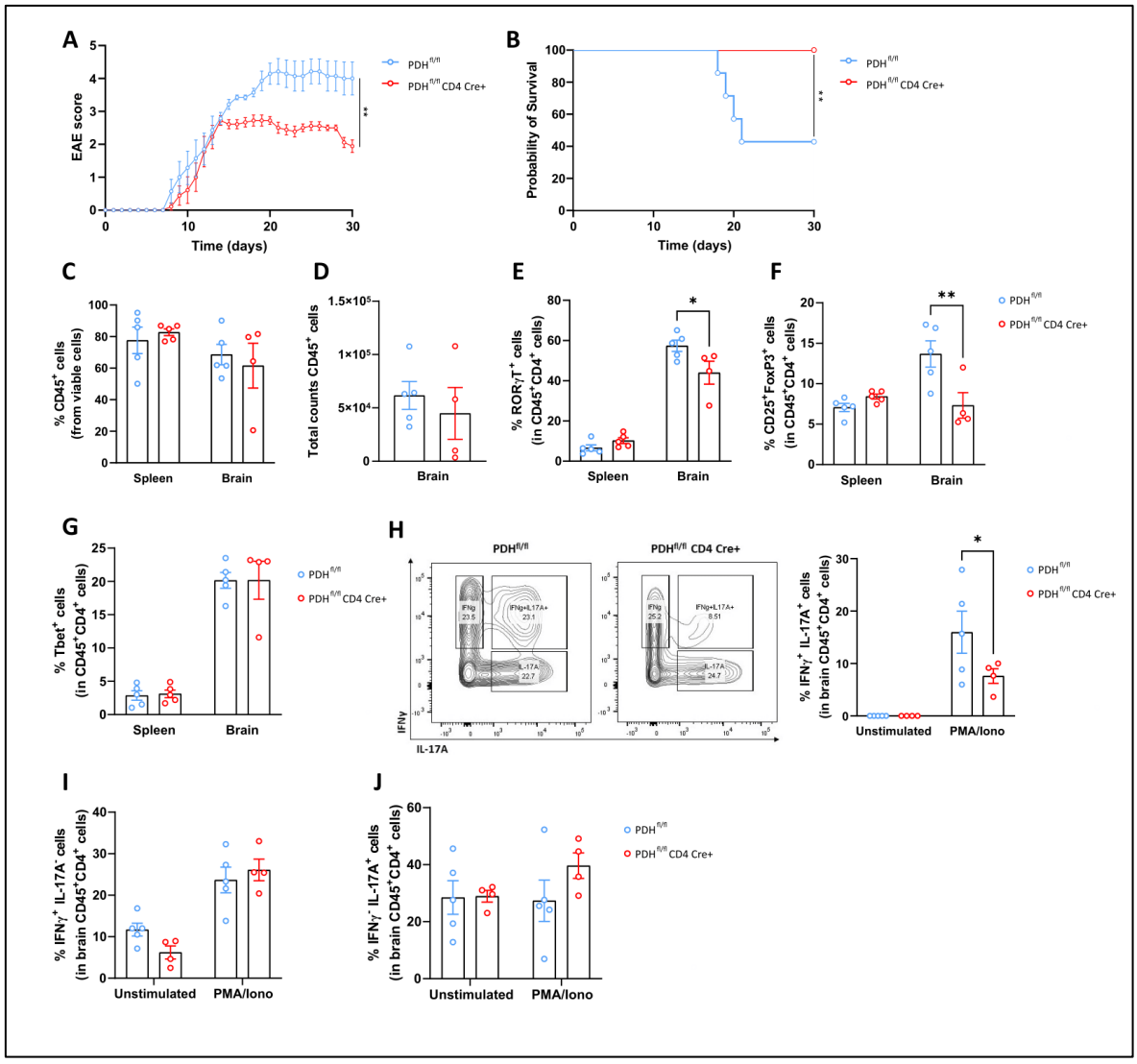

Figure 2: PDH ablation in T cells protects mice from severe EAE symptoms and impairs Th17 effector functions.

(A) EAE clinical scores for 30 days post-induction with pertussis toxin and MOG peptide in PDH$^{fl/fl}$ (n=7) and PDH$^{fl/fl}$ CD4 Cre+ (n=9) mice. Data are means±SEM. **(B)** Survival of the mice in (A). **(C)** Flow cytometric analysis (FCA) of frequencies of CD45^{+} cells from spleen and brain of PDH$^{fl/fl}$ and PDH$^{fl/fl}$ CD4 Cre+ mice at day 14 post-EAE induction amongst living cells. **(D)** FCA of total counts of CD45^{+} cells from the brain of mice in (C), gated from living cells. **(E)** Intracellular FCA of frequencies of RORγT^{+} cells from spleen and brain from mice in (C)

gated from living $CD45^+CD4^+$ cells. **(F)** Intracellular FCA of frequencies of $CD25^+FoxP3^+$ (Treg) cells from spleen and brain from mice in (C) gated from living $CD45^+CD4^+$ cells. **(G)** Intracellular FCA of frequencies of $Tbet^+$ (Th1) cells from spleen and brain from mice in (C) gated from living $CD45^+CD4^+$ cells. **(H)** Left: Representative contour plots of intracellular staining of IL-17A and IFNγ from the brain of mice in (C) gated from living $CD45^+CD4^+$ cells. Cells were stimulated with PMA/calcium ionophore/Brefeldin A (PMA/Iono) for 5h before staining. Plots are representative of 4 mice per genotype. Right: Intracellular FCA of frequencies of $IFN\gamma^+IL\text{-}17A^+$ cells from the brain of mice in (C) gated from living $CD45^+CD4^+$ cells. Cells were left unstimulated or stimulated for 5h with PMA/Iono before staining. **(I)** Intracellular FCA of frequencies of $IFN\gamma^+IL\text{-}17A^-$ cells from the brain of mice in (C) gated from living $CD45^+CD4^+$ cells. Cells were unstimulated or stimulated for 5h with PMA/calcium ionophore/Brefeldin A (PMA/Iono) before staining. **(J)** Intracellular FCA of frequencies of $IFN\gamma^-IL\text{-}17A^+$ cells from the brain of mice in (C) gated from living $CD45^+CD4^+$ cells. Cells were unstimulated or stimulated for 5h with PMA/calcium ionophore/Brefeldin A (PMA/Iono) before staining. **(C-J)** Data are means ±SEM (n=5-4). *p≤0.05; **p≤0.01.

1.3. PDH is needed for the full expression of IL-17 in Th17 cells *in vitro*

To dissect how PDH ablation impairs the functionality of Th17 cells, the differentiation potential of naïve CD4 T cells isolated from control and $PDH^{fl/fl}$ CD4 Cre+ spleens and lymph nodes into Th17 cells *in vitro* was tested. To that end, naïve CD4 T cells were cultured for 3 days under Th17 cell skewing conditions as described in the previous section. Interestingly, only a slight decrease in Th17 cell differentiation as shown by percentages of $ROR\gamma T^{+}$ cells and RORγT mean fluorescence intensity (MFI) was observed (Figure 3A and 3B), while IL-17 production was drastically impaired (Figure 3C, 3D and 3E). Moreover, PDH deletion did not affect the differentiation and function of Th1 and Treg cells (Figure 3F, 3G and 3H). This indicates that Th17 cell differentiation does not rely on PDH as much as its effector function.

Taken together, the *in vitro* data recapitulated the *in vivo* results showing that PDH is essential for Th17 cells' effector functions.

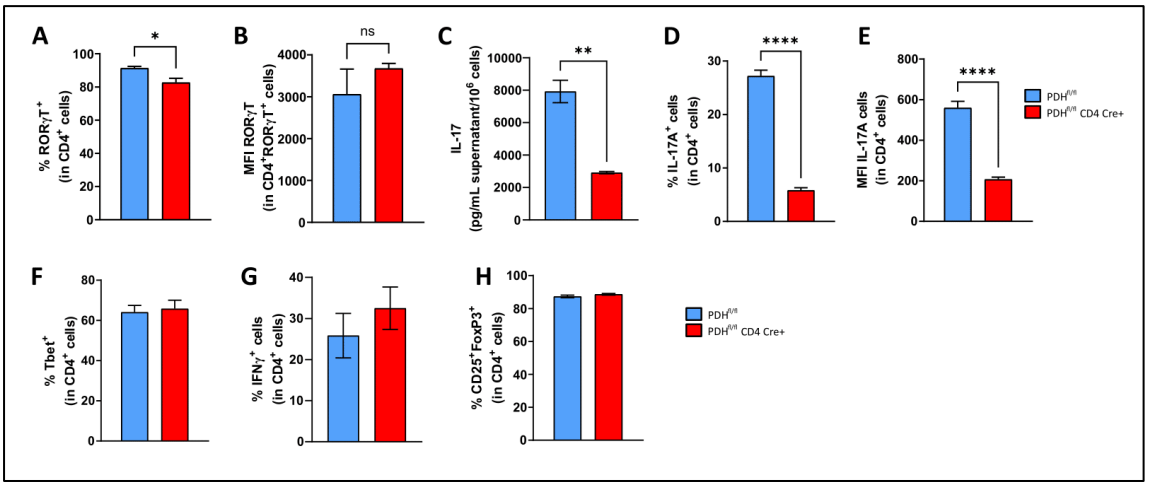

Figure 3: PDH-deficient Th17 cells show reduced production of IL-17A

(A-E) Naïve T cells were isolated from spleen and lymph nodes of $PDH^{fl/fl}$ and $PDH^{fl/fl}$ CD4 Cre+ mice and differentiated *in vitro* into Th17 cells. **(A)** Intracellular FCA of frequencies of RORγT$^+$ cells gated from living CD4$^+$ cells. Data are means ±SEM (n=3) and representative of 4 trials. **(B)** Quantification of FCA from RORγT MFI gated from living CD4$^+$RORγT$^+$ cells. Data are means ±SEM (n=3) and representative of 4 trials. **(C)** ELISA determination of IL-17 protein in supernatants. Data are mean±SEM (n=3) and representative of 3 trials. **(D)** Intracellular FCA of frequencies of IL-17A$^+$ cells gated from living CD4+ cells after 5h stimulation with PMA/Iono. Data are means ±SEM (n=3) and representative of 4 trials. **(E)** Quantification of FCA from IL-17A MFI, gated from living CD4+ cells. Data are means ±SEM (n=3) and representative of 4 trials. **(F-H)** Naïve T cells were isolated from spleen and lymph nodes of $PDH^{fl/fl}$ and $PDH^{fl/fl}$ CD4 Cre+ mice and *in vitro*-differentiated into Th1 (F,G) or Treg (H) cells for 3 days. **(F)** Intracellular FCA of frequencies of Tbet$^+$ cells gated on viable CD4$^+$ cells. **(G)** Intracellular FCA of frequencies of IFNγ$^+$ cells after 5hr stimulation with PMA/Iono, gated on viable CD4$^+$ cells. **(H)** Intracellular FCA of frequencies of CD25$^+$FoxP3$^+$ cells gated on viable CD4+ cells. Data are mean±SEM (n=3) and representative of 3 trials. *p≤0.05; **p≤0.01; **** p≤0.0001; ns: non-significant.

PART II

2.1. PDH restricts glucose metabolism of Th17 cells

PDH exhibits an essential role in glucose metabolism, connecting glycolysis and the mitochondrial TCA cycle. Metabolic rewiring is necessary for effector T cell functions such as cytokine production (DeBrosse and Kerr, 2016). It was therefore speculated that metabolic reprogramming of Th17 cells would be severely affected in the absence of PDH.

The expression of the major glucose transporter of T cells, Glut-1 (Macintyre et al., 2014) was measured via flow cytometry in *in vitro* differentiated Th17 cells. Glut-1 was significantly increased in PDH-ablated Th17 cells compared to their WT counterpart (Figure 4A). This was associated with and increased uptake of the fluorescent glucose analog 2-(N-(7-Nitrobenz-2-oxa-1,3-diazol-4-yl)Amino)-2-Deoxyglucose (2-NBDG) (Zou et al., 2005) (Figure 4B). Consistently, an increased glucose uptake was observed in PDH-deficient Th17 cells using mass spectrometry (MSpec) (Figure 4C). Altogether, these results indicate that Th17 cells might increase glucose metabolism upon PDH ablation.

To analyze the glycolytic activity in these cells, a glycolytic stress test and extracellular flux analysis by Seahorse was performed. This test measures the extracellular acidification rate (ECAR) of the cells after consecutive injections of glucose, oligomycin and 2-deoxyglucose (2-DG). In line with the increased glucose uptake, PDH-deficient Th17 cells showed an increased glycolysis and glycolytic capacity (Figure 4D, 4E and 4F). These data were further confirmed by augmented lactate release in the medium measured by YSI (Figure 4G), as well as the increased expression of hexokinase-1, enzyme that catalyzes the first and rate-limiting step of the glycolytic pathway (glucose to glucose-6-phosphate) (Palmer et al., 2015) (Figure 4H).

To delineate the glucose metabolic profile of Th17 cells and to reveal the differences between WT and $PDH^{fl/fl}$ CD4 Cre+ Th17 cells, ^{13}C-glucose isotopic tracing combined with mass spectrometry (MSpec) was used to track the flux of glucose-derived carbon atoms into glycolytic metabolites (cf. to Illustration 17) (Buescher et al., 2015). Surprisingly, no differences in the contribution of ^{13}C-glucose to pyruvate (M3 label) were observed (Figure 4I). Which would indicate that the flux in the glycolytic pathway remains unchanged despite the increased glucose uptake.

In summary, these data indicate that, in the absence of PDH, Th17 cells upregulate glycolysis without altering the flux to generate glucose-derived pyruvate.

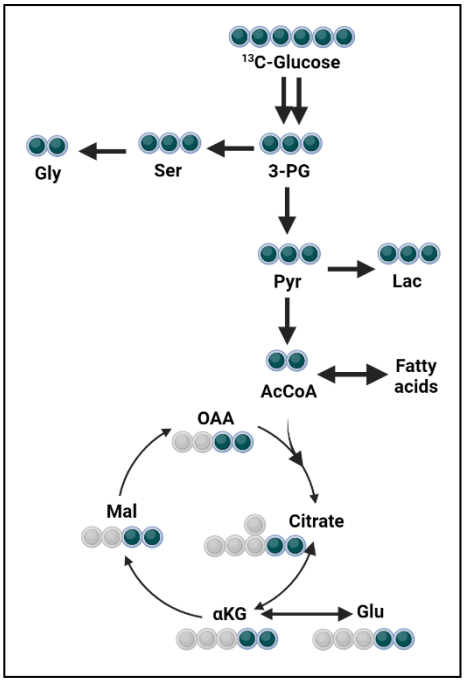

Illustration 17 : Glucose carbon atoms can be traced by following ^{13}C-labelled carbon atoms via MSpec.

Using heavy carbons (^{13}C; green carbons), glucose carbons are labeled and thus able to be detected through mass spectrometry into the different glucose-derived metabolites as the carbons coming from glucose will be heavier than the others (grey carbons). (Created in BioRender)

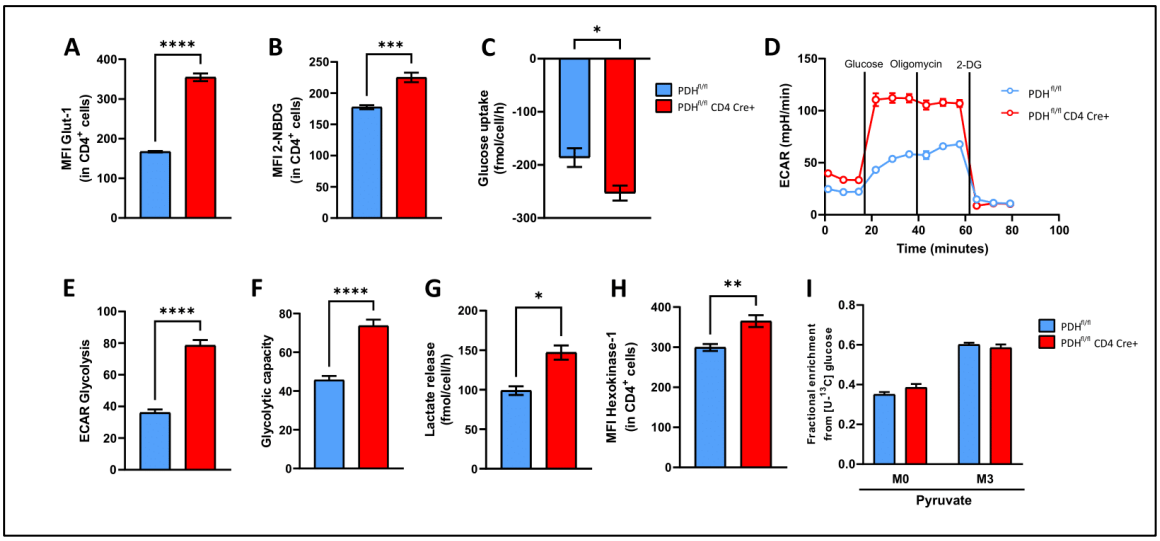

Figure 4 : PDH restricts the glycolytic activity of Th17 cells.

(A) Quantification of FCA from Glut-1 MFI from Th17 cells of PDH$^{fl/fl}$ and PDH$^{fl/fl}$ CD4 Cre+ mice, gated from living CD4+ cells. Data are means ±SEM (n=3) and representative of 3 trials. **(B)** Quantification of FCA from 2-NBDG MFI from Th17 cells of PDH$^{fl/fl}$ and PDH$^{fl/fl}$ CD4 Cre+ mice, gated from living CD4^{+} cells. Data are means ±SEM (n=3) and representative of 3 trials. **(C)** YSI quantification of glucose uptake from the medium of Th17 cells from PDH$^{fl/fl}$ and PDH$^{fl/fl}$ CD4 Cre+ mice. Data are mean±SEM (n=3) and representative of 2 trials. **(D)** Representative seahorse ECAR plot of Th17 cells of PDH$^{fl/fl}$ and PDH$^{fl/fl}$ CD4 Cre+ mice. Data are means ±SEM (n=3) and representative of 3 trials. **(E-F)** Seahorse quantification of glycolysis **(E)** and glycolytic capacity **(F)** from Th17 cells of PDH$^{fl/fl}$ and PDH$^{fl/fl}$ CD4 Cre+ mice. Data are means ±SEM (n=3) and representative of 3 trials. **(G)** YSI quantification of lactate released into the medium of Th17 cells PDH$^{fl/fl}$ and PDH$^{fl/fl}$ CD4 Cre+ mice. Data are mean±SEM (n=3) and representative of 2 trials. **(H)** Quantification of intracellular FCA from Hexokinase-1 MFI from Th17 cells of PDH$^{fl/fl}$ and PDH$^{fl/fl}$ CD4 Cre+ mice, gated from living CD4^{+} cells. Data are means ±SEM (n=3) and representative of 2 trials. **(I)** Mass isotopomer distributions (MID) of M0 and M3 pyruvate from Th17 cells of PDH$^{fl/fl}$ and PDH$^{fl/fl}$ CD4 Cre+ mice following 24h incubation with [U-$^{13}C_6$]-glucose. Data are means ±SEM (n=3) and representative of 2 trials. *p≤0.05; **p≤0.01; *** p≤0.001; **** p≤0.0001.

2.2. PDH stimulates the mitochondrial activity and glucose oxidation of Th17 cells

Glucose-derived pyruvate is either converted into lactate by the lactate dehydrogenase (LDH), or transported into the mitochondria via the mitochondrial pyruvate carrier (MPC) to serve as substrate for PDH and generate acetyl-CoA for the TCA cycle (cf. to illustration 8). Using ^{13}C-glucose isotope tracing, the contribution of glucose-derived carbons into metabolites of the TCA cycle was calculated (cf. to illustration 17). As the conversion of pyruvate into acetyl-CoA is impaired in PDH-deficient Th17 cells, a significant reduction in the levels of M2 labelled TCA metabolites was expected. Indeed, almost no contribution of ^{13}C-glucose to the formation of citrate, fumarate and malate was observed (Figure 5A, 5B and 5C), confirming that there was no flux from glucose into the TCA cycle in PDH$^{fl/fl}$ CD4 Cre+ Th17 cells. Furthermore, increased pyruvate secretion into the medium was measured in PDH-deficient Th17 cells, which suggests these cells are unable to metabolize pyruvate above a certain concentration threshold (Figure 5D).

Taken together, these results indicate that PDH$^{fl/fl}$ CD4 Cre+ Th17 cells are unable to convert pyruvate into acetyl-CoA for the TCA cycle and, thus, cannot metabolize pyruvate any further, forcing them to secrete it into the medium.

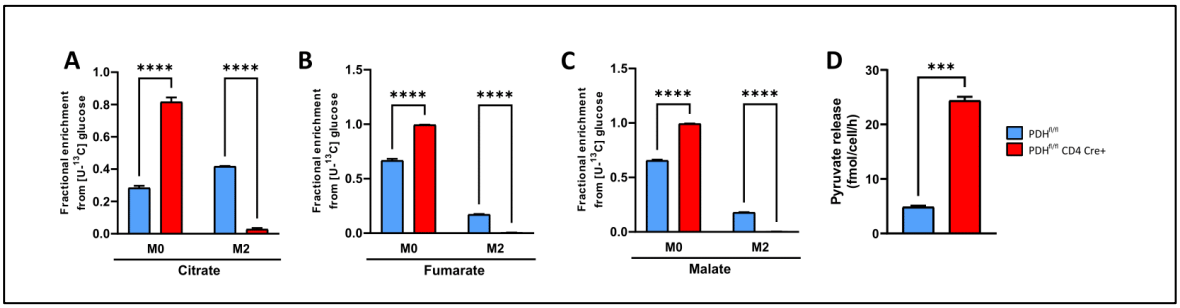

Figure 5 : PDH is essential for the glucose flux into the TCA cycle in Th17 cells.

(A-C) MID of M0 and M2 citrate **(A)**, fumarate **(B)** and malate **(C)** from Th17 cells of $PDH^{fl/fl}$ and $PDH^{fl/fl}$ CD4 Cre+ mice following 24h incubation with [U-$^{13}C_6$]-glucose. Data are means ±SEM (n=3) and representative of 2 trials. **(D)** GC/MS quantification of pyruvate release into the medium of Th17 cells from $PDH^{fl/fl}$ and $PDH^{fl/fl}$ CD4 Cre+ mice. Data are mean±SEM (n=3) and representative of 2 trials. *** p≤0.001; **** p≤0.0001.

2.3. PDH is essential for citrate generation from glutamine in Th17 cells

The previous results indicate that the contribution of glucose into the TCA cycle has been compromised in PDH-deficient Th17 cells. Another source of carbon atoms for the TCA cycle is glutamine. It has been previously shown that in Th17 cells glutamine metabolism is essential for differentiation and function by replenishing the TCA cycle at the level of α-ketoglutarate (cf. to illustration 11) (Johnson et al., 2018; Yoo et al., 2020).

To study the contribution of glutamine in PDH-deficient Th17 cells, ^{13}C-glutamine isotopic tracing was used (cf. to Illustration 18). Indeed, carbon atoms from glutamine were highly incorporated into TCA cycle metabolites such as fumarate and malate (M4 label) of PDH$^{fl/fl}$ CD4 Cre+ Th17 cells (Figure 6A and 6B). Accordingly, glutamine uptake was significantly increased in PDH-deficient Th17 cells (Figure 6C). However, an increased contribution of glutamine-derived carbon atoms into citrate, neither by oxidative (M4 label) nor by reductive (M5 label) metabolism, were detected (Figure 6D and 6E).

These results indicate that although glutamine was able to replenish some of the TCA cycle metabolites, the generation of citrate is dependent on glucose-derived PDH-produced acetyl-CoA.

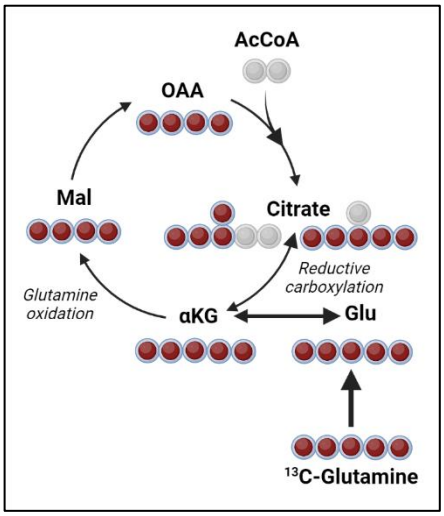

Illustration 18 : Glutamine carbon atoms can be traced by following ^{13}C-labelled carbon atoms via MSpec.

Using heavy carbons (^{13}C; red carbons), glutamine carbons are labeled and thus able to be detected through mass spectrometry into the different glutamine-derived metabolites as the carbons coming from glutamine will be heavier than the others (grey carbons). (Created in BioRender)

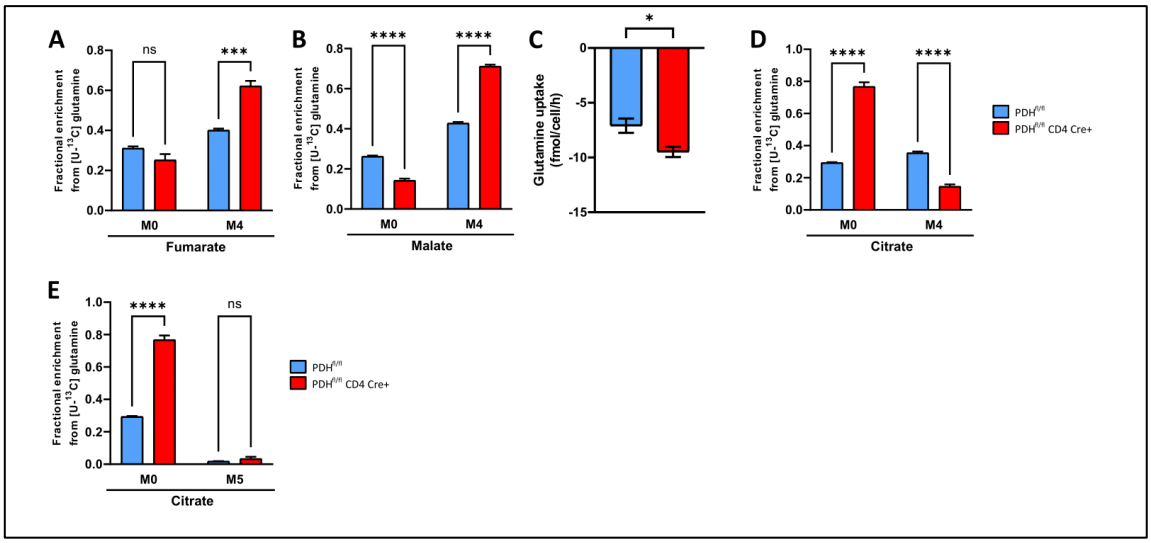

Figure 6 : PDH function is crucial for the generation of glutamine-derived citrate in the TCA cycle in Th17 cells.

(A-B) MID of M0 and M4 fumarate **(A)** and malate **(B)** from Th17 cells of $PDH^{fl/fl}$ and $PDH^{fl/fl}$ CD4 Cre+ mice following 24h incubation with [U-$^{13}C_5$]-glutamine. Data are means ±SEM (n=3) and representative of 2 trials. **(C)** YSI quantification of glutamine uptake from the medium of Th17 cells from $PDH^{fl/fl}$ and $PDH^{fl/fl}$ CD4 Cre+ mice. Data are mean±SEM (n=3) and representative of 2 trials. **(D)** MID of M0 and M4 citrate from Th17 cells of $PDH^{fl/fl}$ and $PDH^{fl/fl}$ CD4 Cre+ mice following 24h incubation with [U-$^{13}C_5$]-glutamine. Data are means ±SEM (n=3) and representative of 2 trials. **(E)** MID of M0 and M5 citrate from Th17 cells of $PDH^{fl/fl}$ and $PDH^{fl/fl}$ CD4 Cre+ mice following 24h incubation with [U-$^{13}C_5$]-glutamine. Data are means ±SEM (n=3) and representative of 2 trials. *** p≤0.001; **** p≤0.0001; ns: non-significant.

2.4. Th17 cells rely on PDH for oxidative phosphorylation

Based on the results obtained by ^{13}C labeled isotope tracing that showed impaired oxidation of glucose within the TCA cycle and an incomplete glutamine anaplerosis, further analysis of the functional state of the mitochondria were warranted. Thus, a mitochondrial stress test using Seahorse on WT and PDH-deficient Th17 cells to analyze the oxygen consumption rate (OCR), a proxy for overall activity of oxidative phosphorylation (OXPHOS) was performed. This test evaluates the OCR after oligomycin, carbonyl cyanide 4-(trifluoromethoxy)phenylhydrazone (FCCP) and antimycin A/rotenone consecutive injections. As expected, a significant reduction in the basal oxygen consumption rate (OCR), maximal respiration, OCR-dependent ATP production and spare respiratory capacity were observed, indicating impaired OXPHOS in $PDH^{fl/fl}$ CD4 Cre+ Th17 cells (Figure 7).

These results are in line with the compromised glucose flux into the TCA cycle and indicate a drastic impairment in mitochondrial respiration in PDH-deficient Th17 cells.

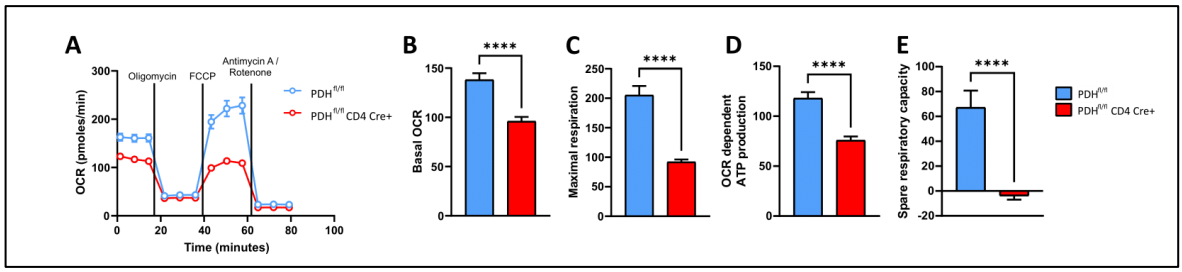

Figure 7 : PDH is required for oxygen consumption in Th17 cells.

(A) Representative seahorse OCR plot of Th17 cells of $PDH^{fl/fl}$ and $PDH^{fl/fl}$ CD4 Cre+ mice. Data are means ±SEM (n=3) and representative of 3 trials. **(B - E)** Seahorse quantification of basal OCR **(B)**, maximal respiration **(C)**, OCR dependent ATP **(D)**, and spare respiratory capacity **(E)** from Th17 cells of $PDH^{fl/fl}$ and $PDH^{fl/fl}$ CD4 Cre+ mice. Data are means ±SEM (n=3) and representative of 3 trials. **** p≤0.0001.

2.5. PDH is crucial for the transcription of enzymes related to mitochondrial metabolism

To reveal the differences in the metabolic rewiring seen in PDH-deficient Th17 cells at the transcriptional level, RNA sequencing (RNA-seq) on *in vitro* differentiated WT and $PDH^{fl/fl}$ CD4 Cre+ Th17 cells was performed. Indeed, an overall reduced expression of TCA cycle enzymes was observed (Figure 8A). Furthermore, a lower expression of genes involved in OXPHOS was also detected (Figure 8B and 8C).

These transcriptomic data support the *in vitro* results, showing impaired TCA cycle enzyme and OXPHOS gene transcription in the absence of PDH in Th17 cells.

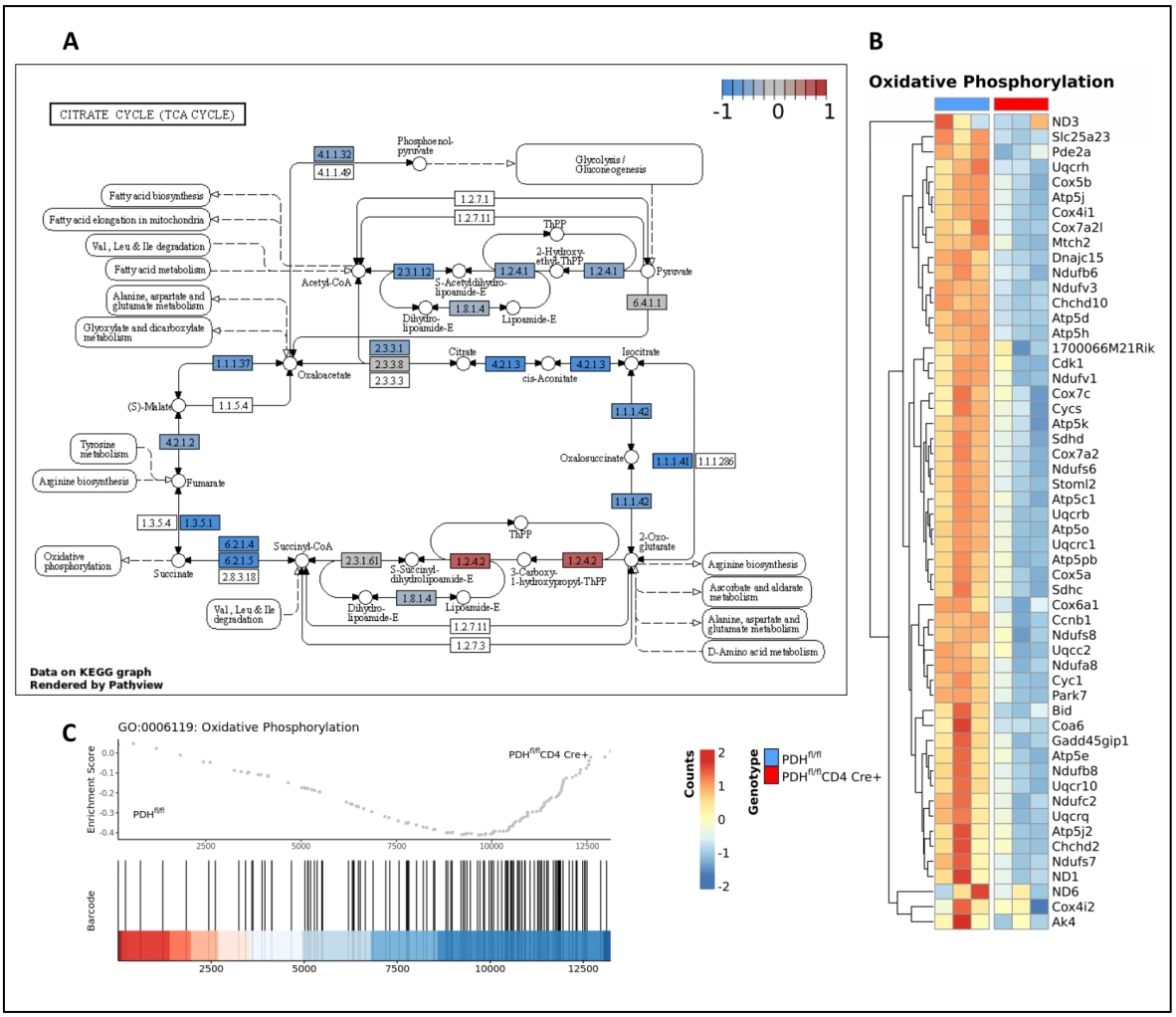

Figure 8 : PDH is crucial for the regulation of the transcription of TCA and OXPHOS-related genes in Th17 cells.

(A) KEGG map of gene expression (log2) changes in the TCA cycle pathway in PDH$^{fl/fl}$ CD4 Cre+ vs. PDH$^{fl/fl}$ Th17 cells. **(B)** Heatmap of the significantly enriched GO:0006119 (Oxidative Phosphorylation) in GSEA of PDH$^{fl/fl}$ CD4 Cre+ vs. PDH$^{fl/fl}$ Th17 cell RNA-Seq. Displayed is the gene expression level for core enriched genes from each sample scaled by gene. **(C)** Barcode plot of significantly enriched GO:0006119 (Oxidative Phosphorylation) in GSEA of PDH$^{fl/fl}$ CD4 Cre+ vs. PDH$^{fl/fl}$ Th17 cell RNA-Seq. Upper panel shows the running enrichment score with the lower showing occurrence of associated genes in the ranked distribution of expression differences. (Normalized enrichment score -1.74, p adjust 0.02).

2.6. Production of TCA metabolites in Th17 cells is dependent on PDH function

As PDH-deficient Th17 cells had impaired mitochondrial respiration, the measurement of total amounts of TCA metabolites in these cells was performed. It was seen that genetic ablation of *Pdha1* in Th17 cells resulted in reduced quantities of all TCA cycle metabolites including, α-ketoglutarate, fumarate, malate and, most significantly, citrate (Figure 9).

In summary, all the results of this part exhibit drastic changes in the central carbon metabolism caused by the absence of PDH in Th17 cells. Namely, $PDH^{fl/fl}$ CD4 Cre+ Th17 cells show impaired glucose flux into the TCA cycle and partial glutamine anaplerosis. This has important consequences in the generation of TCA metabolites, specifically citrate.

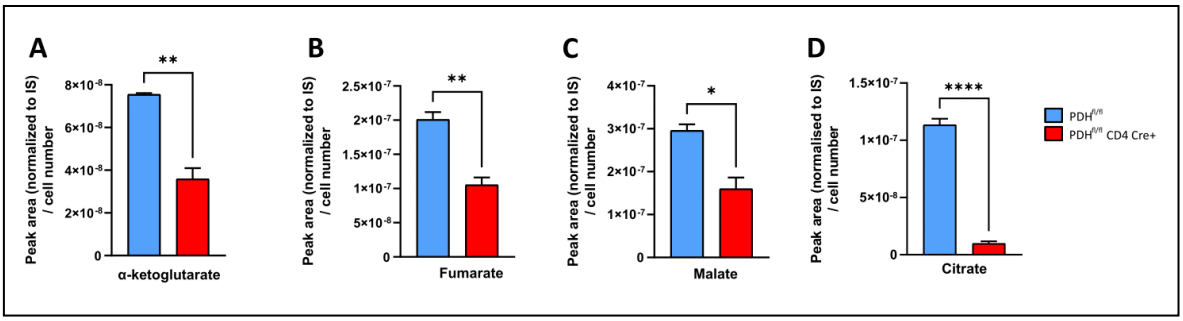

Figure 9 : PDH is necessary for the maintenance of the levels of TCA metabolites pools in Th17 cells.

(A-D) Quantification of intracellular α-ketoglutarate **(A)**, fumarate **(B)**, malate **(C)** and citrate **(D)** in $PDH^{fl/fl}$ and $PDH^{fl/fl}$ CD4 Cre+ Th17 cells by MSpec. Data are mean±SEM (n=3) and representative of 2 trials. *p≤0.05; **p≤0.01; **** p≤0.0001.

PART III

3.1. PDH is essential for *de novo* production of fatty acids and proliferation in Th17 cells

Citrate is an essential metabolite for an array of processes such as *de novo* lipid synthesis. For that purpose, mitochondrial citrate is translocated to the cytoplasm, where ATP citrate lyase (ACLY) converts it to OAA and acetyl-CoA. Acetyl-CoA is used as a building block for lipid synthesis (Pietrocola et al., 2015; Wellen et al., 2009; Zhao et al., 2016).

As previously stated, citrate amounts were drastically impaired in PDH-deficient Th17 cells (Figure 9D). As a consequence, ^{13}C-glucose, as well as ^{13}C-glutamine, isotope tracing revealed almost no contribution of these substrates in the synthesis of octadecenoic acid, also known as oleic acid, required for the fluidity of lipid membranes, in PDH-deficient Th17 cells (Figure 10A, 10B and 10C) (Kurniawan et al., 2017).

Lipids are crucial for the generation of daughter cells upon proliferation, as they are a major constituent of membrane structures such as nucleus and plasma membrane (de Jong et al., 2014; Pietrocola et al., 2015). To determine the effect of the lack of *de novo* lipid synthesis on proliferation, CellTrace Violet (CTV) labeled WT and PDH$^{fl/fl}$ CD4 Cre+ naïve cells after three days of Th17 cell differentiation were analyzed. As expected, a significant decrease in the division index, calculated as previously described (Roederer, 2011), was observed. This result points toward a reduced proliferative potential of PDH$^{fl/fl}$ CD4 Cre+ Th17 cells compared to WT Th17 cells (Figure 10D).

Taken together, these results indicate that PDH-deficient Th17 cells are unable to generate lipids *de novo*, which is associated with impaired proliferation.

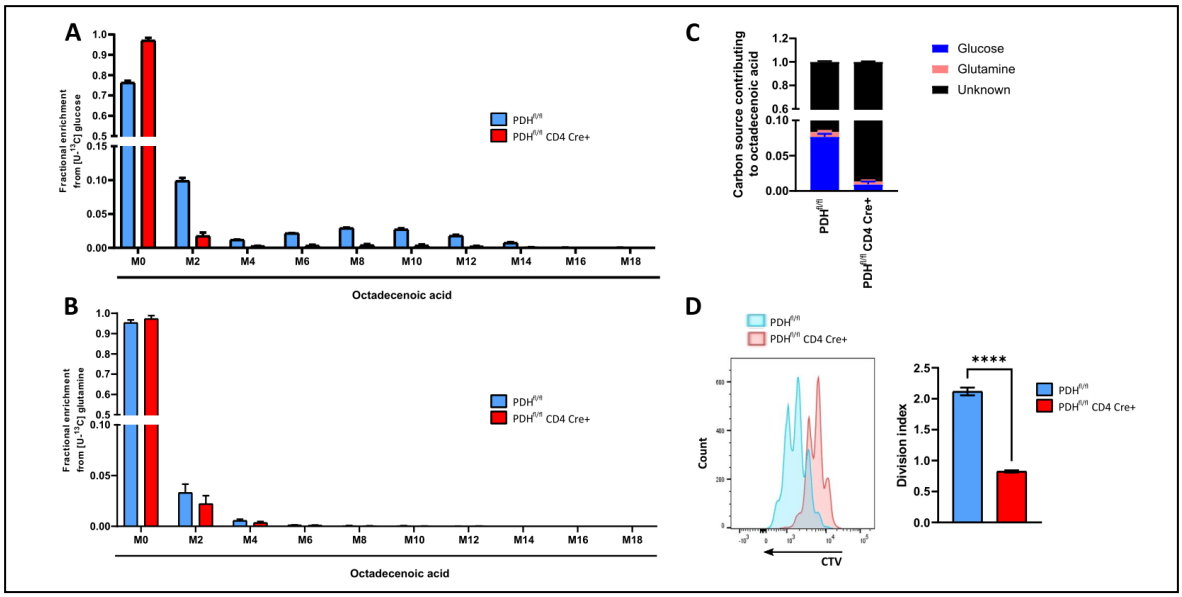

Figure 10 : *De novo* fatty acid generation and consequent proliferation are dependent on PDH in Th17 cells. **(A-B)** MID from M0 to M18 of octadecenoic acid in $PDH^{fl/fl}$ and $PDH^{fl/fl}$ CD4 Cre+ Th17 cells incubated for 24hr with [U-$^{13}C_6$]-glucose **(A)** or [U-$^{13}C_6$]-glutamine **(B)**. Data are mean±SEM (n=3) and representative of 2 trials. **(C)** Distribution of carbon sources contributing to octadecenoic acid in $PDH^{fl/fl}$ and $PDH^{fl/fl}$ CD4 Cre+ Th17 cells. Data are mean±SEM (n=3) and representative of 2 trials. **(D)** Left: representative FCA plot of the proliferation of CTV labeled Th17 cells of $PDH^{fl/fl}$ and $PDH^{fl/fl}$ CD4 Cre+ mice. Right: Division index Th17 cells from FCA. Data are means ±SEM (n=3) and representative of 3 trials. **** p≤0.0001.

3.2. PDH expression in Th17 cells limits extracellular lipid dependence for survival and OXPHOS

In the previous section, it was shown that PDH-deficient Th17 cells were capable of dividing at minimal capacity. This led us to study the source of the lipids necessary for this process.

The ability of PDH-deficient Th17 cells to uptake lipids from the extracellular medium was analyzed. To that end, control and $PDH^{fl/fl}$ CD4 Cre+ Th17 cells were cultured with fluorescently labeled palmitate (Bodipy FL C16) and its uptake was measured via flow cytometry (Field et al., 2020). Interestingly, an increased uptake of Bodipy FL C16 in $PDH^{fl/fl}$ CD4 Cre+ compared to control Th17 cells was observed (Figure 11A).

Analysis of the effects of lipid deprivation on control and PDH-deficient Th17 cells was performed by comparing their survival, proliferation and basal OCR. Differentiating the Th17 cells in medium with (w/) or without (w/o) lipids led to significantly impaired survival and proliferation (Figure 11B, 11C and 11D). Although control Th17 cells were also affected by the lipid deprivation, the effects on PDH-deficient cells were more significant (Figure 11B, 11C and 11D). Furthermore, $PDH^{fl/fl}$ CD4 Cre+ Th17 cells showed a drastic reduction in basal OCR upon lipid deprivation (Figure 11E).

These results indicate that extracellular lipids are essential carbon sources for survival, proliferation and OXPHOS, especially in $PDH^{fl/fl}$ CD4 Cre+ Th17 cells.

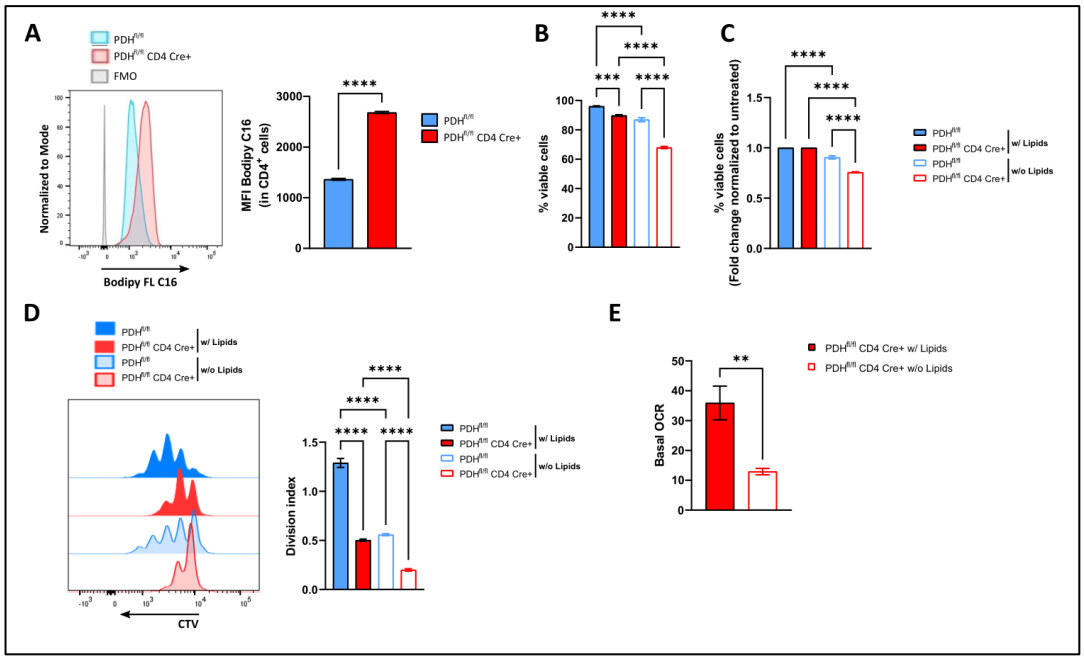

Figure 11 : PDH function is required in Th17 cells to be less dependent on extracellular lipids for basal OXPHOS and survival.

(A) Left: representative FCA of Bodipy FL C16 labeled Th17 cells of PDH$^{fl/fl}$ and PDH$^{fl/fl}$ CD4 Cre+ mice. Right: Quantification of FCA from Bodipy FL C16 MFI from Th17 cells, gated from living CD4^{+} cells. Data are means ±SEM (n=3) and representative of 3 trials. **(B)** Frequencies of living cells of Th17 cells of PDH$^{fl/fl}$ and PDH$^{fl/fl}$ CD4 Cre+ mice differentiated in full IMDM with (w/) lipids or without (w/o) lipids. Data are means ±SEM (n=3) and representative of 3 trials. **(C)** Fold changes of (B) normalized to untreated condition. Data are means ±SEM (n=3) and representative of 3 trials. **(D)** Left: representative FCA of the proliferation of CTV labeled Th17 cells of PDH$^{fl/fl}$ and PDH$^{fl/fl}$ CD4 Cre+ mice in full IMDM with or without lipids. Right: Division index Th17 cells from FCA in full IMDM w/ or w/o lipids. Data are means ±SEM (n=3) and representative of 3 trials. **(E)** Seahorse quantification of basal OCR from Th17 cells of PDH$^{fl/fl}$ CD4 Cre+ mice differentiated in full IMDM w/ or w/o lipids. Data are means ±SEM (n=3) and representative of 3 trials. **p≤0.01; *** p≤0.001; **** p≤0.0001.

3.3. PDH restricts the induction of CD36 and lipid uptake in Th17 cells

Based on the previous results showing an increased lipid uptake by PDH-deficient Th17 cells, the analysis of the mechanism driving this effect was performed. Long-chain fatty acids (LCFA) are dependent on transporters to enter cells, one of the most important ones being CD36 (Koundouros and Poulogiannis, 2020). When measuring CD36 expression via flow cytometry, a significant increase in $PDH^{fl/fl}$ CD4 Cre+ Th17 cells compared to WT Th17 cells was observed (Figure 12A).

FA uptake and increased anabolic processes requires activation of metabolic regulators. In particular, mammalian target of rapamycin complex 1 (mTORC1) that control CD36 expression and proliferation, is central to controlling this process in T cells metabolism (Angela et al., 2016; Wang et al., 2014; Wipperman et al., 2019). Thus, it was hypothesized that increased FA dependency of PDH-deficient CD4 T cells involves a heightened activity of mTORC1.

Indeed, an induction in phosphorylation, and thus, activation, of mTOR (p-mTOR) and its downstream target ribosomal protein S6 (p-S6) were observed (Figure 12B and 12C). Moreover, pharmacological inhibition of mTOR by Torin 1 and rapamycin reduced the levels of Bodipy FL C16 uptake and CD36 of $PDH^{fl/fl}$ CD4 Cre+ Th17 cells similar to that of WT controls (Figure 12D, 12E, 12F and 12G).

These results indicate that in the absence of PDH, mTOR drives and increases the expression of its target CD36 in Th17 cells, leading to an augmented uptake of lipids.

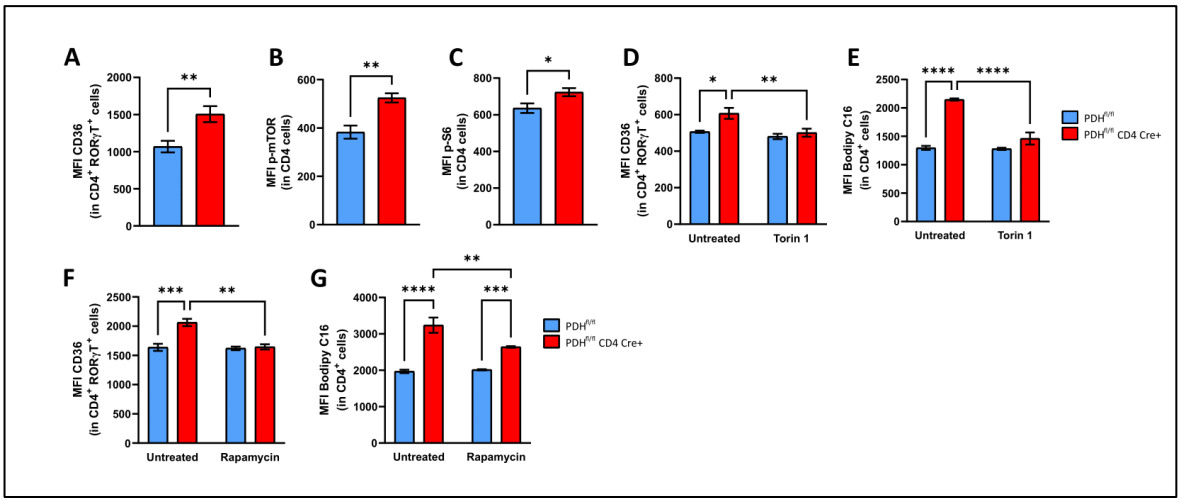

Figure 12 : PDH restricts mTOR-target CD36 expression for lipid uptake in Th17 cells.

(A-C) Quantification of FCA of CD36 MFI **(A)**, intracellular p-mTOR MFI **(B)** and intracellular p-S6 MFI **(C)** from Th17 cells of $PDH^{fl/fl}$ and $PDH^{fl/fl}$ CD4 Cre+ mice, gated from living $CD4^+ROR\gamma T^+$ or living $CD4^+$ cells. Data are means ±SEM (n=3) and representative of 3 trials. **(D-E)** Quantification of FCA of CD36 MFI **(D)** and Bodipy FL C16 MFI **(E)** from Th17 cells of $PDH^{fl/fl}$ and $PDH^{fl/fl}$ CD4 Cre+ mice differentiated with or without Torin 1 (100 nM), gated from living $CD4^+ROR\gamma T^+$ or living $CD4^+$ cells. Data are means ±SEM (n=3) and representative of 3 trials. **(F-G)** Quantification of FCA of CD36 MFI **(F)** and Bodipy FL C16 MFI **(G)** from Th17 cells of $PDH^{fl/fl}$ and $PDH^{fl/fl}$ CD4 Cre+ mice differentiated with or without Rapamycin (100 nM), gated from living $CD4^+ROR\gamma T^+$ or living $CD4^+$ cells. Data are means ±SEM (n=3) and representative of 3 trials. *p≤0.05; **p≤0.01; *** p≤0.001; **** p≤0.0001.

3.4. PDH restricts glutamine-dependent increase of mTOR activity in Th17 cells

mTOR activity is mainly induced by an array of amino acids, including glutamine (Takahara et al., 2020). It was shown in previous sections of this thesis that glutaminolysis as well as glutamine uptake are increased in $PDH^{fl/fl}$ CD4 Cre+ Th17 cells (Figure 6A, 6B and 6C). Thus, it was hypothesized that the induction of the mTOR-CD36 axis is a consequence of the increased glutamine metabolism.

To that end, control and $PDH^{fl/fl}$ CD4 Cre+ Th17 cells were differentiated in media with or without glutamine. Supporting the hypothesis, PDH-deficient Th17 cells differentiated under glutamine deprivation reduced the phosphorylation of mTOR, the expression of CD36 and the lipid uptake to control levels (Figure 13).

Collectively, the data indicate that enhanced glutamine metabolism leads to activation of mTOR-dependent increase in CD36, which sustains FA metabolism, which is required for proliferative potential of PDH-deficient Th17 cells. It was therefore revealed that PDH plays a pivotal role in a metabolic feedback loop regulating Th17 function.

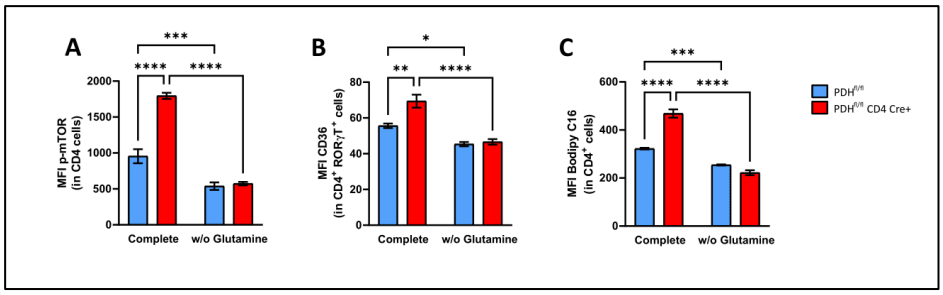

Figure 13 : PDH limits the glutamine-dependent induction of the mTOR-CD36-lipid uptake axis.

(A-C) Quantification by FCA of intracellular p-mTOR MFI **(A)**, CD36 MFI **(B)** and Bodipy FL C16 MFI **(C)** from Th17 cells of $PDH^{fl/fl}$ and $PDH^{fl/fl}$ CD4 Cre+ mice differentiated with (Complete) or without (w/o) glutamine, gated from living $CD4^{+}ROR\gamma T^{+}$ or living $CD4^{+}$ cells. Data are means ±SEM (n=3) and representative of 2 trials. *p≤0.05; **p≤0.01; *** p≤0.001; **** p≤0.0001.

PART IV

4.1. PDH is crucial for histone acetylation in Th17 cells

As previously shown, PDH-deficient Th17 cells generate very low amounts of citrate (Figure 9D). Citrate is essential for the generation of acetyl-CoA, used for post-translational modifications, namely histone acetylation (Pietrocola et al., 2015).

This information indicates that there might be alterations on histone acetylation upon PDH deletion. Thus, histone 3 (H3) acetylation was measured by immunoblotting in control and $PDH^{fl/fl}$ CD4 Cre+ Th17 cells. In line with the decreased intracellular pool of citrate, acetylation at lysine (K) 23 (H3K27Ac) and total H3 acetylation were reduced in PDH-deficient Th17 cells compared to WT (Figure 14A). To track the carbon atoms from glucose to the acetylation of histones, ^{13}C-glucose isotope tracing was used. Thus, the amount of carbon atoms derived from glucose that reached H3 for mono-acetylation (M2 label) or di-acetylation (M4 label) was measured. Consistently with the total histone measurement, a significantly lower M2 and M4 labeling from glucose in H3 acetylation was observed (Figure 14B and 14C).

This data suggest that the metabolic alterations in PDH-deficient Th17 cells impair post-translational modifications such as histone acetylation.

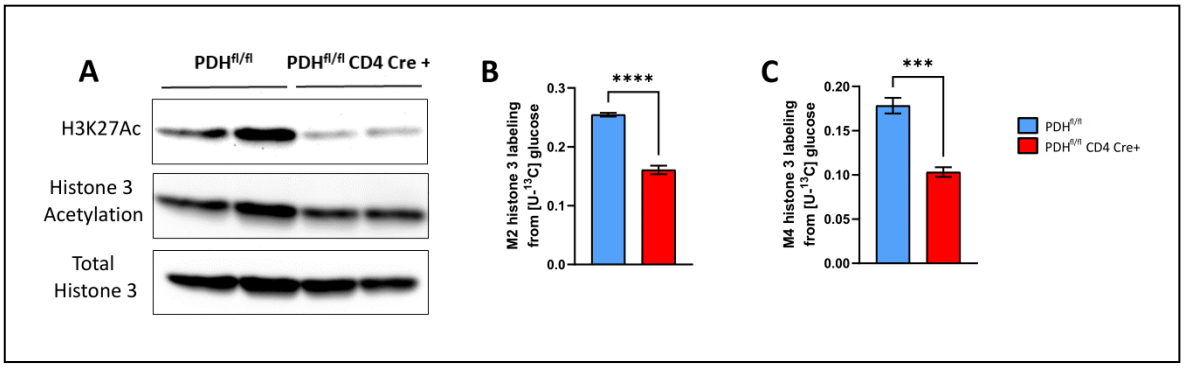

Figure 14 : PDH is required for histone 3 acetylation in Th17 cells.

(A) Representative immunoblots showing histone 3 lysine 27 acetylation (H3K27Ac) and histone 3 acetylation in Th17 cells from two $PDH^{fl/fl}$ and two $PDH^{fl/fl}$ CD4 Cre+ mice. Total histone 3 detection as a loading control. Data are representative of 4 mice per genotype. **(B)** M2 labeling into H3 acetylation from [U-$^{13}C_6$]-glucose in $PDH^{fl/fl}$ and $PDH^{fl/fl}$ CD4 Cre+ Th17 cells**.** Data are mean±SEM (n=4). **(C)** M4 labeling into H3 acetylation from [U-$^{13}C_6$]-glucose in $PDH^{fl/fl}$ and $PDH^{fl/fl}$ CD4 Cre+ Th17 cells**.** Data are mean±SEM (n=4). *** p≤0.001; **** p≤0.0001.

4.2. PDH in Th17 cells is essential for chromatin openness at Th17 cell-signature genes loci

Histone acetylation allows for the chromatin to be permissible for transcription (Li et al., 2007). Based on the previous results, the chromatin accessibility in control and PDH-deficient *in vitro* Th17 cells was studied by assay for transposase-accessible chromatin sequencing (ATAC-seq) as previously described (Buenrostro et al., 2015, 2013).

Consistently with the immunoblot data, a lower median chromatin accessibility in $PDH^{fl/fl}$ CD4 Cre+ Th17 cells compared to control cells was observed (Figure 15A). The ATAC-seq results were combined with the RNA-seq data to explore which loci were the most affected by the epigenetic changes in PDH-deficient Th17 cells and had consequences in their expression. It was observed that the decrease in accessibility and expression was especially pronounced in the *Il17a* and *Il17f* genes, encoding for the cytokines IL-17A and Il-17F, respectively (Figure 15B). Interestingly, although accessibility of the *Rorc* locus that encodes RORγT was reduced, the expression remained unaltered (Figure 15B). This data is in line with the near to normal expression of RORγT observed *in vitro* by flow cytometry (Figure 3A and 3B). Other Th17 cell-signature genes such as *Il23r*, *Smad3* and *Hif1a* also showed decreased chromatin accessibility and gene expression (Figure 15C).

Taken together, these results connect the changes in metabolism observed in PDH-deficient Th17 cells with epigenetic modifications and transcription of Th17 cell-signature genes.

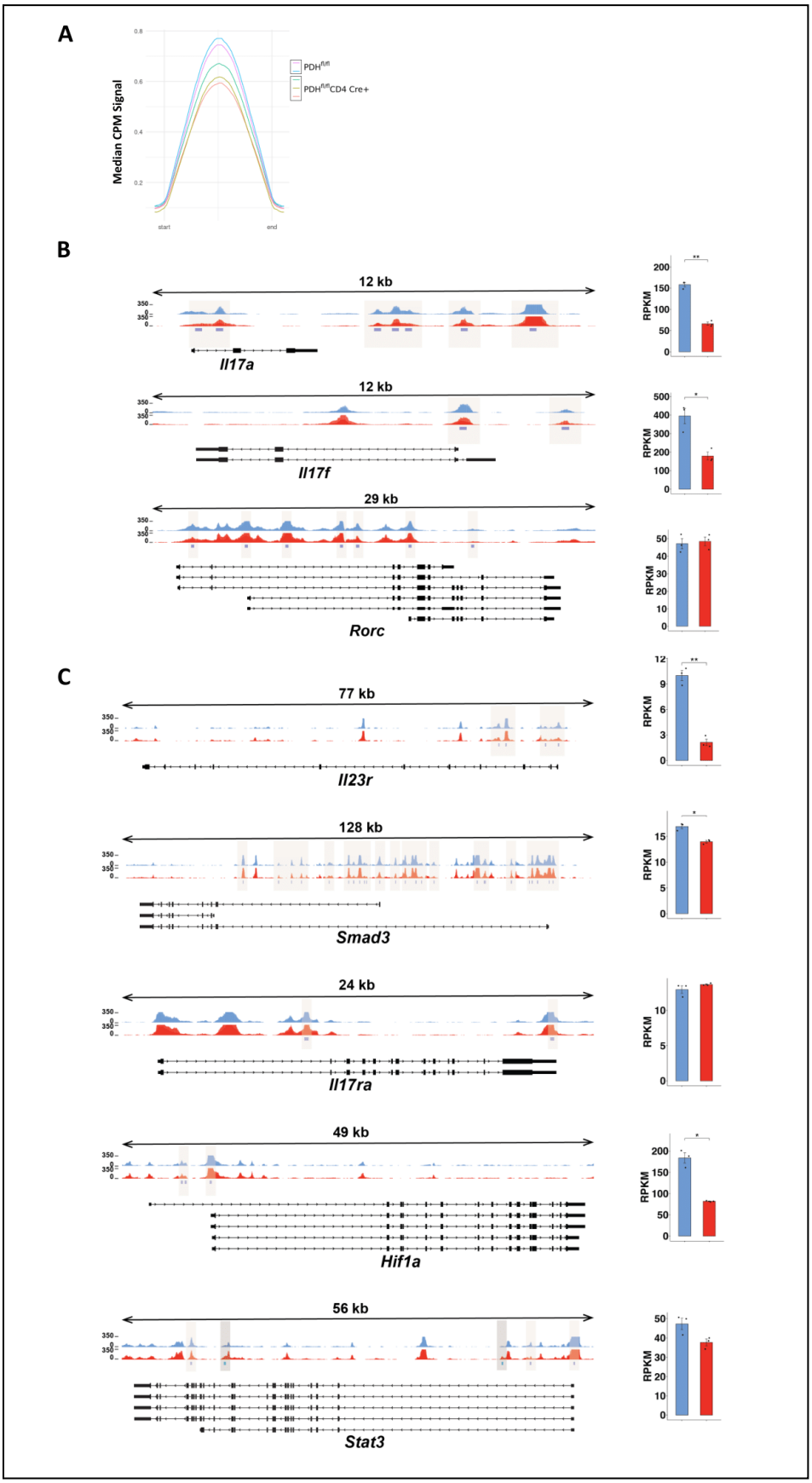

Figure 15 : PDH increases chromatin accessibility at Th17 cell-signature genes loci in Th17 cells.

(A) Metagene plots depicting the binned median chromatin accessibility signal from peak start to peak end for all genomic regions with significantly differential accessibility between $PDH^{fl/fl}$ and $PDH^{fl/fl}$ CD4 Cre+ Th17 cells. Y-axis represents the median CPM signal. Blue and purple lines represent ATAC-seq of two $PDH^{fl/fl}$ samples. Green, brown and red lines represent ATAC-seq of three $PDH^{fl/fl}$ CD4 Cre+ samples. **(B)** Left: Plot of chromatin accessibility at the *Il17a, Il17f* and *Rorc* loci in $PDH^{fl/fl}$ and $PDH^{fl/fl}$ CD4 Cre+ Th17 cells. Light violet bars depict significantly differentially accessible regions (DBS) as identified by DiffBind. Right: Quantitation of *Il17a, Il17f* and *Rorc* mRNA levels (RPKM) in $PDH^{fl/fl}$ and $PDH^{fl/fl}$ CD4 Cre+ Th17 cells as measured by RNA-seq. (C) Left: Chromatin accessibility of the *Il23r, Smad3, Il17ra, Hif1a* and *Stat3* loci in $PDH^{fl/fl}$ and $PDH^{fl/fl}$ CD4 Cre+ Th17 cells. The light violet bars depict significantly differentially accessible regions (DBS) as identified by DiffBind. Right: Levels of *Il23r, Smad3, Il17ra, Hif1a* and *Stat3* mRNA expression (RPKM) in $PDH^{fl/fl}$ and $PDH^{fl/fl}$ CD4 Cre+ Th17 cells as measured by RNA-seq. *p≤0.05; **p≤0.01.

PART V

5.1. Acetate restores histone acetylation and citrate levels in PDH-deficient Th17 cells

PDH is the only enzyme that converts pyruvate to acetyl-CoA, which is required for the generation of citrate (DeBrosse and Kerr, 2016) and it was shown in this thesis that PDH deletion in Th17 cells has severe metabolic, epigenetic and functional consequences.

It is tempting to speculate that treating PDH-deficient Th17 cells with acetate, a short-chain fatty acid (SCFA), would restore their function, as acetate can be converted into acetyl-CoA by acetyl-CoA synthetase (Bulusu et al., 2017; Comerford et al., 2014; Qiu et al., 2019). Hence, it was assumed that the acetate treatment would replenish acetyl-CoA in PDH-deficient cells, bypassing PDH deficiency.

Whether acetate treatment could rescue the deficits on the epigenetic modifications in PDH-deficient Th17 cells was first analyzed. Indeed, acetate treatment restored H3 acetylation to comparable levels as WT Th17 cells (Figure 16A). Thus, ^{13}C-acetate isotope tracing was used to measure the amount of carbon atoms derived from acetate that reached H3 for mono-acetylation (M2 label) or di-acetylation (M4 label). In line with the data in Figure 16A, increased M2 and M4 labeling from acetate in H3 acetylation was detected in PDH-deficient Th17 cells (Figure 16B and 16C). This result would suggest that acetate is the main source of carbon atoms for histone acetylation upon PDH ablation.

In parallel, ^{13}C-acetate contributed to the generation of TCA metabolites: citrate, fumarate and malate to similar or increased levels compared to acetate treatment in WT Th17 cells (Figure 16D, 16E and 16F).

Importantly, acetate treatment restored the citrate pool in PDH-deficient Th17 cells (Figure 16G).

Collectively, these results show that acetate treatment rescues PDH-deficient Th17 cells' epigenetic modifications and restore citrate levels.

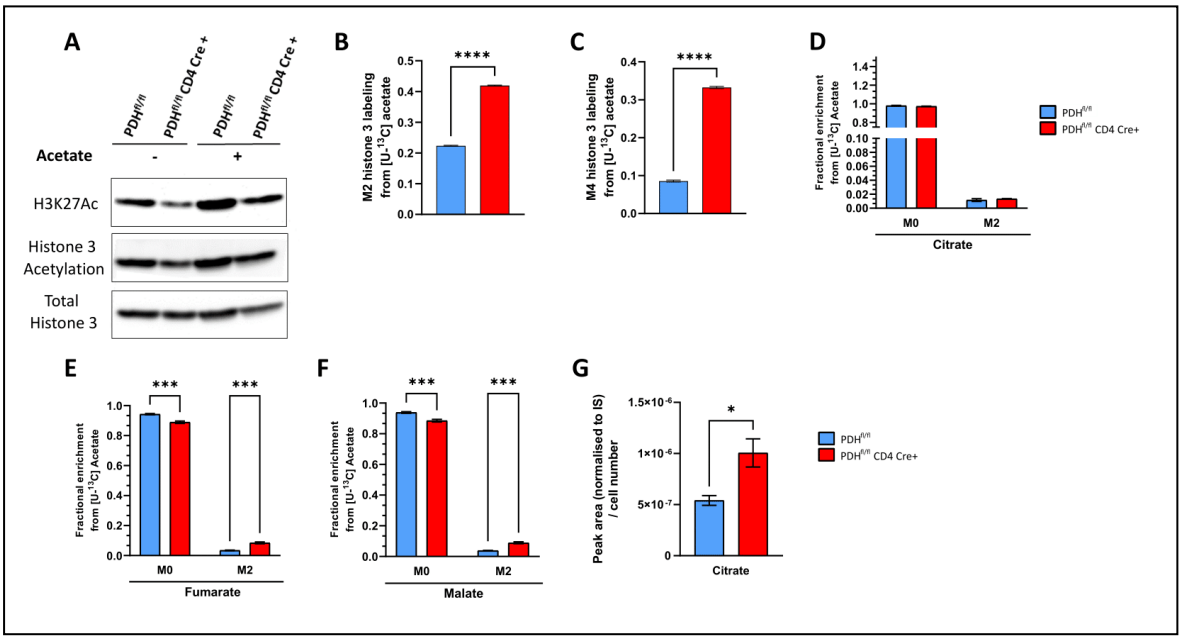

Figure 16 : Acetate treatment rescues H3 acetylation and citrate pool in PDH-deficient Th17 cells.

(A) Representative immunoblots showing histone 3 lysine 27 acetylation (H3K27Ac) and histone 3 acetylation in Th17 cells from two $PDH^{fl/fl}$ and two $PDH^{fl/fl}$ CD4 Cre+ mice treated with or without acetate (10 mM). Total histone 3 detection as a loading control. Data are representative of 4 mice per genotype. **(B)** M2 labeling into H3 acetylation from [U-$^{13}C_2$]-acetate in $PDH^{fl/fl}$ and $PDH^{fl/fl}$ CD4 Cre+ Th17 cells**.** Data are mean±SEM (n=4). **(C)** M4 labeling into H3 acetylation from [U-$^{13}C_2$]-acetate in $PDH^{fl/fl}$ and $PDH^{fl/fl}$ CD4 Cre+ Th17 cells**.** Data are mean±SEM (n=4). **(D-F)** MID of M0 and M2 citrate **(D)**, fumarate **(E)** and malate **(F)** from Th17 cells of $PDH^{fl/fl}$ and $PDH^{fl/fl}$ CD4 Cre+ mice following 72h incubation with [U-$^{13}C_2$]-acetate. Data are means ±SEM (n=3) and representative of 2 trials. **(G)** Quantification of intracellular citrate in Th17 cells from $PDH^{fl/fl}$ and $PDH^{fl/fl}$ CD4 Cre+ mice following 72h differentiation with acetate. Data are mean±SEM (n=3) and representative of 2 trials. *p≤0.05; *** p≤0.001; **** p≤0.0001.

5.2. PDH-deficient Th17 cells recover their ability to generate lipids and proliferate after acetate treatment

Based on the finding that acetate treatment restored the citrate pool of PDH-deficient Th17 cells, it was hypothesized that treatment with acetate would also rescue the ability of PDH-deficient Th17 cells to generate lipids *de novo*. Indeed, when measuring the ^{13}C-acetate contribution to the generation of octadecenoic acid in mutant Th17 cells, similar levels compared to WT Th17 cells were detected (Figure 17A).

In line with the increased fatty acid synthesis, acetate treatment improved PDH$^{fl/fl}$ CD4 Cre+ Th17 cells proliferation (Figure 17B).

These data indicate that acetate restores lipid synthesis and proliferation in PDH$^{fl/fl}$ CD4 Cre+ Th17 cells.

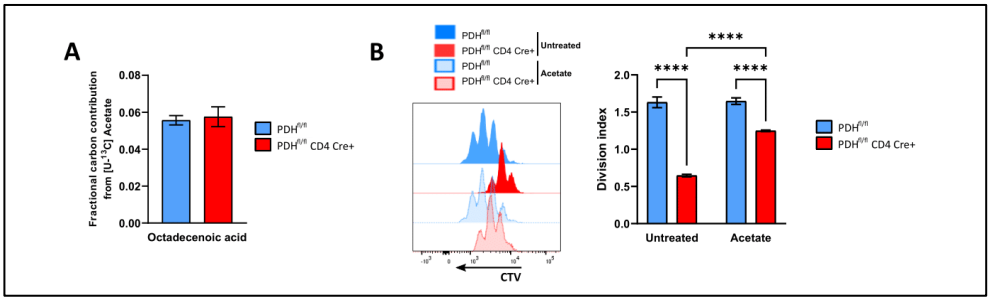

Figure 17 : Acetate rescues *de novo* lipid synthesis and improves PDH-deficient Th17 proliferation.

(A) Fractional carbon contribution of ^{13}C-acetate to octadecenoic acid in PDH$^{fl/fl}$ and PDH$^{fl/fl}$ CD4 Cre+ Th17 cells. Data are mean±SEM (n=3) and representative of 2 trials. **(B)** Left: representative FCA of the proliferation of CTV labeled Th17 cells of PDH$^{fl/fl}$ and PDH$^{fl/fl}$ CD4 Cre+ mice in full IMDM with or without acetate. Right: Division index Th17 cells from FCA in full IMDM with or without acetate. Data are means ±SEM (n=3) and representative of 3 trials. **** p≤0.0001.

5.3. Acetate treatment restores central carbon metabolism in PDH-deficient Th17 cells

As acetate-derived carbon atoms were incorporated into TCA metabolites, a mitochondrial stress test was performed on PDH-deficient and -sufficient Th17 cells, with or without acetate to analyze their OXPHOS. Increased levels of basal OCR in $PDH^{fl/fl}$ CD4 Cre+ Th17 cells after acetate treatment reaching comparable levels to WT Th17 cells were detected (Figure 18A).

In addition, it was examined whether the acetate treatment also affected the glycolytic pathway. An extracellular flux analysis was performed and the ECAR was measured in PDH-deficient and control Th17 cells, with or without acetate treatment. Acetate-treated PDH-deficient Th17 cells reduced their glycolytic rate to WT levels (Figure 18B). In accordance, Glut-1 expression and glucose uptake measured by 2-NBDG were also reduced after acetate treatment in PDH-deficient Th17 cells (Figure 18C and 18D).

Taken together, the data suggest that acetate is able to restore OXPHOS and glycolytic activity in $PDH^{fl/fl}$ CD4 Cre+ to the level of control Th17 cells.

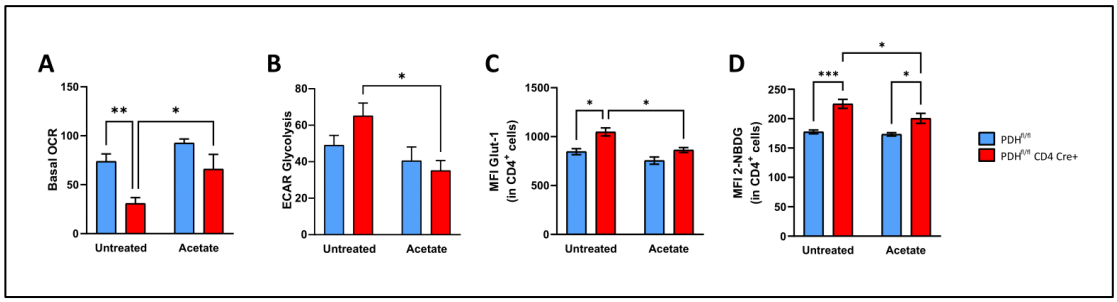

Figure 18 : PDH-deficient Th17 cells adopt wild-type central carbon metabolism upon acetate treatment.

(A-B) Seahorse quantification of basal OCR **(A)** and glycolysis **(B)** from Th17 cells differentiated with or without acetate of $PDH^{fl/fl}$ and $PDH^{fl/fl}$ CD4 Cre+ mice. Data are means ±SEM (n=3) and representative of 3 trials. **(C-D)** Quantification of FCA from Glut-1 MFI **(C)** and 2-NBDG MFI **(D)** from Th17 cells differentiated with or without acetate of $PDH^{fl/fl}$ and $PDH^{fl/fl}$ CD4 Cre+ mice, gated from living $CD4^+$ cells. Data are means ±SEM (n=3) and representative of 3 trials. *p≤0.05; **p≤0.01; ***p≤0.001.

5.4. Acetate treatment downregulates the mTOR-CD36 activity in PDH-deficient Th17 cells

It was shown that PDH-deficient Th17 cells increased glutamine uptake as a partially compensatory mechanism (Figure 6C), which in turn induced the mTOR-CD36 axis and fatty acid uptake (Figure 13). Therefore, it was speculated that acetate treatment would normalize these metabolic parameters in PDH-deficient Th17 cells. As expected, acetate administration normalized glutamine uptake (Figure 19A). Consequently, phosphorylation of mTOR as well as CD36 expression and Bodipy FL C16 uptake of $PDH^{fl/fl}$ CD4 Cre+ Th17 cells were restored to levels similar to that of WT Th17 cells (Figure 19B, 19C and 19D).

These data show that acetate restores the balance of glutamine-mTOR-CD36 axis in PDH-deficient Th17 cells.

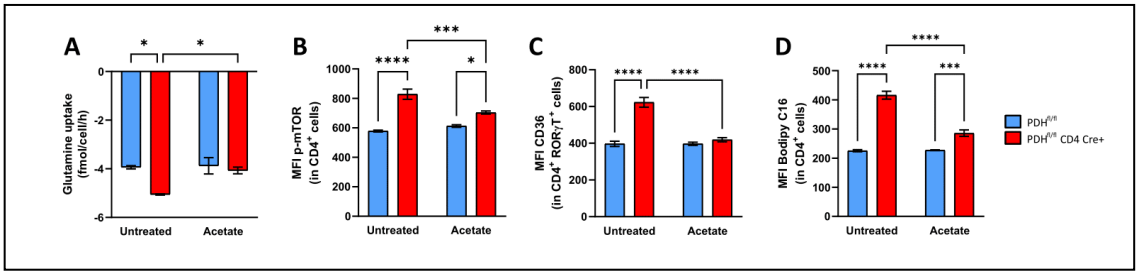

Figure 19 : PDH-deficient Th17 cells restore their mTOR-CD36 axis to WT levels after acetate treatment.

(A) YSI quantification of glutamine uptake from the medium of Th17 cells from $PDH^{fl/fl}$ and $PDH^{fl/fl}$ CD4 Cre+ mice with or without acetate. Data are mean±SEM (n=3) and representative of 2 trials. **(B-D)** Quantification of FCA of intracellular p-mTOR MFI **(B)**, CD36 MFI **(C)** and Bodipy FL C16 MFI **(D)** from Th17 cells of $PDH^{fl/fl}$ and $PDH^{fl/fl}$ CD4 Cre+ mice differentiated with or without acetate, gated from living $CD4^+RORγT^+$ or living $CD4^+$ cells. Data are means ±SEM (n=3) and representative of 2 trials. *p≤0.05; *** p≤0.001; **** p≤0.0001.

5.5. Acetate treatment restores IL-17A production in PDH-deficient Th17 cells

The main effect that PDH ablation has on Th17 cells is the impairment of their effector functions both *in vivo* (Figure 2) and *in vitro* (Figure 3). As acetate treatment restored the observed metabolic and epigenetic defects caused by PDH-ablation, it was tempting to speculate that also IL-17 expression could be increased in mutant Th17 cells by such a treatment. In line with the metabolic and signaling data presented, $PDH^{fl/fl}$ CD4 Cre+ Th17 cells fully restored IL-17A production (Figure 20).

Taken together, the results of this part show that acetate bypasses the need for glucose-derived citrate, and restores the epigenetic, metabolic and functional defects of Th17 cells caused by PDH deficiency.

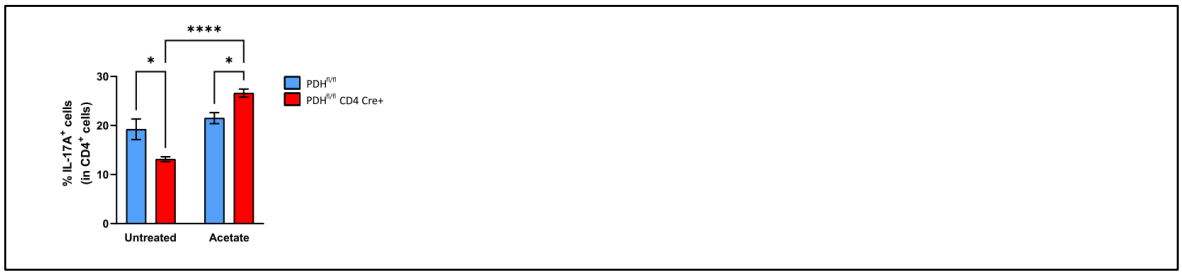

Figure 20 : PDH-deficient Th17 cells recover their production of IL-17A upon acetate treatment.

Intracellular FCA of frequencies of IL-17A$^+$ cells gated from living CD4$^+$ cells after 5h stimulation with PMA/Iono. Data are means ±SEM (n=3) and representative of 4 trials. *p≤0.05; *** p≤0.001.

DISCUSSION AND PERSPECTIVES

Th17 cells' function is crucial for the host's defense against extracellular pathogens. However, their uncontrolled activation can lead to autoimmune diseases like multiple sclerosis and rheumatoid arthritis (Aranami and Yamamura, 2008; Basu et al., 2013).

In the last two decades, it has been shown that there is a tight connection between metabolism and the function of effector T cells (Buck et al., 2015; Chapman et al., 2020; Chapman and Chi, 2022; Rangel Rivera et al., 2021). In this study, the catalytic E1α subunit of PDH in T cells was genetically targeted, thus, disconnecting the glycolytic pathway from the mitochondrial TCA cycle.

Th17 cells have been described to rely on glycolytic ATP and regulators such as myc, HIF-1α, and mTOR for differentiation and function (Angiari et al., 2020; Dang et al., 2011; Michalek et al., 2011; Shi et al., 2011; Wang et al., 2011; K. Xu et al., 2021; Zhang et al., 2019). This study shows that Th17 cells also require PDH for their effector functions *in vivo* and *in vitro*.

In this thesis, it was shown that Th17 cells rewire their metabolism and increase the uptake of glucose, glutamine and fatty acids to ensure their survival and proliferation upon PDH ablation. However, PDH-deficient Th17 cells suffered from the lack of citrate that is essential for *de novo* fatty acid synthesis and histone acetylation. This impairment has severe consequences on cell proliferation and the epigenetic landscape, which confer the functionality and the effector functions of Th17 cells *in vivo* or *in vitro*. Finally, the effects of PDH deletion could be reverted by the addition of exogenous acetate, causing the metabolism to return to a WT phenotype. This allowed the production of the essential pool of citrate, restoring the effector function of PDH-deficient Th17 cells.

PART I. LACK OF PYRUVATE DEHYDROGENASE IN T CELLS PROTECTS MICE FROM SEVERE EXPERIMENTAL AUTOIMMUNE ENCEPHALOMYELITIS SYMPTOMS

Experimental autoimmune encephalomyelitis (EAE) is a commonly used model mimicking multiple sclerosis (MS) symptoms in mice, which is driven by Th17 cells (Aranami and Yamamura, 2008; Rivers et al., 1933; Rivers and Schwentker, 1935). Here, it was shown that PDH is expressed to a high level in Th17 cells and EAE served as a disease model to study the role of this enzyme in Th17 cells *in vivo*.

T cell-specific PDH deletion in mice lead to milder symptoms of EAE while having similar initiation phases. This is in line with the reduced Th17 cell abundance and their impaired effector function in the brain. This data shows that PDH is essential for Th17 effector function *in vivo* during EAE pathogenesis.

The role of PDH is to transform pyruvate into acetyl-CoA once the former is transported into the mitochondria by the mitochondrial pyruvate carrier (MPC) (Bricker et al., 2012; Herzig et al., 2012; Zangari et al., 2020). A recent study has shown that Vav-Cre MPC1 fl/fl mutant mice, which do not express *Mpc1* in hematopoietic cells, suffer more severe EAE symptoms compared to their control littermates (Ramstead et al., 2020). These results are in clear contrast to the findings on the T cell specific deletion of PDH. However, Vav-cre mediated MPC1-deletion occurs during hematopoiesis, which affects T cell development and favors the selection of a more activated T cell pool (Ramstead et al., 2020). This might serve as a likely explanation for these discrepancies between the studies. Alternatively, PDH-dependent pyruvate conversion to acetyl-CoA, and not its transport to the mitochondria, might be essential for the effector functions of Th17 cells during EAE, which would be interesting to investigate in follow up studies.

Similarly, deletion of PDH in bone marrow and hematopoietic stem cells by the use of the Mx1-Cre, showed impaired development of T cells in the thymus which is not the case when using the CD4 Cre as a deleter, as previously shown (Jun et al., 2021). This study shows that the developmental stage in which the deletion takes place is an important point to consider, which can lead to different outcomes.

These studies would suggest that the timing of the PDH deletion as well as its specific function are essential to regulate Th17 effector function *in vivo*.

Another study showed that CD8 T cells' cytotoxic function is reduced by activation of PDH through lactate, which is found in high concentrations in the tumor microenvironment (TME), allowing tumor cells to survive (Elia et al., 2022). Mechanistically, the authors have shown that CD8 T cells rely on pyruvate carboxylase (PC) for anaplerosis of the TCA cycle and succinate production. The latter is secreted and taken up in an autocrine fashion through the succinate receptor 1 (SUCNR1) which signals for the production of cytotoxic molecules. On the other hand, PDH activity promotes the classical TCA cycle function, where succinate is converted into fumarate and not secreted, thus reducing cytotoxic function of the CD8 T cells. In this study, the authors show that in the TME, where lactate concentrations are increased, inhibition of PDH can restore CD8 T cells' cytotoxic abilities by inducing the PC pathway.

Collectively, these studies demonstrate the relevance of PDH in effector T cell function and its therapeutic potential in different contexts.

The importance of other metabolic enzymes in Th17 effector function *in vivo* have been recently shown by others. For instance, Xu et al. showed that in the case of ablation of LDH in T cells, mice were completely protected against EAE (K. Xu et al., 2021). In another study, mice harboring a deletion of the glucose transporter Glut3 were also protected from EAE (Hochrein et al., 2022). Consistently, a study has shown that pharmacological induction of the tetramerization of pyruvate kinase isoform 2 (PKM2), the enzyme catalyzing the conversion of phosphoenolpyruvate to pyruvate reduced the disease severity of mice suffering from EAE (Angiari et al., 2020). Taken together, these reports show that metabolism is essential for Th17 cell function *in vivo*, especially in models of MS.

PART II. PYRUVATE DEHYDROGENASE IS ESSENTIAL FOR TH17 CELLS' CARBON METABOLISM

The metabolic regulation is important for maintenance of Th cell functionality (Marelli-Berg et al., 2012). It has been previously shown that overactive or insufficient glycolysis and/or OXPHOS can impair T cell function (Kurniawan et al., 2020a; Mak et al., 2017).

In this study, it was shown that PDH-deficient Th17 cells increased their glucose uptake and glycolytic activity while the glucose flux into the TCA cycle was drastically impaired as well as OXPHOS. Thus, PDH activity is essential for the physiological flux of glucose in Th17 cells.

Surprisingly, Gerriets et al. have shown that pharmacological inhibition of PDK1, an inhibitor of PDH, activates PDH and also impairs the function of Th17 cells (Gerriets et al., 2015). Thus, it would be tempting to speculate that the overactivation of PDH or the lack of PDH activity could interfere with Th17 cell function. Together, these results would suggest that regulation of PDH and glucose contribution to the TCA cycle is important to maintain Th17 cell functionality. This underlines the important regulatory role of PDH for this Th cell subset.

Although glucose is considered as the main energy source for effector cells, glutamine also contributes to the TCA cycle (Yoo et al., 2020). A previous study demonstrated that the ablation of glutaminase impaired Th17 cell differentiation and function, which led to protection from Th17-driven inflammatory diseases *in vivo* (Johnson et al., 2018). However, in this study, PDH-deficient Th17 cells increase the glutamine uptake and its contribution to the TCA cycle, in an attempt to rescue the lack of glucose-derived carbons in the TCA cycle. Nevertheless, when measuring glutamine's contribution to the production of citrate by oxidative or reductive metabolism, an increased flux to citrate or an increased citrate concentration in mutant Th17 cells was not observed. Thus, glutamine is only able to partially replenish the TCA cycle in Th17 cells upon PDH deletion.

Taken together, these studies show the importance of glutamine metabolism in T cells and further highlight the importance of Th subset-specific requirements. This offers therapeutic possibilities for T cell subset-specific interference at key regulatory points of central carbon metabolism.

Furthermore, here, it was shown that the total levels of TCA metabolites such as α-ketoglutarate, fumarate, malate and especially citrate were reduced in PDH-deficient Th17 cells.

In summary, PDH is essential for the correct functioning of "central" carbon metabolism. PDH-deficient Th17 cells have boosted glycolysis, leading to increased ECAR and lactate production as

well as pyruvate release. On the other hand, mitochondrial function is impaired despite the anaplerosis attempts of glutamine-derived carbon atoms (cf. to illustration 19).

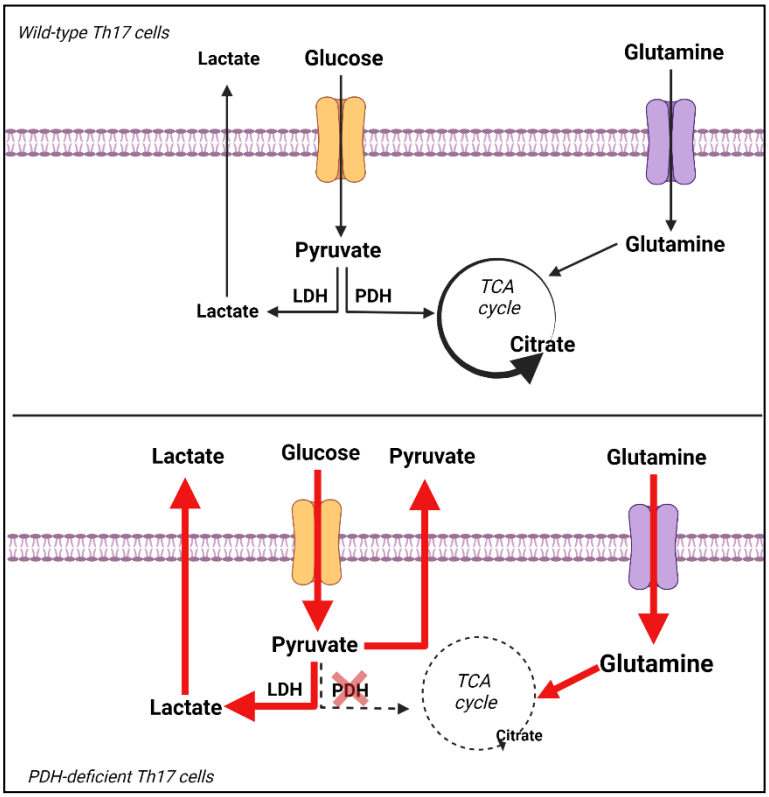

Illustration 19 : PDH is essential for Th17 cells' mitochondrial carbon metabolism.

Upon pyruvate dehydrogenase (PDH) ablation, Th17 cells' mitochondrial glucose metabolism is impaired causing cells to release lactate, generated through lactate dehydrogenase (LDH), and pyruvate to extracellular milieu. On the other hand, glutamine uptake is induced, however the mitochondrial function is downregulated and the total amounts of tricarboxylic acid (TCA) metabolites, especially citrate, is drastically reduced. (Created in BioRender)

PART III. PYRUVATE DEHYDROGENASE RESTRICTS LIPID DEPENDENCE IN TH17 CELLS

In wild-type Th17 cells, mitochondrial acetyl-CoA reacts with OAA to produce citrate (Wang and Green, 2012). Citrate can be oxidized following the TCA cycle to generate the reductive equivalents necessary for ATP production through OXPHOS (Chapman and Chi, 2022). In addition, citrate can exit the mitochondria and can be converted to cytosolic OAA and acetyl-CoA by ACLY (Koundouros and Poulogiannis, 2020; Wellen et al., 2009; Zhao et al., 2016). In mammalian cells, cytosolic acetyl-CoA has two possible fates: lipid synthesis and protein acetylation (Pietrocola et al., 2015; Sivanand et al., 2018).

In this study, it was shown that glucose-derived acetyl-CoA is used for lipid synthesis in wild-type Th17 cells, which is necessary for proliferation. However, upon PDH deletion, Th17 cells are unable to generate lipids *de novo* from glucose, which suppressed their proliferative abilities. As a mean to maintain their lipid levels, PDH-deficient Th17 cells increase extracellular fatty acid uptake through a glutamine-mTOR-dependent upregulation of CD36, making these mutant cells highly dependent on extracellular lipids for their survival. Moreover, the data revealed that both, wild-type and PDH-deficient Th17 cells, rely on extracellular fatty acids for their proliferation.

While CD36 is a target of mTOR signaling, mTOR is also crucial for Th17 differentiation and metabolic rewiring (Delgoffe et al., 2009; Lochner et al., 2015; Nagai et al., 2013; Salmond, 2018). A major activator of mTOR is glutamine (Takahara et al., 2020). The data show that PDH-deficient Th17 cells increase their glutamine uptake, which induces mTOR activation. Consecutively, increased mTOR activity prompts CD36 expression and fatty acid uptake. These results show a metabolic feedback loop connecting glucose, glutamine and fatty acid metabolism with mTOR as a central regulator in Th17 cells.

Collectively, upon PDH deletion, Th17 cells activate a glutamine-mTOR-CD36 axis to maintain their intracellular lipid pools, which become essential for their survival (cf. to illustration 20).

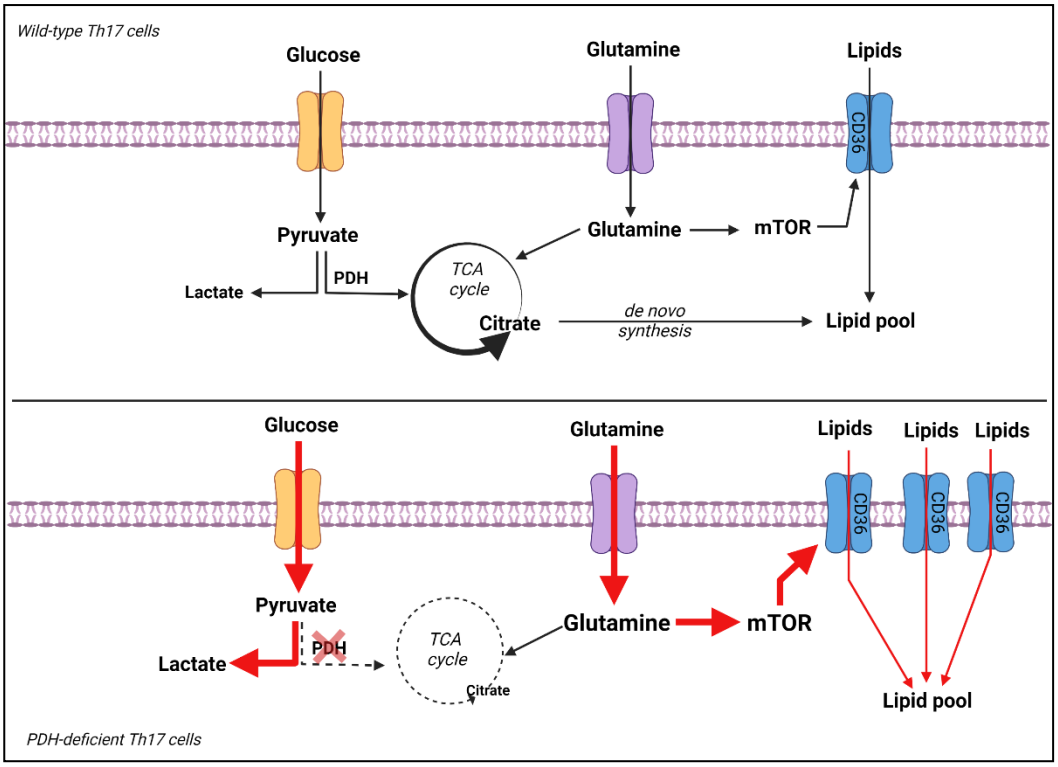

Illustration 20 : PDH ablation in Th17 cells induced a lipid dependence.

In a wild-type setting, Th17 cells use glucose-derived pyruvate for the generation of mitochondrial citrate through the TCA cycle. Citrate exits the mitochondria to be used as a substrate for *de novo* synthesis of lipids, to maintain the intracellular lipid pool. However, upon pyruvate dehydrogenase (PDH) ablation, Th17 cells are not able to generate glucose-derived citrate, inducing glutamine uptake that activates the mTOR axis and thus the expression of CD36 to increase the fatty acid uptake to maintain the levels of the lipid pool. (Created in BioRender)

PART IV. GLUCOSE-DERIVED CITRATE IS ESSENTIAL FOR HISTONE ACETYLATION AND GENE EXPRESSION IN TH17 CELLS

Cytoplasmic citrate can also enter the nucleus, where it can be transformed into acetyl-CoA by the nuclear form of ACLY. Nuclear acetyl-CoA is used as a substrate for histone-acetyl transferases (HATs) for histone acetylation (Koundouros and Poulogiannis, 2020; Wellen et al., 2009; Zhao et al., 2016). The data clearly states that histone 3 acetylation is impaired in PDH-deficient Th17 cells, which correlates with the low concentration of citrate in the cells and thus, the lack of substrate for ACLY activity.

Furthermore, it has been shown that PDH can be localized in the nucleus in constitutively active form, where it generates a mitochondrial-independent pool of acetyl-CoA for histone acetylation (Sutendra et al., 2014). As both forms of PDH (mitochondrial and nuclear) are ablated in this system, the mitochondrial-independent generation of acetyl-CoA through PDH would not be possible either. In line, a largely impaired histone acetylation was observed.

The role of histone acetylation has been intensely studied. Its main function is to keep chromatin open to permit binding of transcription factors and enhancers to promoter regions of genes in order to initiate their expression (Li et al., 2007; Pietrocola et al., 2015; Sivanand et al., 2018). In line with the decreased histone 3 acetylation, the results show that PDH deletion reduced chromatin accessibility in the regions of Th17 cell-signature genes, affecting their expression.

In line with these findings, Hochrein et al. recently showed that the glucose transporter 3 (Glut3) is essential for pathogenic Th17 cells' effector functions *in vivo* and *in vitro*. Mechanistically, they show that Glut3 is linked to glucose oxidation and ACLY-dependent generation of acetyl-CoA to regulate the epigenetic program of these cells and the expression of inflammatory genes (Hochrein et al., 2022). This data shows the importance of the generation of acetyl-CoA in an ACLY-dependent manner in Th17 cells, corroborating the results of this thesis.

Surprisingly, Wenes et al. have shown that inhibition of the MPC, the transporter allowing pyruvate import into the mitochondria, in CD8 T cells resulted in an increased differentiation into memory CD8 T cells by enhancing histone acetylation and chromatin accessibility of pro-memory genes (Wenes et al., 2022). Briefly, they show that upon MPC ablation or inhibition, glutamine and fatty acid metabolism are induced to produce high levels of acetyl-CoA, which is then used for histone acetylation, enhancing the transcription of memory genes. The disparity between our findings could

be due to defective citrate production and generation of acetyl-CoA in PDH-deficient Th17 cells, despite a compensatory upregulation of glutamine metabolism.

Collectively, PDH ablation and the consequential low concentration of citrate have a severe impact on histone acetylation and Th17 specific gene expression (cf. to illustration 21).

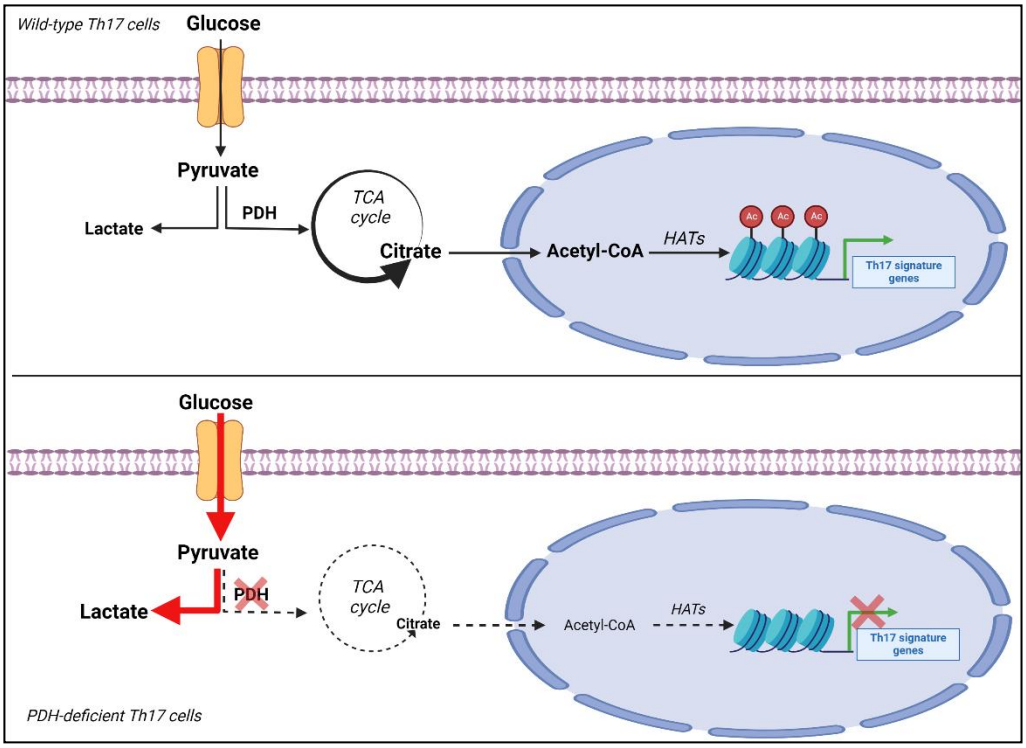

Illustration 21: Glucose-derived citrate is essential for histone acetylation and gene expression in Th17 cells.

Th17 cells use glucose-derived citrate for the generation of acetyl-CoA, which is the substrate of histone acetyl-transferases (HATs) for histone acetylation, essential to allow the transcription of Th17 signature genes. On the other hand, once pyruvate dehydrogenase (PDH) is ablated in Th17 cells, the generation of citrate is impaired and thus the levels of acetyl-CoA are reduced. This limits the substrate availability for HATs to acetylate histones and finally weakens Th17 signature genes' expression. (Created with BioRender)

PART V. ACETATE TREATMENT RESCUES THE METABOLIC CHANGES AND ITS CONSEQUENCES IN PDH-DEFICIENT TH17 CELLS

Acetate is a short-chain fatty acid and it enters the cells through monocarboxylate transporters (MCTs) or aquaporins (Qiu et al., 2019). Once in the cell, acetate can be converted into acetyl-CoA by the acetyl-CoA synthetase (ACSS) and serve its multiple functions (Moffett et al., 2020; Pietrocola et al., 2015; Watkins et al., 2007).

For instance, Balmer et al. showed that acetate is taken up by memory CD8 T cells to expand their acetyl-CoA pool, allowing the acetylation of GAPDH, which boosts glycolysis and recall responses (Balmer et al., 2016). In the tumor microenvironment, where glucose is limited, acetate supplementation enhanced histone acetylation, chromatin accessibility and IFNγ production in $CD8^+$ T cells (Qiu et al., 2019). Another study showed that LDH-deficient Th1 cells, which have impaired IFNγ production, presented low levels of acetyl-CoA. This culminated in a reduced histone acetylation in the *Ifng* promoter, which was reversible by acetate treatment (Peng et al., 2016). In line with the latter study, Xu et al. were able to rescue the reduced histone acetylation found in LDH-deficient Th17 cells by supplementing acetate in the media (K. Xu et al., 2021).

Similarly, in this study, acetate supplementation reverted the histone 3 acetylation to wild-type levels and restored the citrate pool. This allowed mutant Th17 cells to generate fatty acids *de novo*, proliferate, recover a “normal” central carbon metabolism, and, most importantly, restore the production of the effector cytokine IL-17.

In line with these results, Hochrein et al. have shown that the impairment in the effector function of Glut3-deficient Th17 cells was due to the inability of these cells to generate acetyl-CoA from citrate. Accordingly, addition of acetate rescued the production of effector cytokines IL-17A, GM-CSF and IL-2 (Hochrein et al., 2022).

Taken together, these studies highlight the connection between cellular metabolism, epigenetic modifications and effector function in T cells. These results could lead to potential targets for the treatments of autoimmune diseases and cancer.

OUTLOOK

1. Acute PDH ablation in T cells

We have shown the mechanistic consequences of ablating PDH in Th17 cells. However, to confirm that these effects are due to the ablation of the enzyme and not a consequence of the adaptation of the T cells during development, we will acutely ablate PDH expression in peripheral T cells. To that end, we will cross $PDH^{fl/fl}$ mice with tamoxifen (TAM)-inducible CD4 Cre bearing mice generated by Aghajani et al. CD4-$CreER^{T2}$ (Aghajani et al., 2012). The CD4-$CreER^{T2}$ is induced *in vivo* by repeated daily oral gavage of 100 µL of a 50 mg/mL solution of TAM dissolved in sunflower oil. Once the CD4-$CreER^{T2}$ is active, all T cells will have impaired PDH gene expression. We will then isolate the naïve T cells and differentiate them into Th17 cells *in vitro*. It is also possible to induce the CD4-$CreER^{T2}$ *in vitro* by treating the cells with 4-hydroxytamoxifen. Alternatively, we will differentiate WT naïve CD4 T cells into Th17 cells *in vitro* in the presence of the PDH inhibitor 6,8-Bis(benzylthio)octanoic acid. This way, we will be able to perform all the relevant assays to reproduce the data obtained on *in vitro*-differentiated Th17 cells from $PDH^{fl/fl}$ CD4 Cre+ mice and confirm that the effects observed are indeed strictly PDH-dependent.

2. Reconstitution of PDH in PDH-deficient T cells

Another way of confirming the cause-consequence effects would be to reconstitute PDH in PDH-deficient Th17 cells using retroviral transduction of a PDH x CD90.1 vector as previously described (Kurniawan et al., 2020a). This technique will allow us to perform assays on reconstituted Th17 cells to observe the restoration of the effector function of these originally mutant cells.

3. Confirmation on psoriasis model

To confirm that the effects observed *in vivo* in the EAE model is dependent on Th17 cells and not on the organ, we propose, for example, the imiquimod-induced psoriasis-like mouse model (Jabeen et al., 2020). As this disease model has been shown to be highly dependent on IL-17 (Fits et al., 2009), we would expect $PDH^{fl/fl}$ CD4 Cre+ mice to be more resistant to the disease.

4. PDH-deficient Th17 cells in the context of *Citrobacter rodentium*

Although we have not explored this topic, it is important to note that Th17 cells are essential for the mucosal defense of extracellular bacteria (Luckheeram et al., 2012). A standard model to study intestinal mucosal infections in mice is using the attaching and effacing pathogen *Citrobacter rodentium* (C*. rodentium*) (Collins et al., 2014). As studies have shown that IL-17 deficient mice have increased symptoms during *C. rodentium* infection (Ishigame et al., 2009), it would be of interest to assess the impact that the infection would have on $PDH^{fl/fl}$ CD4 Cre+ mice.

5. Acetate treatment *in vivo*

As our *in vitro* results show that the dysfunction of PDH-deficient Th17 cells can be rescued by supplementing the media with acetate, it is likely that acetate addition would modulate the functional effects on Th17 cells *in vivo*. To confirm that hypothesis, the mice will be provided with a specific high acetate-producing diet prior to induction of EAE and during its progression, as previously decribed (Yap et al., 2021). We anticipate to observe increased disease scores in $PDH^{fl/fl}$ CD4 Cre+ mice fed with the high acetate-producing diet compared to the $PDH^{fl/fl}$ CD4 Cre+ mice with the control diet.

6. PDH function in human Th17 cells

While our research is strictly based on murine *in vivo* models and *in vitro* analysis of Th17 cells, PDH deficiency is a rare condition in humans causing lactic acidosis, neuromuscular and neurological degeneration and even death during childhood (DeBrosse and Kerr, 2016; Patel et al., 2012). Thus, it would be of great interest to study Th17 cells derived from PDH-deficient patients and compare them to healthy controls for translational research, as well as the potential effects of increasing acetate levels in these patients (i.e. increasing the amounts of vinegar in the diet). Since PDH-deficiency in Th17 cells reduces their effector functions, inhibition of the enzyme could be beneficial in Th17-driven autoimmune diseases such as MS or psoriasis.

CONCLUSION

In conclusion, our research uncovered a role of PDH as a central regulator of effector function of Th17 cells *in vivo* and *in vitro*. The results show that PDH in Th17 cells is critical for the establishment of a glucose-derived citrate pool that is essential for survival, proliferation, and effector function of this important Th cell subset. The data, thus, indicate that PDH could be a potential target in the treatment of Th17 driven autoimmune diseases (cf. to illustration 22).

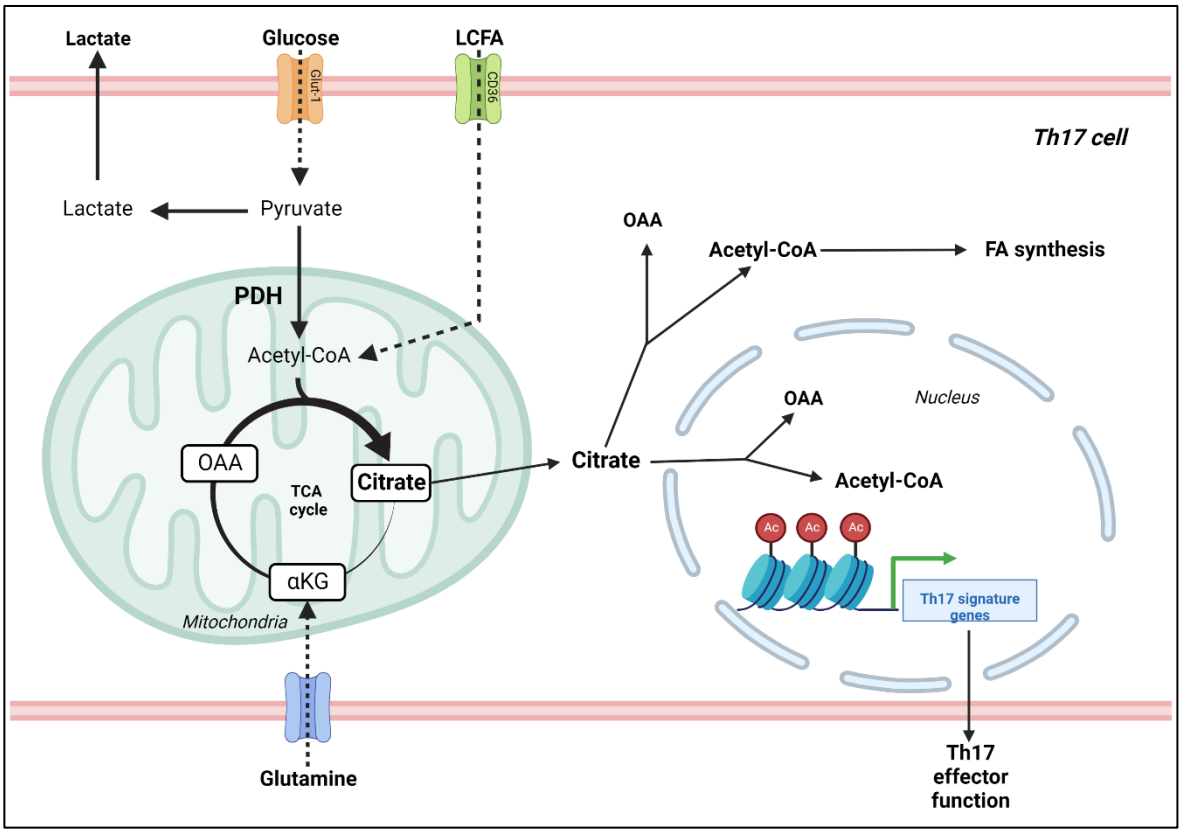

Illustration 22 : Pyruvate dehydrogenase fuels a critical citrate pool that is essential for Th17 cell effector function.

Th17 cells rely on multiple carbon sources such as glucose, glutamine and long-chain fatty acids (LCFA). However, the function of PDH is pivotal for the generation of a glucose-derived citrate pool. The mitochondrial citrate is then shuttled into the cytoplasm to generate acetyl-CoA, which is used for histone acetylation, chromatin openness and expression of Th17 cell's signature genes. The latter is crucial for Th17 cells' effector function. (Created with BioRender)

REFERENCES

REFERENCES

Abbas, A.K., Lichtman, A.H., Pillai, S., 2015. Cellular and molecular immunology, 8th ed. Elsevier Saunders, Philadelphia, PA.

Adams, M.D., Celniker, S.E., Holt, R.A., Evans, C.A., Gocayne, J.D., Amanatides, P.G., Scherer, S.E., Li, P.W., Hoskins, R.A., Galle, R.F., George, R.A., Lewis, S.E., Richards, S., Ashburner, M., Henderson, S.N., Sutton, G.G., Wortman, J.R., Yandell, M.D., Zhang, Q., Chen, L.X., Brandon, R.C., Rogers, Y.-H.C., Blazej, R.G., Champe, M., Pfeiffer, B.D., Wan, K.H., Doyle, C., Baxter, E.G., Helt, G., Nelson, C.R., Gabor, G.L., Miklos, Abril, J.F., Agbayani, A., An, H.-J., Andrews-Pfannkoch, C., Baldwin, D., Ballew, R.M., Basu, A., Baxendale, J., Bayraktaroglu, L., Beasley, E.M., Beeson, K.Y., Benos, P.V., Berman, B.P., Bhandari, D., Bolshakov, S., Borkova, D., Botchan, M.R., Bouck, J., Brokstein, P., Brottier, P., Burtis, K.C., Busam, D.A., Butler, H., Cadieu, E., Center, A., Chandra, I., Cherry, J.M., Cawley, S., Dahlke, C., Davenport, L.B., Davies, P., Pablos, B. de, Delcher, A., Deng, Z., Mays, A.D., Dew, I., Dietz, S.M., Dodson, K., Doup, L.E., Downes, M., Dugan-Rocha, S., Dunkov, B.C., Dunn, P., Durbin, K.J., Evangelista, C.C., Ferraz, C., Ferriera, S., Fleischmann, W., Fosler, C., Gabrielian, A.E., Garg, N.S., Gelbart, W.M., Glasser, K., Glodek, A., Gong, F., Gorrell, J.H., Gu, Z., Guan, P., Harris, M., Harris, N.L., Harvey, D., Heiman, T.J., Hernandez, J.R., Houck, J., Hostin, D., Houston, K.A., Howland, T.J., Wei, M.-H., Ibegwam, C., Jalali, M., Kalush, F., Karpen, G.H., Ke, Z., Kennison, J.A., Ketchum, K.A., Kimmel, B.E., Kodira, C.D., Kraft, C., Kravitz, S., Kulp, D., Lai, Z., Lasko, P., Lei, Y., Levitsky, A.A., Li, J., Li, Z., Liang, Y., Lin, X., Liu, X., Mattei, B., McIntosh, T.C., McLeod, M.P., McPherson, D., Merkulov, G., Milshina, N.V., Mobarry, C., Morris, J., Moshrefi, A., Mount, S.M., Moy, M., Murphy, B., Murphy, L., Muzny, D.M., Nelson, D.L., Nelson, D.R., Nelson, K.A., Nixon, K., Nusskern, D.R., Pacleb, J.M., Palazzolo, M., Pittman, G.S., Pan, S., Pollard, J., Puri, V., Reese, M.G., Reinert, K., Remington, K., Saunders, R.D.C., Scheeler, F., Shen, H., Shue, B.C., Sidén-Kiamos, I., Simpson, M., Skupski, M.P., Smith, T., Spier, E., Spradling, A.C., Stapleton, M., Strong, R., Sun, E., Svirskas, R., Tector, C., Turner, R., Venter, E., Wang, A.H., Wang, X., Wang, Z.-Y., Wassarman, D.A., Weinstock, G.M., Weissenbach, J., Williams, S.M., Woodage, T., Worley, K.C., Wu, D., Yang, S., Yao, Q.A., Ye, J., Yeh, R.-F., Zaveri, J.S., Zhan, M., Zhang, G., Zhao, Q., Zheng, L., Zheng, X.H., Zhong, F.N., Zhong, W., Zhou, X., Zhu, S., Zhu, X., Smith, H.O., Gibbs, R.A., Myers, E.W., Rubin, G.M., Venter, J.C., 2000. The Genome Sequence of *Drosophila melanogaster*. Science 287, 2185–2195. https://doi.org/10.1126/science.287.5461.2185

Aghajani, K., Keerthivasan, S., Yu, Y., Gounari, F., 2012. Generation of CD4CreER ^{T2} transgenic mice to study development of peripheral CD4-T-cells. genesis 50, 908–913. https://doi.org/10.1002/dvg.22052

Andrews, S., 2010. FastQC: a quality control tool for high throughput sequence data.

Angela, M., Endo, Y., Asou, H.K., Yamamoto, T., Tumes, D.J., Tokuyama, H., Yokote, K., Nakayama, T., 2016. Fatty acid metabolic reprogramming via mTOR-mediated inductions of PPARγ directs early activation of T cells. Nat. Commun. 7, 13683. https://doi.org/10.1038/ncomms13683

Angiari, S., Runtsch, M.C., Sutton, C.E., Palsson-McDermott, E.M., Kelly, B., Rana, N., Kane, H., Papadopoulou, G., Pearce, E.L., Mills, K.H.G., O'Neill, L.A.J., 2020. Pharmacological Activation of Pyruvate Kinase M2 Inhibits CD4+ T Cell Pathogenicity and Suppresses Autoimmunity. Cell Metab. 31, 391-405.e8. https://doi.org/10.1016/j.cmet.2019.10.015

Aranami, T., Yamamura, T., 2008. Th17 Cells and Autoimmune Encephalomyelitis (EAE/MS). Allergol. Int. 57, 115–120. https://doi.org/10.2332/allergolint.R-07-159

Balmer, M.L., Ma, E.H., Bantug, G.R., Grählert, J., Pfister, S., Glatter, T., Jauch, A., Dimeloe, S., Slack, E., Dehio, P., Krzyzaniak, M.A., King, C.G., Burgener, A.-V., Fischer, M., Develioglu, L., Belle, R., Recher, M., Bonilla, W.V., Macpherson, A.J., Hapfelmeier, S., Jones, R.G., Hess, C., 2016. Memory CD8 + T Cells Require Increased Concentrations of Acetate Induced by Stress for Optimal Function. Immunity 44, 1312–1324. https://doi.org/10.1016/j.immuni.2016.03.016

Baricza, E., Marton, N., Királyhidi, P., Kovács, O.T., Kovácsné Székely, I., Lajkó, E., Kőhidai, L., Rojkovich, B., Érsek, B., Buzás, E.I., Nagy, G., 2018. Distinct In Vitro T-Helper 17 Differentiation Capacity of Peripheral Naive T Cells in Rheumatoid and Psoriatic Arthritis. Front. Immunol. 9, 606. https://doi.org/10.3389/fimmu.2018.00606

Basu, R., Hatton, R.D., Weaver, C.T., 2013. The Th17 family: flexibility follows function. Immunol. Rev. 252, 89–103. https://doi.org/10.1111/imr.12035

Battello, N., Zimmer, A.D., Goebel, C., Dong, X., Behrmann, I., Haan, C., Hiller, K., Wegner, A., 2016. The role of HIF-1 in oncostatin M-dependent metabolic reprogramming of hepatic cells. Cancer Metab. 4, 3. https://doi.org/10.1186/s40170-016-0141-0

Bettini, M.L., Chou, P.-C., Guy, C., Lee, T., Vignali, K.M., Vignali, D.A.A., 2017. CD3 ITAM diversity is required for optimal T cell receptor signaling and thymocyte development. J. Immunol. Baltim. Md 1950 199, 1555–1560. https://doi.org/10.4049/jimmunol.1700069

Birnbaum, M.E., Berry, R., Hsiao, Y.-S., Chen, Z., Shingu-Vazquez, M.A., Yu, X., Waghray, D., Fischer, S., McCluskey, J., Rossjohn, J., Walz, T., Garcia, K.C., 2014. Molecular architecture of the αβ T cell receptor–CD3 complex. Proc. Natl. Acad. Sci. 111, 17576–17581. https://doi.org/10.1073/pnas.1420936111

Bricker, D.K., Taylor, E.B., Schell, J.C., Orsak, T., Boutron, A., Chen, Y.-C., Cox, J.E., Cardon, C.M., Van Vranken, J.G., Dephoure, N., Redin, C., Boudina, S., Gygi, S.P., Brivet, M., Thummel, C.S., Rutter, J., 2012. A Mitochondrial Pyruvate Carrier Required for Pyruvate Uptake in Yeast, *Drosophila* , and Humans. Science 337, 96–100. https://doi.org/10.1126/science.1218099

Brüstle, A., Brenner, D., Knobbe, C.B., Lang, P.A., Virtanen, C., Hershenfield, B.M., Reardon, C., Lacher, S.M., Ruland, J., Ohashi, P.S., Mak, T.W., 2012. The NF-κB regulator MALT1 determines the encephalitogenic potential of Th17 cells. J. Clin. Invest. 122, 4698–4709. https://doi.org/10.1172/JCI63528

Buck, M.D., O'Sullivan, D., Pearce, E.L., 2015. T cell metabolism drives immunity. J. Exp. Med. 212, 1345–1360. https://doi.org/10.1084/jem.20151159

Buenrostro, J.D., Giresi, P.G., Zaba, L.C., Chang, H.Y., Greenleaf, W.J., 2013. Transposition of native chromatin for fast and sensitive epigenomic profiling of open chromatin, DNA-binding proteins and nucleosome position. Nat. Methods 10, 1213–1218. https://doi.org/10.1038/nmeth.2688

Buenrostro, J.D., Wu, B., Chang, H.Y., Greenleaf, W.J., 2015. ATAC-seq: A Method for Assaying Chromatin Accessibility Genome-Wide. Curr. Protoc. Mol. Biol. 109. https://doi.org/10.1002/0471142727.mb2129s109

Buescher, J.M., Antoniewicz, M.R., Boros, L.G., Burgess, S.C., Brunengraber, H., Clish, C.B., DeBerardinis, R.J., Feron, O., Frezza, C., Ghesquiere, B., Gottlieb, E., Hiller, K., Jones, R.G., Kamphorst, J.J., Kibbey, R.G., Kimmelman, A.C., Locasale, J.W., Lunt, S.Y., Maddocks, O.D., Malloy, C., Metallo, C.M., Meuillet, E.J., Munger, J., Nöh, K., Rabinowitz, J.D., Ralser, M., Sauer, U., Stephanopoulos, G., St-Pierre, J., Tennant, D.A., Wittmann, C., Vander Heiden, M.G., Vazquez, A., Vousden, K., Young, J.D., Zamboni, N., Fendt, S.-M., 2015. A roadmap for interpreting 13 C metabolite labeling patterns from cells. Curr. Opin. Biotechnol. 34, 189–201. https://doi.org/10.1016/j.copbio.2015.02.003

Bulusu, V., Tumanov, S., Michalopoulou, E., van den Broek, N.J., MacKay, G., Nixon, C., Dhayade, S., Schug, Z.T., Vande Voorde, J., Blyth, K., Gottlieb, E., Vazquez, A., Kamphorst, J.J., 2017. Acetate Recapturing by Nuclear Acetyl-CoA Synthetase 2 Prevents Loss of Histone Acetylation during Oxygen and Serum Limitation. Cell Rep. 18, 647–658. https://doi.org/10.1016/j.celrep.2016.12.055

Carbonneau, M., M. Gagné, L., Lalonde, M.-E., Germain, M.-A., Motorina, A., Guiot, M.-C., Secco, B., Vincent, E.E., Tumber, A., Hulea, L., Bergeman, J., Oppermann, U., Jones, R.G., Laplante, M., Topisirovic, I., Petrecca, K., Huot, M.-É., Mallette, F.A., 2016. The oncometabolite 2-hydroxyglutarate activates the mTOR signalling pathway. Nat. Commun. 7, 12700. https://doi.org/10.1038/ncomms12700

Carty, S.A., Gohil, M., Banks, L.B., Cotton, R.M., Johnson, M.E., Stelekati, E., Wells, A.D., Wherry, E.J., Koretzky, G.A., Jordan, M.S., 2018. The Loss of TET2 Promotes CD8 $^{+}$ T Cell Memory Differentiation. J. Immunol. 200, 82–91. https://doi.org/10.4049/jimmunol.1700559

Chapman, N.M., Boothby, M.R., Chi, H., 2020. Metabolic coordination of T cell quiescence and activation. Nat. Rev. Immunol. 20, 55–70. https://doi.org/10.1038/s41577-019-0203-y

Chapman, N.M., Chi, H., 2022. Metabolic adaptation of lymphocytes in immunity and disease. Immunity 55, 14–30. https://doi.org/10.1016/j.immuni.2021.12.012

Chaudhry, R., Varacallo, M., 2022. Biochemistry, Glycolysis, in: StatPearls. StatPearls Publishing, Treasure Island (FL).

Chen, Y., Zhang, J., Cui, W., Silverstein, R.L., 2022. CD36, a signaling receptor and fatty acid transporter that regulates immune cell metabolism and fate. J. Exp. Med. 219, e20211314. https://doi.org/10.1084/jem.20211314

Collins, J.W., Keeney, K.M., Crepin, V.F., Rathinam, V.A.K., Fitzgerald, K.A., Finlay, B.B., Frankel, G., 2014. Citrobacter rodentium: infection, inflammation and the microbiota. Nat. Rev. Microbiol. 12, 612–623. https://doi.org/10.1038/nrmicro3315

Comerford, S.A., Huang, Z., Du, X., Wang, Y., Cai, L., Witkiewicz, A.K., Walters, H., Tantawy, M.N., Fu, A., Manning, H.C., Horton, J.D., Hammer, R.E., McKnight, S.L., Tu, B.P., 2014. Acetate Dependence of Tumors. Cell 159, 1591–1602. https://doi.org/10.1016/j.cell.2014.11.020

Constantinescu, C.S., Farooqi, N., O'Brien, K., Gran, B., 2011. Experimental autoimmune encephalomyelitis (EAE) as a model for multiple sclerosis (MS). Br. J. Pharmacol. 164, 1079–1106. https://doi.org/10.1111/j.1476-5381.2011.01302.x

Corces, M.R., Trevino, A.E., Hamilton, E.G., Greenside, P.G., Sinnott-Armstrong, N.A., Vesuna, S., Satpathy, A.T., Rubin, A.J., Montine, K.S., Wu, B., Kathiria, A., Cho, S.W., Mumbach, M.R., Carter, A.C., Kasowski, M., Orloff, L.A., Risca, V.I., Kundaje, A., Khavari, P.A., Montine, T.J., Greenleaf, W.J., Chang, H.Y., 2017. An improved ATAC-seq protocol reduces background and enables interrogation of frozen tissues. Nat. Methods 14, 959–962. https://doi.org/10.1038/nmeth.4396

Corrado, M., Pearce, E.L., 2022. Targeting memory T cell metabolism to improve immunity [WWW Document]. https://doi.org/10.1172/JCI148546

Cribioli, E., Giordano Attianese, G.M.P., Ginefra, P., Signorino-Gelo, A., Vuillefroy de Silly, R., Vannini, N., Hess, C., Irving, M., Coukos, G., 2022. Enforcing GLUT3 expression in CD8+ T cells improves fitness and tumor control by promoting glucose uptake and energy storage. Front. Immunol. 13.

Cyster, J.G., Allen, C.D.C., 2019. B Cell Responses: Cell Interaction Dynamics and Decisions. Cell 177, 524–540. https://doi.org/10.1016/j.cell.2019.03.016

Dang, E.V., Barbi, J., Yang, H.-Y., Jinasena, D., Yu, H., Zheng, Y., Bordman, Z., Fu, J., Kim, Y., Yen, H.-R., Luo, W., Zeller, K., Shimoda, L., Topalian, S.L., Semenza, G.L., Dang, C.V., Pardoll, D.M., Pan, F., 2011. Control of TH17/Treg Balance by Hypoxia-Inducible Factor 1. Cell 146, 772–784. https://doi.org/10.1016/j.cell.2011.07.033

de Jong, A.J., Kloppenburg, M., Toes, R.E.M., Ioan-Facsinay, A., 2014. Fatty Acids, Lipid Mediators, and T-Cell Function. Front. Immunol. 5. https://doi.org/10.3389/fimmu.2014.00483

DeBrosse, S.D., Kerr, D.S., 2016. Pyruvate Dehydrogenase Complex Deficiency, in: Mitochondrial Case Studies. Elsevier, pp. 93–101. https://doi.org/10.1016/B978-0-12-800877-5.00012-7

Delgoffe, G.M., Kole, T.P., Zheng, Y., Zarek, P.E., Matthews, K.L., Xiao, B., Worley, P.F., Kozma, S.C., Powell, J.D., 2009. mTOR differentially regulates effector and regulatory T cell lineage commitment. Immunity 30, 832–844. https://doi.org/10.1016/j.immuni.2009.04.014

Dobin, A., Davis, C.A., Schlesinger, F., Drenkow, J., Zaleski, C., Jha, S., Batut, P., Chaisson, M., Gingeras, T.R., 2013. STAR: ultrafast universal RNA-seq aligner. Bioinformatics 29, 15–21. https://doi.org/10.1093/bioinformatics/bts635

Domínguez-Amorocho, O., Takiishi, T., da Cunha, F.F., Camara, N.O.S., 2019. Immunometabolism: A target for the comprehension of immune response toward transplantation. World J. Transplant. 9, 27–34. https://doi.org/10.5500/wjt.v9.i2.27

Ducker, G.S., Rabinowitz, J.D., 2017. One-Carbon Metabolism in Health and Disease. Cell Metab. 25, 27–42. https://doi.org/10.1016/j.cmet.2016.08.009

Dutta, A., Venkataganesh, H., Love, P.E., 2021. New Insights into Epigenetic Regulation of T Cell Differentiation. Cells 10, 3459. https://doi.org/10.3390/cells10123459

Elia, I., Rowe, J.H., Johnson, S., Joshi, S., Notarangelo, G., Kurmi, K., Weiss, S., Freeman, G.J., Sharpe, A.H., Haigis, M.C., 2022. Tumor cells dictate anti-tumor immune responses by altering pyruvate utilization and succinate signaling in CD8+ T cells. Cell Metab. 34, 1137-1150.e6. https://doi.org/10.1016/j.cmet.2022.06.008

Ellmeier, W., Seiser, C., 2018. Histone deacetylase function in CD4+ T cells. Nat. Rev. Immunol. 18, 617–634. https://doi.org/10.1038/s41577-018-0037-z

Fendt, S.-M., Bell, E.L., Keibler, M.A., Olenchock, B.A., Mayers, J.R., Wasylenko, T.M., Vokes, N.I., Guarente, L., Vander Heiden, M.G., Stephanopoulos, G., 2013. Reductive glutamine metabolism is a function of the α-ketoglutarate to citrate ratio in cells. Nat. Commun. 4, 2236. https://doi.org/10.1038/ncomms3236

Field, C.S., Baixauli, F., Kyle, R.L., Puleston, D.J., Cameron, A.M., Sanin, D.E., Hippen, K.L., Loschi, M., Thangavelu, G., Corrado, M., Edwards-Hicks, J., Grzes, K.M., Pearce, E.J., Blazar, B.R., Pearce, E.L., 2020. Mitochondrial Integrity Regulated by Lipid Metabolism Is a Cell-Intrinsic Checkpoint for Treg Suppressive Function. Cell Metab. 31, 422-437.e5. https://doi.org/10.1016/j.cmet.2019.11.021

Fits, L. van der, Mourits, S., Voerman, J.S.A., Kant, M., Boon, L., Laman, J.D., Cornelissen, F., Mus, A.-M., Florencia, E., Prens, E.P., Lubberts, E., 2009. Imiquimod-Induced Psoriasis-Like Skin Inflammation in Mice Is Mediated via the IL-23/IL-17 Axis. J. Immunol. 182, 5836–5845. https://doi.org/10.4049/jimmunol.0802999

Franchina, D.G., Dostert, C., Brenner, D., 2018. Reactive Oxygen Species: Involvement in T Cell Signaling and Metabolism. Trends Immunol. 39, 489–502. https://doi.org/10.1016/j.it.2018.01.005

Franchina, D.G., Kurniawan, H., Grusdat, M., Binsfeld, C., Guerra, L., Bonetti, L., Soriano-Baguet, L., Ewen, A., Kobayashi, T., Farinelle, S., Minafra, A.R., Vandamme, N., Carpentier, A., Borgmann, F.K., Jäger, C., Chen, Y., Kleinewietfeld, M., Vasiliou, V., Mittelbronn, M., Hiller, K., Lang, P.A., Brenner, D., 2022. Glutathione-dependent redox balance characterizes the distinct metabolic properties of follicular and marginal zone B cells. Nat. Commun. 13, 1789. https://doi.org/10.1038/s41467-022-29426-x

Frankish, A., Diekhans, M., Ferreira, A.-M., Johnson, R., Jungreis, I., Loveland, J., Mudge, J.M., Sisu, C., Wright, J., Armstrong, J., Barnes, I., Berry, A., Bignell, A., Carbonell Sala, S., Chrast, J., Cunningham, F., Di Domenico, T., Donaldson, S., Fiddes, I.T., García Girón, C., Gonzalez, J.M., Grego, T., Hardy, M., Hourlier, T., Hunt, T., Izuogu, O.G., Lagarde, J., Martin, F.J., Martínez, L., Mohanan, S., Muir, P., Navarro, F.C.P., Parker, A., Pei, B., Pozo, F., Ruffier, M., Schmitt, B.M., Stapleton, E., Suner, M.-M., Sycheva, I., Uszczynska-Ratajczak, B., Xu, J., Yates, A., Zerbino, D., Zhang, Y., Aken, B., Choudhary, J.S., Gerstein, M., Guigó, R., Hubbard, T.J.P., Kellis, M., Paten, B., Reymond, A., Tress, M.L., Flicek, P., 2019. GENCODE reference annotation for the human and mouse genomes. Nucleic Acids Res. 47, D766–D773. https://doi.org/10.1093/nar/gky955

Geiger, R., Rieckmann, J.C., Wolf, T., Basso, C., Feng, Y., Fuhrer, T., Kogadeeva, M., Picotti, P., Meissner, F., Mann, M., Zamboni, N., Sallusto, F., Lanzavecchia, A., 2016. L-Arginine Modulates T Cell Metabolism and Enhances Survival and Anti-tumor Activity. Cell 167, 829-842.e13. https://doi.org/10.1016/j.cell.2016.09.031

Gerriets, V.A., Kishton, R.J., Nichols, A.G., Macintyre, A.N., Inoue, M., Ilkayeva, O., Winter, P.S., Liu, X., Priyadharshini, B., Slawinska, M.E., Haeberli, L., Huck, C., Turka, L.A., Wood, K.C., Hale, L.P., Smith, P.A., Schneider, M.A., MacIver, N.J., Locasale, J.W., Newgard, C.B., Shinohara, M.L., Rathmell, J.C., 2015. Metabolic programming and PDHK1 control CD4+ T cell subsets and inflammation. J. Clin. Invest. 125, 194–207. https://doi.org/10.1172/JCI76012

Ghasemi, N., Razavi, S., Nikzad, E., 2017. Multiple Sclerosis: Pathogenesis, Symptoms, Diagnoses and Cell-Based Therapy. Cell J. Yakhteh 19, 1–10.

Ghoneim, H.E., Fan, Y., Moustaki, A., Abdelsamed, H.A., Dash, P., Dogra, P., Carter, R., Awad, W., Neale, G., Thomas, P.G., Youngblood, B., 2017. De Novo Epigenetic Programs Inhibit PD-1 Blockade-Mediated T Cell Rejuvenation. Cell 170, 142-157.e19. https://doi.org/10.1016/j.cell.2017.06.007

Guerra, L., Bonetti, L., Brenner, D., 2020. Metabolic Modulation of Immunity: A New Concept in Cancer Immunotherapy. Cell Rep. 32, 107848. https://doi.org/10.1016/j.celrep.2020.107848

Herzig, S., Raemy, E., Montessuit, S., Veuthey, J.-L., Zamboni, N., Westermann, B., Kunji, E.R.S., Martinou, J.-C., 2012. Identification and Functional Expression of the Mitochondrial Pyruvate Carrier. Science 337, 93–96. https://doi.org/10.1126/science.1218530

Hiller, K., Hangebrauk, J., Jäger, C., Spura, J., Schreiber, K., Schomburg, D., 2009. MetaboliteDetector: Comprehensive Analysis Tool for Targeted and Nontargeted GC/MS Based Metabolome Analysis. Anal. Chem. 81, 3429–3439. https://doi.org/10.1021/ac802689c

Hitosugi, T., Fan, J., Chung, T.-W., Lythgoe, K., Wang, X., Xie, J., Ge, Q., Gu, T.-L., Polakiewicz, R.D., Roesel, J.L., Chen, G.Z., Boggon, T.J., Lonial, S., Fu, H., Khuri, F.R., Kang, S., Chen, J., 2011. Tyrosine Phosphorylation of Mitochondrial Pyruvate Dehydrogenase Kinase 1 Is Important for Cancer Metabolism. Mol. Cell 44, 864–877. https://doi.org/10.1016/j.molcel.2011.10.015

Hochrein, S.M., Wu, H., Eckstein, M., Arrigoni, L., Herman, J.S., Schumacher, F., Gerecke, C., Rosenfeldt, M., Grün, D., Kleuser, B., Gasteiger, G., Kastenmüller, W., Ghesquière, B., Van den Bossche, J., Abel, E.D., Vaeth, M., 2022. The glucose transporter GLUT3 controls T helper 17 cell responses through glycolytic-epigenetic reprogramming. Cell Metab. 34, 516-532.e11. https://doi.org/10.1016/j.cmet.2022.02.015

Hu, Y., Ota, N., Peng, I., Refino, C.J., Danilenko, D.M., Caplazi, P., Ouyang, W., 2010. IL-17RC Is Required for IL-17A– and IL-17F–Dependent Signaling and the Pathogenesis of Experimental Autoimmune Encephalomyelitis. J. Immunol. 184, 4307–4316. https://doi.org/10.4049/jimmunol.0903614

Ishigame, H., Kakuta, S., Nagai, T., Kadoki, M., Nambu, A., Komiyama, Y., Fujikado, N., Tanahashi, Y., Akitsu, A., Kotaki, H., Sudo, K., Nakae, S., Sasakawa, C., Iwakura, Y., 2009. Differential Roles of Interleukin-17A and -17F in Host Defense against Mucoepithelial Bacterial Infection and Allergic Responses. Immunity 30, 108–119. https://doi.org/10.1016/j.immuni.2008.11.009

Ivanov, I.I., McKenzie, B.S., Zhou, L., Tadokoro, C.E., Lepelley, A., Lafaille, J.J., Cua, D.J., Littman, D.R., 2006. The Orphan Nuclear Receptor RORγt Directs the Differentiation Program of Proinflammatory IL-17+ T Helper Cells. Cell 126, 1121–1133. https://doi.org/10.1016/j.cell.2006.07.035

Jabeen, M., Boisgard, A.-S., Danoy, A., El Kholti, N., Salvi, J.-P., Boulieu, R., Fromy, B., Verrier, B., Lamrayah, M., 2020. Advanced Characterization of Imiquimod-Induced Psoriasis-Like Mouse Model. Pharmaceutics 12, 789. https://doi.org/10.3390/pharmaceutics12090789

Johnson, M.O., Wolf, M.M., Madden, M.Z., Andrejeva, G., Sugiura, A., Contreras, D.C., Maseda, D., Liberti, M.V., Paz, K., Kishton, R.J., Johnson, M.E., de Cubas, A.A., Wu, P., Li, G., Zhang, Y., Newcomb, D.C., Wells, A.D., Restifo, N.P., Rathmell, W.K., Locasale, J.W., Davila, M.L., Blazar, B.R., Rathmell, J.C., 2018. Distinct Regulation of Th17 and Th1 Cell Differentiation by Glutaminase-Dependent Metabolism. Cell 175, 1780-1795.e19. https://doi.org/10.1016/j.cell.2018.10.001

Jones, W., Bianchi, K., 2015. Aerobic Glycolysis: Beyond Proliferation. Front. Immunol. 6. https://doi.org/10.3389/fimmu.2015.00227

Jun, S., Mahesula, S., Mathews, T.P., Martin-Sandoval, M.S., Zhao, Z., Piskounova, E., Agathocleous, M., 2021. The requirement for pyruvate dehydrogenase in leukemogenesis depends on cell lineage. Cell Metab. 33, 1777-1792.e8. https://doi.org/10.1016/j.cmet.2021.07.016

Kaplon, J., Zheng, L., Meissl, K., Chaneton, B., Selivanov, V.A., Mackay, G., van der Burg, S.H., Verdegaal, E.M.E., Cascante, M., Shlomi, T., Gottlieb, E., Peeper, D.S., 2013. A key role for mitochondrial gatekeeper pyruvate dehydrogenase in oncogene-induced senescence. Nature 498, 109–112. https://doi.org/10.1038/nature12154

Kindt, T.J., Goldsby, R.A., Osborne, B.A., Kuby, J., 2007. Kuby Immunology, 6th ed. W.H. Freeman, New York.

Klein Geltink, R.I., Kyle, R.L., Pearce, E.L., 2018. Unraveling the Complex Interplay Between T Cell Metabolism and Function. Annu. Rev. Immunol. 36, 461–488. https://doi.org/10.1146/annurev-immunol-042617-053019

Klein, L., Kyewski, B., Allen, P.M., Hogquist, K.A., 2014. Positive and negative selection of the T cell repertoire: what thymocytes see (and don't see). Nat. Rev. Immunol. 14, 377–391. https://doi.org/10.1038/nri3667

Komiyama, Y., Nakae, S., Matsuki, T., Nambu, A., Ishigame, H., Kakuta, S., Sudo, K., Iwakura, Y., 2006. IL-17 Plays an Important Role in the Development of Experimental Autoimmune Encephalomyelitis. J. Immunol. 177, 566–573. https://doi.org/10.4049/jimmunol.177.1.566

Kopylova, E., Noé, L., Touzet, H., 2012. SortMeRNA: fast and accurate filtering of ribosomal RNAs in metatranscriptomic data. Bioinformatics 28, 3211–3217. https://doi.org/10.1093/bioinformatics/bts611

Korotchkina, L.G., Patel, M.S., 2001. Site Specificity of Four Pyruvate Dehydrogenase Kinase Isoenzymes toward the Three Phosphorylation Sites of Human Pyruvate Dehydrogenase. J. Biol. Chem. 276, 37223–37229. https://doi.org/10.1074/jbc.M103069200

Koundouros, N., Poulogiannis, G., 2020. Reprogramming of fatty acid metabolism in cancer. Br. J. Cancer 122, 4–22. https://doi.org/10.1038/s41416-019-0650-z

Kurniawan, H., Franchina, D.G., Guerra, L., Bonetti, L., - Baguet, L.S., Grusdat, M., Schlicker, L., Hunewald, O., Dostert, C., Merz, M.P., Binsfeld, C., Duncan, G.S., Farinelle, S., Nonnenmacher, Y., Haight, J., Das Gupta, D., Ewen, A., Taskesen, R., Halder, R., Chen, Y., Jäger, C., Ollert, M., Wilmes, P., Vasiliou, V., Harris, I.S., Knobbe-Thomsen, C.B., Turner, J.D., Mak, T.W., Lohoff, M., Meiser, J., Hiller, K., Brenner, D., 2020a. Glutathione Restricts Serine Metabolism to Preserve Regulatory T Cell Function. Cell Metab. 31, 920-936.e7. https://doi.org/10.1016/j.cmet.2020.03.004

Kurniawan, H., Soriano-Baguet, L., Brenner, D., 2020b. Regulatory T cell metabolism at the intersection between autoimmune diseases and cancer. Eur. J. Immunol. 50, 1626–1642. https://doi.org/10.1002/eji.201948470

Kurniawan, J., Suga, K., Kuhl, T.L., 2017. Interaction forces and membrane charge tunability: Oleic acid containing membranes in different pH conditions. Biochim. Biophys. Acta BBA - Biomembr. 1859, 211–217. https://doi.org/10.1016/j.bbamem.2016.11.001

Langrish, C.L., Chen, Y., Blumenschein, W.M., Mattson, J., Basham, B., Sedgwick, J.D., McClanahan, T., Kastelein, R.A., Cua, D.J., 2005. IL-23 drives a pathogenic T cell population that induces autoimmune inflammation. J. Exp. Med. 201, 233–240. https://doi.org/10.1084/jem.20041257

Lauterbach, M.A., Hanke, J.E., Serefidou, M., Mangan, M.S.J., Kolbe, C.-C., Hess, T., Rothe, M., Kaiser, R., Hoss, F., Gehlen, J., Engels, G., Kreutzenbeck, M., Schmidt, S.V., Christ, A., Imhof, A., Hiller, K., Latz, E., 2019. Toll-like Receptor Signaling Rewires Macrophage Metabolism and Promotes Histone Acetylation via ATP-Citrate Lyase. Immunity 51, 997-1011.e7. https://doi.org/10.1016/j.immuni.2019.11.009

Li, B., Carey, M., Workman, J.L., 2007. The Role of Chromatin during Transcription. Cell 128, 707–719. https://doi.org/10.1016/j.cell.2007.01.015

Li, H., Handsaker, B., Wysoker, A., Fennell, T., Ruan, J., Homer, N., Marth, G., Abecasis, G., Durbin, R., 1000 Genome Project Data Processing Subgroup, 2009. The Sequence Alignment/Map format and SAMtools. Bioinformatics 25, 2078–2079. https://doi.org/10.1093/bioinformatics/btp352

Li, J., Hardy, K., Olshansky, M., Barugahare, A., Gearing, L.J., Prier, J.E., Sng, X.Y.X., Nguyen, M.L.T., Piovesan, D., Russ, B.E., Gruta, N.L.L., Hertzog, P.J., Rao, S., Turner, S.J., 2021. KDM6B-dependent chromatin remodeling underpins effective virus-specific CD8+ T cell differentiation. Cell Rep. 34. https://doi.org/10.1016/j.celrep.2021.108839

Ligthart-Melis, G.C., van de Poll, M.C., Boelens, P.G., Dejong, C.H., Deutz, N.E., van Leeuwen, P.A., 2008. Glutamine is an important precursor for de novo synthesis of arginine in humans. Am. J. Clin. Nutr. 87, 1282–1289. https://doi.org/10.1093/ajcn/87.5.1282

Lim, S.A., Su, W., Chapman, N.M., Chi, H., 2022. Lipid metabolism in T cell signaling and function. Nat. Chem. Biol. 18, 470–481. https://doi.org/10.1038/s41589-022-01017-3

Liotti, A., Ferrara, A.L., Loffredo, S., Galdiero, M.R., Varricchi, G., Di Rella, F., Maniscalco, G.T., Belardo, M., Vastano, R., Prencipe, R., Pignata, L., Romano, R., Spadaro, G., de Candia, P., Pezone, A., De Rosa, V., 2022. Epigenetics: An opportunity to shape innate and adaptive immune responses. Immunology n/a. https://doi.org/DOI: 10.1111/imm.13571

Lochner, M., Berod, L., Sparwasser, T., 2015. Fatty acid metabolism in the regulation of T cell function. Trends Immunol. 36, 81–91. https://doi.org/10.1016/j.it.2014.12.005

Love, M.I., Huber, W., Anders, S., 2014. Moderated estimation of fold change and dispersion for RNA-seq data with DESeq2. Genome Biol. 15, 550. https://doi.org/10.1186/s13059-014-0550-8

Love, M.I., Soneson, C., Hickey, P.F., Johnson, L.K., Pierce, N.T., Shepherd, L., Morgan, M., Patro, R., 2020. Tximeta: Reference sequence checksums for provenance identification in RNA-seq. PLOS Comput. Biol. 16, e1007664. https://doi.org/10.1371/journal.pcbi.1007664

Luckheeram, R.V., Zhou, R., Verma, A.D., Xia, B., 2012. CD4 $^{+}$ T Cells: Differentiation and Functions. Clin. Dev. Immunol. 2012, 1–12. https://doi.org/10.1155/2012/925135

Luo, W., Brouwer, C., 2013. Pathview: an R/Bioconductor package for pathway-based data integration and visualization. Bioinformatics 29, 1830–1831. https://doi.org/10.1093/bioinformatics/btt285

Ma, E.H., Bantug, G., Griss, T., Condotta, S., Johnson, R.M., Samborska, B., Mainolfi, N., Suri, V., Guak, H., Balmer, M.L., Verway, M.J., Raissi, T.C., Tsui, H., Boukhaled, G., Henriques da Costa, S., Frezza, C., Krawczyk, C.M., Friedman, A., Manfredi, M., Richer, M.J., Hess, C., Jones, R.G., 2017. Serine Is an Essential Metabolite for Effector T Cell Expansion. Cell Metab. 25, 345–357. https://doi.org/10.1016/j.cmet.2016.12.011

Macintyre, A.N., Gerriets, V.A., Nichols, A.G., Michalek, R.D., Rudolph, M.C., Deoliveira, D., Anderson, S.M., Abel, E.D., Chen, B.J., Hale, L.P., Rathmell, J.C., 2014. The Glucose Transporter Glut1 Is Selectively Essential for CD4 T Cell Activation and Effector Function. Cell Metab. 20, 61–72. https://doi.org/10.1016/j.cmet.2014.05.004

MacIver, N.J., Jacobs, S.R., Wieman, H.L., Wofford, J.A., Coloff, J.L., Rathmell, J.C., 2008. Glucose metabolism in lymphocytes is a regulated process with significant effects on immune cell function and survival. J. Leukoc. Biol. 84, 949–957. https://doi.org/10.1189/jlb.0108024

Mak, T.W., Grusdat, M., Duncan, G.S., Dostert, C., Nonnenmacher, Y., Cox, M., Binsfeld, C., Hao, Z., Brüstle, A., Itsumi, M., Jäger, C., Chen, Y., Pinkenburg, O., Camara, B., Ollert, M., Bindslev-Jensen, C., Vasiliou, V., Gorrini, C., Lang, P.A., Lohoff, M., Harris, I.S., Hiller, K., Brenner, D., 2017. Glutathione Primes T Cell Metabolism for Inflammation. Immunity 46, 675–689. https://doi.org/10.1016/j.immuni.2017.03.019

Male, D.K. (Ed.), 2013. Immunology: study smart with student consult, 8th ed. Elsevier Saunders, Amsterdam.

Marelli-Berg, F.M., Fu, H., Mauro, C., 2012. Molecular mechanisms of metabolic reprogramming in proliferating cells: implications for T-cell-mediated immunity: The metabolic control of T-cell immunity. Immunology 136, 363–369. https://doi.org/10.1111/j.1365-2567.2012.03583.x

Martinez, N.E., Sato, F., Omura, S., Kawai, E., Takahashi, S., Yoh, K., Tsunoda, I., 2014. RORγt, but not T-bet, Overexpression Exacerbates an Autoimmune Model for Multiple Sclerosis. J. Neuroimmunol. 276, 142–149. https://doi.org/10.1016/j.jneuroim.2014.09.006

Meiser, J., Tumanov, S., Maddocks, O., Labuschagne, C.F., Athineos, D., Van Den Broek, N., Mackay, G.M., Gottlieb, E., Blyth, K., Vousden, K., Kamphorst, J.J., Vazquez, A., 2016. Serine one-carbon catabolism with formate overflow. Sci. Adv. 2, e1601273. https://doi.org/10.1126/sciadv.1601273

Michalek, R.D., Gerriets, V.A., Jacobs, S.R., Macintyre, A.N., MacIver, N.J., Mason, E.F., Sullivan, S.A., Nichols, A.G., Rathmell, J.C., 2011. Cutting Edge: Distinct Glycolytic and Lipid Oxidative Metabolic Programs Are Essential for Effector and Regulatory CD4 $^{+}$ T Cell Subsets. J. Immunol. 186, 3299–3303. https://doi.org/10.4049/jimmunol.1003613

Modamio, J., Saraiva, C., Giro, G.G., Nickels, S.L., Jarazo, J., Antony, P., Barbuti, P., Hadler, R., Jäger, C., Krüger, R., Glaab, E., Schwamborn, J.C., 2021. Synaptic decline precedes dopaminergic neuronal loss in human midbrain organoids harboring a triplication of the *SNCA* gene (preprint). Neuroscience. https://doi.org/10.1101/2021.07.15.452499

Moffett, J.R., Puthillathu, N., Vengilote, R., Jaworski, D.M., Namboodiri, A.M., 2020. Acetate Revisited: A Key Biomolecule at the Nexus of Metabolism, Epigenetics and Oncogenesis—Part 1: Acetyl-CoA, Acetogenesis and Acyl-CoA Short-Chain Synthetases. Front. Physiol. 11.

Møller, S.H., Hsueh, P.-C., Yu, Y.-R., Zhang, L., Ho, P.-C., 2022. Metabolic programs tailor T cell immunity in viral infection, cancer, and aging. Cell Metab. 34, 378–395. https://doi.org/10.1016/j.cmet.2022.02.003

Moser, M., Leo, O., 2010. Key concepts in immunology. Vaccine 28, C2–C13. https://doi.org/10.1016/j.vaccine.2010.07.022

Murphy, K., Weaver, C., Mowat, A., Berg, L., Chaplin, D., 2017. Janeway's immunobiology, 8th ed. Garland Science, Taylor & Francis Group, New York.

Nagai, S., Kurebayashi, Y., Koyasu, S., 2013. Role of PI3K/Akt and mTOR complexes in Th17 cell differentiation: Th17 cells and PI3K-Akt-mTOR complexes. Ann. N. Y. Acad. Sci. 1280, 30–34. https://doi.org/10.1111/nyas.12059

Navale, A.M., Paranjape, A.N., 2016. Glucose transporters: physiological and pathological roles. Biophys. Rev. 8, 5–9. https://doi.org/10.1007/s12551-015-0186-2

Nolfi-Donegan, D., Braganza, A., Shiva, S., 2020. Mitochondrial electron transport chain: Oxidative phosphorylation, oxidant production, and methods of measurement. Redox Biol. 37, 101674. https://doi.org/10.1016/j.redox.2020.101674

O'Connor, R.A., Cambrook, H., Huettner, K., Anderton, S.M., 2013. T-bet is essential for Th1-mediated, but not Th17-mediated, CNS autoimmune disease. Eur. J. Immunol. 43, 2818–2823. https://doi.org/10.1002/eji.201343689

O'Neill, L.A.J., Kishton, R.J., Rathmell, J., 2016. A guide to immunometabolism for immunologists. Nat. Rev. Immunol. 16, 553–565. https://doi.org/10.1038/nri.2016.70

Ouyang, X., Han, Y., Qu, G., Li, M., Wu, N., Liu, H., Arojo, O., Sun, H., Liu, X., Liu, D., Chen, L., Zou, Q., Su, B., 2019. Metabolic regulation of T cell development by Sin1–mTORC2 is mediated by pyruvate kinase M2. J. Mol. Cell Biol. 11, 93–106. https://doi.org/10.1093/jmcb/mjy065

Palmer, C.S., Ostrowski, M., Balderson, B., Christian, N., Crowe, S.M., 2015. Glucose Metabolism Regulates T Cell Activation, Differentiation, and Functions. Front. Immunol. 6. https://doi.org/10.3389/fimmu.2015.00001

Park, H., Li, Z., Yang, X.O., Chang, S.H., Nurieva, R., Wang, Y.-H., Wang, Y., Hood, L., Zhu, Z., Tian, Q., Dong, C., 2005. A distinct lineage of CD4 T cells regulates tissue inflammation by producing interleukin 17. Nat. Immunol. 6, 1133–1141. https://doi.org/10.1038/ni1261

Patel, K.P., O'Brien, T.W., Subramony, S.H., Shuster, J., Stacpoole, P.W., 2012. The Spectrum of Pyruvate Dehydrogenase Complex Deficiency: Clinical, Biochemical and Genetic Features in 371 Patients. Mol. Genet. Metab. 105, 34–43. https://doi.org/10.1016/j.ymgme.2011.09.032

Patel, M.S., Nemeria, N.S., Furey, W., Jordan, F., 2014. The Pyruvate Dehydrogenase Complexes: Structure-based Function and Regulation. J. Biol. Chem. 289, 16615–16623. https://doi.org/10.1074/jbc.R114.563148

Patro, R., Duggal, G., Love, M.I., Irizarry, R.A., Kingsford, C., 2017. Salmon provides fast and bias-aware quantification of transcript expression. Nat. Methods 14, 417–419. https://doi.org/10.1038/nmeth.4197

Pearce, E.L., Pearce, E.J., 2013. Metabolic Pathways in Immune Cell Activation and Quiescence. Immunity 38, 633–643. https://doi.org/10.1016/j.immuni.2013.04.005

Pearce, E.L., Poffenberger, M.C., Chang, C.-H., Jones, R.G., 2013. Fueling Immunity: Insights into Metabolism and Lymphocyte Function. Science 342, 1242454. https://doi.org/10.1126/science.1242454

Peng, M., Yin, N., Chhangawala, S., Xu, K., Leslie, C.S., Li, M.O., 2016. Aerobic glycolysis promotes T helper 1 cell differentiation through an epigenetic mechanism. Science 354, 481–484. https://doi.org/10.1126/science.aaf6284

Pietrocola, F., Galluzzi, L., Bravo-San Pedro, J.M., Madeo, F., Kroemer, G., 2015. Acetyl Coenzyme A: A Central Metabolite and Second Messenger. Cell Metab. 21, 805–821. https://doi.org/10.1016/j.cmet.2015.05.014

Pishesha, N., Harmand, T.J., Ploegh, H.L., 2022. A guide to antigen processing and presentation. Nat. Rev. Immunol. https://doi.org/10.1038/s41577-022-00707-2

Qiu, J., Villa, M., Sanin, D.E., Buck, M.D., O'Sullivan, D., Ching, R., Matsushita, M., Grzes, K.M., Winkler, F., Chang, C.-H., Curtis, J.D., Kyle, R.L., Van Teijlingen Bakker, N., Corrado, M., Haessler, F., Alfei, F., Edwards-Hicks, J., Maggi, L.B., Zehn, D., Egawa, T., Bengsch, B., Klein Geltink, R.I., Jenuwein, T., Pearce, E.J., Pearce, E.L., 2019. Acetate Promotes T Cell Effector Function during Glucose Restriction. Cell Rep. 27, 2063-2074.e5. https://doi.org/10.1016/j.celrep.2019.04.022

Ramírez, F., Bhardwaj, V., Arrigoni, L., Lam, K.C., Grüning, B.A., Villaveces, J., Habermann, B., Akhtar, A., Manke, T., 2018. High-resolution TADs reveal DNA sequences underlying genome organization in flies. Nat. Commun. 9, 189. https://doi.org/10.1038/s41467-017-02525-w

Ramstead, A.G., Wallace, J.A., Lee, S.-H., Bauer, K.M., Tang, W.W., Ekiz, H.A., Lane, T.E., Cluntun, A.A., Bettini, M.L., Round, J.L., Rutter, J., O'Connell, R.M., 2020. Mitochondrial Pyruvate Carrier 1 Promotes Peripheral T Cell Homeostasis through Metabolic Regulation of Thymic Development. Cell Rep. 30, 2889-2899.e6. https://doi.org/10.1016/j.celrep.2020.02.042

Rangachari, M., Kuchroo, V.K., 2013. Using EAE to better understand principles of immune function and autoimmune pathology. J. Autoimmun. 45, 31–39. https://doi.org/10.1016/j.jaut.2013.06.008

Rangel Rivera, G.O., Knochelmann, H.M., Dwyer, C.J., Smith, A.S., Wyatt, M.M., Rivera-Reyes, A.M., Thaxton, J.E., Paulos, C.M., 2021. Fundamentals of T Cell Metabolism and Strategies to Enhance Cancer Immunotherapy. Front. Immunol. 12, 645242. https://doi.org/10.3389/fimmu.2021.645242

Rhodes, C.T., Lin, C.-H.A., 2023. Role of the histone methyltransferases Ezh2 and Suv4-20h1/Suv4-20h2 in neurogenesis. Neural Regen. Res. 18, 469–473. https://doi.org/10.4103/1673-5374.350188

Riezman, H., 2007. The Long and Short of Fatty Acid Synthesis. Cell 130, 587–588. https://doi.org/10.1016/j.cell.2007.08.008

Rivers, T.M., Schwentker, F.F., 1935. ENCEPHALOMYELITIS ACCOMPANIED BY MYELIN DESTRUCTION EXPERIMENTALLY PRODUCED IN MONKEYS. J. Exp. Med. 61, 689–702.

Rivers, T.M., Sprunt, D.H., Berry, G.P., 1933. OBSERVATIONS ON ATTEMPTS TO PRODUCE ACUTE DISSEMINATED ENCEPHALOMYELITIS IN MONKEYS. J. Exp. Med. 58, 39–53.

Roederer, M., 2011. Interpretation of cellular proliferation data: Avoid the panglossian. Cytometry A 79A, 95–101. https://doi.org/10.1002/cyto.a.21010

Ross-Innes, C.S., Stark, R., Teschendorff, A.E., Holmes, K.A., Ali, H.R., Dunning, M.J., Brown, G.D., Gojis, O., Ellis, I.O., Green, A.R., Ali, S., Chin, S.-F., Palmieri, C., Caldas, C., Carroll, J.S., 2012. Differential oestrogen receptor binding is associated with clinical outcome in breast cancer. Nature 481, 389–393. https://doi.org/10.1038/nature10730

Salmond, R.J., 2018. mTOR Regulation of Glycolytic Metabolism in T Cells. Front. Cell Dev. Biol. 6, 122. https://doi.org/10.3389/fcell.2018.00122

Saravia, J., Chapman, N.M., Chi, H., 2019. Helper T cell differentiation. Cell. Mol. Immunol. 16, 634–643. https://doi.org/10.1038/s41423-019-0220-6

Sarma, J.D., Ciric, B., Marek, R., Sadhukhan, S., Caruso, M.L., Shafagh, J., Fitzgerald, D.C., Shindler, K.S., Rostami, A., 2009. Functional interleukin-17 receptor A is expressed in central nervous system glia and upregulated in experimental autoimmune encephalomyelitis. J. Neuroinflammation 6, 14. https://doi.org/10.1186/1742-2094-6-14

Schubert, M., Ermini, L., Sarkissian, C.D., Jónsson, H., Ginolhac, A., Schaefer, R., Martin, M.D., Fernández, R., Kircher, M., McCue, M., Willerslev, E., Orlando, L., 2014. Characterization of ancient and modern genomes by SNP detection and phylogenomic and metagenomic analysis using PALEOMIX. Nat. Protoc. 9, 1056–1082. https://doi.org/10.1038/nprot.2014.063

Shi, L.Z., Wang, R., Huang, G., Vogel, P., Neale, G., Green, D.R., Chi, H., 2011. HIF1α–dependent glycolytic pathway orchestrates a metabolic checkpoint for the differentiation of TH17 and Treg cells. J. Exp. Med. 208, 1367–1376. https://doi.org/10.1084/jem.20110278

Sieper, J., Poddubnyy, D., 2017. Axial spondyloarthritis. The Lancet 390, 73–84. https://doi.org/10.1016/S0140-6736(16)31591-4

Sivanand, S., Viney, I., Wellen, K.E., 2018. Spatiotemporal Control of Acetyl-CoA Metabolism in Chromatin Regulation. Trends Biochem. Sci. 43, 61–74. https://doi.org/10.1016/j.tibs.2017.11.004

Spits, H., Artis, D., Colonna, M., Diefenbach, A., Di Santo, J.P., Eberl, G., Koyasu, S., Locksley, R.M., McKenzie, A.N.J., Mebius, R.E., Powrie, F., Vivier, E., 2013. Innate lymphoid cells - a proposal for uniform nomenclature. Nat. Rev. Immunol. 13, 145–149. https://doi.org/10.1038/nri3365

Stavnezer, J., Schrader, C.E., 2014. Ig heavy chain class switch recombination: mechanism and regulation. J. Immunol. Baltim. Md 1950 193, 5370–5378. https://doi.org/10.4049/jimmunol.1401849

Sugiura, A., Andrejeva, G., Voss, K., Heintzman, D.R., Xu, X., Madden, M.Z., Ye, X., Beier, K.L., Chowdhury, N.U., Wolf, M.M., Young, A.C., Greenwood, D.L., Sewell, A.E., Shahi, S.K., Freedman, S.N., Cameron, A.M., Foerch, P., Bourne, T., Garcia-Canaveras, J.C., Karijolich, J., Newcomb, D.C., Mangalam, A.K., Rabinowitz, J.D., Rathmell, J.C., 2022. MTHFD2 is a metabolic checkpoint controlling effector and regulatory T cell fate and function. Immunity 55, 65-81.e9. https://doi.org/10.1016/j.immuni.2021.10.011

Sun, X.-J., Man, N., Tan, Y., Nimer, S.D., Wang, L., 2015. The Role of Histone Acetyltransferases in Normal and Malignant Hematopoiesis. Front. Oncol. 5, 108. https://doi.org/10.3389/fonc.2015.00108

Sutendra, G., Kinnaird, A., Dromparis, P., Paulin, R., Stenson, T.H., Haromy, A., Hashimoto, K., Zhang, N., Flaim, E., Michelakis, E.D., 2014. A Nuclear Pyruvate Dehydrogenase Complex Is Important for the Generation of Acetyl-CoA and Histone Acetylation. Cell 158, 84–97. https://doi.org/10.1016/j.cell.2014.04.046

Takahara, T., Amemiya, Y., Sugiyama, R., Maki, M., Shibata, H., 2020. Amino acid-dependent control of mTORC1 signaling: a variety of regulatory modes. J. Biomed. Sci. 27, 87. https://doi.org/10.1186/s12929-020-00679-2

Talley, J.T., Mohiuddin, S.S., 2022. Biochemistry, Fatty Acid Oxidation, in: StatPearls. StatPearls Publishing, Treasure Island (FL).

Tomé, D., 2021. Amino acid metabolism and signalling pathways: potential targets in the control of infection and immunity. Nutr. Diabetes 11, 20. https://doi.org/10.1038/s41387-021-00164-1

Tran, K.A., Dillingham, C.M., Sridharan, R., 2019. The role of α-ketoglutarate–dependent proteins in pluripotency acquisition and maintenance. J. Biol. Chem. 294, 5408–5419. https://doi.org/10.1074/jbc.TM118.000831

Tyrakis, P.A., Palazon, A., Macias, D., Lee, Kian.L., Phan, Anthony.T., Veliça, P., You, J., Chia, G.S., Sim, J., Doedens, A., Abelanet, A., Evans, C.E., Griffiths, J.R., Poellinger, L., Goldrath, Ananda.W., Johnson, R.S., 2016. The immunometabolite S-2-hydroxyglutarate regulates CD8+ T-lymphocyte fate. Nature 540, 236–241. https://doi.org/10.1038/nature20165

van der Windt, G.J.W., Pearce, E.L., 2012. Metabolic switching and fuel choice during T-cell differentiation and memory development. Immunol. Rev. 249, 27–42. https://doi.org/10.1111/j.1600-065X.2012.01150.x

Vivier, E., Artis, D., Colonna, M., Diefenbach, A., Di Santo, J.P., Eberl, G., Koyasu, S., Locksley, R.M., McKenzie, A.N.J., Mebius, R.E., Powrie, F., Spits, H., 2018. Innate Lymphoid Cells: 10 Years On. Cell 174, 1054–1066. https://doi.org/10.1016/j.cell.2018.07.017

Wang, C., Yan, Y., Hu, L., Zhao, L., Yang, P., Moorhead, J.F., Varghese, Z., Chen, Y., Ruan, X.Z., 2014. Rapamycin-mediated CD36 translational suppression contributes to alleviation of hepatic steatosis. Biochem. Biophys. Res. Commun. 447, 57–63. https://doi.org/10.1016/j.bbrc.2014.03.103

Wang, R., Dillon, C.P., Shi, L.Z., Milasta, S., Carter, R., Finkelstein, D., McCormick, L.L., Fitzgerald, P., Chi, H., Munger, J., Green, D.R., 2011. The Transcription Factor Myc Controls Metabolic Reprogramming upon T Lymphocyte Activation. Immunity 35, 871–882. https://doi.org/10.1016/j.immuni.2011.09.021

Wang, R., Green, D.R., 2012. Metabolic reprogramming and metabolic dependency in T cells. Immunol. Rev. 249, 14–26. https://doi.org/10.1111/j.1600-065X.2012.01155.x

Warburg, Otto, 1956. On the Origin of Cancer Cells. Science 123, 309–314. https://doi.org/10.1126/science.123.3191.309

Warburg, O., 1956. On respiratory impairment in cancer cells. Science 124, 269–270.

Watkins, P.A., Maiguel, D., Jia, Z., Pevsner, J., 2007. Evidence for 26 distinct acyl-coenzyme A synthetase genes in the human genome. J. Lipid Res. 48, 2736–2750. https://doi.org/10.1194/jlr.M700378-JLR200

Wellen, K.E., Hatzivassiliou, G., Sachdeva, U.M., Bui, T.V., Cross, J.R., Thompson, C.B., 2009. ATP-Citrate Lyase Links Cellular Metabolism to Histone Acetylation. Science 324, 1076–1080. https://doi.org/10.1126/science.1164097

Wenes, M., Jaccard, A., Wyss, T., Maldonado-Pérez, N., Teoh, S.T., Lepez, A., Renaud, F., Franco, F., Waridel, P., Yacoub Maroun, C., Tschumi, B., Dumauthioz, N., Zhang, L., Donda, A., Martín, F., Migliorini, D., Lunt, S.Y., Ho, P.-C., Romero, P., 2022. The mitochondrial pyruvate carrier regulates memory T cell differentiation and antitumor function. Cell Metab. 34, 731-746.e9. https://doi.org/10.1016/j.cmet.2022.03.013

Wipperman, M.F., Montrose, D.C., Gotto, A.M., Hajjar, D.P., 2019. Mammalian Target of Rapamycin. Am. J. Pathol. 189, 492–501. https://doi.org/10.1016/j.ajpath.2018.11.013

Wu, B., Wan, Y., 2020. Molecular control of pathogenic Th17 cells in autoimmune diseases. Int. Immunopharmacol. 80, 106187. https://doi.org/10.1016/j.intimp.2020.106187

Xu, K., Yin, N., Peng, M., Stamatiades, E.G., Chhangawala, S., Shyu, A., Li, P., Zhang, X., Do, M.H., Capistrano, K.J., Chou, C., Leslie, C.S., Li, M.O., 2021. Glycolytic ATP fuels phosphoinositide 3-kinase signaling to support effector T helper 17 cell responses. Immunity 54, 976-987.e7. https://doi.org/10.1016/j.immuni.2021.04.008

Xu, T., Schutte, A., Jimenez, L., Gonçalves, A.N.A., Keller, A., Pipkin, M.E., Nakaya, H.I., Pereira, R.M., Martinez, G.J., 2021. Kdm6b Regulates the Generation of Effector CD8+ T Cells by Inducing Chromatin Accessibility in Effector-Associated Genes. J. Immunol. https://doi.org/10.4049/jimmunol.2001459

Xu, T., Stewart, K.M., Wang, X., Liu, K., Xie, M., Ryu, J.K., Li, K., Ma, T., Wang, H., Ni, L., Zhu, S., Cao, N., Zhu, D., Zhang, Y., Akassoglou, K., Dong, C., Driggers, E.M., Ding, S., 2017. Metabolic control of TH17 and induced Treg cell balance by an epigenetic mechanism. Nature 548, 228–233. https://doi.org/10.1038/nature23475

Yang, M., Vousden, K.H., 2016. Serine and one-carbon metabolism in cancer. Nat. Rev. Cancer 16, 650–662. https://doi.org/10.1038/nrc.2016.81

Yang, W., Pang, D., Chen, M., Du, C., Jia, L., Wang, L., He, Y., Jiang, W., Luo, L., Yu, Z., Mao, M., Yuan, Q., Tang, P., Xia, X., Cui, Y., Jing, B., Platero, A., Liu, Y., Wei, Y., Worley, P.F., Xiao, B., 2021. Rheb mediates neuronal-activity-induced mitochondrial energetics through mTORC1-independent PDH activation. Dev. Cell 56, 811-825.e6. https://doi.org/10.1016/j.devcel.2021.02.022

Yang, Z., Matteson, E.L., Goronzy, J.J., Weyand, C.M., 2015. T-cell metabolism in autoimmune disease. Arthritis Res. Ther. 17, 29. https://doi.org/10.1186/s13075-015-0542-4

Yap, Y.A., McLeod, K.H., McKenzie, C.I., Gavin, P.G., Davalos-Salas, M., Richards, J.L., Moore, R.J., Lockett, T.J., Clarke, J.M., Eng, V.V., Pearson, J.S., Hamilton-Williams, E.E., Mackay, C.R., Mariño, E., 2021. An acetate-yielding diet imprints an immune and anti-microbial programme against enteric infection. Clin. Transl. Immunol. 10, e1233. https://doi.org/10.1002/cti2.1233

Yoo, H.C., Yu, Y.C., Sung, Y., Han, J.M., 2020. Glutamine reliance in cell metabolism. Exp. Mol. Med. 52, 1496–1516. https://doi.org/10.1038/s12276-020-00504-8

Yu, G., Wang, L.-G., Han, Y., He, Q.-Y., 2012. clusterProfiler: an R Package for Comparing Biological Themes Among Gene Clusters. OMICS J. Integr. Biol. 16, 284–287. https://doi.org/10.1089/omi.2011.0118

Yu, G., Wang, L.-G., He, Q.-Y., 2015. ChIPseeker: an R/Bioconductor package for ChIP peak annotation, comparison and visualization. Bioinformatics 31, 2382–2383. https://doi.org/10.1093/bioinformatics/btv145

Zangari, J., Petrelli, F., Maillot, B., Martinou, J.-C., 2020. The Multifaceted Pyruvate Metabolism: Role of the Mitochondrial Pyruvate Carrier. Biomolecules 10, 1068. https://doi.org/10.3390/biom10071068

Zhang, D., Jin, W., Wu, R., Li, J., Park, S.-A., Tu, E., Zanvit, P., Xu, J., Liu, O., Cain, A., Chen, W., 2019. High Glucose Intake Exacerbates Autoimmunity through Reactive-Oxygen-Species-Mediated TGF-β Cytokine Activation. Immunity 51, 671-681.e5. https://doi.org/10.1016/j.immuni.2019.08.001

Zhao, S., Torres, A., Henry, R.A., Trefely, S., Wallace, M., Lee, J.V., Carrer, A., Sengupta, A., Campbell, S.L., Kuo, Y.-M., Frey, A.J., Meurs, N., Viola, J.M., Blair, I.A., Weljie, A.M., Metallo, C.M., Snyder, N.W., Andrews, A.J., Wellen, K.E., 2016. ATP-Citrate Lyase Controls a Glucose-to-Acetate Metabolic Switch. Cell Rep. 17, 1037–1052. https://doi.org/10.1016/j.celrep.2016.09.069

Zou, C., Wang, Y., Shen, Z., 2005. 2-NBDG as a fluorescent indicator for direct glucose uptake measurement. J. Biochem. Biophys. Methods 64, 207–215. https://doi.org/10.1016/j.jbbm.2005.08.001

APPENDICES

APPENDIX 1

Submitted Manuscript from Thesis Project

(First author)

SORIANO-BAGUET, L., GRUSDAT, M., KURNIAWAN, H., BENZARTI, M., BONETTI, L., EWEN, A., GUERRA, L., FRANCHINA, D.G., KOBAYASHI, T., LONGWORTH, J., BINSFELD, C., VERSCHUEREN, C., HELGUETA-ROMERO, S., GERARD, D., MORE, T., HENNE, A., DOSTERT, C., FARINELLE, S., JÄGER, C., MITTELBRONN, M., SINKKONEN, L., HILLER, K., MEISER, J., BRENNER, D. **Pyruvate dehydrogenase fuels a critical citrate pool that is essential for Th17 cell effector functions.** *In submission.*

Pyruvate dehydrogenase fuels a critical citrate pool that is essential for Th17 cell effector function

Graphical Abstract

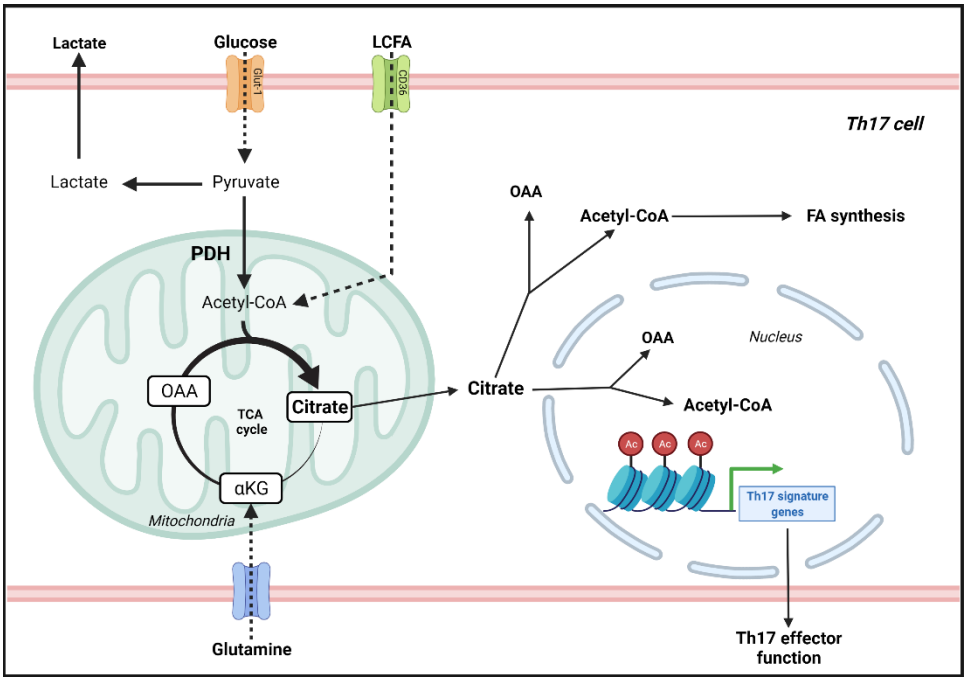

Authors

Leticia Soriano-Baguet, Melanie Grusdat, Henry Kurniawan,…, Karsten Hiller, Johannes Meiser, Dirk Brenner

Correspondence

dirk.brenner@lih.lu

In Brief

The pyruvate dehydrogenase (PDH) connects glycolysis with the mitochondrial tricarboxylic acid (TCA) cycle. Soriano-Baguet *et al.* show that PDH directs a glucose-derived citrate pool that coordinates central carbon metabolism, histone acetylation and is essential for Th17 cell function.

Highlights

- **T cell-specific deficiency of PDH protects mice against severe EAE**
- **PDH function is essential for Th17 cells and IL-17 production**
- **PDH coordinates a citrate pool that controls glycolysis, glutaminolysis and lipid metabolism in an mTOR-dependent manner**
- **The PDH-dependent citrate pool is crucial for histone acetylation and signature gene transcription**

Pyruvate dehydrogenase fuels a critical citrate pool that is essential for Th17 cell effector functions

Leticia Soriano-Baguet[1,2], Melanie Grusdat[1,2], Henry Kurniawan[1,2], Mohaned Benzarti[3], Lynn Bonetti[1,2], Anouk Ewen[1,2], Luana Guerra[1,2], Davide G. Franchina[1,2], Takumi Kobayashi[1,2], Joseph Longworth[1,2], Carole Binsfeld[1,2], Charlène Verschueren[1,2], Sergio Helgueta-Romero[4,5], Déborah Gerard[5], Tushar More[6], Antonia Henne[6], Catherine Dostert[1,2], Sophie Farinelle[1,2], Christian Jäger[7], Michel Mittelbronn[4,7,8,9,10,11], Lasse Sinkkonen[5], Karsten Hiller[6], Johannes Meiser[3] and Dirk Brenner[1,2,12, #,++]

[1]Experimental and Molecular Immunology, Department of Infection and Immunity, Luxembourg Institute of Health, Esch-sur-Alzette, Luxembourg.

[2]Immunology and Genetics, Luxembourg Centre for Systems Biomedicine, University of Luxembourg, 7, Avenue des Hauts Fourneaux, Esch-sur-Alzette, Luxembourg.

[3]Cancer Metabolism Group, Department of Oncology, Luxembourg Institute of Health, Luxembourg, Luxembourg.

[4]National Center of Pathology (NCP), Laboratoire National de Santé (LNS), Dudelange, Luxembourg.

[5]Epigenetics Team, Systems Biology Group, Life Science Research Unit (LSRU), University of Luxembourg, Esch-sur-Alzette, Luxembourg.

[6]Department for Bioinformatics and Biochemistry, Braunschweig Integrated Center of Systems Biology (BRICS), Technische Universität Braunschweig, Rebenring 56, 38106 Braunschweig, Germany.

[7]Luxembourg Centre for Systems Biomedicine (LCSB), University of Luxembourg, Esch-sur-Alzette, L-4362, Luxembourg.

[8]Luxembourg Center of Neuropathology (LCNP), Dudelange, L-3555, Luxembourg.

[9]Department of Life Sciences and Medicine (DLSM), University of Luxembourg, Esch-sur-Alzette, Luxembourg.

[10]Faculty of Science, Technology and Medicine, University of Luxembourg, Esch-sur-Alzette, Luxembourg.

[11]Department of Oncology (DONC), Luxembourg Institute of Health (LIH), Luxembourg, L-1526, Luxembourg.

[12]Odense Research Center for Anaphylaxis (ORCA), Department of Dermatology and Allergy Center, Odense University Hospital, University of Southern Denmark, Odense, Denmark.

[#]Corresponding author:

Dirk Brenner, PhD ([++]lead author)

Deputy Head of Research & Strategy

Department of Infection and Immunity, Experimental and Molecular Immunology, Luxembourg Institute of Health, 29, rue Henri Koch, L-4354 Esch-sur-Alzette, Luxembourg

Telephone: +352 26970-319 Fax: +352 26970-390 Email: dirk.brenner@lih.lu

SUMMARY

Pyruvate dehydrogenase (PDH) is the central enzyme connecting glycolysis and the tricarboxylic acid (TCA) cycle. The importance of PDH function in Th17 cells is unknown. Here, we show that PDH is essential for the generation of a unique glucose-derived citrate pool needed for Th17 cell proliferation, survival and effector function. *In vivo*, mice harboring a T cell-specific deletion of PDH were less susceptible to experimental autoimmune encephalomyelitis. Mechanistically, the absence of PDH in Th17 cells increased glutaminolysis, glycolysis, and lipid uptake in an mTOR-dependent manner. However, cellular citrate remained critically low in mutant Th17 cells, which interfered with oxidative phosphorylation (OXPHOS), lipid synthesis and histone acetylation crucial for the transcription of Th17 signature genes. Increasing cellular citrate in PDH-deficient Th17 cells restored their metabolism and function, identifying a metabolic feedback loop within central carbon metabolism that may offer possibilities for therapeutically targeting Th17 cell-driven autoimmunity.

KEYWORDS: pyruvate dehydrogenase, glucose metabolism, citrate, T cells, Th17 cells, experimental autoimmune encephalomyelitis, histone acetylation, IL-17

INTRODUCTION

T cells are essential for adaptive immune responses, and T helper 17 (Th17) cells are the $CD4^+$ subset that protects the host against extracellular bacteria and fungi (Pearce *et al.*, 2013). However, Th17 cells are also linked to autoimmune diseases such as multiple sclerosis and rheumatoid arthritis (Aranami and Yamamura, 2008; Basu, Hatton and Weaver, 2013). Th17 cells are defined by their expression of RORγT and the ability to produce IL-17 (Basu, Hatton and Weaver, 2013; Wu and Wan, 2020).

All T cells adapt their metabolism according to their energy demands (Franchina, Dostert and Brenner, 2018; Guerra, Bonetti and Brenner, 2020). Upon activation, $CD4^+$ T cells switch from mitochondrial metabolism [i.e. tricarboxylic citric acid cycle (TCA), oxidative phosphorylation (OXPHOS), and fatty acid beta-oxidation] to glycolysis and glutaminolysis to generate ATP and biosynthetic precursors, a process dubbed "metabolic reprogramming". This metabolic rewiring then supports the molecular signaling needed for T cell proliferation and effector functions (Pearce and Pearce, 2013; Buck, O'Sullivan and Pearce, 2015; Kurniawan, Soriano-Baguet and Brenner, 2020; Rangel Rivera *et al.*, 2021). However, aspects of metabolic reprogramming differ in different Th subsets (Chapman and Chi, 2022), and the details of this process in Th17 cells are not fully understood.

The mitochondrial pyruvate dehydrogenase (PDH) complex regulates the flux of cytoplasmic glucose into the TCA cycle (DeBrosse and Kerr, 2016). PDH catalyzes the conversion of glucose-derived pyruvate into acetyl-coenzyme A (CoA), which then condenses with oxaloacetate (OAA) to generate citrate (Pearce *et al.*, 2013; O'Neill, Kishton and Rathmell, 2016). Citrate enters the TCA cycle to produce the reducing equivalents necessary for ATP production via OXPHOS. In addition, citrate is transported out of the mitochondria into the cytoplasm and can even enter the nucleus, where it is converted back into acetyl-CoA and OAA by ATP-citrate lyase (ACLY) (Wellen *et al.*, 2009; Wang and Green, 2012; Zhao *et al.*, 2016; Koundouros and Poulogiannis, 2020; Chapman and Chi, 2022). Cytoplasmic acetyl-CoA drives lipid synthesis, whereas nuclear acetyl-CoA participates in histone acetylation regulating cell type-specific gene expression (Li, Carey and Workman, 2007; Pietrocola *et al.*, 2015; Sivanand, Viney and Wellen, 2018).

In this study, we investigated the role of PDH in the adaptation of Th17 cell metabolism. Our results demonstrate that PDH is critical for the generation of a citrate pool that is indispensable to support histone acetylation, Th17 cell-dependent gene expression and normal Th17 cell function.

Here, we show that PDH has a crucial role in the adaptation of Th17 cell metabolism and for their functions. Mechanistically, the ablation of PDH reduces cellular citrate below a critical level, which triggered metabolic alterations including increased glycolysis, glutaminolysis and fatty acid uptake to support survival and proliferation. However, these alterations could not sustain Th17 cell effector functions *in vivo* and *vitro*. In Th17 cells, PDH-synthesized citrate was found to be essential for histone

acetylation and Th17 cell-dependent gene expression. Consequently, replenishing the citrate pool by exogenous addition of acetate could reinstate normal Th17 cell metabolism and function. Our results demonstrate a novel role for PDH in the generation of a critical citrate pool that is indispensable to support Th17 cell function.

RESULTS

Loss of *Pdh* in T cells protects mice from severe EAE symptoms

To investigate PDH's importance in T cell metabolic adaptation, we analyzed *Pdh* mRNA levels in various $CD4^+$ Th subsets induced to differentiate *in vitro*. Th17 cells showed greater *Pdh* expression than Th0, Th1 or Treg cells (Figure 1A). We then crossed CD4 Cre+ mice with $Pdha1^{flox8}$ mice to generate a mutant mouse strain ($PDH^{fl/fl}$ CD4 Cre+) in which T cells did not express *Pdha1* (Figure 1B, 1C). *Pdha1* encodes the PDH-E1α subunit, which catalyzes the rate-limiting step of pyruvate conversion into acetyl-CoA (Yang *et al.*, 2021). $PDH^{fl/fl}$ CD4 Cre+ T cells still expressed the *Pdhb* gene (Figure S1A), which encodes the other PDH-E1 subunit, which does not harbor a catalytic activity without PDH-E1α (Figure S1A) (Yang *et al.*, 2021).

Next, we induced experimental autoimmune encephalomyelitis (EAE), a mouse model of multiple sclerosis known to depend on Th17 cells (Aranami and Yamamura, 2008), in control $PDH^{fl/fl}$ and $PDH^{fl/fl}$ CD4 Cre+ mice. $PDH^{fl/fl}$ CD4 Cre+ mice showed significant reductions in disease burden and mortality compared to littermate controls (Figure 1D, 1E). T cells isolated from brains and spleens of control and $PDH^{fl/fl}$ CD4 Cre+ mice at day 14 post-EAE induction showed comparable percentages and numbers of $CD45^+$ infiltrating cells (Figure 1F, S1B). However, while brains of $PDH^{fl/fl}$ CD4 Cre+ mice showed normal infiltration of $Tbet^+$ Th1 cells, the percentages of infiltrating $ROR\gamma T^+$ Th17 cells and $CD25^+Foxp3^+$ Treg cells were reduced (Figure 1G, S1C, S1D). We then analyzed Th17 cell function by measuring IFNγ and IL-17A production. The pathogenic $IFN\gamma^+IL\text{-}17A^+$ Th17 cell subset was significantly decreased in $PDH^{fl/fl}$ CD4 Cre+ brains whereas the frequencies of $IFN\gamma^+IL\text{-}17A^-$ and $IFN\gamma^-IL\text{-}17A^+$ $CD4^+$ T cells were unaffected (Figure 1H, S1E, S1F). Thus, PDH is critical for Th17 cell function *in vivo*.

To gain mechanistic insight into PDH's role in Th17 cells, we induced naïve $CD4^+$ T cells isolated from spleens and lymph nodes of control and $PDH^{fl/fl}$ CD4 Cre+ mice to differentiate into Th17 cells *in vitro* by exposing them to anti-CD3/CD28, IL-6 and TGFβ (Baricza *et al.*, 2018; Wu and Wan, 2020). Although the PDH-deficient Th17 cells showed only marginally decreased RORγT expression, their production of IL-17 was markedly impaired (Figure 1I-L, S1G). In contrast, Th1 differentiation and effector function and Treg induction were not affected by PDH ablation (Figure S1H, I, J). Thus, Th17 cell effector functions, but not differentiation *per se,* depend on PDH.

PDH is essential for central metabolism in Th17 cells

We hypothesized that PDH loss in Th17 cells would trigger drastic metabolic shifts impeding their function. Flow cytometric analysis (FCA) revealed that expression of Glut-1, the major glucose transporter in T cells (Macintyre *et al.*, 2014), was increased in PDH-deficient Th17 cells compared to controls (Figure 2A). This result aligned with the PDH-deficient cells' elevated glucose uptake as determined by mass spectrometry (MS) and enhanced uptake of the fluorescent glucose analog [2-(N-(7-Nitrobenz-2-oxa-1,3-diazol-4-yl)amino)-2-deoxyglucose] (2-NBDG) (Zou, Wang and Shen, 2005) (Figure 2B, S2A). Extracellular flux analyses by Seahorse confirmed significantly increased glycolysis and glycolytic capacity in PDH-deficient Th17 cells that were associated with heightened lactate release (Figure 2C-E, S2B). Furthermore, the mutant cells exhibited increased expression of hexokinase-1, which catalyzes the conversion of glucose to glucose-6-phosphate (Katsen, Soderman and Nitowsky, 1965), as well as enhanced pyruvate release (Figure 2F, S2C). All these data pointed to increased flux through glycolysis that, because PDH-deficient Th17 cells cannot metabolize pyruvate further, resulted in pyruvate release into the culture medium.

Despite the above, glycolytic flux analysis using an exogenous ^{13}C-glucose tracer (Buescher *et al.*, 2015) revealed no difference in the contribution of ^{13}C-glucose to pyruvate (M3 label) between control and PDH-deficient Th17 cells (Figure 2G). This result further substantiated our findings that glycolytic activity was increased but that glucose flux through glycolysis itself was not altered in the absence of PDH. In contrast, there was minimal ^{13}C-glucose incorporation into the TCA metabolites citrate, fumarate, and malate (M2 label) in PDH-deficient Th17 cells (Figure 2H-J). RNAseq analysis showed an overall reduction in expression of TCA cycle genes in mutant Th17 cells compared to controls (Figure S2D). Thus, without PDH-E1α, Th17 cells cannot convert pyruvate into acetyl-CoA to feed into the TCA cycle, and this deficit compromises Th17 cell effector functions.

Glutamine can replenish the TCA cycle at the stage of α-ketoglutarate (αKG) (Yoo *et al.*, 2020), and we observed that ^{13}C-glutamine incorporation into TCA metabolites such as fumarate and malate (M4 label) was elevated in PDH-deficient Th17 cells (Figure 2K, 2L). Glutamine uptake was also increased (Figure S2E). Nonetheless, we did not detect an increased flux to citrate, either by oxidative (M4 label) or by reductive (M5 label) glutamine metabolism (Figure 2M, 2N). These results bolster our finding that citrate production in Th17 cells requires PDH-generated acetyl-CoA.

In line with their decreased glucose flux into the TCA cycle and reduced expression of TCA enzymes, PDH-deficient Th17 cells showed deficits in basal oxygen consumption rate (OCR), OCR-dependent ATP production, and spare respiratory capacity (Figure 2O-S). Expression levels of OXPHOS-related genes and pathways were also decreased (Figure 2T, S2F). Thus, an absence of PDH in Th17 cells drastically alters central oxidative metabolism, prevents glucose flux into the TCA cycle, and impairs citrate formation such that it cannot be replenished by glutamine.

PDH ablation induces fatty acid metabolism in Th17 cells

Because the contribution of glucose carbons to citrate was impaired in PDH-deficient Th17 cells, we used MS to measure total intracellular TCA metabolites in these cells. Absolute citrate levels were minimal in PDH-deficient Th17 cells (Figure 3A), and fumarate and malate were reduced (Figure S3A, S3B). When citrate exits the mitochondria, it is converted by ACLY into OAA and acetyl-CoA used for *de novo* lipid synthesis (Wellen *et al.*, 2009; Pietrocola *et al.*, 2015; Zhao *et al.*, 2016). However, our ^{13}C-glucose and ^{13}C-glutamine tracing revealed almost no contribution of these carbon sources to the synthesis of the lipid octadecenoic acid in PDH-deficient Th17 cells (Figure 3B, S3C, S3D). Thus, the absence of citrate in PDH-deficient Th17 cells affects the biosynthesis of critical metabolites such as lipids.

Because lipids are essential for proliferation (de Jong *et al.*, 2014; Pietrocola *et al.*, 2015), we used CellTrace Violet (CTV) to monitor the proliferation of PDH-deficient Th17 cells in culture. Although PDH$^{fl/fl}$ CD4 Cre+ Th17 cells showed significantly decreased proliferation compared to controls, it was still substantial (Figure 3C), suggesting that the necessary lipids were derived from a citrate-independent source. We measured the uptake of extracellular lipids by the mutant cells using fluorescently labeled palmitate (Bodipy FL C16) and observed a marked increase (Figure 3D). When we cultured mutant and control Th17 cells in medium lacking extracellular lipids, the proliferation and basal OCR of PDH$^{fl/fl}$ CD4 Cre+ Th17 cells were impaired (Figure 3E-G), affirming our contention that the mutant cells rely on the import of extracellular lipids.

Long-chain fatty acids (LCFA) require transporters such as CD36 to enter cells (Koundouros and Poulogiannis, 2020), and we observed increased CD36 expression in PDH$^{fl/fl}$ CD4 Cre+ Th17 cells (Figure 3H). CD36 expression is controlled by mTOR (Wang *et al.*, 2014; Angela *et al.*, 2016; Wipperman *et al.*, 2019), and we detected increased phosphorylation of both mTOR (p-mTOR) and its downstream target ribosomal protein S6 (p-S6) in the mutant cells (Figure 3I, 3J). CD36 induction and the observed increase in lipid uptake by PDH-deficient Th17 cells could be reversed by two chemical inhibitors of mTOR, Torin 1 and rapamycin (Figure 3K, 3L, S3E, S3F). mTOR is activated by amino acids, particularly glutamine (Takahara *et al.*, 2020), and we had already established that PDH-deficient Th17 cells showed increased glutamine uptake and glutaminolysis (Figure S2E, 2K, 2L). Glutamine deprivation decreased p-mTOR and CD36 levels as well as lipid uptake in PDH-deficient Th17 cells (Figure S3G, S3H, S3I), exposing a metabolic feedback loop regulating central carbon metabolism. Thus, the increased activity of mTOR in PDH-deficient Th17 cells promotes extracellular lipid uptake, which is critical for the survival and functionality of these cells.

PDH-derived citrate is crucial for histone acetylation and epigenetic modifications

Citrate-derived acetyl-CoA is required for post-translational histone acetylation (Pietrocola *et al.*, 2015), which is an important epigenetic modification that opens up condensed chromatin and fosters

transcriptional activity (Li, Carey and Workman, 2007). Strikingly, histone 3 (H3) acetylation was not detected in PDH-deficient Th17 cells (Figure 4A). ATACseq analysis (Buenrostro *et al.*, 2013, 2015) of *in vitro*-differentiated control and PDH-deficient Th17 cells showed drastic decreases in mean chromatin accessibility in the PDH-deficient Th17 cells (Figure 4B). The *IL-17A, IL-17F, Il23r, Smad3,* and *Hif1a* loci all showed decreased chromatin accessibility and mRNA expression (Figure 4C, S4A). Interestingly, although the accessibility of the *Rorc* locus encoding RORγT was reduced, RORγT expression was not affected (Figure 4C), in line with the near-normal RORγT levels in mutant Th17 cells (Figure 1I, 1J).

Next, we treated PDH-deficient and control Th17 cells with the short-chain fatty acid (SCFA) acetate (Bulusu *et al.*, 2017; Qiu *et al.*, 2019). Acetate is converted by acetyl-CoA synthetases into acetyl-CoA (Comerford *et al.*, 2014), and so can bypass the lack of citrate in PDH-deficient Th17 cells. Indeed, upon acetate supplementation, PDH-deficient Th17 cells showed wild-type H3 acetylation levels (Figure 4D). To test if acetate reaches the TCA cycle in the mutant Th17 cells, we treated them with ^{13}C-labelled acetate and observed that it did contribute to TCA metabolites such as citrate, fumarate and malate (Figure 4E, 4F, S4B). Indeed, these contributions were increased over those in control Th17 cells due to the lack of glucose flux into the TCA cycle in the mutant cells. The citrate pool was also restored in acetate-treated PDH-deficient Th17 cells (Figure 4G), re-establishing lipid synthesis and proliferative potential (Figure 4H, 4I). Acetate treatment also allowed mutant Th17 cell to normalize their basal OCR and glycolytic capacity (Figure 4L, S4C) and return their levels of p-mTOR, CD36 and lipid uptake to normal (Figure 4M-O). Finally, acetate-treated PDH-deficient Th17 cells regained the capacity to produce IL-17A (Figure 4P).

Thus, PDH-generated acetyl-CoA contributes to a critical citrate pool that cannot be derived from other carbon sources. This citrate is crucial for epigenetic-mediated chromatin accessibility allowing Th17 signature gene transcription, and thereby coordinates the metabolism, proliferation and functionality of these cells.

DISCUSSION

Previous work has shown that the metabolism and functions of effector T cells are closely connected (Buck, O'Sullivan and Pearce, 2015; Chapman, Boothby and Chi, 2020; Rangel Rivera *et al.*, 2021; Chapman and Chi, 2022). In our study, we genetically targeted the PDH-E1α subunit specifically in T cells, disconnecting glycolysis from the TCA cycle. Th17 cells are known to rely on glycolytic ATP and regulators such as myc, HIF-1α, and mTOR for their differentiation and function (Dang *et al.*, 2011; Michalek *et al.*, 2011; Shi *et al.*, 2011; Wang *et al.*, 2011; Zhang *et al.*, 2019; Xu *et al.*, 2021), and we have added PDH to this list. Without PDH, Th17 cells rewire their metabolism to increase their uptake of glucose, glutamine, and fatty acids to ensure their survival and proliferation. However, our mutant Th17 cells lacked a critical citrate pool that could not be generated in a PDH-independent manner and was essential for the functionality of Th17 cells *in vivo* and *in vitro*.

The mitochondrial pyruvate carrier (MPC) imports pyruvate into the mitochondria where it is converted into acetyl-CoA (Bricker *et al.*, 2012; Herzig *et al.*, 2012; Zangari *et al.*, 2020). MPC1$^{fl/fl}$ Vav Cre mutant mice, which do not express *Mpc1* in any hematopoietic cells, suffer from more severe EAE than control littermates (Ramstead *et al.*, 2020), a finding that contrasts with the effects of T cell-specific PDH deletion we observed. However, glutamine can also generate pyruvate in the mitochondria and thus, provide a substrate for PDH while bypassing the need for MPC-mediated pyruvate import. Which would indicate that PDH-dependent pyruvate conversion to acetyl-CoA, and not its transport to the mitochondria, might be essential for Th17 cell effector function during EAE. Furthermore, VavCre-mediated MPC1 deletion occurs very early during hematopoiesis and so affects T cell development, which favors the establishment of a more activated T cell pool (Ramstead *et al.*, 2020); this difference may also explain this discrepancy. Similarly, when Mx1Cre is employed to delete PDH in bone marrow and hematopoietic stem cells, T cell development in the thymus is impaired, which is not the case when CD4 Cre is used (Jun *et al.*, 2021). Thus, the developmental stage at which pyruvate metabolism is disrupted may define its effects.

Tight regulation of metabolism is important for maintaining Th cell functionality (Marelli-Berg, Fu and Mauro, 2012), and too much or too little glycolysis and/or OXPHOS impairs T cell functions (Mak *et al.*, 2017; Kurniawan *et al.*, 2020). Our data show that, not surprisingly, abrogation of PDH activity affects Th17 cell functionality. Conversely, sustained PDH activation achieved by pharmacological inhibition of PDK1 (an inhibitor of PDH) also has a negative effect on Th17 cells (Gerriets *et al.*, 2015). Thus, PDH is a vital regulator of Th17 cells, and too little or too much flux through this metabolic gatekeeper is detrimental to this Th cell subset.

Glutamine contributes to the energy produced via the TCA cycle (Yoo *et al.*, 2020), and ablation of glutaminase impairs Th17 cell differentiation and function such that Th17-driven inflammatory diseases are mitigated *in vivo* (Johnson *et al.*, 2018). Glutamine is also required for the synthesis of glutathione

(GSH), an important antioxidant in T cells that is essential for effector T cell reprogramming and Treg suppressive capacity (Mak *et al.*, 2017; Kurniawan *et al.*, 2020). However, we showed that increased glutamine uptake did not relieve the functional defects of PDH-deficient Th17 cells because glutamine could not replenish the critical PDH-dependent citrate pool in these cells. Thus, only the stringent control of a specific metabolic program in a given Th subset can ensure its functionality. Fortunately, this restriction offers the possibility of subset-specific therapeutic interference at key regulatory points.

In mammalian cells, cytosolic acetyl-CoA has two possible fates: lipid synthesis and protein acetylation (Pietrocola *et al.*, 2015; Sivanand, Viney and Wellen, 2018). In our study of Th17 cells, glucose-derived acetyl-CoA was used for lipid synthesis and proliferation. Upon PDH deletion, Th17 cells increased their extracellular fatty acid uptake through mTOR-dependent upregulation of CD36. Although CD36 is a target of mTOR signaling, mTOR is also crucial for Th17 cell differentiation and metabolic rewiring (Delgoffe *et al.*, 2009; Nagai, Kurebayashi and Koyasu, 2013; Salmond, 2018). A major activator of mTOR is glutamine (Takahara *et al.*, 2020), and the increased mTOR activation in our PDH-deficient Th17 cells was causally linked to their heightened glutamine uptake. These data reveal a metabolic feedback loop between glycolysis and glutaminolysis in Th17 cells that can respond to exogenous acetyl-CoA in the form of acetate. Acetate treatment of PDH-deficient Th17 cells reverted the metabolic dysregulation in these cells and restored their functionality. Similarly, other studies have shown that acetate can serve as a source of acetyl-CoA to regulate effector T cell functions (Peng *et al.*, 2016; Qiu *et al.*, 2019; Xu *et al.*, 2021). These aspects of cellular metabolism are closely linked to epigenetic modifications. When PDH localizes in the nucleus in constitutively active form, it generates a mitochondria-independent pool of acetyl-CoA for histone acetylation (Sutendra *et al.*, 2014). We demonstrated that an absence of PDH impairs H3 acetylation in a manner that can be restored by acetate treatment, bolstering the importance of PDH for maintaining normal epigenetics in Th17 cells.

In conclusion, our study has uncovered an unexpected role for PDH as a central regulator of Th17 cells *in vivo* and *in vitro*. We show that PDH in Th17 cells is critical for the establishment of a glucose-derived citrate pool that is essential for the survival, proliferation, and effector functions of this important Th cell subset.

Acknowledgements

We are grateful to Max Löhning (Charité – Univ. Berlin) and Alexander Skupin (Univ. Luxembourg) for helpful discussions; the Metabolomics Platform of Luxembourg Centre for Systems Biomedicine (LCSB) for metabolomics data; and the National Cytometry Platform (LIH, Luxembourg) for support with flow cytometry. We also thank Samantha Storn, Anaïs Oudin, all Animal Facility staff, and LIH's Animal Welfare Structure for animal services at LIH, Luxembourg; and Djalil Coowar, Jennifer Behm, Marthe Schmit and all Animal Facility staff for animal services at Univ. Luxembourg.

D.B. is supported by FNR-ATTRACT (A14/BM/7632103) and FNR-CORE grants (C21/BM/15796788), (C18/BM/12691266). D.B., T.K. and C.D. are supported by FNRS-Televie grants No. 7.4587.20 and/or No. 7.497.19. D.B., L.B., L.G. and L.S-B. by FNR-PRIDE (PRIDE/11012546/NEXTIMMUNE); D.B. and A.E. by (PRIDE17/11823097/MicrOH); D.B. and D.G.F. by FNR-RIKEN (TregBar/11228353), J.M. by FNR-ATTRACT (A18/BM/11809970) and M.M. by FNR PEARL P16/BM/11192868.

Author Contributions

L.S-B. performed most experiments assisted by M.G., H.K, L.B., A.E., L.G., D.G.F, C.B., C.V. and S.F. L.S-B., M.G. and C.B isolated brains and spleens from EAE mice. L.S-B., H.K., A.E. and D.G.F. performed Seahorse flux assays. Isotopic and metabolic tracing experiments were performed by L.S-B., M.G. and H.K. and analyzed by M.B. and J.M. Analysis of RNA-sequencing data was performed by J.L. and S.H-R. ATAC-sequencing and data analysis were performed by S.H-R., D.G. and L.S. T.K., C.D., J-J.G., C.J., M.M., L.S. and J.M. provided reagents and expert comments. D.B. supervised the project. L.S-B. and D.B. conceptualized the work, designed all experiments, analyzed data, and wrote the manuscript. All authors reviewed and edited the final manuscript.

Declaration of Interests

The authors declare no competing interests.

Figure 1

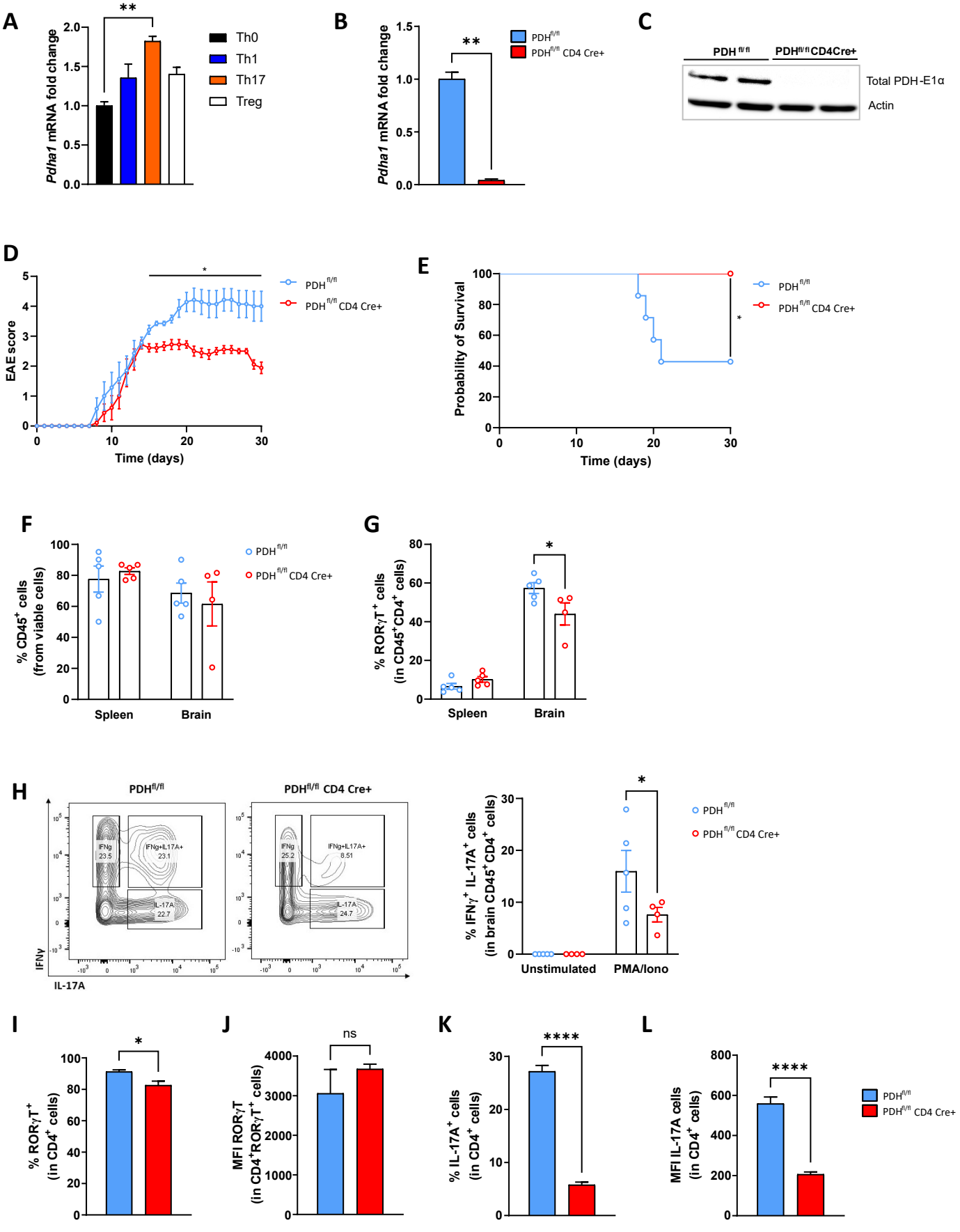
A
Pdha1 mRNA fold change
Th0
Th1
Th17
Treg
B
Pdha1 mRNA fold change
PDH fl/fl
PDH fl/fl CD4 Cre+
C
PDH fl/fl
PDH fl/fl CD4Cre+
Total PDH-E1α
Actin
D
EAE score
Time (days)
E
Probability of Survival
Time (days)
F
% CD45+ cells (from viable cells)
Spleen
Brain
G
% RORγT+ cells (in CD45+CD4+ cells)
Spleen
Brain
H
PDH fl/fl
PDH fl/fl CD4 Cre+
IFNg 23.5
IFNg+IL17A+ 23.1
IL-17A 22.7
IFNg 25.2
IFNg+IL17A+ 8.51
IL-17A 24.7
IFNγ
IL-17A
% IFNγ+ IL-17A+ cells (in brain CD45+CD4+ cells)
Unstimulated
PMA/Iono
I
% RORγT+ (in CD4+ cells)
J
MFI RORγT (in CD4+RORγT+ cells)
ns
K
% IL-17A+ cells (in CD4+ cells)
L
MFI IL-17A cells (in CD4+ cells)

Figure 2

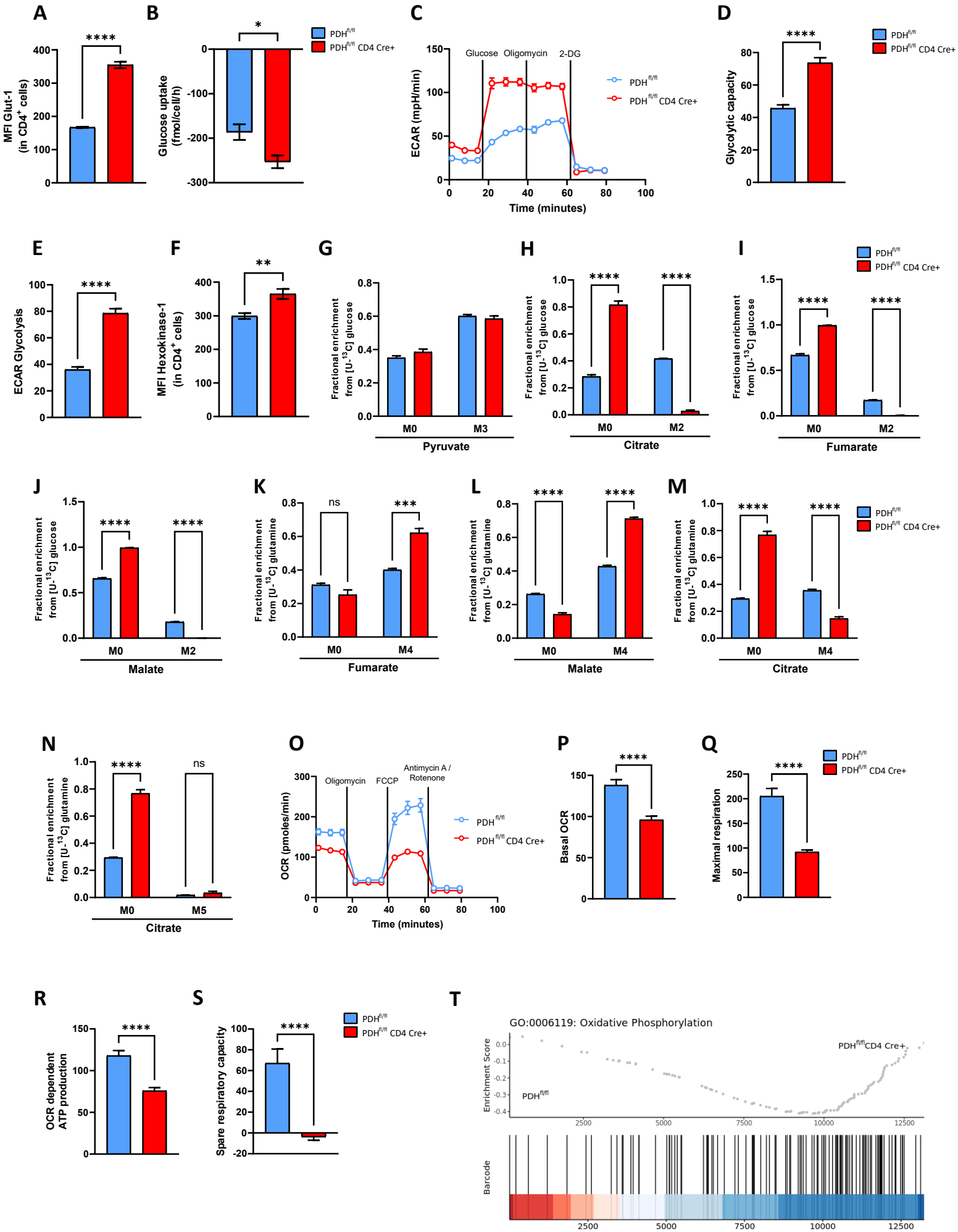
A
MFI Glut-1 (in CD4+ cells)
****
B
Glucose uptake (fmol/cell/h)
*
PDHfl/fl
PDHfl/fl CD4 Cre+
C
ECAR (mpH/min)
Glucose
Oligomycin
2-DG
Time (minutes)
D
Glycolytic capacity
E
ECAR Glycolysis
F
MFI Hexokinase-1 (in CD4+ cells)
**
G
Fractional enrichment from [U-13C] glucose
M0
M3
Pyruvate
H
M0
M2
Citrate
I
Fumarate
J
Malate
K
ns
***
M4
L
M
N
Fractional enrichment from [U-13C] glutamine
M5
O
OCR (pmoles/min)
Oligomycin
FCCP
Antimycin A / Rotenone
P
Basal OCR
Q
Maximal respiration
R
OCR dependent ATP production
S
Spare respiratory capacity
T
GO:0006119: Oxidative Phosphorylation
Enrichment Score
Barcode

Figure 3

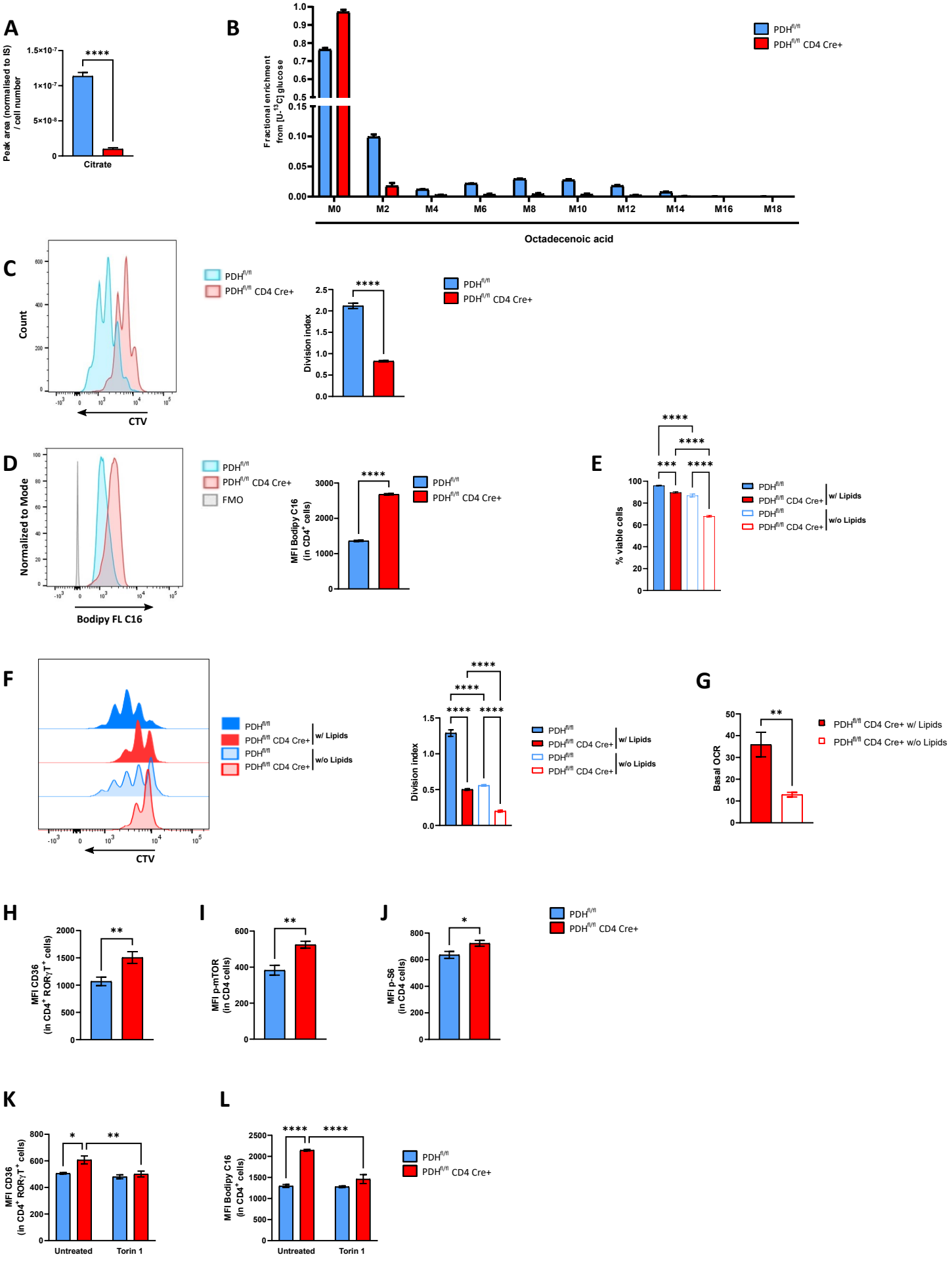
A
Peak area (normalised to IS) / cell number
Citrate
****
B
Fractional enrichment from [U-13C] glucose
M0
M2
M4
M6
M8
M10
M12
M14
M16
M18
Octadecenoic acid
PDHfl/fl
PDHfl/fl CD4 Cre+
C
Count
CTV
Division index
D
Normalized to Mode
Bodipy FL C16
FMO
MFI Bodipy C16 (in CD4+ cells)
E
% viable cells
***
w/ Lipids
w/o Lipids
F
Division index
G
Basal OCR
PDHfl/fl CD4 Cre+ w/ Lipids
PDHfl/fl CD4 Cre+ w/o Lipids
H
MFI CD36 (in CD4+ RORγT+ cells)
I
MFI p-mTOR (in CD4 cells)
J
MFI p-S6 (in CD4 cells)
K
Untreated
Torin 1
L

Figure 4

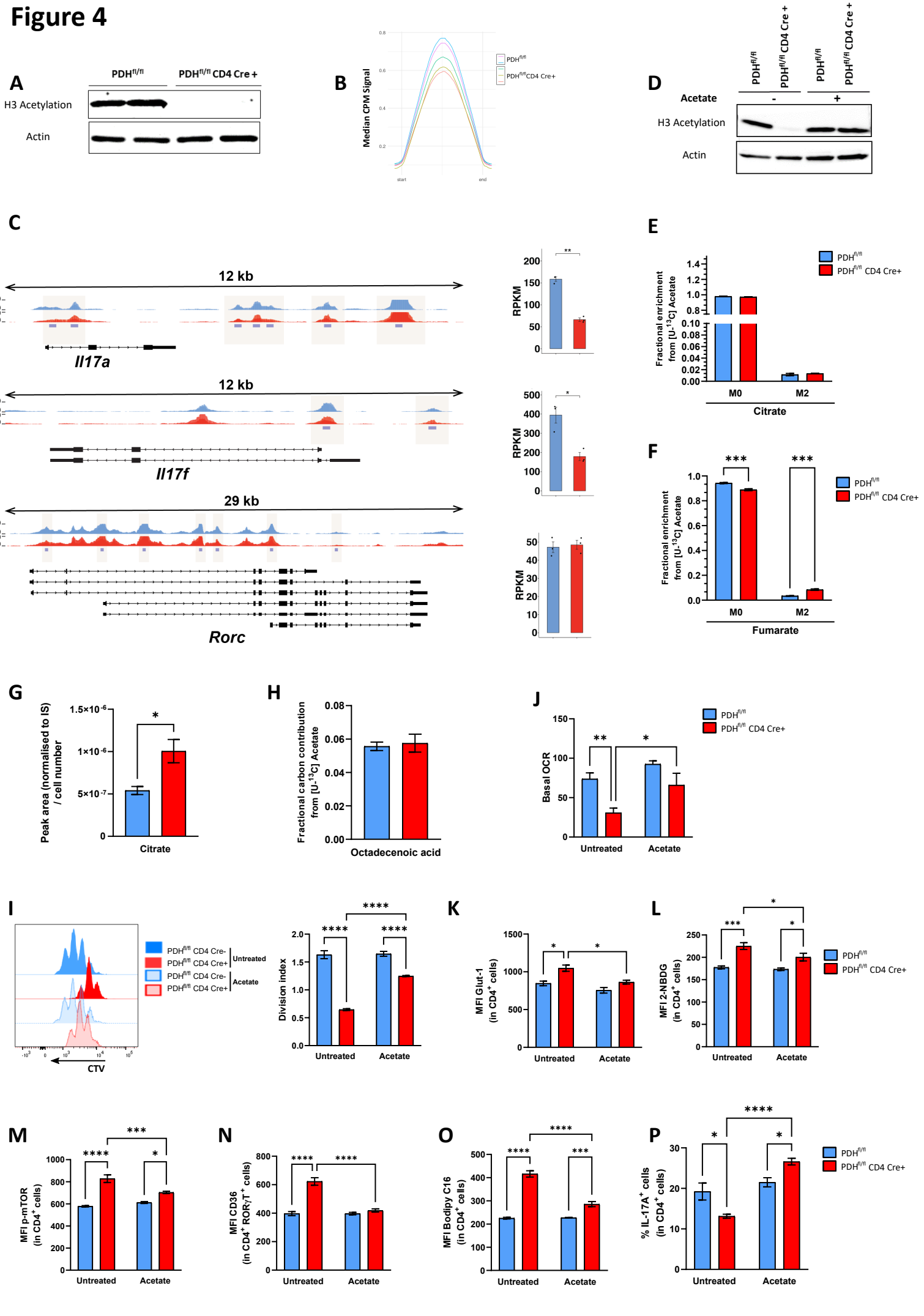
A
PDHfl/fl
PDHfl/fl CD4 Cre+
H3 Acetylation
Actin
B
Median CPM Signal
PDHfl/fl
PDHfl/fl CD4 Cre+
start
end
D
PDHfl/fl
PDHfl/fl CD4 Cre +
PDHfl/fl
PDHfl/fl CD4 Cre +
Acetate
-
+
H3 Acetylation
Actin
C
12 kb
Il17a
12 kb
Il17f
29 kb
Rorc
RPKM
RPKM
RPKM
E
PDHfl/fl
PDHfl/fl CD4 Cre+
Fractional enrichment from [U-13C] Acetate
M0
M2
Citrate
F
PDHfl/fl
PDHfl/fl CD4 Cre+
Fractional enrichment from [U-13C] Acetate
M0
M2
Fumarate
G
Peak area (normalised to IS) / cell number
Citrate
H
Fractional carbon contribution from [U-13C] Acetate
Octadecenoic acid
J
PDHfl/fl
PDHfl/fl CD4 Cre+
Basal OCR
Untreated
Acetate
I
PDHfl/fl CD4 Cre-
PDHfl/fl CD4 Cre+
PDHfl/fl CD4 Cre-
PDHfl/fl CD4 Cre+
Untreated
Acetate
CTV
Division index
Untreated
Acetate
K
MFI Glut-1 (in CD4+ cells)
Untreated
Acetate
L
PDHfl/fl
PDHfl/fl CD4 Cre+
MFI 2-NBDG (in CD4+ cells)
Untreated
Acetate
M
MFI p-mTOR (in CD4+ cells)
Untreated
Acetate
N
MFI CD36 (in CD4+ RORγT+ cells)
Untreated
Acetate
O
MFI Bodipy C16 (in CD4+ cells)
Untreated
Acetate
P
PDHfl/fl
PDHfl/fl CD4 Cre+
% IL-17A+ cells (in CD4+ cells)
Untreated
Acetate

Figure S1

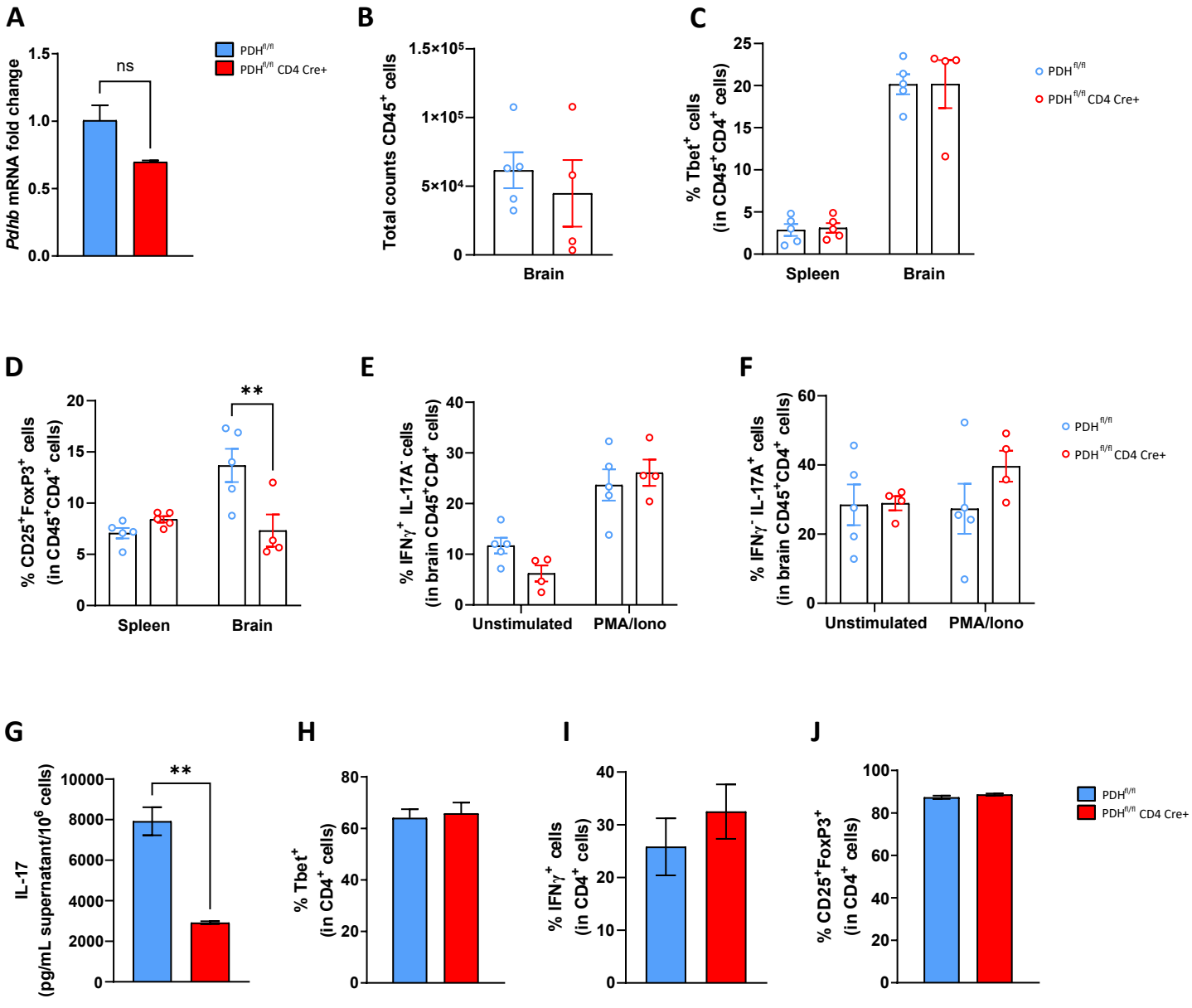
A
Pdhb mRNA fold change
1.5
1.0
0.5
0.0
ns
PDH fl/fl
PDH fl/fl CD4 Cre+
B
Total counts CD45+ cells
1.5×10^5
1×10^5
5×10^4
0
Brain
C
% Tbet+ cells
(in CD45+CD4+ cells)
25
20
15
10
5
0
Spleen
Brain
PDH fl/fl
PDH fl/fl CD4 Cre+
D
% CD25+FoxP3+ cells
(in CD45+CD4+ cells)
20
15
10
5
0
**
Spleen
Brain
E
% IFNγ+ IL-17A- cells
(in brain CD45+CD4+ cells)
40
30
20
10
0
Unstimulated
PMA/Iono
F
% IFNγ- IL-17A+ cells
(in brain CD45+CD4+ cells)
60
40
20
0
Unstimulated
PMA/Iono
PDH fl/fl
PDH fl/fl CD4 Cre+
G
IL-17
(pg/mL supernatant/10^6 cells)
10000
8000
6000
4000
2000
0
**
H
% Tbet+
(in CD4+ cells)
80
60
40
20
0
I
% IFNγ+ cells
(in CD4+ cells)
40
30
20
10
0
J
% CD25+FoxP3+
(in CD4+ cells)
100
80
60
40
20
0
PDH fl/fl
PDH fl/fl CD4 Cre+

Figure S2

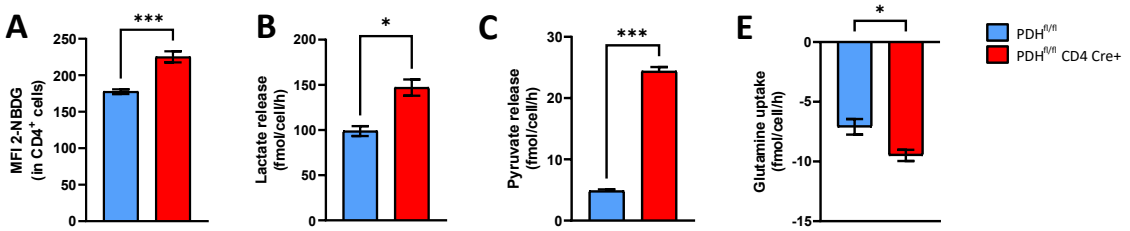
A
MFI 2-NBDG (in CD4+ cells)
***
B
Lactate release (fmol/cell/h)
*
C
Pyruvate release (fmol/cell/h)
***
E
Glutamine uptake (fmol/cell/h)
*
PDHfl/fl
PDHfl/fl CD4 Cre+

D

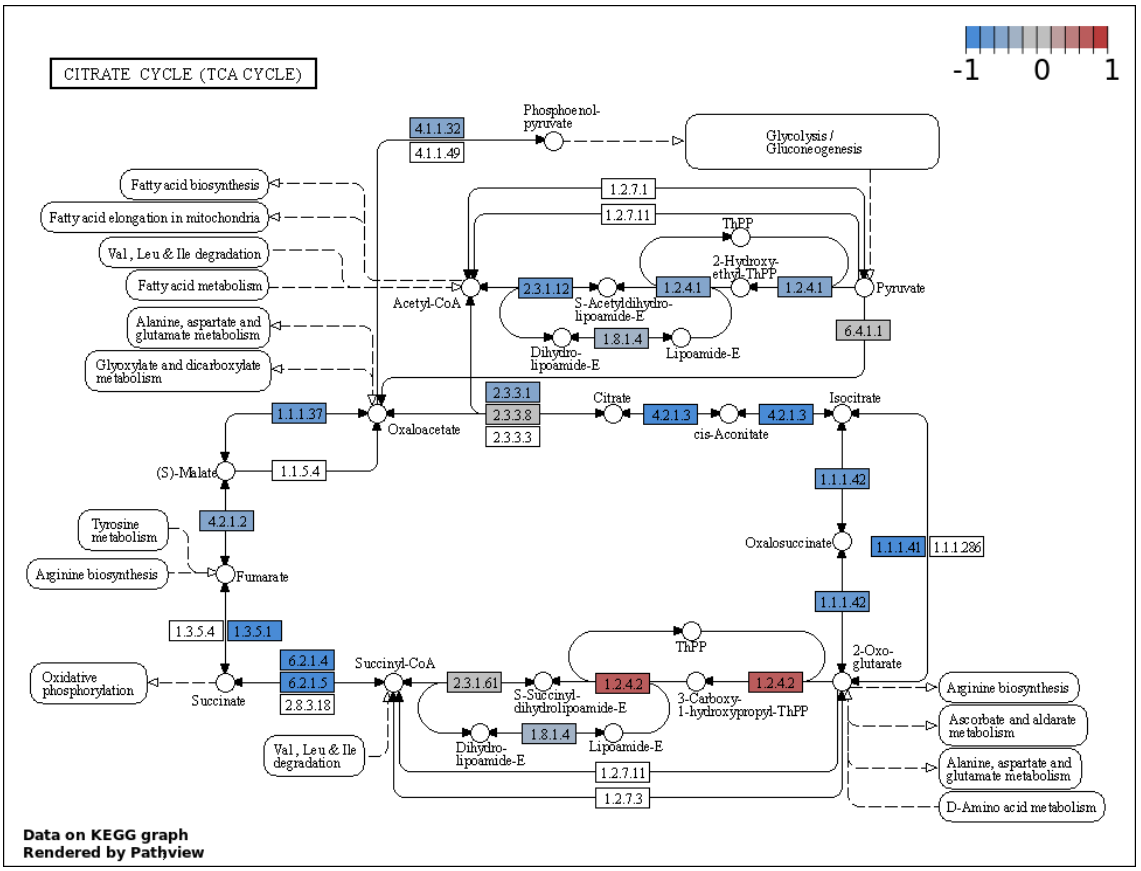
CITRATE CYCLE (TCA CYCLE)
-1 0 1
Phosphoenol-pyruvate
Glycolysis / Gluconeogenesis
Fatty acid biosynthesis
Fatty acid elongation in mitochondria
Val, Leu & Ile degradation
Fatty acid metabolism
Alanine, aspartate and glutamate metabolism
Glyoxylate and dicarboxylate metabolism
Acetyl-CoA
Pyruvate
ThPP
2-Hydroxy-ethyl-ThPP
S-Acetyldihydro-lipoamide-E
Dihydro-lipoamide-E
Lipoamide-E
Oxaloacetate
Citrate
cis-Aconitate
Isocitrate
(S)-Malate
Fumarate
Oxalosuccinate
2-Oxo-glutarate
Tyrosine metabolism
Arginine biosynthesis
Oxidative phosphorylation
Succinate
Succinyl-CoA
S-Succinyl-dihydrolipoamide-E
3-Carboxy-1-hydroxypropyl-ThPP
Arginine biosynthesis
Ascorbate and aldarate metabolism
Alanine, aspartate and glutamate metabolism
D-Amino acid metabolism
Data on KEGG graph
Rendered by Pathview

F

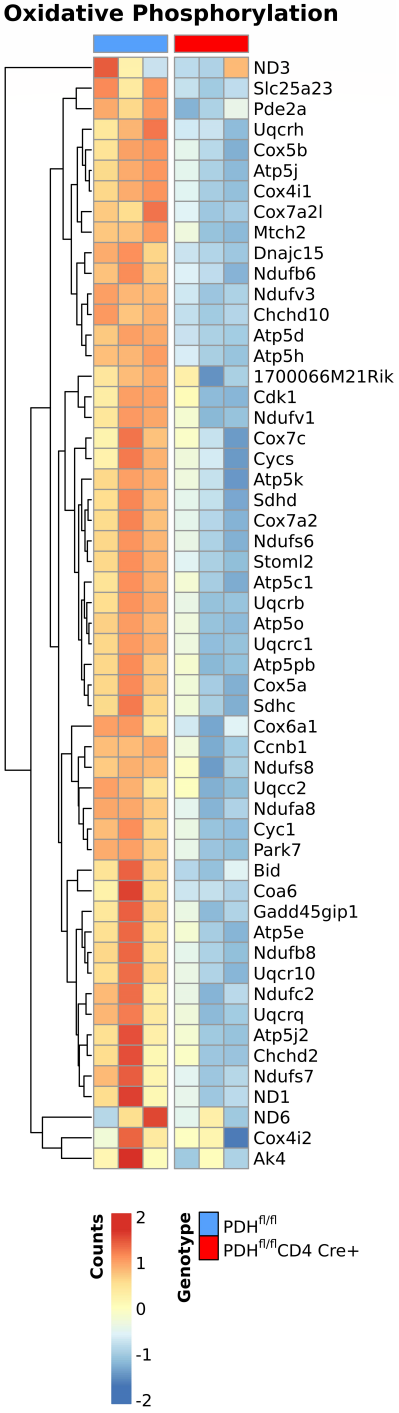
Oxidative Phosphorylation
ND3
Slc25a23
Pde2a
Uqcrh
Cox5b
Atp5j
Cox4i1
Cox7a2l
Mtch2
Dnajc15
Ndufb6
Ndufv3
Chchd10
Atp5d
Atp5h
1700066M21Rik
Cdk1
Ndufv1
Cox7c
Cycs
Atp5k
Sdhd
Cox7a2
Ndufs6
Stoml2
Atp5c1
Uqcrb
Atp5o
Uqcrc1
Atp5pb
Cox5a
Sdhc
Cox6a1
Ccnb1
Ndufs8
Uqcc2
Ndufa8
Cyc1
Park7
Bid
Coa6
Gadd45gip1
Atp5e
Ndufb8
Uqcr10
Ndufc2
Uqcrq
Atp5j2
Chchd2
Ndufs7
ND1
ND6
Cox4i2
Ak4
Counts
2
1
0
-1
-2
Genotype
PDHfl/fl
PDHfl/flCD4 Cre+

Figure S3

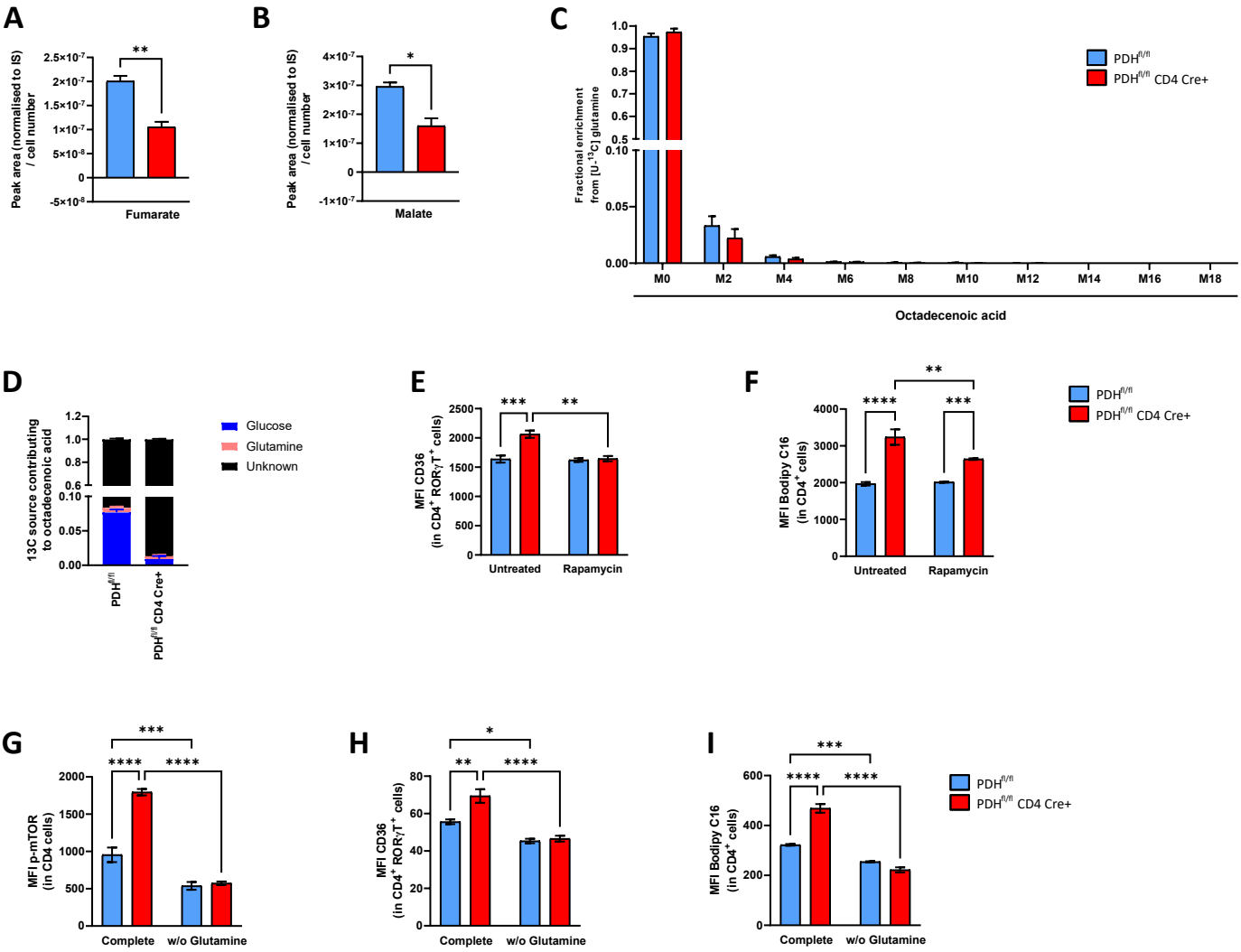
A
Peak area (normalised to IS) / cell number
Fumarate
B
Peak area (normalised to IS) / cell number
Malate
C
Fractional enrichment from [U-13C] glutamine
PDHfl/fl
PDHfl/fl CD4 Cre+
M0
M2
M4
M6
M8
M10
M12
M14
M16
M18
Octadecenoic acid
D
13C source contributing to octadecenoic acid
Glucose
Glutamine
Unknown
PDHfl/fl
PDHfl/fl CD4 Cre+
E
MFI CD36 (in CD4+ RORγT+ cells)
Untreated
Rapamycin
F
MFI Bodipy C16 (in CD4+ cells)
Untreated
Rapamycin
PDHfl/fl
PDHfl/fl CD4 Cre+
G
MFI p-mTOR (in CD4 cells)
Complete
w/o Glutamine
H
MFI CD36 (in CD4+ RORγT+ cells)
Complete
w/o Glutamine
I
MFI Bodipy C16 (in CD4+ cells)
Complete
w/o Glutamine
PDHfl/fl
PDHfl/fl CD4 Cre+

Figure S4

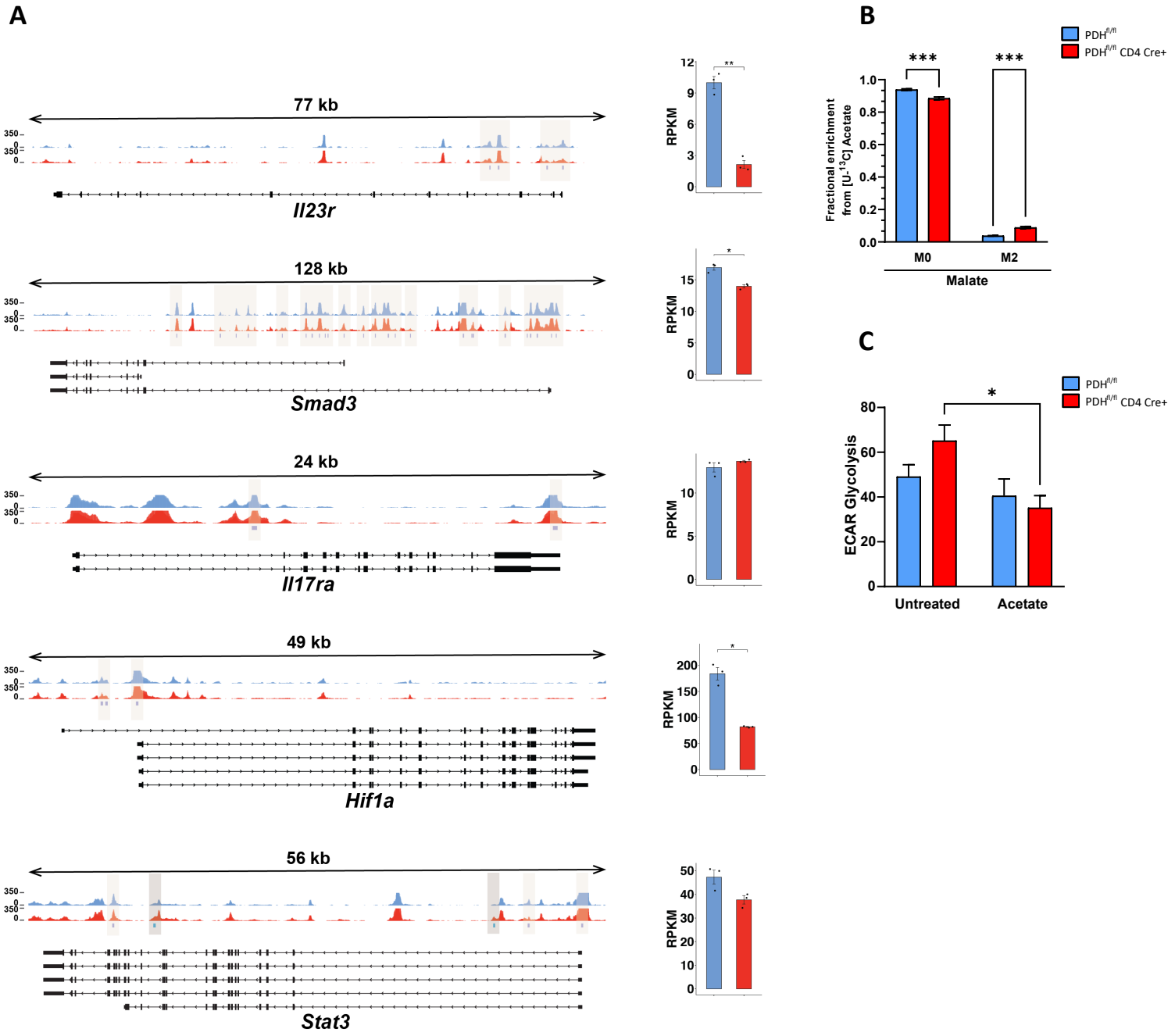
A
77 kb
Il23r
128 kb
Smad3
24 kb
Il17ra
49 kb
Hif1a
56 kb
Stat3
RPKM
B
PDH^fl/fl
PDH^fl/fl CD4 Cre+
Fractional enrichment from [U-13C] Acetate
M0
M2
Malate
C
ECAR Glycolysis
Untreated
Acetate

FIGURE LEGENDS

Figure 1: *Pdh* ablation in T cells protects mice from severe EAE and impairs IL-17 production.

(A) qPCR determination of fold change in *Pdhα1* mRNA levels in the indicated WT T cell subsets that were induced to differentiate *in vitro* as described in Methods. ΔΔCt values were normalized to Tbp expression. Data are mean±SEM (n=3) and representative of 2 trials.

(B) qPCR determination as in (A) of *Pdhα1* mRNA levels in total $CD4^+$ T cells that were isolated from spleen and lymph nodes of control ($PDH^{fl/fl}$) and PDH-deficient ($PDH^{fl/fl}$CD4Cre+) mice and activated *in vitro* for 24hr with anti-CD3/anti-CD28. Data are mean±SEM (n=3) and representative of 2 trials.

(C) Representative immunoblot to detect total PDH-E1α protein in total $CD4^+$ T cells that were isolated from spleen and lymph nodes of two $PDH^{fl/fl}$ and two $PDH^{fl/fl}$ CD4 Cre+ mice and activated *in vitro* as in (B). Actin, loading control. Data are representative of 4 mice/genotype.

(D, E) EAE clinical scores (D) and survival (E) of $PDH^{fl/fl}$ (n=7) and $PDH^{fl/fl}$ CD4 Cre+ (n=9) mice at 30 days post-induction. Data in (D) are mean±SEM.

(F) Flow cytometric analysis (FCA) of frequencies of $CD45^+$ cells among viable cells isolated from spleens and brains of $PDH^{fl/fl}$ and $PDH^{fl/fl}$ CD4 Cre+ mice at day 14 post-EAE induction. Data are mean±SEM (n=4-5/group).

(G) Intracellular FCA of frequencies of $ROR\gamma T^+$ cells among viable $CD45^+CD4^+$ cells isolated from spleens and brains of the mice in (F). Data are mean±SEM (n=4-5/group).

(H) Left: Representative contour plots of intracellular staining of IL-17A and IFNγ among viable $CD45^+CD4^+$ cells isolated from brains of the mice in (F) (n=4/genotype). Cells were stimulated *in vitro* with PMA/calcium ionophore/Brefeldin A (PMA/Iono) for 5hr before staining. Right: Quantification of frequencies of the $IFN\gamma^+IL\text{-}17A^+$ cells in the left panel. Data are mean±SEM (n=4-5/group).

(I-L) Naïve T cells were isolated from spleen and lymph nodes of $PDH^{fl/fl}$ and $PDH^{fl/fl}$ CD4 Cre+ mice and *in vitro*-differentiated into Th17 cells for 3 days. (I) Intracellular FCA of frequencies of $ROR\gamma T^+$ cells, and (J) quantification of RORγT MFI, gated on viable $CD4^+ROR\gamma T^+$ cells. (K) Intracellular FCA of frequencies of $IL\text{-}17A^+$ cells after 5hr stimulation with PMA/Iono, and (L) quantification of IL-17A MFI, gated on viable $CD4^+$ cells. Data are mean±SEM (n=3) and representative of 4 trials.

Figure 2: PDH in T cells is essential for central metabolism function.

(A) Quantification of Glut-1 MFI in $PDH^{fl/fl}$ and $PDH^{fl/fl}$ CD4 Cre+ Th17 cells, gated on viable $CD4^+$ cells. Data are mean±SEM (n=3) and representative of 3 trials.

(B) YSI quantification of glucose uptake from the culture medium of $PDH^{fl/fl}$ and $PDH^{fl/fl}$ CD4 Cre+ Th17 cells. Data are mean±SEM (n=3) and representative of 2 trials.

(C) Representative Seahorse ECAR plot of $PDH^{fl/fl}$ and $PDH^{fl/fl}$ CD4 Cre+ Th17 cells. Data are mean±SEM (n=3) and representative of 3 trials.

(D, E) Quantification of Seahorse determinations of glycolytic capacity (D) and glycolysis (E) in $PDH^{fl/fl}$ and $PDH^{fl/fl}$ CD4 Cre+ Th17 cells. Data are mean±SEM (n=3) and representative of 3 trials.

(F) Quantification of hexokinase-1 MFI in $PDH^{fl/fl}$ and $PDH^{fl/fl}$ CD4 Cre+ Th17 cells, gated on viable $CD4^+$ cells. Data are mean±SEM (n=3) and representative of 2 trials.

(G-J) Mass isotopomer distributions (MID) of (G) M0 and M3 pyruvate, (H) M0 and M2 citrate, (I) M0 and M2 fumarate, and (J) M0 and M2 malate in $PDH^{fl/fl}$ and $PDH^{fl/fl}$ CD4 Cre+ Th17 cells incubated for 24hr with [U-$^{13}C_6$]-glucose. Data are mean±SEM (n=3) and representative of 2 trials.

(K-N) MID of (K) M0 and M4 fumarate, (L) M0 and M4 malate, (M) M0 and M4 citrate, and (N) M0 and M5 citrate in $PDH^{fl/fl}$ and $PDH^{fl/fl}$ CD4 Cre+ Th17 cells incubated for 24hr with [U-$^{13}C_5$]-glutamine. Data are mean±SEM (n=3) and representative of 2 trials.

(O) Representative Seahorse OCR plot of $PDH^{fl/fl}$ and $PDH^{fl/fl}$ CD4 Cre+ Th17 cells. Data are mean±SEM (n=3) and representative of 3 trials.

(P-S) Quantification of Seahorse determinations of basal OCR (P), maximal respiration (Q), OCR dependent ATP (R), and spare respiratory capacity (S) in $PDH^{fl/fl}$ and $PDH^{fl/fl}$ CD4 Cre+ Th17 cells. Data are mean±SEM (n=3) and representative of 3 trials.

(T) Barcode plot of significantly enriched GO:0006119 (Oxidative Phosphorylation) in GSEA of $PDH^{fl/fl}$ CD4 Cre+ vs. $PDH^{fl/fl}$ Th17 cell RNA-Seq. Upper panel shows the running enrichment score with the lower showing occurrence of associated genes in the ranked distribution of expression differences. (Normalised enrichment score -1.74, p adjust 0.02).

Figure 3: Ablation of PDH in Th17 cells induces fatty acid metabolism.

(A) Quantification of intracellular citrate in $PDH^{fl/fl}$ and $PDH^{fl/fl}$ CD4 Cre+ Th17 cells. Data are mean±SEM (n=3) and representative of 2 trials.

(B) MID from M0 to M18 of octadecenoic acid in $PDH^{fl/fl}$ and $PDH^{fl/fl}$ CD4 Cre+ Th17 cells incubated for 24hr with [U-$^{13}C_6$]-glucose. Data are mean±SEM (n=3) and representative of 2 trials.

(C) Left: Representative FCA of the proliferation of cell-trace violet (CTV)-labeled $PDH^{fl/fl}$ and $PDH^{fl/fl}$ CD4 Cre+ Th17 cells. Right: Division index of the Th17 cells in the left panel. Data are mean±SEM (n=3) and representative of 3 trials.

(D) Left: Representative FCA of BODIPY FL C16-labeled $PDH^{fl/fl}$, $PDH^{fl/fl}$ CD4 Cre+ Th17 cells and fluorescence minus one (FMO) of unlabeled Th17 cells. Right: Quantification of BODIPY FL C16 MFI in the Th17 cells in the left panel, gated on viable $CD4^+$ cells. Data are mean±SEM (n=3) and representative of 3 trials.

(E) Frequencies of viable $PDH^{fl/fl}$ and $PDH^{fl/fl}$ CD4 Cre+ *in vitro*-differentiated Th17 cells cultured in complete IMDM with (w/) or without (w/o) lipids, gated on viable cells. Data are mean±SEM (n=3) and representative of 3 trials.

(F) Left: Representative FCA of the proliferation of CTV-labeled $PDH^{fl/fl}$ and $PDH^{fl/fl}$ CD4 Cre+ Th17 cells in complete IMDM w/ or w/o lipids. Right: Division index of the Th17 cells in the left panel. Data are mean±SEM (n=3) and representative of 3 trials.

(G) Quantification of Seahorse determination of basal OCR in $PDH^{fl/fl}$ CD4 Cre+ *in vitro*-differentiated Th17 cells cultured in complete IMDM w/ or w/o lipids. Data are mean±SEM (n=3) and representative of 3 trials.

(H-J) Quantification of (H) CD36 MFI, (I) intracellular p-mTOR MFI, and (J) intracellular p-S6 MFI in $PDH^{fl/fl}$ and $PDH^{fl/fl}$ CD4 Cre+ Th17 cells, gated on viable $CD4^+RORγT^+$ cells. Data are mean±SEM (n=3) and representative of 3 trials.

(K, L) Quantification of (K) CD36 MFI and (L) BODIPY FL C16 MFI in $PDH^{fl/fl}$ and $PDH^{fl/fl}$ CD4 Cre+ *in vitro*-differentiated Th17 cells cultured w/ or w/o Torin 1 (100 nM), gated on viable $CD4^+RORγT^+$ cells. Data are mean±SEM (n=3) and representative of 3 trials.

Figure 4: PDH is crucial for histone acetylation and epigenetic modifications in Th17 cells.

(A) Representative immunoblot to detect histone 3 (H3) acetylation in Th17 cells from two $PDH^{fl/fl}$ and two $PDH^{fl/fl}$ CD4 Cre+ mice. Actin, loading control. Data are representative of 4 mice/genotype.

(B) Metagene plots depicting the binned median chromatin accessibility signal from peak start to peak end for all genomic regions with significantly differential accessibility between $PDH^{fl/fl}$ and $PDH^{fl/fl}$ CD4 Cre+ Th17 cells. Y-axis represents the median CPM signal. Blue and purple lines represent ATAC-seq of two $PDH^{fl/fl}$ samples. Green, brown and red lines represent ATAC-seq of three $PDH^{fl/fl}$ CD4 Cre+ samples.

(C) Left: Plot of chromatin accessibility at the *Il17a, Il17f* and *Rorc* loci in $PDH^{fl/fl}$ and $PDH^{fl/fl}$ CD4 Cre+ Th17 cells. Light violet bars depict significantly differentially accessible regions (DBS) as identified by

DiffBind. Right: Quantitation of *Il17a, Il17f* and *Rorc* mRNA levels (RPKM) in $PDH^{fl/fl}$ and $PDH^{fl/fl}$ CD4 Cre+ Th17 cells as measured by RNA-seq.

(D) Representative immunoblot to detect H3 acetylation in $PDH^{fl/fl}$ and $PDH^{fl/fl}$ CD4 Cre+ Th17 cells treated w/ or w/o acetate (10 mM). Actin, loading control. Data are representative of 4 mice/genotype.

(E, F) MID of (E) M0 and M2 citrate and (F) M0 and M2 fumarate in $PDH^{fl/fl}$ and $PDH^{fl/fl}$ CD4 Cre+ Th17 cells incubated for 72hr with [U-$^{13}C_2$]-acetate. Data are mean±SEM (n=3) and representative of 2 trials.

(G) Quantification of intracellular citrate in $PDH^{fl/fl}$ and $PDH^{fl/fl}$ CD4 Cre+ Th17 cells incubated for 72hr with acetate (10 mM). Data are mean±SEM (n=3) and representative of 2 trials.

(H) Fractional carbon contribution of ^{13}C-acetate to octadecenoic acid in $PDH^{fl/fl}$ and $PDH^{fl/fl}$ CD4 Cre+ Th17 cells. Data are mean±SEM (n=3) and representative of 2 trials.

(I) Left: Representative FCA of the proliferation of CTV-labeled $PDH^{fl/fl}$ and $PDH^{fl/fl}$ CD4 Cre+ Th17 cells cultured in complete IMDM w/ or w/o acetate (10 mM). Right: Division index of the Th17 cells in the left panel. Data are mean±SEM (n=3) and representative of 3 trials.

(J) Quantification of Seahorse determination of basal OCR in $PDH^{fl/fl}$ and $PDH^{fl/fl}$ CD4 Cre+ *in vitro*-differentiated Th17 cells cultured w/ or w/o acetate (10 mM). Data are mean±SEM (n=3) and representative of 3 trials.

(K-O) Quantification of (K) Glut-1 MFI, (L) 2-NBDG MFI, (M) intracellular p-mTOR MFI, (N) CD36 MFI and (O) BODIPY FL C16 MFI in $PDH^{fl/fl}$ and $PDH^{fl/fl}$ CD4 Cre+ *in vitro*-differentiated Th17 cells cultured w/ or w/o acetate (10 mM), gated on viable $CD4^+$ cells. Data are mean±SEM (n=3) and representative of 3 trials.

(P) Intracellular FCA of frequencies of IL-$17A^+$ cells among $PDH^{fl/fl}$ and $PDH^{fl/fl}$ CD4 Cre+ cultured w/ or w/o acetate (10 mM) and stimulated for 5hr with PMA/Iono, gated on viable $CD4^+$ cells. Data are mean±SEM (n=3) and representative of 4 trials.

SUPPLEMENTARY FIGURE LEGENDS

Supplementary Figure 1: PDH-E1α deficiency in T cells does not affect PDH-E1β expression or the frequencies of Th1 and Th17 cells in EAE-affected mice.

(A) qPCR determination of fold change in *Pdhb* mRNA levels in total $CD4^+$ T cells that were isolated from spleen and lymph nodes of control ($PDH^{fl/fl}$) and PDH-deficient ($PDH^{fl/fl}$ CD4 Cre+) mice and activated *in vitro* for 24hr with anti-CD3 and anti-CD28 antibodies. Data are mean±SEM (n=3) and representative of 2 trials. ΔΔCt values were normalized to Tbp expression.

(B) Flow cytometric analysis (FCA) of total counts of $CD45^+$ cells from the brains of $PDH^{fl/fl}$ and $PDH^{fl/fl}$ CD4 Cre+ mice at day 14 post-EAE induction, gated on viable cells. Data are mean±SEM (n=4-5/group).

(C, D) Intracellular FCA of frequencies of (C) $Tbet^+$ (Th1) and (D) $CD25^+FoxP3^+$ (Treg) cells from spleens and brains of the mice in (B), gated on viable $CD45^+CD4^+$ cells. Data are mean±SEM (n=4-5/group).

(E, F) Intracellular FCA of frequencies of (E) $IFNγ^+IL\text{-}17A^-$ and (F) $IFNγ^-IL\text{-}17A^+$ cells from the brains of the mice in (B), gated on viable $CD45^+CD4^+$ cells. Cells were left unstimulated or stimulated *in vitro* for 5hr with PMA/calcium ionophore/Brefeldin A (PMA/Iono) before staining. Data are mean±SEM (n=4-5/group).

(G) ELISA determination of IL-17 protein in culture supernatants of *in vitro*-differentiated Th17 cells of the indicated genotypes. Naïve T cells were isolated from spleens and lymph nodes of $PDH^{fl/fl}$ and $PDH^{fl/fl}$ CD4 Cre+ mice and cultured for 3 days with anti-CD3, anti-CD28, IL-6, anti-IFNγ, and TGFβ. Data are mean±SEM (n=3) and representative of 3 trials.

(H-J) Naïve T cells were isolated from spleen and lymph nodes of $PDH^{fl/fl}$ and $PDH^{fl/fl}$ CD4 Cre+ mice and *in vitro*-differentiated into Th1 (H,I) or Treg (J) cells for 3 days. (H) Intracellular FCA of frequencies of $Tbet^+$ cells, gated on viable $CD4^+$ cells. (I) Intracellular FCA of frequencies of $IFNγ^+$ cells after 5hr stimulation with PMA/Iono, gated on viable $CD4^+$ cells. (J) Intracellular FCA of frequencies of $CD25^+FoxP3^+$ cells gated on viable $CD4^+$ cells. Data are mean±SEM (n=3) and representative of 3 trials.

Supplementary Figure 2: PDH ablation impairs mitochondrial glucose metabolism and related gene expression patterns.

(A) Quantification of 2-NBDG MFI in $PDH^{fl/fl}$ and $PDH^{fl/fl}$ CD4 Cre+ Th17 cells, gated on viable $CD4^+$ cells. Data are mean±SEM (n=3) and representative of 3 trials.

(B) YSI quantification of lactate released into the culture medium of $PDH^{fl/fl}$ and $PDH^{fl/fl}$ CD4 Cre+ Th17 cells. Data are mean±SEM (n=3) and representative of 2 trials.

(C) GC/MS quantification of pyruvate release into the medium of $PDH^{fl/fl}$ and $PDH^{fl/fl}$ CD4 Cre+ Th17 cells. Data are mean±SEM (n=3) and representative of 2 trials.

(D) Coloured KEGG map of gene expression (log2) changes in the TCA cycle pathway in $PDH^{fl/fl}$ CD4 Cre+ vs. $PDH^{fl/fl}$ Th17 cells.

(E) YSI quantification of glutamine uptake from the medium of $PDH^{fl/fl}$ and $PDH^{fl/fl}$CD4Cre+ Th17 cells. Data are mean±SEM (n=3) and representative of 2 trials.

(F) Heatmap of the significantly enriched GO:0006119 (Oxidative Phosphorylation) in GSEA of $PDH^{fl/fl}$ CD4 Cre+ vs. $PDH^{fl/fl}$ Th17 cell RNA-Seq. Displayed is the gene expression level for core enriched genes from the each sample scaled by gene.

Supplementary Figure 3: PDH deficiency in T cells alters central metabolism in Th17 cells

(A, B) Quantification of intracellular fumarate (A) and malate (B) in $PDH^{fl/fl}$ and $PDH^{fl/fl}$ CD4 Cre+ Th17 cells. Data are mean±SEM (n=3) and representative of 2 trials.

(C) MID from M0 to M18 of octadecenoic acid in $PDH^{fl/fl}$ and $PDH^{fl/fl}$ CD4 Cre+ Th17 cells incubated for 24hr with [U-$^{13}C_6$]-glutamine. Data are mean±SEM (n=3) and representative of 2 trials.

(D) Distribution of ^{13}C sources contributing to octadecenoic acid in $PDH^{fl/fl}$ and $PDH^{fl/fl}$ CD4 Cre+ Th17 cells. Data are mean±SEM (n=3) and representative of 2 trials.

(E,F) Quantification of (E) CD36 MFI and (F) BODIPY FL C16 MFI in $PDH^{fl/fl}$ and $PDH^{fl/fl}$ CD4 Cre+ *in vitro*-differentiated Th17 cells cultured w/ or w/o rapamycin (100 nM), gated on viable $CD4^+RORγT^+$ (E) or $CD4^+$ (F) cells. Data are mean±SEM (n=3) and representative of 3 trials.

(G,H,I) Quantification of (G) intracellular p-mTOR MFI, (H) CD36 MFI and (I) BODIPY FL C16 MFI in $PDH^{fl/fl}$ and $PDH^{fl/fl}$ CD4 Cre+ *in vitro*-differentiated Th17 cells cultured in RPMI w/ (Complete) or w/o 1% L-glutamine (w/o Glutamine), gated on viable $CD4^+$ (G,I) or $CD4^+RORγT^+$ (H) cells. Data are mean±SEM (n=3) and representative of 2 trials.

Supplementary Figure 4: PDH deficiency in T cells alters chromatin accessibility and acetate incorporation in Th17 cells

(A) Left: Chromatin accessibility of the *Il23r, Smad3, Il17ra, Hif1a* and *Stat3* loci in $PDH^{fl/fl}$ and $PDH^{fl/fl}$ CD4 Cre+ Th17 cells. The light violet bars depict significantly differentially accessible regions (DBS) as identified by DiffBind. Right: Levels of *Il23r, Smad3, Il17ra, Hif1a* and *Stat3* mRNA expression (RPKM) in $PDH^{fl/fl}$ and $PDH^{fl/fl}$ CD4 Cre+ Th17 cells as measured by RNA-seq.

(B) MID of M0 and M2 malate in $PDH^{fl/fl}$ and $PDH^{fl/fl}$ CD4 Cre+ Th17 cells incubated for 72hr with [U-$^{13}C_2$]-acetate. Data are mean±SEM (n=3) and representative of 2 trials.

(C) Quantification of Seahorse determination of ECAR glycolysis in $PDH^{fl/fl}$ and $PDH^{fl/fl}$ CD4 Cre+ *in vitro*-differentiated Th17 cells cultured w/ or w/o acetate (10 mM). Data are mean±SEM (n=3) and representative of 3 trials.

MATERIALS AND METHODS

Mice

$PDH^{fl/fl}$ mice [B6.129P2-Pdha1tm1Ptl/J] were purchased from The Jackson Laboratory and crossed with CD4 Cre-expressing mice also obtained from The Jackson Laboratory. All experiments used sex- and age-matched mice (8-12 weeks old) with corresponding littermate controls. All animal experimentation protocols were approved and conducted according to the LIH Animal Welfare Structure guidelines.

EAE mouse model

Induction of EAE was performed and clinical scores determined as described (Brüstle *et al.*, 2012). Briefly, $PDH^{fl/fl}$ and $PDH^{fl/fl}$ CD4 Cre+ mice were injected subcutaneously with MOG_{35-55}/CFA emulsion, followed by two intraperitoneal injections of pertussis toxin (Hooke Labs). Mouse brains and spleens were analyzed at day 14 post-induction.

Naïve T cell isolation from spleen and lymph nodes

Naïve $CD4^+$ T cells were isolated from $PDH^{fl/fl}$ and $PDH^{fl/fl}$ CD4 Cre+ mouse spleen and lymph nodes by magnetic bead sorting (MACS) using the Naïve $CD4^+$ T cell isolation kit (Miltenyi Biotec) according to the manufacturer's protocol. Sorting was performed using an autoMACS® pro-Separator (Miltenyi Biotec). Cell number calculations were performed using a CASY cell counter (Omni Life Science).

Isolation of lymphocytes from mouse brain

Isolation of lymphocytes from the brains of EAE-affected mice at day 14 post-induction was performed as described (Brüstle *et al.*, 2012). Briefly, mice were sacrificed and brains were perfused with 20 mL cold PBS through the left ventricle. Brains were digested in RPMI supplemented with 50 µg/mL collagenase D (Roche) and 10 µg/mL DNAseI (Sigma-Aldrich) for 1 hr at 37°C in a mixer (Labortechnik). Lymphocyte enrichment was obtained by centrifugation using a two-layer Percoll gradient (40% and 70%), followed by two washes in RPMI.

In vitro differentiation of Th cell subsets

Naïve T cells isolated from $PDH^{fl/fl}$ and $PDH^{fl/fl}$CD4Cre+ spleen and lymph nodes as described above were seeded at $2x10^6$ cells/mL in complete medium consisting of IMDM (Westburg) supplemented with 10% FBS (Biochrom GmbH), 55µM 2-mercaptoethanol (Gibco) and 1% penicillin/streptomycin (Gibco), and incubated for 3 days in the presence of the appropriate Th subset-specific cytokine mix (cf. Table 1). For acetate-treated cells, *in vitro* Th cell differentiation was performed in the presence of 10 mM sodium acetate (Sigma-Aldrich) diluted in culture medium.

For experiments comparing media with and without glutamine, cells were cultured in RPMI-1640 medium (Lonza) supplemented with 10% FBS (Biochrom GmbH), 55µM 2-mercaptoethanol (Gibco) and

1% penicillin/streptomycin (Gibco) with (Complete) or without (w/o Glutamine) 1% L-Glutamine (Westburg).

Th subset	Cytokine	Concentration	Source
Th0	anti-CD3 (plate-bound)	5 µg/mL	Biolegend
	anti-CD28	1 µg/mL	Biolegend
	anti-IFNγ	5 µg/mL	BD Biosciences
	IL-2	50 U/mL	Miltenyi Biotec
Th1	anti-CD3 (plate-bound)	5 µg/mL	Biolegend
	anti-CD28	1 µg/mL	Biolegend
	IL-12	2 ng/mL	Miltenyi Biotec
	IL-2	50 U/mL	Miltenyi Biotec
Th17	anti-CD3 (plate-bound)	5 µg/mL	Biolegend
	anti-CD28	1 µg/mL	Biolegend
	IL-6	30 ng/mL	Miltenyi Biotec
	anti-IFNγ	5 µg/mL	BD Biosciences
	TGFβ	2 ng/mL	Bio-Techne
Treg	anti-CD3 (plate-bound)	5 µg/mL	Biolegend
	anti-CD28	1 µg/mL	Biolegend
	IL-2	50 U/mL	Miltenyi Biotec
	anti-IFNγ	5 µg/mL	BD Biosciences
	TGFβ	4 ng/mL	Bio-Techne

Table 1: Th subset-specific cytokine cocktails used for the differentiation of naïve T cells *in vitro*.

Immunoblotting

Cells were lysed in lysis buffer (CST 9803S) containing protease and phosphatase inhibitors (Bioké) following manufacturer's instructions. Blotting was performed as previously described (Kurniawan *et al.*, 2020). Antibodies used for protein detection were anti-Pdha1 (Abcam, ab168379), anti-actin (Sigma Aldrich) and anti-acetyl-histone H3 (Millipore, 06-599).

Flow cytometry

For the detection of surface markers, cells were stained for 30 min at 4°C in FACS buffer (PBS with 1% FBS and 5 mM EDTA, pH 8.0) containing antibodies (cf. Key Resources Table; 1:200 dilution) and either live/dead dye (DAPI (Thermo Fisher Scientific), LIVE/DEAD® Fixable Near-IR or Green Dye (Biolegend), or 7-AAD (Thermo Fisher Scientific); 1:1000-1:3000 dilution). Cells were washed in FACS buffer before flow cytometry measurements.

For intracellular staining of transcription factors, cells were fixed at 4°C for 1hr in the eBioscience™ FoxP3/Transcription Factor Fixation kit (Thermo Fisher Scientific) and permeabilized using the buffer provided by the kit. To measure intracellular cytokine expression, cells were restimulated for 5hr *in vitro* with phorbol 12-myristate 13-acetate (PMA; Sigma, 50 ng/mL), calcium ionophore A23187 (Ionomycin, Sigma, 750 ng/mL), and BD GolgiPlug™ Protein Transport Inhibitor (BECTON DICKINSON, 1:1000 dilution). Cells were washed once with FACS buffer before extracellular staining, then fixed for 20 min at 4°C with BD Cytofix/Cytoperm and permeabilized with BD Perm/Wash™ buffer (BD Biosciences). To

detect hexokinase-1, cells were fixed in 4% formaldehyde (Sigma-Aldrich) for 10 min at room temperature (RT), then permeabilized in PBS 0.1% Tween-20. For p-mTOR and p-S6 detection, cells were fixed in 2% formaldehyde (Sigma-Aldrich) for 10 min at RT, then permeabilized in 0.01% saponin (Sigma-Aldrich). Antibodies used for intracellular staining were diluted 1:200 in the appropriate permeabilization buffer prior to incubation with cells for 30 min at 4°C.

To measure 2-NBDG uptake, cells were incubated in glucose-free RPMI for 2hr at 37°C in the presence of 50 µM 2-NBDG (Thermo Fisher Scientific). To measure lipid uptake, cells were incubated in IMDM with 1 µM BODIPY™ FL C16 (Invitrogen) for 30 min at 37°C. Cells were washed once with PBS prior to flow cytometric measurements.

All flow cytometric measurements were obtained using a BD Fortessa instrument (BD Biosciences) and analyses were performed using FlowJo v10.6.2 software (Tree Star).

Cytokine quantification

Measurement of IL-17 in culture supernatants of *in vitro*-differentiated Th17 cells was performed using the Mouse IL-17 DuoSet ELISA kit (Bio-Techne) following the manufacturer's instructions.

Metabolic flux measurements and analysis

In vitro-differentiated Th17 cells were seeded at $3x10^5$ cells/well in a pre-coated XFe96 cell culture plate (Agilent Technologies) using Corning™ Cell-Tak Cell and Tissue Adhesive (Thermo Fisher Scientific) and 0.1 M sodium bicarbonate (Sigma-Aldrich).

For OCR measurements, plated cells were cultured in XF Seahorse DMEM medium (Agilent Technologies) containing 2 mM glutamine (Westburg), 1 mM sodium pyruvate (Gibco) and 25 mM glucose (Sigma-Aldrich). OCR was measured using the XF Cell Mito Stress Test (Agilent Technologies) following the manufacturer's protocol, which involved sequential injections of oligomycin A (1 µM), carbonyl cyanide 4-(trifluoromethoxy)phenylhydrazone (FCCP; 3 µM) and antimycin A/rotenone (1 µM) (all from Sigma-Aldrich).

For ECAR measurements, plated cells were cultured in XF Seahorse DMEM medium (Agilent Technologies) containing 2 mM glutamine (Westburg), and ECAR was determined by the XF Glycolysis Stress Test Kit (Agilent Technologies). Measurements were taken during sequential injections of glucose (10 mM), oligomycin (1 µM) and 2-deoxy-D-glucose (2-DG; 50 mM) (all from Sigma-Aldrich).

Experiments were performed using an XFe96 Extracellular Flux Analyzer (Agilent), and results were analyzed using Wave 2.6.1 software (Agilent Technologies). All measurements were calculated from raw OCR or ECAR data as described in Table 2 below.

Parameter	Raw data source	Calculations
Basal OCR	OCR	3^{rd} minus 12^{th} measurement

Maximal respiration	OCR	9^{th} minus 12^{th} measurement
OCR-dependent ATP production	OCR	3^{rd} minus 6^{th} measurement
Spare respiratory capacity	OCR	9^{th} minus 3^{rd} measurement
Glycolytic capacity	ECAR	9^{th} minus 12^{th} measurement
ECAR glycolysis	ECAR	6^{th} minus 3^{rd} measurement

Table 2: Calculations of OCR and ECAR measurements.

Isotopic labelling

For glucose and glutamine isotopic tracing, naïve T cells were incubated for 3 days with the appropriate cytokine cocktail to induce Th cell differentiation *in vitro*. At day 3, cells were counted, washed and seeded for 24hr in tracing medium consisting of SILAC RPMI 1640 (Fisher Scientific) supplemented with 10% FBS (Biochrom GmbH), 55µM 2-mercaptoethanol (Gibco), 1% penicillin/streptomycin (Gibco), L-arginine (Sigma Aldrich) and L-lysine (Sigma Aldrich), and containing [U-$^{13}C_6$]-glucose (11.1 mmol/L; Cambridge Isotope Laboratories) or [U-$^{13}C_5$]-glutamine (2 mmol/L; Cambridge Isotope Laboratories). For acetate isotopic tracing, naïve T cells were incubated for 3 days with complete IMDM media with cytokine cocktail and [U-$^{13}C_2$]-Acetate. Extraction of intracellular metabolites, MID and carbon contribution determinations, GC and LC-MS measurements, and substractions of natural isotope abundance, were performed as previously described (Battello *et al.*, 2016) using MetaboliteDetector software. Glucose, lactate and glutamine concentrations in medium were measured by a YSI 2950D Biochemistry Analyzer (YSI Incorporated).

Proliferation

$1x10^6$ cells were labeled with 5µM cell-trace violet (CVT; Thermo Fisher Scientific) for 72hr and analyzed by flow cytometry. Division index was calculated as described by FlowJo software.

RNA extraction and quantitative RT-PCR

RNA was extracted using a NucleoSpin RNA Kit (Macherey-Nagel) according to the manufacturer's protocol. RNA concentrations were measured by a NanoDrop 2000c Spectrophotometer (Thermo Fisher Scientific). RT-qPCR was carried out by mixing 2µL RNA (150 ng) with 5µL Master Mix (Luna Universal One-Step RT-qPCR Kits; Bioké), 2pmol forward primer, 2pmol reverse primer, 0.3µL reverse transcriptase and 2.7µL RNAse-free water (cf. Key Resources Table). Reactions were run on a CFX384 instrument (Bio-Rad). Data were normalized to tbp and analyzed using the ΔΔCt method as previously described (Mak *et al.*, 2017).

RNA-seq sample preparation

RNA was extracted as described above. RNA-seq and ATAC-seq were performed on the same pools of $PDH^{fl/fl}$ and $PDH^{fl/fl}$CD4Cre+ naïve T cells induced to differentiate into Th17 cells *in vitro* for 72 hr. mRNA sequencing was performed by the Sequencing Platform of the Luxembourg Centre for Systems Biomedicine (LCSB) of the University of Luxembourg. Single-end, stranded sequencing was executed by an Illumina NextSeq 500 machine with a read length of 75 bp. The TruSeq Stranded mRNA Library Prep kit (Illumina) was used for library preparation.

RNA-seq data analysis

Raw fastq files were uploaded to **GEO XXX** and FastQC (v0.11.5) was used to assess the quality control of the raw reads (Andrews, S., 2010). Adapter removal was performed using the PALEOMIX pipeline (v1.2.12) (Schubert *et al.*, 2014), with a minimum length of the remaining reads set to 25 bp. SortMeRNA (v2.1) was used to remove rRNA reads (Kopylova, Noé and Touzet, 2012), followed by mapping using STAR (v.2.5.2b) (Dobin *et al.*, 2013). RNA-seq transcript alignment was performed with Salmon (Patro *et al.*, 2017) against the Mouse Transcriptome from Genecode v.M27 (Frankish *et al.*, 2019). Subsequent analysis was conducted in R, and tximeta (Love *et al.*, 2020) was used to assign transcripts to genes before differential analysis with DESeq2 (Love, Huber and Anders, 2014). Gene set enrichment analysis (GSEA) was performed using ClusterProfiler (Yu *et al.*, 2012). Coloured KEGG view pathways were prepared using Pathview (Luo and Brouwer, 2013).

ATAC-seq sample preparation

RNA-seq and ATAC-seq were performed on the same pools of $PDH^{fl/fl}$ and $PDH^{fl/fl}$ CD4 Cre+ naïve T cells induced to differentiate into Th17 cells *in vitro* for 72 hr. ATAC-seq was performed using OMNI-ATAC supplementary protocol 1 as described (Corces *et al.*, 2017) with some modifications. Viable cells ($1x10^5$) were resuspended in 50 µL cold ATAC-Resuspension Buffer (RSB) containing 0.1% NP40, 0.1% Tween-20 and 0.01% digitonin, and lysed for 3 min on ice. Lysates were washed with 1 mL cold ATAC-RSB containing 0.1% Tween-20 but no NP40 or digitonin. Samples were centrifuged for 10 min at 500×g at 4°C, the supernatants removed, and the pellets resuspended in 50 µL transposition mix (Tagment DNA buffer from Illumina, #15027866) containing 2.5 µL Tagment DNA TDE1 Enzyme (Illumina #15027865). After 45 min incubation at 37°C and 1000 rpm in an Eppendorf ThermoMixer, chromatin fragments were isolated using the Zymo Research DNA Clean & Concentrator kit (ZymoResearch ZY-D4013). For pre-amplification of transposed fragments, 5 PCR cycles were run using primers Ad1 and Ad2.x (Buenrostro *et al.*, 2015). The remaining cycles of library amplification were determined by qPCR (Adams *et al.*, 2000). Another cleanup was performed using the Zymo Research DNA Clean & Concentrator kit (21 µL elution volume) followed by AMPure XP bead (Beckman Coulter #A63880) size selection, with samples adjusted to 100 µL plus 55 µL of beads to remove large fragments. Samples were incubated for 5 min before separation of beads using a magnetic stand and transfer of the supernatant to a new tube. Another 225

µL of beads were added followed by incubation for 10 min and separation on a magnetic stand. After washing with 80% ethanol, beads were resuspended in 20 µL elution buffer and incubated for 5 min. After separation on a magnetic stand, the eluate was transferred to a new tube. Library quality control was performed using the Agilent DNA High Sensitivity Bioanalyzer chip (Agilent #5067-4626). The sequencing of ATAC-seq libraries was performed by the Sequencing Platform of the Luxembourg Centre for Systems Biomedicine (LCSB) of the University of Luxembourg. Paired-end, unstranded library sequencing was performed using the Illumina NextSeq 500/550 75 cycles High Output Kit.

ATAC-seq data analysis

FastQC (v0.11.5) was used to assess the quality control of raw reads (Andrews, S., 2010). Alignment and mapping to generate BAM files were performed with BWA (v.0.7.16a) (Li et al., 2009). The mouse reference genome used for mapping was GRCm38 release 102 downloaded from GENCODE (https://www.gencodegenes.org/). The Picard tool (v2.10.9) (Adams et al., 2000) was used to validate BAM files. Genrich (https://github.com/jsh58/Genrich) was used for peak calling with parameters "-r -m 30 -j -a 200 -g 15 -l 15 -d 50" to remove PCR duplicates and include only reads with mapping quality of at least 30. Also, to achieve a minimum AUC for a peak of 200 bp, a maximum distance between significant sites of 15 bp, a minimum length of a peak of 15 bp, and for defining expand cut sites to 50 bp.

Differentially accessible regions were detected using DiffBind (3.4.3) (Ross-Innes *et al.*, 2012) (10.18129/B9.bioc.DiffBind) in R (4.1.2). Briefly, peaks from all samples were overlapped, resulting in 119,671 unique regions. Of these, 103,563 peaks were identified in at least two samples and constituted the peakset. The number of mapped reads was calculated for each peak included in the peakset and background normalization was performed. Differential analysis was then carried out using DESeq2. Differentially accessible regions were annotated using the ChIPseeker R package (1.30.3) (Yu, Wang and He, 2015).

For metagene plots, the BAMs from the ATAC-seq analysis were filtered for a minimal mapping quality of 30 and processed by bamCoverage (Ramírez *et al.*, 2018) (deepTools v3.5.0) using the CountsPerMillion (CPM) normalization to generate bigwigs. These bigwigs were further used as input for ComputeMatrix (Ramírez *et al.*, 2018) (deepTools v3.5.0) using the command "scale-regions -m 450 -b 50 -a 50 -bs 10" for all peaks with significant differential accessibility according to DiffBind. The CPM signal was binned per 10 bp and each peak was scaled to 450 bp (the median peak width across samples), with an additional flanking region of 50 bp included.

Quantification and statistical analysis

Data are presented as the mean±SEM with a minimum n=3 per group (for more information, please refer to the Figure Legends). P values were calculated using the unpaired Student's t test, or one or two-way ANOVA, and Prism 9.3.1 (GraphPad). Statistical significance was set as $p \leq 0.05$, with levels indicated by asterisks as follows: * $p \leq 0.05$; ** $p \leq 0.01$; *** $p \leq 0.001$; **** $p \leq 0.0001$; ns, not significant.

KEY RESOURCES TABLE

REAGENT or RESOURCE	SOURCE	IDENTIFIER
Antibodies		
CD4-APC Clone GK1.5 (1:200)	Biolegend	#100412
CD3ε-PE-Cy7 Clone 145-2C11 (1:200)	Biolegend	#100320
CD4-PE Clone GK1.5 (1:200)	Biolegend	#100408
CD4-BV785 Clone GK1.5 (1:200)	Biolegend	#100453
CD4-BUV737 Clone GK1.5 (RUO) (1:200)	BD Biosciences	#612761
IL17A-BV605 Clone TC11-18H10 (1 :200)	BD Biosciences	#564169
IFN-γ-APC Clone XMG1.2 (1:200)	Biolegend	#505810
RORγT-BV421 Clone Q31-378 (1:200)	BD Biosciences	#562894
Tbet-PE/Cy7 Clone 4B10 (1:200)	Biolegend	#644824
FoxP3-APC Clone FJK-16 s (1:200)	Thermo Fisher	#17-5773-82
CD25-PE Clone PC61 (1:200)	Biolegend	#102008
pmTOR-PE Clone MRRBY (1:200)	Thermo Fisher	#12-9718-42
pS6-APC Clone cupk43k (1:200)	Thermo Fisher	#17-9007-42
CD45-PerCP/Cyanine5.5 Clone 30-F11 (1:200)	Biolegend	#103132
Glut-1 – Alexa Fluor® 647 Clone EPR3915 (1:200)	Abcam	#ab195020
Hexokinase-1 - Alexa Fluor® 488 Clone EPR10134(B) (1:200)	Abcam	#ab184818
CD36-PerCP/Cyanine5.5 Clone HM36 (1:200)	Biolegend	#102620
Ultra-LEAF™ Purified anti-mouse CD3ε Clone 145-2C11	Biolegend	# 100340
Ultra-LEAF™ Purified anti-mouse CD28 Clone 37.51	Biolegend	# 102116
Purified NA/LE Rat Anti-Mouse IFN-γ Clone XMG1.2	BD Biosciences	#554408
Anti-pyruvate dehydrogenase E1-alpha subunit antibody	Abcam	#ab168379
Anti-acetyl-histone H3 antibody	Millipore	#06-599
Anti-actin antibody produced in rabbit	Sigma-Aldrich	# A2066-.2ML
Mouse anti-rabbit IgG-HRP	Santa Cruz Biotechnology	#sc-2357
Chemicals, Peptides and Recombinant Proteins		
PBS (1X) without Ca++, Mg++, 500ml	Westburg	#BE17-516F
FBS Superior Lot: 0193F	Biochrom GmbH	#S0615
Penicillin-Streptomycin (10,000 U/mL)	Gibco	#11548876
L-Glutamine	Westburg	#BE17-605E
2-Mercaptoethanol	Gibco	#11508916
Methanol	Sigma-Aldrich	#1060351000
Chloroform	Sigma-Aldrich	#34854-1L-M
Ethanol absolute	VWR	#20821.330
Ethanol eurodenatured	VWR	#85823.440
Sodium acetate trihydrate	Sigma-Aldrich	#71188-250MG
HEPES	Sigma-Aldrich	#H4034-100G

EDTA	Sigma-Aldrich	#EDS-100G
DL-Dithiothreitol solution (DTT)	Sigma-Aldrich	#43816-10ML
Bovine serum albumin (BSA)	Sigma-Aldrich	#A9647-500G
RPMI 1640 (without L-Glutamine)	Westburg	#BE12-167F
IMDM with HEPES and L-Glutamine	Westburg	#BE12-722F
Collagenase D from *Clostridium histolyticum*	Roche	#11088866001
DNAseI	Sigma-Aldrich	#D4513-1VL
Percoll®	Sigma-Aldrich	#GE17-0891-01
Recombinant human TGF-β	Bio-Techne	#240-B-002
Mouse IL-6, research grade	Miltenyi Biotec	#130-094-065
Mouse IL-2, research grade	Miltenyi Biotec	#130-098-221
Mouse IL-12, research grade	Miltenyi Biotec	#130-096-707
Cell Trace Violet	Thermo Fisher	#C34557
Molecular Probes™ 2-NBDG	Thermo Fisher Scientific	#11569116
SYBR™ Fast Green Master Mix	Thermo Fisher Scientific	#4385612
Luna Universal One-Step RT-qPCR Kit	Bioké	#E3005E
Formaldehyde	Sigma-Aldrich	#252549-1L
Saponin	Sigma-Aldrich	#S4521-25G
DAPI (1:2000)	Thermo Fisher Scientific	#D1306
Zombie NIR™ Fixable Viability Kit	Biolegend	#423106
Zombie Green™ Fixable Viability Kit	Biolegend	#423112
7-AAD	Thermo Fisher Scientific	#A1310
Bodipy™ FL C16	Thermo Fisher Scientific	#10654623
Corning™ Cell-Tak Cell and Tissue Adhesive	Thermo Fisher Scientific	#10317081
Oligomycin A	Sigma-Aldrich	#75351-5MG
FCCP	Sigma-Aldrich	#C2920-10MG
Antimycin A	Sigma-Aldrich	#A8674-25MG
Rotenone	Sigma-Aldrich	#R8875-1G
2-Deoxy-D-glucose	Sigma-Aldrich	#D6134-1G
Sodium pyruvate	Gibco	#12539059
Phorbol 12-myristate 13-acetate (PMA)	Sigma-Aldrich	#P8139-1MG
Calcium ionophore A23187	Sigma-Aldrich	#C7522-1MG
Rapamycin	Invivogen	#tlrl-rap
Torin 1	Sigma-Aldrich	#475991-10MG
SILAC RPMI 1640 Flex Medium	Gibco	#15347143
$^{13}C_6$-glucose	Cambridge Isotope Lab	#CLM-1396
$^{13}C_5$-L-Glutamine	Cambridge Isotope Lab	#CLM-1822-H

$^{13}C_2$-Acetate	Sigma-Aldrich	#282014-250MG
D-(+)-Glucose solution	Sigma-Aldrich	#G8769-100ML
GolgiPlug™ (Protein Transport Inhibitor)	BD Biosciences	#555029
Tween 20	Sigma-Aldrich	#P7949-500ML
NaCl	Sigma-Aldrich	# S9888-5KG
Sodium bicarbonate solution	Sigma-Aldrich	#S8761-100ML
Protease/Phosphatase Inhibitor Cocktail (100x)	Bioké	#5872
Powdered milk	Carl Roth	#T145.2
Luminata™ Crescendo Western HRP substrate	Thermo Fisher Scientific	#10776189
Seahorse XF DMEM medium	Agilent Technologies	#103575-100
Critical Commercial Assays and Kits		
$CD4^+$ T Cell Isolation Kit	Miltenyi Biotec	#130-104-454
Naive $CD4^+$ T Cell Isolation Kit, mouse	Miltenyi Biotec	#130-104-453
NucleoSpin RNA 250	Macherey-Nagel	#740955.250
Foxp3/Transcription Factor Staining Buffer Set	Thermo Fisher Scientific	#15151976
BD Cytofix/Cytoperm Fixation/Permeabilization kit	BD Biosciences	#554714
Mouse IL17 DuoSet ELISA	BIO-TECHNE	#DY421
Seahorse XFe96 Fluxpak	Agilent Technologies	#102416-100
EAE induction kit: MOG35-55/CFA Emulsion PTX	Hooke Laboratories, Inc	#EK-2110
Experimental Models: Organisms/Strains		
$PDH^{fl/fl}$:B6 mice	The Jackson laboratory	#17443
CD4 Cre+:B6 mice	The Jackson laboratory	#022071
Deposited Data		
RNA-seq	This paper	N/A
ATAC-seq	This paper	N/A
Oligonucleotides		
Tbp F: GAAGAACAATCCAGACTAGCAGCA R: CCTTATAGGGAACTTCACATCACAG	(Kurniawan et al., 2020)	
Pdha1 F: CGT CTG TTG AGA GAG CAG CA R: CGC ACA AGA TAT CCA TTC CA	This paper	
Pdhb F: AGGAGGGAATTGAATGTGAGGT R: ACTGGCTTCTATGGCTTCGAT	This paper	
Software and Algorithms		
FlowJo Software	Tree Star	N/A
Graphpad Prism	GraphPad Software, Inc	N/A

Wave Software	Agilent	N/A
Inkscape	Inkscape	N/A

REFERENCES

Adams, M.D. *et al.* (2000) 'The Genome Sequence of *Drosophila melanogaster*', *Science*, 287(5461), pp. 2185–2195. doi:10.1126/science.287.5461.2185.

Andrews, S. (2010) 'FastQC: a quality control tool for high throughput sequence data'.

Angela, M. *et al.* (2016) 'Fatty acid metabolic reprogramming via mTOR-mediated inductions of PPARγ directs early activation of T cells', *Nature Communications*, 7(1), p. 13683. doi:10.1038/ncomms13683.

Aranami, T. and Yamamura, T. (2008) 'Th17 Cells and Autoimmune Encephalomyelitis (EAE/MS)', *Allergology International*, 57(2), pp. 115–120. doi:10.2332/allergolint.R-07-159.

Baricza, E. *et al.* (2018) 'Distinct In Vitro T-Helper 17 Differentiation Capacity of Peripheral Naive T Cells in Rheumatoid and Psoriatic Arthritis', *Frontiers in Immunology*, 9, p. 606. doi:10.3389/fimmu.2018.00606.

Basu, R., Hatton, R.D. and Weaver, C.T. (2013) 'The Th17 family: flexibility follows function', *Immunological Reviews*, 252(1), pp. 89–103. doi:10.1111/imr.12035.

Battello, N. *et al.* (2016) 'The role of HIF-1 in oncostatin M-dependent metabolic reprogramming of hepatic cells', *Cancer & Metabolism*, 4, p. 3. doi:10.1186/s40170-016-0141-0.

Bricker, D.K. *et al.* (2012) 'A Mitochondrial Pyruvate Carrier Required for Pyruvate Uptake in Yeast, *Drosophila* , and Humans', *Science*, 337(6090), pp. 96–100. doi:10.1126/science.1218099.

Brüstle, A. *et al.* (2012) 'The NF-κB regulator MALT1 determines the encephalitogenic potential of Th17 cells', *Journal of Clinical Investigation*, 122(12), pp. 4698–4709. doi:10.1172/JCI63528.

Buck, M.D., O'Sullivan, D. and Pearce, E.L. (2015) 'T cell metabolism drives immunity', *Journal of Experimental Medicine*, 212(9), pp. 1345–1360. doi:10.1084/jem.20151159.

Buenrostro, J.D. *et al.* (2013) 'Transposition of native chromatin for fast and sensitive epigenomic profiling of open chromatin, DNA-binding proteins and nucleosome position', *Nature Methods*, 10(12), pp. 1213–1218. doi:10.1038/nmeth.2688.

Buenrostro, J.D. *et al.* (2015) 'ATAC-seq: A Method for Assaying Chromatin Accessibility Genome-Wide', *Current Protocols in Molecular Biology*, 109(1). doi:10.1002/0471142727.mb2129s109.

Buescher, J.M. *et al.* (2015) 'A roadmap for interpreting 13 C metabolite labeling patterns from cells', *Current Opinion in Biotechnology*, 34, pp. 189–201. doi:10.1016/j.copbio.2015.02.003.

Bulusu, V. *et al.* (2017) 'Acetate Recapturing by Nuclear Acetyl-CoA Synthetase 2 Prevents Loss of Histone Acetylation during Oxygen and Serum Limitation', *Cell Reports*, 18(3), pp. 647–658. doi:10.1016/j.celrep.2016.12.055.

Chapman, N.M., Boothby, M.R. and Chi, H. (2020) 'Metabolic coordination of T cell quiescence and activation', *Nature Reviews Immunology*, 20(1), pp. 55–70. doi:10.1038/s41577-019-0203-y.

Chapman, N.M. and Chi, H. (2022) 'Metabolic adaptation of lymphocytes in immunity and disease', *Immunity*, 55(1), pp. 14–30. doi:10.1016/j.immuni.2021.12.012.

Comerford, S.A. *et al.* (2014) 'Acetate Dependence of Tumors', *Cell*, 159(7), pp. 1591–1602. doi:10.1016/j.cell.2014.11.020.

Corces, M.R. *et al.* (2017) 'An improved ATAC-seq protocol reduces background and enables interrogation of frozen tissues', *Nature Methods*, 14(10), pp. 959–962. doi:10.1038/nmeth.4396.

Dang, E.V. *et al.* (2011) 'Control of TH17/Treg Balance by Hypoxia-Inducible Factor 1', *Cell*, 146(5), pp. 772–784. doi:10.1016/j.cell.2011.07.033.

DeBrosse, S.D. and Kerr, D.S. (2016) 'Pyruvate Dehydrogenase Complex Deficiency', in *Mitochondrial Case Studies*. Elsevier, pp. 93–101. doi:10.1016/B978-0-12-800877-5.00012-7.

Delgoffe, G.M. *et al.* (2009) 'mTOR differentially regulates effector and regulatory T cell lineage commitment', *Immunity*, 30(6), pp. 832–844. doi:10.1016/j.immuni.2009.04.014.

Dobin, A. *et al.* (2013) 'STAR: ultrafast universal RNA-seq aligner', *Bioinformatics*, 29(1), pp. 15–21. doi:10.1093/bioinformatics/bts635.

Franchina, D.G., Dostert, C. and Brenner, D. (2018) 'Reactive Oxygen Species: Involvement in T Cell Signaling and Metabolism', *Trends in Immunology*, 39(6), pp. 489–502. doi:10.1016/j.it.2018.01.005.

Frankish, A. *et al.* (2019) 'GENCODE reference annotation for the human and mouse genomes', *Nucleic Acids Research*, 47(D1), pp. D766–D773. doi:10.1093/nar/gky955.
Gerriets, V.A. *et al.* (2015) 'Metabolic programming and PDHK1 control CD4+ T cell subsets and inflammation', *Journal of Clinical Investigation*, 125(1), pp. 194–207. doi:10.1172/JCI76012.
Guerra, L., Bonetti, L. and Brenner, D. (2020) 'Metabolic Modulation of Immunity: A New Concept in Cancer Immunotherapy', *Cell Reports*, 32(1), p. 107848. doi:10.1016/j.celrep.2020.107848.
Herzig, S. *et al.* (2012) 'Identification and Functional Expression of the Mitochondrial Pyruvate Carrier', *Science*, 337(6090), pp. 93–96. doi:10.1126/science.1218530.
Johnson, M.O. *et al.* (2018) 'Distinct Regulation of Th17 and Th1 Cell Differentiation by Glutaminase-Dependent Metabolism', *Cell*, 175(7), pp. 1780-1795.e19. doi:10.1016/j.cell.2018.10.001.
de Jong, A.J. *et al.* (2014) 'Fatty Acids, Lipid Mediators, and T-Cell Function', *Frontiers in Immunology*, 5. doi:10.3389/fimmu.2014.00483.
Jun, S. *et al.* (2021) 'The requirement for pyruvate dehydrogenase in leukemogenesis depends on cell lineage', *Cell Metabolism*, 33(9), pp. 1777-1792.e8. doi:10.1016/j.cmet.2021.07.016.
Katsen, M., Soderman, D. and Nitowsky, M. (1965) 'Kinetic and Electrophoretic Evidence For Multiple Forms of Glucose-ATP Phosphotransferase Activity From Human Cell Cultures and Rat Liver', *Biochemical and Biophysical Research Communications*, 19(3), p. 6.
Kopylova, E., Noé, L. and Touzet, H. (2012) 'SortMeRNA: fast and accurate filtering of ribosomal RNAs in metatranscriptomic data', *Bioinformatics*, 28(24), pp. 3211–3217. doi:10.1093/bioinformatics/bts611.
Koundouros, N. and Poulogiannis, G. (2020) 'Reprogramming of fatty acid metabolism in cancer', *British Journal of Cancer*, 122(1), pp. 4–22. doi:10.1038/s41416-019-0650-z.
Kurniawan, H. *et al.* (2020) 'Glutathione Restricts Serine Metabolism to Preserve Regulatory T Cell Function', *Cell Metabolism*, 31(5), pp. 920-936.e7. doi:10.1016/j.cmet.2020.03.004.
Kurniawan, H., Soriano-Baguet, L. and Brenner, D. (2020) 'Regulatory T cell metabolism at the intersection between autoimmune diseases and cancer', *European Journal of Immunology*, 50(11), pp. 1626–1642. doi:10.1002/eji.201948470.
Li, B., Carey, M. and Workman, J.L. (2007) 'The Role of Chromatin during Transcription', *Cell*, 128(4), pp. 707–719. doi:10.1016/j.cell.2007.01.015.
Li, H. *et al.* (2009) 'The Sequence Alignment/Map format and SAMtools', *Bioinformatics*, 25(16), pp. 2078–2079. doi:10.1093/bioinformatics/btp352.
Love, M.I. *et al.* (2020) 'Tximeta: Reference sequence checksums for provenance identification in RNA-seq', *PLOS Computational Biology*. Edited by M. Pertea, 16(2), p. e1007664. doi:10.1371/journal.pcbi.1007664.
Love, M.I., Huber, W. and Anders, S. (2014) 'Moderated estimation of fold change and dispersion for RNA-seq data with DESeq2', *Genome Biology*, 15(12), p. 550. doi:10.1186/s13059-014-0550-8.
Luo, W. and Brouwer, C. (2013) 'Pathview: an R/Bioconductor package for pathway-based data integration and visualization', *Bioinformatics*, 29(14), pp. 1830–1831. doi:10.1093/bioinformatics/btt285.
Macintyre, A.N. *et al.* (2014) 'The Glucose Transporter Glut1 Is Selectively Essential for CD4 T Cell Activation and Effector Function', *Cell Metabolism*, 20(1), pp. 61–72. doi:10.1016/j.cmet.2014.05.004.
Mak, T.W. *et al.* (2017) 'Glutathione Primes T Cell Metabolism for Inflammation', *Immunity*, 46(4), pp. 675–689. doi:10.1016/j.immuni.2017.03.019.
Marelli-Berg, F.M., Fu, H. and Mauro, C. (2012) 'Molecular mechanisms of metabolic reprogramming in proliferating cells: implications for T-cell-mediated immunity: The metabolic control of T-cell immunity', *Immunology*, 136(4), pp. 363–369. doi:10.1111/j.1365-2567.2012.03583.x.
Michalek, R.D. *et al.* (2011) 'Cutting Edge: Distinct Glycolytic and Lipid Oxidative Metabolic Programs Are Essential for Effector and Regulatory CD4 $^{+}$ T Cell Subsets', *The Journal of Immunology*, 186(6), pp. 3299–3303. doi:10.4049/jimmunol.1003613.
Nagai, S., Kurebayashi, Y. and Koyasu, S. (2013) 'Role of PI3K/Akt and mTOR complexes in Th17 cell differentiation: Th17 cells and PI3K-Akt-mTOR complexes', *Annals of the New York Academy of Sciences*, 1280(1), pp. 30–34. doi:10.1111/nyas.12059.

O'Neill, L.A.J., Kishton, R.J. and Rathmell, J. (2016) 'A guide to immunometabolism for immunologists', *Nature Reviews Immunology*, 16(9), pp. 553–565. doi:10.1038/nri.2016.70.
Patro, R. *et al.* (2017) 'Salmon provides fast and bias-aware quantification of transcript expression', *Nature Methods*, 14(4), pp. 417–419. doi:10.1038/nmeth.4197.
Pearce, E.L. *et al.* (2013) 'Fueling Immunity: Insights into Metabolism and Lymphocyte Function', *Science*, 342(6155), p. 1242454. doi:10.1126/science.1242454.
Pearce, E.L. and Pearce, E.J. (2013) 'Metabolic Pathways in Immune Cell Activation and Quiescence', *Immunity*, 38(4), pp. 633–643. doi:10.1016/j.immuni.2013.04.005.
Peng, M. *et al.* (2016) 'Aerobic glycolysis promotes T helper 1 cell differentiation through an epigenetic mechanism', *Science*, 354(6311), pp. 481–484. doi:10.1126/science.aaf6284.
Pietrocola, F. *et al.* (2015) 'Acetyl Coenzyme A: A Central Metabolite and Second Messenger', *Cell Metabolism*, 21(6), pp. 805–821. doi:10.1016/j.cmet.2015.05.014.
Qiu, J. *et al.* (2019) 'Acetate Promotes T Cell Effector Function during Glucose Restriction', *Cell Reports*, 27(7), pp. 2063-2074.e5. doi:10.1016/j.celrep.2019.04.022.
Ramírez, F. *et al.* (2018) 'High-resolution TADs reveal DNA sequences underlying genome organization in flies', *Nature Communications*, 9(1), p. 189. doi:10.1038/s41467-017-02525-w.
Ramstead, A.G. *et al.* (2020) 'Mitochondrial Pyruvate Carrier 1 Promotes Peripheral T Cell Homeostasis through Metabolic Regulation of Thymic Development', *Cell Reports*, 30(9), pp. 2889-2899.e6. doi:10.1016/j.celrep.2020.02.042.
Rangel Rivera, G.O. *et al.* (2021) 'Fundamentals of T Cell Metabolism and Strategies to Enhance Cancer Immunotherapy', *Frontiers in Immunology*, 12, p. 645242. doi:10.3389/fimmu.2021.645242.
Ross-Innes, C.S. *et al.* (2012) 'Differential oestrogen receptor binding is associated with clinical outcome in breast cancer', *Nature*, 481(7381), pp. 389–393. doi:10.1038/nature10730.
Salmond, R.J. (2018) 'mTOR Regulation of Glycolytic Metabolism in T Cells', *Frontiers in Cell and Developmental Biology*, 6, p. 122. doi:10.3389/fcell.2018.00122.
Schubert, M. *et al.* (2014) 'Characterization of ancient and modern genomes by SNP detection and phylogenomic and metagenomic analysis using PALEOMIX', *Nature Protocols*, 9(5), pp. 1056–1082. doi:10.1038/nprot.2014.063.
Shi, L.Z. *et al.* (2011) 'HIF1α–dependent glycolytic pathway orchestrates a metabolic checkpoint for the differentiation of TH17 and Treg cells', *Journal of Experimental Medicine*, 208(7), pp. 1367–1376. doi:10.1084/jem.20110278.
Sivanand, S., Viney, I. and Wellen, K.E. (2018) 'Spatiotemporal Control of Acetyl-CoA Metabolism in Chromatin Regulation', *Trends in Biochemical Sciences*, 43(1), pp. 61–74. doi:10.1016/j.tibs.2017.11.004.
Sutendra, G. *et al.* (2014) 'A Nuclear Pyruvate Dehydrogenase Complex Is Important for the Generation of Acetyl-CoA and Histone Acetylation', *Cell*, 158(1), pp. 84–97. doi:10.1016/j.cell.2014.04.046.
Takahara, T. *et al.* (2020) 'Amino acid-dependent control of mTORC1 signaling: a variety of regulatory modes', *Journal of Biomedical Science*, 27(1), p. 87. doi:10.1186/s12929-020-00679-2.
Wang, C. *et al.* (2014) 'Rapamycin-mediated CD36 translational suppression contributes to alleviation of hepatic steatosis', *Biochemical and Biophysical Research Communications*, 447(1), pp. 57–63. doi:10.1016/j.bbrc.2014.03.103.
Wang, R. *et al.* (2011) 'The Transcription Factor Myc Controls Metabolic Reprogramming upon T Lymphocyte Activation', *Immunity*, 35(6), pp. 871–882. doi:10.1016/j.immuni.2011.09.021.
Wang, R. and Green, D.R. (2012) 'Metabolic reprogramming and metabolic dependency in T cells', *Immunological Reviews*, 249(1), pp. 14–26. doi:10.1111/j.1600-065X.2012.01155.x.
Wellen, K.E. *et al.* (2009) 'ATP-Citrate Lyase Links Cellular Metabolism to Histone Acetylation', *Science*, 324(5930), pp. 1076–1080. doi:10.1126/science.1164097.
Wipperman, M.F. *et al.* (2019) 'Mammalian Target of Rapamycin', *The American Journal of Pathology*, 189(3), pp. 492–501. doi:10.1016/j.ajpath.2018.11.013.
Wu, B. and Wan, Y. (2020) 'Molecular control of pathogenic Th17 cells in autoimmune diseases', *International Immunopharmacology*, 80, p. 106187. doi:10.1016/j.intimp.2020.106187.

Xu, K. *et al.* (2021) 'Glycolytic ATP fuels phosphoinositide 3-kinase signaling to support effector T helper 17 cell responses', *Immunity*, 54(5), pp. 976-987.e7. doi:10.1016/j.immuni.2021.04.008.

Yang, W. *et al.* (2021) 'Rheb mediates neuronal-activity-induced mitochondrial energetics through mTORC1-independent PDH activation', *Developmental Cell*, 56(6), pp. 811-825.e6. doi:10.1016/j.devcel.2021.02.022.

Yoo, H.C. *et al.* (2020) 'Glutamine reliance in cell metabolism', *Experimental & Molecular Medicine*, 52(9), pp. 1496–1516. doi:10.1038/s12276-020-00504-8.

Yu, G. *et al.* (2012) 'clusterProfiler: an R Package for Comparing Biological Themes Among Gene Clusters', *OMICS: A Journal of Integrative Biology*, 16(5), pp. 284–287. doi:10.1089/omi.2011.0118.

Yu, G., Wang, L.-G. and He, Q.-Y. (2015) 'ChIPseeker: an R/Bioconductor package for ChIP peak annotation, comparison and visualization', *Bioinformatics*, 31(14), pp. 2382–2383. doi:10.1093/bioinformatics/btv145.

Zangari, J. *et al.* (2020) 'The Multifaceted Pyruvate Metabolism: Role of the Mitochondrial Pyruvate Carrier', *Biomolecules*, 10(7), p. 1068. doi:10.3390/biom10071068.

Zhang, D. *et al.* (2019) 'High Glucose Intake Exacerbates Autoimmunity through Reactive-Oxygen-Species-Mediated TGF-β Cytokine Activation', *Immunity*, 51(4), pp. 671-681.e5. doi:10.1016/j.immuni.2019.08.001.

Zhao, S. *et al.* (2016) 'ATP-Citrate Lyase Controls a Glucose-to-Acetate Metabolic Switch', *Cell Reports*, 17(4), pp. 1037–1052. doi:10.1016/j.celrep.2016.09.069.

Zou, C., Wang, Y. and Shen, Z. (2005) '2-NBDG as a fluorescent indicator for direct glucose uptake measurement', *Journal of Biochemical and Biophysical Methods*, 64(3), pp. 207–215. doi:10.1016/j.jbbm.2005.08.001.

APPENDIX 2

Review Publication

(Shared first author)

KURNIAWAN, H.*, SORIANO-BAGUET, L.*, BRENNER, D., 2020. **Regulatory T cell metabolism at the intersection between autoimmune diseases and cancer.** *Eur. J. Immunol.* 50, 1626–1642.

*Authors contributed equally

European Journal of Immunology

HIGHLIGHTS

Basic

REVIEW

Regulatory T cell metabolism at the intersection between autoimmune diseases and cancer

Henry Kurniawan[*1,2], *Leticia Soriano-Baguet*[*1,2,3] *and Dirk Brenner*[1,2,4]

[1] Experimental and Molecular Immunology, Department of Infection and Immunity, Luxembourg Institute of Health, Esch-sur-Alzette, Luxembourg
[2] Immunology and Genetics, Luxembourg Centre for Systems Biomedicine (LCSB), University of Luxembourg, Belvaux, Luxembourg
[3] Faculty of Science, Technology and Medicine, University of Luxembourg, Esch-sur-Alzette, Luxembourg
[4] Odense Research Center for Anaphylaxis, Department of Dermatology and Allergy Center, Odense University HospitalUniversity of Southern Denmark, Odense, Denmark

Regulatory T cells (Tregs) are critical for peripheral immune tolerance and homeostasis, and altered Treg behavior is involved in many pathologies, including autoimmunity and cancer. The expression of the transcription factor FoxP3 in Tregs is fundamental to maintaining their stability and immunosuppressive function. Recent studies have highlighted the crucial role that metabolic reprogramming plays in controlling Treg plasticity, stability, and function. In this review, we summarize how the availability and use of various nutrients and metabolites influence Treg metabolic pathways and activity. We also discuss how Treg-intrinsic metabolic programs define and shape their differentiation, FoxP3 expression, and suppressive capacity. Lastly, we explore how manipulating the regulation of Treg metabolism might be exploited in different disease settings to achieve novel immunotherapies.

Keywords: autoimmunity · cancer · metabolism · regulatory T cells

Introduction

Regulatory T cells (Tregs) are a subset of $CD4^+$ T helper (Th) cells that is indispensable for the maintenance of peripheral tolerance and immune homeostasis [1,2]. Tregs account for ~5–10% of total circulating $CD4^+$ T cells. The majority of Tregs originate and mature in the thymus, constituting the thymus-derived Treg population (tTregs). A fraction of the body's Tregs arises from naïve $CD4^+$ T cells upon antigen stimulation and differentiates in the periphery, constituting the peripherally derived Treg population (pTregs) [3]. While both tTregs and pTregs have been linked to the establishment of peripheral tolerance, how each exerts its Treg suppressive function in various contexts remains to be further clarified.

The discovery of Forkhead box P3 (FoxP3) as the lineage-specific master transcriptional regulator of all Tregs opened up new avenues for characterizing transcriptional regulation in this subset [4]. FoxP3 expression is essential for normal Treg identity and function [5–7]. Mutations in this gene result in severe immune dysregulation and initiate the autoimmune (AI) disease polyendocrinopahthy enteropathy X-linked (IPEX) syndrome in humans as well as a severe, spontaneous autoimmune disorder in mice [8]. Tregs also express the α-subunit of the IL-2 receptor (CD25) and require constitutive IL-2 signaling to maintain their

Correspondence: Prof. Dirk Brenner
e-mail: dirk.brenner@lih.lu

*Both authors contributed equally.

homeostasis and function [9,10]. The loss of CD25 in Tregs abrogates Treg development and FoxP3 expression, but not in mature Treg [11,12].

It has become clear that the metabolic reprogramming that occurs in activated immune cells is essential for their proper functions, leading to the creation of a new field of research termed "immunometabolism" [13]. Recent studies have underlined the role of cellular metabolism in the generation and maintenance of various types of immune cells, including Tregs [14], and have revealed that distinct T cell subsets utilize different energetic and biosynthetic pathways to sustain their activities. Both human and murine naive $CD4^+$ Th cells use oxidative phosphorylation (OXPHOS) for energy generation in the quiescent state. Upon activation by antigen, these cells proliferate and differentiate into $CD4^+$ Th effector cells (Teffs), such as Th1, Th2, and/or Th17 cells and switch from OXPHOS to a highly glycolytic form of metabolism. In contrast, upon activation, Tregs employ glycolysis at a low rate and high lipid oxidation [15,16]. This divergent use of metabolic pathways can influence cell fate in various ways. For instance, fatty acid oxidation (FAO) fosters the generation of Tregs while dampening the polarization of Teffs [15]. Researchers have therefore focused on investigating how cellular metabolism affects cellular functions in specific contexts. A key goal is to identify the metabolic checkpoints that interfere with cellular activity in the context of abnormal immune homeostasis.

In this review, we discuss the metabolic features of Tregs and delineate how the metabolic strictures shape Treg induction and function. In addition, we describe the relevance of these metabolic pathways in AI diseases and cancer, and explore how their manipulation might lead to new therapeutic avenues.

Overview of metabolic control in Treg cells

Nutrients and metabolites are critical for normal immune cell function, and it is now well known that both under- and overnutrition can contribute to dysregulation of the immune system. However, the precise pathways modulating nutrients and metabolites so as to influence the functions of particular immune cell types remain obscure.

Tregs engage a nutrient-sensing mechanism to adapt to both intrinsic and extrinsic environmental cues and trigger metabolic reprogramming to maintain their activity. These pathways of cellular metabolism are highly interconnected and critical for Treg function [17]. Tregs can select their usage of substrates and metabolic pathways to ensure their survival and function [18]. Under normal homeostatic conditions, where FoxP3 expression is maintained, the majority of Tregs are stable in phenotype and function. However, this stability depends on each cell's ability to prevent disruption of FoxP3 expression and the acquisition of an inflammatory effector function [10,19]. In the context of pathologies, changes in nutrient availability or alterations to genes associated with metabolic regulation can affect Treg stability and function [20–22]. Managing the balance of these metabolic shifts is critical for the maintenance of Treg suppressive capacity. Of note, any difference in the metabolic regulation between tTreg and pTreg is still yet to be determined. Vitamins, glucose, lipids, and amino acids (AAs) are the major groups of metabolic substrates accessed by Tregs. Although each substrate is important for distinct functions and aspects of Treg regulation, they are closely interconnected and can be utilized simultaneously.

We will first discuss how the sensing of nutrients and metabolites can influence Treg function, and then highlight the signaling pathways that establish this metabolism-dependent control of FoxP3 expression and other Treg-specific characteristics.

Vitamins that shape Treg activity

Vitamins are important regulators of Treg cell development, proliferation, and function. Among these, vitamins A, B_9, C, and D have been the best studied and implicated in Treg biology [13].

Vitamin A

The metabolite all-*trans* retinoic acid (ATRA), which is derived from vitamin A, promotes FoxP3 expression and thus Treg development. Upon the induction of TGF-β signaling during murine Treg differentiation, ATRA stimulates signaling by extracellular-related kinase (ERK1/2). This enhanced ERK signaling leads to increased histone methylation and acetylation of the FoxP3 promoter as well as the "conserved non-coding DNA sequence" (CNS) element in this locus, without altering its DNA methylation [21,23,24]. FoxP3 expression is induced while pro-inflammatory cytokine gene expression programs are suppressed. This ATRA-induced stabilization of FoxP3 expression has also been observed in the cultures of expanding human Tregs during inflammation [25]. These findings have clinical relevance, since retinoic acid is superior to the mTORC1 inhibitor rapamycin in promoting stable FoxP3 expression and rapamycin is a drug widely used as an immunosuppressant for graft rejection in the clinic (Table 1) [26–28].

Vitamin B9

The enzyme dihydrofolate reductase converts dietary vitamin B_9, also known as folic acid (FAc), into tetrahydrofolate. Tetrahydrofolate is an essential precursor for one-carbon metabolism (1CM), which is a metabolic cycle predominantly involved in DNA synthesis, methylation, and redox regulation. Tetrahydrofolate is methylated to generate 5-methyltetrahydrofolate, which binds with high affinity to folate receptors to drive 1CM [29]. Tregs express high levels of folate receptor 4 (FR4), and FAc deficiency leads to colonic inflammation in mice. These data establish the importance of FAc and 1CM in sustaining Treg-mediated suppression of inflammations *in vivo* [30].

Table 1. Pharmacological inhibitors of the energy-generating metabolic pathways and their regulators in Tregs, effects and diseases applied

Metabolic Pathway	Target	Drug	Effect on Tregs	Associated Disease	Species	Reference
Glucose metabolism	Glut-1	CG-5	Induce Treg differentiation	SLE	Mouse	[99]
	Glycolysis	2-DG	Induce Treg differentiation and suppression	Experimental autoimmune neuritis	Mouse	[102]
				Skin and heart transplantation	Mouse	[105]
	PDHK	DCA	Increase Treg expansion	EAE	Mouse	[55]
	One-carbon metabolism	Methotrexate	Increase Treg expansion	Rheumatoid arthritis, psoriasis, Crohn's disease and multiple sclerosis	Human	[39]
Lipid Metabolism	Mevalonate pathway	Statins	Dampen Treg stability and function			
	PPARγ (FA oxidation)	Pioglitazone	Induce VAT Tregs	Obesity	Mouse	[77]
	ACC (FA synthesis)	Soraphen A	Induce Treg differentiation	EAE	Mouse	[70]
	ACC (FA synthesis)	TOFA	Impair Treg proliferation	Glioblastoma	Mouse	[117]
	Lipid uptake	SSO	Impair Treg suppression			
Glutamine Metabolism	Glutamine uptake	DON	In combination with metformin and 2-DG, promote Treg generation	Skin and heart transplantation	Mouse	[105]
Metabolic Regulators	mTORC1	Rapamycin	Increase Treg stability, generation and function	Graft rejection	Human	[26, 27]
				Autoimmune phenotype	Mouse	[61]
	AMPK	Metformin	Induce Treg differentiation	Type II diabetes	Human	[103]
				Skin and heart transplantation	Mouse	[105]
				Inflammatory bowel disease	Mouse	[103]
				EAE	Mouse	[104]
	mtROS	MitoTEMPO	Inhibit Treg damage and apoptosis	EAE	Mouse	[107]

SLE, Systemic lupus erythematosus; 2-DG, 2-Deoxy-D-Glucose; PDHK, Pyruvate dehydrogenase kinase; DCA, Dichloroacetate; EAE, Experimental autoimmune encephalomyelitis; SSO, Sulfo-N-succinimidyl oleate; TOFA, 5-tetradecyl-oxy-2-furoic acid, ACC: Acetyl-CoA carboxylase; DON, 6-diazo-5-oxo-L-norleucine; mtROS, mitochondrial reactive oxygen species.

Vitamin C

Vitamin C increases the induction and stability of murine FoxP3$^+$ pTregs by promoting demethylation of the Treg-specific demethylation region (TSDR), a conserved CpG-rich region within the FoxP3 locus [31]. Interestingly, vitamin C seems to have differing effects on pTregs and tTregs. Oyarce et al. and others showed in mice that, whereas vitamin C did not affect tTreg suppressive capacity, it greatly enhanced the function in pTregs both *in vitro* and *in vivo* [32]. It is intriguing to speculate that this difference may be due to distinct modes of metabolic control in tTregs versus pTregs, an issue that needs to be further clarified. Kasahara et al. further showed that vitamin C promoted the induction of Treg differentiation from human naïve T cells, which was very stable even in the presence of IL-6 *in vitro* [33].

Vitamin D

The vitamin D-derived metabolite calcitriol increases CTLA-4 and FoxP3 expression in human Tregs and also enhances their

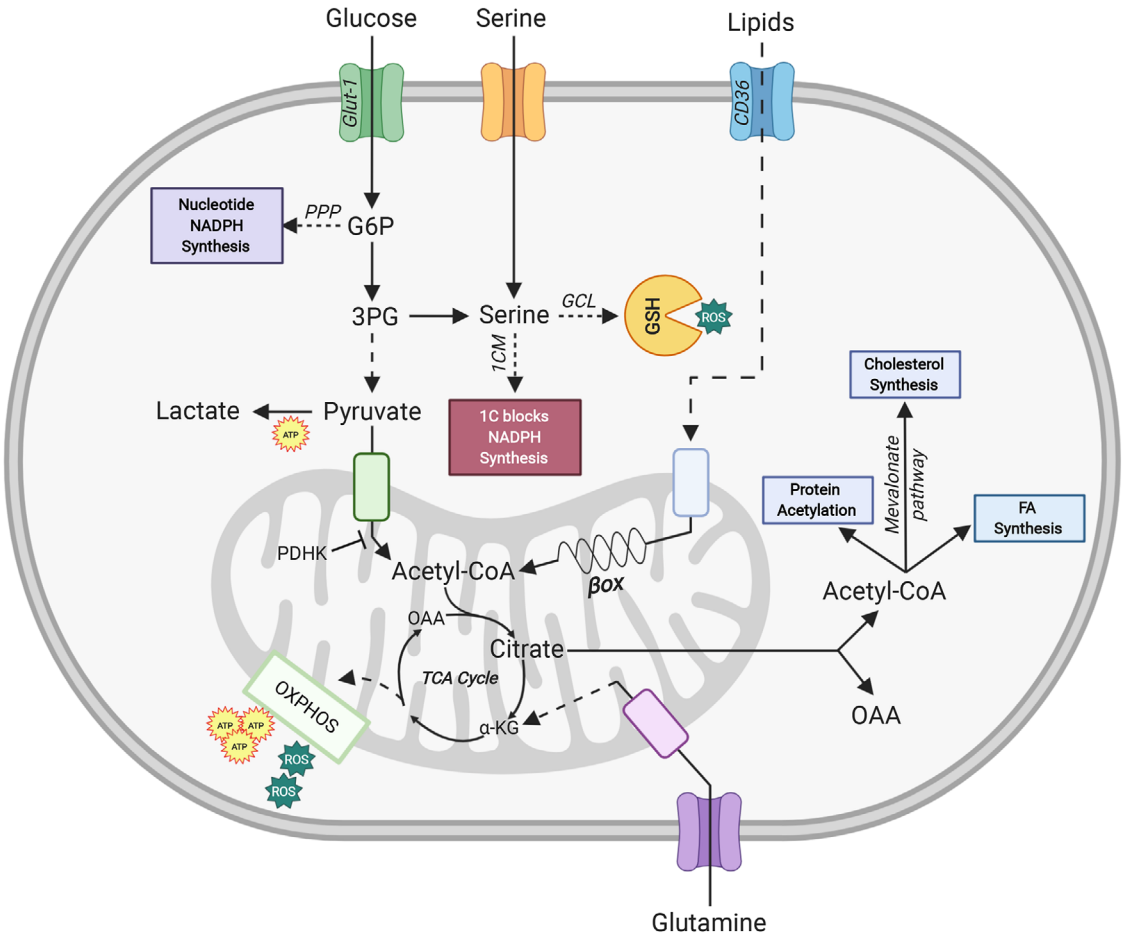

Figure 1. Schematic diagram of energy-generating metabolic pathways and their regulators in Tregs. Upon TCR engagement and CD28 co-stimulation, glucose enters the Tregs via the Glut-1 transporter and is converted via glycolysis into pyruvate in the cytoplasm. Pyruvate enters the mitochondria and is converted into acetyl-CoA, which drives the TCA cycle and thus energy production via oxidative phosphorylation (OXPHOS). OXPHOS is an efficient but slow route of cellular ATP production, and also generates ROS as by-products. Under anaerobic conditions, cytosolic pyruvate is converted into lactate, generating less ATP. Depending on a cell's requirements, glucose entering the cell can also drive nucleotide and NADPH synthesis via the pentose phosphate pathway (PPP). Serine either enters the cell from the extracellular space or is synthesized from 3-phosphoglycerate (3PG) generated from cytosolic glucose. This serine then either enters one-carbon metabolism (1CM) to produce one-carbon (1C) building blocks for anabolism, or generates the ROS scavenger glutathione (GSH). Lipids enter T cells via the CD36 transporter and then move to the mitochondria where the β-oxidation (βox) of fatty acids (FA) is initiated. FA oxidation (FAO) generates acetyl-CoA, which enters the TCA cycle to drive OXPHOS and provide energy. The TCA cycle metabolite citrate can be shuttled out of the mitochondria and converted back into cytosolic oxaloacetate (OAA) and acetyl-CoA. The latter can be used for protein acetylation, cholesterol synthesis via the mevalonate pathway, and FA synthesis. Lastly, glutamine enters T cells, enters the mitochondria, and is converted into glutamate and α-ketoglutarate (α-KG). This α-KG enters the TCA cycle to drive OXPHOS.

suppressive capacity [34]. In murine models of systemic lupus erythematosus (SLE), as well as in patients who suffer from this disease, vitamin D supplementation increases the percentage of Tregs and decreases levels of Th1 and Th17 cells, B cells, and anti-dsDNA antibodies [35,36]. The reduction in these inflammatory parameters corresponds to the amelioration of disease severity. Other work has shown that vitamin D can induce the generation of tolerogenic dendritic cells (DCs) to support pTreg generation, increase tolerogenic cytokines IL-10 and TGF-β, and attenuate the development of colitis in mice [37]. Despite these advances, however, the molecular mechanism by which vitamin D regulates function of Tregs is yet not clear.

Glucose metabolism and signaling pathways controlling Tregs cells

General pathways of energy production in T cells

When a naive conventional $CD4^+$ T cell experiences T cell receptor (TCR) engagement and CD28 co-stimulation, the T cell uses the Glut1 transporter to take up glucose from the environment and initiate the glycolytic pathway [38]. This pathway converts glucose into various metabolites that can feed multiple branch pathways, such as the pentose phosphate pathway (PPP) that supports nucleotide production (Fig. 1). Glucose also feeds into

serine biosynthesis plus 1CM to produce one-carbon building blocks for macromolecule biosynthesis [39]. The final step of the glycolytic pathway is the generation of pyruvate, which either enters the TCA cycle in the mitochondria and is converted into acetyl-CoA by pyruvate dehydrogenase (PDH), or remains in the cytosol and is converted into lactate by lactate dehydrogenase (LDH) [39]. Acetyl-CoA within the TCA cycle reacts with oxaloacetate (OAA) to generate citrate that further fuels the TCA, the electron transport chain (ETC), and OXPHOS. OXPHOS is considered to be highly energetically efficient since it results in up to 36 molecules of ATP produced per molecule of glucose consumed [14, 39]. Alternatively, the citrate produced by the TCA cycle can exit the mitochondria and be converted back into cytosolic OAA and acetyl-CoA by ATP-citrate lyase (ACLY). Cytosolic acetyl-CoA can be used for the synthesis of cholesterol or fatty acids (FA), or for protein acetylation (such as that of histones) to modulate gene expression [14,39].

The generation of lactate from pyruvate in the cytosol was originally described as an inefficient energy pathway used predominantly during hypoxia due to the fact that only two ATP molecules are produced per glucose molecule consumed [14,39]. However, activated Teffs use this route even under normoxic conditions, as it is the fastest way to generate energy and intermediate metabolites to build biomass for proliferation. This phenomenon was first described in cancer cells and is known as the Warburg effect [40,41].

Signaling pathways controlling energy production in Tregs

In contrast to Teffs, both human and murine Tregs rely mostly on the oxidative pathway of glucose metabolism for their function in a manner tightly regulated by several key signaling cascades. An especially important pathway in this context is the PI3K/AKT/mTOR axis, which is activated in a T cell upon TCR engagement plus CD28 co-stimulation [39]. Activated PI3K in turn phosphorylates AKT kinase, which leads to engagement of mTOR complex 1 (mTORC1) [42]. mTORC1 is the master regulator of anabolism and activates downstream targets such as S6 kinase and 4EBP1 to promote protein translation. mTORC1 also stimulates SREBP-1 to trigger FA synthesis, and HIF1-α to induce glycolysis (Fig. 2). mTORC1 is also activated by growth factors and nutrients, including the AAs leucine, arginine, and glutamine [39]. It has been shown that a lack of mTOR activity, or its specific inhibition by rapamycin, increases FoxP3 expression and causes naïve $CD4^+$ T cells to differentiate into Tregs rather than Teffs both *in vitro* and *in vivo* [43,44]. However, it has also been shown that mTORC1 is necessary for the suppressive function of Tregs, since *in vivo* deletion of raptor, a central component of mTORC1, specifically in mouse Tregs causes loss of Treg suppressive capacity, spontaneous Teff activation, and a fatal inflammatory disorder [45,46]. In addition, Kishore et al. have shown that mTOR-induced glycolysis is required *in vivo* and *in vitro* for human and murine Treg migration to inflammatory sites via the PI3K-mTORC2-mediated pathway [47]. mTOR also regulates the glycolytic-lipogenic switch important for Treg cell growth and proliferation [48]. Despite mTOR levels in Treg being relatively low compared to Tconv, this nutrient sensor is still crucial for Treg function [49]. Tregs have been shown to have a dynamic mTOR requirement throughout their activity. Early downregulation of mTOR, followed by an increase in mTOR activation is critical for Treg cell expansion to occur [50]. Thus, delicate balance of mTOR is critical for normal Treg activity, and dysregulation of mTOR activity impairs Treg function. These observations reveal the dual role of mTOR signaling in Tregs: on one hand, mTOR induction promotes Treg proliferation and migration; on the other hand, it dampens Treg suppressive capacity [22].

mTORC1 signaling in T cells is negatively regulated by AMPK-dependent signaling [39]. AMPK is a sensor of a cell's AMP/ATP ratio and becomes active when this energy balance is low (Fig. 2). AMPK signaling thus has the opposite effect on mTORC1-responsive pathways, promoting mitochondrial OXPHOS and FA oxidation [42].

Negative regulators of mTOR critical for Treg function include protein phosphatase 2A (PP2A) and tuberous sclerosis 1 (TSC1) (Fig. 2). Genetic deletion specifically in murine Tregs of either of these two regulators impairs Treg suppressive capacity, resulting in spontaneous autoimmunity [51,52].

The lipid phosphatase PTEN prevents PI3K activation and so is another inhibitor of the mTOR signaling pathway (Fig. 2). Consistent with other studies, ablation of PTEN in murine Tregs results in a spontaneous autoimmune lymphoproliferative disease [53]. PTEN-deficient tTregs gradually lose CD25 and FoxP3 expression and increase glycolysis while reducing their mitochondrial fitness [53, 54]. In mice suffering from experimental autoimmune encephalomyelitis (EAE), a mouse model of human multiple sclerosis (MS), PTEN-deficient Tregs are unable to suppress Teff functions, allowing autoreactive Teffs to attack the host's central nervous system [53].

HIF1α itself is also important in balancing Treg generation. HIF1α signaling induced by hypoxia blocks mitochondrial respiration and activates PDH kinase (PDHK), which inhibits PDH and so interferes with the conversion of pyruvate into acetyl-CoA [39, 55]. It has also been reported that HIF1α promotes FoxP3 degradation by binding to this transcription factor, targeting it for ubiquitination and proteasomal degradation [56]. In line with these findings, HIF1α expression in murine T cells favors Th17 cell commitment over Treg generation *in vitro* [56].

FoxP3 expression in Tregs

As noted above, FoxP3 is the master transcription factor controlling Treg development. However, FoxP3 also regulates metabolism in mature Tregs by increasing their oxidative metabolism, catabolism, and OXPHOS (Fig. 2). Specifically, FoxP3 promotes the production of ETC proteins and enzymes involved in FAO, while simultaneously blocking PI3K-AKT-mTORC1-driven glycolysis and anabolism [22,57,58]. In a low glucose/high lactate environment, FoxP3 is able to reprogram mouse Tregs

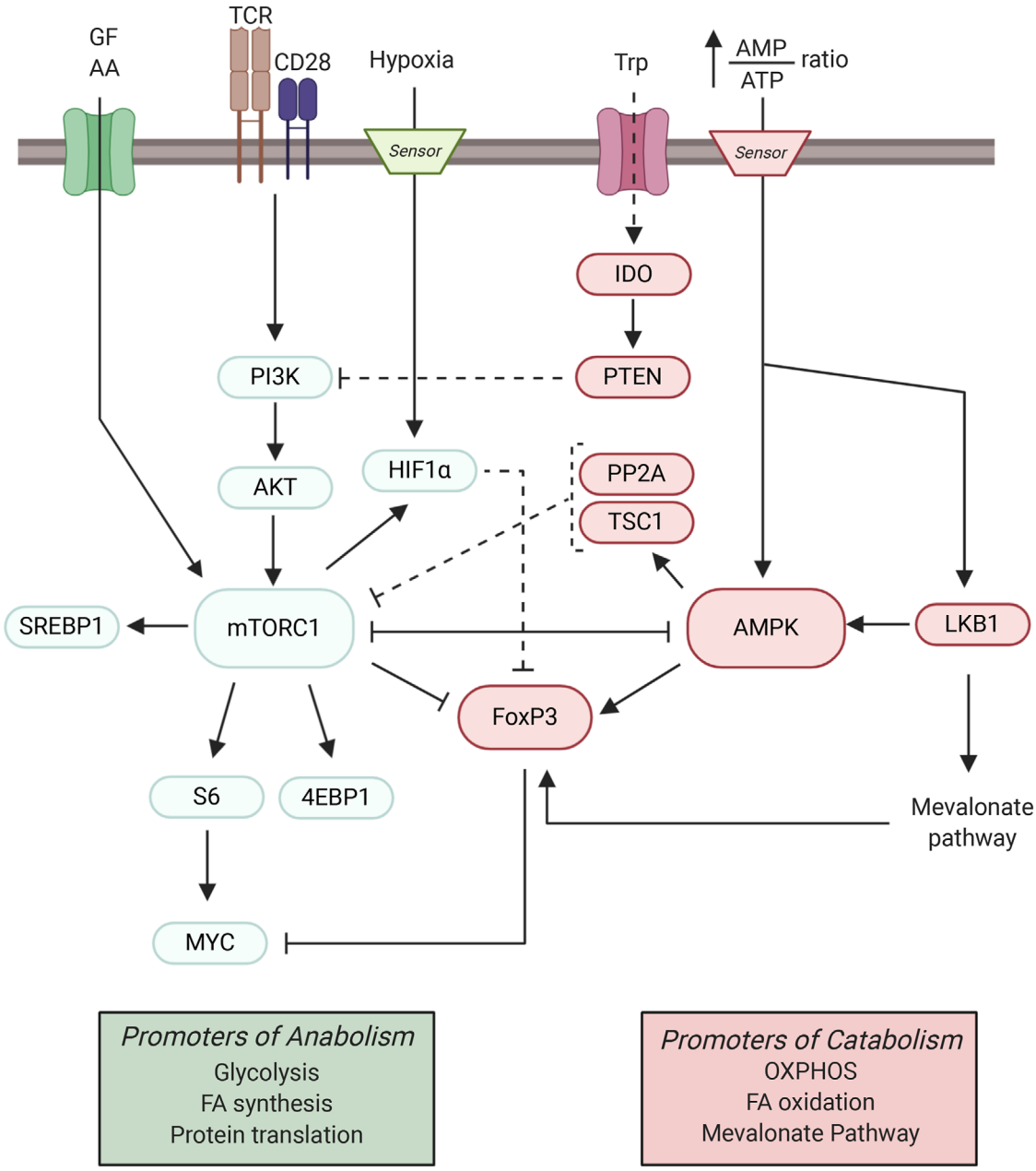

Figure 2. Schematic diagram of energy-generating regulators in Tregs. The mTORC1 and AMPK signaling pathways are major metabolic checkpoints that modulate the FoxP3 expression and immunosuppressive activity of Tregs. Upon TCR engagement and CD28 co-stimulation, the PI3K/AKT pathway is activated and induces mTORC1 signaling. The mTORC1 pathway can also be stimulated by the sensing of growth factor (GF) or amino acid (AA) availability. mTORC1 activation represses FoxP3 expression and thus Treg function. FoxP3 inhibits MYC, a downstream target of mTORC1, and so exerts direct metabolic control. FoxP3 is also downregulated by HIF1α, which is activated either directly by hypoxia or via mTORC1. HIF1α is therefore also a modulator of Treg function. Indoleamine 2,3-dioxygenase (IDO), an enzyme involved in tryptophan (Trp) catabolism, activates PTEN. PTEN opposes PI3K-dependent mTOR activation and thus supports Treg function. mTORC1 negatively regulates AMPK, which is a major promotor of catabolism and also regulates FoxP3 expression. AMPK is activated when energy supplies become low (high AMP/ATP ratio). LKB1 drives both AMPK activity and the mevalonate pathway, which is critical for Treg metabolism and function. Activated AMPK can also signal via TSC1 to inhibit the mTORC1 pathway. Likewise, protein phosphatase 2A (PP2A) is a negative regulator of the mTORC1 pathway.

to survive by blocking the anabolic mTORC1 target Myc and glycolysis, while increasing respiratory capacity via OXPHOS to increase the NAD/NADH ratio [39,42,57,59]. OXPHOS is indispensable for Treg function since Treg-specific ablation of Rieske iron-sulfur protein (RISP) in mice, an element of ETC complex III, causes an autoimmune "scurfy-like" disease [60]. Lastly, it was shown that increased Glut1 expression in murine Tregs enhances glycolysis and proliferation driven by mTORC1. The increased mTORC1 activity impairs tTreg and pTreg suppressive capacity and decreases FoxP3 expression both *in vitro* and *in vivo* [22,61].

Collectively, current studies of energy metabolism in Tregs indicate that Treg proliferation and suppressive activity can be influenced by a variety of metabolic pathways, including anabolic signals driven by the mTORC1 axis and those arising from FoxP3-dependent oxidative metabolism [22,61].

Lipid metabolism in regulatory T cells

Fatty acid oxidation

Lipid metabolism is essential for providing many cell types with an adequate supply of energy (Fig. 1) [62]. FA are a subgroup of lipids that have been implicated in human and murine Treg differentiation, survival, and function, although the exact contribution of the different lipids in both Treg population remain to be addressed [15,55,63]. Tregs recognize and take up FA via various receptors, including G protein-coupled receptors (GPCRs), CD36, fatty acid-binding protein (FABP), and fatty acid transport protein (FATP) [63,64]. High levels of mitochondrial FAO then ensue in these Tregs to generate the energy needed to support their development [15]. In the absence of exogenous FA *in vitro* TGF-β-induced generation of FoxP3$^+$ Tregs is abrogated in mice [15].

Several studies have indicated that FAO is critically needed to support Treg function [15,55,65,66]. Carnitine palmitoyl transferase-1 (CPT1) enzyme is essential for FAO. CPT1 attaches carnitine to long-chain FA (LC-FA) to facilitate LC-FA transport from the cytosol into the mitochondria, where FAO occurs. Interestingly, Raud et al. showed that genetic deletion of CPT1a had no effect on the development or function of murine tTregs and pTregs [67], which is in stark contrast to the studies using the CPT1a inhibitor etomoxir [15]. When applied at higher concentrations the studies from Raud et al. and Divakaruni et al. indicated that etomoxir inhibits different targets beside CPT1a [67,68]. However, it should be noted that Tregs can use CPT1a-independent pathways to utilize fatty acids and that the translocation of short- or medium-chain FAs does not involve CPT1a [66].

A balance between FAO and FA synthesis in Treg is determined by nutrient levels in the surrounding environment and intracellular energy status. Although Tregs primarily depend on FAO, they also require the balance between certain degree of *de novo* FA synthesis (which costs the cell energy) and FAO (which generates energy) [65, 69]. In contrast, Teffs are highly proliferative when functioning and require FA synthesis [70].

AMPK and LBK1

AMPK is part of a sensor system that is activated when a cell is in a low energy environment (Fig. 2). Activation of AMPK drives mitochondrial FAO while inhibiting *de novo* FA synthesis. To support their high demand for FAs, Tregs store substantial amounts of lipids within intracellular lipid droplets [71]. AMPK activation in Tregs stimulates mitochondrial oxidation of these lipids, while inhibiting *de novo* FA synthesis. Multiple studies have shown that tilting the balance towards lipid oxidation by modulating upstream targets of AMPK or pathways implicated in β-oxidation *in vivo* promotes Treg development [70,72,73].

Liver kinase B1 (LKB1) is a kinase acting upstream of AMPK and another important metabolic sensor in Tregs (Fig. 2) [42]. Ablation of LKB1 in mice significantly reduces tTreg numbers and impairs their function. LKB1-deficient Tregs lack functional mitochondria, abrogate FA oxidation and curtail OXPHOS, resulting in ATP depletion [72, 73].

LKB1 also modulates the mevalonate pathway that synthesizes the more complex lipids needed by Tregs. The mevalonate pathway produces cholesterol and the isoprenoid geranylgeranylpyrophosphate (GGPP), two metabolites that promote Treg proliferation and stability (Fig. 1 and 2) [74]. Blocking the mevalonate pathway *in vivo* via either ablation of HMG-CoA reductase (HMGCR), a rate-controlling enzyme in this pathway, or by pharmacological blockade using statins (Table 1), stimulates the conversion of murine Tregs into Th1-like and Th17-like Teffs and impairs tTreg suppressive capacity [74].

Acetyl-CoA carboxylase and FA-binding proteins

Acetyl-CoA carboxylase (ACC) is an important enzyme for the initiation of FA synthesis. Blockade of ACC both *in vitro* and *in vivo* restrains the formation of Th17 cells and dampens IL-17 production, but induces murine FoxP3$^+$ Treg generation [70]. Likewise, FA-binding proteins (FABPs) are pivotal for Treg suppressive function. Genetic or pharmacological inhibition of FABP5 leads to impaired lipid uptake and trafficking, which results in decreased FAO and OXPHOS, impaired lipid metabolism, and loss of murine pTreg suppressive capacity [66].

Dietary lipids

Dietary lipids are also linked to Treg biology, especially for Tregs in the colon (cTregs). Short-chain fatty acids (SCFAs), such as butyrate, acetate, and propionate, are the major metabolites derived from bacterial fermentation of dietary fiber [63]. Several studies have shown that butyrate is involved in epigenetic modification by inhibiting histone deacetylases; in mice, exogenous butyrate increases histone acetylation of the FoxP3 locus, thereby supporting cTreg generation and stability [75, 76]. In addition, SCFAs can act via GPCR 109a to influence Tregs. The binding of butyrate to GPCR 109a on macrophages and DCs induces IL-10 production, and this cytokine in turn promotes Treg generation in mice [76].

Peroxisome proliferator-activated receptor-γ

Peroxisome proliferator-activated receptor (PPAR)-γ is a regulator of lipid metabolism that has been associated with maintaining the homeostasis of Tregs in visceral adipose tissue (VAT). Interestingly, Treg-specific deletion of PPAR-γ in mice significantly

abrogates the generation of Tregs in VAT but not in other organs [77]. Likewise, PPAR-γ agonist pioglitazone (Table 1) upregulates expression of the FA transporter CD36 and increases FAO. These events result in the induction of VAT Tregs, which have positive suppressive effects on obesity-associated metabolic disorders [77].

Polyunsaturated fatty acid

Long-chain polyunsaturated fatty acid (PUFA), which is the preferred ligand for PPAR-γ, has also been shown to shape the Th cell balance and the outcome of autoimmunity. Mice fed with PUFA show a significant reduction of Th1 and Th17 cells, inflammatory cytokines IFN- γ, IL-17, IL-6, TNF, and exhibit a higher number of Tregs [78]. Moreover, these mice have lower incidence of type 1 diabetes. A similar study using fat-1 transgenic mice expressing *Caenorhabditis elegans* fat-1 gene, which led to accumulation of PUFA, showed that these mice had a higher induction of Treg cells *in vitro* and *in vivo*, and lower clinical arthritis score [79].

Lipid metabolism clearly plays a critical role in Treg homeostasis, but further study is required to clarify exactly how LC-FAO supports Tregs as well as the balance between FAO and FA synthesis in Treg biology. It is also possible that short- or medium-chain FA may regulate Tregs differently than LC-FA. These issues remain to be addressed.

Amino acid metabolism in Tregs cells

AA transporters

Amino acids serve not only as a source of energy but also provide building blocks for protein and nucleic acid biosynthesis. There are two types of AAs: essential AAs, which are obtained from the diet, and non-essential AAs, which can be synthesized by the host [80]. Amino acids that are not synthesized have to be imported into cells via AA transporter proteins. A single AA transporter can often facilitate the transport of multiple AAs, raising the complexity of their regulation [81]. Tregs express various AA transporters, with Slc7a5 being the most extensively studied. Slc7a5 interacts with Slc3a2 to form a large neutral AA transporter called LAT1 [82]. The regulation of AA transport via LAT1 directly influences mTOR activity [83,84]. Given the prominence of mTOR in regulating Treg metabolism, additional study of other AA transporters and their effects on Treg function is warranted.

Branched-chain AA and arginine

The branched-chain AAs (BCAAs), leucine, isoleucine, and valine play a particularly important role in the metabolic reprogramming that supports Treg maintenance. Mice fed on a diet containing reduced BCAA exhibit decreased numbers of FoxP3$^+$ Tregs in the periphery [85]. Similarly, genetic deletion of the BCAA transporter Slc3a2 specifically in murine Tregs abrogates their mTOR activity, resulting in loss of tTreg numbers and function, and thus spontaneous inflammation in the mutant mice [85]. In addition, a recent study has shown that Tregs cultured in the presence of arginine and leucine show sustained mTOR activity upon TCR stimulation. The absence of either AA in murine Tregs result in a reduced number of activated Tregs and these mice develop fatal autoimmune disease [86]. Lastly, in human CD4$^+$CD25$^+$FoxP3$^+$ Tregs, exogenous arginine induces DNA hypomethylation rather than histone modification of the IL-10 promoter, which leads to higher IL-10 production by these cells [87].

Kynurenine and glutamine

Kynurenine is a product of tryptophan catabolism that is generated by IDO and is important for murine Treg generation, expansion, and suppressive function [88]. IDO inhibits mTOR signaling via PTEN and thereby inhibits Teff proliferation while promoting Treg induction (Fig. 2) [17].

Glutamine fuels the TCA cycle via glutaminolysis and is critical for reprogramming Teff metabolism upon activation (Fig. 1). Accordingly, glutamine depletion blocks Teff proliferation and cytokine production [89]. Perhaps surprisingly, depending on the model used, glutamine has an opposing effect on Tregs. *In vitro*, glutamine restriction shifts murine naïve T cell differentiation under Th1 polarizing conditions toward FoxP3$^+$ pTregs [90]. However, *in vivo* study using an acute graft-versus-host disease (GVHD) mouse model showed that glutamine supplementation markedly increased the proportion of Tregs and inhibited GVHD-induced inflammation in the intestine, liver, skin, and spleen [91]. Thus, the role of glutamine in Treg homeostasis needs to be further clarified.

Serine

Our group has recently shown that serine metabolism and redox regulation are intimately linked to Treg function. Serine feeds into the synthesis of glutathione (GSH), a major cellular antioxidant [92]. GSH synthesis also depends on the catalytic subunit of glutamate cysteine ligase (*Gclc*). Conditional deletion of *Gclc* in murine Tregs impairs their production of GSH [61]. These mutant Tregs consequently display increased levels of ROS but no apparent defects in both tTreg and pTreg homeostasis, stability or differentiation. However, *Gclc*-deficient Tregs do show increased proliferation, activation, glycolysis, and OXPHOS, and the mutant mice develop spontaneous autoimmunity [61]. Importantly, *Gclc*-deficient Tregs show elevations in both their synthesis and uptake of serine. Accordingly, dietary intervention in the form of feeding the mutant mice on serine/glycine-deficient chow prevents the onset of autoimmunity. In line with this finding, dampening of serine metabolism reinstated the suppressive function of Tregs, firmly linking serine metabolism to Treg function [61].

The high serine levels in *Gclc*-deficient Tregs lead to elevated mTOR activity, which in turn reduces FoxP3 expression and so Treg function [61]. Interestingly, this increase in mTOR activity

in *Gclc*-deficient Tregs stands in striking contrast to the opposite effect seen in *Gclc*-deficient conventional T cells [93], and indicates that GSH exhibits subset-specific functions. In Tregs, GSH controls a feedback loop between GSH and serine availability that controls Treg suppressive capacity [61].

Collectively, these observations clearly establish that a delicate balance of forces within AA metabolism determines the functionality of Tregs.

Distinct metabolic regulation of human Tregs

The metabolic characterization of Tregs has been mainly focused on murine Tregs. Studies on the metabolic control of human Treg cells are still sparse. To complicate matters, it is well accepted that the human Treg population is highly heterogeneous. Mass cytometry analysis of circulating human Tregs identify over 22 subsets, depending on the expression level of surface markers such as CD45RA, CCR4, CD39, CD127, HLA-DR, and Foxp3 [94]. Because of this and the lack of detailed information on each subset, we only discuss the common human Tregs subset that highly express CD25, Foxp3, and low expression of CD127.

There are many commonalties in the metabolic regulation of human and mouse Tregs, however, striking differences have been observed as well. Unlike murine Tregs that are low in glycolysis and high in FAO, human tTregs are highly glycolytic and show high mTOR activity [95]. Along the lines, *in vitro* proliferating human Tregs express high levels of genes linked to glycolysis (similar to murine Tregs) and FAO (different to murine Tregs), such as mTOR and AMPK. Similar to murine Tregs, human Tregs rely on a balanced metabolism, but the molecular consequences are different. In human Tregs blocking glycolysis with the inhibitor 2-DG leads to differential expression of human FoxP3 splicing variants, which support their suppressive function [96]. Unrestrained glycolysis impairs human as well as murine Treg function. In human Tregs, the glycolytic enzyme Enolase-1 has been shown to bind to the FoxP3 promoter and the CNS2 region. Enolase-1 then represses the transcription of the isoform FoxP3-E2, which is important for Treg mediated suppression [96].

Our group has shown that human pTregs also require well-adjusted AA metabolism for their optimal function. Improper redox balance upon *Gclc* inhibition in human pTregs increases serine metabolism that consequently impairs FoxP3 expression and Treg function. Restoring a balanced serine metabolism can reestablish FoxP3 expression in human pTregs as well as in murine Tregs [61].

Modulating Treg metabolism as a therapy for autoimmune diseases: Lessons learned from murine models

One of the most important aspects of the immune system is its ability to differentiate between foreign and self-antigens. Autoimmunity arises when the immune system loses its tolerance to self-antigens and starts to attack host tissues expressing these antigens. Autoimmune (AI) diseases affect ∼7–9% of the general population, with women being at higher risk than men. AI diseases are divided into two categories according to the extent of the affected tissue. Organ-specific AI diseases, such as MS and inflammatory bowel disease (IBD), affect primarily one organ or system. Systemic AI diseases, such as SLE and rheumatoid arthritis (RA), disrupt homeostasis widely throughout the body. In all AI diseases, Th cells play an important role, either as disease contributors or as rescuers attempting to mitigate inflammation [64]. Autoreactive Teffs attack self-tissues and cause AI disease, whereas Tregs, with their ability to shut down Teffs, are important for preventing AI disease [97, 98]. Therefore, enhancing the immunosuppressive activities of Tregs by modulating their cellular metabolism could represent a potential new therapeutic strategy for the treatment of AI diseases.

CG-5 and 2-DG

As previously discussed, Tregs rely mostly on the oxidative metabolism of lipids and minor amounts of glucose to generate energy and maintain their suppressive capacity. In contrast, Teffs employ glycolysis and FA synthesis to sustain their effector functions [14, 42]. Therefore, drugs that favor the oxidative metabolism of Tregs and/or block the anabolic metabolism of Teffs could have a beneficial impact in the context of AI. For example, in both spontaneous and induced mouse model of SLE, reducing glucose intake using the Glut1 inhibitor CG-5 (Table 1) ameliorated AI disease symptoms. *In vitro*, CG-5 treatment of naive murine Th cells promoted Treg differentiation while blocking Th1 and Th17 polarization [99].

Another example is treatment with 2-deoxy-D-glucose (2-DG), which is a known inhibitor of glycolysis because it blocks the generation of glucose-6-phosphate (Table 1). Treatment of mouse naïve cells with 2-DG *in vitro* limits Th17 generation while inducing Treg differentiation [100]. Our group has recently shown that, if ROS are uncontrolled in tTregs and pTregs these cells increase glycolysis at the cost of their suppressive activity, which causes severe autoimmunity [61]. Accordingly, we found that 2-DG-mediated glycolytic restriction was able to reverse the functional deficit of the mutant Tregs *in vitro* [61]. Others have shown that blocking glycolysis with 2-DG *in vitro* reduces ATP levels, increases the AMP/ATP ratio, and thus activates AMPK signaling [101]. AMPK promotes catabolic reactions such as the oxidation of glucose and lipids, which are the pathways preferentially used by Tregs. Liu et al. showed that 2-DG-treated mice with experimental autoimmune neuritis, which is a mouse model of human Guillain-Barré syndrome, blocked disease initiation and progression. 2-DG promoted Treg differentiation while inhibiting that of Th1 and Th17 cells [102].

Metformin

Metformin is another drug that promotes Treg differentiation and is already widely used in the clinic for the treatment of type II

diabetes (Table 1) [103]. Metformin induces FAO through AMPK activation but also inhibits ETC complex I [42]. Studies have shown that the use of metformin in several mouse models of AI diseases, such as IBD and EAE, induces Treg generation while inhibiting Th17 differentiation. This skewing leads to a reduced disease burden in the metformin-treated mice [103, 104]. These observations underline the importance of coordinating the balance between glycolysis and OXPHOS, a balance that is crucial for Treg suppressive capacity [61].

In addition to promoting Treg function, it can be advantageous to use metformin to help decrease the functions of self-reactive Teffs. Glutaminolysis is a major pathway that is important for Teffs, less so for Tregs [90]. Lee et al. showed that a combination of metformin, 2-DG and 6-diazo-5-oxo-L-norleucine (DON), which is a glutamine antagonist (Table 1), blocked Teff proliferation and cytokine production in a mouse model of skin and heart transplantation [105]. Most helpfully, the same cocktail fostered Treg generation and so also promoted the tolerogenic response *in vivo*.

Dichloroacetate

Another way of inducing oxidative metabolism of glucose is to inhibit the positive regulators of glycolysis. Dichloroacetate (DCA) blocks PDH kinase (PDHK), an inhibitor of PDH, and so maintains PDH in its active form (Table 1). Thus, the connection between glucose metabolism and the TCA cycle remains open in DCA-treated cells and the oxidation of pyruvate in the TCA cycle is favored over its reduction into lactate. Gerriets et al. showed using the EAE model that mice treated with DCA presented with a lower disease burden due to increased Treg generation coupled with inhibition of Teff function [55].

Rapamycin and HIF1α deletion

Teffs show highly active mTORC1. mTORC1 inhibition with rapamycin induces FAO, dampens Teff proliferation, and reinforces Treg generation [15,101]. Rapamycin treatment of mice showing AI symptoms reverses their inflammatory phenotype, restores Treg functionality, and prolong the lifespan (Table 1) [61].

HIF1α has also been described as a key regulator in systemic and organ-specific AI diseases, particularly SLE, IBD, and RA [42]. In the EAE mouse model, ablation of HIF1α leads to increased Treg differentiation and reduced Th17 development, which in turn dramatically decreases the AI disease score [56,100].

Methotrexate

In contrast to Tregs, Teffs rely on serine metabolism for macromolecule biosynthesis. Indeed, blocking this pathway with the chemotherapeutic drug methotrexate (Table 1) is used to treat patients with RA, psoriasis, Crohn's disease or MS in the clinic. This strategy induces Tregs while dampening Teff functions [39]. Again, these findings align with our demonstration that modulating serine metabolism, which is linked to a stress-sensitive feedback loop in Tregs, controls Treg suppressive capacity, and is important for limiting autoimmunity in mice [61].

Soraphen A

Tregs rely on lipid oxidation, while Teffs use FA synthesis. Therefore, activating FAO or inhibiting FA synthesis could be a therapeutic intervention for AI diseases. For example, ACC is the first enzyme in the *de novo* FA synthesis pathway [106]. *In vitro*, inhibiting ACC isoform 1 with the specific inhibitor Soraphen A (Table 1) induces Treg differentiation and impairs Th17 differentiation. In line with this result, Soraphen A administration *in vivo* attenuates EAE development in mice [70].

Modulation of ROS

ROS is an important regulator of Treg function [61]. Our group has shown that disturbed redox signaling due to the genetic ablation of antioxidative GSH synthesis in murine Tregs leads to ROS accumulation. Increased ROS in Tregs skew the metabolic programs and lead to increased glycolysis, OXPHOS, and serine metabolism, which impaired Treg function and induce spontaneous autoimmunity [61]. In line with that, Alissafi et al. have recently shown that human and murine Tregs experience a specific metabolic reprogramming during autoimmunity [107]. Tregs from MS and SLE patients show elevated mitochondrial oxidative stress and a DNA damage response. Murine Tregs during EAE exhibited a similarly prominent mitochondrial ROS (mtROS) signature and ROS scavenging with mitoTEMPO reduced the disease burden (Table 1) [107].

Taken together, these data support the concept that fostering a metabolic state favorable to Treg function may be a promising strategy for the treatment of various AI diseases.

Targeting Treg metabolism for cancer therapy

Incipient cancer cells evade immune recognition in a dynamic process of competition between immunosurveillance and tumor cell growth. Escaped tumor cells survive and are able to grow unchallenged, leading to cancer pathogenesis. Studies to delineate the mechanisms that promote adaptive anti-tumor responses and exploit cancer cell vulnerabilities to restrain tumor growth are at the forefront of today's anticancer research [108]. The tumor microenvironment (TME) surrounding a growing malignancy is a complex and heterogeneous milieu that undergoes fluctuating changes in its physical and chemical properties [109]. For example, cellular signaling via HIF1α, extracellular acidity generated by the lactate released by both tumor and stromal cells, and

metabolic competition for nutrients within the TME can all significantly alter the progress of tumorigenesis [48, 110, 111].

The contribution of Tregs to preventing/promoting tumor progression remains controversial. Tregs expressing unusually high levels of FoxP3 have been associated with improved patient survival in several cancer settings, including colorectal and esophageal malignancies [112]. However, it has become evident that, in most solid tumors, Tregs are a negative player and detrimental to robust antitumor immunity [111,113,114]. Most Tregs within the TME exhibit an increase in suppressive capacity and produce signaling molecules that disable antitumor immunity [48]. There are several clinical trials that aim to deplete Tregs by targeting surface markers such as CD25, GITR, OX40, and CCR4 [115]. However, many do not show effective anti-tumor responses. A possible explanation might be that some of these targeted surface markers are also important for immune effector functions. Thus, a better understanding of Treg biology and how to manipulate Treg metabolism and function with minimal effect on effector function within the TME has become a major focus of researchers' intent on devising novel anticancer therapies.

Treg metabolism in the TME

As described above, even in normal tissues Tregs and Teffs display metabolic differences that determine their fates. Inevitably, all types of T cells entering the TME have to undergo metabolic reprogramming to adapt to this harsh environment such as imbalanced metabolic nutrients, increased ROS and low oxygen level (hypoxia) [111,116]. For example, in murine MC38 colorectal carcinomas model, intra-tumoral Tregs invoke supplemental energy production routes involving increases in glycolysis and lipid metabolism [117]. This enhanced glucose and lipid uptake may fuel oxidative metabolism in a manner that confers a metabolic benefit and relative advantage on Tregs in the TME. This situation stands in stark contrast to the case in non-cancerous tissues, where an intrinsic increase in glycolysis is linked to a reduction in FoxP3 and decreased Treg suppressive capacity [22,61]. Once in the TME, Tregs are able to oxidize lactate into pyruvate when metabolic conditions are normal, or if a low glucose/high lactate environment prevails. In contrast, high lactate environment profoundly suppress effector T cell functions [48]. This adaptability of Tregs is due to FoxP3, which suppresses Myc and glycolysis and reprograms the metabolism of Tregs such that they can thrive in a low glucose/high lactate environment [57]. Moreover, Tregs are less susceptible to lactate overload than Teffs due to their decreased dependence on glycolysis and their generation of high levels of NAD during OXPHOS. These metabolic adaptations allow Tregs to carry out their task of promoting peripheral tolerance in the TME, disabling antitumor Teffs and thus perhaps partially explaining how cancer cells evade immune responses [57,118].

Increased ROS level in the TME present an additional challenge for effective antitumor immunity. Several studies have shown the antagonistic effect of ROS on dampening Teff activity that results in deleterious effect on antitumor immunity [93, 111, 119]. Nevertheless, the effect of ROS on Treg biology within the TME is less clear. It has been shown that Treg contain higher thiol as well as antioxidant glutathione, which may provide Tregs the advantage against the oxidative microenvironment due to the accumulation ROS in the TME [61,120]. Indeed, our group has recently shown that modulating ROS level in murine Treg result in an improved antitumor immunity [61]. Upon the ablation of glutathione in Tregs, these mice exhibited impaired Treg function and stronger anti-tumor response upon the inoculation with B16F10 melanoma [61].

Inhibition of Treg glycolysis or migration

Pretreatment of human Tregs *in vitro* with TLR8 agonist or 2-DG to inhibit glycolysis impairs the Tregs' ability to induce the senescence of $CD8^+$ Teffs [121]. Interestingly, Kishore et al. showed that deletion of the glycolytic enzyme glucokinase in murine Tregs does not affect their suppressive function *in vitro*. However, glucokinase is critical for Treg trafficking and that glucokinase-deficient Tregs do suffer from impairments to cytoskeletal rearrangement and actin remodeling that render them unable to migrate to the periphery [47]. Such a treatment in the cancer setting might provide the benefit of sustaining systemic immune tolerance, while at the same time blocking Treg migration to a tumor site and thereby preventing Tregs from dampening antitumor Teff responses. Evidence supporting this notion comes from a study of ovarian cancer patients in which both tumor cells and tumor-associated macrophages were found to secrete the chemokine CCL2. CCL2 induces Tregs to preferentially migrate into the TME where they promote immune tolerance [122]. Thus, blocking metabolites that support Treg trafficking may help to preserve the functionality of anti-tumor Teffs, determining the outcome of tumor growth in various cancer settings.

Blocking HIF1α

Under hypoxic conditions (which are common in solid tumors), HIF1α is activated and orchestrates signaling cascades promoting cellular metabolism and survival. HIF1α is associated with control of the Th17/Treg balance, although its effect on Treg function is controversial [56,123]. Several studies have reported that HIF1α activation positively drives the differentiation of $FoxP3^+$ T cells both *in vitro* and *in vivo* [123, 124]. On the other hand, Dang et al. showed that HIF1α had an inhibitory effect that attenuated Treg differentiation while promoting Th17 induction *in vivo* [56]. Hsiao et al. have further shown that inhibition of HIF1α preserves Treg stability *in vitro*, although the suppressive ability is greatly impaired *in vivo* [125]. To clarify these discrepancies, Miska et al. deleted HIF1α specifically in murine Tregs and found that their suppressive capacity was enhanced *in vitro* [126].

They further showed that conditional deletion of HIF1α in Tregs restricts their glucose uptake, leaving them to use FA for the mitochondrial metabolism needed to support Treg function. On the other hand, in a mouse model of glioblastoma, mutant mice bearing HIF1α-deficient Tregs showed better survival than controls due to impaired Treg migration to tumor sites [126]. Thus, HIF1α seems to play an important role in Tregs as a metabolic switch between glycolysis-driven migration and FA-dependent OXPHOS supporting Treg suppressive function.

Manipulating FA

During tumorigenesis, free FA are released from more complex lipids, altering the FA composition of the TME [127]. Tregs in this setting express high levels of the FA transporters CD36 and SLC27A1, which allow these cells access to additional energetic sources to fuel FA metabolism [10,128]. This exploitation of FA by Tregs in the TME provides the Tregs with the nutrients they need to survive and be fully functional, resulting in the barring of Teffs from attacking cancer cells. In addition, FA synthesis is enhanced in Tregs located in the TME, but not in those resident in the secondary lymphoid organs [117].

A recent study has shown that tumor-infiltrating Tregs in mice exhibit higher glucose uptake. Higher glucose uptake has been shown to increase FA synthesis [117]. The increase in glycolysis and glycolytic-derived FA pool lead to increased oxidative metabolism and support Treg expansion and proliferation without compromising Treg function, which dampen anti-tumor immunity. *De novo* synthesized FA may be utilized not only to support cellular metabolism, but also to support histone acetylation and epigenetic reprogramming, an important factor for FoxP3 stability [129]. Likewise, Wang et al. showed that dampening FA metabolism via genetic deletion of CD36 in murine Tregs results specifically in lower numbers of tumor-infiltrating Treg and decelerated tumor growth. Interestingly, the ablation of CD36 did not alter the homeostasis and functionality of splenic Treg cells [128]. This shows that FA metabolism via CD36 uniquely shape metabolic adaptation which supports the functionality of tumor-infiltrating Treg cells.

In another study, inhibition of lipid uptake with sulfo-*N*-succinimidyl oleate (SSO) (Table 1) has been shown to significantly reduce the immunosuppressive capacity of Tregs *in vitro* [126]. Similarly, 5-(tetradexyloxy)-2-furoic acid (TOFA), an inhibitor of ACC and thus FA synthesis (Table 1), significantly suppressed tumor development in mice [117]. TOFA's antitumor activity may be accounted for by its direct toxic effects on tumor cells (as evidenced by their reduced viability). However, *in vitro*, TOFA-treated Tregs show a significantly decreased lipid pool and impaired proliferation, indicating that FA synthesis may play a vital role in Treg biology in this context [117]. Further studies are needed to elaborate whether the connections between FA metabolism in the TME and Tregs are in fact promoting tumor cell development, and whether this scenario could point to new strategies for cancer therapy.

AA modulation

Manipulation of AA metabolism may serve as another mode of cancer immunotherapy, although most AAs are important for both tumor cells and adaptive immune cells [118]. As noted above, IDO metabolizes tryptophan to kynurenine, a metabolite important for Treg induction [88,130]. Many types of cancer cells overexpress IDO, which might then drive Treg activity and so dampen anti-tumor Teffs [18]. Cyclooxygenase2 (COX2) is involved in the upregulation of IDO expression in myeloid cells [131]. Accordingly, pharmacological inhibition of COX2 is under testing in various cancer models. For example, in a murine bladder tumor model, IDO inhibition reduced numbers of circulating Tregs and enhanced antitumor responses [132]. IDO is also implicated in Treg regulation because it stabilizes PTEN, which Tregs require to retain their functionality. PTEN dysregulation leads to aberrant mTOR activity, loss of Treg function, and spontaneous development of autoimmunity in mice [54]. In a mouse model of Lewis lung carcinoma, PTEN inhibition in Tregs plus IDO neutralization produced synergistic effects that greatly delayed disease relapse [133].

Lastly, we have linked the serine metabolism in Tregs to antitumor immunity. The absence of GSH in Tregs and increased ROS levels, leads to enhanced serine metabolism and higher mTOR signaling, which in turn impairs tTreg and pTreg suppressive activity [61]. This defect in Tregs consequently increases anti-tumor immunity and significantly reduces cancer cell growth *in vivo*.

Taken together, the various studies described above point to the possibility of altering key aspects of AA metabolism in Tregs to improve cancer immunotherapy.

Concluding remarks

Our current understanding of the role of metabolism in immune regulation in general and in Tregs in particular is rapidly expanding, but many aspects remain to be addressed. We do know that Tregs are indispensable regulators of immune homeostasis. Accordingly, their dysregulation is implicated in numerous pathologies. The studies we have reviewed highlight the multifaceted relationships between the intrinsic and extrinsic metabolic pathways modulating Treg function, and their significant implications for the treatment of immune-related diseases.

Tregs have a metabolic profile that is distinct from that of Teffs. Specific nutrients and metabolites obtained from the diet and/or extracellular milieu can influence Treg metabolism and affect their function. These factors also play important roles in Treg-intrinsic metabolic regulation. Treg metabolism is highly plastic and adapts to the environmental context. Although their chief preference is FA utilization, Tregs are able to use various substrates to support their metabolism. Metabolic regulators such as mTOR and AMPK are indispensable for orchestrating Treg metabolism in several different ways, such that their dysregulation has differential effects on Treg functionality. For example,

increased glycolysis leads to upregulation of mTOR and impaired Treg suppressive capacity, but also supports Treg migration.

Furthermore, it is also worth noting that the effects of pharmacological treatment *in vivo* may have dual action on both Teff and Treg simultaneously, in which the significance on one or the other cells still needs to be further evaluated.

Overall, although extensive studies on murine Treg have been conducted, significant challenges are still unsolved. There is Treg heterogeneity between subpopulations and their specific metabolic regulations remain to be explored. It is also important to acknowledge that that human and murine Tregs have different Treg subtypes such as the human type 1 regulatory T cells (Tr1), which only rely on glycolysis instead of fatty acid oxidation. Tr1 cells are also an important source of IL-10 and TGF-β [134]. Additionally, more work remains to be invested to evaluate the differences in metabolic requirement between similar subtypes of human and murine Treg; *in vitro* murine tTreg cells display low glycolysis and high FAO whereas human tTreg cells rely on high glycolysis and FAO [95].

In conclusion, modulating Treg metabolism may provide new tools that can be exploited in diverse disease settings. Inhibition of various metabolic enzymes has been suggested or is currently being studied in order to influence Treg function in AI diseases and cancer. Thus, novel Treg cell-based immune metabolic interventions for the treatment of these disorders may prove to be beneficial in the near future.

Acknowledgements: We acknowledge the valuable work of all investigators that we were unable to cite due to space limitations. The figures were created using Biorender.com. D.B. and H.K. are supported by the FNR-ATTRACT program (A14/BM/7632103) and D.B. by FNR-CORE (C18/BM/12691266). D.B. and L.S.B. are funded by the FNR-PRIDE (PRIDE/11012546/NEXTIMMUNE) scheme.

Conflict of interest: The authors declare no commercial or financial conflict of interest

References

1 **Wing, K.** and **Sakaguchi, S.**, Regulatory T cells exert checks and balances on self tolerance and autoimmunity. *Nat. Immunol.* 2010. **11**: 7–13.

2 **Lahl, K.**, **Loddenkemper, C.**, **Drouin, C.**, **Freyer, J.**, **Arnason, J.**, **Eberl, G.**, **Hamann, A.** et al., Selective depletion of Foxp3+ regulatory T cells induces a scurfy-like disease. *J. Exp. Med.* 2007. **204**: 57–63.

3 **Shevach, E. M.** and **Thornton, A. M.**, tTregs, pTregs, and iTregs: similarities and differences. *Immunol. Rev.* 2014. **259**: 88–102.

4 **Hori, S.**, **Nomura, T.** and **Sakaguchi, S.**, Control of regulatory T cell development by the transcription factor Foxp3. *Science* 2003. **299**: 1057–1061.

5 **Deng, G.**, **Song, X.**, **Fujimoto, S.**, **Piccirillo, C. A.**, **Nagai, Y.** and **Greene, M. I.**, Foxp3 Post-translational Modifications and Treg Suppressive Activity. *Front. Immunol.* 2019. **10**: 2486.

6 **Dhamne, C.**, **Chung, Y.**, **Alousi, A. M.**, **Cooper, L. J.** and **Tran, D. Q.**, Peripheral and thymic foxp3(+) regulatory T cells in search of origin, distinction, and function. *Front. Immunol.* 2013. **4**: 253.

7 **Fontenot, J. D.**, **Gavin, M. A.** and **Rudensky, A. Y.**, Foxp3 programs the development and function of CD4+CD25+ regulatory T cells. *Nat. Immunol.* 2003. **4**: 330–336.

8 **Van Gool, F.**, **Nguyen, M. L. T.**, **Mumbach, M. R.**, **Satpathy, A. T.**, **Rosenthal, W. L.**, **Giacometti, S.**, **Le, D. T.** et al., A Mutation in the Transcription Factor Foxp3 Drives T Helper 2 Effector Function in Regulatory T Cells. *Immunity* 2019. **50**: 362–377 e366.

9 **Josefowicz, S. Z.**, **Lu, L.-F.** and **Rudensky, A. Y.**, Regulatory T Cells: Mechanisms of Differentiation and Function. *Ann Rev Immunol* 2012. **30**: 531–564.

10 **Shi, H.** and **Chi, H.**, Metabolic Control of Treg Cell Stability, Plasticity, and Tissue-Specific Heterogeneity. *Front. Immunol.* 2019. **10**: 2716.

11 **Fan, M. Y.**, **Low, J. S.**, **Tanimine, N.**, **Finn, K. K.**, **Priyadharshini, B.**, **Germana, S. K.**, **Kaech, S. M.** and **Turka, L. A.**, Differential Roles of IL-2 Signaling in Developing versus Mature Tregs. *Cell Rep.* 2018. **25**: 1204–1213 e1204.

12 **Setiady, Y. Y.**, **Coccia, J. A.** and **Park, P. U.**, In vivo depletion of CD4+FOXP3+ Treg cells by the PC61 anti-CD25 monoclonal antibody is mediated by FcgammaRIII+ phagocytes. *Eur. J. Immunol.* 2010. **40**: 780–786.

13 **Zeng, H.** and **Chi, H.**, Metabolic control of regulatory T cell development and function. *Trends Immunol.* 2015. **36**: 3–12.

14 **O'Neill, L. A.**, **Kishton, R. J.** and **Rathmell, J.**, A guide to immunometabolism for immunologists. *Nat. Rev. Immunol.* 2016. **16**: 553–565.

15 **Michalek, R. D.**, **Gerriets, V. A.**, **Jacobs, S. R.**, **Macintyre, A. N.**, **MacIver, N. J.**, **Mason, E. F.**, **Sullivan, S. A.** et al., Cutting edge: distinct glycolytic and lipid oxidative metabolic programs are essential for effector and regulatory CD4+ T cell subsets. *J. Immunol.* 2011. **186**: 3299–3303.

16 **Wang, R.**, **Dillon, C. P.**, **Shi, L. Z.**, **Milasta, S.**, **Carter, R.**, **Finkelstein, D.**, **McCormick, L. L.** et al., The transcription factor Myc controls metabolic reprogramming upon T lymphocyte activation. *Immunity* 2011. **35**: 871–882.

17 **Sharabi, A.** and **Tsokos, G. C.**, T cell metabolism: new insights in systemic lupus erythematosus pathogenesis and therapy. *Nat Rev Rheumatol* 2020. **16**: 100–112.

18 **Galgani, M.**, **De Rosa, V.**, **La Cava, A.** and **Matarese, G.**, Role of Metabolism in the Immunobiology of Regulatory T Cells. *J. Immunol.* 2016. **197**: 2567–2575.

19 **Rubtsov, Y. P.**, **Niec, R. E.**, **Josefowicz, S.**, **Li, L.**, **Darce, J.**, **Mathis, D.**, **Benoist, C.** et al., Stability of the regulatory T cell lineage in vivo. *Science* 2010. **329**: 1667–1671.

20 **Kastner, L.**, **Dwyer, D.** and **Qin, F. X.**, Synergistic effect of IL-6 and IL-4 in driving fate revision of natural Foxp3+ regulatory T cells. *J. Immunol.* 2010. **185**: 5778–5786.

21 **Mucida, D.**, **Park, Y.**, **Kim, G.**, **Turovskaya, O.**, **Scott, I.**, **Kronenberg, M.** and **Cheroutre, H.**, Reciprocal TH17 and regulatory T cell differentiation mediated by retinoic acid. *Science* 2007. **317**: 256–260.

22 **Gerriets, V. A.**, **Kishton, R. J.**, **Johnson, M. O.**, **Cohen, S.**, **Siska, P. J.**, **Nichols, A. G.**, **Warmoes, M. O.** et al., Foxp3 and Toll-like receptor signaling balance Treg cell anabolic metabolism for suppression. *Nat. Immunol.* 2016. **17**: 1459–1466.

23 **Lu, L.**, **Ma, J.**, **Li, Z.**, **Lan, Q.**, **Chen, M.**, **Liu, Y.**, **Xia, Z.** et al., All-trans retinoic acid promotes TGF-beta-induced Tregs via histone modification but not DNA demethylation on Foxp3 gene locus. *PLoS One* 2011. **6**: e24590.

24 **Liu, H.**, **Yao, S.**, **Dann, S. M.**, **Qin, H.**, **Elson, C. O.** and **Cong, Y.**, ERK differentially regulates Th17- and Treg-cell development and contributes to the pathogenesis of colitis. *Eur. J. Immunol.* 2013. **43**: 1716–1726.

25 **Hill, J. A.**, **Hall, J. A.**, **Sun, C.-M.**, **Cai, Q.**, **Ghyselinck, N.**, **Chambon, P.**, **Belkaid, Y.** et al., Retinoic Acid Enhances Foxp3 Induction Indirectly by Relieving Inhibition from CD4+CD44hi Cells. *Immunity* 2008. **29**: 758–770.

26 **Passerini, L.**, **Barzaghi, F.**, **Curto, R.**, **Sartirana, C.**, **Barera, G.**, **Tucci, F.**, **Albarello, L.** et al., Treatment with rapamycin can restore regulatory T-cell function in IPEX patients. *J. Allergy Clin. Immunol.* 2020. **145**: 1262–1271 e1213.

27 **Monti, P.**, **Scirpoli, M.**, **Maffi, P.**, **Piemonti, L.**, **Secchi, A.**, **Bonifacio, E.**, **Roncarolo, M. G.** et al., Rapamycin monotherapy in patients with type 1 diabetes modifies CD4+CD25+FOXP3+ regulatory T-cells. *Diabetes* 2008. **57**: 2341–2347.

28 **Lu, L.**, **Lan, Q.**, **Li, Z.**, **Zhou, X.**, **Gu, J.**, **Li, Q.**, **Wang, J.** et al., Critical role of all-trans retinoic acid in stabilizing human natural regulatory T cells under inflammatory conditions. *Proc. Natl. Acad. Sci. U. S. A.* 2014. **111**: E3432-3440.

29 **Shen, F.**, **Ross, J. F.**, **Wang, X.** and **Ratnam, M.**, Identification of a novel folate receptor, a truncated receptor, and receptor type beta in hematopoietic cells: cDNA cloning, expression, immunoreactivity, and tissue specificity. *Biochemistry* 1994. **33**: 1209–1215.

30 **Kinoshita, M.**, **Kayama, H.**, **Kusu, T.**, **Yamaguchi, T.**, **Kunisawa, J.**, **Kiyono, H.**, **Sakaguchi, S.** et al., Dietary folic acid promotes survival of Foxp3+ regulatory T cells in the colon. *J. Immunol.* 2012. **189**: 2869–2878.

31 **Nikolouli, E.**, **Hardtke-Wolenski, M.**, **Hapke, M.**, **Beckstette, M.**, **Geffers, R.**, **Floess, S.**, **Jaeckel, E.** et al., Alloantigen-Induced Regulatory T Cells Generated in Presence of Vitamin C Display Enhanced Stability of Foxp3 Expression and Promote Skin Allograft Acceptance. *Front. Immunol.* 2017. **8**: 748.

32 **Oyarce, K.**, **Campos-Mora, M.**, **Gajardo-Carrasco, T.** and **Pino-Lagos, K.**, Vitamin C Fosters the In Vivo Differentiation of Peripheral CD4(+) Foxp3(-) T Cells into CD4(+) Foxp3(+) Regulatory T Cells but Impairs Their Ability to Prolong Skin Allograft Survival. *Front. Immunol.* 2018. **9**: 112.

33 **Kasahara, H.**, **Kondo, T.**, **Nakatsukasa, H.**, **Chikuma, S.**, **Ito, M.**, **Ando, M.**, **Kurebayashi, Y.** et al., Generation of allo-antigen-specific induced Treg stabilized by vitamin C treatment and its application for prevention of acute graft versus host disease model. *International Immunology* 2017. **29**: 457–469.

34 **Jeffery, L. E.**, **Burke, F.**, **Mura, M.**, **Zheng, Y.**, **Qureshi, O. S.**, **Hewison, M.**, **Walker, L. S.** et al., 1,25-Dihydroxyvitamin D3 and IL-2 combine to inhibit T cell production of inflammatory cytokines and promote development of regulatory T cells expressing CTLA-4 and FoxP3. *J. Immunol.* 2009. **183**: 5458–5467.

35 **Gorman, S.**, **Geldenhuys, S.**, **Judge, M.**, **Weeden, C. E.**, **Waithman, J.** and **Hart, P. H.**, Dietary Vitamin D Increases Percentages and Function of Regulatory T Cells in the Skin-Draining Lymph Nodes and Suppresses Dermal Inflammation. *Journal of Immunology Research* 2016. **2016**: 1–13.

36 **Terrier, B.**, **Derian, N.**, **Schoindre, Y.**, **Chaara, W.**, **Geri, G.**, **Zahr, N.**, **Mariampillai, K.** et al., Restoration of regulatory and effector T cell balance and B cell homeostasis in systemic lupus erythematosus patients through vitamin D supplementation. *Arthritis Res. Ther.* 2012. **14**: R221.

37 **Daniel, C.**, **Sartory, N. A.**, **Zahn, N.**, **Radeke, H. H.** and **Stein, J. M.**, Immune modulatory treatment of trinitrobenzene sulfonic acid colitis with calcitriol is associated with a change of a T helper (Th) 1/Th17 to a Th2 and regulatory T cell profile. *J. Pharmacol. Exp. Ther.* 2008. **324**: 23–33.

38 **Chapman, N. M.**, **Boothby, M. R.** and **Chi, H.**, Metabolic coordination of T cell quiescence and activation. *Nat. Rev. Immunol.* 2020. **20**: 55–70.

39 **Andrejeva, G.** and **Rathmell, J. C.**, Similarities and Distinctions of Cancer and Immune Metabolism in Inflammation and Tumors. *Cell Metab.* 2017. **26**: 49–70.

40 **Warburg, O.**, On the origin of cancer cells. *Science* 1956. **123**: 309–314.

41 **Warburg, O.**, **Wind, F.** and **Negelein, E.**, The Metabolism of Tumors in the Body. *J. Gen. Physiol.* 1927. **8**: 519–530.

42 **Chen, Y.**, **Colello, J.**, **Jarjour, W.** and **Zheng, S. G.**, Cellular Metabolic Regulation in the Differentiation and Function of Regulatory T Cells. *Cells* 2019. **8**.

43 **Powell, J. D.**, **Pollizzi, K. N.**, **Heikamp, E. B.** and **Horton, M. R.**, Regulation of immune responses by mTOR. *Annu. Rev. Immunol.* 2012. **30**: 39–68.

44 **Delgoffe, G. M.**, **Kole, T. P.**, **Zheng, Y.**, **Zarek, P. E.**, **Matthews, K. L.**, **Xiao, B.**, **Worley, P. F.** et al., The mTOR kinase differentially regulates effector and regulatory T cell lineage commitment. *Immunity* 2009. **30**: 832–844.

45 **Zeng, H.**, **Yang, K.**, **Cloer, C.**, **Neale, G.**, **Vogel, P.** and **Chi, H.**, mTORC1 couples immune signals and metabolic programming to establish T(reg)-cell function. *Nature* 2013. **499**: 485–490.

46 **Chapman, N. M.**, **Zeng, H.**, **Nguyen, T. M.**, **Wang, Y.**, **Vogel, P.**, **Dhungana, Y.**, **Liu, X.** et al., mTOR coordinates transcriptional programs and mitochondrial metabolism of activated Treg subsets to protect tissue homeostasis. *Nat. Commun.* 2018. **9**: 2095.

47 **Kishore, M.**, **Cheung, K. C. P.**, **Fu, H.**, **Bonacina, F.**, **Wang, G.**, **Coe, D.**, **Ward, E. J.** et al., Regulatory T Cell Migration Is Dependent on Glucokinase-Mediated Glycolysis. *Immunity* 2017. **47**: 875–889 e810.

48 **Pacella, I.** and **Piconese, S.**, Immunometabolic Checkpoints of Treg Dynamics: Adaptation to Microenvironmental Opportunities and Challenges. *Front. Immunol.* 2019. **10**: 1889.

49 **Delgoffe, G. M.**, **Pollizzi, K. N.**, **Waickman, A. T.**, **Heikamp, E.**, **Meyers, D. J.**, **Horton, M. R.**, **Xiao, B.** et al., The kinase mTOR regulates the differentiation of helper T cells through the selective activation of signaling by mTORC1 and mTORC2. *Nat. Immunol.* 2011. **12**: 295–303.

50 **Procaccini, C.**, **De Rosa, V.**, **Galgani, M.**, **Abanni, L.**, **Cali, G.**, **Porcellini, A.**, **Carbone, F.** et al., An oscillatory switch in mTOR kinase activity sets regulatory T cell responsiveness. *Immunity* 2010. **33**: 929–941.

51 **Park, Y.**, **Jin, H. S.**, **Lopez, J.**, **Elly, C.**, **Kim, G.**, **Murai, M.**, **Kronenberg, M.** et al., TSC1 regulates the balance between effector and regulatory T cells. *J. Clin. Invest.* 2013. **123**: 5165–5178.

52 **Apostolidis, S. A.**, **Rodriguez-Rodriguez, N.**, **Suarez-Fueyo, A.**, **Dioufa, N.**, **Ozcan, E.**, **Crispin, J. C.**, **Tsokos, M. G.** et al., Phosphatase PP2A is requisite for the function of regulatory T cells. *Nat. Immunol.* 2016. **17**: 556–564.

53 **Huynh, A.**, **DuPage, M.**, **Priyadharshini, B.**, **Sage, P. T.**, **Quiros, J.**, **Borges, C. M.**, **Townamchai, N.** et al., Control of PI(3) kinase in Treg cells maintains homeostasis and lineage stability. *Nat. Immunol.* 2015. **16**: 188–196.

54 **Shrestha, S.**, **Yang, K.**, **Guy, C.**, **Vogel, P.**, **Neale, G.** and **Chi, H.**, Treg cells require the phosphatase PTEN to restrain TH1 and TFH cell responses. *Nat. Immunol.* 2015. **16**: 178–187.

55 **Gerriets, V. A.**, **Kishton, R. J.**, **Nichols, A. G.**, **Macintyre, A. N.**, **Inoue, M.**, **Ilkayeva, O.**, **Winter, P. S.** et al., Metabolic programming and PDHK1 control CD4+ T cell subsets and inflammation. *J. Clin. Invest.* 2015. **125**: 194–207.

56 **Dang, E. V.**, **Barbi, J.**, **Yang, H. Y.**, **Jinasena, D.**, **Yu, H.**, **Zheng, Y.**, **Bordman, Z.** et al., Control of T(H)17/T(reg) balance by hypoxia-inducible factor 1. *Cell* 2011. **146**: 772–784.

57 **Angelin, A.**, **Gil-de-Gomez, L.**, **Dahiya, S.**, **Jiao, J.**, **Guo, L.**, **Levine, M. H.**, **Wang, Z.** et al., Foxp3 Reprograms T Cell Metabolism to Function in

Low-Glucose, High-Lactate Environments. *Cell Metab.* 2017. **25**: 1282–1293 e1287.

58 **Howie, D.**, **Cobbold, S. P.**, **Adams, E.**, **Ten Bokum, A.**, **Necula, A. S.**, **Zhang, W.**, **Huang, H.** et al., Foxp3 drives oxidative phosphorylation and protection from lipotoxicity. *JCI Insight* 2017. **2**: e89160.

59 **Csibi, A.**, **Lee, G.**, **Yoon, S. O.**, **Tong, H.**, **Ilter, D.**, **Elia, I.**, **Fendt, S. M.** et al., The mTORC1/S6K1 pathway regulates glutamine metabolism through the eIF4B-dependent control of c-Myc translation. *Curr. Biol.* 2014. **24**: 2274–2280.

60 **Weinberg, S. E.**, **Singer, B. D.**, **Steinert, E. M.**, **Martinez, C. A.**, **Mehta, M. M.**, **Martinez-Reyes, I.**, **Gao, P.** et al., Mitochondrial complex III is essential for suppressive function of regulatory T cells. *Nature* 2019. **565**: 495–499.

61 **Kurniawan, H.**, **Franchina, D. G.**, **Guerra, L.**, **Bonetti, L.**, **Baguet, L. S.**, **Grusdat, M.**, **Schlicker, L.** et al., Glutathione Restricts Serine Metabolism to Preserve Regulatory T Cell Function. *Cell Metab.* 2020. **31**: 920–936 e927.

62 **Ko, C. W.**, **Qu, J.**, **Black, D. D.** and **Tso, P.**, Regulation of intestinal lipid metabolism: current concepts and relevance to disease. *Nat. Rev. Gastroenterol. Hepatol.* 2020. **17**: 169–183.

63 **Howie, D.**, **Ten Bokum, A.**, **Necula, A. S.**, **Cobbold, S. P.** and **Waldmann, H.**, The Role of Lipid Metabolism in T Lymphocyte Differentiation and Survival. *Front. Immunol.* 2017. **8**: 1949.

64 **Theofilopoulos, A. N.**, **Kono, D. H.** and **Baccala, R.**, The multiple pathways to autoimmunity. *Nat. Immunol.* 2017. **18**: 716–724.

65 **Cluxton, D.**, **Petrasca, A.**, **Moran, B.** and **Fletcher, J. M.**, Differential Regulation of Human Treg and Th17 Cells by Fatty Acid Synthesis and Glycolysis. *Front. Immunol.* 2019. **10**: 115.

66 **Field, C. S.**, **Baixauli, F.**, **Kyle, R. L.**, **Puleston, D. J.**, **Cameron, A. M.**, **Sanin, D. E.**, **Hippen, K. L.** et al., Mitochondrial Integrity Regulated by Lipid Metabolism Is a Cell-Intrinsic Checkpoint for Treg Suppressive Function. *Cell Metab.* 2020. **31**: 422–437 e425.

67 **Raud, B.**, **Roy, D. G.**, **Divakaruni, A. S.**, **Tarasenko, T. N.**, **Franke, R.**, **Ma, E. H.**, **Samborska, B.** et al., Etomoxir Actions on Regulatory and Memory T Cells Are Independent of Cpt1a-Mediated Fatty Acid Oxidation. *Cell Metab.* 2018. **28**: 504–515 e507.

68 **Divakaruni, A. S.**, **Hsieh, W. Y.**, **Minarrieta, L.**, **Duong, T. N.**, **Kim, K. K. O.**, **Desousa, B. R.**, **Andreyev, A. Y.** et al., Etomoxir Inhibits Macrophage Polarization by Disrupting CoA Homeostasis. *Cell Metab.* 2018. **28**: 490–503 e497.

69 **O'Sullivan, D.** and **Pearce, E. L.**, Fatty acid synthesis tips the TH17-Treg cell balance. *Nat. Med.* 2014. **20**: 1235–1236.

70 **Berod, L.**, **Friedrich, C.**, **Nandan, A.**, **Freitag, J.**, **Hagemann, S.**, **Harmrolfs, K.**, **Sandouk, A.** et al., De novo fatty acid synthesis controls the fate between regulatory T and T helper 17 cells. *Nat. Med.* 2014. **20**: 1327–1333.

71 **Howie, D.**, **Ten Bokum, A.**, **Cobbold, S. P.**, **Yu, Z.**, **Kessler, B. M.** and **Waldmann, H.**, A Novel Role for Triglyceride Metabolism in Foxp3 Expression. *Front. Immunol.* 2019. **10**: 1860.

72 **He, N.**, **Fan, W.**, **Henriquez, B.**, **Yu, R. T.**, **Atkins, A. R.**, **Liddle, C.**, **Zheng, Y.** et al., Metabolic control of regulatory T cell (Treg) survival and function by Lkb1. *Proc. Natl. Acad. Sci. U. S. A.* 2017. **114**: 12542–12547.

73 **Yang, K.**, **Blanco, D. B.**, **Neale, G.**, **Vogel, P.**, **Avila, J.**, **Clish, C. B.**, **Wu, C.** et al., Homeostatic control of metabolic and functional fitness of Treg cells by LKB1 signalling. *Nature* 2017. **548**: 602–606.

74 **Timilshina, M.**, **You, Z.**, **Lacher, S. M.**, **Acharya, S.**, **Jiang, L.**, **Kang, Y.**, **Kim, J. A.** et al., Activation of Mevalonate Pathway via LKB1 Is Essential for Stability of Treg Cells. *Cell Rep.* 2019. **27**: 2948–2961 e2947.

75 **Furusawa, Y.**, **Obata, Y.**, **Fukuda, S.**, **Endo, T. A.**, **Nakato, G.**, **Takahashi, D.**, **Nakanishi, Y.** et al., Commensal microbe-derived butyrate induces the differentiation of colonic regulatory T cells. *Nature* 2013. **504**: 446–450.

76 **Smith, P. M.**, **Howitt, M. R.**, **Panikov, N.**, **Michaud, M.**, **Gallini, C. A.**, **Bohlooly, Y. M.**, **Glickman, J. N.** et al., The microbial metabolites, short-chain fatty acids, regulate colonic Treg cell homeostasis. *Science* 2013. **341**: 569–573.

77 **Cipolletta, D.**, **Feuerer, M.**, **Li, A.**, **Kamei, N.**, **Lee, J.**, **Shoelson, S. E.**, **Benoist, C.** et al., PPAR-gamma is a major driver of the accumulation and phenotype of adipose tissue Treg cells. *Nature* 2012. **486**: 549–553.

78 **Bi, X.**, **Li, F.**, **Liu, S.**, **Jin, Y.**, **Zhang, X.**, **Yang, T.**, **Dai, Y.** et al., omega-3 polyunsaturated fatty acids ameliorate type 1 diabetes and autoimmunity. *J. Clin. Invest.* 2017. **127**: 1757–1771.

79 **Kim, J. Y.**, **Lim, K.**, **Kim, K. H.**, **Kim, J. H.**, **Choi, J. S.** and **Shim, S. C.**, N-3 polyunsaturated fatty acids restore Th17 and Treg balance in collagen antibody-induced arthritis. *PLoS One* 2018. **13**: e0194331.

80 **Hou, Y.**, **Yin, Y.** and **Wu, G.**, Dietary essentiality of "nutritionally non-essential amino acids" for animals and humans. *Exp. Biol. Med. (Maywood)* 2015. **240**: 997–1007.

81 **Ren, W.**, **Liu, G.**, **Yin, J.**, **Tan, B.**, **Wu, G.**, **Bazer, F. W.**, **Peng, Y.** et al., Amino-acid transporters in T-cell activation and differentiation. *Cell Death. Dis.* 2017. **8**: e2655.

82 **Kanai, Y.**, **Segawa, H.**, **Miyamoto, K.**, **Uchino, H.**, **Takeda, E.** and **Endou, H.**, Expression cloning and characterization of a transporter for large neutral amino acids activated by the heavy chain of 4F2 antigen (CD98). *J. Biol. Chem.* 1998. **273**: 23629–23632.

83 **Nicklin, P.**, **Bergman, P.**, **Zhang, B.**, **Triantafellow, E.**, **Wang, H.**, **Nyfeler, B.**, **Yang, H.** et al., Bidirectional transport of amino acids regulates mTOR and autophagy. *Cell* 2009. **136**: 521–534.

84 **Bond, P.**, Regulation of mTORC1 by growth factors, energy status, amino acids and mechanical stimuli at a glance. *J Int Soc Sports Nutr* 2016. **13**.

85 **Ikeda, K.**, **Kinoshita, M.**, **Kayama, H.**, **Nagamori, S.**, **Kongpracha, P.**, **Umemoto, E.**, **Okumura, R.** et al., Slc3a2 mediates branched-chain amino-acid-dependent maintenance of regulatory T cells. *Cell Rep.* 2017. **21**: 1824–1838.

86 **Shi, H.**, **Chapman, N. M.**, **Wen, J.**, **Guy, C.**, **Long, L.**, **Dhungana, Y.**, **Rankin, S.** et al., Amino acids license kinase mTORC1 activity and Treg cell function via small G proteins Rag and Rheb. *Immunity* 2019. **51**: 1012–1027 e1017.

87 **Yu, H. R.**, **Tsai, C. C.**, **Chang, L. S.**, **Huang, H. C.**, **Cheng, H. H.**, **Wang, J. Y.**, **Sheen, J. M.** et al., L-Arginine-dependent epigenetic regulation of interleukin-10, but not transforming growth factor-beta, production by neonatal regulatory T lymphocytes. *Front. Immunol.* 2017. **8**: 487.

88 **Curran, T. A.**, **Jalili, R. B.**, **Farrokhi, A.** and **Ghahary, A.**, IDO expressing fibroblasts promote the expansion of antigen specific regulatory T cells. *Immunobiology* 2014. **219**: 17–24.

89 **Carr, E. L.**, **Kelman, A.**, **Wu, G. S.**, **Gopaul, R.**, **Senkevitch, E.**, **Aghvanyan, A.**, **Turay, A. M.** and **Frauwirth, K. A.**, Glutamine uptake and metabolism are coordinately regulated by ERK/MAPK during T lymphocyte activation. *J. Immunol.* 2010. **185**: 1037–1044.

90 **Klysz, D.**, **Tai, X.**, **Robert, P. A.**, **Craveiro, M.**, **Cretenet, G.**, **Oburoglu, L.**, **Mongellaz, C.** et al., Glutamine-dependent alpha-ketoglutarate production regulates the balance between T helper 1 cell and regulatory T cell generation. *Sci. Signal* 2015. **8**: ra97.

91 **Song, E. K.**, **Yim, J. M.**, **Yim, J. Y.**, **Song, M. Y.**, **Rho, H. W.**, **Yim, S. K.**, **Han, Y. H.** et al., Glutamine protects mice from acute graft-versus-host disease (aGVHD). *Biochem. Biophys. Res. Commun.* 2013. **435**: 94–99.

92 **Ye, J.**, **Fan, J.**, **Venneti, S.**, **Wan, Y. W.**, **Pawel, B. R.**, **Zhang, J.**, **Finley, L. W.** et al., Serine catabolism regulates mitochondrial redox control during hypoxia. *Cancer Discov.* 2014. **4**: 1406–1417.

93 **Mak, T. W.**, **Grusdat, M.**, **Duncan, G. S.**, **Dostert, C.**, **Nonnenmacher, Y.**, **Cox, M.**, **Binsfeld, C.** et al., Glutathione primes T cell metabolism for inflammation. *Immunity* 2017. **46**: 675–689.

94 **Mason, G. M.**, **Lowe, K.**, **Melchiotti, R.**, **Ellis, R.**, **de Rinaldis, E.**, **Peakman, M.**, **Heck, S.** et al., Phenotypic complexity of the human regulatory T cell compartment revealed by mass cytometry. *J. Immunol.* 2015. **195**: 2030–2037.

95 **Procaccini, C.**, **Carbone, F.**, **Di Silvestre, D.**, **Brambilla, F.**, **De Rosa, V.**, **Galgani, M.**, **Faicchia, D.** et al., The proteomic landscape of human ex vivo regulatory and conventional T cells reveals specific metabolic requirements. *Immunity* 2016. **44**: 712.

96 **De Rosa, V.**, **Galgani, M.**, **Porcellini, A.**, **Colamatteo, A.**, **Santopaolo, M.**, **Zuchegna, C.**, **Romano, A.** et al., Glycolysis controls the induction of human regulatory T cells by modulating the expression of FOXP3 exon 2 splicing variants. *Nat. Immunol.* 2015. **16**: 1174–1184.

97 **Miyara, M.**, **Gorochov, G.**, **Ehrenstein, M.**, **Musset, L.**, **Sakaguchi, S.** and **Amoura, Z.**, Human FoxP3+ regulatory T cells in systemic autoimmune diseases. *Autoimmun. Rev.* 2011. **10**: 744–755.

98 **Dominguez-Villar, M.** and **Hafler, D. A.**, Regulatory T cells in autoimmune disease. *Nat. Immunol.* 2018. **19**: 665–673.

99 **Li, W.**, **Qu, G.**, **Choi, S. C.**, **Cornaby, C.**, **Titov, A.**, **Kanda, N.**, **Teng, X.** et al., Targeting T cell activation and lupus autoimmune phenotypes by inhibiting glucose transporters. *Front. Immunol.* 2019. **10**: 833.

100 **Shi, L. Z.**, **Wang, R.**, **Huang, G.**, **Vogel, P.**, **Neale, G.**, **Green, D. R.** and **Chi, H.**, HIF1alpha-dependent glycolytic pathway orchestrates a metabolic checkpoint for the differentiation of TH17 and Treg cells. *J. Exp. Med.* 2011. **208**: 1367–1376.

101 **Patel, C. H.** and **Powell, J. D.**, Targeting T cell metabolism to regulate T cell activation, differentiation and function in disease. *Curr. Opin. Immunol.* 2017. **46**: 82–88.

102 **Liu, R. T.**, **Zhang, M.**, **Yang, C. L.**, **Zhang, P.**, **Zhang, N.**, **Du, T.**, **Ge, M. R.** et al., Enhanced glycolysis contributes to the pathogenesis of experimental autoimmune neuritis. *J Neuroinflammation* 2018. **15**: 51.

103 **Lee, S. Y.**, **Lee, S. H.**, **Yang, E. J.**, **Kim, E. K.**, **Kim, J. K.**, **Shin, D. Y.** and **Cho, M. L.**, Metformin ameliorates inflammatory bowel disease by suppression of the STAT3 signaling pathway and regulation of the between Th17/Treg balance. *PLoS One* 2015. **10**: e0135858.

104 **Sun, Y.**, **Tian, T.**, **Gao, J.**, **Liu, X.**, **Hou, H.**, **Cao, R.**, **Li, B.** et al., Metformin ameliorates the development of experimental autoimmune encephalomyelitis by regulating T helper 17 and regulatory T cells in mice. *J. Neuroimmunol.* 2016. **292**: 58–67.

105 **Lee, C. F.**, **Lo, Y. C.**, **Cheng, C. H.**, **Furtmuller, G. J.**, **Oh, B.**, **Andrade-Oliveira, V.**, **Thomas, A. G.** et al., Preventing allograft rejection by targeting immune metabolism. *Cell Rep.* 2015. **13**: 760–770.

106 **Berg, J.**, **Tymoczko, J.** and **Stryer, L.**, Fatty acids are synthesized and degraded by different pathways. *Biochemistry*. 5th ed. W. H. Freeman, New York 2002.

107 **Alissafi, T.**, **Kalafati, L.**, **Lazari, M.**, **Filia, A.**, **Kloukina, I.**, **Manifava, M.**, **Lim, J. H.** et al., Mitochondrial oxidative damage underlies regulatory T cell defects in autoimmunity. *Cell Metab.* 2020. **32**: P591-604.

108 **Vinay, D. S.**, **Ryan, E. P.**, **Pawelec, G.**, **Talib, W. H.**, **Stagg, J.**, **Elkord, E.**, **Lichtor, T.** et al., Immune evasion in cancer: Mechanistic basis and therapeutic strategies. *Semin. Cancer Biol.* 2015. **35**: S185-S198.

109 **Wang, Y. A.**, **Li, X. L.**, **Mo, Y. Z.**, **Fan, C. M.**, **Tang, L.**, **Xiong, F.**, **Guo, C.** et al., Effects of tumor metabolic microenvironment on regulatory T cells. *Mol. Cancer* 2018. **17**: 168.

110 **Franchina, D. G.**, **He, F.** and **Brenner, D.**, Survival of the fittest: cancer challenges T cell metabolism. *Cancer Lett.* 2018. **412**: 216–223.

111 **Guerra, L.**, **Bonetti, L.** and **Brenner, D.**, Metabolic modulation of immunity: a new concept in cancer immunotherapy. *Cell Rep.* 2020. **32**: 107848.

112 **Shang, B.**, **Liu, Y.**, **Jiang, S. J.** and **Liu, Y.**, Prognostic value of tumor-infiltrating FoxP3+ regulatory T cells in cancers: a systematic review and meta-analysis. *Sci. Rep.* 2015. **5**: 15179.

113 **Liu, C.**, **Workman, C. J.** and **Vignali, D. A.**, Targeting regulatory T cells in tumors. *FEBS J.* 2016. **283**: 2731–2748.

114 **Chao, J. L.** and **Savage, P. A.**, Unlocking the complexities of tumor-associated regulatory T cells. *J. Immunol.* 2018. **200**: 415–421.

115 **Ohue, Y.** and **Nishikawa, H.**, Regulatory T (Treg) cells in cancer: can Treg cells be a new therapeutic target? *Cancer Sci.* 2019. **110**: 2080–2089.

116 **Rivadeneira, D. B.** and **Delgoffe, G. M.**, Antitumor T-cell reconditioning: improving metabolic fitness for optimal cancer immunotherapy. *Clinical Cancer Research* 2018. **24**: 2473–2481.

117 **Pacella, I.**, **Procaccini, C.**, **Focaccetti, C.**, **Miacci, S.**, **Timperi, E.**, **Faicchia, D.**, **Severa, M.** et al., Fatty acid metabolism complements glycolysis in the selective regulatory T cell expansion during tumor growth. *Proc. Natl. Acad. Sci. U. S. A.* 2018. **115**: E6546-E6555.

118 **Renner, K.**, **Singer, K.**, **Koehl, G. E.**, **Geissler, E. K.**, **Peter, K.**, **Siska, P. J.** and **Kreutz, M.**, Metabolic hallmarks of tumor and immune cells in the tumor microenvironment. *Front. Immunol.* 2017. **8**: 248.

119 **Franchina, D. G.**, **Dostert, C.** and **Brenner, D.**, Reactive oxygen species: involvement in T cell signaling and metabolism. *Trends Immunol.* 2018. **39**: 489–502.

120 **Mougiakakos, D.**, **Johansson, C. C.** and **Kiessling, R.**, Naturally occurring regulatory T cells show reduced sensitivity toward oxidative stress-induced cell death. *Blood* 2009. **113**: 3542–3545.

121 **Liu, X.**, **Mo, W.**, **Ye, J.**, **Li, L.**, **Zhang, Y.**, **Hsueh, E. C.**, **Hoft, D. F.** et al., Regulatory T cells trigger effector T cell DNA damage and senescence caused by metabolic competition. *Nat. Commun.* 2018. **9**: 249.

122 **Curiel, T. J.**, **Coukos, G.**, **Zou, L.**, **Alvarez, X.**, **Cheng, P.**, **Mottram, P.**, **Evdemon-Hogan, M.** et al., Specific recruitment of regulatory T cells in ovarian carcinoma fosters immune privilege and predicts reduced survival. *Nat. Med.* 2004. **10**: 942–949.

123 **Clambey, E. T.**, **McNamee, E. N.**, **Westrich, J. A.**, **Glover, L. E.**, **Campbell, E. L.**, **Jedlicka, P.**, **de Zoeten, E. F.** et al., Hypoxia-inducible factor-1 alpha-dependent induction of FoxP3 drives regulatory T-cell abundance and function during inflammatory hypoxia of the mucosa. *Proc. Natl. Acad. Sci. U. S. A.* 2012. **109**: E2784-2793.

124 **Ben-Shoshan, J.**, **Maysel-Auslender, S.**, **Mor, A.**, **Keren, G.** and **George, J.**, Hypoxia controls CD4+CD25+ regulatory T-cell homeostasis via hypoxia-inducible factor-1alpha. *Eur. J. Immunol.* 2008. **38**: 2412–2418.

125 **Hsiao, H. W.**, **Hsu, T. S.**, **Liu, W. H.**, **Hsieh, W. C.**, **Chou, T. F.**, **Wu, Y. J.**, **Jiang, S. T.** et al., Deltex1 antagonizes HIF-1alpha and sustains the stability of regulatory T cells in vivo. *Nat. Commun.* 2015. **6**: 6353.

126 **Miska, J.**, **Lee-Chang, C.**, **Rashidi, A.**, **Muroski, M. E.**, **Chang, A. L.**, **Lopez-Rosas, A.**, **Zhang, P.** et al., HIF-1alpha Is a Metabolic Switch between Glycolytic-Driven Migration and Oxidative Phosphorylation-Driven Immunosuppression of Tregs in Glioblastoma. *Cell Rep.* 2019. **27**: 226–237 e224.

127 **Pavlova, Natalya N.**, and **Thompson, Craig B.**, The emerging hallmarks of cancer metabolism. *Cell Metab.* 2016. **23**: 27–47.

128 **Wang, H.**, **Franco, F.**, **Tsui, Y. C.**, **Xie, X.**, **Trefny, M. P.**, **Zappasodi, R.**, **Mohmood, S. R.** et al., CD36-mediated metabolic adaptation supports

regulatory T cell survival and function in tumors. *Nat. Immunol.* 2020. **21**: 298–308.

129 **McDonnell, E., Crown, S. B., Fox, D. B., Kitir, B., Ilkayeva, O. R., Olsen, C. A., Grimsrud, P. A.** et al., Lipids reprogram metabolism to become a major carbon source for histone acetylation. *Cell Rep.* 2016. **17**: 1463–1472.

130 **Opitz, C. A., Litzenburger, U. M., Sahm, F., Ott, M., Tritschler, I., Trump, S., Schumacher, T.** et al., An endogenous tumour-promoting ligand of the human aryl hydrocarbon receptor. *Nature* 2011. **478**: 197–203.

131 **Braun, D., Longman, R. S.** and **Albert, M. L.**, A two-step induction of indoleamine 2,3 dioxygenase (IDO) activity during dendritic-cell maturation. *Blood* 2005. **106**: 2375–2381.

132 **Platten, M., von Knebel Doeberitz, N., Oezen, I., Wick, W.** and **Ochs, K.**, Cancer immunotherapy by targeting IDO1/TDO and their downstream effectors. *Front. Immunol.* 2014. **5**: 673.

133 **Sharma, M. D., Shinde, R., McGaha, T. L., Huang, L., Holmgaard, R. B., Wolchok, J. D., Mautino, M. R.** et al., The PTEN pathway in Tregs is a critical driver of the suppressive tumor microenvironment. *Sci Adv* 2015. **1**: e1500845.

134 **Mascanfroni, I. D., Takenaka, M. C., Yeste, A., Patel, B., Wu, Y., Kenison, J. E., Siddiqui, S.** et al., Metabolic control of type 1 regulatory T cell differentiation by AHR and HIF1-alpha. *Nat. Med.* 2015. **21**: 638–646.

Abbreviations: **2-DG**: 2-deoxy-D-glucose · **AA**: amino acid · **ACC**: acetyl-CoA carboxylase · **ACLY**: ATP-citrate lyase · **AI**: autoimmune · **ATRA**: all-*trans* retinoic acid · **BCAA**: branched-chain AA · **CNS**: conserved non-coding DNA sequence · **CPT-1**: carnitine palmitoyl transferase-1 · **DCA**: dichloroacetate · **ETC**: electron transport chain · **FA**: fatty acid · **FAO**: fatty acid oxidation · **GGPP**: geranylgeranylpyrophosphate · **GSH**: glutathione · **GVHD**: graft-versus-host disease · **HMGCR**: HMG-CoA reductase · **IBD**: inflammatory bowel disease · **LC-FA**: long-chain fatty acid · **LDH**: lactate dehydrogenase · **LKB1**: liver kinase B1 · **OAA**: oxaloacetate · **OXPHOS**: oxidative phosphorylation · **PDH**: pyruvate dehydrogenase · **PP2A**: protein phosphatase 2A · **PPAR-γ**: Peroxisome proliferator-activated receptor-γ · **PPP**: pentose phosphate pathway · **pTreg**: peripherally derived Treg · **RA**: rheumatoid arthritis · **SCFA**: short-chain fatty acid · **SLE**: systemic lupus erythematosus · **TCR**: T cell receptor · **Th cell**: T helper cell · **TME**: tumor microenvironment · **TOFA**: 5-(tetradexyloxy)-2-furoic acid · **Treg**: regulatory T cell · **TSC1**: tuberous sclerosis 1 · **TSDR**: Treg-specific demethylation region · **tTreg**: thymus-derived Treg

Full correspondence: : Prof.Dirk Brenner, Ph.D., Deputy Head of Research & Strategy, Department of Infection and Immunity, Experimental and Molecular Immunology, Luxembourg Institute of Health, 29, rue Henri Koch, L-4354 Esch-sur-Alzette, Luxembourg Luxembourg Centre for Systems Biomedicine, Immunology and Genetics, University of Luxembourg, 6, avenue du Swing, L-4367 Belvaux, Luxembourg, Telephone: +352 26970-319, Fax: +352 26970-390.
e-mail: dirk.brenner@lih.lu

Received: 28/5/2020
Revised: 28/8/2020
Accepted: 14/10/2020
Accepted article online: 16/10/2020

APPENDIX 3

Research Publication

(Co-author)

FRANCHINA, D.G., KURNIAWAN, H., GRUSDAT, M., BINSFELD, C., GUERRA, L., BONETTI, L., SORIANO-BAGUET, L., EWEN, A., KOBAYASHI, T., FARINELLE, S., MINAFRA, A.R., VANDAMME, N., CARPENTIER, A., BORGMANN, F.K., JÄGER, C., CHEN, Y., KLEINEWIETFELD, M., VASILIOU, V., MITTELBRONN, M., HILLER, K., LANG, P.A., BRENNER, D., 2022. **Glutathione-dependent redox balance characterizes the distinct metabolic properties of follicular and marginal zone B cells.** *Nat Commun* 13, 1789.

nature COMMUNICATIONS

ARTICLE

https://doi.org/10.1038/s41467-022-29426-x OPEN

Check for updates

Glutathione-dependent redox balance characterizes the distinct metabolic properties of follicular and marginal zone B cells

Davide G. Franchina[1,2], Henry Kurniawan[1,2], Melanie Grusdat[1,2], Carole Binsfeld[1,2], Luana Guerra[1,2], Lynn Bonetti[1,2], Leticia Soriano-Baguet[1,2], Anouk Ewen[1,2], Takumi Kobayashi[1,2], Sophie Farinelle[1,2], Anna Rita Minafra[3], Niels Vandamme[4,5], Anaïs Carpentier[6], Felix K. Borgmann[6,7], Christian Jäger[8], Ying Chen[9], Markus Kleinewietfeld[10,11], Vasilis Vasiliou[9], Michel Mittelbronn[6,7,12,13,14,15], Karsten Hiller[16], Philipp A. Lang[3] & Dirk Brenner[1,2,17]✉

The metabolic principles underlying the differences between follicular and marginal zone B cells (FoB and MZB, respectively) are not well understood. Here we show, by studying mice with B cell-specific ablation of the catalytic subunit of glutamate cysteine ligase (*Gclc*), that glutathione synthesis affects homeostasis and differentiation of MZB to a larger extent than FoB, while glutathione-dependent redox control contributes to the metabolic dependencies of FoB. Specifically, *Gclc* ablation in FoB induces metabolic features of wild-type MZB such as increased ATP levels, glucose metabolism, mTOR activation, and protein synthesis. Furthermore, *Gclc*-deficient FoB have a block in the mitochondrial electron transport chain (ETC) due to diminished complex I and II activity and thereby accumulate the tricarboxylic acid cycle metabolite succinate. Finally, *Gclc* deficiency hampers FoB activation and antibody responses in vitro and in vivo, and induces susceptibility to viral infections. Our results thus suggest that *Gclc* is required to ensure the development of MZB, the mitochondrial ETC integrity in FoB, and the efficacy of antiviral humoral immunity.

[1] Experimental and Molecular Immunology, Department of Infection and Immunity, Luxembourg Institute of Health, Esch-sur-Alzette, Luxembourg. [2] Immunology & Genetics, Luxembourg Centre for Systems Biomedicine, University of Luxembourg, 7, Avenue des Hauts Fourneaux, Esch-sur-Alzette, Luxembourg. [3] Department of Molecular Medicine II, Medical Faculty, Heinrich-Heine-University, 40225 Düsseldorf, Germany. [4] National Data Mining and Modelling for Biomedicine, VIB Center for Inflammation Research, Ghent, Belgium. [5] Department of Applied Mathematics, Computer Science and Statistics, Ghent University, Ghent, Belgium. [6] National Center of Pathology (NCP), Laboratoire National de Santé (LNS), Dudelange, Luxembourg. [7] Luxembourg Center of Neuropathology (LCNP), Dudelange L-3555, Luxembourg. [8] Luxembourg Centre for Systems Biomedicine, University of Luxembourg, 7 Avenue des Hauts Fourneaux, Esch-sur-Alzette, Luxembourg. [9] Department of Environmental Health Sciences, Yale School of Public Health, New Haven, CT, USA. [10] VIB Laboratory of Translational Immunomodulation, VIB Center for Inflammation Research (IRC) Hasselt University, Diepenbeek, Belgium. [11] Department of Immunology, Biomedical Research Institute, Hasselt University, Diepenbeek, Belgium. [12] Faculty of Science, Technology and Medicine, University of Luxembourg, Esch-sur-Alzette, Luxembourg. [13] Department of Life Sciences and Medicine (DLSM), University of Luxembourg, Esch-sur-Alzette, Luxembourg. [14] Luxembourg Centre for Systems Biomedicine (LCSB), University of Luxembourg, Esch-sur-Alzette L-4362, Luxembourg. [15] Department of Oncology (DONC), Luxembourg Institute of Health (LIH), Luxembourg, L-1526 Dudelange, Luxembourg. [16] Department for Bioinformatics and Biochemistry, Braunschweig Integrated Center of Systems Biology (BRICS), Technische Universität Braunschweig, Rebenring 56, 38106 Braunschweig, Germany. [17] Odense Research Center for Anaphylaxis (ORCA), Department of Dermatology and Allergy Center, Odense University Hospital, University of Southern Denmark, Odense, Denmark. ✉email: dirk.brenner@lih.lu

B cells regulate many functions required for immune homeostasis and can present antigens very efficiently through their major histocompatibility complexes to T cells[1,2]. Furthermore, B cells can release immunomodulatory cytokines that are critical for the normal immune system maintenance, and differentiate into effector subsets that secrete polarized cytokines depending on the environment[3]. However, the principal function of a B lymphocyte is to secrete antibodies that provide humoral immunity. Antibody protection is a key component of the innate and adaptive phases of the immune response and is mediated mainly by two distinct splenic B cell subsets: marginal zone B cells (MZB) and follicular B cells (FoB)[4–6]. Previous studies have described developmental, phenotypic, functional and transcriptomic differences between MZB and FoB[7–14]. Moreover, distinct homeostatic control mechanisms regulate FoB and MZB distribution in the spleen[15,16]. FoB persist in the follicles in a quiescent state as they recirculate until activated by recognition of the antigen by their B cell receptors and the T cell-mediated cognate help, whereupon they proliferate and undergo germinal center (GC) reactions[6,17]. In contrast, MZB do not recirculate between lymphoid organs, are proximal to blood vessels, and can self-propagate[18]. Furthermore, MZB possess innate-like properties and are activated earlier during an immune challenge than FoB[8]. Nevertheless, like FoB, MZB can undergo GC reactions[19,20].

Redox balance is essential for maintaining cellular signaling and activation[21]. Glutathione (GSH) is a key intracellular antioxidant that scavenges excess reactive oxygen species (ROS)[22–24], and it is an important molecule for the regulation of lymphocytes activation[25–27]. Moreover, early studies on HIV-1-infected subjects associated GSH deficiency with a poor lymphocytic response and impaired survival following HIV-1 infections[28–30], implying a role for GSH in disease. In B cells, ROS are instrumental in regulating activation[31,32], but the contribution to B cell subsets and functions of mitochondrial ROS (mtROS), which are generated principally within mitochondria, is poorly understood. It is, therefore, possible that redox thresholds in B cells are subset-specific, and that these thresholds mediate homeostatic functions that could account for the differing properties of MZB and FoB. To this end, Muri et al. have previously shown that GSH-dependent glutathione peroxidase 4 (Gpx4) activity is critical for MZB compared to FoB[33]. However, the precise role of the tripeptide GSH in B cell metabolism remains unknown.

The mechanistic target of rapamycin (mTOR) signaling is a key modulator of anabolic and catabolic reactions[34], which in turn could affect ROS balance. mTOR has emerged as a crucial control point for B cell functions[35]. Previous reports have shown that relatively high levels of mTOR complex 1 (mTORC1) signaling prevail in MZB[36,37], but that the maturation of FoB down-regulates the mTORC1/Akt pathway[38]. However, other groups have shown that efficient mTORC1 suppression is necessary to avoid MZB loss[39]. Because mTORC1 is a well-known regulator of metabolic functions, these findings imply that specific metabolic programs may underlie the unique characteristics of different B cell subsets.

Here, we report that blocking GSH synthesis by ablation of *Gclc* causes loss of MZB. In the absence of GSH synthesis, FoB upregulate mTORC1 and reprogram their metabolism towards glycolysis, which is similar to the metabolic program of wild-type MZB. However, GSH-deficient FoB accumulate defective mitochondria and do not activate upon viral challenge. In summary, our analysis shows that GSH is crucial for the development of MZB and for the control of mitochondrial metabolic functions in FoB. Therefore, our results demonstrate a subset-specific role for GSH in controlling the redox balance underlying the metabolic properties between MZB and FoB.

Results

FoB and MZB exhibit distinct glutathione-based redox dependencies. To dissect the redox state of MZB and FoB in relation to the main antioxidant GSH, we studied the expression of *Gclc*, which is necessary for GSH synthesis[24], in isolated MZB and FoB from spleens of C57BL/6J (B6 or wild-type) mice. We found that both mRNA and protein levels of Gclc were significantly higher in B6 MZB compared to B6 FoB (Fig. 1a). However, the ratio of reduced to oxidized GSH (GSH/GSSG) was lower in B6 MZB than in B6 FoB indicating increased ROS in MZB (Fig. 1b). Indeed, staining of $CD23^{high}$ $CD21/35^{low}$ FoB and $CD23^{low}$ $CD21/35^{high}$ MZB (gated as shown in Supplementary Fig. 1a) with DCFDA, a fluorescent sensor of hydrogen peroxide[40], revealed increased ROS in B6 MZB compared to B6 FoB (Fig. 1c). Metabolic reactions intrinsically generate oxygen radicals, and mitochondria are the major source of metabolic ROS[41]. Evaluation of mtROS with MitoSOX staining[42] indicated that B6 MZB generate more mtROS compared to FoB (Fig. 1d). Accordingly, the absolute levels of GSH were increased in isolated mitochondria (gated as shown in Supplementary Fig. 1a) from B6 MZB compared to B6 FoB (Fig. 1e). These data suggest that MZB experience higher ROS generation and GSH consumption, a notion that correlates with a more sustained metabolic activity of MZB at steady-state.

Given the potential role of GSH in the regulation of immune functions[43,44] and the distinct expression of *Gclc* in mature B cell subsets, we studied FoB and MZB activation in the presence of buthionine sulfoximine (BSO), a Gclc inhibitor[45]. In order to assess activation, B6 FoB and MZB where stimulated with anti-IgM, CD40 ligand and IL-4 or LPS for 4 days and treated with BSO. We found that wild-type MZB were more susceptible to Gclc inhibition as shown by a stronger BSO concentration-dependent decrease in viability and total immunoglobulin secretion in the culture supernatants when compared to FoB (Fig. 1f). Altogether, these data indicate that GSH is differentially important in FoB and MZB at steady state, and that MZB show higher dependency on GSH upon in vitro activation.

To explore the relevance of GSH to the distinct redox properties of FoB and MZB in vivo, we generated B cell-specific *Gclc*-deficient mice by crossing $Gclc^{fl/fl}$ mice with *Mb1-Cre*$^{+}$ mice ($Gclc^{fl/fl}$ *Mb1-Cre*$^{+}$), in which the *Cre* recombinase gene is expressed under the control of the B cell-specific promoter *Mb1*[46]. First, we aimed to compare the transcriptome of MZB and FoB. Therefore, we FACS-sorted splenic B cells from $Gclc^{fl/fl}$ mice (gated as in Supplementary Fig. 1b) and applied single-cell CITE-sequencing (CITE-seq) proteomics[47]. FoB and MZB express specific surface markers, such as $CD19^{+}$ $CD23^{high}$ $CD21/35^{low}$ IgD^{high} and $CD19^{+}$ $CD23^{low}$ $CD21/35^{high}$ $CD1d^{high}$, respectively[7,48–50]. By using CD23, IgD, CD21/CD35, and CD1d antibody-derived tag (ADT) signals, we identified FoB and MZB in the CITE-seq dataset, assigned each cell type using SCINA (Fig. 1g)[51] and conducted downstream analyses. The gene expression PCA plot confirmed transcriptomic-wide differences between GSH-sufficient $Gclc^{fl/fl}$ MZB and $Gclc^{fl/fl}$ FoB (Fig. 1h). Differential expression analysis indicated a general upregulation of transcription in $Gclc^{fl/fl}$ MZB compared to $Gclc^{fl/fl}$ FoB (Fig. 1i), consistent with previous reports[10,37]. Moreover, together with MZB-related signature transcripts such as *Cr2* and *Ighm*, *Gclc* was also upregulated in $Gclc^{fl/fl}$ MZB compared to FoB (Fig. 1i), validating the dataset. Additionally, gene ontology analysis identified that *Gclc*-sufficient MZB transcriptomes showed upregulation of genes that are related to ROS metabolic processes when compared to *Gclc*-sufficient FoB (Fig. 1j and Supplementary Data 1). These data indicate that genes associated with metabolic ROS generation tend to be upregulated in MZB compared to FoB, suggesting that differences in the control of ROS signaling might

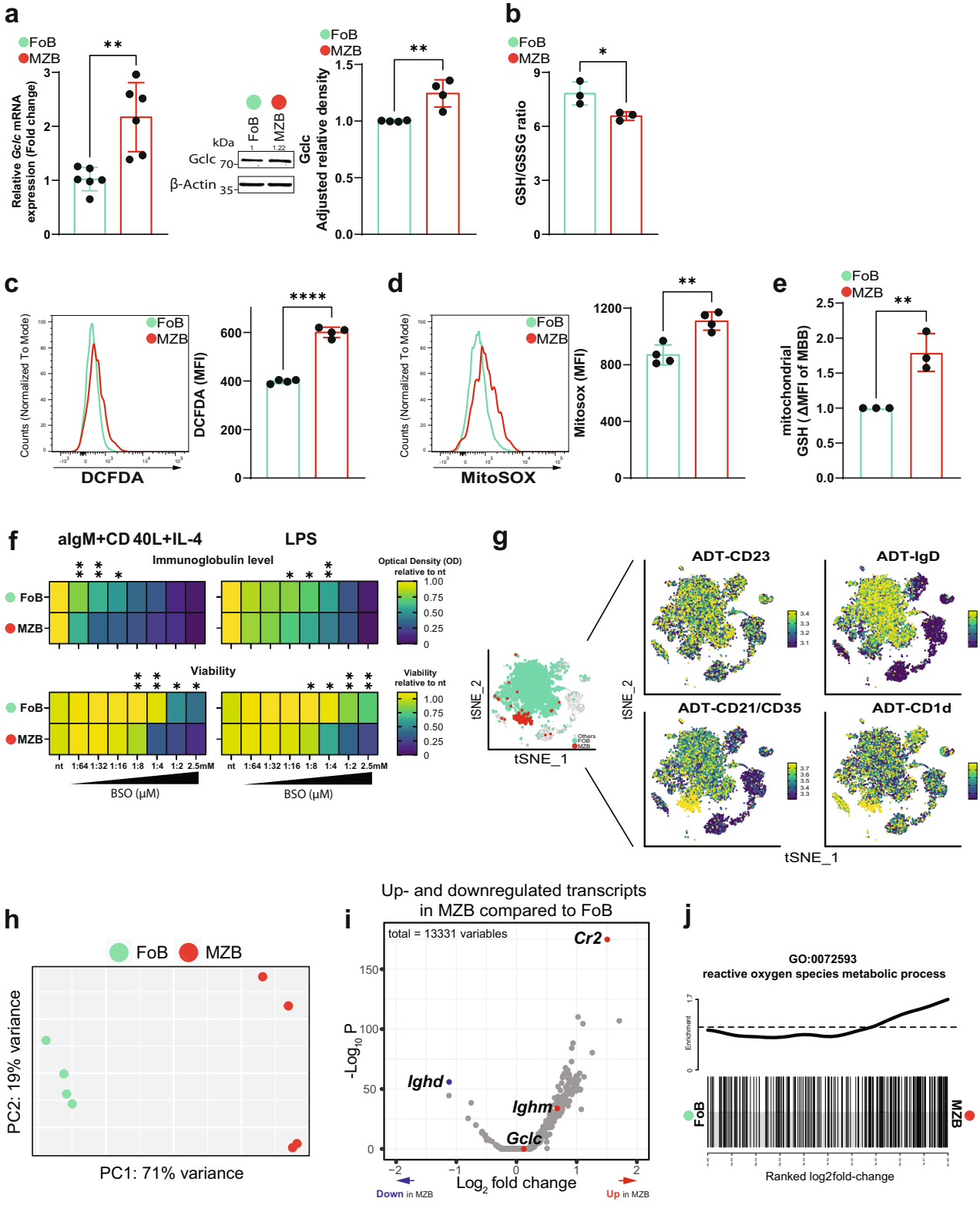

contribute to the classical distinctions between these two mature B cell subsets.

Deletion of *Gclc* results in a drastic decrease of splenic MZB. We next examined the macroscopic structure of splenic B cell follicles and the distribution of FoB and MZB in control $Gclc^{fl/fl}$ and mutant $Gclc^{fl/fl}$ *Mb1-Cre*$^{+}$ mice. At steady-state, histological examination did not reveal major macroscopic anomalies in the follicle architecture of mutant animals (Fig. 2a). However, follicles from $Gclc^{fl/fl}$ *Mb1-Cre*$^{+}$ mice showed partial loss of cellularity around the edges (Fig. 2a, insert). Ablation of *Gclc* in total splenic B cells was confirmed at both the mRNA and protein levels (Fig. 2b). Importantly, deletion of *Gclc* blocked reduced glutathione (GSH) synthesis, and, therefore, oxidized glutathione (GSSG) abundance was minimal in total B cells (Fig. 2c). This confirmed the efficient *Cre*-mediated deletion of the *Gclc* and also

Fig. 1 GSH-dependent redox activity differs between FoB and MZB. a Left: RT-qPCR of *Gclc* mRNA expression in resting *Gclc*-sufficient FoB (green) and MZB (red) isolated from spleen of B6 mice ($n = 5$ animals examined over three independent experiments). Middle: representative blot of Gclc protein from total cell lysis of resting B6 FoB and MZB ($n = 3$ animals examined over three independent experiments). Right: relative density of Gclc protein expression in resting B6 FoB and MZB ($n = 3$ animals examined over three independent experiments). **b** Luminescence-based quantitation of intracellular GSH/GSSG ratio in resting FoB and MZB isolated from B6 mice ($n = 3$ animals examined over three independent experiments). (**c**–**d**) Representative histogram and quantitation of DCFDA (**c**) and MitoSOX (**d**) staining for intracellular ROS and mitochondrial (mt) ROS detection in splenic B6 FoB and MZB (gated as in Supplementary Fig. 1a). **e** Flow-cytometry-based quantitation of monobromobimane (MBB) for the detection of GSH in purified Tom20$^+$ mitochondria from B6 FoB and MZB (gated as in Supplementary Fig. 1a) ($n = 3$–4 animals examined over two independent experiments). **f** Heatmap showing relative expression of immunoglobulin level (top) and viability (bottom) of 4d activated B6 FoB and MZB with increasing concentration of BSO. **g** tSNE plot showing SCINA assignments of *Gclc*-sufficient FoB and MZB (left) isolated from spleen of *Gclc*$^{fl/fl}$ mice (gated as in Supplementary Fig. 1b) and based on the ADT signals of CD23, IgD, CD21/35, and CD1d markers (right). Green: FoB; Red: MZB; Grey: unassigned B cells. Data are pooled from 4 *Gclc*$^{fl/fl}$ mice. Sidebars represent the ADT expression scale. **h** PCA plot showing distinct transcriptome patterns of *Gclc*-sufficient FoB and MZB transcriptomes from 4 *Gclc*$^{fl/fl}$ mice. **i** Volcano plot of differentially expressed genes in resting *Gclc*-sufficient FoB vs. MZB. Data represent up- and downregulated transcripts in *Gclc*-sufficient MZB compared to *Gclc*-sufficient FoB. Red/blue dots indicate upregulated/downregulated signature genes in resting *Gclc*-sufficient MZB compared to FoB. **j** Barcode plot showing enrichment of GO:0072593 gene list (reactive oxygen species metabolic processes) in resting *Gclc*-sufficient MZB compared to FoB. For all applicable figure panels, data are mean ± SD and each dot represents one single mouse. Significance (P) was calculated with unpaired t-test, except for (**f**) (2 way ANOVA). $^*P \le 0.05$; $^{**}P \le 0.01$; $^{****}P \le 0.0001$.

suggested that steady state B cells do not import GSH from the environment. As a consequence of GSH-deficiency, total B cells showed higher cytosolic and mitochondrial ROS (Supplementary Fig. 2a, b), although they were decreased in frequency and numbers (Supplementary Fig. 2c).

Comparative flow cytometric analysis of MZB (CD19$^+$ CD23^{low} CD21/35^{high}) and FoB (CD19$^+$ CD23^{high} CD21/35^{low}) in *Gclc*$^{fl/fl}$ *Mb1-Cre*$^+$ and control mice showed that *Gclc* deletion caused a stark decrease in MZB but not in FoB (Fig. 2d). However, in *Gclc*-deficient FoB no GSH was detectable and these cells accumulated ROS (Fig. 2e–g). Muri et al. have shown that MZB display increased sensitivity to lipid peroxidation in *Gpx4*-deficient mice[33]. Gpx4 uses GSH as cofactor and is needed to prevent lipid peroxidation, which depends on ROS. In line, lipid ROS accumulated in *Gclc*-deficient cells at steady state (Supplementary Fig. 2d).

Analysis of alternative MZB-specific surface proteins (i.e. IgM, CD1d, and CD24)[4,7] (Supplementary Fig. 2e) and immunofluorescence microscopy (Fig. 2h) confirmed the lack of MZB in *Gclc*$^{fl/fl}$ *Mb1-Cre*$^+$ mice. Importantly, flow cytometric analysis of MZB both excluded any gene-dosage effect of *Gclc* expression and confirmed that loss of MZB was independent of any *Cre*-associated toxicity (Supplementary Fig. 2f, g), a concern raised in a previous study[52]. In line with the greater baseline expression of *Gclc* in B6 MZB compared to B6 FoB (Fig. 1a), these data suggest that GSH is required for the homeostatic persistence of MZB in the spleen.

MZB differentiation is blocked in *Gclc*-deficient mice. The loss of MZB in *Gclc*$^{fl/fl}$ *Mb1-Cre*$^+$ mice prompted us to investigate the possibility of defects in the trafficking of MZB in the spleen. To this extent, previous reports have shown that the control of MZB localization in the spleen depends on signals delivered by integrins and chemokines such as ICAM-1 and VCAM-1[16,53]. Moreover, MZB entry and retention in the splenic marginal zone are tightly regulated by chemotactic molecules, such as C-X-C Motif Chemokine Ligand 13 (CXCL13) and sphingosine-1-phosphate (S1P)[54]. However, the expression level of ICAM-1 and VCAM-1 in total splenocytes and serum levels of chemotactic factors (i.e. CXCL13 and S1P) were unchanged in *Gclc*-deficient mice when compared to control littermates (Supplementary Fig. 3a, b). Furthermore, it has been shown that trafficking and retention of MZB require specific macrophage-B cell interactions[53,55–57]. However, both Siglec-1$^+$ marginal zone and MARCO$^+$ metallophilic macrophages (MZM and MMM)[58] formed similar structures in the spleen of *Gclc*$^{fl/fl}$ *Mb1-Cre*$^+$ mice compared to controls (Supplementary Fig. 3c). These data indicated that the factors responsible for MZB positioning in the marginal zone were not affected in *Gclc*-deficient mice.

To assess whether *Gclc* interferes with the development of MZB, which generally populate the spleen 2–3 weeks after birth[59], we investigated the distribution of discrete maturation steps in the spleen. In line with an earlier study[60], we identified three distinct B cell splenic maturation stages using CD21/35 and IgM (Fig. 2i, left): immature type 1 (T1), type 2 (T2), and mature (M) B cells. MZB cells are thought to develop from M B cells but also from T2 B cells[60,61]. We found that *Gclc* ablation prevented the formation of T1 B cells by 2 weeks of age, indicating that a block in the B cell differentiation process occurred at the very early stage in the spleen (Fig. 2i). Accordingly, T2 B cells did not develop in *Gclc*-deficient hosts (Fig. 2i, right). By 8 weeks, M B cells frequency dropped significantly, indicating that *Gclc*-deficient T1 B cells limit M B cells development and that *Gclc* is crucial for the transition from T1 to T2 B cells. Importantly, the lack of T2 B cells indicated that *Gclc* is needed in the transition to MZB or their precursors. To this extent, we studied the distribution of MZB precursors (MZP) in adult mice. As expected, *Gclc*-deficient mice showed lower frequencies of MZP compared to control mice (Fig. 2j), corroborating the data shown in Fig. 2i. Therefore, we concluded that defective B cell development causes the decrease of MZB content in *Gclc*$^{fl/fl}$ *Mb1-Cre*$^+$ mice.

Additionally, later studies have defined three subsets of CD93$^+$ immature or "transitional" B cells (TrB1-3) in the spleen of adult mice by the expression of CD23 and IgM[62]. Using this phenotypical characterization, most of FoB and MZB are thought to derive from TrB1 that have transitioned to TrB2[61,62]. Thus, to better understand at which stage GSH is essential in the maintenance of B cells in the adult mouse, we measured *Gclc* expression and total GSH in TrB from mutant and control mice. *Gclc* was efficiently deleted in TrB cells (Supplementary Fig. 3d). Of note, wild-type TrB showed intermediate levels of *Gclc* mRNA compared to FoB and in MZB (Supplementary Fig. 3e), implying that *Gclc* expression might characterize distinct stages of splenic B cell development. Thus, we measured TrB1-3 distribution in B cell-specific *Gclc*-deficient mice and found that TrB1 were increased in *Gclc*-deficient mice compared to controls (Supplementary Fig. 3f), despite showing low GSH content (Supplementary Fig. 3g). A possible scenario is that *Gclc* deficiency causes a mild block at the TrB1 stage, possibly impacting the maturation of MZB precursors. Therefore, these data support the existence of regulatory functions of *Gclc* in the FoB-MZB fate decision.

Overall, the results shown above confirmed that migratory inputs are not affected by the absence of *Gclc* in B cells, and that

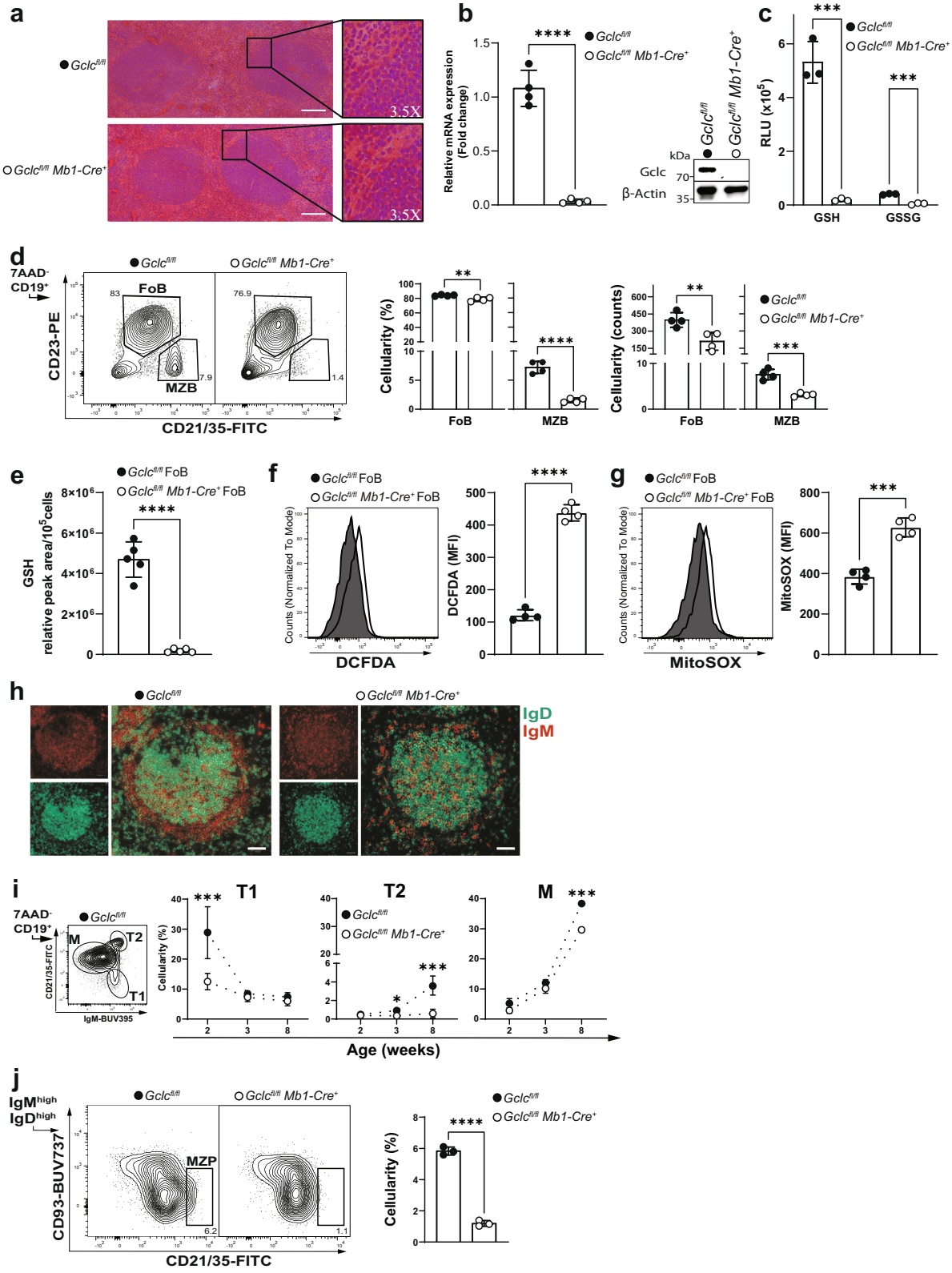

failure to detect MZB in B cell-specific *Gclc*-deficient mice is not due to altered environmental cues. Instead, we have shown that in vivo ablation of *Gclc* in B cells caused a block in B cell differentiation, which results in the absence of MZP. This implies that the difference in redox flexibility between FoB and MZB precursors is necessary to allow B cell differentiation.

The mTOR pathway confers MZB-like properties to GSH-deficient FoB. To investigate further the function of GSH in total splenic B cells, we performed a comparative single-cell CITE-seq analysis on B cells from *Gclc*$^{fl/fl}$ and *Gclc*$^{fl/fl}$ *Mb1-Cre*$^{+}$ mice. tSNE visualization of the total B cell transcriptomic landscape revealed minor changes in the distribution of single-cell transcriptomes in

Fig. 2 *Gclc* depletion induces a stark reduction in MZB. a Histology of spleen follicles resected from one *Gclc*$^{fl/fl}$ and one *Gclc*$^{fl/fl}$ *Mb1-Cre*$^{+}$ mouse and stained with haematoxylin and eosin. Scale bars, 50 µm. Insert digital magnification, 3.5×. **b** Left: RT-qPCR of *Gclc* mRNA of total splenic B cells isolated from *Gclc*$^{fl/fl}$ and *Gclc*$^{fl/fl}$ *Mb1-Cre*$^{+}$ mice ($n = 4$ animals examined over four independent experiments). Right: Representative immunoblot of Gclc protein in total splenic B cells isolated from spleen of *Gclc*$^{fl/fl}$ and *Gclc*$^{fl/fl}$ *Mb1-Cre*$^{+}$ mice ($n = 4$ animals examined over three independent experiments). **c** Luminescence-based quantitation of intracellular GSH and GSSG in total splenic B cells isolated from *Gclc*$^{fl/fl}$ and *Gclc*$^{fl/fl}$ *Mb1-Cre*$^{+}$ mice ($n = 3$ animals examined over three independent experiments). **d** Representative contour plot (left), percentages (middle) and numbers (right) statistic of splenic FoB and MZB from *Gclc*$^{fl/fl}$ and *Gclc*$^{fl/fl}$ *Mb1-Cre*$^{+}$ mice (gated as in Supplementary Fig. 1a) ($n = 4$ animals examined over five independent experiments). **e** Relative quantitation via LC-MS of GSH from resting FoB of *Gclc*$^{fl/fl}$ and *Gclc*$^{fl/fl}$ *Mb1-Cre*$^{+}$ mice ($n = 5$ animals examined over two independent experiments). Representative histogram and quantitation of DCFDA (**f**) and MitoSOX (**g**) staining for intracellular ROS and mitochondrial (mt) ROS detection in splenic FoB from *Gclc*$^{fl/fl}$ and *Gclc*$^{fl/fl}$ *Mb1-Cre*$^{+}$ mice (gated as in Supplementary Fig. 1a) ($n = 4$ animals examined over three independent experiments). **h** Representative immunofluorescence staining to detect IgD (green) and IgM (red) in a single spleen follicle resected from one *Gclc*$^{fl/fl}$ and one *Gclc*$^{fl/fl}$ *Mb1-Cre*$^{+}$ mouse. Scale bars: 50 µm. **i** Representative contour plot of splenic *Gclc*$^{fl/fl}$ M, T1, and T2 B cells used to determine the percentages over time (weeks) of the gated population from spleens of *Gclc*$^{fl/fl}$ and *Gclc*$^{fl/fl}$ *Mb1-Cre*$^{+}$ mice ($n = 2$–3 animals examined over three independent experiments). **j** Representative contour plot (left) and percentages statistic (right) of splenic MZP from *Gclc*$^{fl/fl}$ and *Gclc*$^{fl/fl}$ *Mb1-Cre*$^{+}$ mice (gated as in Supplementary Fig. 1a) ($n = 3$ animals examined over three independent experiments). For all applicable figure panels, data are mean ± SD and each dot represents one single mouse, except for (**f**) where each panel represents the mean of 2–3 mice. In contour plots, numbers represent percentages of the cells gated. Significance (*P*) was calculated with unpaired t-test, except for (**c**) (2way ANOVA). $^{*}P \leq 0.05$; $^{**}P \leq 0.01$; $^{***}P \leq 0.001$; $^{****}P \leq 0.0001$.

the absence of *Gclc* (Supplementary Fig. 4a). Mirroring our flow cytometric analyses (Fig. 2d and Supplementary Fig. 2e), ADT signals and the SCINA assignments confirmed the loss of MZB in *Gclc*$^{fl/fl}$ *Mb1-Cre*$^{+}$ mice (Supplementary Fig. 4b, c). As expected, FoB were clearly detectable in *Gclc*$^{fl/fl}$ *Mb1-Cre*$^{+}$ mice by the expression of CD23-ADT and IgD-ADT (Supplementary Fig. 4c). To investigate the transcriptomic changes induced by *Gclc* deletion, we performed downstream analyses of FoB (Supplementary Fig. 4d). As shown in Supplementary Fig. 4e, PCA analysis indicated that principal component 1 (PC1) covered most of the variation in gene expression (58% of total variance), likely including the effect caused by *Gclc* deletion. Analysis of total gene transcripts per cell further suggested that the deletion of *Gclc*, and therefore the lack of GSH (Fig. 2e), influenced gene expression levels in FoB (Supplementary Fig. 4f).

As noted above, mTOR signaling has emerged as a key control point for B cell functions[35]. As already shown, GSH-deficiency in B cells resulted in the absence of MZB but not of FoB (Fig. 2d, h). This prevented the direct analysis of *Gclc*-deficient MZB. This implies the existence of a GSH-dependent process that is more important for MZB than for FoB. To elucidate these regulation circuits and to investigate whether mTOR signaling might be involved in this abnormality, we performed gene set enrichment analysis (GSEA) on differentially expressed genes of *Gclc*-sufficient MZB vs. FoB (*Gclc*$^{fl/fl}$ MZB vs. *Gclc*$^{fl/fl}$ FoB) and of *Gclc*-deficient FoB vs. control FoB (*Gclc*$^{fl/fl}$ *Mb1-cre*$^{+}$ FoB vs. *Gclc*$^{fl/fl}$ FoB). In accordance with previous reports[36,37], our GSEA analysis revealed positive enrichment for genes of the mTORC1 signaling pathway in *Gclc*-sufficient MZB compared to FoB (Fig. 3a). Indeed, flow cytometric evaluation of resting B6 MZB confirmed increased phosphorylation of both mTOR and its canonical target S6 (Fig. 3b, c). Strikingly, our GSEA analysis also showed that ablation of *Gclc* in FoB displayed a similar increase in mTORC1 signaling genes compared to *Gclc*$^{fl/fl}$ FoB and *Gclc*$^{fl/fl}$ MZB (Fig. 3d). Corresponding increases in phosphorylated mTOR and S6 were detected in mutant FoB compared to control FoB (Fig. 3e, f and Supplementary Fig. 5a). These data pointed to an unexpected similarity between *Gclc*-deficient FoB and *Gclc*-sufficient MZB.

mTOR is also an important regulator of translation[63], and supports an enhanced secretory apparatus and superior secretory activity of MZB compared to FoB[7,14]. Accordingly, we found that B6 MZB had a higher endoplasmic reticulum (ER)/Golgi ratio than B6 FoB as measured by their greater staining intensity of ER-tracker and giantin (Supplementary Fig. 5b), as well as by their increased phosphorylation of the translation initiation factor eIF4E (Supplementary Fig. 5c). In addition, our differential expression analysis identified upregulation of a considerable number of transcripts related to ribosomal proteins in *Gclc*$^{fl/fl}$ MZB compared to *Gclc*$^{fl/fl}$ FoB (Supplementary Fig. 5d). Additionally, gene ontology analysis detected accumulation of transcripts related to the three steps of protein synthesis (initiation, elongation, termination) in *Gclc*$^{fl/fl}$ MZB compared to *Gclc*$^{fl/fl}$ FoB (Supplementary Fig. 5e). To confirm this heightened protein translation in vitro, B6 FoB and B6 MZB were activated with anti-IgM, CD40 ligand and IL-4 or LPS, pulsed with puromycin, and chased for up to 6 h[64]. B6 MZB indeed showed greater protein synthesis compared to B6 FoB over time (Supplementary Fig. 5f). Strikingly, the absence of *Gclc* in FoB resulted in secretory properties that recapitulated those of *Gclc*-sufficient MZB at both the transcriptional and protein levels (Supplementary Fig. 5g–k). These findings confirmed a certain degree of similarity between *Gclc*-deficient FoB and *Gclc*-sufficient MZB, which was further substantiated by comparing differentially expressed genes between the two groups *Gclc*$^{fl/fl}$ MZB vs. FoB and *Gclc*$^{fl/fl}$ *Mb1-Cre*$^{+}$ vs. control FoB (Supplementary Fig. 5l). This suggests that MZB and FoB depend on a different redox state and that the loss of GSH in FoB may induce MZB-like properties.

mTORC1 is regulated through the phosphatidylinositol 3 kinase (PI3K)/Protein kinase B (Akt)-dependent pathway[65]. In particular, the PI3K/AKT axis converts phosphatidylinositol-4,5-bisphosphate (PIP_2) to phosphatidylinositol 3,4,5-trisphosphate (PIP_3). A key repressor of this signaling, phosphatase and tensin homolog deleted on chromosome 10 (PTEN), dephosphorylates PIP_3 to PIP_2 regulating the activity of PI3K/AKT[66]. Time course in vitro activation showed that PIP_3 levels were higher in GSH-deficient FoB compared to control cells (Fig. 3g). This suggested that the PI3K/AKT pathway is increased in *Gclc*-deficient FoB, and in turn can sustain increased mTORC1 activity. Importantly, *Gclc*-deficient FoB accumulate ROS (Fig. 2f, g), which are known inducers of PI3K/AKT[67,68] and suppressors of PTEN[69]. Therefore, it is possible that the increased mTORC1 activation measured in FoB upon *Gclc* deletion can be a consequence of ROS accumulation and activation of the PI3K/AKT axis.

Collectively, these data might indicate that the diminished ROS buffering of GSH-deficient cells leads to an increased activation of the mTOR pathway which could drive to the MZB-like properties of *Gclc*-deficient FoB. We were thus prompted to explore the intriguing hypothesis that GSH-dependent control of ROS could play a role in defining the distinctive metabolic signaling of MZB and FoB.

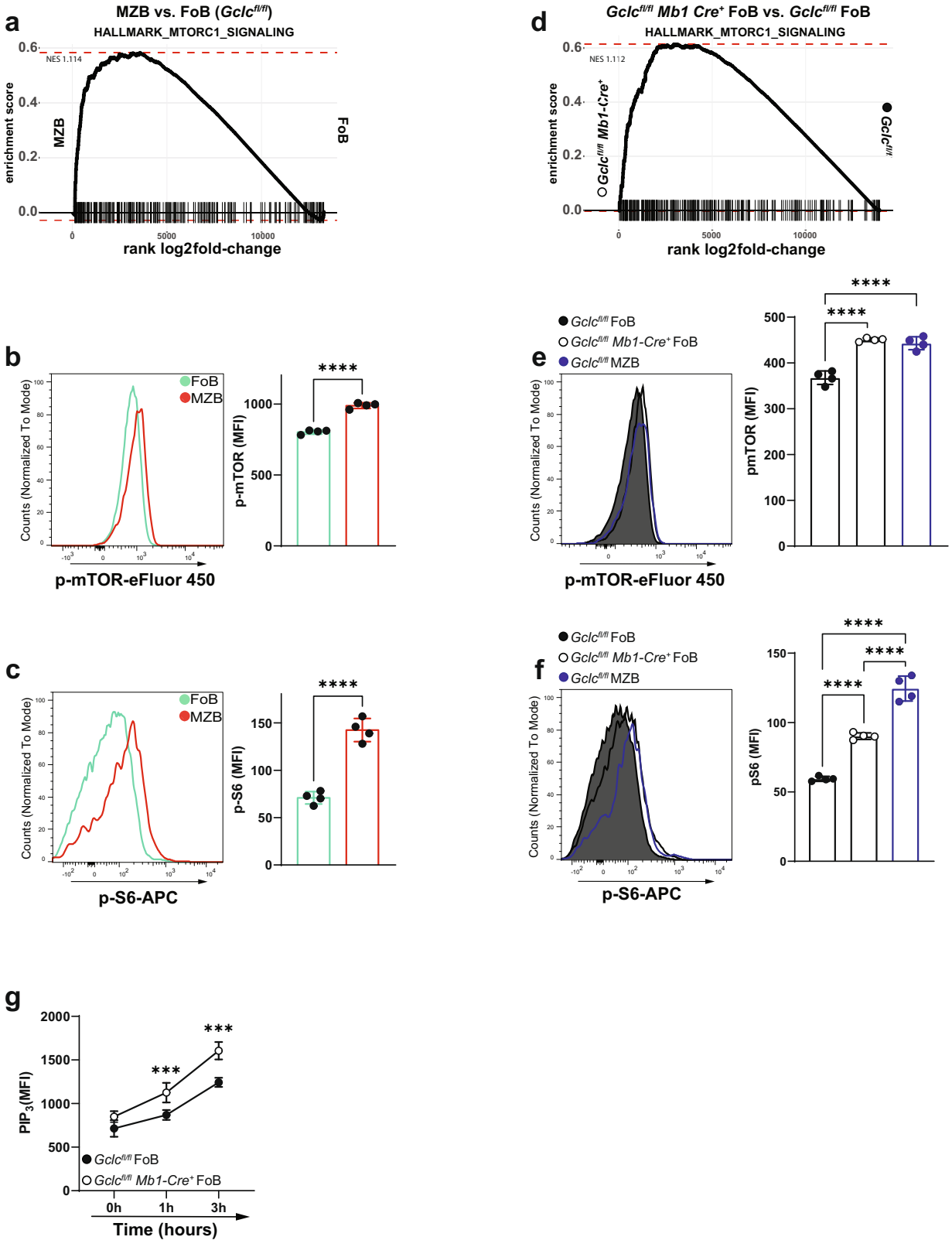

***Gclc* deletion enhances glycolytic reactions and glucose uptake in FoB**. mTORC1 signaling plays a role in maturation and activation of both MZB and FoB[36–39], and is key for the regulation of various metabolic pathways[34]. Therefore, in order to contextualize the complexity of the metabolic network and the impact of *Gclc* on it, we analyzed our transcriptomic data using Compass, a flux balance analysis-based approach that allows the characterization and interpretation of metabolic diversity at the single cell level[70,71]. Using this computational prediction method, we found that $Gclc^{fl/fl}$ MZB exhibited increased glucose catabolism compared to $Gclc^{fl/fl}$ FoB (Fig. 4a, top and Supplementary Data 2). Glucose can be catabolized to lactate during glycolysis or glucose-derived carbons can enter the tricarboxylic acid cycle (TCA). We, therefore, sorted the metabolic reactions identified by

Fig. 3 mTORC1 is comparably elevated in *Gclc*-sufficient MZB and *Gclc*-deficient FoB. a GSEA plot comparing expression of mTORC1 signaling hallmark gene sets between $Gclc^{fl/fl}$ FoB and $Gclc^{fl/fl}$ MZB. Representative histogram (left) and quantitation (right) of immunostaining to detect p-mTOR (**b**) and p-S6 (**c**) in B6 FoB and MZB (gated as in Supplementary Fig. 1a) ($n = 4$ animals examined over three independent experiments). **d** GSEA plot comparing the expression of mTORC1 signaling hallmark gene sets between $Gclc^{fl/fl}$ and $Gclc^{fl/fl}$ *Mb1-Cre*$^{+}$ FoB. Representative histogram (left) and quantitation (right) of immunostaining to detect p-mTOR (**e**) and p-S6 (**f**) in $Gclc^{fl/fl}$ and $Gclc^{fl/fl}$ *Mb1-Cre*$^{+}$ FoB, including $Gclc^{fl/fl}$ MZB as control (gated as in Supplementary Fig. 1a) ($n = 4$ animals examined over four independent experiments). **g** Flow-cytometry measurements kinetic of PIP_3 in sorted FoB from spleens of $Gclc^{fl/fl}$ and $Gclc^{fl/fl}$ *Mb1-Cre*$^{+}$ at the indicated time points after stimulation with anti-IgM ($n = 3$ animals examined over two independent experiments). Data are mean ± SD. Significance (*P*) was calculated with unpaired t-test, except for **e**, **f** (one-way ANOVA), and **g** (2 way ANOVA). ***$P \leq 0.001$; ****$P \leq 0.0001$.

the Compass algorithm into two groups: glycolysis and TCA. This analysis indicated that glycolysis was upregulated in $Gclc^{fl/fl}$ MZB compared to $Gclc^{fl/fl}$ FoB (Fig. 4a, bottom and Supplementary Data 2), suggesting that MZB rely on glycolysis rather than oxidative metabolism at steady-state. To confirm these predictions, we measured glucose uptake with 2-(N-(7-Nitrobenz-2-oxa-1,3-diazol-4-yl)Amino)-2-Deoxyglucose (2-NBDG)[72] in B6 MZB and FoB. In line with our Compass results, B6 MZB showed increased 2-NBDG uptake compared to B6 FoB (Fig. 4b) as well as higher expression of the glucose transporter Glut-1 as measured by flow cytometry (Fig. 4c). Moreover, total intracellular glucose measured by mass spectrometry was elevated in freshly isolated MZB compared to FoB (Fig. 4d), although the size difference between FoB and MZB[7] might influence total glucose level.

Our data above indicated that GSH deficiency upregulated mTORC1 signaling in mutant FoB. Therefore, we sought to determine whether this heightened mTORC1 skewed FoB metabolism towards glycolysis. Indeed, our Compass analysis reflected a global increase in glucose catabolism in FoB when *Gclc* was ablated (Fig. 4e and Supplementary Data 3), just as occurred in *Gclc*-sufficient MZB (Fig. 4a). Mutant FoB also showed increased 2-NBDG uptake at steady-state (Fig. 4f), higher Glut-1 expression (Fig. 4g), and accumulation of glucose (Fig. 4h) compared to $Gclc^{fl/fl}$ FoB and MZB. These data indicate that mutant FoB undergo an increase in oxidative state (i.e. low GSH and high ROS) that might induce some metabolic traits similar to those observed in *Gclc*-sufficient MZB.

GSH-deficient FoB upregulate glycolysis but accumulate defective mitochondria. Based on our scRNA analyses and the effect of *Gclc* deficiency on glucose uptake (Fig. 4e–h), we compared ATP levels in $Gclc^{fl/fl}$ and $Gclc^{fl/fl}$ *Mb1-Cre*$^{+}$ FoB prior to activation. Interestingly, we detected increased total ATP in *Gclc*-deficient FoB (Fig. 5a). This finding was confirmed by flux analysis (Fig. 5b) and further suggests an increased glycolytic activity of *Gclc*-deficient FoB, a dependence that is not observed in *Gclc*-deficient T cells[43]. Importantly, we also confirmed that $Gclc^{fl/fl}$ MZB and B6 MZB showed increased glycolysis-derived ATP (Fig. 5b and Supplementary Fig. 6a). These data further confirm our Compass predictions (Fig. 4a, e) and strengthen the metabolic parallel between GSH-deficient FoB and GSH-sufficient MZB.

To further study the dynamics of glucose fluxes in B cell subsets, we measured glucose levels in the culture medium of $Gclc^{fl/fl}$ and $Gclc^{fl/fl}$ *Mb1-Cre*$^{+}$ FoB after 5 h activation with anti-IgM, CD40 ligand and IL-4. We found that the activated mutant cells consumed more glucose than controls (Fig. 5c). Moreover, following ^{13}C-glucose tracing in activated $Gclc^{fl/fl}$ and $Gclc^{fl/fl}$ *Mb1-Cre*$^{+}$ FoB, we detected an increased contribution of glycolytic carbon to lactate within the mutant cells (Fig. 5d, left). In line, lactate also accumulated to a higher extent in the culture medium of $Gclc^{fl/fl}$ *Mb1-Cre*$^{+}$ FoB as compared to control cells (Fig. 5d, right). To further substantiate these results, we measured the expression of hexokinase 1 (HK1), a rate limiting enzyme of glycolysis. HK1 content increased upon *Gclc*-ablation in FoB and in $Gclc^{fl/fl}$ MZB (Supplementary Fig. 6b). This was paralleled by the accumulation of glucose-6-phosphate (6P) in steady state GSH-deficient FoB (Supplementary Fig. 6c). Concomitantly, we measured increased pyruvate levels in mutant compared to control cells (Supplementary Fig. 6d), confirming increased glycolysis upon *Gclc*-ablation.

Furthermore, we determined the flux of glycolytic carbon through the pyruvate dehydrogenase complex (PDC) by stable-isotope labeling with ^{13}C-glucose. Glycolysis converts the ^{13}C-glucose tracer to M3-pyruvate isotopologues which are oxidized to M2-acetyl-CoA by PDC and finally condensed with oxaloacetate to M2-citrate. We found that the glycolytic flux into the TCA cycle was reduced in $Gclc^{fl/fl}$ *Mb1-Cre*$^{+}$ FoB compared to $Gclc^{fl/fl}$ FoB, as indicated by increased M3-lactate and reduced M2-citrate (Supplementary Fig. 6e) and a higher M3-lactate/M2-citrate ratio in the mutant cells (Fig. 5e). In line, expression of the catalytic alpha subunit of PDC (Pdha-1) was decreased in *Gclc*-deficient cells (Fig. 5e), which provides a possible explanation for the reduced carbon flux into the TCA. Thus, blocking GSH synthesis in FoB preferentially promotes ATP production through aerobic glycolysis.

Most of the ATP in a cell is generated by the combined action of the TCA cycle and oxidative phosphorylation (OXPHOS) within the mitochondria[73,74]. Our data showed that loss of *Gclc* decreased glucose flux into the TCA cycle (Fig. 5e and Supplementary Fig. 6e), suggesting a disturbance in mitochondrial ATP generation. Indeed, flux analysis showed that, similarly to GSH-sufficient MZB, *Gclc*-deficient FoB at rest showed decreased amounts of mitochondria-derived ATP (Fig. 5f and Supplementary Fig. 6f), implying that *Gclc* deficiency alters mitochondrial metabolism in FoB. In turn, we speculated that this impairment of mitochondrial metabolism in FoB might explain the increase in aerobic glycolysis for ATP production.

To acquire more information about the mitochondrial function of *Gclc*-deficient FoB, we investigated mitochondrial size and conformation. Interestingly, the lack of mitochondrial GSH (mtGSH) in $Gclc^{fl/fl}$ *Mb1-Cre*$^{+}$ FoB (Supplementary Fig. 6g) resulted in an increased mitochondrial area compared to control FoB (Fig. 5g) as well as a lower mitochondrial DNA/nuclear DNA ratio as measured by quantitative PCR (Fig. 5h). Crucially, wild-type MZB are known to be prone to activation compared to FoB[7,8,75], and we found that both $Gclc^{fl/fl}$ *Mb1-Cre*$^{+}$ FoB and B6 MZB showed a similar increase in mitochondrial mass (Fig. 5h and Supplementary Fig. 6h), further substantiating similarity. Thus, interference with GSH synthesis in FoB induced an increase in mitochondrial mass without concomitant mtDNA replication. Next, we visualized mitochondria of FoB by electron microscopy to examine the mitochondrial inner space and the conformation of mitochondrial cristae. This analysis confirmed the accumulation of fragmented mitochondria, which exhibited a dilated intercristae space, in *Gclc*-deficient FoB (Fig. 5i). This is in line with the higher expression of the major mitochondrial fission GTPase, dynamin-related protein 1 (DRP1)[76] (Fig. 5j). Taken together, these data imply that loss of *Gclc* alters mitochondrial structure and metabolism of FoB.

To gain more insight into the effect of GSH paucity on mitochondria, we used MitoTracker (MT) green and MT red

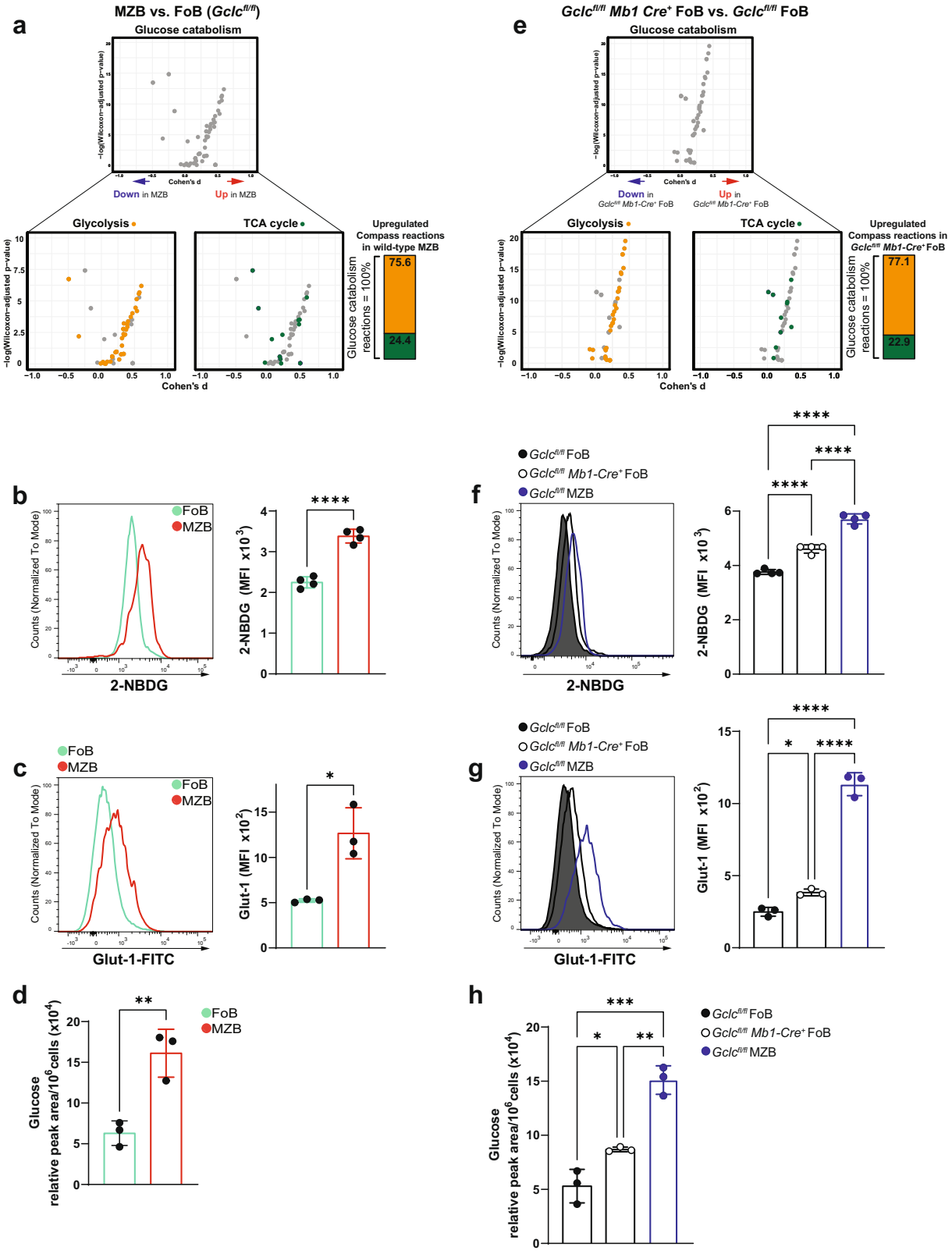

staining to assess mitochondrial membrane potential ($\Delta\Psi_m$) with flow cytometry. We found that *Gclc* deficiency increased $\Delta\Psi_m$ in mutant FoB compared to controls (Fig. 5k). However, loose mitochondrial cristae have been associated with poor electron transport chain (ETC) efficiency in T cells[77], suggesting that other factors might be responsible for the increased $|\Delta\Psi_m|$ in mutant FoB. Coupled with our data, this observation suggests that GSH is critical for the steady state function of mitochondria, whose fitness is crucial for the maintenance of MZB. In FoB, we found that ATP levels in *Gclc*-deficient, but not in *Gclc*-sufficient FoB dropped in a dose-dependent fashion in response to inhibition of glycolysis with 2-deoxy-D-glucose (2-DG) or galactose (Fig. 5l and Supplementary Fig. 6i). In parallel, glycolysis inhibition increased cell death in *Gclc*-deficient FoB to a stronger extent

Fig. 4 *Gclc*-deficient FoB show increased glycolytic reactions and glucose uptake, mirroring *Gclc*-sufficient MZB. a Compass analysis to compare glucose catabolism (top) and its components (glycolysis and TCA cycle) (bottom) in $Gclc^{fl/fl}$ MZB vs. FoB. Each dot represents a single biochemical reaction. Means difference (Cohen's d) and Wilcoxon rank sum *p* values were computed as described previously[70,71]. Vertical bar shows relative contributions (percentages) of upregulated glycolytic reactions and TCA reactions to total glucose catabolism computed from glycolysis and TCA cycle reactions in $Gclc^{fl/fl}$ MZB vs. FoB. (**b**-**c**) Representative histogram (left) and quantitation (right) of 2-NBDG (**b**) and Glut-1 (**c**) staining in resting splenic B6 FoB and MZB (gated as in Supplementary Fig. 1a) ($n = 3$ animals examined over 3–4 independent experiments). **d** Quantitation of intracellular glucose level measured by LC-MS in resting *Gclc*-sufficient FoB and MZB ($n = 3$ animals examined over two independent experiments). **e**–**h** Same analyses as shown in (**a**–**d**), but comparing $Gclc^{fl/fl}$ versus $Gclc^{fl/fl}$ *Mb1-Cre*$^{+}$ FoB and including $Gclc^{fl/fl}$ MZB as control (gated as in Supplementary Fig. 1a) ($n = 3$–4 animals examined over 2–3 independent experiments). For all applicable figure panels, data are mean ± SD and each dot represents one single metabolic reaction or mouse. Significance (*P*) was calculated with unpaired t-test, with exception of (**f**)-(**h**) (one-way ANOVA). $^{*}P \le 0.05$; $^{**}P \le 0.01$; $^{***}P \le 0.001$; $^{****}P \le 0.0001$.

when compared to controls (Fig. 5m and Supplementary Fig. 6j), confirming the dependency of GSH-deficient FoB on glycolysis.

Taken together, our data indicate that the loss of GSH triggered by *Gclc* deletion induces a defective mitochondrial accumulation in FoB, which may lead to compensation through upregulation of glycolytic metabolism. This observation implies the existence of a regulatory function for GSH in the context of energy metabolism shifts in B cells.

Absence of *Gclc* impairs mitochondrial respiration in FoB. Our data above showed that glucose-derived fluxes into the TCA cycle were reduced in GSH-deficient FoB. However, in our analyses of ^{13}C-glucose, we found that total and labelled succinate accumulated to higher levels in mutant cells than in $Gclc^{fl/fl}$ FoB (Fig. 6a and Supplementary Fig. 6k). Within the TCA cycle, succinate is converted into fumarate by the succinate dehydrogenase (SDH) which represents the respiratory ETC complex II (CII)[73] (Supplementary Fig. 6l). Accordingly, SDH flux showed lower conversion into M2-fumarate in $Gclc^{fl/fl}$ *Mb1-Cre*$^{+}$ FoB compared to control cells (Supplementary Fig. 6m). Because SDH is the only enzyme that participates in both the TCA cycle and the ETC, we speculated that the ETC might be compromised in *Gclc*-deficient FoB, thus explaining the inhibition of SDH and the accumulation of succinate. Indeed, the basal oxygen consumption rate (OCR) of *Gclc*-deficient FoB measured by extracellular flux analysis was slightly reduced compared to $Gclc^{fl/fl}$ FoB (Fig. 6b and Supplementary Fig. 6n), indicating that loss of GSH results in dysfunctional mitochondrial respiration in FoB at steady state. However, no difference in the OCR profiles of mutant and control FoB was detected upon treatment with oligomycin A (Fig. 6b and Supplementary Fig. 6o) which inhibits the ATP synthase, and thus, suggests that ADP phosphorylation capacity is unchanged. Interestingly, the most striking respiratory difference attributable to loss of GSH emerged upon treatment of $Gclc^{fl/fl}$ and $Gclc^{fl/fl}$ *Mb1-Cre*$^{+}$ FoB with the mitochondrial ionophore FCCP, which increases the OCR to the maximal respiration (i.e. reserve capacity)[78]. Upon FCCP treatment, the ETC activity rate increases in the attempt to restore the proton gradient and re-couple it to OXPHOS. We found that an absence of *Gclc* in FoB prevented this FCCP-mediated uncoupling (Fig. 6b and Supplementary Fig. 6p), suggesting that GSH promotes electron transport through the ETC in FoB. However, transient treatment with GSH did not recover mitochondrial function (Supplementary Fig. 6q), possibly because of irreversible ROS-mediated modifications.

Previous work has established that any residual OCR detected after oligomycin A treatment is due to non-respiratory oxygen consumption, which is usually ascribed to proton leakage through the mitochondrial inner membrane[79]. We found that, despite the similar oligomycin A-dependent OCR profiles in $Gclc^{fl/fl}$ and $Gclc^{fl/fl}$ *Mb1-Cre*$^{+}$ FoB (Fig. 6b and Supplementary Fig. 6o), the contributions to the maximal OCR value in each genotype by ATP-linked OCR, proton leakage, reserve capacity, and non-mitochondrial OCR were altered by *Gclc* deficiency (Fig. 6c). In particular, *Gclc*-deficient FoB experienced greater proton leakage (Fig. 6c, d), which together with increased ROS (Fig. 2f, g) might lead to damage of the mitochondrial membrane and/or ETC malfunction. In this regard, it is tempting to speculate that the accumulation of succinate (the CII substrate in the TCA cycle) in GSH-deficient FoB (Fig. 6a and Supplementary Fig. 6k) might be associated with the observed ETC insensitivity to FCCP treatment (Fig. 6b and Supplementary Fig. 6p).

Mitochondrial damage is often defined as a deviation of respiratory parameters or states, which were originally defined in vitro using isolated mitochondria[80–82]. However, these measurements can also be derived from measurements with whole cells (Supplementary Fig. 6r). In particular, state 3 respiration is equivalent to the OCR after FCCP treatment (i.e. maximal respiration induced by the substrate + ADP), and state 4 corresponds to the consumption rate upon oligomycin A addition (i.e. absence of substrate-dependent respiration)[83]. These assumptions allow for the calculation of the intermediate respiratory state or $state_{apparent}$ (Supplementary Fig. 6s)[84,85], which is an indicator of mitochondrial workload. From the assay performed in Fig. 6b, we determined a $state_{apparent}$ value of 2.94 ± 0.15 in *Gclc*-deficient FoB (Fig. 6e), suggesting that FoB with *Gclc* deficiency experience a higher basal rate of mitochondrial activity compared to control cells. This higher activity results from the insensitivity of ETC to FCCP treatment and is consistent with the limited reserve capacity of *Gclc*-deficient FoB (Fig. 6b and Supplementary Fig. 6p). Taken together, these results establish that loss of GSH in FoB impairs mitochondrial respiration.

Oxidative phosphorylation is disrupted at complex I and II in GSH-deficient follicular B cells. To determine whether the accumulation of succinate in *Gclc*-deficient FoB was caused by a dysfunctional ETC, we assessed the respiratory parameters of each ETC complex. First, we performed extracellular flux analysis to assay the mitochondrial complex-dependent OCR profile in saponin-permeabilized $Gclc^{fl/fl}$ and $Gclc^{fl/fl}$ *Mb1-Cre*$^{+}$ FoB. Under normal conditions, CI regenerates the reducing equivalent NADH to NAD^{+} (Supplementary Fig. 6l). However, CI showed no activation upon substrate injection (pyruvate + malate) in *Gclc*-deficient FoB (Fig. 6f). Moreover, CII activation in $Gclc^{fl/fl}$ *Mb1-Cre*$^{+}$ FoB was also negligible compared to CII from control cells (Fig. 6g). Thus, both CI and CII exhibited a significant lower activity, which was confirmed by a lower $state_{apparent}$ upon *Gclc* ablation (Supplementary Fig. 6t). However, substrate-dependent CIII and CIV OCR showed a tendency, although not significant, to be increased in GSH-deficient FoB cells compared to control FoB (Fig. 6h, i). CIII and CIV (together with CI) of the ETC act as H^{+} pump and build up the membrane potential. This suggests the possibility of a mild compensatory activation of CIII and CIV

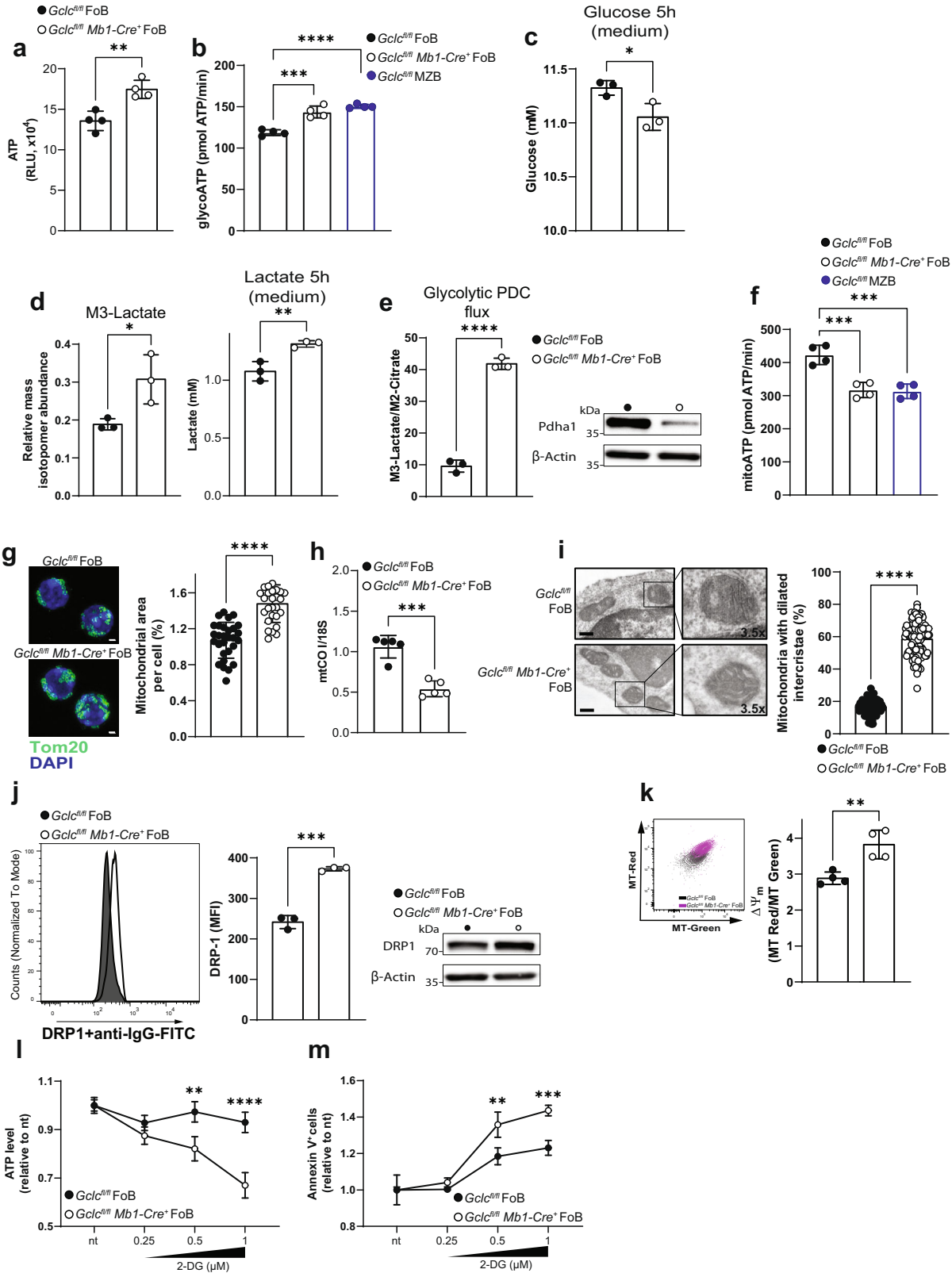

that may explain the higher intensity of MT red binding (i.e. higher $\Delta\Psi_m$) in mutant FoB (Fig. 5k) despite the higher membrane leak (Fig. 6d). These data indicate that GSH-dependent ETC dysfunction mostly affected the activity of CI and CII. In line with these results, we detected lower CI activity in total lysates of *Gclc*-deficient FoB compared to control FoB (Fig. 6j). Consequently, NADH levels were increased in the mutant cells (Fig. 6k) due to reduced NAD^+ regeneration which resulted in a lower NAD^+/NADH ratio (Fig. 6l). Moreover, the expression level of the main subunit of CII (succinate dehydrogenase A, Sdha) was decreased in *Gclc*-deficient FoB (Fig. 6m). In line, ETC complex protein levels were reduced in mutant FoB compared to controls (Supplementary Fig. 6u). This included the CIII subunit core protein 2 and CIV subunit MTCO1, indicating that

Fig. 5 GSH deficiency increases glucose flux through glycolysis and leads to mitochondria accumulation in FoB. a Total ATP levels expressed in relative luminescence unit (RLU) in resting *Gclc*$^{fl/fl}$ and *Gclc*$^{fl/fl}$ *Mb1-Cre*$^{+}$ FoB ($n = 4$ animals examined over 4 independent experiments). **b** Seahorse quantitation of glycolysis-derived ATP in resting *Gclc*$^{fl/fl}$ and *Gclc*$^{fl/fl}$ *Mb1-Cre*$^{+}$ FoB and resting *Gclc*$^{fl/fl}$ MZB ($n = 3$ animals examined over three independent experiments). **c** Quantitation of total glucose in culture supernatants of *Gclc*$^{fl/fl}$ and *Gclc*$^{fl/fl}$ *Mb1-Cre*$^{+}$ FoB at 5 h post-stimulation with anti-IgM, CD40 ligand, and IL-4 ($n = 3$ animals examined over two independent experiments). **d** Left: Mass isotopomeric distribution (MID) of M3-lactate in *Gclc*$^{fl/fl}$ and *Gclc*$^{fl/fl}$ *Mb1-Cre*$^{+}$ FoB that were incubated with ^{13}C-glucose and assayed at 5 h post-activation with anti-IgM, CD40 ligand and IL-4. Right: quantitation of total lactate in culture supernatants of the cells in the left panel ($n = 3$ animals examined over three independent experiments). **e** Left: ratio of M3-lactate/M2-citrate in *Gclc*$^{fl/fl}$ and *Gclc*$^{fl/fl}$ *Mb1-Cre*$^{+}$ FoB that were incubated with ^{13}C-glucose and assayed at 5 h post-activation. Right: representative blot of Pdha1 protein from total cell lysis of resting *Gclc*$^{fl/fl}$ and *Gclc*$^{fl/fl}$ *Mb1-Cre*$^{+}$ FoB ($n = 3$ animals examined over three independent experiments). **f** Seahorse quantitation of mitochondria-derived ATP in resting *Gclc*$^{fl/fl}$ and *Gclc*$^{fl/fl}$ *Mb1-Cre*$^{+}$ FoB and *Gclc*$^{fl/fl}$ MZB ($n = 4$ animals examined over three independent experiments). **g** Left: Representative confocal microscopic image of mitochondrial morphology in resting *Gclc*$^{fl/fl}$ and *Gclc*$^{fl/fl}$ *Mb1-Cre*$^{+}$ FoB. Mitochondria are green (Tom20) and nuclei are blue (DAPI). Scale bars, 1 μm; Right: Quantitation of mitochondrial area (Tom20 area) per cell. Each dot represents a single cell ($n = 2$ animals examined over three independent experiments). **h** Mitochondrial mass quantitation [ratio between mitochondrial cytochrome c oxidase subunit I (CO I) and nuclear 18S ribosomal RNA] as determined by RT-qPCR of DNA from *Gclc*$^{fl/fl}$ and *Gclc*$^{fl/fl}$ *Mb1-Cre*$^{+}$ FoB ($n = 5$ animals examined over three independent experiments). **i** Left: representative TEM image of ultrastructural mitochondrial morphology in *Gclc*$^{fl/fl}$ and *Gclc*$^{fl/fl}$ *Mb1-Cre*$^{+}$ FoB. Scale bars, 300 nm. Insert digital magnification, 3.5×. Right: percentage of mitochondria with enlarged intercristae counted from 25 cells/genotype ($n = 3$ animals examined over 2 independent experiments). Each dot represents a single mitochondrium. **j** Representative flow-cytometry histogram (left) and quantitation (middle), and blot (right) of DRP1 in resting splenic *Gclc*$^{fl/fl}$ and *Gclc*$^{fl/fl}$ *Mb1-Cre*$^{+}$ FoB (gated as in Supplementary Fig. 1a) ($n = 3$ animals examined over two independent experiments). **k** Representative contour plot (left) and quantitation of derived $\Delta\Psi_m$ values (right) of Mitotracker dyes in *Gclc*$^{fl/fl}$ and *Gclc*$^{fl/fl}$ *Mb1-Cre*$^{+}$ FoB (gated as in Supplementary Fig. 1a) ($n = 4$ animals examined over three independent experiments). (**l**-**m**) Normalized ATP levels (RLU) (**l**) and percentage of Annexin V-expressing cells (**m**), in *Gclc*$^{fl/fl}$ and *Gclc*$^{fl/fl}$ *Mb1-Cre*$^{+}$ FoB after 5 h incubation with the indicated concentrations of 2-DG ($n = 3$ animals examined over two independent experiments). For all applicable figure panels, data are mean ± SD and each dot represents one single mouse, except for (**l**) and (**m**) where each dot represents the mean of triplicates. Significance (*P*) was calculated with unpaired t-test, except for **b**, **f** (one-way ANOVA), and **l**, **m** (2 way ANOVA). $^{*}P \le 0.05$; $^{**}P \le 0.01$; $^{***}P \le 0.001$; $^{****}P \le 0.0001$. MFI: mean fluorescence intensity.

GSH-deficiency altered protein expression independently of the overall activity of CIII and CIV.

These data indicate that GSH plays a role in sustaining the activities of CI and CII, and so of the overall ETC. In particular, our energetic steady-state analyses (Fig. 6f and Supplementary Fig. 6t) show that loss of GSH induces a partial uncoupling of ETC from OXPHOS, suggesting that *Gclc* function has a direct effect on the metabolic dependencies of FoB. GSH deficiency has a large negative impact on the mitochondrial respiration machinery, slowing down the TCA cycle at the ETC branch point (i.e. CII). Thus, we have identified a previously unknown role of GSH in B cells: maintaining mitochondrial ETC activity.

***Gclc* is required for T cell-independent and -dependent B cell immune responses**. Next, we aimed to understand how the metabolic perturbations caused by B cell-specific *Gclc* ablation impinge on immune responses and in particular how the impaired mitochondrial metabolism affects the antibody response. Therefore, we treated in vitro activated B6 FoB with various mitochondrial inhibitors and the Gclc inhibitor BSO and measured total immunoglobulins from the supernatants. After 4 days of activation with anti-IgM, CD40 ligand, and IL-4, we found that blocking of mitochondrial metabolism with mitochondrial inhibitors or blocking GSH synthesis by BSO had lowered antibody production of FoB in a dose-dependent manner (Fig. 7a). Thus, we reasoned that *Gclc* expression and GSH are needed upon activation of FoB. Indeed, levels of *Gclc* transcripts and reduced glutathione (GSH) increased upon activation B6 FoB in vitro (Fig. 7b), confirming our hypothesis.

Next, we studied B cell functions in vivo and measured antibody production. As expected, T cell-independent (TI) type II immunization with TNP-Ficoll to evaluate MZB-dependent antigen binding and early antibody production[86–88] confirmed the deficit of MZB in *Gclc*$^{fl/fl}$ *Mb1-Cre*$^{+}$ mice (Supplementary Fig. 7a, b). The absence of MZB-mediated immunity was substantiated by the lack of anti-TNP IgM at 7 days post-immunization with TNP-Ficoll in *Gclc*$^{fl/fl}$ *Mb1-Cre*$^{+}$ mice (Supplementary Fig. 7c). Furthermore, to study the long-term antibody response and FoB function, we infected *Gclc*$^{fl/fl}$ *Mb1-Cre*$^{+}$ mice with lymphocytic choriomeningitis virus Clone 13 (LCMV Cl13), which causes a chronic infection[89–93]. We monitored levels of antibodies against LCMV Cl13 glycoprotein 1 (Gp1) by ELISA at various time points after infection and observed that both early (IgM) and late (IgG) responses were undetectable in serum of infected mutant mice, in contrast to infected controls (Fig. 7c). Indeed, viremia in multiple tissues of infected *Gclc*$^{fl/fl}$ *Mb1-Cre*$^{+}$ animals was detected by 130 days post-infection (Fig. 7d), suggesting that *Gclc*$^{fl/fl}$ *Mb1-Cre*$^{+}$ animals are unable to efficiently control LCMV Cl13 replication.

The lack of LCMV-specific antibodies in our mutant mice could be caused by either a failure of the GC reaction or a defect in antibody production. To this extent, we detected a reduction in CD95^{+}GL-7^{+} GC B cells in *Gclc*$^{fl/fl}$ *Mb1-Cre*$^{+}$ mice compared to controls (Fig. 7e) at 12 days post-infection. These data imply that the absence of *Gclc* prevents B cells from establishing GC reactions, and therefore, hinders antibody production.

LCMV is a non-cytopathic virus that replicates slowly, which favors its persistence due to the failure of the host to mount an efficient cytotoxic T cell response[89,94]. In order to exclude any virus-dependent effects, we further investigated the T cell-dependent (TD) response in *Gclc*$^{fl/fl}$ *Mb1-Cre*$^{+}$ mice using a stronger, T cell-driven model of cytopathic viral infection. Vesicular stomatitis virus (VSV) first induces the antiviral activity of endogenously-produced interferon and then the generation of neutralizing antibodies to the VSV-G glycoprotein, measures that are critical for the control of this virus[95,96]. We infected *Gclc*$^{fl/fl}$ and *Gclc*$^{fl/fl}$ *Mb1-Cre*$^{+}$ mice with VSV and found that the mutants succumbed more rapidly to the infection than controls (Fig. 7f) and lacked neutralizing IgM and IgG antibodies against VSV-G glycoprotein (Fig. 7g). Accordingly, we found that in vitro activation and the costimulatory potential of GSH-deficient FoB was decreased compared to control cells upon 24h stimulation as indicated by lower expression of CD25, CD69, GL-7 and CD80/CD86 (Supplementary Fig. 7d). Consequently, low activation prevented proliferation in vitro (Supplementary Fig. 7e) and adds another layer that explains the lack of humoral response upon in vivo immunizations.

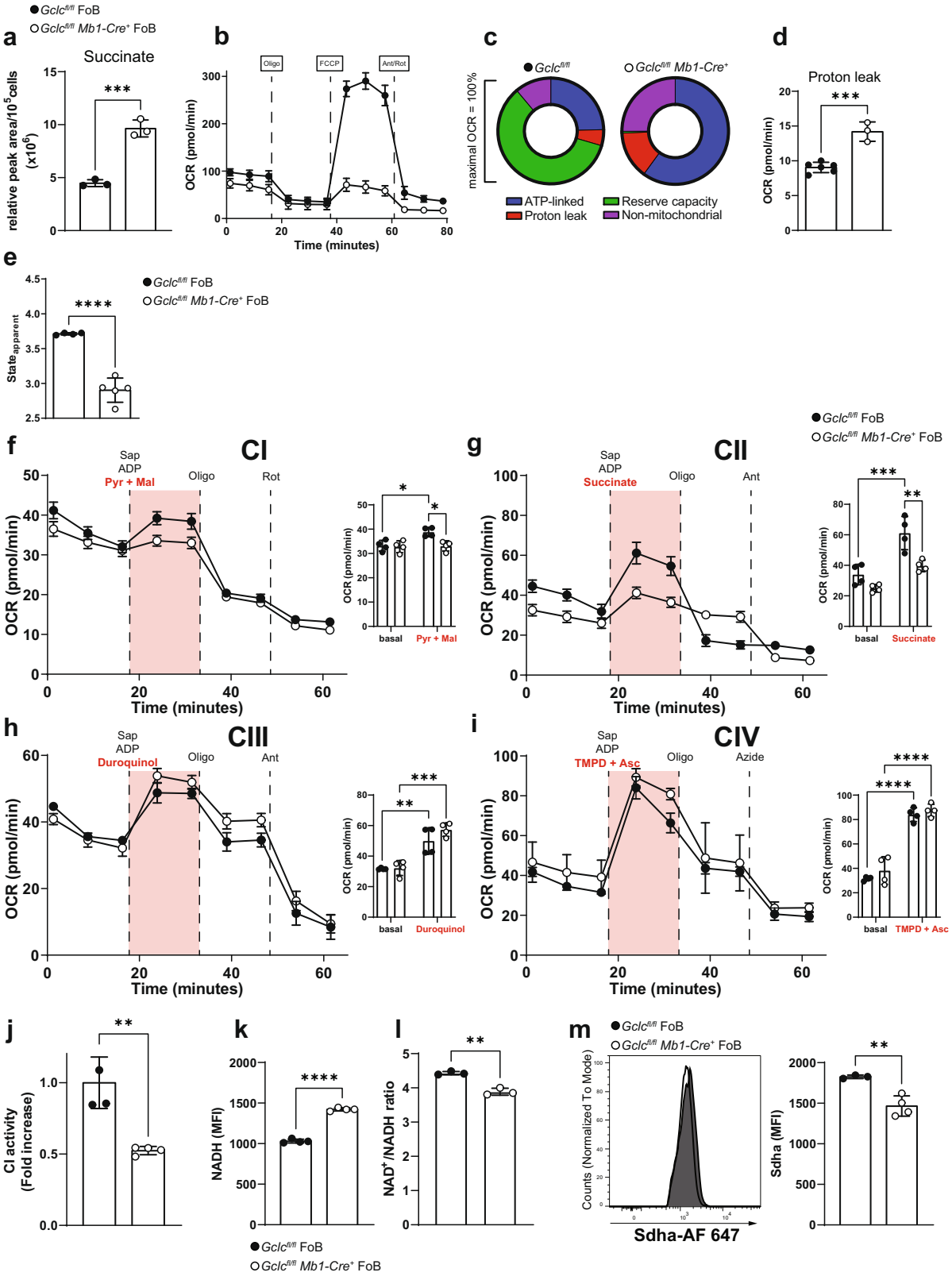

Collectively, these data confirm the functional absence of MZB in *Gclc*$^{fl/fl}$ *Mb1-Cre*$^{+}$ mice and demonstrate that *Gclc* is critical for FoB-mediated GC reactions and antibody-mediated immunity to infections. We have therefore established a link between a metabolic switch in response to GSH loss to the inability to mount antibody-mediated immune responses in vivo.

Discussion

ROS-induced signals regulate B cell activation and early metabolic reprogramming[97,98], and a flexible redox system controls B cell differentiation[31,99,100]. Compared to FoB, MZB were previously shown to use GSH through Gpx4 for protection from excessive lipid peroxidation[33], suggesting a differential dependency on redox

Fig. 6 Mitochondrial respiratory complex I and II are dysfunctional in *Gclc*-deficient FoB. a Quantitation of intracellular succinate level measured by LC-MS in resting $Gclc^{fl/fl}$ and $Gclc^{fl/fl}$ *Mb1-Cre*$^{+}$ FoB ($n = 3$ animals examined over two independent experiments). **b** Seahorse quantitation of OCR of resting $Gclc^{fl/fl}$ and $Gclc^{fl/fl}$ *Mb1-Cre*$^{+}$ FoB at the indicated time points ($n = 3$–4 animals examined over 5 independent experiments). **c** OCR components from (**b**) plotted as proportions of maximal OCR (after FCCP treatment) ($n = 3$–4 animals examined over five independent experiments). **d** Quantitation of the contribution of proton leakage from (**b**) as determined by Ant/Rot treatment ($n = 3$–4 animals examined over five independent experiments). **e** Respiratory status of $Gclc^{fl/fl}$ and $Gclc^{fl/fl}$ *Mb1-Cre*$^{+}$ FoB in (**b**) displayed as $state_{apparent}$ ($n = 3$–4 animals examined over five independent experiments). **f–i** OCR of $Gclc^{fl/fl}$ and $Gclc^{fl/fl}$ *Mb1-Cre*$^{+}$ FoB sequentially treated with saponin (Sap), adenosine diphosphate (ADP), and the indicated substrates (red) for ETC complexes CI (**f**), CII (**g**), CIII (**h**) and CIV (**i**), as indicated. Side bar graphs show basal and substrate-induced (red) OCR. Oligo: oligomycin A; Rot: rotenone; Ant: antimycin A; TMPD: N,N,N′,N′-Tetramethyl-p-phenylenediamine; Asc: ascorbate; Pyr: pyruvate; Mal: malate ($n = 4$ animals examined over two independent experiments). **j** Quantitation of relative activity of CI in $Gclc^{fl/fl}$ and $Gclc^{fl/fl}$ *Mb1-Cre*$^{+}$ FoB as measured by colorimetric assay ($n = 3$–4 animals examined over two independent experiments). **k** Quantitation of NADH autofluorescence in $Gclc^{fl/fl}$ and $Gclc^{fl/fl}$ *Mb1-Cre*$^{+}$ FoB (gated as in Supplementary Fig. 1a) as measured by FACS ($n = 4$ animals examined over three independent experiments). **l** CI activity in $Gclc^{fl/fl}$ and $Gclc^{fl/fl}$ *Mb1-Cre*$^{+}$ FoB expressed as the ratio of NAD^{+} (CI substrate) to NADH (CI product), as measured by colorimetric assay ($n = 3$–4 animals examined over two independent experiments). **m** Representative histogram (left) and quantitation (right) of immunostaining to detect the expression of succinate dehydrogenase a (Sdha, the major subunit of CII) in $Gclc^{fl/fl}$ and $Gclc^{fl/fl}$ *Mb1-Cre*$^{+}$ FoB (gated as in Supplementary Fig. 1a) ($n = 3$ animals examined over three independent experiments). For all applicable figure panels, data are mean ± SD and each dot represents one single mouse, except for (**b**) and (**f**)–(**i**) where each dot represents the mean of 3–5 mice. Significance (P) was calculated with unpaired t-test, except for **f–i** (2 way ANOVA). $^{**}P \leq 0.01$; $^{***}P \leq 0.001$; $^{****}P \leq 0.0001$.

functions downstream of GSH synthesis. However, the impact of GSH itself, its role in B cell metabolism and B cell responses has so far been elusive. The present study has uncovered the contribution of GSH to B cell homeostasis and function. In particular, we have shown that genetic deletion of *Gclc*, and therefore loss of GSH, in B cells has important and subset-specific effects on FoB and MZB (Supplementary Fig. 7f). Our data further indicate that GSH acts as a rheostat to regulate metabolism, mitochondrial function and ETC activity in B cells.

The intracellular environment of MZB operates at a higher oxidative level compared to that in FoB. In MZB, higher levels of GSH are necessary to sustain their homeostasis and function (i.e. antibody secretion). In contrast, FoB exhibit lower intracellular ROS and maintain a metabolic setup that is distinct from that in MZB. Upon genetic deletion of *Gclc*, MZB differentiation is halted because the GSH-dependent buffering capacity is lost. Notably, FoB persist in *Gclc*-deficient mice and are characterized by increased ROS and acquire characteristics of *Gclc*-sufficient MZB. This indicates an interesting GSH-dependent threshold regulation that is important for the subset-specific functions of B cells and a differential redox-dependent regulation of metabolic activities in these cells. These metabolic states appear to be related to the divergent functions of FoB and MZB, which have been documented in numerous studies[7–14]. In particular, the differences between FoB and MZB in recirculation properties[49], the exposure to oxygen levels, and in degree of activation upon stimulation[48], have raised interest in their metabolic dependencies. MZB have the potential to self-renew[18] and are activated more quickly than FoB[7,8], properties consistent with a requirement for glycolytic reprogramming in activated B cells[101].

The development of FoB in B cell-specific *Gclc*-deficient mice can be linked to the metabolic quiescence which characterizes wild-type FoB[38]. This basal metabolic dormancy might facilitate *Gclc*-deficient FoB to sustain the deficiency of GSH, and therefore, increased oxidative stress. Thus, when depleted of GSH, FoB experience a change in their redox buffering potential which results in a metabolic adaptation (i.e. lower mitochondrial activity but increased glycolysis) that partially mirrors the metabolic properties of wild-type MZB. In accordance with this observation, we demonstrated that resting wild-type MZB show increased glucose uptake and glycolysis compared to resting FoB. Resting wild-type FoB are instead characterized by downregulation of mTORC1 and its downstream targets[37–39], which is indicative of metabolic quiescence. Strikingly, *Gclc* ablation increased mTORC1 activation in FoB to a level similar to that found in MZB. However, mTORC1 activation only promoted metabolic reprogramming of *Gclc*-deficient FoB but was not sufficient to ensure antibody production, in contrast to B cell cells isolated from tuberous sclerosis complex 1 (TSC1)-deficient mice[102].

In immune cells, upregulation of metabolic pathways upon activation is necessary to generate ATP to support functions such as antibody production[101]. However, this increase in metabolic activity is also associated with elevated ROS, which are known modulators of the functions of immune cells[32,41,43,44,103]. mtROS are generated by inefficient electron transfer through the ETC[104], and defects in the ETC have been shown to increase mtROS even further[105]. Although cells benefit from low or moderate ROS levels, high ROS impose irreversible oxidative damage and so efficient ROS removal is necessary to maintain homeostasis[21,106] and controlled cellular activation.

Balanced mtROS are critical for the correct function of the redox-sensitive ETC proteins, which are susceptible to inactivation by these reactive molecules[107–111]. In our study, we found that activities of ETC CI and CII were reduced in GSH-deficient FoB. However, protein levels of CII and CIV were also affected, thus implying that other modifications (i.e. s-glutathionylation) or factors, such as active site availability, substrate availability, and kinetic of the reaction might play a role in the stability of these complexes. Moreover, these multi-protein complexes are continuously exposed to a GSH-depleted environment in *Gclc*-deficient FoB, which might alter protein folding or their targeting to the mitochondria. In our study, transient ROS-scavenging was not able to revert these modifications and to reinstate the functionality of these cells. This might be due to the chronic exposure to high ROS concentrations of these cells. Indeed, chronic ROS can cause protein oxidation of methionine and cysteine residues[112,113], which in the absence of GSH becomes permanent and might decrease irreversibly CI and CII functionality. Another possible explanation why ROS-scavenging by antioxidants did not restore the functionality of *Gclc*-deficient B cells is the altered redox state caused by this treatment. Thus, antioxidants could expose these cells to reductive stress, which is also associated with cellular dysfunctionality[114,115]. We speculate that the redox state of B cells must be very precisely balanced to ensure proper functionality of these cells. Most interestingly, this is very important for B cells, while in our previous studies we could restore functionality of *Gclc*-deficient T cells by ROS-scavenging with N-acetyl cysteine and GSH[43,44]. However, we cannot rule out ROS-independent functions of GSH in B cells that contribute to our observed effects. For example GSH has been shown to be important for the

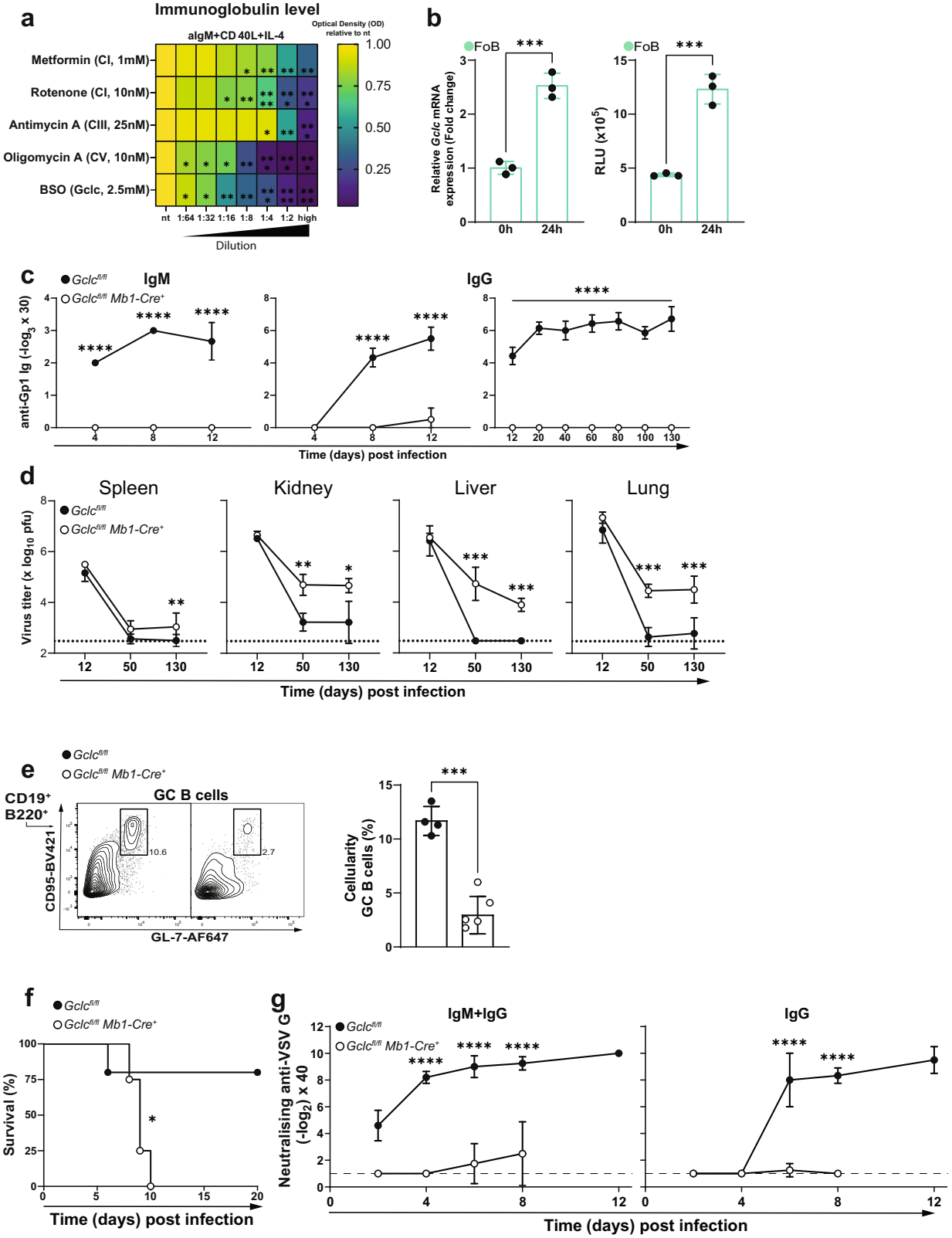

regulation of cellular labile copper pools[116]. These labile copper pools are important for the assembly of iron-sulfur (FeS) clusters, which are directly linked to mitochondrial function[117,118]. Moreover, GSH-independent roles of Gclc associated with its direct product—γ-glutamylcysteine (γ-GluCys)—might influence the downstream regulation of biosynthetic pathways of amino acids (and/or their transport)[119] in MZB and FoB.

CI activity, in particular, requires adequate levels of reduced GSH in the mitochondria for its function[120,121]. GSH-dependent mitochondrial functions are influenced by changes in levels of cytosolic GSH because GSH is synthesized in the cytosol and must be imported into the mitochondria to exert its function as antioxidant[122,123]. In addition to decreased CI, we found compromised CII activity in *Gclc*-deficient B cells. Reduced CII

Fig. 7 *Gclc* deficiency impairs B cell-mediated immune responses in vivo. a Heatmap showing relative expression of immunoglobulin level of 4d activated B6 FoB with increasing concentration of mitochondrial inhibitors and BSO. High concentration shown in brackets. Statistics are relative to nt. **b** Left: RT-qPCR of *Gclc* mRNA in B6 FoB at 0 or 24h after activation in vitro with anti-IgM, CD40 ligand and IL-4. Right: Luminescence-based quantitation of intracellular ROS in resting and 24h stimulated B6 FoB ($n = 3$ animals examined over two independent experiments). **c** Titers of IgM (left) and IgG (middle and right) in serum of LCMV Cl13-infected $Gclc^{fl/fl}$ and $Gclc^{fl/fl}$ *Mb1-Cre*$^{+}$ mice as measured by ELISA at the indicated time points ($n = 7$ animals examined over 3–5 independent experiments). **d** LCMV Cl13 viral titers in the indicated organs of LCMV Cl13-infected $Gclc^{fl/fl}$ and $Gclc^{fl/fl}$ *Mb1-Cre*$^{+}$ mice as measured by plaque assay at the indicated time points ($n = 7$ animals examined over 3–5 independent experiments). **e** Representative contour plot (left) and quantitation (right) of GC B cells (gated as in Supplementary Fig. 1a) in spleens of $Gclc^{fl/fl}$ and $Gclc^{fl/fl}$ *Mb1-Cre*$^{+}$ mice as measured by FACS on day 12 post-LCMV Cl13 infection ($n = 3$ animals examined over two independent experiments). **f** Survival curve of $Gclc^{fl/fl}$ and $Gclc^{fl/fl}$ *Mb1-Cre*$^{+}$ mice upon infection with VSV ($n = 7$ animals examined over two independent experiments). **g** Titers of neutralizing IgM and/or IgG antibodies against VSV-G protein in serum of $Gclc^{fl/fl}$ and $Gclc^{fl/fl}$ *Mb1-Cre*$^{+}$ mice as measured by ELISA at the indicated time points ($n = 7$ animals examined over two independent experiments). Dotted/dashed lines represent the detection limit of the assay. For all applicable figure panels, data are mean ± SD and each dot represents one single mouse, except for (**a**), (**c**), (**d**), (**f**) and (**g**), where each panel or dot represents the mean of 3–7 mice. In contour plots, numbers represent percentages of the cells gated. Significance (*P*) was calculated with 2 way ANOVA, except for **b** and **e** (unpaired t-test) and **f** (log-rank test). $^{*}P \leq 0.5$; $^{**}P \leq 0.01$; $^{***}P \leq 0.001$; $^{****}P \leq 0.0001$.

activity has consequences for central carbon metabolism because CII is involved in the conversion of succinate to fumarate within the TCA cycle[73]. Our metabolic analyses showed that *Gclc* deficiency led to an accumulation of succinate, indicating a block in the TCA cycle. Interestingly, we found that succinate accumulated only in *Gclc*-deficient B cells and not in *Gclc*-deficient effector T cells nor Tregs[43,44]. This result identifies an unexpected B cell-specific function of GSH in the regulation of the TCA cycle and the ETC.

Based on the results above, we suggest that GSH activity is essential to preserve ETC integrity in MZB at steady state. Because of their lower activation threshold at baseline[7], MZB need mitochondrial GSH for their correct metabolic reprogramming and therefore *Gclc*-ablation leads to MZB loss. On the other hand, FoB rely on OXPHOS to a lower extent: *Gclc*-deficient FoB lose CI and CII functionality, but these cells increase glycolysis to replenish their ATP pool to the extent that they persist in $Gclc^{fl/fl}$ *Mb1 Cre*$^{+}$ hosts. Similarly, alterations of redox metabolism have previously been shown to have negative effects on MZB but not on FoB[103,124]. These findings support the notion that differential redox capacity exists in different B cell subsets, and suggest that steady-state MZB require greater redox buffering capacity. Our data have revealed that MZB and FoB rely on activities that differ in their dependence on GSH. Accordingly, deletion of *Gclc* in B cells leads to a specific loss of MZB content but not FoB. We have shown that GSH modulates redox functions in steady-state B cells in a subset-specific manner, adding a new element of complexity to the distinct homeostatic properties of FoB and MZB[4,48,50]. However, we cannot exclude that commitment of the FoB compartment and the reflection of wild-type MZB-like properties by FoB in B cell-specific *Gclc*-deficient hosts, might be the consequence of a physiological attempt to fill the empty MZB compartment.

Furthermore, the importance of GSH to the B cell lineage is not limited to steady-state subset-specific roles. Once FoB are activated, their demand for GSH increases to cope with accumulating ROS. Our data showed that, despite the higher mTORC1 signaling in *Gclc*-deficient FoB cells, these cells dampened antibody production and could not ensure GC formation following activation in vivo and antibody production in vitro. In a previous study, enhanced mTORC1 signaling was found to be dispensable for GC formation and serum antibody responses[102]. Thus, our data further indicate that the increased mTORC1 signaling is a consequence of GSH depletion, but it is not sufficient to sustain humoral immunity. Instead, it reflects the ability of FoB to metabolically adapt to oxidative stress.

In line, intracellular GSH levels in B cells of HIV-1-infected individuals showed a tendency to be decreased compared to uninfected donors[30,125,126], supporting the link between GSH and the regulation of B cell activation in human infections. The effect of GSH-deficit was exacerbated upon VSV infection, resulting in the drastically reduced survival of infected $Gclc^{fl/fl}$ *Mb1-Cre*$^{+}$ mice. These results highlight the important and non-redundant role of GSH in B cell humoral immunity in vivo, but does not exclude impairment of other B cell functions such as antigen presentation or cytokine secretion.

In conclusion, we have shown that GSH is critical for B cell homeostasis and regulates metabolic pathways of MZB and FoB. GSH regulates the TCA cycle and ETC activity in a B cell-specific manner that stands in stark contrast to its functions in T cells. Our work highlights B cell-specific alterations that offer novel insights for the understanding of the role of GSH in the regulation of B cells function and defects during disease, such as those caused by viral infections.

Methods

Mice. Wild-type C57BL/6J (B6) were purchased from Charles River (stock number JAX 000664). $Gclc^{fl/fl}$ mice were described previously[127] and were crossed to *Mb1-Cre*$^{+}$ expressing mice[46] to obtain the $Gclc^{fl/fl}$*Mb1-cre* strain. The mice were housed and bred under specific pathogen-free conditions at the Luxembourg Institute of Health (LIH) and the BTA facility of the University of Luxembourg. Female or male age-matched mice (7–12 weeks old) were used for all experiments (unless otherwise stated) and euthanasia was performed by cervical dislocation. All protocols were conducted and approved in the accordance to the LIH Animal Welfare Structure guidelines.

Cryosections staining and microscopy. Hematoxylin and eosin (H&E) and immunofluorescence of tissues were performed on snap-frozen tissue samples in O.C.T. (Sakura 4583). For H&E staining sections were processed following standard laboratory procedures. For immunofluorescence, cryosections were dried for 2 h at RT, fixed in pure acetone for 10 min and blocked with PBS 10% FCS for 30 min at RT. After washing in PBS, primary antibodies (IgM-PE BioLegend 406507, IgD-APC BioLegend 405713, MARCO Santa Cruz sc-65353/ anti-rat PE Abcam ab97058 and Siglec-1 Biolegend 142417) diluted in PBS 10% FCS were incubated overnight at 4 °C. DAPI mounting medium (SouthernBiotech 0100-20) was used to counterstain the nucleus. For Tom20 staining (Abcam ab186734), 10^6 FACS-sorted FoB were washed in PBS and fixed in fix/perm buffer (BD 554714) for 20 min at 4 °C. Cells were washed with perm/wash buffer (BD 554714) and fixed in fix/perm buffer. After 30 min at 4 °C, cells were washed in perm/wash buffer and resuspended with secondary Ab anti-Rabbit IgG FITC (Fisher Scientific 15303926) or PE (CST 79408 S). After the last wash, cells were resuspended in DAPI mounting medium and seeded on Cell-Tak (Fisher Scientific 10317081) coated glass slides. Tissues were visualized with ZEISS Axio Observer and cells with ZEISS LSM 880. Images were analyzed with ZEISS ZEN Blue and Fiji softwares. Nuclear and mitochondrial area were calculated using the Analyze particle function in Fiji.

For ultrastructural microscopy, $10–20 \times 10^6$ FoB were fixed in complete RPMI medium + 2.5% glutaraldehyde (EMS 16220) for 1 h at RT. After spinning, supernatant was removed and pellet was resuspended in 0.1 M sodium cacodylate buffer (pH 7,4) + 2.5% glutaraldehyde and stored overnight at 4 °C. Cells were centrifuged and resuspended in 0.1 M sodium cacodylate buffer and post-fixed for 1 h with 1% osmium + 0.1 M sodium cacodylate buffer, then dehydrated and embedded in Agar 100 resin. Pelleted cells were sectioned in a RMC Boeckeler

ultramicrotome using a Diatome diamond knife at a thickness setting of 60 nm. Sections were stained with 2% uranyl acetate, and lead citrate. The sections were examined using a ZEISS GEMINI 300 at 30 kV with the STEM detector. For identification of dilated intercristae space, mitochondria were counted in 25 cells per condition. Based on mitochondria from *Gclc*$^{fl/fl}$ FoB (measured intercristae space 60 nm), a cutoff of >100 nm was set for identification of dilated intercristae space.

T-dependent B cell immunization (LCMV Cl13 and VSV). Mice were intravenously infected with 2×10^6 pfu of LCMV Cl13. Blood was collected at the indicated time points for antibody detection in the serum. At the endpoint, mice were euthanized and blood, spleen, kidney, liver and lung were collected and snap-frozen until further analysis.

VSV, Indiana strain (VSV-IND, Mudd-Summers isolate), was originally obtained from D. Kolakofsky (University of Geneva, Geneva, Switzerland). Mice were infected with 10^5 PFU of VSV. Upon appearance of clinical signs of VSV replication in the central nervous system, such as paralysis, mice were removed from the experiment.

T-independent B cell immunization (TNP-Ficoll). To study Ag-trapping by MZB, mice were injected i.v. with 100 µg TNP-Ficoll FITC (Biosearch Technologies F-1300F) and 30 min later tissues were analyzed with flow cytometry (splenocytes were stained with surface markers for the detection of FoB and MZB, with the addition of biotinylated anti-TNP (BD Pharmingen 554055) + Streptavidin-APC (Biolegend 405207 for TNP detection) or snap-frozen for immunofluorescence microscopy in OCT (Sakura 4583). To measure the early IgM response, the same dose of TNP-Ficoll (Biosearch Technologies F-1300-100) was administered i.p., and blood was collected one day previous injection and 3, 5, and 7 days post injection.

Single-cell sequencing (CITE-seq): preparation, pre-processing, and analysis. For CITE-seq labelling, a total of 2 million cells/genotype were FACS sorted, counted, isolated, and spun down. The cell pellet was resuspended and incubated for 30 min on ice with 25 µL of staining mix in PBS containing 0.04% BSA, TruStain FcX Block (BioLegend 101320), and the mouse cell surface protein antibody panel containing the following oligo-conjugated anti-mouse antibodies (TotalSeq-A BioLegend) diluted 1:500: CD23 (Cat. Number 101635), IgD (Cat. Number 405745), CD1d (Cat. Number 123529), CD21/CD35 (Cat. Number 123427), IgM (Cat. Number 406535).

Sorted single-cell suspensions were resuspended at an estimated final concentration of 1000 cells/µl and loaded on a Chromium GemCode Single Cell Instrument (10x Genomics) to generate single-cell gel beads-in-emulsion (GEM). Biological replicates ($n = 4$ for each group) were multiplexed using TotalSeq-A Cell Hashing Antibodies. The scRNA/CITE-seq libraries were prepared using the GemCode Single Cell 3′ Gel Bead and Library kit, version 3 (10x Genomics 1000128) according to the manufacturer's instructions with the addition of amplification primer (3 nM, 5′CCTTGGCACCCGAGAATT*C*C) during cDNA amplification to enrich the TotalSeq-A cell surface protein oligos. Sequencing libraries were loaded on an Illumina HiSeq4000 flow cell at VIB Nucleomics core with sequencing settings according to the recommendations of 10x Genomics, pooled in a 85:15 ratio for the gene expression and antibody-derived libraries, respectively. The Cell Ranger pipeline (10x Genomics version 3.1.0) was used to perform sample demultiplexing and to generate FASTQ files for read 1, read 2, and the i7 sample index for the gene expression and cell surface protein libraries. Read 2 of the gene expression libraries was mapped to the reference genome (mouse mm10, v3.0.0) using STAR. For cellular identification and clustering of the gene-barcode matrix was passed to the R (version 4.04) package Seurat (v. 4.0)[128] for all downstream analyses. Analysis was conducted on cells that expressed a minimum of 800 genes, of which less than 15% was of mitochondrial origin. Count data were derived through the SCTransform function. To identify FoB and MZB, Antibody-derived signals (ADT) were used in combination with the SCINA algorithm[51] with the following signatures: CD23-ADT, IgD-ADT for FoB; CD1d-ADT, CD21-CD35-ADT, IgM-ADT for MZB. For principal component analysis (PCA), counts of each cell group/mouse for each genotype where extracted and analyzed using DESeq2[129]. Cluster-based marker identification and differential expression were performed using Seurat's FindMarkers/DESeq2 with logfc.threshold = 0.2 comparing specific groups (i.e. MZB vs. FoB for *Gclc*$^{fl/fl}$, or FoB *Gclc*$^{fl/fl}$ *Mb1 Cre*$^{+}$ vs. FoB *Gclc*$^{fl/fl}$). Visualization of differentially expressed genes was done with EnhancedVolcano[130]. For gene ontology (GO) analysis, the Seurat's FindMarkers output for the specified groups was used to plot gene ontology terms with the barcodeplot functions from limma[131]. For GSEA analyses, the fgsea package was used[132].

scRNA-seq data were analyzed as above and the gene expression matrix of 156 cells/group (MZB and FoB from *Gclc*$^{fl/fl}$ mice) or 1700 FoB/genotype (i.e. *Gclc*$^{fl/fl}$ or *Gclc*$^{fl/fl}$ *Mb1 Cre*$^{+}$ mice) was used as input for the Compass algorithm[70,71]. Downstream analysis was conducted with the compassR package and differential metabolic states were determined with a Wilcoxon Rank Sum Test on the Compass reactions.

Flow cytometry and sorting. For surface staining cells were incubated at 4–8 °C, in the dark with fluorochrome-conjugated CD19, CD23, CD21-CD35 or CD35, IgD, IgM, CD1d, CD24, CD93, CD95, and GL-7 diluted 1:200 (refer to Supplementary Data 4 for details). The antibody mix was washed from the cells after 20–30 min. Samples from in vivo LCMV experiments were fixed for 10 min at RT in a volume of at least 100 µL 2% formaldehyde (FA) after staining. All antibodies dilutions are made from stock solutions prepared as per the manufacturer's instructions, where applicable.

For intracellular staining of phospho(p)-mTOR (Fisher Scientific 15549836) and p-S6 (eBioscience 15528216), cells were first stained for extracellular markers, fixed in 2% FA at RT, and stained for p-mTOR and p-S6 diluted 1:200 in saponin 5 µg/mL. p-eIF4E staining was done using mouse anti-elF4E (pS209) (BD 560229) diluted 1:100 and cells were fixed with BD Cytofix/Perm and intracellular staining was done in BD Perm (BD 554714). For intracellular staining of hexokinase-1, cells were stained for extracellular markers, fixed in 4% FA at RT, and stained with Anti-Hexokinase 1 (Abcam ab184818) diluted 1:100 in PBS 0.1% Tween-20 at RT. For viability, 7-aminoactinomycin D (7AAD) (Thermo fisher A1310) or Zombie NIR (BioLegend 423106) diluted 1:3000 was stained concurrently with antibodies in all flow cytometry assays. For glucose uptake and GLUT-1 surface detection splenocytes were washed with glucose-free RPMI medium (Lonza BE12-752F). Pellet was resuspended in glucose-free RPMI medium supplemented with 2-NBDG (Thermo Fisher N13195) at 50 µM and incubated for 30 min at 37 °C. Anti-GLUT1 (Abcam ab195359) diluted 1:200 was used and expression was measured on FoB gated on total splenocytes as described above. For detection of DRP1, cells were washed and fixed in 4% FA at RT after surface staining. Then, cells were washed and stained in Triton 0.1% containing DRP1 antibody (Abcam ab184247) diluted 1:100. After 30 min at RT, cells were washed and incubated with secondary Ab anti-Rabbit IgG FITC (Fisher Scientific 15303926).

Sdha detection was performed on FoB from total spleen with the MitoBiogenesis Flow Cytometry Kit (Abcam ab168540) following the manufacturer's instructions. Lipid peroxidation was measured with using Bodipy 581/591 C11 (Fisher Scientific D3861) at 1 µM following the manufacturer's protocol. For quantitation of mitochondrial potential and mass of FoB and MZB, splenocytes were stained with 100 nM MitoTracker Deep Red FM and 10 nM MitoTracker Green FM (Fisher Scientific 15754272 and 15784272) as follows. Splenocytes were washed with warm RPMI 1640, stained at 37 °C for 30 min with Abs diluted in RPMI 1640, and washed with PBS. To detect intracellular ROS, cells were incubated with dichlorofluorescein diacetate (Carboxy-H2DCFDA; Thermo Fisher 11500146) diluted 1:5000 or MitoSOX Red (Thermo Fisher 11579096) diluted 1:2500 as follows. Splenocytes were washed with warm RPMI 1640, stained for surface markers detection at 37 °C for 30 min in RPMI 1640, and washed with PBS. Detection of cellular thiols was done using monobromobimane (MBB, ThermoFisher M1378) added 10 min before acquisition at 50 µM. Mitochondrial thiols were detected by measuring the MFI of MBB in CD19^{-} Tom20^{+} (Abcam ab186734) isolated mitochondria from the enriched FoB and MZB fractions. NADH levels were measured in FoB from splenocytes, and were measured as mean autofluorescence intensity upon excitation with UV laser and recorded with a band pass filter BP465/30[133,134]. ER and Golgi apparatus were stained using ER-Tracker Red (Fisher Scientific 11584746) diluted 1:2000 and anti-Giantin (BioLegend 908701)[135] diluted 1:500. Briefly, after surface staining, cells were fixed in FA and permeabilized with Triton 0.1%. ER and Golgi stain were performed in Triton 0.1%, 20 min, RT. Annexin V^{+} cells were detected upon 5 h treatment with 2-Deoxy-D-glucose. Briefly, FoB were washed and stained with Annexin binding buffer (Invitrogen BMS500BB). Cells were stained with CD19, 7-AAD, and anti-Annexin V-PE diluted 1:200 (BioLegend, 640908) for 20 min, RT.

Cell counts (cellularity) was determined as follows for each individual tube: 10^4 unlabeled beads (BD Calibrite 3, 340486) were added prior to acquisition. Beads were distinguished from lymphocytes through FSC-A/SSC-A profile. Beads count and the cells of interest (i.e. total live CD19^{+} cells) were retrieved with FlowJo v10.6.1. Cell counts of the population of interest was normalized by the beads counts acquired. The following calculation was used:

$$\text{Cellularity (counts)} = \frac{\text{Acquired number of cells of interest}}{\text{acquired total live lymphocytes}} \times \frac{10^4}{\text{acquired number of beads}}$$

FoB cell sorting for confocal microscopy and TEM was performed by MACS pre-enrichment with B cell isolation kit (Miltenyi Biotech 130-090-862). Untouched B cells were then stained with CD19, CD21/CD35, and CD23. Live CD23^{high}CD21/35^{low} FoB cells were FACS-sorted using Aria IIu (BD). For CITE-seq, 10^4 B cells were identified as CD11b^{-}TCR-beta^{-}CD19^{+}B220^{+} and FACS-sorted using Aria II (BD). Flow cytometry was performed using a BD Fortessa instrument (BD) or NovoCyte Quanteon and data were analyzed using FlowJo v10.6.1 software (Tree Star).

Cell culture and assays. Total B cells and FoB/MZB were magnetically enriched from mouse spleen using a B cell or MZ and FO B Cell Isolation Kit, respectively (Miltenyi Biotec 130-090-862 and 130-100-366) as per manufacturer's protocol. Mitochondria were isolated (Miltenyi Biotec 130-096-946) from 10×10^6 pooled cells from 2 to 3 mice following the manufacturer's protocol. Most of the experiments were performed with MACS-sorted FoB cells, unless clearly specified. Cells were seeded in complete medium consisting of RPMI-1640 supplemented with 10% FCS (Sigma), 1% Penicillin/Streptomycin (GIBCO), 1% L-Glutamine (Sigma),

and 55 mM β-mercaptoethanol (GIBCO). Cells were seeded in 96-well plates at 2×10^5 cells/well unless otherwise indicated. FoB were activated with 5 µg/mL anti-IgM (Jackson Immunoresearch 715-006-020), 50 ng/mL CD40 ligand (Bio-techne 8230-CL-050) and 10 ng/mL IL-4 (Miltenyi Biotec 130-097-757). Reduced GSH was purchased from Sigma (G4251). MZB were stimulated with 1ug/mL of LPS (Sigma L2630). To inhibit glycolysis, 2-Deoxy-D-glucose (2-DG, Sigma D8375) or galactose (D-(+)-Galactose, Sigma G0750) was used at the indicated concentration. The GSH/GSSG content and ATP levels of $0.5–1 \times 10^5$ cells/well were measured by a luminescent-based assay (Promega V6612 for GSH/GSSG and Promega G7571 or Sigma MAK135 for ATP) following the manufacturer's protocol. Complex I activity was measured with the Complex I Enzyme Activity Kit (Abcam ab109721). To inhibit mitochondrial metabolism and GSH synthesis, the following chemicals were purchased from Sigma: metformin, rotenone, antimycin A, oligomycin A and BSO.

To measure PIP_3, FoB were stimulated with 5 µg/mL anti-IgM (Jackson Immunoresearch 715-006-020) for the indicated time points, then fixed in 2% FA and permeabilized with 0.1% saponin. Biotinylated Anti-PtdIns(3,4,5)P3 IgG (echelon biosciences Z-B345b) and Invitrogen eBioscience Streptavidin-PE (Fisher scientific 11500607) were used for detection.

ELISAs. ELISA assays were performed in 96-well NUNC plates (Fisher Scientific 11371605) unless otherwise indicated. Readings were recorded with SpectraMax ELISA plate reader instrument (Molecular Devices). Washes were done with PBS Tween 0.05% (PBS-T).

Detection of CXCL13 (biotechne MCX130) and S1P (tebu-bio K-1900-1ea) were measured in the serum following the manufacturer's recommendation. For total Ig detection from cell supernatants, plates were coated at 4 °C overnight with goat Anti-Mouse Ig (Southern Biotech 1010-01) at 1 µg/mL. After tipping off the supernatant, plates were washed, blotted on paper and blocked with PBS 1% BSA for 30 min at RT. After tipping off the supernatant, diluted supernatants were incubated for 2 hr at RT. After washing, 50 µL/well of HRP-conjugated detection antibody anti-Ig-HRP (Cytiva NA9310-1ML) was added for 1 h at RT. Plates were developed by adding 50 µL of RT TMB solution (ThermoFisher 12750000). Reaction was stopped by adding 2N H_2SO_4 and absorbance was recorded at 450 nm.

For TNP-specific antibody detection, plates were coated at 4 °C overnight with $NP_{(7)}$-BSA (Biosearch Technologies N-5050L) at 1 µg/mL. After tipping off the supernatant, plates were washed, blotted on paper, and blocked with PBS 1% BSA for 30 min at RT. After tipping off the supernatant, diluted serum samples were incubated for 2 h at RT. After washing, 50 µL/well of HRP-conjugated detection antibody (anti-IgM-HRP Sigma A8786) was added for 1 h at RT. Plates were developed by adding 50 µL of RT TMB solution (ThermoFisher 12750000). Reaction was stopped by adding 2N H_2SO_4 and absorbance was recorded at 450 nm.

Analysis of IgM and IgG anti-LCMV-Gp specific antibodies was performed as previously described[93]. Briefly, plates were coated overnight with anti-human Fc (Jackson ImmunoResearch Laboratories 109-001-008), blocked for 2 h with PBS 2% BSA at RT, and incubated overnight at 4 °C with recombinant Gp1-Fc protein derived from HEK293 cells transfected with LCMV glycoprotein vector. Diluted sera of LCMV Cl13 infected mice were serially diluted and incubated for 90 min at RT. Plates were washed with PBS-T and anti-mouse IgM-HRP or anti-mouse IgG-HRP (Sigma A8786 and A3673) was used for detection. Plates were washed and a green color reaction was produced with 2,2′azino-bis(3-ethylbenzothiazoline-6-sulfonate) (ABST, Sigma 10102946001) diluted in 0.1 M NaH_2PO_4 (pH = 4). Plates were read at 405 nm and titers were defined as the $\log_3$ serum dilution two-fold above background.

RNA, DNA isolation and PCR. RNA was isolated using NucleoSpin RNA Kit (Macherey-Nagel 740955250). RT-qPCR was carried out using Luna Universal One-Step RT-qPCR Kit (Bioké E3005E) with the following primers: *Gclc* forward (F) GGCTCTCTGCACCATCACTT and reverse (R) GTTAGAGTACCGAAGCGGGG; *Tbp* F GAAGAACAATCCAGACTAGCAGCA and R CCTTATAGGGAACTTCA CATCACAG; *Cox1* F GCCCCAGATATAGCATTCCC and R GTTCATCCTGTTC CTGCTCC; *18S* F TAGAGGGACAAGTGGCGTTC and R CGCTGAGCCAGTCA GTGT.

Reactions were run on a CFX384 instrument (Bio-Rad). Data were normalized to *Tbp* and analyzed using the ΔΔCt method as previously described[136]. DNA isolation from MACS-sorted FoB and MZB was performed with NucleoSpin 96 Tissue kit (Macherey-Nagel 740454.4). RT-qPCR was carried out using Fast SYBR Green Master Mix (Thermo Fisher 4385610) and the mitochondrial/nuclear DNA ratio was derived as described previously[137].

Immunoblot analysis. For detection of Gclc (Santa Cruz Biotechnology sc-390811), Pdha-1 (Abcam ab168379), DRP1 (Abcam ab184247), eIF4E (Abcam ab33766), p-eIF4E (Abcam ab76256), 4E-BP1 (Cell signaling 9452), p-4E-BP1 (Cell signaling 2855), DRP1 (Abcam ab184247), mTOR (Cell Signaling 2972), p-mTOR (Ser2448) (Cell Signaling 2971), p70 S6 (Cell Signaling 9202), p-p70 S6 (Thr421/Ser424) (Cell Signaling 9204), $1–5 \times 10^6$ cells were lysed with lysis buffer (CST 9803S) and protein/phosphatases inhibitors as per manufacturer's protocol and blotted as described[44]. Briefly, cells were washed and lysed on ice for 30 min and spun. Supernatants were assayed for total protein concentration with Bradford assay (BioRad 5000006) and 50–100 µg of protein was mixed with loading buffer and loaded in a 12 or 16% gradient gel (Thermo 1Fisher XP00162). Proteins were transferred onto a NC or PVDF membrane (Fisher Scientific) and blocked with 5% milk for 1 h. OXPHOS complexes were revealed with total OXPHOS Rodent WB Antibody Cocktail (Abcam ab110413). Lysis was carried out with the addition of lauryl maltoside at 1.5%.

Isotopic labelling and mass spectrometry. FoB cells were incubated for 5 h in SILAC RPMI containing [U-$^{13}C_6$]-glucose (11 mmol/L; Cambridge Isotope Laboratories). Extraction of intracellular metabolites, GC-MS measurement, MID calculations, determinations of fractional carbon contributions, and subtractions of natural isotope abundance were performed as described[44]. Total glucose and lactate concentrations from medium were determined using a YSI 2950D. Intracellular metabolites (GSH, glucose, glucose-6P, pyruvate, succinate) were measured by liquid chromatography (Vanquish HPLC Thermo Scientific) coupled to high resolution mass spectrometry (QExactive HF Thermo Scientific). Briefly, extraction of $3–30 \times 10^5$ cells was done in a 2:2:1 mixture of acetonitrile:MeOH:H_2O + 0.5% formic acid on ice. Following neutralization with $(NH)_4HCO_3$, samples were frozen at −20 °C for 20 min, spun and supernatants measured directly.

Seahorse flux analysis. Assays were performed using an XFe96 Extracellular Flux Analyzer (Agilent). FoB or MZB cells were seeded in XF Seahorse RPMI medium at 10^6/well on Seahorse XFe96 culture plates pre-coated with Cell-Tak. Oxygen consumption rate (OCR) of intact cells were determined using the XF Cell Mitochondrial Stress Test according to the manufacturer's protocol. Briefly, three basal OCR measurements were taken, followed by sequential injections of 1 µM oligomycin A, 3 µM FCCP, and 1 µM antimycin A, taking three measurements following each treatment. GlycoATP and mitoATP were derived from cells sequentially treated with oligomycin A and Rot/Antimycin A. Activity measurements for each respiratory chain complex in permeabilized cells were performed according to previous research[85,138]. Briefly, after enrichment, FoB were washed and resuspended in mannitol and sucrose-BSA (MAS-B) buffer pH 7.2 (70 mM sucrose, 220 mM Mannitol, 10 mM KH_2PO_4, 5 mM $MgCl_2$, 2 mM Hepes, 1 mM EGTA, and 0.4% fatty acid-free BSA), and flux measurements were started. After three basal measurements, cells were permeabilized by injection of saponin (1 µg/mL, Sigma S4521), together with 1 mM ADP (Sigma 01905) and the following respiratory complex substrates: CI, pyruvate/malate (5 mM/2.5 mM); CII, succinate/rotenone (5 mM/1 µM); CIII, duroquinol (0.5 mM); CIV, N,N,N,N-tetramethyl-p-phenylenediamine (TMPD)/ascorbate (0.5 mM/2 mM). These were followed by injections with oligomycin A (1 µM) and respective complex inhibitors (CI, 1 µM rotenone; CII and CIII, 20 µM antimycin A; CIV, 20 mM potassium azide).

Statistical analyses. Data are graphed as the mean ± SD (refer to figure legends for detailed information) and *P* value were determined by unpaired Student's t-test (two-tailed), one-way or 2 way ANOVA using Prism (GraphPad version 9.0.1). Significance is indicated with asterisks * and a minimum *P* value of 0.05 was considered statistically significant (refer to figure legends for details).

Reporting summary. Further information on research design is available in the Nature Research Reporting Summary linked to this article.

Data availability

The data sets generated during and/or analyzed during the current study are available upon reasonable request. The CITE-seq data from control and *Gclc*-deficient B cells have been deposited in GEO under the accession code GSE194419. Where applicable, source data are provided as a Source Data file for each figure. Source data are provided with this paper.

Received: 9 December 2021; Accepted: 11 March 2022;
Published online: 04 April 2022

References

1. Janeway, C. A., Ron, J. J. & Katz, M. E. The B cell is the initiating antigen-presenting cell in peripheral lymph nodes. *J. Immunol.* http://www.jimmunol.org/content/138/4/1051 (1987).
2. Bouaziz, J. D. et al. Therapeutic B cell depletion impairs adaptive and autoreactive CD4+ T cell activation in mice. *Proc. Natl Acad. Sci. USA* **104**, 20878–20883 (2007).
3. Harris, D. P. et al. Reciprocal regulation of polarized cytokine production by effector B and T cells. *Nat. Immunol.* **1**, 475–482 (2000).
4. Cerutti, A., Cols, M. & Puga, I. Marginal zone B cells: Virtues of innate-like antibody-producing lymphocytes. *Nat. Rev. Immunol.* **13**, 118–132 (2013).

5. Zandvoort, A. & Timens, W. The dual function of the splenic marginal zone: Essential for initiation of anti-TI-2 responses but also vital in the general first-line defense against blood-borne antigens. *Clin. Exp. Immunol.* **130**, 4–11 (2002).
6. Nutt, S. L., Hodgkin, P. D., Tarlinton, D. M. & Corcoran, L. M. The generation of antibody-secreting plasma cells. *Nat. Rev. Immunol.* **15**, 160–171 (2015).
7. Oliver, A. M., Martin, F., Gartland, G. L., Carter, R. H. & Kearney, J. F. Marginal zone B cells exhibit unique activation, proliferative, and immunoglobulin secretory responses. *Eur. J. Immunol.* **27**, 2366–2374 (1997).
8. Oliver, A. M., Martin, F. & Kearney, J. F. IgMhighCD21high lymphocytes enriched in the splenic marginal zone generate effector cells more rapidly than the bulk of follicular B cells. *J. Immunol.* **162**, 7198–7207 (1999).
9. Martin, F., Oliver, A. M. & Kearney, J. F. Marginal zone and B1 B cells unite in the early response against T-independent blood-borne particulate antigens. *Immunity* **14**, 617–629 (2001).
10. Haines, R. R., Scharer, C. D., Lobby, J. L. & Boss, J. M. LSD1 cooperates with noncanonical NF-kappaB signaling to regulate marginal zone B cell development. *J. Immunol.* **203**, 1867–1881 (2019).
11. Kleiman, E. et al. Distinct transcriptomic features are associated with transitional and mature B-cell populations in the mouse spleen. *Front. Immunol.* **6**, 30 (2015).
12. Mabbott, N. A. & Gray, D. Identification of co-expressed gene signatures in mouse B1, marginal zone, and B2 B-cell populations. *Immunology* **141**, 79–95 (2014).
13. Shi, W. et al. Transcriptional profiling of mouse B cell terminal differentiation defines a signature for antibody-secreting plasma cells. *Nat. Immunol.* **16**, 663–673 (2015).
14. Gunn, K. E. & Brewer, J. W. Evidence that marginal zone B cells possess an enhanced secretory apparatus and exhibit superior secretory activity. *J. Immunol.* **177**, 3791–3798 (2006).
15. Arnon, T. I. & Cyster, J. G. Blood, sphingosine-1-phosphate and lymphocyte migration dynamics in the spleen. *Curr. Top. Microbiol. Immunol.* **378**, 107–128 (2014).
16. Lu, T. T. & Cyster, J. G. Integrin-mediated long-term B cell retention in the splenic marginal zone. *Science* **297**, 409–412 (2002).
17. Manser, T. Textbook germinal centers? *J. Immunol.* **172**, 3369–3375 (2004).
18. Hao, Z. & Rajewsky, K. Homeostasis of peripheral B cells in the absence of B cell influx from the bone marrow. *J. Exp. Med.* **194**, 1151–1164 (2001).
19. Song, H. & Cerny, J. Functional heterogeneity of marginal zone B cells revealed by their ability to generate both early antibody-forming cells and germinal centers with hypermutation and memory in response to a T-dependent antigen. *J. Exp. Med.* **198**, 1923–1935 (2003).
20. Liu, Y. J., Oldfield, S. & MacLennan, I. C. Memory B cells in T cell-dependent antibody responses colonize the splenic marginal zones. *Eur. J. Immunol.* **18**, 355–362 (1988).
21. Sies, H. & Jones, D. P. Reactive oxygen species (ROS) as pleiotropic physiological signalling agents. *Nat. Rev. Mol. Cell Biol.* https://doi.org/10.1038/s41580-020-0230-3 (2020).
22. Deponte, M. Glutathione catalysis and the reaction mechanisms of glutathione-dependent enzymes. *Biochim. Biophys. Acta* **1830**, 3217–3266 (2013).
23. Wu, G., Fang, Y. Z., Yang, S., Lupton, J. R. & Turner, N. D. Glutathione metabolism and its implications for health. *J. Nutr.* **134**, 489–492 (2004).
24. Meister, A. & Anderson, M. E. Glutathione. *Annu. Rev. Biochem.* **52**, 711–760 (1983).
25. Hamilos, D. L. & Wedner, H. J. The role of glutathione in lymphocyte activation. I. Comparison of inhibitory effects of buthionine sulfoximine and 2-cyclohexene-1-one by nuclear size transformation. *J. Immunol.* **135**, 2740–2747 (1985).
26. Fidelus, R. K. & Tsan, M. F. Enhancement of intracellular glutathione promotes lymphocyte activation by mitogen. *Cell Immunol.* **97**, 155–163 (1986).
27. Droge, W., Pottmeyer-Gerber, C., Schmidt, H. & Nick, S. Glutathione augments the activation of cytotoxic T lymphocytes in vivo. *Immunobiology* **172**, 151–156 (1986).
28. Staal, F. J., Roederer, M., Herzenberg, L. A. & Herzenberg, L. A. Glutathione and immunophenotypes of T and B lymphocytes in HIV-infected individuals. *Ann. N. Y Acad. Sci.* **651**, 453–463 (1992).
29. Herzenberg, L. A. et al. Glutathione deficiency is associated with impaired survival in HIV disease. *Proc. Natl Acad. Sci. USA* **94**, 1967–1972 (1997).
30. Staal, F. J. et al. Intracellular glutathione levels in T cell subsets decrease in HIV-infected individuals. *AIDS Res. Hum. Retroviruses* **8**, 305–311 (1992).
31. Vene, R. et al. Redox remodeling allows and controls B-cell activation and differentiation. *Antioxid. Redox Signal* **13**, 1145–1155 (2010).
32. Franchina, D. G., Grusdat, M. & Brenner, D. B-cell metabolic remodeling and cancer. *Trends Cancer* **4**, 138–150 (2018).
33. Muri, J., Thut, H., Bornkamm, G. W. & Kopf, M. B1 and marginal zone B cells but not follicular B2 cells require Gpx4 to prevent lipid peroxidation and ferroptosis. *Cell Rep.* **29**, 2731–2744 e2734 (2019).
34. Saxton, R. A. & Sabatini, D. M. mTOR signaling in growth, metabolism, and disease. *Cell* **168**, 960–976 (2017).
35. Limon, J. J. & Fruman, D. A. Akt and mTOR in B cell activation and differentiation. *Front. Immunol.* **3**, 228 (2012).
36. Donahue, A. C. & Fruman, D. A. Distinct signaling mechanisms activate the target of rapamycin in response to different B-cell stimuli. *Eur. J. Immunol.* **37**, 2923–2936 (2007).
37. Gaudette, B. T., Jones, D. D., Bortnick, A., Argon, Y. & Allman, D. mTORC1 coordinates an immediate unfolded protein response-related transcriptome in activated B cells preceding antibody secretion. *Nat. Commun.* **11**, 723 (2020).
38. Farmer, J. R. et al. Induction of metabolic quiescence defines the transitional to follicular B cell switch. *Sci. Signal*, https://doi.org/10.1126/scisignal.aaw5573 (2019).
39. Benhamron, S. & Tirosh, B. Direct activation of mTOR in B lymphocytes confers impairment in B-cell maturation and loss of marginal zone B cells. *Eur. J. Immunol.* **41**, 2390–2396 (2011).
40. Bass, D. A. et al. Flow cytometric studies of oxidative product formation by neutrophils: a graded response to membrane stimulation. *J. Immunol.* **130**, 1910–1917 (1983).
41. Franchina, D. G., Dostert, C. & Brenner, D. Reactive oxygen species: Involvement in T cell signaling and metabolism. *Trends Immunol.* **39**, 489–502 (2018).
42. Robinson, K. M. et al. Selective fluorescent imaging of superoxide in vivo using ethidium-based probes. *Proc. Natl Acad. Sci. USA* **103**, 15038–15043 (2006).
43. Mak, T. W. et al. Glutathione primes T cell metabolism for inflammation. *Immunity* **46**, 675–689 (2017).
44. Kurniawan, H. et al. Glutathione restricts serine metabolism to preserve regulatory T cell function. *Cell Metab.* https://doi.org/10.1016/j.cmet.2020.03.004 (2020).
45. Griffith, O. W. & Meister, A. Potent and specific inhibition of glutathione synthesis by buthionine sulfoximine (S-n-butyl homocysteine sulfoximine). *J. Biol. Chem.* **254**, 7558–7560 (1979).
46. Hobeika, E. et al. Testing gene function early in the B cell lineage in mb1-cre mice. *Proc. Natl Acad. Sci. USA* **103**, 13789–13794 (2006).
47. Stoeckius, M. et al. Simultaneous epitope and transcriptome measurement in single cells. *Nat. Methods* **14**, 865–868 (2017).
48. Martin, F. & Kearney, J. F. Marginal-zone B cells. *Nat. Rev. Immunol.* **2**, 323–335 (2002).
49. Arnon, T. I., Horton, R. M., Grigorova, I. L. & Cyster, J. G. Visualization of splenic marginal zone B-cell shuttling and follicular B-cell egress. *Nature* **493**, 684–688 (2013).
50. Pillai, S., Cariappa, A. & Moran, S. T. Marginal zone B cells. *Annu. Rev. Immunol.* **23**, 161–196 (2005).
51. Zhang, Z. et al. SCINA: A semi-supervised subtyping algorithm of single cells and bulk samples. *Genes*, https://doi.org/10.3390/genes10070531 (2019).
52. Schmidt-Supprian, M. & Rajewsky, K. Vagaries of conditional gene targeting. *Nat. Immunol.* **8**, 665–668 (2007).
53. Karlsson, M. C. et al. Macrophages control the retention and trafficking of B lymphocytes in the splenic marginal zone. *J. Exp. Med.* **198**, 333–340 (2003).
54. Cinamon, G. et al. Sphingosine 1-phosphate receptor 1 promotes B cell localization in the splenic marginal zone. *Nat. Immunol.* **5**, 713–720 (2004).
55. Chen, Y. et al. Defective microarchitecture of the spleen marginal zone and impaired response to a thymus-independent type 2 antigen in mice lacking scavenger receptors MARCO and SR-A. *J. Immunol.* **175**, 8173–8180 (2005).
56. You, Y. et al. Marginal zone B cells regulate antigen capture by marginal zone macrophages. *J. Immunol.* **186**, 2172–2181 (2011).
57. You, Y., Zhao, H., Wang, Y. & Carter, R. H. Cutting edge: Primary and secondary effects of CD19 deficiency on cells of the marginal zone. *J. Immunol.* **182**, 7343–7347 (2009).
58. Borges da Silva, H. et al. Splenic macrophage subsets and their function during blood-borne infections. *Front. Immunol.* **6**, 480 (2015).
59. Pillai, S. & Cariappa, A. The follicular versus marginal zone B lymphocyte cell fate decision. *Nat. Rev. Immunol.* **9**, 767–777 (2009).
60. Loder, F. et al. B cell development in the spleen takes place in discrete steps and is determined by the quality of B cell receptor-derived signals. *J. Exp. Med.* **190**, 75–89 (1999).
61. Allman, D. & Pillai, S. Peripheral B cell subsets. *Curr. Opin. Immunol.* **20**, 149–157 (2008).
62. Allman, D. et al. Resolution of three nonproliferative immature splenic B cell subsets reveals multiple selection points during peripheral B cell maturation. *J. Immunol.* **167**, 6834–6840 (2001).
63. Ma, X. M. & Blenis, J. Molecular mechanisms of mTOR-mediated translational control. *Nat. Rev. Mol. Cell Biol.* **10**, 307–318 (2009).
64. Schmidt, E. K., Clavarino, G., Ceppi, M. & Pierre, P. SUnSET, a nonradioactive method to monitor protein synthesis. *Nat. Methods* **6**, 275–277 (2009).
65. Dibble, C. C. & Cantley, L. C. Regulation of mTORC1 by PI3K signaling. *Trends Cell Biol.* **25**, 545–555 (2015).
66. Carracedo, A. & Pandolfi, P. P. The PTEN-PI3K pathway: of feedbacks and cross-talks. *Oncogene* **27**, 5527–5541 (2008).

67. Okoh, V. O., Felty, Q., Parkash, J., Poppiti, R. & Roy, D. Reactive oxygen species via redox signaling to PI3K/AKT pathway contribute to the malignant growth of 4-hydroxy estradiol-transformed mammary epithelial cells. *PLoS One* **8**, e54206 (2013).
68. Silva, A. et al. Intracellular reactive oxygen species are essential for PI3K/Akt/mTOR-dependent IL-7-mediated viability of T-cell acute lymphoblastic leukemia cells. *Leukemia* **25**, 960–967 (2011).
69. Kwon, J. et al. Reversible oxidation and inactivation of the tumor suppressor PTEN in cells stimulated with peptide growth factors. *Proc. Natl Acad. Sci. USA* **101**, 16419–16424 (2004).
70. Wagner, A. et al. In silico modeling of metabolic state in single Th17 cells reveals novel regulators of inflammation and autoimmunity. *J. Immunol.* https://doi.org/10.1101/2020.01.23.912717 (2020).
71. Wang, C. et al. Metabolic and epigenomic regulation of Th17/Treg balance by the polyamine pathway. *Cell*, https://doi.org/10.1101/2020.01.23.911966 (2020).
72. Zou, C., Wang, Y. & Shen, Z. 2-NBDG as a fluorescent indicator for direct glucose uptake measurement. *J. Biochem. Biophys. Methods* **64**, 207–215 (2005).
73. Martinez-Reyes, I. & Chandel, N. S. Mitochondrial TCA cycle metabolites control physiology and disease. *Nat. Commun.* **11**, 102 (2020).
74. Boyer, P. D. et al. Oxidative phosphorylation and photophosphorylation. *Annu. Rev. Biochem.* **46**, 955–966 (1977).
75. Martin, F. & Kearney, J. F. B-cell subsets and the mature preimmune repertoire. Marginal zone and B1 B cells as part of a "natural immune memory". *Immunol. Rev.* **175**, 70–79 (2000).
76. Lee, J. E., Westrate, L. M., Wu, H., Page, C. & Voeltz, G. K. Multiple dynamin family members collaborate to drive mitochondrial division. *Nature* **540**, 139–143 (2016).
77. Buck, M. D. et al. Mitochondrial dynamics controls T cell fate through metabolic programming. *Cell* **166**, 63–76 (2016).
78. Little, A. C. et al. High-content fluorescence imaging with the metabolic flux assay reveals insights into mitochondrial properties and functions. *Commun. Biol.* **3**, 271 (2020).
79. Brand, M. D. The proton leak across the mitochondrial inner membrane. *Biochim. Biophys. Acta (BBA) - Bioenerg.* **1018**, 128–133 (1990).
80. Chance, B. & Williams, G. R. Respiratory enzymes in oxidative phosphorylation. II. Difference spectra. *J. Biol. Chem.* **217**, 395–407 (1955).
81. Chance, B. & Williams, G. R. Respiratory enzymes in oxidative phosphorylation. *J. Biol. Chem.* **221**, 477–489 (1956).
82. Chance, B. & Williams, G. R. Respiratory enzymes in oxidative phosphorylation. III. The steady state. *J. Biol. Chem.* **217**, 409–427 (1955).
83. Brown, G. C., Lakin-Thomas, P. L. & Brand, M. D. Control of respiration and oxidative phosphorylation in isolated rat liver cells. *Eur. J. Biochem.* **192**, 355–362 (1990).
84. Choi, S. W., Gerencser, A. A. & Nicholls, D. G. Bioenergetic analysis of isolated cerebrocortical nerve terminals on a microgram scale: spare respiratory capacity and stochastic mitochondrial failure. *J. Neurochem.* **109**, 1179–1191 (2009).
85. Salabei, J. K., Gibb, A. A. & Hill, B. G. Comprehensive measurement of respiratory activity in permeabilized cells using extracellular flux analysis. *Nat. Protoc.* **9**, 421–438 (2014).
86. Cariappa, A., Liou, H. C., Horwitz, B. H. & Pillai, S. Nuclear factor kappa B is required for the development of marginal zone B lymphocytes. *J. Exp. Med.* **192**, 1175–1182 (2000).
87. Girkontaite, I. et al. Lsc is required for marginal zone B cells, regulation of lymphocyte motility, and immune responses. *Nat. Immunol.* **2**, 855–862 (2001).
88. Guinamard, R., Okigaki, M., Schlessinger, J. & Ravetch, J. V. Absence of marginal zone B cells in Pyk-2-deficient mice defines their role in the humoral response. *Nat. Immunol.* **1**, 31–36 (2000).
89. Sullivan, B. M. et al. Point mutation in the glycoprotein of lymphocytic choriomeningitis virus is necessary for receptor binding, dendritic cell infection, and long-term persistence. *Proc. Natl Acad. Sci. USA* **108**, 2969–2974 (2011).
90. Matloubian, M., Kolhekar, S. R., Somasundaram, T. & Ahmed, R. Molecular determinants of macrophage tropism and viral persistence: Importance of single amino acid changes in the polymerase and glycoprotein of lymphocytic choriomeningitis virus. *J. Virol.* **67**, 7340–7349 (1993).
91. Matloubian, M., Somasundaram, T., Kolhekar, S. R., Selvakumar, R. & Ahmed, R. Genetic basis of viral persistence: single amino acid change in the viral glycoprotein affects ability of lymphocytic choriomeningitis virus to persist in adult mice. *J. Exp. Med.* **172**, 1043–1048 (1990).
92. McIlwain, D. R. et al. T-cell STAT3 is required for the maintenance of humoral immunity to LCMV. *Eur. J. Immunol.* **45**, 418–427 (2015).
93. Recher, M. et al. Deliberate removal of T cell help improves virus-neutralizing antibody production. *Nat. Immunol.* **5**, 934–942 (2004).
94. Borrow, P., Evans, C. F. & Oldstone, M. B. Virus-induced immunosuppression: Immune system-mediated destruction of virus-infected dendritic cells results in generalized immune suppression. *J. Virol.* **69**, 1059–1070 (1995).
95. Lefrancois, L. Protection against lethal viral infection by neutralizing and nonneutralizing monoclonal antibodies: Distinct mechanisms of action in vivo. *J. Virol.* **51**, 208–214 (1984).
96. Vandepol, S. B., Lefrancois, L. & Holland, J. J. Sequences of the major antibody binding epitopes of the Indiana serotype of vesicular stomatitis virus. *Virology* **148**, 312–325 (1986).
97. Akkaya, M. et al. Second signals rescue B cells from activation-induced mitochondrial dysfunction and death. *Nat. Immunol.* **19**, 871–884 (2018).
98. Wheeler, M. L. & Defranco, A. L. Prolonged production of reactive oxygen species in response to B cell receptor stimulation promotes B cell activation and proliferation. *J. Immunol.* **189**, 4405–4416 (2012).
99. Bertolotti, M. et al. B- to plasma-cell terminal differentiation entails oxidative stress and profound reshaping of the antioxidant responses. *Antioxid. Redox Signal* **13**, 1133–1144 (2010).
100. van Anken, E. et al. Sequential waves of functionally related proteins are expressed when B cells prepare for antibody secretion. *Immunity* **18**, 243–253 (2003).
101. Caro-Maldonado, A. et al. Metabolic reprogramming is required for antibody production that is suppressed in anergic but exaggerated in chronically BAFF-exposed B cells. *J. Immunol.* **192**, 3626–3636 (2014).
102. Ci, X. et al. TSC1 promotes B cell maturation but is dispensable for germinal center formation. *PLoS One* **10**, e0127527 (2015).
103. Muri, J. & Kopf, M. Redox regulation of immunometabolism. *Nat. Rev. Immunol.* https://doi.org/10.1038/s41577-1123020-00478-8 (2020).
104. Boveris, A., Oshino, N. & Chance, B. The cellular production of hydrogen peroxide. *Biochem. J.* **128**, 617–630 (1972).
105. Sena, L. A. et al. Mitochondria are required for antigen-specific T cell activation through reactive oxygen species signaling. *Immunity* **38**, 225–236 (2013).
106. Finkel, T. Signal transduction by reactive oxygen species. *J. Cell Biol.* **194**, 7–15 (2011).
107. Brand, M. D. The sites and topology of mitochondrial superoxide production. *Exp. Gerontol.* **45**, 466–472 (2010).
108. Wang, S. B., Murray, C. I., Chung, H. S. & Van Eyk, J. E. Redox regulation of mitochondrial ATP synthase. *Trends Cardiovasc. Med.* **23**, 14–18 (2013).
109. Garcia, J. et al. Regulation of mitochondrial glutathione redox status and protein glutathionylation by respiratory substrates. *J. Biol. Chem.* **285**, 39646–39654 (2010).
110. Mailloux, R. J., McBride, S. L. & Harper, M. E. Unearthing the secrets of mitochondrial ROS and glutathione in bioenergetics. *Trends Biochem. Sci.* **38**, 592–602 (2013).
111. Zhang, Y., Marcillat, O., Giulivi, C., Ernster, L. & Davies, K. J. The oxidative inactivation of mitochondrial electron transport chain components and ATPase. *J. Biol. Chem.* **265**, 16330–16336 (1990).
112. Stadtman, E. R. & Levine, R. L. Free radical-mediated oxidation of free amino acids and amino acid residues in proteins. *Amino Acids* **25**, 207–218 (2003).
113. Danielson, S. R. et al. Quantitative mapping of reversible mitochondrial Complex I cysteine oxidation in a Parkinson disease mouse model. *J. Biol. Chem.* **286**, 7601–7608 (2011).
114. Zhang, H. et al. Glutathione-dependent reductive stress triggers mitochondrial oxidation and cytotoxicity. *FASEB J.* **26**, 1442–1451 (2012).
115. Perez-Torres, I., Guarner-Lans, V. & Rubio-Ruiz, M. E. Reductive stress in inflammation-associated diseases and the pro-oxidant effect of antioxidant agents. *Int. J. Mol. Sci.* **18**, 2098 (2017).
116. Chung, C. Y. et al. Activity-based ratiometric FRET probe reveals oncogene-driven changes in labile copper pools induced by altered glutathione metabolism. *Proc. Natl Acad. Sci. USA* **116**, 18285–18294 (2019).
117. Vallieres, C., Holland, S. L. & Avery, S. V. Mitochondrial ferredoxin determines vulnerability of cells to copper excess. *Cell Chem. Biol.* **24**, 1228–1237 e1223 (2017).
118. Brancaccio, D. et al. [4Fe-4S] cluster assembly in mitochondria and its impairment by copper. *J. Am. Chem. Soc.* **139**, 719–730 (2017).
119. Orlowski, M. & Meister, A. The gamma-glutamyl cycle: A possible transport system for amino acids. *Proc. Natl Acad. Sci. USA* **67**, 1248–1255 (1970).
120. Balijepalli, S., Annepu, J., Boyd, M. R. & Ravindranath, V. Effect of thiol modification on brain mitochondrial complex I activity. *Neurosci. Lett.* **272**, 203–206 (1999).
121. Beer, S. M. et al. Glutaredoxin 2 catalyzes the reversible oxidation and glutathionylation of mitochondrial membrane thiol proteins: Implications for mitochondrial redox regulation and antioxidant DEFENSE. *J. Biol. Chem.* **279**, 47939–47951 (2004).
122. Martensson, J., Lai, J. C. & Meister, A. High-affinity transport of glutathione is part of a multicomponent system essential for mitochondrial function. *Proc. Natl Acad. Sci. USA* **87**, 7185–7189 (1990).

123. Masini, A., Ceccarelli, D., Trenti, T., Gallesi, D. & Muscatello, U. Mitochondrial inner membrane permeability changes induced by octadecadienoic acid hydroperoxide. Role of mitochondrial GSH pool. *Biochim. Biophys. Acta* **1101**, 84–89 (1992).
124. Muri, J. et al. The thioredoxin-1 and glutathione/glutaredoxin-1 systems redundantly fuel murine B-cell development and responses. *Eur. J. Immunol.* **49**, 709–723 (2019).
125. Staal, F. J. et al. CD20 expression is increased on B lymphocytes from HIV-infected individuals *J. Acquir. Immune Defic. Syndr.* **5**, 627–632 (1992).
126. Moir, S. & Fauci, A. S. B cells in HIV infection and disease. *Nat. Rev. Immunol.* **9**, 235–245 (2009).
127. Chen, Y. et al. Hepatocyte-specific Gclc deletion leads to rapid onset of steatosis with mitochondrial injury and liver failure. *Hepatology* **45**, 1118–1128 (2007).
128. Butler, A., Hoffman, P., Smibert, P., Papalexi, E. & Satija, R. Integrating single-cell transcriptomic data across different conditions, technologies, and species. *Nat. Biotechnol.* **36**, 411–420 (2018).
129. Love, M. I., Huber, W. & Anders, S. Moderated estimation of fold change and dispersion for RNA-seq data with DESeq2. *Genome Biol.* **15**, 550 (2014).
130. Blighe, K., Rana, S. & Lewis, M. EnhancedVolcano: Publication-ready volcano plots with enhanced colouring and labeling. R package version 1.8.0, https://github.com/kevinblighe/EnhancedVolcano (2020).
131. Ritchie, M. E. et al. limma powers differential expression analyses for RNA-sequencing and microarray studies. *Nucleic Acids Res.* **43**, e47 (2015).
132. Korotkevich, G. et al. Fast gene set enrichment analysis. Preprint at *bioRxiv*, https://doi.org/10.1101/060012 (2021).
133. Schaefer, P. M., Kalinina, S., Rueck, A., von Arnim, C. A. F. & von Einem, B. NADH autofluorescence-A marker on its way to boost bioenergetic research. *Cytom. A* **95**, 34–46 (2019).
134. Bartolome, F. & Abramov, A. Y. Measurement of mitochondrial NADH and FAD autofluorescence in live cells. *Methods Mol. Biol.* **1264**, 263–270 (2015).
135. Kirk, S. J., Cliff, J. M., Thomas, J. A. & Ward, T. H. Biogenesis of secretory organelles during B cell differentiation. *J. Leukoc. Biol.* **87**, 245–255 (2010).
136. Livak, K. J. & Schmittgen, T. D. Analysis of relative gene expression data using real-time quantitative PCR and the 2(−Delta Delta C(T)) method. *Methods* **25**, 402–408 (2001).
137. Quiros, P. M., Goyal, A., Jha, P. & Auwerx, J. Analysis of mtDNA/nDNA ratio in mice. *Curr. Protoc. Mouse Biol.* **7**, 47–54 (2017).
138. Kory, N. et al. MCART1/SLC25A51 is required for mitochondrial NAD transport. *Sci. Adv.* https://doi.org/10.1126/sciadv.abe5310 (2020).

Acknowledgements

We would like to thank Hans-Martin Jäck (FAU) and Elisabeth Letellier (Uni.Lu) for constructive feedback and continuous support; Vitaly Pozdeev (Uni.Lu), Dominique Revets (LIH), Thomas Cerutti (LIH), and Gert Van Isterdael (VIB) for tissue section microscopy and FACS sorting; the Metabolomics Platform of the LCSB (Uni.Lu); Samantha Storn (LIH) and Anaïs Oudin (LIH) and the Luxembourg Institute of Health's Animal Welfare Structure; Charlène Verschueren (LIH) and Catherine Dostert (LIH) for assistance. D.B. is supported by the FNR-ATTRACT (A14/BM/7632103) and the FNR-CORE (C21/BM/15796788) programs. D.B., L.B., L.G., and A.E. are funded by FNR-PRIDE (PRIDE/11012546/NEXTIMMUNE), and D.B., A.E. by (PRIDE17/11823097/MicrOH). D.B. and D.G.F. are supported by FNR-RIKEN (TregBar/11228353). V.V. holds grant NIH/NIAAA (5R24AA022057). D.B and K.H. are supported by binational FNR/DFG program: the FNR-CORE grant (C18/BM/12691266) and the Deutsche Forschungsgemeinschaft (DFG, German Research Foundation) project HI1400/3-1. M.K. was supported by a SALK-grant from the government of Flanders and by an Odysseus-grant of the Research Foundation Flanders, Belgium (FWO). P.A.L. is supported by the DFG (SFB974, GRK1949) and the Jürgen Manchot Foundation (MOI). M.M. would like to thank the Luxembourg National Research Fund (FNR) for the support (FNR PEARL P16/BM/11192868 grant). The authors would like to thank the Roger de Spoelberch Foundation for funding the electron microscopy platform (LCSB/LNS).

Author contributions

D.G.F. carried out most experimental work, with help from H.K., M.G., L.G., L.B., L.S.-B., A.E., and S.F. N.V. performed CITE-seq preparation and pre-processing. D.G.F. performed CITE-seq analyses. D.G.F. and H.K. performed seahorse flux assays and tracing experiments. D.G.F., C.J., and L.B. analyzed stable isotope tracing experiments. D.G.F., M.G., and C.B. performed and analyzed LCMV experiments. A.M. performed and analyzed VSV experiments. T.K. helped with experiment design. A.C. and F.K.B. performed and analyzed electron microscopy. C.J., Y.C., V.V., M.K., M.M., K.H., and P.A.L. provided expert comments and reagents. D.G.F. and D.B. conceptualized the work, designed all experiments, analyzed the data, and wrote the manuscript. All authors reviewed and edited the final manuscript.

Competing interests

The authors declare no competing interests.

Additional information

Supplementary information The online version contains supplementary material available at https://doi.org/10.1038/s41467-022-29426-x.

Correspondence and requests for materials should be addressed to Dirk Brenner.

Peer review information *Nature Communications* thanks Matteo Villa, and the other, anonymous, reviewer(s) for their contribution to the peer review of this work.

Reprints and permission information is available at http://www.nature.com/reprints

Publisher's note Springer Nature remains neutral with regard to jurisdictional claims in published maps and institutional affiliations.

APPENDIX 4

Research Publication

(Co-author)

KURNIAWAN, H., FRANCHINA, D. G., GUERRA, L., BONETTI, L., SORIANO-BAGUET, L., GRUSDAT, M., SCHLICKER, L., HUNEWALD, O., DOSTERT, C., MERZ, M. P., BINSFELD, C., DUNCAN, G. S., FARINELLE, S., NONNENMACHER, Y., HAIGHT, J., DAS GUPTA, D., EWEN, A., TASKESEN, R., HALDER, R., CHEN, Y., JÄGER, C., OLLERT, M., WILMES, P., VASILIOU, V., HARRIS, I. S., KNOBBETHOMSEN, C. B., TURNER, J. D., MAK, T. W., LOHOFF, M., MEISER, J., HILLER, K. & BRENNER, D. 2020. **Glutathione Restricts Serine Metabolism to Preserve Regulatory T Cell Function.** *Cell Metab*, 31, 920-936.e7.

Article

Cell Metabolism

Glutathione Restricts Serine Metabolism to Preserve Regulatory T Cell Function

Graphical Abstract

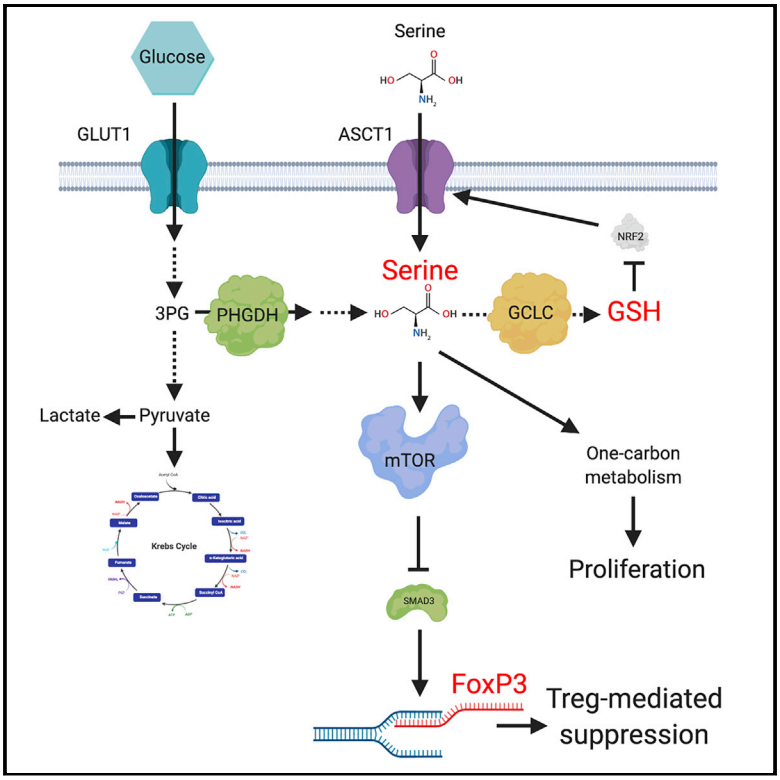

Highlights

- Ablation of *Gclc* in Tregs causes autoimmunity and increases anti-tumor responses
- *Gclc*-derived GSH is needed for the suppressive function of Tregs *in vitro* and *in vivo*
- GSH in Tregs regulates serine concentrations and metabolism. which impact mTOR and FoxP3
- Serine- and glycine-deficient diet rescues mutant mice from lethal inflammation

Authors

Henry Kurniawan, Davide G. Franchina, Luana Guerra, ..., Johannes Meiser, Karsten Hiller, Dirk Brenner

Correspondence

dirk.brenner@lih.lu

In Brief

Regulatory T cells (Tregs) rely on oxidative metabolism, which triggers the generation of reactive oxygen species (ROS). Accumulating ROS are controlled by the antioxidant glutathione (GSH). Kurniawan et al. reveal an unexpected subset-specific role of GSH in serine metabolism and Treg function.

Kurniawan et al., 2020, Cell Metabolism *31*, 1–17
May 5, 2020
https://doi.org/10.1016/j.cmet.2020.03.004

CellPress

Please cite this article in press as: Kurniawan et al., Glutathione Restricts Serine Metabolism to Preserve Regulatory T Cell Function, Cell Metabolism (2020), https://doi.org/10.1016/j.cmet.2020.03.004

Cell Metabolism
Article

Glutathione Restricts Serine Metabolism to Preserve Regulatory T Cell Function

Henry Kurniawan,[1] Davide G. Franchina,[1] Luana Guerra,[1] Lynn Bonetti,[1] Leticia Soriano - Baguet,[1] Melanie Grusdat,[1] Lisa Schlicker,[2,3] Oliver Hunewald,[4] Catherine Dostert,[1] Myriam P. Merz,[5] Carole Binsfeld,[1] Gordon S. Duncan,[6] Sophie Farinelle,[1] Yannic Nonnenmacher,[2,3] Jillian Haight,[6] Dennis Das Gupta,[7] Anouk Ewen,[1] Rabia Taskesen,[12] Rashi Halder,[8] Ying Chen,[9] Christian Jäger,[8] Markus Ollert,[4,10] Paul Wilmes,[8] Vasilis Vasiliou,[9] Isaac S. Harris,[11] Christiane B. Knobbe-Thomsen,[12] Jonathan D. Turner,[5] Tak W. Mak,[6,12,13] Michael Lohoff,[7] Johannes Meiser,[14] Karsten Hiller,[2,3] and Dirk Brenner[1,10,15,16,*]

[1]Experimental & Molecular Immunology, Department of Infection and Immunity, Luxembourg Institute of Health, 29 Rue Henri Koch, Esch-sur-Alzette, Luxembourg
[2]Braunschweig Integrated Center of Systems Biology (BRICS), Technische Universität Braunschweig, Rebenring 56, 38106 Braunschweig
[3]Computational Biology of Infection Research, Helmholtz Centre for Infection Research, Inhoffenstraße 7, 38124 Braunschweig, Germany
[4]Allergy and Clinical Immunology, Department of Infection and Immunity, Luxembourg Institute of Health, 29 Rue Henri Koch, L-4354 Esch-sur-Alzette, Luxembourg
[5]Immune Endocrine Epigenetics Research Group, Department of Infection and Immunity, Luxembourg Institute of Health, 29 Rue Henri Koch, L-4354 Esch-sur-Alzette, Grand Duchy of Luxembourg
[6]The Campbell Family Cancer Research Institute, Ontario Cancer Institute University Health Network, Toronto, ON, Canada
[7]Institute for Medical Microbiology and Hospital Hygiene, University of Marburg, Marburg, Germany
[8]Luxembourg Centre for Systems Biomedicine, University of Luxembourg, 7 Avenue des Hauts Fourneaux, Esch-sur-Alzette, Luxembourg
[9]Department of Environmental Health Sciences, Yale School of Public Health, New Haven, CT, USA
[10]Odense Research Center for Anaphylaxis (ORCA), Department of Dermatology and Allergy Center, Odense University Hospital, University of Southern Denmark, Odense, Denmark
[11]Department of Biomedical Genetics and Wilmot Cancer Institute, University of Rochester Medical Center, 601 Elmwood Ave, Rochester, New York, USA
[12]Departments of Medical Biophysics and Immunology, Faculty of Medicine, University of Toronto, Toronto, ON, Canada
[13]The University of Hong Kong, Hong Kong SAR, China
[14]Cancer Metabolism Group, Department of Oncology, 84 Val Fleuri, Luxembourg, Luxembourg
[15]Immunology & Genetics, Luxembourg Centre for Systems Biomedicine, University of Luxembourg, 7 Avenue des Hauts Fourneaux, Esch-sur-Alzette, Luxembourg
[16]Lead Contact
*Correspondence: dirk.brenner@lih.lu
https://doi.org/10.1016/j.cmet.2020.03.004

SUMMARY

Regulatory T cells (Tregs) maintain immune homeostasis and prevent autoimmunity. Serine stimulates glutathione (GSH) synthesis and feeds into the one-carbon metabolic network (1CMet) essential for effector T cell (Teff) responses. However, serine's functions, linkage to GSH, and role in stress responses in Tregs are unknown. Here, we show, using mice with Treg-specific ablation of the catalytic subunit of glutamate cysteine ligase (*Gclc*), that GSH loss in Tregs alters serine import and synthesis and that the integrity of this feedback loop is critical for Treg suppressive capacity. Although *Gclc* ablation does not impair Treg differentiation, mutant mice exhibit severe autoimmunity and enhanced anti-tumor responses. *Gclc*-deficient Tregs show increased serine metabolism, mTOR activation, and proliferation but downregulated FoxP3. Limitation of cellular serine *in vitro* and *in vivo* restores FoxP3 expression and suppressive capacity of *Gclc*-deficient Tregs. Our work reveals an unexpected role for GSH in restricting serine availability to preserve Treg functionality.

Context and Significance

Regulatory T cells (Tregs) restrict inflammation to maintain healthy body functions. Dysregulation of Treg metabolism thus leads to inflammatory disease; however, our knowledge of their metabolic needs is limited. Researchers of the Luxembourg Institute of Health describe a novel metabolic control mechanism in Tregs that serves as a barrier against autoimmunity. The antioxidant glutathione restricts serine metabolism in Tregs to preserve their suppressive function such that glutathione depletion boosts anti-tumor immunity. Glutathione is thus a stress sensor in Tregs whose manipulation holds promise for anti-inflammatory and anti-tumor therapies. The authors further show that elucidation of the metabolic mechanism of a disease can lead to its mitigation by a rationally designed diet, setting a new direction for future treatment of metabolic diseases.

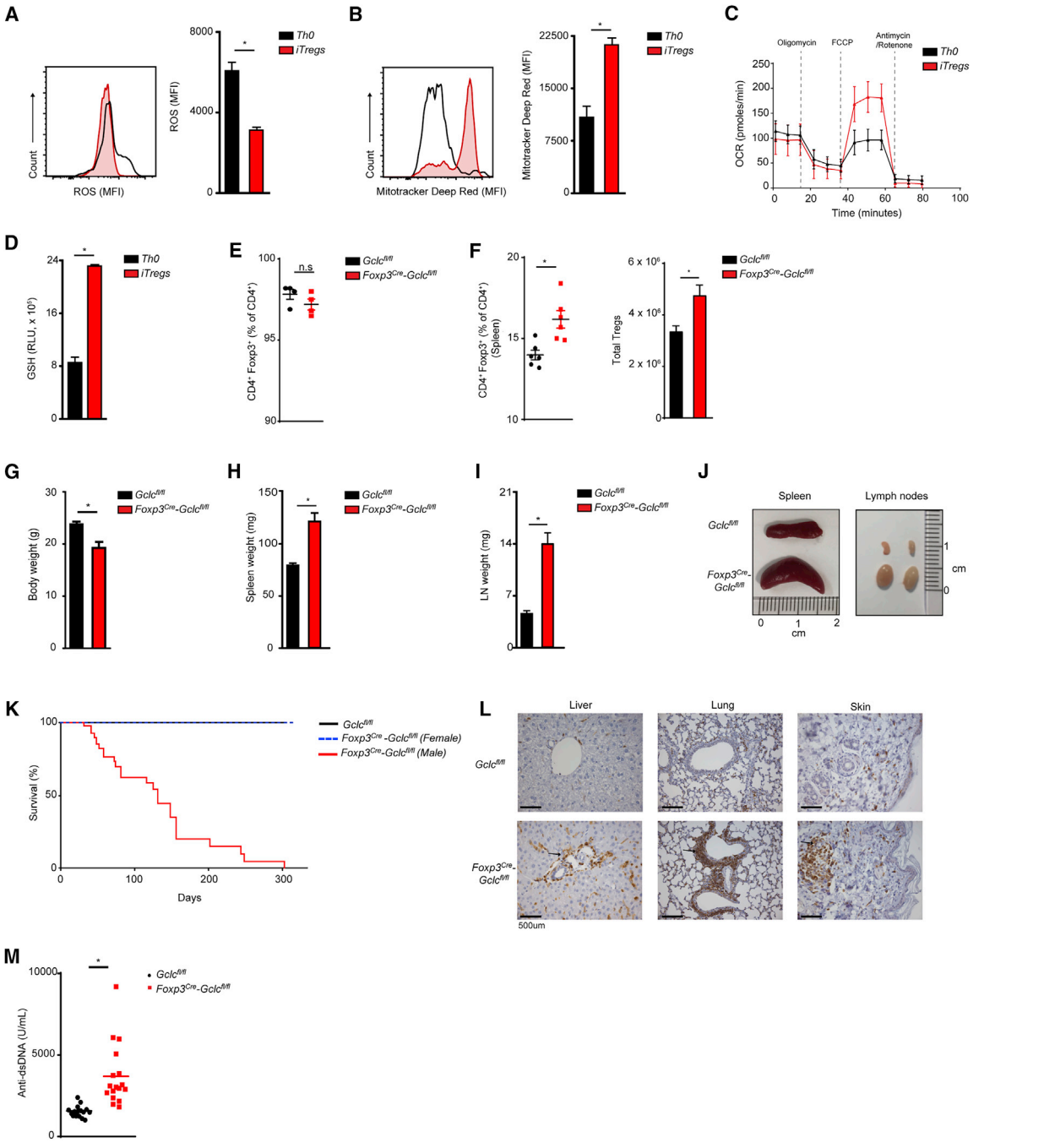

Figure 1. *Gclc* Deficiency Does Not Affect Treg Homeostasis but Does Lead to Multi-organ Inflammation

(A–D) Splenic naive T cells from C57BL/6 mice were treated with αCD3+αCD28+IL2, with or without TGFβ, to generate iTreg or Th0 cells, respectively. Cells were stained with (A) DCF-DA to detect ROS, or (B) Mitotracker Deep Red to assess mitochondrial function, followed by flow cytometry (FC).

(C) Seahorse determination of OCR.

(D) Luminescence-based quantification of intracellular GSH. Data are mean ± SEM (n = 3) and are representative of 3 independent trials.

(E) FC quantitation of $CD4^+Foxp3^+$ iTregs among splenic naive T cells isolated from $Gclc^{fl/fl}$ (control) or $Foxp3^{cre}$-$Gclc^{fl/fl}$ mice and treated *in vitro* with αCD3+αCD28+IL2+TGF-β. Data are mean ± SEM (n = 4); 5 trials.

(F) Flow cytometric analysis (FCA) of $CD4^+Foxp3^+$ nTregs from spleens of $Gclc^{fl/fl}$ and $Foxp3^{cre}$-$Gclc^{fl/fl}$ mice. Data are mean ± SEM (n = 6); 5 trials.

(G–I) Weights of (G) whole body, (H) spleen, and (I) LN from $Gclc^{fl/fl}$ and $Foxp3^{cre}$-$Gclc^{fl/fl}$ mice at 8–12 weeks of age. Data are mean ± SEM (n = 13).

(J) Images of spleens and LN from $Gclc^{fl/fl}$ and $Foxp3^{cre}$-$Gclc^{fl/fl}$ mice (8 weeks of age).

(K) Survival of $Gclc^{fl/fl}$ (n = 48) and $Foxp3^{cre}$-$Gclc^{fl/fl}$ (male n = 38, female = 21) mice.

(legend continued on next page)

INTRODUCTION

Tregs suppress Teffs to maintain peripheral tolerance and prevent autoimmunity (Wing and Sakaguchi, 2010). Metabolic reprogramming in activated Tregs is distinct from that in Teffs (Dang et al., 2011; Delgoffe et al., 2009; Shi et al., 2011), implying that specific nutrients may affect the function and differentiation of T cell subsets differently.

Serine is a non-essential amino acid (NEAA) and fosters Teff function (Ma et al., 2017; Ron-Harel et al., 2016), but its role in Tregs is unknown. Serine is either taken up directly by cells or synthesized *de novo* from the glycolytic metabolite 3-phosphoglycerate (3-PG). Intracellular serine is the major carbon source for folate-mediated one-carbon metabolism (1CMet), which operates in the cytosol and mitochondria to provide building blocks for S-adenosylmethionine (SAM), nucleotides, NAD(P)H, and ATP. 1CMet thus supports AA homeostasis, epigenetic maintenance, and redox defense (Ducker and Rabinowitz, 2017; Tibbetts and Appling, 2010). Serine is also a source of glycine and cysteine used to synthesize glutathione (GSH), the main antioxidant preserving intracellular redox balance (Meister, 1983; Ye et al., 2014). GSH, composed of glycine, glutamine, and cysteine, is synthesized by glutamate cysteine ligase (GCL; containing Gclc and Gclm subunits) and glutathione synthase (Lu, 2009). GSH is vital for Teff functions and proliferation (Mak et al., 2017).

We report here, using Treg-specific *Gclc*-deficient mice, that a feedback loop involving GSH and serine unexpectedly regulates Treg functionality. GSH-deficient Tregs display increased serine uptake and *de novo* synthesis, enhancing 1CMet. Inhibition of serine uptake restores the suppressive capacity in *Gclc*-deficient Tregs. GSH not only controls a Treg's redox state but also acts as negative feedback regulator to restrict serine import and synthesis. Strikingly, GSH-deficient Tregs are linked to both autoimmunity and increased tumor rejection *in vivo*. Our results demonstrate a novel role for GSH in restricting serine metabolism to support Treg's suppressive capacity.

RESULTS

Gclc Ablation in Tregs Leads to Multi-organ Autoimmunity

Considering that Tregs rely on oxidative metabolism (Almeida et al., 2016; Pearce et al., 2013), we investigated whether wild-type (WT) Tregs generate more ROS than WT Teffs. Naive T cells isolated from C57BL/6 mice were treated *in vitro* with anti (α)-CD3 antibody (Ab), αCD28 Ab, and interleukin (IL)2, with or without transforming growth factor (TGF)β, to trigger the differentiation of induced Tregs (iTregs) or Th0 cells, respectively. Unexpectedly, ROS were lower (Figure 1A) but mitochondrial membrane potential and maximal oxygen consumption rate (OCR) were higher in WT iTregs compared to WT Th0 cells (Figures 1B and 1C), suggesting that ROS scavenging is very efficient in iTregs. In line, iTregs contained ~3-fold more GSH than Th0 cells (Figure 1D), conferring superior buffering of oxidative stress.

To explore GSH loss specifically in Tregs, we crossed $Gclc^{fl/fl}$ mice with $Foxp3^{cre}$ mice to generate $Foxp3^{cre}$-$Gclc^{fl/fl}$ animals (Rubtsov et al., 2008). We isolated naive T cells from male mutants (6 week old) and $Gclc^{fl/fl}$ littermate controls and generated iTregs *in vitro*. Under conditions of optimal TCR stimulation, iTreg differentiation was not impaired by *Gclc* ablation (Figure 1E), and STAT5 phosphorylation (Figure S1A) and cell size (Figure S1B) were normal. In accordance with a previous report, suboptimal TCR stimulation of *Gclc*-deficient naive T cells led to more iTregs than in controls (Figure S1C) (Lian et al., 2018). Quantitative RT-PCR and mass spectrometry confirmed loss of *Gclc* mRNA and GSSG/GSH in mutant FoxP3$^+$ iTregs (Figures S1D and S1E), in line with their higher ROS (Figure S1F). *Gclc* deletion in all T cell subsets reduces CD4$^+$ and CD8$^+$ T cell numbers and homeostasis (Mak et al., 2017). However, Treg-specific *Gclc* deletion did not impair natural Treg (nTreg) homeostasis in the spleen or thymus of male mice. Indeed, percentages and absolute numbers of peripheral nTregs were slightly increased (Figures 1F and S1G).

By 8 weeks of age, male $Foxp3^{cre}$-$Gclc^{fl/fl}$ mice showed inflammation and reduced body weight and size (Figures 1G and S1H). By 12 weeks, most exhibited severe lymphadenopathy and splenomegaly (Figures 1H–1J) and a shorter lifespan (Figure 1K). Female $Foxp3^{cre}$-$Gclc^{fl/fl}$ mice, which possess an active $Foxp3^{cre}$-expressing or WT X chromosome and so retain some $Gclc^+$ nTregs, did not develop disease and had a normal lifespan (Figure 1K). Diseased male mice showed organ infiltration by T cells and macrophages (Figures 1L, S1I, and S1J) and increased serum anti-dsDNA Abs (Figure 1M). Thus, although *Gclc* ablation in Tregs does not impair Treg homeostasis, mice bearing these mutated cells develop multi-organ autoimmunity.

Teff Accumulation and Increased IFNγ Drive Lethal Auto-inflammation

Diseased male $Foxp3^{cre}$-$Gclc^{fl/fl}$ mice showed increased lymphocytic cellularity in the spleen and in lymph nodes (LN) (Figure 2A). Relative and absolute numbers of naive T cells (CD62L^{high}CD44^{low}) were decreased in the mutants, whereas the frequency and absolute numbers of activated CD4$^+$ and CD8$^+$ Teffs (CD62L^{low}CD44^{high}) were increased (Figures 2B, 2C, S2A, and S2B). These differences were not observed in female $Foxp3^{cre}$-$Gclc^{fl/fl}$ mice, indicating that non-targeted Tregs can suppress the inflammatory disease (Figure S2C). T cells from male $Foxp3^{cre}$-$Gclc^{fl/fl}$ mice produced more IFNγ, IL2 (CD4$^+$), and TNF (CD8$^+$), but not IL17 (CD4$^+$) (Figures 2D and 2E). Tbet expression was enhanced in mutant CD4$^+$ T cells (Figure S2D). ELISA confirmed high systemic levels of IFNγ, TNF, and IL2 in the serum of male mutants (Figure 2F). T cell frequencies, activation, and IFNγ production were increased in the lamina propria in male mutants (Figures S2E–S2G). T follicular helper cells (PD1$^+$CXCR5$^+$) and germinal center B cells (GL-7$^+$CD95$^+$) were elevated in mutant spleen (Figures S2H

(L) Histology of the indicated tissues resected from one $Gclc^{fl/fl}$ and one Foxp3^{cre}-$Gclc^{fl/fl}$ mouse and stained with αCD3. Scale bars, 500 μm. Results are representative of 5 mice/group; 2 trials.

(M) ELISA of anti-dsDNA Ab in serum of $Gclc^{fl/fl}$ (n = 17) and $Foxp3^{cre}$-$Gclc^{fl/fl}$ (n = 17) mice (8–12 weeks of age). *p < 0.05.

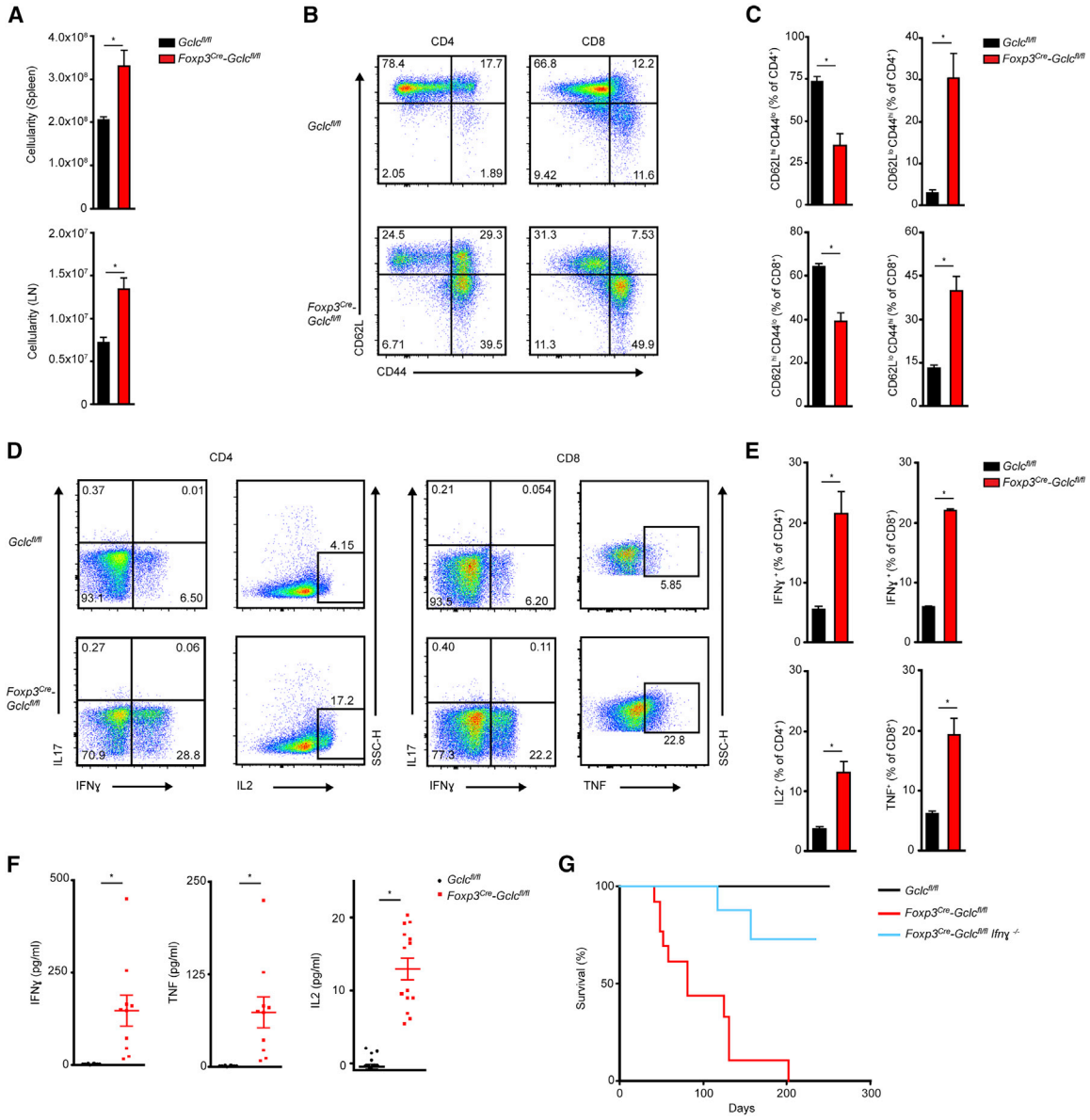

Figure 2. Treg-Specific *Gclc* Deletion Impairs Homeostasis

(A) Total lymphocyte numbers in spleen and LN of *Gclc*$^{fl/fl}$ and *Foxp3*^{cre}-*Gclc*$^{fl/fl}$ mice. Data are mean ± SEM (n = 6); 2 trials.

(B and C) FCA of naive (CD62L^{hi}CD44^{lo}), central memory (CD62L^{hi}CD44^{hi}), and effector (CD62L^{lo}CD44^{hi}) subsets (B), and quantification within the CD4$^+$ population (top) and CD8$^+$ population (bottom) (C), from *Gclc*$^{fl/fl}$ and *Foxp3*^{cre}-*Gclc*$^{fl/fl}$ mice as in (A). Data are mean ± SEM (n = 3); 5 trials.

(D and E) Intracellular staining and FCA of IFNγ, IL17, IL2, and TNF production by purified CD4$^+$ (left) and CD8$^+$ (right) splenic *Gclc*$^{fl/fl}$ and *Foxp3*^{cre}-*Gclc*$^{fl/fl}$ T cells re-stimulated *in vitro* with 50 ng PMA + 750 ng Iono for 6 h. Data are mean ± SEM (n = 3); 3 trials.

(F) ELISA of IFNγ, TNF, and IL2 in serum of *Gclc*$^{fl/fl}$ and *Foxp3*^{cre}-*Gclc*$^{fl/fl}$ mice (8–12 weeks of age). Each symbol represents an individual mouse. Data are mean ± SEM (*Gclc*$^{fl/fl}$ n = 10; *Foxp3*^{cre}-*Gclc*$^{fl/fl}$ n = 17); 2 trials.

(G) Survival of *Gclc*$^{fl/fl}$ (n = 23), *Foxp3*^{cre}-*Gclc*$^{fl/fl}$ (n = 13), and Foxp3^{cre}-*Gclc*$^{fl/fl}$ x *Ifnγ*$^{-/-}$ (n = 14) mice. *p < 0.05.

and S2I), and serum concentrations of IgG1, IgG2a, IgG3, and IgA were elevated (Figure S2J).

We next crossed male *Foxp3*^{cre}-*Gclc*$^{fl/fl}$ mice to *Ifnγ*$^{-/-}$ mice and monitored autoimmune disease onset in the progeny. *Ifnγ* deletion significantly reduced disease burden and prolonged survival (Figure 2G). Thus, *Gclc* function allows Tregs to suppress IFNγ-mediated autoimmunity and spontaneous Teff activation *in vivo*.

GSH in Tregs Is Crucial for Their Suppressive Capacity

Flow cytometric analysis of splenic nTregs from *Foxp3*^{cre}-*Gclc*$^{fl/fl}$ and control mice revealed that surface levels of CD25, ICOS, CTLA4, GITR, and OX40 were comparable (Figure 3A). However, CD44 and CD69 were elevated on *Gclc*-deficient nTregs and iTregs (Figure S3A), indicating enhanced activation. PD1 was also higher on mutant nTregs. Although PD1 supports nTregs in normal tissues of WT mice (Francisco et al., 2009), PD1 is

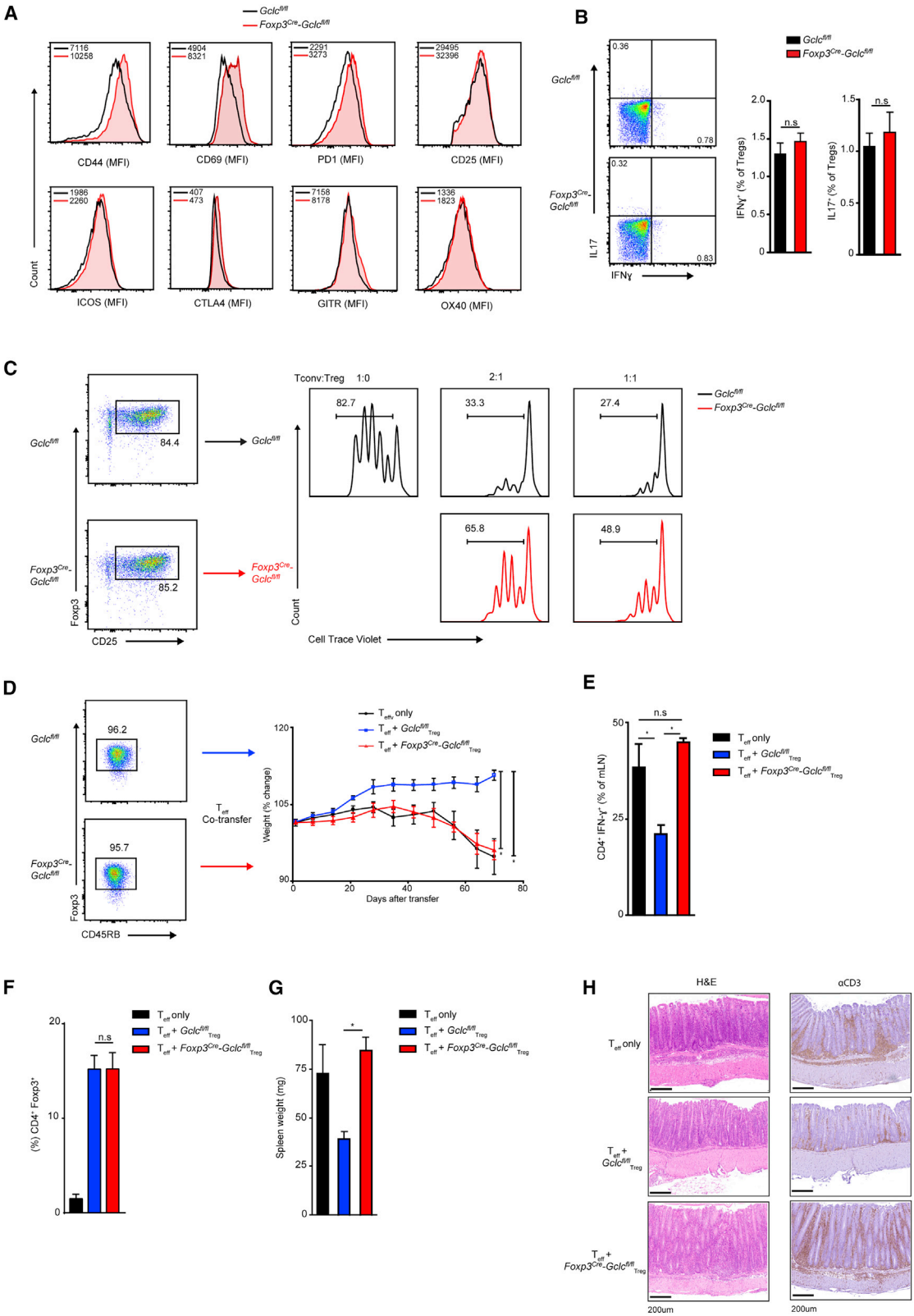

(legend on next page)

linked to Treg dysfunction and increased IFNγ in tumors (Lowther et al., 2016). Notably, *Gclc*-deficient nTregs did not produce more IFNγ after restimulation (Figure 3B), implying that they are stable and do not become Teffs. In line, Helios (Kim et al., 2015; Nakagawa et al., 2016) and IRF4 expression were normal in mutant splenic nTregs (Figure S3B). We next co-cultured control conventional T cells (Tconv) with control or *Foxp3*^{cre}-*Gclc*$^{fl/fl}$ iTregs or freshly isolated nTregs and measured Tconv proliferation. *Gclc*-deficient nTregs and iTregs suffered a dramatic reduction in suppressive capacity independent of the Treg:Tconv ratio (Figures 3C, S3C, and S3D) and expressed less IL10 and TGFβ (Figure S3E).

To explore these data *in vivo*, we employed a T-cell-dependent colitis model (Reardon et al., 2011). WT Teffs (CD4$^+$ CD45RB^{high}) were adoptively transferred alone, or with control or *Gclc*-deficient nTregs (CD4$^+$CD45RB^{low}), into *Rag1*$^{-/-}$ recipient mice. Colitis (represented by mouse weight loss) was induced by control Teffs alone but not if control nTregs were co-transferred (Figure 3D). In contrast, mice receiving control Teffs plus *Gclc*-deficient nTregs developed colitis (Figure 3D). Teffs from mice receiving control Teffs only, or control Teffs plus *Gclc*-deficient nTregs, produced more IFNγ (Figure 3E). Numbers of nTregs in all recipients after 50 days were equal, ruling out colitis due to mutant Treg death (Figure 3F). Recipients of control Teffs plus *Gclc*-deficient nTregs exhibited splenomegaly (Figure 3G), and intestinal crypts of these recipients showed T cell infiltration (Figure 3H). Thus, *Gclc* in Tregs is indispensable for suppression *in vitro* and *in vivo*.

FoxP3 Is Reduced in *Gclc*-Deficient Tregs Due to Increased mTOR Activation

To determine if *Gclc* deficiency alters Treg gene transcription, we used RNA sequencing (RNA-seq) and principal component analysis (PCA) to examine *Foxp3*^{cre}-*Gclc*$^{fl/fl}$ and *Gclc*$^{fl/fl}$ iTreg transcriptomes (Figure S4A). *Foxp3* was the most downregulated gene in mutant iTregs (Figure 4A) and splenic nTregs (Figure S4B). Although FoxP3$^+$ nTreg numbers were slightly increased in *Foxp3*^{cre}-*Gclc*$^{fl/fl}$ mice (Figures 1F), intracellular FoxP3 expression was reduced in mutant nTregs and iTregs (Figure 4B).

Reciprocity exists between mTOR and Foxp3 in Tregs (Delgoffe et al., 2009; Gerriets et al., 2015; Huynh et al., 2015). Phosphorylation (p) of mTOR and its target S6 were increased in nTregs and iTregs from male *Foxp3*^{cre}-*Gclc*$^{fl/fl}$ mice (Figure 4C). To rule out any effects of inflammation, we analyzed nTregs from female mutants heterozygously expressing a *Foxp3*^{cre}-YFP$^+$ reporter gene. Due to random X chromosome inactivation, these disease-free animals contain YFP$^+$ nTregs (activated Cre, *Gclc* absent) and YFP$^-$ nTregs (no Cre, *Gclc* intact). Higher pS6 and pmTOR were detected in YFP$^+$ nTregs than in YFP$^-$ nTregs (Figure S4C). To confirm this result, we generated tamoxifen (TAM)-inducible Treg-specific *Gclc*-deficient mice (*Foxp3*$^{ER\text{-}cre}$-*Gclc*$^{fl/fl}$), which showed no inflammation without TAM. We isolated naive T cells from these mutants and controls and induced iTregs *in vitro*. In parallel, we triggered acute *Gclc* deletion by adding 4-hydroxytamoxifen (4-OHT). Again, we observed increased pS6, decreased FoxP3, and reduced iTreg mediated suppression (Figures S4D and S4E). Conversely, retroviral transduction of *Gclc* into *Gclc*-deficient iTregs reduced pS6, increased FoxP3, and restored their suppressive capacity (Figures 4D and 4E). Thus, *Gclc's* effects on mTOR and FoxP3 are not compromised by an inflammatory environment.

When we treated *Gclc*-deficient iTregs with the mTOR inhibitor rapamycin (Rap) (Dumont and Su, 1996), pS6 was reduced and FoxP3 was restored (Figures 4F and 4G), confirming that increased mTOR in GSH-deficient cells decreases FoxP3. We isolated nTregs from spleen and LN of male *Foxp3*^{cre}-*Gclc*$^{fl/fl}$ and control mice, incubated these cells with or without Rap for 24 h, removed Rap, and measured nTregs' suppressive capacity. Again, Rap normalized *Gclc*-deficient nTreg-mediated suppression (Figure 4H). Smad3 is linked to FoxP3 induction in Tregs (Tone et al., 2008). Smad 3 is suppressed and inactivated by mTOR, and hyperphosphorylated in mTOR-deficient cells (Delgoffe et al., 2009). In consistency, our *Gclc*-deficient iTregs showed increased mTOR activation and reduced pSmad3, which was reversed by Rap (Figure 4I). We next infected control and *Gclc*-deficient iTregs with retrovirus expressing Smad3. FoxP3 increased in Smad3-transduced mutant cells, which regained their suppressive function (Figures 4J and 4K). Retroviral expression of constitutively active STAT5 had no effect (Figure S4F). Thus, mTOR inactivation mediated by GSH is critical for Smad3-dependent FoxP3 induction and iTregs' suppressive capacity.

To explore these findings *in vivo*, we intraperitoneally (i.p.) injected male control and *Foxp3*^{cre}-*Gclc*$^{fl/fl}$ mice (6 weeks) with Rap or vehicle every other day for 30 days. Rap ameliorated inflammatory disease in the mutants due to its immunosuppressive effect (Figures S4G–S4L). Rap also restored *Gclc*-deficient nTreg function such that Teff proliferation was suppressed *in vitro* (Figure S4M). To determine whether FoxP3 reconstitution alone in *Gclc*-deficient Tregs could rescue their suppressive

Figure 3. GSH Modulates Treg Functionality *In Vitro* and *In Vivo*

(A) FCA of the indicated surface markers on splenic nTregs from *Gclc*$^{fl/fl}$ and *Foxp3*^{cre}-*Gclc*$^{fl/fl}$ mice (n = 3); 4 trials.

(B) FC quantification of intracellular IFNγ and IL17 in splenic nTregs of *Gclc*$^{fl/fl}$ and *Foxp3*^{cre}-*Gclc*$^{fl/fl}$ mice re-stimulated *in vitro* with PMA + Iono for 6 h. Data are mean ± SEM (n = 3); 3 trials.

(C) *In vitro* suppression assay of splenic nTregs from *Gclc*$^{fl/fl}$ and *Foxp3*^{cre}-*Gclc*$^{fl/fl}$ mice incubated at the indicated ratios with Tconv labeled with 5 μM cell-trace violet (CTV). Suppression was determined by FC as a decrease in Tconv proliferation; 5 trials.

(D) *In vivo* assay of Treg suppression using a T cell adoptive transfer-based induced colitis model. *Rag1*$^{-/-}$ mice received WT Teff (CD4$^+$CD45RB^{high}) alone or together with FACS-sorted nTregs (CD4$^+$ CD45RB^{low}) from *Gclc*$^{fl/fl}$ or *Foxp3*^{cre}-*Gclc*$^{fl/fl}$ mice. Results are presented as post-transfer body weight relative to initial weight of recipients. Data are mean ± SEM (n = 4); 2 trials.

(E) Intracellular staining and FCA of IFNγ produced by CD4$^+$ Teff isolated from mesenteric LN of the mice in (D) at day 70 post-transfer and re-stimulated *in vitro* with PMA+Iono. Data are mean ± SEM (n = 4); 2 trials.

(F) Quantification of nTregs in peripheral blood of *Rag1*$^{-/-}$ recipients treated as in (D) at 50 days post-transfer. Data are mean ± SEM (n = 2–3). 2 trials.

(G) Quantification of spleen weights of the *Rag1*$^{-/-}$ recipients in (D) at experimental endpoint. Data are mean ± SEM (n = 4); 2 trials.

(H) Histology of large intestine of the mice in (D) after staining with H&E or αCD3. Scale bars, 200 μm. Data are mean ± SEM (n = 4); 2 trials. *p < 0.05.

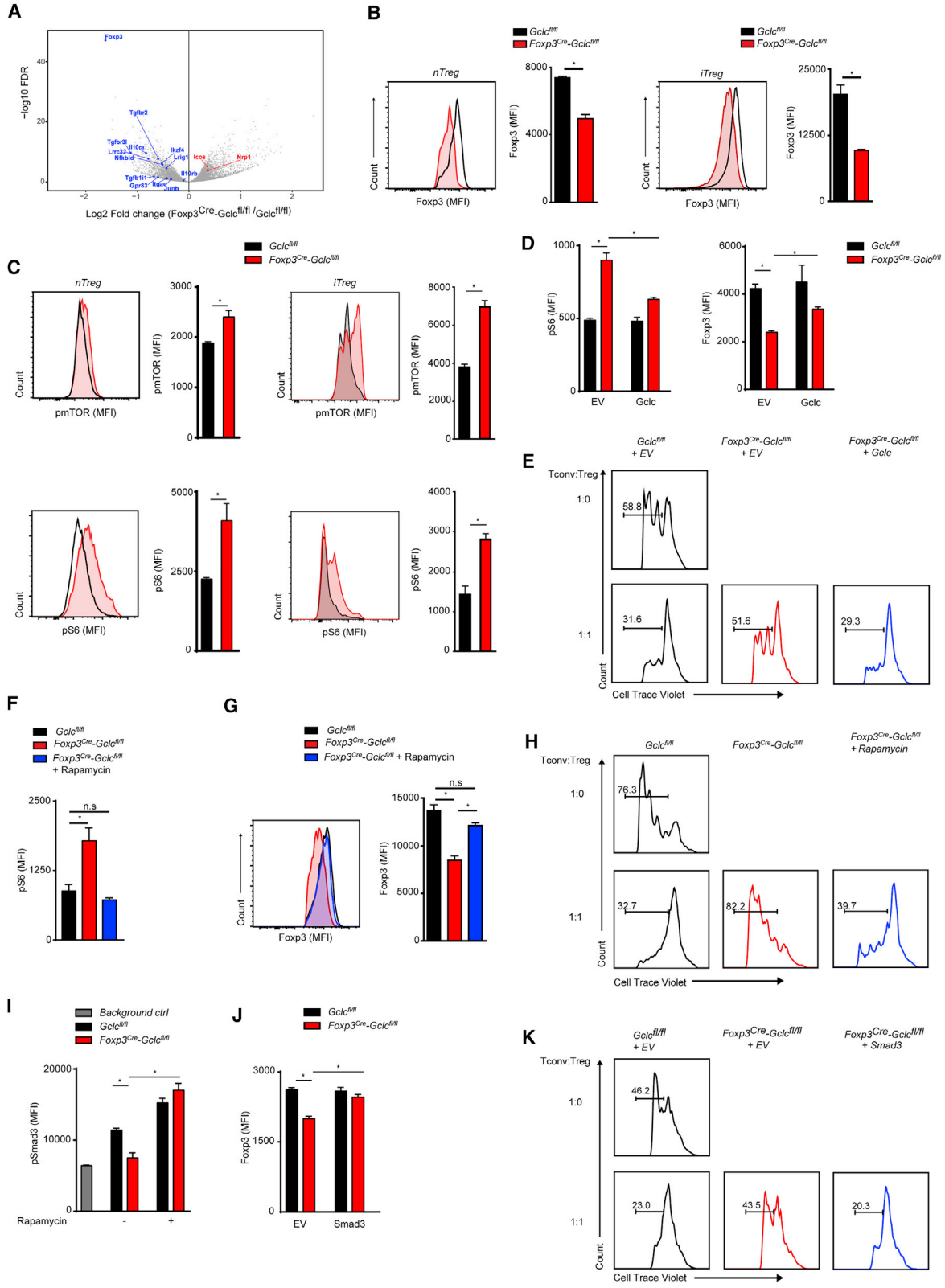

Figure 4. Lack of GSH Alters mTOR Signaling and Impairs FoxP3 Expression

(A) Volcano plot comparing mRNAs of the indicated Treg-associated genes in *Foxp3^{cre}-Gclc$^{fl/fl}$ and Gclc$^{fl/fl}$* iTregs. Downregulated (blue) and upregulated (red) transcripts in *Foxp3^{cre}-Gclc$^{fl/fl}$* are shown.

(legend continued on next page)

capacity, we transduced *Foxp3*^{cre}-*Gclc*$^{fl/fl}$ Tregs with control or *Foxp3*-expressing retrovirus and subjected transduced CD90.1^{+} iTregs to *in vitro* suppression assays. Indeed, retroviral *Foxp3* expression restored FoxP3 and the suppressive activity of *Gclc*-deficient Tregs (Figures S4N and S4O). Thus, GSH is crucial *in vitro* and *in vivo* for maintaining Treg suppression through effects on mTOR and FoxP3.

Regulation of Serine Availability by GSH Is Required for Treg Function

mTOR is an energy sensor that is activated by AA levels (Goberdhan et al., 2016). Gene set enrichment analysis revealed that *Gclc*-deficient iTregs and nTregs showed elevated expression of genes associated with AA metabolism or 1CMet (Figures 5A, 5B, S5A, and S5B). Heightened 1CMet is linked to increased Teff proliferation (Ma et al., 2017; Ron-Harel et al., 2016). In line, *Gclc*-deficient iTregs proliferated more vigorously than controls (Figure 5C), in striking contrast to *Gclc*-deficient Tconv, where GSH loss blocks proliferation (Mak et al., 2017). Thus, GSH has a surprising, subset-specific role in Tregs.

Serine drives 1CMet because it provides its hydroxymethyl group as a one-carbon unit to tetrahydrofolate (Ducker and Rabinowitz, 2017; Herbig et al., 2002; Tibbetts and Appling, 2010). *Gclc*-deficient iTregs showed increased expression of genes involved in serine metabolism (Figure 5D). When we cultured *Gclc*-deficient iTregs or 4-OHT-inducible *Gclc*-deficient iTregs without serine, pS6 was reduced to control levels (Figure 5E), while FoxP3 was increased (Figure 5F). Serine deprivation had only minor effects on pS6 and Foxp3 in control iTregs. Although glycine is also a 1CMet donor, its deprivation neither decreased pS6 nor restored FoxP3 in *Gclc*-deficient iTregs (Figure S5C). To assess when serine suppresses FoxP3 in GSH-deficient Tregs, we cultured *Gclc*-deficient iTregs with or without serine for various times. When mutant iTregs were induced from naive T cells in the absence of serine for 96 h, FoxP3 rose (Figure S5D). However, serine deprivation for only 48 h (followed by serine supplementation for the next 48 h) had no effect, and FoxP3 remained low in mutant iTregs. Conversely, mutant iTregs incubated with serine for the first 48 h followed by serine starvation for 48 h showed increased FoxP3. Thus, serine exerts its effect during later stages of Treg differentiation.

Cells import serine via the alanine-serine-cysteine-threonine transporters (ASCTs) 1 and 2, which are encoded by the *SLC1A4* and *SLC1A5* genes, respectively (Bröer and Bröer, 2017; Kaplan et al., 2018; Yamamoto et al., 2004). *SLC1A4* and *SLC1A5* are expressed by T cells (Ren et al., 2017). *SLC1A4* (but not *SLC1A5*) mRNA was upregulated in *Gclc*-deficient iTregs (Figures 5G and S5E). *SLC1A4* is a target of the master antioxidant transcription factor NRF2 (Christensen, 1990; Fu et al., 2019; Hirotsu et al., 2012; Schäfer et al., 2010), and NRF2 responses are triggered by increased intracellular ROS (Kong and Chandel, 2018). Thus, cells with elevated ROS might increase *SLC1A4*. Both iTregs and nTregs lacking *Gclc* (which have high ROS; Figure S1E) exhibited enriched expression of ROS metabolism genes (Figure S5F) and increased NRF2 target gene activation (Figure S5G). *SLC1A4* mRNA was increased in *Gclc*-deficient iTregs and normalized when treated with the ROS scavenger N-acetyl-cysteine (NAC) (Figure 5G). In line with increased *SLC1A4*, *Gclc*-deficient iTregs consumed more serine and secreted more glycine and formate than did controls (Figure 5H), and antioxidant treatment of these cells decreased intracellular serine (Figure 5I) and restored FoxP3 (Figure S5H).

The ASCT AA transporters are inhibited by L-phenylglycine (Foster et al., 2017). We treated control and *Gclc*-deficient iTregs with L-phenylglycine to block ASCTs and detected reduced intracellular serine in the mutant cells (Figure S5I) as well as decreased formate secretion (Figure 5J). L-phenylglycine restored FoxP3 in *Gclc*-deficient iTregs and 4-OHT-inducible *Gclc*-deficient iTregs (Figure 5K). CRISPR/Cas9-mediated downregulation of ASCT1 increased FoxP3 in mutant iTregs (Figure S5J). ASCT blockade also reinstated *Gclc*-deficient nTregs suppressive function (Figure 5L). Thus, restriction of serine uptake is crucial for maintaining Tregs' suppressive capacity.

Serine hydroxymethyltransferase (SHMT) mediates serine's contribution to 1CMet. Isotopic tracing with [U-$^{13}C_3$]-serine confirmed increased M1-labeling of formate in mutant iTregs (Figure 5M). While formate secretion by *Gclc*-deficient iTregs decreased upon SHMT inhibition (Figure S5K), Foxp3 did not increase (Figure S5L), but proliferation was normalized (Figure S5M). Thus, serine stimulates 1CMet to increase mutant Treg proliferation, but it also acts to decrease Foxp3- and Treg-mediated suppression independently of SHMT and 1CMet.

GSH Restricts Treg Metabolism and Controls Treg Function via Effects on FoxP3

Increased glycolysis is linked to decreased FoxP3 and diminished Treg suppressive capacity (Gerriets et al., 2015; Huynh et al., 2015). Indeed, *Gclc*-deficient iTregs consumed more

(B) FCA of FoxP3 in *Foxp3*^{cre}-*Gclc*$^{fl/fl}$ *and Gclc*$^{fl/fl}$ Tregs isolated from spleen (left) or induced *in vitro* (right). Data are mean ± SEM (n = 3); 5 trials.
(C) Intracellular staining and FCA of pmTOR and pS6 in *Gclc*$^{fl/fl}$ and Foxp3^{cre}-*Gclc*$^{fl/fl}$ Tregs as in (B). Data are mean ± SEM (n = 3); 5 trials.
(D) Intracellular staining and FCA of pS6 and Foxp3 in *Gclc*$^{fl/fl}$ and *Foxp3*^{cre}-*Gclc*$^{fl/fl}$ iTregs transduced with retrovirus expressing EV or *Gclc*. Data are mean ± SEM (n = 3); 3 trials.
(E) *In vitro* suppression assay of *Gclc*$^{fl/fl}$ and Foxp3^{cre}-*Gclc*$^{fl/fl}$ iTregs transduced with retrovirus expressing EV or *Gclc*. Transduced Tregs were FACS sorted and incubated with CTV-labeled Tconv at the indicated ratios; 2 trials.
(F) FCA of pS6 in *Foxp3*^{cre}-*Gclc*$^{fl/fl}$ and *Gclc*$^{fl/fl}$ iTregs incubated with/without Rap. Data are mean ± SEM (n = 3); 3 trials.
(G) Intracellular staining and FCA of FoxP3 in *Foxp3*^{cre}-*Gclc*$^{fl/fl}$ *and Gclc*$^{fl/fl}$ iTregs incubated with/without 100 nM Rap. Data are mean ± SEM (n = 3); 3 trials.
(H) *In vitro* suppression assay of splenic nTregs from *Gclc*$^{fl/fl}$ and Foxp3^{cre}-*Gclc*$^{fl/fl}$ mice that were incubated with/without Rap for 24 h and mixed with Tconv at the indicated ratios; 5 trials.
(I) Intracellular staining and FCA of pSmad3 in *Foxp3*^{cre}-*Gclc*$^{fl/fl}$ *and Gclc*$^{fl/fl}$ iTregs incubated with/without Rap. Data are mean ± SEM (n = 3); 2 trials.
(J) Intracellular staining and FCA of Foxp3 in *Gclc*$^{fl/fl}$ and *Foxp3*^{cre}-*Gclc*$^{fl/fl}$ iTregs transduced with retrovirus expressing EV or Smad3. Data are mean ± SEM (n = 3); 3 trials.
(K) *In vitro* suppression assay of *Gclc*$^{fl/fl}$ and Foxp3^{cre}-*Gclc*$^{fl/fl}$ iTregs transduced with retrovirus expressing EV or Smad3. Transduced Tregs were FACS sorted and incubated with CTV-labeled Tconv at the indicated ratios; 2 trials. *p < 0.05.

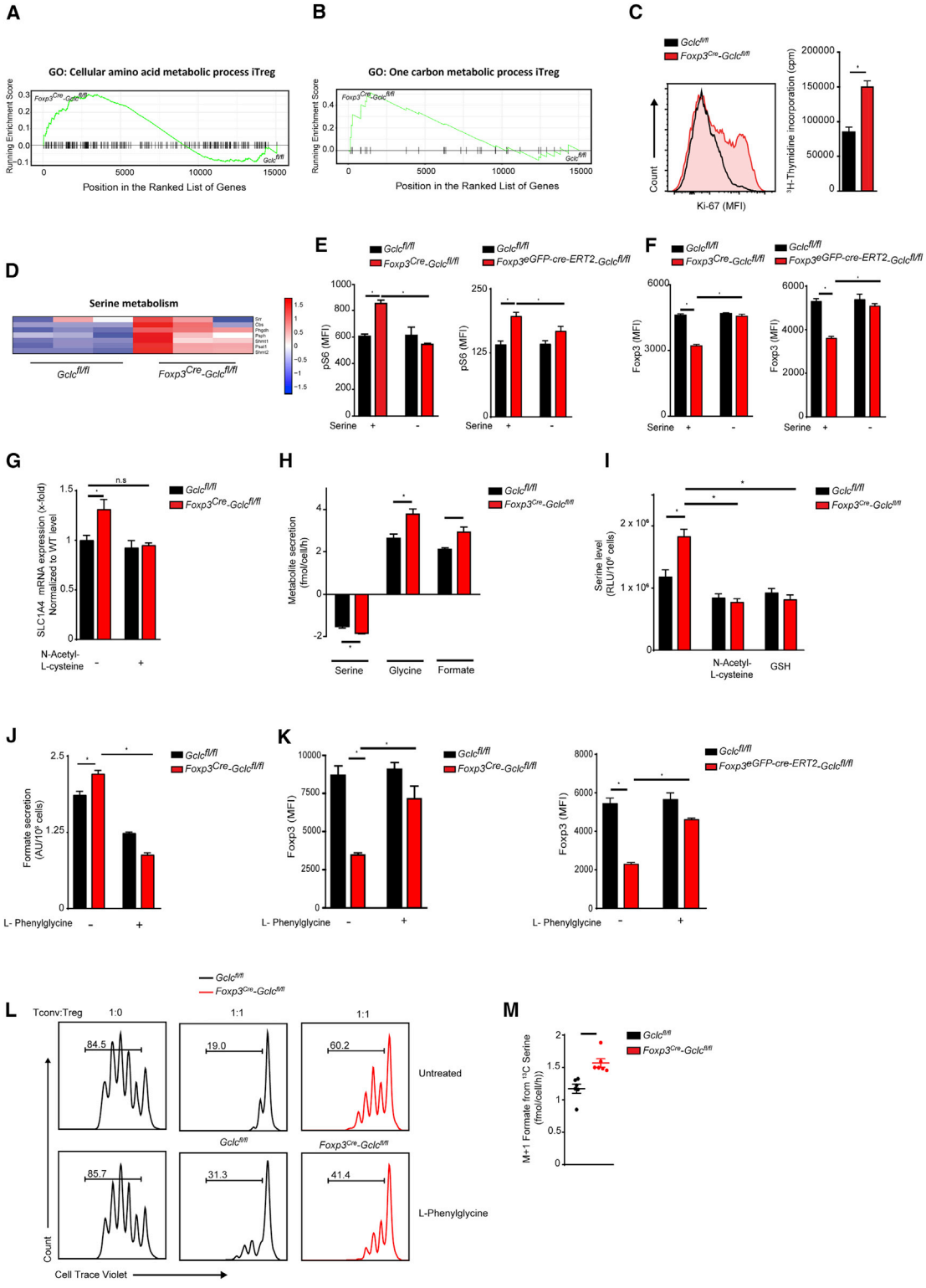

Figure 5. GSH-Mediated Regulation of the Serine Pool Is Required for Treg Function

(A) Barcode enrichment plot of KEGG pathway GO:0006520 (Cellular amino acid metabolic processes) for *Gclc*$^{fl/fl}$ and Foxp3^{cre}-*Gclc*$^{fl/fl}$ iTregs.

(B) Barcode enrichment plot of KEGG pathway GO:0006730 (1CMet) for *Gclc*$^{fl/fl}$ and Foxp3^{cre}-*Gclc*$^{fl/fl}$ iTregs.

(C) Determination of proliferation of *Gclc*$^{fl/fl}$ and Foxp3^{cre}-*Gclc*$^{fl/fl}$ iTregs by Ki-67 staining (left) and ^{3}H-thymidine incorporation (right). Data are mean ± SEM (n = 3); 3 trials.

(legend continued on next page)

glucose, secreted more lactate, and expressed more of the glucose transporter Glut1 than did controls (Figures 6A and S6A). Glycolysis stress testing of *Gclc*-deficient iTregs and 4-OHT-inducible *Gclc*-deficient iTregs revealed that the extracellular acidification rate (ECAR) of culture medium and cellular glycolytic capacity were increased whether *Gclc* ablation was constitutive or 4-OHT induced (Figures 6B and 6C). We then determined [U-$^{13}C_6$]-glucose incorporation into TCA cycle metabolites in *Gclc*-deficient and control iTregs over 24 h and measured mass isotopomer distributions (MIDs) by GC-MS. M2 isotopologues of citrate were elevated in mutant iTregs (Figure S6B), demonstrating an increased relative flux of glucose-derived carbon into the TCA cycle. Accordingly, OCR values in *Gclc*-deficient iTregs and 4-OHT-inducible *Gclc*-deficient iTregs were increased (Figures 6D and 6E).

To determine if enhanced metabolism interfered with iTreg mediated suppression, we incubated *Gclc*-deficient and control iTregs with 2-deoxyglucose (2-DG) or oligomycin to restrict glycolysis or oxidative phosphorylation (OXPHOS), respectively. Restriction of either pathway induced control levels of FoxP3 in the mutant cells and restored their suppressive function (Figures 6F and 6G). To investigate a direct link between FoxP3 and increased metabolism, we transduced *Gclc*-deficient and control iTregs with retrovirus expressing FoxP3 or empty vector (EV). In mutant iTregs, FoxP3 expression decreased uptake of the glucose analog 2-NDBG as well as Glut1 expression and glycolysis (ECAR) (Figures 6H–6J). *Gclc* deficiency in Tconv is associated with impaired mTOR activation and decreased MYC (Mak et al., 2017), but mTOR was more activated (Figure 4C) and MYC was normal in *Gclc*-deficient iTregs (Figure S6C), again pointing to a subset-specific function for GSH. To determine whether FoxP3 could alter a T cell's response to GSH depletion, we transduced activated WT Tconv with retrovirus expressing FoxP3 or EV and treated these cells with the GCLC inhibitor buthionine sulfoximine (BSO). In line with previous work (Gerriets et al., 2016), FoxP3 expression in activated Tconv reduced pS6 (Figures 6K and S6D). BSO decreased pS6 in activated Tconv expressing EV (Figure 6K), but FoxP3 expression altered the Tconv response to BSO and increased pS6 (Figure 6K). Thus, it is FoxP3 in Tregs that shapes responses to GSH depletion; that is, the decreased mTOR activation in activated Tconv lacking GSH shifts to activation of this pathway in *Gclc*-deficient Tregs.

De Novo Serine Synthesis in Tregs Interferes with Foxp3 Expression

During glycolysis, 3-phosphoglycerate dehydrogenase (PHGDH) redirects some 3-PG to serine synthesis. To determine if *Gclc*-deficient Tregs increased glycolysis to produce the 3-PG needed for their enhanced serine production, we incubated *Gclc*-deficient and control iTregs for 24 h with the PHGDH inhibitor PKUMDL-WQ-2101 (Wang et al., 2017) and found equivalent decreases in ECAR (Figure 7A). Thus, regardless of GSH, glycolysis in Tregs is driven partly by the need for intermediates for serine synthesis. [U-$^{13}C_6$]-glucose incorporation into serine and formate was enhanced in *Gclc*-deficient iTregs and reduced by PHGDH inhibition (Figures 7B and 7C). PHGDH inhibition or CRISPR/CAS9 mediated *Phgdh* deletion also elevated FoxP3 in *Gclc*-deficient iTregs and 4-OHT-inducible *Gclc*-deficient iTregs (Figures 7D and 7E). Consequently, PHGDH inhibition restored mutant iTregs suppressive capacity (Figure 7F). Thus, limitation of serine availability by GSH preserves FoxP3 expression and Treg function.

GSH regulates serine uptake and synthesis. Serine deprivation of control iTregs increased glucose-dependent GSH synthesis (Figure S7A), supporting interconnection of these pathways in a feedback loop. To investigate serine's relevance *in vivo*, we fed serine- and glycine-deficient food to 3-week-old control and mutant mice. Serine/glycine-deficient food is well tolerated, measurably decreases circulating serine/glycine, and does not interfere with immune cell subsets (Ma et al., 2017; Maddocks et al., 2013; Maddocks et al., 2017). Serine deprivation *in vivo* increased FoxP3 but reduced pS6 and CD44 in mutant nTregs (Figure 7G), and it decreased serum IFNγ and TNF as well as inflammatory T cells in mutant mice (Figures 7H and 7I). Strikingly, serine/glycine deprivation prevented mutant mouse spontaneous inflammation and death (Figure 7J), confirming the importance of serine metabolism and 1CMet *in vivo*.

To replicate our data in human Tregs, we isolated naive T cells from peripheral blood of healthy donors and induced iTreg differentiation *in vitro* with TGFβ in the absence or presence of BSO. GSH was reduced in BSO-treated human iTregs (Figure S7B). FoxP3 was also decreased, but pS6 was increased (Figures S7C and S7D). Serine deprivation of BSO-treated human iTregs restored FoxP3 and pS6 to control levels (Figures S7E and S7F). FoxP3 in BSO-treated human iTregs was also increased by

(D) Heatmap showing normalized differential gene expression patterns of genes associated with serine metabolism in *Gclc*$^{fl/fl}$ versus *Foxp3*^{cre}-*Gclc*$^{fl/fl}$ iTregs.
(E and F) Intracellular staining and FCA of (E) pS6 and (F) Foxp3 in *Gclc*$^{fl/fl}$ versus Foxp3^{cre}-*Gclc*$^{fl/fl}$ (left) and *Gclc*$^{fl/fl}$ versus Foxp3$^{eGPF\text{-}cre\text{-}ERT2}$-*Gclc*$^{fl/fl}$ (right) iTregs cultured in normal or serine-deficient medium. *Gclc*$^{fl/fl}$ versus Foxp3$^{eGPF\text{-}cre\text{-}ERT2}$-*Gclc*$^{fl/fl}$ iTregs were co-incubated with 1μM 4-OHT. Data are mean ± SEM (n = 3); 3 trials.
(G) RT-qPCR of *ASCT1* mRNA in *Gclc*$^{fl/fl}$ and Foxp3^{cre}-*Gclc*$^{fl/fl}$ iTregs. Data are mean ± SEM (n = 7); 2 trials.
(H) LC/MS quantification of serine uptake from, and glycine and formate secretion into, culture medium of *Gclc*$^{fl/fl}$ and Foxp3^{cre}-*Gclc*$^{fl/fl}$ iTregs. Data are mean ± SEM (n = 3); 2 trials.
(I) Quantification of intracellular serine in *Gclc*$^{fl/fl}$ and Foxp3^{cre}-*Gclc*$^{fl/fl}$ iTregs treated with/without 200 μM NAC or 0.5 mM GSH. Data are mean ± SEM (n = 3); 2 trials.
(J) Quantification of formate secretion into culture medium of *Gclc*$^{fl/fl}$ and Foxp3^{cre}-*Gclc*$^{fl/fl}$ iTregs treated with/without 50 μM L-phenylglycine. Data are mean ± SEM (n = 3); 2 trials.
(K) Intracellular staining and FCA of Foxp3 in *Gclc*$^{fl/fl}$ versus Foxp3^{cre}-*Gclc*$^{fl/fl}$ (left), and *Gclc*$^{fl/fl}$ versus Foxp3$^{eGPF\text{-}cre\text{-}ERT2}$-*Gclc*$^{fl/fl}$ (right), iTregs treated with/without L-phenylglycine. *Gclc*$^{fl/fl}$ versus Foxp3$^{eGPF\text{-}cre\text{-}ERT2}$-*Gclc*$^{fl/fl}$ iTregs were co-incubated with 4-OHT. Data are mean ± SEM (n = 3); 3 trials.
(L) *In vitro* suppression assay of nTregs that were isolated from *Gclc*$^{fl/fl}$ and Foxp3^{cre}-*Gclc*$^{fl/fl}$ mice, incubated with/without L-phenylglycine, and mixed *in vitro* with Tconv at the indicated ratios; 3 trials.
(M) Mass isotopomer distribution of M+1 formate following incubation of *Gclc*$^{fl/fl}$ and Foxp3^{cre}-*Gclc*$^{fl/fl}$ iTregs with [U-$^{13}C_3$]-serine for 24 h. Data are mean ± SEM (n = 3); 2 trials. *p < 0.05.

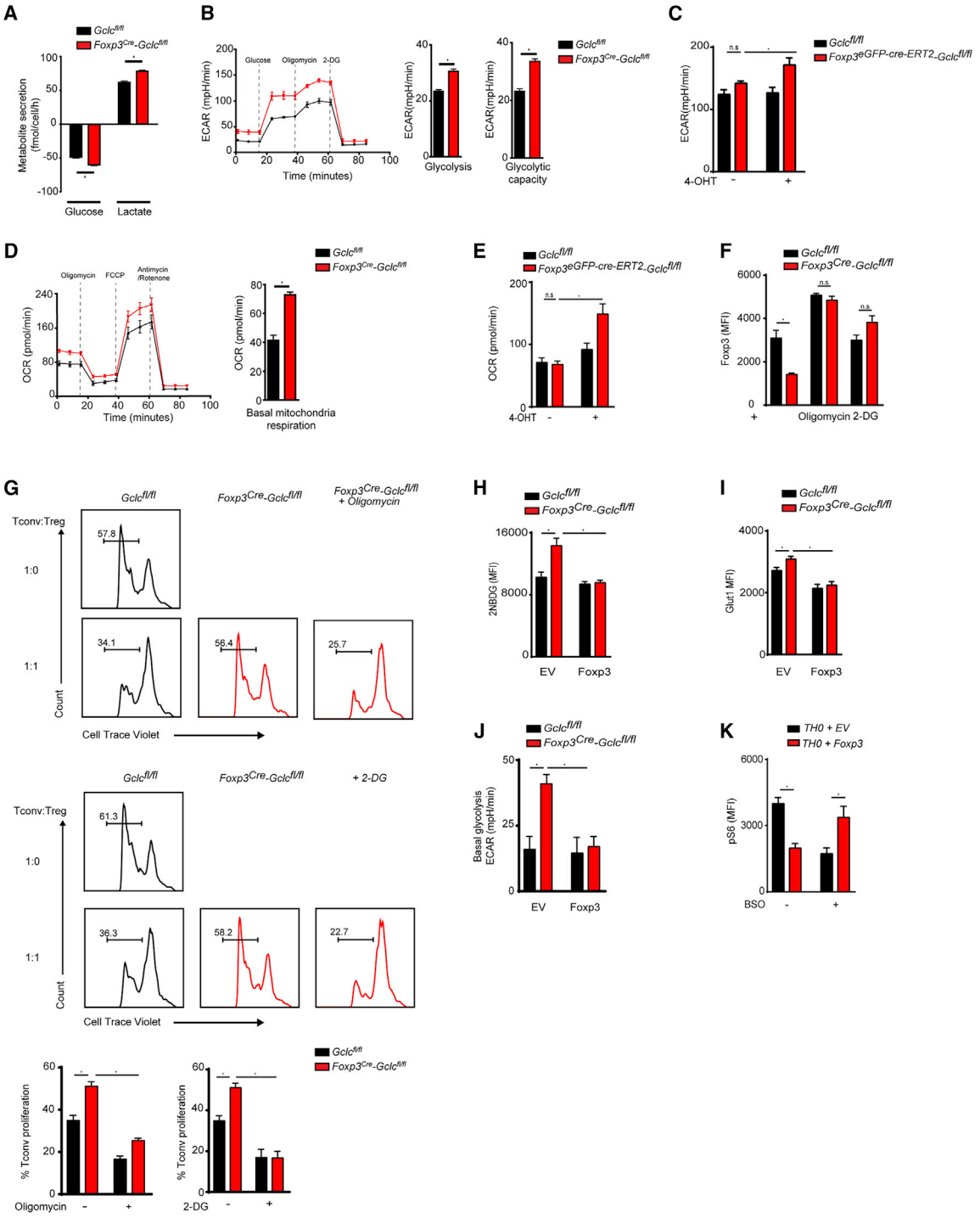

Figure 6. *Gclc* Expression Is Required to Modulate Treg Metabolism Supporting Treg Function

(A) Quantification of glucose uptake from and lactate secretion into culture medium of *Gclc*$^{fl/fl}$ and *Foxp3*^{cre}-*Gclc*$^{fl/fl}$ iTregs. Data are mean ± SEM (n = 3); 3 trials.

(B) Quantification of ECAR of *Gclc*$^{fl/fl}$ versus *Foxp3*^{cre}-*Gclc*$^{fl/fl}$ iTregs. Data are mean ± SEM (n = 4); 4 trials.

(C) Quantification of ECAR of *Gclc*$^{fl/fl}$ versus *Foxp3*$^{eGPF\text{-}cre\text{-}ERT2}$-*Gclc*$^{fl/fl}$ iTregs incubated with 4-OHT. Data are mean ± SEM (n = 3); 2 trials.

(D) Quantification of OCR of *Gclc*$^{fl/fl}$ versus *Foxp3*^{cre}-*Gclc*$^{fl/fl}$ iTregs. Data are mean ± SEM (n = 4); 4 trials.

(E) Quantification of OCR of *Gclc*$^{fl/fl}$ versus *Foxp3*$^{eGPF\text{-}cre\text{-}ERT2}$-*Gclc*$^{fl/fl}$ iTregs incubated with 4-OHT. Data are mean ± SEM (n = 3); 2 trials.

(F) Intracellular staining and FCA of FoxP3 in *Gclc*$^{fl/fl}$ versus *Foxp3*^{cre}-*Gclc*$^{fl/fl}$ iTregs treated with or without suboptimal doses of 0.5 nM oligomycin or 100 μM 2-DG for 24 h. Data are mean ± SEM (n = 3); 3 trials.

(G) *In vitro* suppression assay of *Gclc*$^{fl/fl}$ versus *Foxp3*^{cre}-*Gclc*$^{fl/fl}$ iTregs treated (or not) with suboptimal doses of oligomycin (top) or 2-DG (bottom) prior to incubation with CTV-labeled Tconv at the indicated ratios; 3 trials.

(legend continued on next page)

blocking serine synthesis or restricting serine influx (Figure S7G). Lastly, BSO-treated human iTregs showed a profound loss of suppression (Figure S7H). All these data parallel the results obtained using our mouse model of Treg-specific *Gclc* deficiency.

Anti-tumor Immunity Is Enhanced in *Foxp3^{cre}-Gclc$^{fl/fl}$* Mice

Tregs can promote tumor growth by inhibiting Teff-mediated anti-tumor responses, and some tumors secrete substances driving Treg differentiation (Franchina et al., 2018b). Tumors often generate high ROS due to hypoxia or activities of cancer-associated macrophages or fibroblasts (Bhattacharyya and Saha, 2015; Henze and Mazzone, 2016; Sabharwal and Schumacker, 2014). These ROS inactivate Teffs and so dampen anti-tumor immunity (Bhattacharyya and Saha, 2015; Franchina et al., 2018b; Mak et al., 2017; Pilipow et al., 2018). GSH synthesis by T cells is thus a major defense against tumor-associated ROS. Our iTregs contained more intracellular GSH than Teffs (Figure 1D), in line with their greater ROS resistance (Huynh et al., 2015). This enhanced ROS resistance may allow Tregs to survive in the tumor microenvironment long enough to suppress anti-tumor responses by Teffs. Conversely, a loss of GSH that compromises Tregs' suppressive capacity might allow Teff anti-tumor responses to proceed unchecked to limit cancer growth. To test this hypothesis, we examined anti-tumor immunity in *Foxp3^{cre}-Gclc$^{fl/fl}$* mice.

We subcutaneously (s.c.) injected *Foxp3^{cre}-Gclc$^{fl/fl}$* and control mice with B16 melanoma cells or MC38 colon adenocarcinoma cells and monitored cancer progression. In both cases, tumor growth was slower in *Foxp3^{cre}-Gclc$^{fl/fl}$* mice (Figures 7K and S7I), and tumor weight and size were reduced (Figures 7L, 7M, and S7J). Tumor-infiltrating lymphocytes (TILs) were increased in tumors of mutant mice (Figure 7N). Absolute numbers and frequencies of $CD4^+$ TILs were comparable, but absolute numbers and frequencies of $CD8^+PD1^+GranzymeB^+$ Teffs and $CD8^+IFN\gamma^+$ Teffs were increased in tumors of mutant mice (Figures 7O and S7K). Treg frequency was decreased in tumors of mutant mice, and these Tregs showed reduced FoxP3 (Figure 7O). Adoptive transfer of control or *Gclc*-deficient nTregs into FoxP3-Cre-*Gclc$^{fl/fl}$* mice on the day prior to B16 melanoma cell inoculation resulted in significant tumor development in mutant mice receiving control nTregs, whereas mutant mice receiving *Gclc*-deficient nTregs had still a greatly decreased tumor burden (Figure 7p). Thus, loss of *Gclc* in Tregs reduces their ability to impair anti-cancer Teff responses and thus boosts anti-tumor immunity.

DISCUSSION

ROS are both detrimental byproducts of metabolism and important signaling molecules during cellular activation and differentiation (Franchina et al., 2018a; Sena and Chandel, 2012). In Tconv, mitochondrial ROS are linked to activation, proliferation, and effector functions (Devadas et al., 2002; Gülow et al., 2005; Jackson et al., 2004; Sena et al., 2013; Yi et al., 2006). Nevertheless, excessive ROS accumulation in these cells must be prevented by antioxidants like GSH. Accordingly, *Gclc* ablation in all T cells abrogates autoimmunity but also interferes with anti-viral responses (Lian et al., 2018; Mak et al., 2017). Prior to our study, GSH's function in Tregs was unknown. Targeting *Gclc* specifically in this subset has revealed an unexpected mechanism by which GSH-mediated ROS scavenging preserves mouse and human Treg functionality through restriction of serine metabolism.

Male *Foxp3^{cre}-Gclc$^{fl/fl}$* mice developed an IFNγ-driven lethal lymphoproliferative disease but were better able to suppress tumorigenesis. We have shown, *in vitro* and *in vivo*, that these effects are due to *Gclc*'s crucial role in Treg suppressive function. A lack of GSH in Tregs reduced their FoxP3 and thus their suppressive capacity, a property restored by FoxP3 reconstitution. Surprisingly, Treg proliferation was increased in the absence of GSH, rather than decreased as in Tconv with genetic deletion of *Gclc* or subjected to pharmacological GCL inhibition (Hamilos et al., 1989; Mak et al., 2017; Suthanthiran et al., 1990). Thus, GSH has a unique function in Tregs.

Serine uptake and *de novo* synthesis were both increased in *Gclc*-deficient Tregs. Serine is utilized by Teffs and cancer cells to support proliferation (Labuschagne et al., 2014; Locasale et al., 2011; Ma et al., 2017; Maddocks et al., 2017; Possemato et al., 2011; Ron-Harel et al., 2016) and tumor invasion (Meiser et al., 2018), but we showed that serine interferes with Treg-mediated suppression. Blocking serine uptake or *de novo* synthesis restored FoxP3 and the suppressive capacity of mutants Tregs. Serine is a major substrate of 1CMet (Ducker and Rabinowitz, 2017), and we showed that formate production is increased in mutant Tregs in a manner driven by serine. Glycine starvation did not rescue FoxP3 in mutant Tregs, indicating a critical role for SHMT but not glycine cleavage. Previous studies have shown that glycine and serine are not always interchangeable (Labuschagne et al., 2014; Ma et al., 2017; Maddocks et al., 2017). However, while blocking SHMT in *Gclc*-deficient Tregs restored normal formate secretion and cell proliferation, it did not increase Foxp3. Thus, serine engages at least two distinct pathways in *Gclc*-deficient Tregs.

In vivo, inflammation and morbidity were drastically reduced in mutant mice fed on a serine/glycine-deficient diet. Serine and glycine are two NEAAs whose deprivation is well tolerated *in vivo* (Maddocks et al., 2013; Maddocks et al., 2017). Because an absence of dietary serine/glycine interferes with $CD8^+$ T cell responses (Ma et al., 2017), the reduction of T cell activation in *Gclc*-deficient mice is likely due at least in part to a direct effect of serine/glycine deprivation on Teff responses. However, the complete absence of inflammation in serine/glycine-starved mutant mice points to a more profound effect. While we cannot rule out that other immune cell subsets are affected, *Gclc*-deficient Tregs of serine/glycine-deprived animals showed restored FoxP3, reduced mTOR signaling, and dampened cellular activation, validating our *in vitro* findings *in vivo*. Importantly,

(H and I) FCA of (H) 2-NBDG uptake and (I) Glut-1 expression by *Gclc$^{fl/fl}$* versus *Foxp3^{cre}-Gclc$^{fl/fl}$* iTregs transduced with retrovirus expressing EV or Foxp3.
(J) Quantification of ECAR for the iTregs in (H) as determined in (B). For (H–J), data are the mean ± SEM (n = 3); 2 trials.
(K) Intracellular staining and FCA of pS6 in activated WT Tconv transduced with retrovirus expressing EV or FoxP3 as in (H) and treated with BSO for 48 h. Data are mean ± SEM (n = 3); 3 trials. *$p < 0.05$.

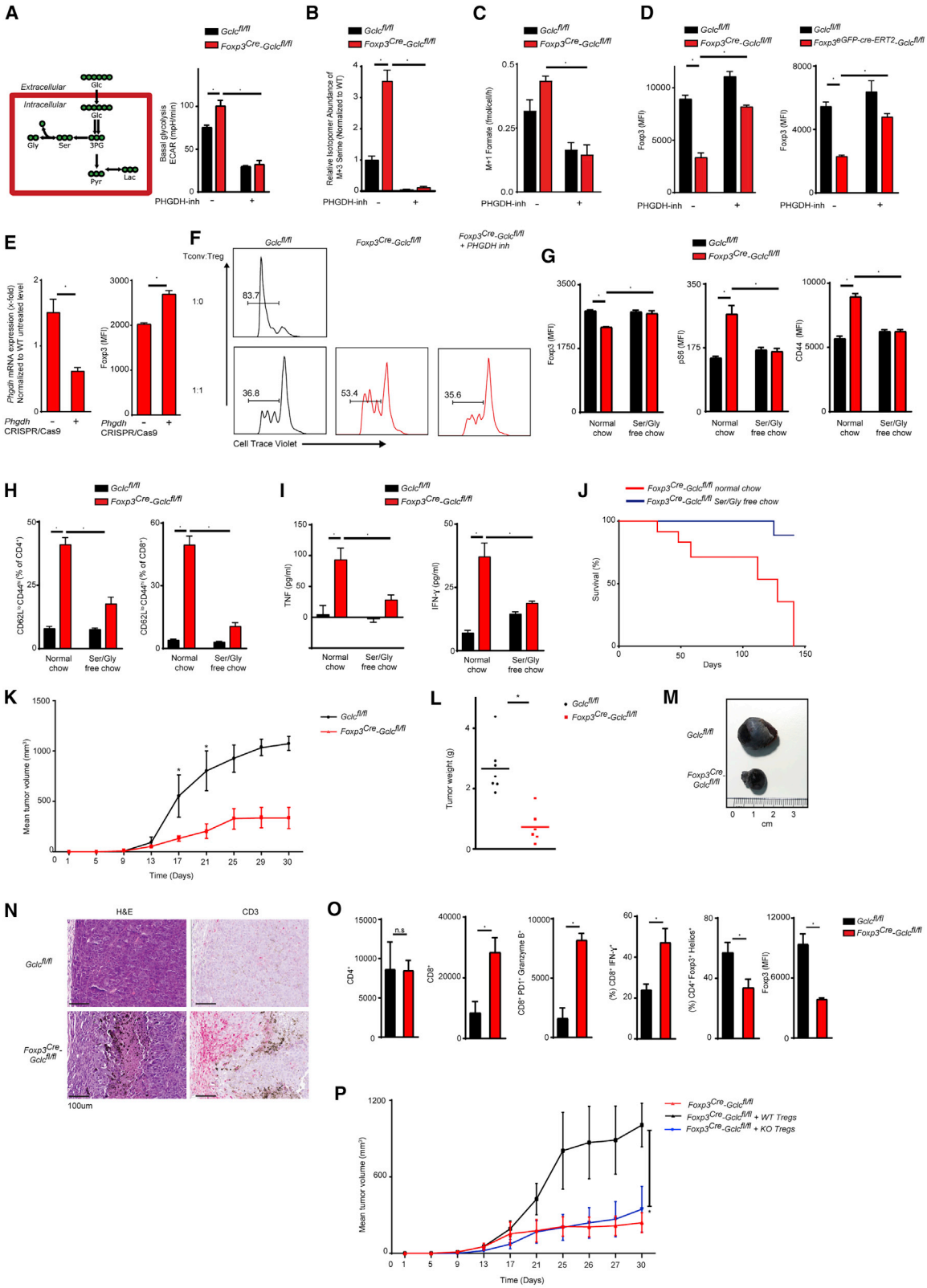

Figure 7. Glutathione Restricts *De Novo* Serine Synthesis and Enhances Anti-tumor Immune Responses

(A) Diagram of serine synthesis pathway (left) and quantification of ECAR of *Gclc*$^{fl/fl}$ and *Foxp3*^{cre}-*Gclc*$^{fl/fl}$ iTregs cultured with/without 10 μM PHGDH inhibitor (right). Data are mean ± SEM (n = 3); 2 trials.

(legend continued on next page)

our study shows that elucidating the exact metabolic and molecular basis of a disease allows potential correction of the metabolic abnormality via a special diet that is aligned with the delineated disease mechanism. Our study might thus be a first step toward personalized treatment of metabolic diseases.

mTOR activation relies mainly on glutamine and leucine (Hara et al., 1998; Nicklin et al., 2009). However, we found that the enhanced serine uptake in mutant Tregs elevated their mTOR activity, paralleling a previous study (Ye et al., 2012). mTOR drives the expression of methylenetetrahydrofolate dehydrogenase (MTHFD)-2 to stimulate 1CMet and purine synthesis (Ben-Sahra et al., 2016), suggesting a feed-forward loop. Such a mechanism might explain how the increased serine levels and mTOR activity in *Gclc*-deficient Tregs support 1CMet. That these pathways are interlinked is indicated by our finding that preventing serine accumulation and inhibiting increased mTOR in mutant Tregs restored their FoxP3 and suppressive function. We therefore propose that in normal Tregs, GSH limits serine uptake and *de novo* synthesis to keep mTOR in check and that this control is critical for Treg function (Figure S7L).

To avoid any effects of inflammation, we assessed FACS-sorted nTregs from non-inflamed female *Foxp3*^{cre}-*Gclc*$^{fl/fl}$ mice, iTregs in which *Gclc* deletion was 4-OHT induced, mutant iTregs subjected to retroviral *Gclc* reconstitution, and human iTregs subjected to pharmacological GCLC blockade. All of these experiments confirmed our findings in male *Foxp3*^{cre}-*Gclc*$^{fl/fl}$ mice. Furthermore, our hypothesis that GSH limits serine and blocks mTOR matches a report that proliferating WT Tregs exhibit stronger mTOR signaling and glycolysis but reduced suppressive capacity (Gerriets et al., 2016). Similarly, constitutive mTOR activation due to deletion of PTEN, PP2A, or TSC1 increases Treg numbers but impairs Treg-mediated suppression (Apostolidis et al., 2016; Huynh et al., 2015; Park et al., 2013; Shrestha et al., 2015). Again, all of these observations align with our findings that *Gclc*-deficient Tregs exhibit increased metabolic activity but are less functional, and that restriction of Treg metabolism reinstates a normal suppressive capacity.

Foxp3 expression in *Gclc*-deficient Tregs was increased by mTOR inhibition or Smad3 overexpression, in line with previous studies showing that mTOR blockade or genetic ablation favors Smad3-dependent induction of FoxP3^{+} T cells over other Th subsets (Delgoffe et al., 2009; Delgoffe et al., 2011). While *Gclc* ablation in Tconv reduced mTOR activation (Mak et al., 2017), the same mutation has the opposite effect in Tregs, implying a subset-specific function of GSH. Treg identity is largely determined by FoxP3 (Rudensky, 2011), and FoxP3 expression in non-Treg T cells induces certain Treg properties (Fontenot et al., 2003; Hori et al., 2003; Khattri et al., 2003). We found that FoxP3 expression in activated T cells shifted responses to BSO from mTOR inhibition to mTOR activation. Thus, FoxP3 expression combined with pharmacological GCLC inhibition recapitulated results obtained using *Gclc*-deficient mice. It appears that lineage-specific transcription factors shape metabolic responses in a subset-specific way.

We demonstrated that *Gclc* ablation increases ROS in Tregs. Mitochondrial ROS are decreased in Tconv with genetic deletion of mitochondrial complex III (Sena et al., 2013). Loss of complex III in Tregs abrogates their suppressive activity but does so independently of FoxP3 (Weinberg et al., 2019). Although ROS levels were not determined in the latter study, it seems that too much or too little ROS is detrimental to Treg function and that multiple regulatory mechanisms can be engaged. Increased ROS triggers an NRF2 response (Kong and Chandel, 2018), as we observed in *Gclc*-deficient Tregs. A key NRF2 target is ASCT1 (Christensen, 1990; Fu et al., 2019; Hirotsu et al., 2012; Schäfer et al., 2010), which is upregulated when T cells grow in an oxidative environment (Yang et al., 2018). We showed that *SLC1A4* mRNA was upregulated in *Gclc*-deficient Tregs and that ROS scavenging decreased ASCT1 and serine uptake in these cells. In contrast, ASCT2 is not an NRF2 target and was equally expressed in control and *Gclc*-deficient Tregs. Inhibition of serine transport in mutant Tregs, or serine deprivation, increased FoxP3 and normalized their suppressive function. Thus, in Tregs, GSH controls ROS to limit NRF2 activation, which decreases ASCT1 and reduces serine import, thereby permitting full

(B) Mass isotopomer distribution of M+3 serine in the cells in (A) following incubation with [U-$^{13}C_6$]-glucose for 24 h.
(C) Mass isotopomer distribution of M+1 formate in the cells in (A) following incubation with [U-$^{13}C_6$]-glucose for 24 h.
(D) Intracellular staining and FCA of FoxP3 in *Gclc*$^{fl/fl}$ versus *Foxp3*^{cre}-*Gclc*$^{fl/fl}$ (left) and *Gclc*$^{fl/fl}$ versus *Foxp3*$^{eGPF\text{-}cre\text{-}ERT2}$-*Gclc*$^{fl/fl}$ (right) iTregs treated with/without PHGDH inhibitor. *Gclc*$^{fl/fl}$ versus *Foxp3*$^{eGPF\text{-}cre\text{-}ERT2}$-*Gclc*$^{fl/fl}$ iTregs were co-incubated with 4-OHT. Data are mean ± SEM (n = 3); 3 trials.
(E) *Phgdh* mRNA expression (left) and intracellular staining and FCA of FoxP3 (right) in *Gclc*$^{fl/fl}$ versus *Foxp3*^{cre}-*Gclc*$^{fl/fl}$ iTregs that were nucleofected with sgRNAs specific for *Phgdh* or controls. Data are mean ± SEM (n = 3); 2 trials.
(F) *In vitro* suppression assay of *Gclc*$^{fl/fl}$ versus *Foxp3*^{cre}-*Gclc*$^{fl/fl}$ iTregs treated with PHGDH inhibitor prior to incubation with CTV-labeled Tconv at the indicated ratios; 3 trials.
(G) Intracellular staining and FCA of FoxP3, pS6, and CD44 in splenic Tregs of *Gclc*$^{fl/fl}$ versus *Foxp3*^{cre}-*Gclc*$^{fl/fl}$ mice (12 weeks of age) fed with normal chow or a serine- and glycine- (Ser/Gly) free chow for 9 weeks. Data are mean ± SEM (n = 4–11); 2 trials.
(H) FCA and quantification of Teff (CD44^{hi}CD62L^{lo}) within CD4^{+} (left) and CD8^{+} (right) T cell populations in blood of the mice in (G). Data are mean ± SEM (n = 4–11); 2 trials.
(I) ELISA of IFNγ and TNF in serum of the mice in (G). Data are mean ± SEM (n = 4–11); 2 trials.
(J) Survival of *Foxp3*^{cre}-*Gclc*$^{fl/fl}$ mice on normal chow (n = 12) or a Ser/Gly- free chow (n = 9);
(K–N) *Gclc*$^{fl/fl}$ and *Foxp3*^{cre}-*Gclc*$^{fl/fl}$ mice (8 weeks of age) were transplanted s.c. with B16F10 melanoma cells.
(K) Mean tumor volumes determined at the indicated times.
(L) Quantification of tumor weights at time of sacrifice. Each dot represents an individual mouse.
(M) Representative macroscopic images of tumors from transplanted *Gclc*$^{fl/fl}$ and *Foxp3*^{cre}-*Gclc*$^{fl/fl}$ mice.
(N) Histology of tumor sections from the mice in (F) stained with H&E or αCD3. Scale bars, 100 μm. Results are representative of 4 mice/group; 2 trials.
(O) Quantification of the indicated TIL subsets in tumors of *Gclc*$^{fl/fl}$ and *Foxp3*^{cre}-*Gclc*$^{fl/fl}$ mice treated as in (K). Data are mean ± SEM (n = 5).
(P) Mean tumor volumes at the indicated times in *Foxp3*^{cre}-*Gclc*$^{fl/fl}$ mice (8 weeks of age) transplanted s.c. with B16F10 melanoma cells and injected intravenously with nTregs from *Gclc*$^{fl/fl}$ (WT) or *Foxp3*^{cre}-*Gclc*$^{fl/fl}$ (KO) mice at day 0. Data are mean ± SEM (n = 4); 2 trials. *p < 0.05.

FoxP3 expression. We propose that in Tregs, GSH is a stress sensor, and it routinely scavenges ROS to prevent redox imbalance. Without GSH, ROS accumulate and initiate an NRF2 stress response that increases serine import and synthesis in an effort to produce GSH. The intracellular accumulation of this serine fuels 1CMet driving Treg expansion but also stimulates mTOR, which reduces FoxP3 and dampens Tregs suppressive capacity (Figure S7L). Thus, there is a crucial stress-sensitive feedback loop between GSH and serine availability that controls Treg function.

In conclusion, we have shown that GSH is critical for maintaining Treg function crucial for immune homeostasis. This unexpected, subset-specific role for GSH in restraining serine metabolism in Tregs may offer novel opportunities to modulate their activities. In particular, our results may point the way to new therapies for cancers where subverted Tregs contribute to tumor progression.

Limitations of Study

(1) We observed that *Gclc* regulates Treg metabolism in a subset-specific way that is clearly distinct from its function in conventional T cells. However, it is difficult to postulate a mechanistic explanation. Notably, FoxP3 expression alters the response to GSH depletion, a finding that would be interesting to study in detail. (2) We validated our mouse data in FoxP3-expressing human Tregs, but additional human Treg subsets exist that do not rely on FoxP3. It will be important to investigate whether and how GSH affects the metabolism and function of these subsets. (3) Our study depends on GSH depletion achieved using *in vitro* and *in vivo* mouse and human models. We show that GSH depletion interferes with Treg metabolism and increases ROS and that ROS scavenging normalizes cellular serine concentrations. However, we cannot exclude the possibility that GSH-dependent, but ROS-independent, mechanisms might contribute to our findings.

STAR★METHODS

Detailed methods are provided in the online version of this paper and include the following:

SUPPLEMENTAL INFORMATION

Supplemental Information can be found online at https://doi.org/10.1016/j.cmet.2020.03.004.

ACKNOWLEDGMENTS

We thank S. Storn, A. Oudin (LIH, Luxembourg), and LIH's Animal Welfare Structure for animal services, and we are grateful to the Metabolomics Platform of Luxembourg Centre for Systems Biomedicine (LCSB). We also thank B. Camara (Univ. Marburg, Germany) for technical help; M. Brenner for general support; and Croix-Rouge Luxembourgeoise and all study blood donors. D.B. is supported by FNR-ATTRACT (A14/BM/7632103) and FNR-CORE grants (C15/BM/10355103) and (C18/BM/12691266). D.B., L.B., L.G., J.T., M.Z., and L.S.B are funded by FNR-PRIDE (PRIDE/11012546/NEXTIMMUNE) and D.B., A.E., and P.W. by (PRIDE17/11823097/MicrOH). D.B. and D.G.F. are supported by FNR-RIKEN (TregBar/11228353). V.V. holds grant NIH/NIAAA (5R24AA022057). J.T. was funded by FNR-CORE (C16/BM/11342695). M.L. and D.D.G. are funded by Deutsches Zentrum für Infektionsforschung and University Hospital Giessen Marburg. T.W.M. is funded by grants from the National Multiple Sclerosis Society and Canadian Institutes of Health Research. C.B.K.T. and R.T. are supported by DKH (110663, CBKT, RT) and BMBF (01ZX1401B, CBKT). J.M. is supported by FNR-ATTRACT (A18/BM/11809970) and INTER-BMBF grant (18/13399110).

AUTHOR CONTRIBUTIONS

D.B. and H.K.: study conception and manuscript writing. H.K., D.G.F., L.G., L.B., L.S.B., M.G., L.S., C.D., M.P.M., C.B., G.S.D., S.F., Y.N., J.H., D.D.G., and A.E.: data generation and analysis. R.T. and C.B.K.: histology. R.H. and P.W.: RNA sequencing. O.H.: bioinformatics. H.K., D.G.F., L.S.B., L.S., C.J., J.M., K.H., Y.N., and D.B.: metabolic analyses. T.W.M., M.L., I.S.H., Y.C., M.O., and V.V.: expert comments and reagents. D.B.: study supervision.

DECLARATION OF INTERESTS

The authors declare no competing interests.

Received: June 20, 2019
Revised: December 26, 2019
Accepted: March 2, 2020
Published: March 25, 2020

REFERENCES

Almeida, L., Lochner, M., Berod, L., and Sparwasser, T. (2016). Metabolic pathways in T cell activation and lineage differentiation. Semin. Immunol. *28*, 514–524.

Apostolidis, S.A., Rodríguez-Rodríguez, N., Suárez-Fueyo, A., Dioufa, N., Ozcan, E., Crispín, J.C., Tsokos, M.G., and Tsokos, G.C. (2016). Phosphatase PP2A is requisite for the function of regulatory T cells. Nat. Immunol. *17*, 556–564.

Battello, N., Zimmer, A.D., Goebel, C., Dong, X., Behrmann, I., Haan, C., Hiller, K., and Wegner, A. (2016). The role of HIF-1 in oncostatin M-dependent metabolic reprogramming of hepatic cells. Cancer & Metabolism *4*, 3.

Ben-Sahra, I., Hoxhaj, G., Ricoult, S.J.H., Asara, J.M., and Manning, B.D. (2016). mTORC1 induces purine synthesis through control of the mitochondrial tetrahydrofolate cycle. Science *351*, 728–733.

Bhattacharyya, S., and Saha, J. (2015). Tumour, oxidative stress and host T cell response: cementing the dominance. Scand. J. Immunol. *82*, 477–488.

Bothur, E., Raifer, H., Haftmann, C., Stittrich, A.B., Brüstle, A., Brenner, D., Bollig, N., Bieringer, M., Kang, C.H., Reinhard, K., et al. (2015). Antigen receptor-mediated depletion of FOXP3 in induced regulatory T-lymphocytes via PTPN2 and FOXO1. Nat. Commun. *6*, 8576.

Brenner, D., Brüstle, A., Lin, G.H., Lang, P.A., Duncan, G.S., Knobbe-Thomsen, C.B., St Paul, M., Reardon, C., Tusche, M.W., Snow, B., et al. (2014). Toso controls encephalitogenic immune responses by dendritic cells and regulatory T cells. Proc. Natl. Acad. Sci. USA *111*, 1060–1065.

Bröer, S., and Bröer, A. (2017). Amino acid homeostasis and signalling in mammalian cells and organisms. Biochem. J. *474*, 1935–1963.

Chen, Y., Yang, Y., Miller, M.L., Shen, D., Shertzer, H.G., Stringer, K.F., Wang, B., Schneider, S.N., Nebert, D.W., and Dalton, T.P. (2007). Hepatocyte-specific Gclc deletion leads to rapid onset of steatosis with mitochondrial injury and liver failure. Hepatology *45*, 1118–1128.

Christensen, H.N. (1990). Role of amino acid transport and countertransport in nutrition and metabolism. Physiol. Rev. *70*, 43–77.

Cossarizza, A., Chang, H.D., Radbruch, A., Acs, A., Adam, D., Adam-Klages, S., Agace, W.W., Aghaeepour, N., Akdis, M., Allez, M., et al. (2019). Guidelines for the use of flow cytometry and cell sorting in immunological studies (second edition). Eur. J. Immunol. *49*, 1457–1973.

Dang, E.V., Barbi, J., Yang, H.Y., Jinasena, D., Yu, H., Zheng, Y., Bordman, Z., Fu, J., Kim, Y., Yen, H.R., et al. (2011). Control of T(H)17/T(reg) balance by hypoxia-inducible factor 1. Cell *146*, 772–784.

Delgoffe, G.M., Kole, T.P., Zheng, Y., Zarek, P.E., Matthews, K.L., Xiao, B., Worley, P.F., Kozma, S.C., and Powell, J.D. (2009). The mTOR kinase differentially regulates effector and regulatory T cell lineage commitment. Immunity *30*, 832–844.

Delgoffe, G.M., Pollizzi, K.N., Waickman, A.T., Heikamp, E., Meyers, D.J., Horton, M.R., Xiao, B., Worley, P.F., and Powell, J.D. (2011). The kinase mTOR regulates the differentiation of helper T cells through the selective activation of signaling by mTORC1 and mTORC2. Nat. Immunol. *12*, 295–303.

Devadas, S., Zaritskaya, L., Rhee, S.G., Oberley, L., and Williams, M.S. (2002). Discrete generation of superoxide and hydrogen peroxide by T cell receptor stimulation: selective regulation of mitogen-activated protein kinase activation and fas ligand expression. J. Exp. Med. *195*, 59–70.

Ducker, G.S., and Rabinowitz, J.D. (2017). One-Carbon Metabolism in Health and Disease. Cell Metab. *25*, 27–42.

Dumont, F.J., and Su, Q. (1996). Mechanism of action of the immunosuppressant rapamycin. Life Sci. *58*, 373–395.

Fontenot, J.D., Gavin, M.A., and Rudensky, A.Y. (2003). Foxp3 programs the development and function of CD4+CD25+ regulatory T cells. Nat. Immunol. *4*, 330–336.

Foster, A.C., Rangel-Diaz, N., Staubli, U., Yang, J.Y., Penjwini, M., Viswanath, V., and Li, Y.X. (2017). Phenylglycine analogs are inhibitors of the neutral amino acid transporters ASCT1 and ASCT2 and enhance NMDA receptor-mediated LTP in rat visual cortex slices. Neuropharmacology *126*, 70–83.

Franchina, D.G., Dostert, C., and Brenner, D. (2018a). Reactive oxygen species: involvement in T cell signaling and metabolism. Trends Immunol. *39*, 489–502.

Franchina, D.G., He, F., and Brenner, D. (2018b). Survival of the fittest: Cancer challenges T cell metabolism. Cancer Lett. *412*, 216–223.

Francisco, L.M., Salinas, V.H., Brown, K.E., Vanguri, V.K., Freeman, G.J., Kuchroo, V.K., and Sharpe, A.H. (2009). PD-L1 regulates the development, maintenance, and function of induced regulatory T cells. J. Exp. Med. *206*, 3015–3029.

Fu, J., Xiong, Z., Huang, C., Li, J., Yang, W., Han, Y., Paiboonrungruan, C., Major, M.B., Chen, K.N., Kang, X., and Chen, X. (2019). Hyperactivity of the transcription factor Nrf2 causes metabolic reprogramming in mouse esophagus. J. Biol. Chem. *294*, 327–340.

Gerriets, V.A., Kishton, R.J., Nichols, A.G., Macintyre, A.N., Inoue, M., Ilkayeva, O., Winter, P.S., Liu, X., Priyadharshini, B., Slawinska, M.E., et al. (2015). Metabolic programming and PDHK1 control CD4+ T cell subsets and inflammation. J. Clin. Invest. *125*, 194–207.

Gerriets, V.A., Kishton, R.J., Johnson, M.O., Cohen, S., Siska, P.J., Nichols, A.G., Warmoes, M.O., de Cubas, A.A., MacIver, N.J., Locasale, J.W., et al. (2016). Foxp3 and Toll-like receptor signaling balance T_{reg} cell anabolic metabolism for suppression. Nat. Immunol. *17*, 1459–1466.

Goberdhan, D.C., Wilson, C., and Harris, A.L. (2016). Amino Acid Sensing by mTORC1: Intracellular Transporters Mark the Spot. Cell Metab. *23*, 580–589.

Gülow, K., Kaminski, M., Darvas, K., Süss, D., Li-Weber, M., and Krammer, P.H. (2005). HIV-1 trans-activator of transcription substitutes for oxidative signaling in activation-induced T cell death. J. Immunol. *174*, 5249–5260.

Hamilos, D.L., Zelarney, P., and Mascali, J.J. (1989). Lymphocyte proliferation in glutathione-depleted lymphocytes: direct relationship between glutathione availability and the proliferative response. Immunopharmacology *18*, 223–235.

Hara, K., Yonezawa, K., Weng, Q.P., Kozlowski, M.T., Belham, C., and Avruch, J. (1998). Amino acid sufficiency and mTOR regulate p70 S6 kinase and eIF-4E BP1 through a common effector mechanism. J. Biol. Chem. *273*, 14484–14494.

Henze, A.T., and Mazzone, M. (2016). The impact of hypoxia on tumor-associated macrophages. J. Clin. Invest. *126*, 3672–3679.

Herbig, K., Chiang, E.P., Lee, L.R., Hills, J., Shane, B., and Stover, P.J. (2002). Cytoplasmic serine hydroxymethyltransferase mediates competition between folate-dependent deoxyribonucleotide and S-adenosylmethionine biosyntheses. J. Biol. Chem. *277*, 38381–38389.

Hirotsu, Y., Katsuoka, F., Funayama, R., Nagashima, T., Nishida, Y., Nakayama, K., Engel, J.D., and Yamamoto, M. (2012). Nrf2-MafG heterodimers contribute globally to antioxidant and metabolic networks. Nucleic Acids Res. *40*, 10228–10239.

Hori, S., Nomura, T., and Sakaguchi, S. (2003). Control of regulatory T cell development by the transcription factor Foxp3. Science *299*, 1057–1061.

Huynh, A., DuPage, M., Priyadharshini, B., Sage, P.T., Quiros, J., Borges, C.M., Townamchai, N., Gerriets, V.A., Rathmell, J.C., Sharpe, A.H., et al. (2015). Control of PI(3) kinase in Treg cells maintains homeostasis and lineage stability. Nat. Immunol. *16*, 188–196.

Jackson, S.H., Devadas, S., Kwon, J., Pinto, L.A., and Williams, M.S. (2004). T cells express a phagocyte-type NADPH oxidase that is activated after T cell receptor stimulation. Nat. Immunol. *5*, 818–827.

Kaplan, E., Zubedat, S., Radzishevsky, I., Valenta, A.C., Rechnitz, O., Sason, H., Sajrawi, C., Bodner, O., Konno, K., Esaki, K., et al. (2018). ASCT1 (Slc1a4) transporter is a physiologic regulator of brain d-serine and neurodevelopment. Proc. Natl. Acad. Sci. USA *115*, 9628–9633.

Khattri, R., Cox, T., Yasayko, S.A., and Ramsdell, F. (2003). An essential role for Scurfin in CD4+CD25+ T regulatory cells. Nat. Immunol. *4*, 337–342.

Kim, H.J., Barnitz, R.A., Kreslavsky, T., Brown, F.D., Moffett, H., Lemieux, M.E., Kaygusuz, Y., Meissner, T., Holderried, T.A., Chan, S., et al. (2015). Stable inhibitory activity of regulatory T cells requires the transcription factor Helios. Science *350*, 334–339.

Kong, H., and Chandel, N.S. (2018). Regulation of redox balance in cancer and T cells. J. Biol. Chem. *293*, 7499–7507.

Labuschagne, C.F., van den Broek, N.J., Mackay, G.M., Vousden, K.H., and Maddocks, O.D. (2014). Serine, but not glycine, supports one-carbon metabolism and proliferation of cancer cells. Cell Rep. *7*, 1248–1258.

Lian, G., Gnanaprakasam, J.R., Wang, T., Wu, R., Chen, X., Liu, L., Shen, Y., Yang, M., Yang, J., Chen, Y., et al. (2018). Glutathione de novo synthesis but not recycling process coordinates with glutamine catabolism to control redox homeostasis and directs murine T cell differentiation. eLife *7*, e36158.

Locasale, J.W., Grassian, A.R., Melman, T., Lyssiotis, C.A., Mattaini, K.R., Bass, A.J., Heffron, G., Metallo, C.M., Muranen, T., Sharfi, H., et al. (2011). Phosphoglycerate dehydrogenase diverts glycolytic flux and contributes to oncogenesis. Nat. Genet. *43*, 869–874.

Lowther, D.E., Goods, B.A., Lucca, L.E., Lerner, B.A., Raddassi, K., van Dijk, D., Hernandez, A.L., Duan, X., Gunel, M., Coric, V., et al. (2016). PD-1 marks dysfunctional regulatory T cells in malignant gliomas. JCI Insight *1*, e85935.

Lu, S.C. (2009). Regulation of glutathione synthesis. Mol. Aspects Med. *30*, 42–59.

Ma, E.H., Bantug, G., Griss, T., Condotta, S., Johnson, R.M., Samborska, B., Mainolfi, N., Suri, V., Guak, H., Balmer, M.L., et al. (2017). Serine Is an Essential Metabolite for Effector T Cell Expansion. Cell Metab. *25*, 345–357.

Maddocks, O.D., Berkers, C.R., Mason, S.M., Zheng, L., Blyth, K., Gottlieb, E., and Vousden, K.H. (2013). Serine starvation induces stress and p53-dependent metabolic remodelling in cancer cells. Nature *493*, 542–546.

Maddocks, O.D.K., Athineos, D., Cheung, E.C., Lee, P., Zhang, T., van den Broek, N.J.F., Mackay, G.M., Labuschagne, C.F., Gay, D., Kruiswijk, F., et al. (2017). Modulating the therapeutic response of tumours to dietary serine and glycine starvation. Nature *544*, 372–376.

Mak, T.W., Grusdat, M., Duncan, G.S., Dostert, C., Nonnenmacher, Y., Cox, M., Binsfeld, C., Hao, Z., Brüstle, A., Itsumi, M., et al. (2017). Glutathione Primes T Cell Metabolism for Inflammation. Immunity *46*, 675–689.

Meiser, J., Tumanov, S., Maddocks, O., Labuschagne, C.F., Athineos, D., Van Den Broek, N., Mackay, G.M., Gottlieb, E., Blyth, K., Vousden, K., et al. (2016). Serine one-carbon catabolism with formate overflow. Sci. Adv. *2*, e1601273.

Meiser, J., Schuster, A., Pietzke, M., Vande Voorde, J., Athineos, D., Oizel, K., Burgos-Barragan, G., Wit, N., Dhayade, S., Morton, J.P., et al. (2018). Increased formate overflow is a hallmark of oxidative cancer. Nat. Commun. *9*, 1368.

Meister, A. (1983). Selective modification of glutathione metabolism. Science *220*, 472–477.

Nakagawa, H., Sido, J.M., Reyes, E.E., Kiers, V., Cantor, H., and Kim, H.J. (2016). Instability of Helios-deficient Tregs is associated with conversion to a T-effector phenotype and enhanced antitumor immunity. Proc. Natl. Acad. Sci. USA *113*, 6248–6253.

Nicklin, P., Bergman, P., Zhang, B., Triantafellow, E., Wang, H., Nyfeler, B., Yang, H., Hild, M., Kung, C., Wilson, C., et al. (2009). Bidirectional transport of amino acids regulates mTOR and autophagy. Cell *136*, 521–534.

Nüssing, S., House, I.G., Kearney, C.J., Vervoort, S.J., Beavis, P.A., Oliaro, J., Johnstone, R.W., Trapani, J.A., and Parish, I.A. (2019). Efficient CRISPR/Cas9 gene ablation in uncultured naïve mouse T cells for in vivo studies. bioRxiv. https://doi.org/10.1101/730812.

Park, Y., Jin, H.S., Lopez, J., Elly, C., Kim, G., Murai, M., Kronenberg, M., and Liu, Y.C. (2013). TSC1 regulates the balance between effector and regulatory T cells. J. Clin. Invest. *123*, 5165–5178.

Pearce, E.L., Poffenberger, M.C., Chang, C.H., and Jones, R.G. (2013). Fueling immunity: insights into metabolism and lymphocyte function. Science *342*, 1242454.

Pilipow, K., Scamardella, E., Puccio, S., Gautam, S., De Paoli, F., Mazza, E.M., De Simone, G., Polletti, S., Buccilli, M., Zanon, V., et al. (2018). Antioxidant metabolism regulates CD8+ T memory stem cell formation and antitumor immunity. JCI Insight *3*, 122299.

Possemato, R., Marks, K.M., Shaul, Y.D., Pacold, M.E., Kim, D., Birsoy, K., Sethumadhavan, S., Woo, H.K., Jang, H.G., Jha, A.K., et al. (2011). Functional genomics reveal that the serine synthesis pathway is essential in breast cancer. Nature *476*, 346–350.

Reardon, C., Lechmann, M., Brüstle, A., Gareau, M.G., Shuman, N., Philpott, D., Ziegler, S.F., and Mak, T.W. (2011). Thymic stromal lymphopoetin-induced expression of the endogenous inhibitory enzyme SLPI mediates recovery from colonic inflammation. Immunity *35*, 223–235.

Ren, W., Liu, G., Yin, J., Tan, B., Wu, G., Bazer, F.W., Peng, Y., and Yin, Y. (2017). Amino-acid transporters in T-cell activation and differentiation. Cell Death Dis. *8*, e2655.

Ron-Harel, N., Santos, D., Ghergurovich, J.M., Sage, P.T., Reddy, A., Lovitch, S.B., Dephoure, N., Satterstrom, F.K., Sheffer, M., Spinelli, J.B., et al. (2016). Mitochondrial biogenesis and proteome remodeling promote one-carbon metabolism for T cell activation. Cell Metab. *24*, 104–117.

Rubtsov, Y.P., Rasmussen, J.P., Chi, E.Y., Fontenot, J., Castelli, L., Ye, X., Treuting, P., Siewe, L., Roers, A., Henderson, W.R., Jr., et al. (2008). Regulatory T cell-derived interleukin-10 limits inflammation at environmental interfaces. Immunity *28*, 546–558.

Rudensky, A.Y. (2011). Regulatory T cells and Foxp3. Immunol. Rev. *241*, 260–268.

Sabharwal, S.S., and Schumacker, P.T. (2014). Mitochondrial ROS in cancer: initiators, amplifiers or an Achilles' heel? Nat. Rev. Cancer *14*, 709–721.

Schäfer, M., Dütsch, S., auf dem Keller, U., Navid, F., Schwarz, A., Johnson, D.A., Johnson, J.A., and Werner, S. (2010). Nrf2 establishes a glutathione-mediated gradient of UVB cytoprotection in the epidermis. Genes Dev. *24*, 1045–1058.

Sena, L.A., and Chandel, N.S. (2012). Physiological roles of mitochondrial reactive oxygen species. Mol. Cell *48*, 158–167.

Sena, L.A., Li, S., Jairaman, A., Prakriya, M., Ezponda, T., Hildeman, D.A., Wang, C.R., Schumacker, P.T., Licht, J.D., Perlman, H., et al. (2013). Mitochondria are required for antigen-specific T cell activation through reactive oxygen species signaling. Immunity *38*, 225–236.

Shi, L.Z., Wang, R., Huang, G., Vogel, P., Neale, G., Green, D.R., and Chi, H. (2011). HIF1alpha-dependent glycolytic pathway orchestrates a metabolic checkpoint for the differentiation of TH17 and Treg cells. J. Exp. Med. *208*, 1367–1376.

Shrestha, S., Yang, K., Guy, C., Vogel, P., Neale, G., and Chi, H. (2015). Treg cells require the phosphatase PTEN to restrain TH1 and TFH cell responses. Nat. Immunol. *16*, 178–187.

Suthanthiran, M., Anderson, M.E., Sharma, V.K., and Meister, A. (1990). Glutathione regulates activation-dependent DNA synthesis in highly purified normal human T lymphocytes stimulated via the CD2 and CD3 antigens. Proc. Natl. Acad. Sci. USA *87*, 3343–3347.

Tibbetts, A.S., and Appling, D.R. (2010). Compartmentalization of Mammalian folate-mediated one-carbon metabolism. Annu. Rev. Nutr. *30*, 57–81.

Tone, Y., Furuuchi, K., Kojima, Y., Tykocinski, M.L., Greene, M.I., and Tone, M. (2008). Smad3 and NFAT cooperate to induce Foxp3 expression through its enhancer. Nat. Immunol. *9*, 194–202.

Wang, Q., Liberti, M.V., Liu, P., Deng, X., Liu, Y., Locasale, J.W., and Lai, L. (2017). Rational design of selective allosteric inhibitors of PHGDH and serine synthesis with anti-tumor activity. Cell Chem. Biol. *24*, 55–65.

Weinberg, S.E., Singer, B.D., Steinert, E.M., Martinez, C.A., Mehta, M.M., Martinez-Reyes, I., Gao, P., Helmin, K.A., Abdala-Valencia, H., Sena, L.A., et al. (2019). Mitochondrial complex III is essential for SC of regulatory T cells. Nature *565*, 495–499.

Wing, K., and Sakaguchi, S. (2010). Regulatory T cells exert checks and balances on self tolerance and autoimmunity. Nat. Immunol. *11*, 7–13.

Yamamoto, T., Nishizaki, I., Nukada, T., Kamegaya, E., Furuya, S., Hirabayashi, Y., Ikeda, K., Hata, H., Kobayashi, H., Sora, I., and Yamamoto, H. (2004). Functional identification of ASCT1 neutral amino acid transporter as the predominant system for the uptake of L-serine in rat neurons in primary culture. Neurosci. Res. *49*, 101–111.

Yang, X., Xia, R., Yue, C., Zhai, W., Du, W., Yang, Q., Cao, H., Chen, X., Obando, D., Zhu, Y., et al. (2018). ATF4 regulates $CD4^+$ T cell immune responses through metabolic reprogramming. Cell Rep. *23*, 1754–1766.

Ye, J., Mancuso, A., Tong, X., Ward, P.S., Fan, J., Rabinowitz, J.D., and Thompson, C.B. (2012). Pyruvate kinase M2 promotes de novo serine synthesis to sustain mTORC1 activity and cell proliferation. Proc. Natl. Acad. Sci. USA *109*, 6904–6909.

Ye, J., Fan, J., Venneti, S., Wan, Y.W., Pawel, B.R., Zhang, J., Finley, L.W., Lu, C., Lindsten, T., Cross, J.R., et al. (2014). Serine catabolism regulates mitochondrial redox control during hypoxia. Cancer Discov. *4*, 1406–1417.

Yi, J.S., Holbrook, B.C., Michalek, R.D., Laniewski, N.G., and Grayson, J.M. (2006). Electron transport complex I is required for CD8+ T cell function. J. Immunol. *177*, 852–862.

STAR★METHODS

KEY RESOURCES TABLE

REAGENT or RESOURCE	SOURCE	IDENTIFIER
Antibodies		
CD4-PE Clone GK1.5 (1:200)	Biolegend	Cat #100408; RRID:AB_312693
CD25-PE Clone PC61 (1:200)	Biolegend	Cat #102008; RRID:AB_312857
IRF4-PE Clone IRF4.3F4 (1:200)	Biolegend	Cat #646404; RRID:AB_2563005
F4/80-PE Clone BM8 (1:200)	Biolegend	Cat #123110 ;RRID:AB_893486
CD185-PE Clone L138D7 (1:200)	Biolegend	Cat #145504; RRID:AB_2561968
CD90.1-PE Clone HIS51 (1:200)	Thermo Fisher	Cat #12-0900-81; RRID:AB_465773
CD45RB-PE Clone C363-16A (1:200)	Biolegend	Cat #103308; RRID:AB_313015
Ki-67-PE Clone 16A8 (1:200)	Biolegend	Cat #652404; RRID:AB_2561525
TGF-β1,-β2,-β3-PE Clone 1D11 (1:200)	R&D Systems	Cat #IC1835P; RRID:AB_884508
Tbet-PE/Cy7 Clone 4B10 (1:200)	Biolegend	Cat #644824; RRID:AB_2561761
F4/80-PE/Cy7 Clone BM8 (1:200)	Biolegend	Cat #123114; RRID:AB_893478
Bcl6-PE/Cy7 Clone 7D1 (1:200)	Biolegend	Cat #358512; RRID:AB_2566196
Helios-PE/Cy7 Clone 22F6 (1:200)	Biolegend	Cat #137236; RRID:AB_2565990
pSTAT5-PE/Cy7 Clone SRBCZY (1:200)	Thermo Fisher	Cat #25-9010-42; RRID:AB_2573534
CD8a-APC Clone 53-6.7 (1:200)	Biolegend	Cat #100712; RRID:AB_312751
IFN-γ-APC Clone XMG1.2 (1:200)	Biolegend	Cat #505810; RRID:AB_315404
Foxp3-APC Clone FJK-16 s (1:200)	Thermo Fisher	Cat #17-5773-82; RRID:AB_469457
pS6-APC Clone cupk43k (1:200)	Therno Fisher	Cat #17-9007-42; RRID:AB_2573270
GL7-APC Clone GL7 (1:200)	Biolegend	Cat #144606; RRID:AB_2562185
I-A/I-E-APC Clone M5/114.15.2 (1:200)	Biolegend	Cat #107614; AB_313329
CD98-APC Clone RL388 (1:200)	Biolegend	Cat #128210; RRID:AB_2254922
pS473-APC Clone M89-61 (1:200)	BD Biosciences	Cat #560343; RRID:AB_1645397
Granzyme B-APC Clone NGZB (1:200)	Thermo Fisher	Cat #50-8898-82; RRID:AB_11219679
IgG (H+L)-APC (1:500)	Thermo Fisher	Cat #A21244; RRID:AB_141663
CD3ϵ-APC-Cy7 Clone 145-2C11(1:200)	Biolegend	Cat #100330; RRID:AB_1877170
CD86-FITC Clone GL-1 (1:200)	Biolegend	Cat #105006; RRID:AB_313149
Perforin-FITC Clone eBioOMAK-D (1:200)	Thermo Fisher	Cat #11-9392-82; RRID:AB_465447
RORγT-BV421 Clone Q31-378 (1:200)	BD Biosciences	Cat #562894; RRID:AB_2687545
CD95-BV421 Clone Jo2 (1:200)	BD Biosciences	Cat #562633; RRID:AB_2737690
CD152-BV421 Clone UC10-4B9 (1:200)	Biolegend	Cat #106312; RRID:AB_2563063
CD134-BV421 Clone OX-86 (1:200)	Biolegend	Cat #119411; RRID:AB_10962569
CD62L-Pacific Blue Clone MEL-14 (1:200)	Biolegend	Cat #104424; RRID:AB_493380
CD25-Pacific Blue Clone PC61 (1:200)	Biolegend	Cat #102022; RRID:AB_493643
TNF-α-Pacific Blue Clone MP6-XT22 (1:200)	Biolegend	Cat #506318; RRID:AB_893639
pmTOR-Pacific Blue Clone MRRBY (1:200)	Biolegend	Cat #48-9718-42; RRID:AB_2574127
c-Myc-Pacific Blue Clone D84C12 (1:200)	Cell Signaling	Cat #14426; RRID:AB_2798478
Foxp3-V450 Clone MF23 (1:200)	BD Biosciences	Cat #561293; RRID:AB_10611728
CD44-PerCP/Cy5.5 Clone IM7 (1:200)	Biolegend	Cat #103032; RRID:AB_2076204
CD86-PerCP Clone GL-1 (1:200)	Biolegend	Cat #105026; RRID:AB_893417
CD45R/B220-BV510 Clone RA3-6B2 (1:200)	Biolegend	Cat #103248; RRID:AB_2650679
CD69-BV605 Clone H1.2F3 (1:200)	Biolegend	Cat #104530; RRID:AB_2563062
IL-17A-BV605 Clone TC11-18H10 (1:200)	BD Biosciences	Cat #564169; RRID:AB_2738640
CD279-BV605 Clone 29F.1A12 (1:200)	Biolegend	Cat #135220; RRID:AB_2562616
CD4-BV785 Clone GK1.5 (1:200)	Biolegend	Cat #100453; RRID:AB_2565843

(*Continued on next page*)

Continued

REAGENT or RESOURCE	SOURCE	IDENTIFIER
CD19-BV785 Clone 6D5 (1:200)	Biolegend	Cat #115543; RRID:AB_11218994
Glut1-Alexa Fluor®488 Clone EPR3915 (1:200)	Abcam	Cat #ab195359; RRID:AB_2714026
pSMAD3 Ser423, Ser425	Thermo Fisher	Cat #44-246G; RRID:AB_2533615
pAMPK alpha-1,2 (Thr172)	Thermo Fisher	Cat #44-1150G; RRID:AB_2533585
Purified anti-mouse CD3ϵ Clone 145-2C11	Biolegend	Cat #100340; RRID:AB_11149115
Purified anti-mouse CD28 Clone	Biolegend	Cat #102112; RRID:AB_312877
Human CD3/CD28 T Cell activator	StemCell Technologies, Inc.	Cat #10911 10971; RRID:AB_2827806
Anti-Mouse IFN-γ Clone XMG1.2	BD Biosciences	Cat #554408; RRID:AB_395373
Biological Samples		
Healthy control buffy coat	Croix-Rouge Luxembourgeoise	N/A
Chemicals, Peptides, and Recombinant Proteins		
RPMI 1640 (without L-Glutamine)	Lonza	#BE12-167F
RMPI 1640 (without glucose, serine, glycine)	Teknova	#50-190-8105
DMEM (with glucose and L-Glutamine)	Lonza	#BE12-604F
Hank's Balanced Salt Solutions	Lonza	#BE10-543F
SILAC RPMI 1640 Flex Media	GIBCO	#15347143
Seahorse XF base medium without phenol red	Agilent Technologies	#103335-100
PBS	Lonza	#BE17-516F
FBS	Sigma-Aldrich	#TMS-013-B
Penicillin/Streptomycin	GIBCO	#11548876
L-Glutamine	Sigma-Aldrich	#G3126-100G
2-mercaptoethanol	GIBCO	#11508916
Sodium pyruvate	GIBCO	#12539059
Recombinant human TGF-β	R&D Systems	#240-B-002
recombinant human IL-2	Miltenyi Biotec	#130-120-333
2-Deoxy-D-glucose	Sigma-Aldrich	#D6134-1G
D-(+)-glucose	Sigma-Aldrich	#G8270-5KG
Oligomycin A	Sigma-Aldrich	#75351-5MG
FCCP	Sigma-Aldrich	#C2920-10MG
Antimycin A	Sigma-Aldrich	#A8674-25MG
Rotenone	Sigma-Aldrich	#R8875-1G
Phorbol 12-myristate 13-acetate (PMA)	Sigma-Aldrich	#P8139-1MG
Calcium Ionophore	Sigma-Aldrich	#C7522-1MG
N-Acetyl-L-cysteine	Sigma-Aldrich	#A7250-50G
L-Glutathione reduced	Sigma-Aldrich	#G4251-10G
Rapamycin	Invivogen	#tlrl-rap
Rapamycin	LC Laboratories	N/A
L−(+)-α-Phenylglycine	Sigma-Aldrich	#237647-25G
4-Hydroxytamoxifen	Sigma-Aldrich	#H6278-10MG
PKUMDL-WQ-2101	Sigma-Aldrich	#SML1970-5MG
L-buthionine-sulfoximine	Sigma-Aldrich	#B2515-1G
SHIN1	Aobious	#AOB36697
Thymidine, [6-3H]-, 5mCi (185MBq)	Perkin Elmer	# NET355005MC
SYBR™ Fast Green Master Mix	Applied Biosystems	# 10459604
Corning™ Cell-Tak Cell and Tissue Adhesive	Thermo Fisher	# 10317081
$^{13}C_6$-glucose	Cambridge Isotope Lab	# CLM-1396
$^{13}C_5$-L-Glutamine	Cambridge Isotope Lab	# CLM-1822-H
$^{13}C_3$-serine	Cambridge Isotope Lab	#CLM-1574-H
GolgiPlug™	BD Biosciences	#555029

(*Continued on next page*)

Continued

REAGENT or RESOURCE	SOURCE	IDENTIFIER
Cell Trace Violet	Thermo Fisher	#C34557
Mitotracker Deep Red	Thermo Fisher	# M22426
Molecular Probes™ Carboxy-H2DCFDA	Thermo Fisher	#11500146
Molecular Probes™ 2-NBDG	Thermo Fisher	#11569116
Zombie NIR™ Fixable Viability Kit	Biolegend	#423106
Saponin	Sigma-Aldrich	#S4521-25G
Formaldehyde	Sigma-Aldrich	#252549-1L
HEPES	Sigma-Aldrich	#H4034-100G
EDTA	Sigma-Aldrich	#E9884-100G
Polyethylene glycol	Sigma-Aldrich	#P1458-50ML
Ethanol	VWR	#20821330
Tween 80	Sigma-Aldrich	#P1754-1L
Methanol	Sigma-Aldrich	#1060351000
Chloroform	Sigma-Aldrich	#34854-1L-M
Trichloroacetic acid	Sigma-Aldrich	#T6399-100G
DNase I	Sigma-Aldrich	#10104159001
Liberase	Sigma-Aldrich	#5401020001
Percoll®	Sigma-Aldrich	#GE17-0891-01
HiSep™ LSM 1077	HiMedia Laboratory	#LS001-500ML
Critical Commercial Assays		
Naive $CD4^+$ T Cell Isolation Kit	Miltenyi Biotec	#130-104-453
CD4+ T Cell Isolation Kit	Miltenyi Biotec	#130-104-454
CD90.1 Microbeads	Miltenyi Biotec	#130-094-523
$CD4^+$ $CD25^+$ Regulatory T Cell Isolation Kit	Miltenyi Biotec	#130-091-041
Tumor Dissociation Kit	Miltenyi Biotec	#130-096-730
CD45 (TIL) Microbeads	Miltenyi Biotec	#130-110-618
Naive CD4+ T Cell Isolation Kit II, human	Miltenyi Biotec	#130-094131
Seahorse XFe96 Fluxpak	Agilent Technologies	#102416-100
Foxp3/Transcription Factor Staining Buffer Set	Thermo Fisher	#15151976
Fixation/Permeabilization solution kit	BD Biosciences	#554701
Lyse/Fix Buffer 5x	BD Biosciences	#558049
Perm buffer III	BD Biosciences	#558050
QuantiTect Reverse Transcription Kit	QIAGEN	#205314
RNA 6000 Nano Kit	Agilent Technologies	#5067-1511
NucleoSpin RNA 250	Macherey-Nagel	#740 955 250
IFN gamma Mouse Uncoated ELISA Kit	Thermo Fisher	#88-7314-88
TNF alpha Mouse Uncoated ELISA Kit	Thermo Fisher	#88-7324-88
Invitrogen ™ IL-2 Mouse Uncoated ELISA Kit	Thermo Fisher	#15520997
Experimental Models: Cell Lines		
B16F10	Dr. Philipp Lang	N/A
MC38	ATCC	N/A
Experimental Models: Organisms/Strains		
$Gclc^{fl/fl}$: B6	Mak et al., 2017	N/A
$Foxp3^{YFP\text{-}Cre}$: B6	The Jackson laboratory	#016959
$Foxp3^{eGFP\text{-}Cre\text{-}ERT2}$: B6	The Jackson laboratory	#016961
$Rag1^{-/-}$: B6	The Jackson laboratory	#002216
$IFN\gamma^{-/-}$: B6	The Jackson laboratory	#002287

(*Continued on next page*)

Continued

REAGENT or RESOURCE	SOURCE	IDENTIFIER
Deposited Data		
RNA-Seq	This paper	N/A
Oligonucleotides		
Gclc: F:GGCTCTCTGCACCATCACTT R:GTTAGAGTACCGAAGCGGGG	This paper	N/A
Foxp3: F:CCCATCCCCAGGAGTCTTG R:ACCATGACTAGGGGCACTGTA	This paper	N/A
Slc1a4: F:TGCTCTGGCGTTCATCATCA R:AGTGAATGCGGCAACCACAA	This paper	N/A
Slc1a5: F:TGGCCAGCAAGATTGTGGAGAT R:TTTGCGGGTGAAGAGGAAGT	This paper	N/A
HPRT: F:TCAGTCAACGGGGGACATAAA R:GGGGCTGTACTGCTTAACCAG	This paper	N/A
TBP: F:GAAGAACAATCCAGACTAGCAGCA R:CCTTATAGGGAACTTCACATCACAG	This paper	N/A
PHGDH: F:ATGGCCTTCGCAAATCTGC R:AGTTCAGCTATCAGCTCCTCC	This paper	N/A
sgRNA Phgdh C*U*U*GCCUUGCCUUGCCCAUG G*G*C*AAGAGCUCACCUUCUUC U*U*C*UUACAGGCAGAUUCCCC	Synthego	N/A
sgRNA Slc1a4 A*C*C*AGGCUGCAAACCACCAG G*C*A*UCUCGCCCGGGAAGGCC C*C*U*CAGCGCCGCGCCCAUGC	Synthego	N/A
Recombinant DNA		
pMIT-Foxp3-CD90.1	Dr. Michael Lohoff	N/A
pMIT-CD90.1	Dr. Michael Lohoff	N/A
pMIG-RI-STAT5-CA	Dr. Michael Lohoff	N/A
pMIG-RI	Dr. Russell Jones	N/A
pMIG-RI-Gclc	This paper	N/A
pMIG-RI-Smad3	This paper	N/A
Software and Algorithms		
FlowJo Software	Tree Star	N/A
Graphpad Prism	GraphPad Software, Inc	N/A
Wave Software	Agilent	N/A
Adobe Illustrator	Adobe systems	N/A

LEAD CONTACT AND RESOURCE SHARING

Further information and requests for resources or reagents should be directed to and will be made available upon reasonable request by the Lead Contact, Dirk Brenner (dirk.brenner@lih.lu).

EXPERIMENTAL MODEL AND SUBJECT DETAILS

Primary Cell Culture

Natural regulatory T cells (nTregs), naive $CD4^+$ T cells, and $CD4^+$ and $CD8^+$ Tconv were isolated from mouse spleen and LN by magnetic bead sorting (Miltenyi Biotec). To induce regulatory T cells (iTregs), 2×10^5 naive T cells were cultured for four days in the

presence of plate bound anti-CD3 antibody (αCD3; 5 μg/mL, Biolegend), soluble anti-CD28 antibody (αCD28; 1 μg/mL, Biolegend), recombinant human TGF-β1 (4 ng/mL, Bio-Techne), IL-2 (50U/mL, Miltenyi Biotec) and anti-IFNγ antibody (αIFNγ; 5 μg/mL, BD Biosciences). Naive T cells were cultured in T cell media consisting of RPMI-1640 medium supplemented with 10% FCS (Sigma), 1% Penicillin/Streptomycin (GIBCO), 1% L-Glutamine (Sigma), and 55μM β-mercaptoethanol (GIBCO). To isolate nTregs, the cells were labeled using the $CD4^+CD25^+$ Regulatory T cells isolation kit (Miltenyi Biotec) and magnetically sorted using the autoMACS® Pro Separator (Miltenyi Biotec) according to the manufacturer's protocol. nTregs were cultured in T cell media in the presence of plate bound anti-CD3 antibody (αCD3; 5 μg/mL, Biolegend), soluble anti-CD28 antibody (αCD28; 5 μg/mL, Biolegend), IL-2 (500U, Miltenyi Biotec). To induce acute Gclc deletion, naive $CD4^+$ T cells were differentiated into iTregs *in vitro* in the presence of vehicle or 100 nM 4-hydroxytamoxifen (4-OHT) (Sigma) for 4 days.

For the human studies, buffy coats from healthy donors were provided by Croix-Rouge Luxembougeoise. The experimental setup was approved by the Croix-Rouge Luxembourgeoise (LIH-2019-0006). Human PBMCs were isolated using the Ficoll separation (HiSep™ LSM 1077, HiMedia Laboratory GmbH). Human naive $CD4^+$ T cells were isolated using the Human Naive $CD4^+$ T cells isolation kit II (Miltenyi Biotec). 2×10^5 naive $CD4^+$ T cells were cultured for six days with ImmunoCult™ Human CD3/CD28 T cell activator (StemCell Technologies, Inc.), according to the manufacturer's instructions. IL-2 (100U/mL) and TGF-β1 (4 ng/mL, Bio-Techne) were supplemented. The cells were differentiated in T cell media containing RPMI-1640 medium supplemented with 10% FCS (Sigma), 1% Penicillin/Streptomycin (GIBCO), 1% L-Glutamine (Sigma), and 100μM sodium pyruvate (GIBCO).

Mouse Models

Gclc$^{fl/fl}$ mice have been previously described (Chen et al., 2007) and were crossed to *Foxp3*^{cre}-expressing mice [B6.129(Cg)-*Foxp3*$^{tm4(YFP/icre)Ayr}$/J] and *Foxp3*$^{tm9(EGFP/cre/ERT2)Ayr}$/J (Jackson Laboratory). B6.129S7-Ifng^{tm1Ts}/J mice were obtained from The Jackson Laboratory. C57BL/6 and *Rag1*$^{-/-}$ mice were originally purchased from The Jackson Laboratory and bred in the SPF facility of the Luxembourg Institute of Health (LIH). Male and age-matched mice (6-12 weeks old) were used for all experiments unless otherwise indicated. For the serine- and glycine-free chow experiments, the mice were fed with normal or serine- and glycine-free chow as of 3 weeks of age (post weaning). The food was purchased from Special Diets Services (SDS, diet code 827030).

METHOD DETAILS

Cell Sorting and Flow Cytometry

To stain extracellular surface molecules, the cells were incubated in FACS buffer (PBS with 1% FCS and 5mM EDTA pH 8.0) together with specific antibodies for at least 30 min at 4°C protected from light. To detect intracellular phosphoproteins, the cells were fixed in 2% formaldehyde and permeabilized in 0.01% saponin. To identify transcription factors and intracellular nuclear proteins, the cells were fixed using the eBioscience Foxp3/Transcription Factor Fixation kit and permeabilized using the respective permeabilization buffer, according to the manufacturer's protocol. For cytokine stainings, the cells were fixed using the BD Cytofix/Cytoperm solution according to the manufacturers instructions. To stain intracellular ROS, the cells were incubated with dichlorofluorescein diacetate (DCF-DA, Sigma) for 30 min at 37°C in RPMI medium (non-supplemented). To measure NBDG uptake, the cells were incubated with 50 μM2-NBDG (Thermo Fisher Scientific) for 2 h at 37°C in glucose free RPMI (non-supplemented). For cell sorting, the cells were sorted using Aria II (BD Biosciences). Experiments were done in accordance with the guidelines for flow cytometry and cell sorting (Cossarizza et al., 2019).

Treg Suppression Assay

Purified nTregs ($CD4^+CD25^+$) and Tconv (Tconv; $CD4^+$ $CD25^-$) were magnetically sorted using a $CD4^+CD25^+$ Regulatory T cell Isolation Kit (Miltenyi Biotec). Tconv were labeled with CellTrace™ Violet Cell Proliferation (ThermoFisher Scientific) and cultured with irradiated antigen-presenting cells plus αCD3, with or without Tregs at various Tconv:Treg ratios. After 72 h, the proliferation of Teff cells was analyzed by flow cytometry.

T Cell Transfer-Induced Colitis

Rag1$^{-/-}$ mice were adoptively transferred with 4×10^5 WT Teffs ($CD4^+CD45RB^{hi}$), either alone or in combination with 2×10^5 Tregs ($CD4^+CD45RB^{low}$) from *Gclc*$^{fl/fl}$ or *Foxp3*^{cre}-*Gclc*$^{fl/f}$ mice. To this end, cells were purified by FACS sorting (Aria II, BD) prior to intravenous (i.v.) injection into mice. Recipient mice were weighed and examined every day for signs of disease. Cells from mesenteric LN were subjected to flow cytometric analysis. Colonic tissues were fixed and stained with H&E and αCD3 Ab and subjected to histological analyses.

Isotopic Labeling

Tregs were incubated for 24 h in RPMI 1640 containing [U-$^{13}C_6$]-glucose (11.1 mmol/L; Cambridge Isotope Laboratories) or [U-^{13}C]-glutamine (2 mmol/L; Cambridge Isotope Laboratories), both conjugated to bovine serum albumin (Sigma). For serine tracing, cells were cultured for 24 h in serine/glycine-free medium (Teknova) supplemented with 0.01 g/l glycine plus 400μM [U-$^{13}C_3$]-serine (Eurisotop (CLM-1574-H). Extraction of intracellular metabolites, GC-MS measurement, MID calculations, determinations of fractional carbon contributions, and substractions of natural isotope abundance were performed as described (Battello et al., 2016) using the MetaboliteDetector software package. Glucose, lactate and amino acid concentrations were determined using an YSI 2950D

Biochemistry Analyzer (YSI Incorporated). Formate quantification was performed following MCF derivatization and GC-MS analysis as previously described (Meiser et al., 2016).

Tumor Model and Treg Adoptive Transfer

B16F10 melanoma cells (2x10^5; ATCC) in 100 μl sterile PBS were injected subcutaneously into the shaved left flank of each mouse. Tumor volume was calculated daily: tumor volume = $\frac{length * diameter^2}{2}$. Mice were sacrificed at day 30 or when tumor volume exceeded 1.2 cm^3. For the Treg transfers, 1x10^6 of *Gclc*$^{fl/fl}$ and *Foxp3*^{cre}-*Gclc*$^{fl/fl}$ Tregs were magnetically sorted using the CD4$^+$CD25$^+$ Regulatory T cells isolation kit (Miltenyi Biotec) and magnetically sorted using the autoMACS® Pro Separator (Miltenyi Biotec) according to the manufacturer's protocol. Purified Tregs were intravenously injected prior B16 melanoma inoculation at experimental day 0.

TILs Isolation

Isolated tumors were cut into small pieces and digested with enzymes A, D, and R obtained from the Mouse Tumor Dissociation Kit (Miltenyi Biotec) according to the manufacturer's protocol. The digestion was followed by tumor dissociation using GentleMACS Octo Dissociator (37C_m_TDK_1). The cells were then filtered through 70 μm filter and washed with RPMI. The TILS were isolated using CD45 (TIL) Microbeads (Miltenyi Biotec) according to the manufacturer's protocol. The TILs were analyzed by flow cytometry or stimulated by PMA/Ionomycin for cytokine analysis.

In Vivo Rapamycin Treatment

Rapamycin was prepared in 100% ethanol and diluted in vehicle (5% polyethylene glycol and 5% Tween 80). Male *Gclc*$^{fl/fl}$ and *Foxp3*^{cre}-*Gclc*$^{fl/fl}$ mice of age 6 weeks were intraperitoneally injected with 100μg rapamycin (LC Laboratories) or vehicle every other day for 30 days. Mice were sacrificed at day 30 and organs extracted for analysis.

Expression Plasmids and Retroviral Transduction

The plasmids pMIT-Foxp3-CD90.1, pMIT-CD90.1 and pMig-RI-STAT5-CA (constitutively active) were provided by M. Lohoff (University of Marburg, Germany) (Bothur et al., 2015). pMigRI-GFP was provided by R. Jones (Van Andel Institute, USA). Murine full length cDNA of *Gclc* and *Smad3* were synthesized into pMigRI-GFP using the EcoRI restriction site (GeneCust, France). For retroviral transduction, retroviral supernatants were added to *in vitro*-differentiated iTreg cells whose culture medium had been stored. Cells and viral supernatants were centrifuged at 2700 rpm for 1.5 h at 37°C to achieve spin infection. Infected cells were re-cultured in the stored culture medium for 72 h before MACS-sorting to identify CD90.1 co-expression or fluorescence based FACS cell sorting. Infected iTreg cells were used for experiments as described in the main text.

Cytokine Quantification

To induce intracellular cytokine expression, T cells were restimulated *in vitro* with phorbol 12-myristate 13-acetate (PMA; Sigma, 50ng/mL) plus calcium ionophore A23187 (Ionomycin; Sigma, 750ng/mL) for 6 h. The cells were analyzed with flow cytometry. Serum concentrations of IL-2, TNF, IFNγ, and immunoglobulins were quantified by ELISA using the appropriate kits and protocols from eBioscience.

CRISPR/Cas9 Genomic Editing

1x10^6 enriched naive CD4 T cells were cultured in Treg skewing media for 48 h prior transfection with sgRNAs. sgRNAs targeting murine *Asct1* and *Phgdh* were obtained from Synthego (CRISPRevolution sgRNA EZ Kit, Synthego). sgRNAs were electroporated as described previously (Nüssing et al., 2019). Briefly, 1 μl of 0.3 nmol sgRNAs were incubated with 0.3 μl Cas9 Nuclease to a final volume of 5 μl for 10 min at room temperature. Pre differentiated CD4 regulatory T cells were resuspended in 95 μl P3 buffer (P3 primary cell 4D-Nucleofector™ system, mixed with the pre-prepared sgRNA/Cas9 solution, and subjected to electroporation. The cells were transferred to 1ml RPMI containing 10% FCS, glutamine, pen/strep and 100U IL-2 and cultured for 72 h before further analysis.

Quantitative PCR

RNA was isolated using a NucleoSpin RNA Kit (Macherey-Nagel) and cDNA was prepared using a QuantiTect Rev. Transcription Kit (QIAGEN). RT-PCR was carried out using Sybrgreen Master Mix (ABI) and the primers listed under 'Oligonucleotides'. Reactions were run on an ABI 7500HT Fast qRT-PCR instrument. Data were normalized to GAPDH transcription and analyzed using the ΔΔCt method as previously described (Mak et al., 2017).

Histology and Immunohistochemistry

Specimens for histology and immunohistochemistry analyses were prepared and examined as previously described (Brenner et al., 2014).

GSH, GSSG, and Formate Determination

The GSH content of 2x10^5 Treg cells/well was measured by GSH-Glo (Promega). Formate release into culture medium was quantified using a formate assay kit (Sigma). Intracellular GSH and GSSG was quantified as reported by (Meiser et al., 2016). Briefly, 2 million Treg cells were harvested and washed with 0.9% saline solution before adding 100 μl ice-cold MilliQ water with 20 μg/mL labeled

GSH (13C2, 15N; Cambridge Isotope Laboratories) as internal standard, followed by an equal volume of ice-cold 5% trichloroacetic acid. Cells were shaken at 1400 rpm at 4°C for 10 min and subsequently centrifuged at 21.000xg and 4°C for 5 min. 150 μl of the supernatant were transferred into a 2-ml-LC vial with micro insert. 10 μl of the extract were injected into an Agilent 1290 Infinity II equipped with a Waters Acquity UPLC HSS T3 (100 × 2.1 mm, 1.8 μm). Mobile phase A was composed of 0.1% formic acid and B was composed of methanol with 0.1% formic acid. The system was operated at 0.45 mL/min. The total run time of the method was 20 min starting with 1% B for 10 min, then increasing to 99% B at 12 min, which was held for 2 min. B was reduced to 1% after 15 min and kept for the rest of the run. Mass spectra were acquired in positive mode using a Bruker maXis.

Lamina Propria Isolation

Colons were cut longitudinally and incubated for 10 min at 37°C in Hank's Balanced Salt Solution (HBSS) containing 15mM HEPES, 10% FCS and 5mM EDTA. The colonic tissue was recovered in a 100 μM strainer and transferred again in HBSS (15mM HEPES, 10% FCS, 5mM EDTA) to re-incubate once more. After collection in a 100 μM strainer, the tissue was washed in RPMI containing 15mM HEPES, 10% FCS for 5 min at 37°C. Then the tissue was cut into small pieces, and digested for 30 min at 37°C in 10ml RPMI containing 0.1 mg/mL DNase I (Roche) and 0.083 mg/mL Liberase (Roche). Tissue suspensions were passed through a 40 μM strainer, pelleted, and overlayed on a 40%–75% Percoll gradient. After centrifugation at 800 g for 20 min at 20°C (without break), lamina propria lymphocytes (LPLs) were collected at the 40%–75% Percoll interface, washed, and resuspended in RPMI containing 10% FCS. Lamina propria lymphocytes were identified by flow cytometric analysis.

Metabolic Phenotyping

iTreg cells were seeded XF Seahorse DMEM medium in a density of 3×10^5 cells/well. The extracellular acidification rate (ECAR) and oxygen consumption rate (OCR) were determined using the XF Glycolytic Stress Test and XF Cell Mitochondrial Stress Test kits, respectively, according to the manufacturer's protocol (Agilent).

RNA-Sequencing

Libraries were prepared with 500 ng total RNA using the Total RNA TruSeq mRNA Stranded Library Prep Kit (Illumina) according to the manufacturer's protocol. Briefly, mRNA pulldown was performed using an oligodT primer attached to magnetic beads. To preserve strandness information, the second strand synthesis was performed using dUTP incorporation, ensuring that only the first strand was PCR-amplified. The libraries were quantified using the Qubit dsDNA HS assay kit (Thermofisher) and an Agilent 2100 Bioanalyzer. The pooled library was sequenced on an Illumina NextSeq500 instrument according to the manufacturer's instructions.

Transcriptomic and Data Analyses

Demultiplexing of the sequenced libraries was performed using bcl2fastq (v2.18.0.12). Mapping was performed using star aligner (v 2.5.2b), and the count matrix was produced using the featureCounts function from the subread package (v 1.5.2) using mouse annotation v GRCm38.87. *Foxp3*^{cre}-*Gclc*$^{fl/fl}$ and *Gclc*$^{fl/fl}$ mRNA data were analyzed using R statistical software (3.5.1) and DESeq2 (v 1.14.1) with default parameters to detect differential gene expression. We selected 1163 genes as having significant differences in expression based on a minimum log2 fold change of 0.58 and an adjusted p value < 0.05. Gene Set Enrichment Analysis on KEGG gene sets was performed using Bioconductor (v 3.7) and clusterProfiler (v 3.9.2). The Signaling Pathway Impact Analysis tool SPIA was used to identify activated or inhibited pathways.

QUANTIFICATION AND STATISTICAL ANALYSIS

Data are represented as the mean ± SEM and have at least n = 3 per group (refer to figure legend to detailed information), with p values determined by unpaired Student's t test or two-way ANOVA test using Prism 7.0 (GraphPad). P values were indicated with asterisks * and p values $\leq$0.05 were considered significant.

DATA AND CODE AVAILABILITY

The GEO accession number for the RNA-seq data from control and FoxP3-deficient Tregs file in this paper is GEO: GSE145311

APPENDIX 5

Research Publication

(Co-author)

KIWELER, N., DELBROUCK, C., POZDEEV, V.I., NEISES, L., SORIANO-BAGUET, L., EIDEN, K., XIAN, F., BENZARTI, M., HAASE, L., KONCINA, E., SCHMOETTEN, M., JAEGER, C., NOMAN, M.Z., VAZQUEZ, A., JANJI, B., DITTMAR, G., BRENNER, D., LETELLIER, E., MEISER, J., 2022. **Mitochondria preserve an autarkic one-carbon cycle to confer growth-independent cancer cell migration and metastasis.** *Nat Commun* 13, 2699.

nature COMMUNICATIONS

ARTICLE

https://doi.org/10.1038/s41467-022-30363-y OPEN

Mitochondria preserve an autarkic one-carbon cycle to confer growth-independent cancer cell migration and metastasis

Nicole Kiweler[1], Catherine Delbrouck[1,2], Vitaly I. Pozdeev[3], Laura Neises[1], Leticia Soriano-Baguet[2,4,5], Kim Eiden[1,2], Feng Xian[6], Mohaned Benzarti[1,2], Lara Haase[1,2,7], Eric Koncina[3], Maryse Schmoetten[3], Christian Jaeger[7], Muhammad Zaeem Noman[8], Alexei Vazquez[9], Bassam Janji[8], Gunnar Dittmar[2,6], Dirk Brenner[4,5,10], Elisabeth Letellier[3] & Johannes Meiser[1]✉

Metastasis is the most common cause of death in cancer patients. Canonical drugs target mainly the proliferative capacity of cancer cells, which leaves slow-proliferating, persistent cancer cells unaffected. Metabolic determinants that contribute to growth-independent functions are still poorly understood. Here we show that antifolate treatment results in an uncoupled and autarkic mitochondrial one-carbon (1C) metabolism during cytosolic 1C metabolism impairment. Interestingly, antifolate dependent growth-arrest does not correlate with decreased migration capacity. Therefore, using methotrexate as a tool compound allows us to disentangle proliferation and migration to profile the metabolic phenotype of migrating cells. We observe that increased serine de novo synthesis (SSP) supports mitochondrial serine catabolism and inhibition of SSP using the competitive PHGDH-inhibitor BI-4916 reduces cancer cell migration. Furthermore, we show that sole inhibition of mitochondrial serine catabolism does not affect primary breast tumor growth but strongly inhibits pulmonary metastasis. We conclude that mitochondrial 1C metabolism, despite being dispensable for proliferative capacities, confers an advantage to cancer cells by supporting their motility potential.

[1] Cancer Metabolism Group, Department of Cancer Research, Luxembourg Institute of Health, Luxembourg, Luxembourg. [2] Faculty of Science, Technology and Medicine, University of Luxembourg, 2 avenue de Université, Esch-sur-Alzette, Luxembourg. [3] Faculty of Science, Technology and Medicine, Department of Life Sciences and Medicine, Molecular Disease Mechanisms Group, University of Luxembourg, Esch-sur-Alzette, Luxembourg. [4] Experimental & Molecular Immunology, Department of Infection and Immunity, Luxembourg Institute of Health, 29 Rue Henri Koch, Esch-sur-Alzette, Luxembourg. [5] Immunology & Genetics, Luxembourg Centre for Systems Biomedicine, University of Luxembourg, 7 Avenue des Hauts Fourneaux, Esch-sur-Alzette, Luxembourg. [6] Proteomics of cellular signaling, Department of Infection and Immunity, Luxembourg Institute of Health,1a Rue Thomas Edison, Strassen, Luxembourg. [7] Luxembourg Centre for Systems Biomedicine, University of Luxembourg, Esch-sur-Alzette, Luxembourg. [8] Tumor Immunotherapy and Microenvironment (TIME) Group, Department of Cancer Research, Luxembourg Institute of Health, Luxembourg, Luxembourg. [9] Institute of Cancer Sciences, University of Glasgow, Glasgow, UK. [10] Odense Research Center for Anaphylaxis (ORCA), Department of Dermatology and Allergy Center, Odense University Hospital, University of Southern Denmark, Odense, Denmark. ✉email: johannes.meiser@lih.lu

The survival rates of patients harboring primary tumors steadily increase due to targeted treatment schemes. However, in case of tumor relapse and metastatic disease, effective therapies are mostly lacking with the consequence that secondary tumors account for the majority of cancer deaths[1]. Classical chemotherapeutic approaches to counteract cancer growth aim to target biomass production by interfering with the synthesis of proteins, lipids, and nucleotides and thereby directly interfere with central pathways of cancer cell metabolism[2,3]. Prospectively, therapeutic approaches targeting metabolic pathways that also support the invasive and migratory properties of cancer cells would help to prevent metastatic progression of the initial disease. However, profound knowledge of specific metabolic dependencies that support growth-independent processes during the metastatic cascade, are only starting to be understood[4].

Nucleotide synthesis is an essential requirement for cancer cell proliferation. Consequently, antifolates such as Methotrexate (MTX) and related compounds have been proven as successful chemotherapeutics for several decades. Although differences between the various antifolates exist, a shared mode of action is the inhibition of one-carbon (1C) metabolism which provides essential building blocks for thymidylate and purine synthesis. Additionally, 1C metabolism has implications in supporting methylation reactions, glutathione, heme, sphingolipid and protein synthesis[5]. 1C metabolism describes a metabolic cycle that is spread across mitochondrion and cytoplasm and it is mainly fueled by the non-essential amino acid serine. De-novo serine synthesis is catalyzed by the rate limiting enzyme phosphoglycerate dehydrogenase (PHGDH) which is amplified in different tumors[6–8]. Hence, targeting serine synthesis, serine catabolism or serine availability by starvation or inhibition of PHDGH has been proven successful to inhibit cancer progression[9–17]. To support the various anabolic programs, cytosolic 1C metabolism is of particular importance, while mitochondrial 1C metabolism is dispensable due to the reversibility of the cytosolic 1C metabolism[16]. In fact, depending on intracellular folate levels, cytosolic 1C metabolism can be the dominant route to provide one-carbon units for nucleotide synthesis[17]. In that light, reasons for conserved mitochondrial 1C metabolism are still not fully understood. Previous evidence suggests implications of mitochondrial 1C metabolism for mitochondrial translation[18,19]. One additional explanation resides in the observation that mitochondrial derived formate lowers the pool of free cytosolic folates by increasing the 10-CHO-THF pool thereby protecting it from degradation. Upon MTX, degradation is facilitated as folates accumulate in the oxidized DHF form, impeding the 10-CHO-THF synthetase activity of MTHFD1[20]. However, if mitochondrial folate-dependent 1C metabolism and formate production remains functional under conditions of cytosolic 1C metabolism impairment and whether mitochondrial 1C metabolism itself confers additional functions that contribute to tumorigenesis remains unknown.

We have previously shown that a reduction of biomass demand can result in increased formate release from cancer cells to their surrounding microenvironment[21] and that the rate of serine catabolism to formate is significantly increased in adenomas of the small intestine and breast tumors compared to normal tissue[22]. Importantly, enhanced formate release rates and increased extracellular formate concentrations have been shown to increase the invasiveness of glioblastoma cells in vitro[22].

Apart from our previous findings on formate overflow and its potential implications for cancer cell invasion[21,22], other reports substantiate a role of serine metabolism in the context of metastasis[7,14,23–25]. However, such studies were so far focused on the relevance of serine de novo synthesis via PHGDH or extracellular serine availability for metastatic outgrowth (proliferative aspect) in the secondary tissue[7,14,23–25]. In contrast, whether mitochondrial serine catabolism also has a growth-independent role in promoting cancer cell motility that potentially increases the rate of cancer cell escape from the primary tumor has not been addressed so far. Being able to identify and target metabolic programs that promote the early steps of the metastatic cascade would help to contain the tumor, a clinical phenotype with more favorable therapeutic outcome compared to advanced metastatic stages.

In the present study, we observed that antifolates, albeit being strongly cytostatic, did not decrease the cell's motility potential. Using MTX as a tool compound to selectively inhibit cytosolic 1C metabolism, we show that mitochondrial 1C metabolism runs as an autarkic, compartmentalized pathway that is important to drive cancer cell motility. In contrast, the cytosolic part of 1C metabolism, which is essential for nucleotide synthesis during proliferation, is dispensable for the cellular motility potential. Hence, we provide mechanistic evidence that one selective advantage of mitochondrial 1C metabolism is to support cell motility. We corroborate this hypothesis in an orthotopic breast cancer model. Here, we demonstrate that ablating mitochondrial 1C metabolism effectively blocks mitochondrial serine catabolism but does not affect primary tumor growth. Yet, it strongly inhibits pulmonary metastasis formation.

Results

Inhibition of anabolic synthesis routes differentially impacts the motility potential of cancer cells. To assess the relative importance of different anabolic pathways for cancer cell migration, we employed a panel of metabolic perturbations targeting glycolysis, mitochondrial electron transport chain (ETC) as well as lipid, protein, and nucleotide synthesis (Fig. 1a). As expected, the chosen metabolic interventions inhibited proliferation and affected cell cycle progression of MDA-MB-468 breast cancer cells with no to mild toxic effects after 48 h treatment (Fig. 1b–c, S1A). Inhibition of glycolysis, ETC, lipid, and protein synthesis significantly reduced migration of MDA-MB-468 cells (Fig. 1d). Surprisingly and in contrast to all other growth-inhibiting conditions, inhibition of nucleotide synthesis with various drugs did not diminish migration of MDA-MB-468 cells (Fig. 1e). Calculation of the area under curve (AUC) allowed us to quantitatively compare wound closure over time (Fig. 1d, e) and confirmed that wound closure was significantly reduced upon treatment with rotenone (Rot), galactose (Gal), simvastatin (SIM) and sirolimus (rapamycin, SIR). However, treatment with the antifolates methotrexate (MTX) and pemetrexed (PEM), as well as with hydroxyurea (HU) and clofarabine (CLO) did not affect or did even significantly increase wound closure in scratch assays in comparison to fully proliferative, untreated control cells. While cell migration correlates with reduced cell growth for all other metabolic perturbations, nucleotide synthesis inhibition does not reduce cell migration in correlation to growth inhibition (Fig. 1f, g). Sustained migration in response to nucleotide synthesis inhibition was verified in LN229 glioblastoma and 4T1 breast cancer cells (Fig. S1B–D). Of note, using dialyzed or normal FBS did not change the result (Fig. S1E). This observation was also confirmed in trans-well migration assays using Boyden chambers (Fig. 1h, S1F, G). Furthermore, using ECM-collagen coating in trans-well assay, we found that nucleotide synthesis inhibition also had no impact on the invasive capacity of MDA-MB-468 cells (Fig. 1h), LN229 and 4T1 cells (Fig. S1F, G). To validate if MTX resistance results in a pro-migratory effect, we generated MTX-resistant MDA-MB-468 cells by long-term cultivation in 50 nM MTX for 2 months. The resulting MTX-resistant MDA-MB-468 cells proliferate in the presence of increasing

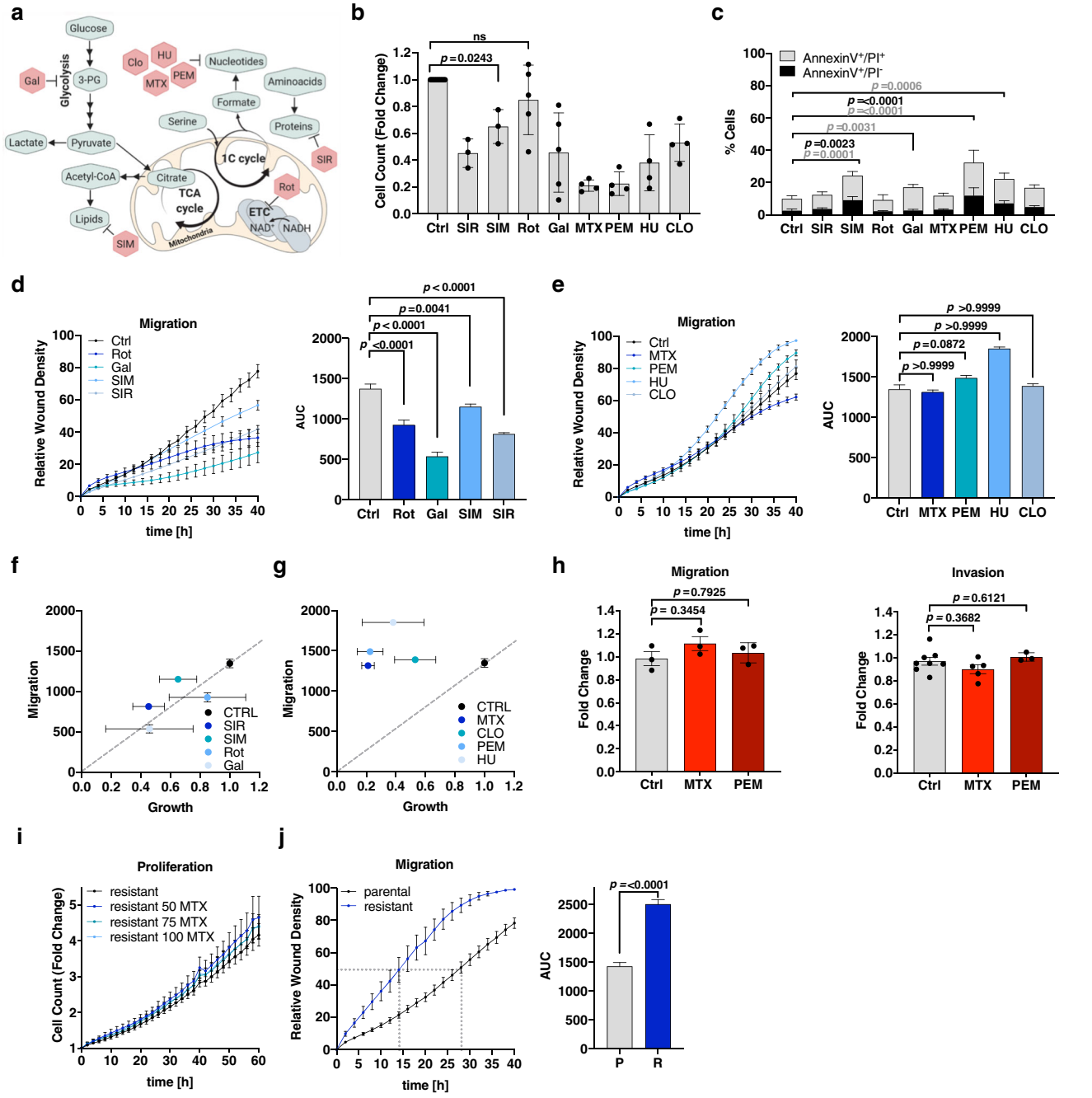

Fig. 1 Inhibition of major anabolic synthesis routes differentially impacts the motility potential of cancer cells. a Synthesis routes of metabolic building blocks (lipids, nucleotides, and proteins) and pharmacologic intervention points of the selected drug panel. **b** MDA-MB-468 cells were counted after 48 h treatment with 100 nM Sirolimus (SIR) ($n = 3$), 1 µM Simvastatin (SIM) ($n = 3$), 50 nM Rotenone (Rot) ($n = 5$), galactose (Gal) ($n = 5$) supplementation, 50 nM Methotrexate (MTX) ($n = 4$), 1 µM Pemetrexed (PEM) ($n = 4$), 0.5 mM hydroxyurea (HU) ($n = 4$), and 100 nM Clofarabine (CLO) ($n = 4$). Mean ± SD; ordinary one-way ANOVA with Dunnett's multiple comparisons test. Unlabeled comparisons to Ctrl are all significant with $p < 0.0001$. **c** MDA-MB-468 cells were treated as in (**b**). Cell death was assessed by flow cytometry and AnnexinV-FITC/PI-staining; mean ± SD of independent experiments ($n = 8$ (Ctrl), $n = 4$ (SIR, SIM, PEM, CLO), $n = 3$ (Rot, Gal, MTX, HU)). Two-way ANOVA with Dunnett's multiple comparisons test. **d**, **e** Migration of MDA-MB-468 cells upon (**d**) 50 nM Rot ($n = 5$), Gal ($n = 5$), 1 µM SIM ($n = 3$), and 100 nM SIR ($n = 4$) or (**e**) 50 nM MTX ($n = 7$), 1 µM PEM ($n = 3$), 0.5 mM HU ($n = 4$), and 100 nM CLO (n = 4) and respective area under curve (AUC); mean ± SEM of independent experiments; Brown-Forsythe and Welch one-way ANOVA with Dunnett's multiple comparisons test. **f**, **g** Correlation of cell migration (AUC over 40 h, mean ± SEM, ($n =$ as in (**d**, **e**)) and proliferation (fold cell growth after 48 h, mean ± SD ($n =$ as in (**b**)). MDA-MB-468 cells were treated as in (**b**) and (**d**, **e**). **h** Migration and invasion of MDA-MB-468 cells treated for 24 h with 50 nM MTX using non-coated (migration) or ECM-Collagen-coated (invasion) Boyden chambers. Mean ± SEM (Migration: $n = 3$, Invasion: $n = 7$ (Ctrl), 5 (MTX, 3 (Pem)); Brown-Forsythe and Welch one-way ANOVA with Dunnett's multiple comparisons test. **i** Proliferation of MTX-resistant MDA-MB-468 cells upon the indicated concentrations of MTX [nM]; mean ± SEM of independent experiments ($n = 4$). **j** Migration of parental and MTX-resistant MDA-MB-468 cells and respective AUC; mean ± SEM of independent experiments (parental $n = 15$, resistant $n = 6$); unpaired, two-tailed *t*-test with Welch's correction. Time point of 50% wound closure is indicated. Source data are provided as a Source Data file.

concentrations of MTX (Fig. 1i) and display enhanced migratory capacity compared to the parental MDA-MB-468 cell line (Fig. 1j).

In conclusion, the perturbation of any major anabolic route results in growth repression. However, the impact on cell migration highly depends on the targeted metabolic pathway, with nucleotide synthesis being an ineffective target to abrogate cell motility. Furthermore, prolonged nucleotide synthesis inhibition in drug-resistant cells acts as a selection pressure for more motile cancer subpopulations.

Sustained motility upon MTX is supported by a ROS-driven EMT phenotype. As MTX induced the strongest growth repression without increasing cell death (Fig. 1b, c), we used it as a tool compound to disentangle proliferation from migration to investigate the metabolic processes that support cancer cell migration. After testing multiple concentrations (Fig. S2A), we chose a concentration of 50 nM MTX for subsequent experiments. 50 nM MTX is significantly growth- and cell cycle-arresting in MDA-MB-468 cells (Fig. 1b, S1A) and has also been shown to be within the therapeutic window[26–29]. As this concentration of 50 nM is significantly lower compared to earlier in vitro studies[20,30–33], we first set out to validate known drug effects of MTX in our system. We observed that 48 h MTX treatment of MDA-MB-468 cells resulted in altered cellular morphology with individual cells visibly increasing in cell size and exhibiting an outstretched cell shape with protruding edges (Fig. 2a). MTX-resistant MDA-MB-468 cells showed comparable morphologic alterations (Fig. S2B). While the observed cell cycle and proliferation arrest upon MTX treatment was rapidly reversible (Fig. S2C, D) upon MTX removal, [U-^{13}C]serine tracing and metabolic flux analysis confirmed that 50 nM MTX did strongly inhibit nucleotide synthesis (Fig. 2b). Of note, nucleotide synthesis was partially restored in MTX-resistant MDA-MB-468 cells (Fig. S2E). Stable isotope labeling by amino acids in cell culture (SILAC) and quantitative proteomics analysis further confirmed the efficacy of the selected MTX dose as mechanistic targets of MTX such as dihydrofolate reductase (DHFR), thymidylate synthase (TYMS), and thymidine kinase (TK1) were upregulated by treatment as expected (Fig. S2F). DHFR expression was also increased in MTX resistant cells, while FolRa expression was slightly decreased (Fig. S2G). Moreover, superoxide dismutase (SOD) was one of the most significantly upregulated proteins in response to treatment (Fig. S2F), which corresponds to prior reports that depict MTX as a potent inducer of oxidative stress[30,34,35]. We validated these prior findings with our low dose of MTX by measuring a moderate but significant increase of mitochondrial and cytosolic reactive oxidant species (ROS) upon acute MTX treatment and in the MTX resistant cells (Fig. S2H, I, J). In line with increased ROS levels we observed NRF2 stabilization, however, this did not result in activation of the BACH1 axis, as reported earlier for metastatic lung cancer[36,37] (Fig. S2K, I). Increased ROS levels upon MTX correspond to earlier reports that highlight the potential of oxidative stress as a driver of cancer cell transformation via epithelial-mesenchymal transition (EMT)[38–44]. EMT is also a known general mechanism to escape chemotherapy induced effects.

In line with previous reports, we found that *ZEB1* and *ZEB2* expression as well as *VIM* expression was upregulated in a time-dependent manner in response to acute MTX treatment and in the MTX-resistant cell line (Fig. 2c, d, S2F, M, N). MTX-treatment also induced the expression of the collagenase *MMP9* (Fig. S2O), an enzyme which is involved in the degradation of the extracellular matrix during cancer cell invasion[45]. Treatment of cells with the antioxidant N-acetylcysteine (NAC) reduced ROS levels in MTX-treated MDA-MB-468 cells (Fig. S2P) and resulted in a significant reduction of MTX-induced cell migration (Fig. 2e) and EMT phenotype induction (Fig. 2f). These findings confirm that the chosen low dose of MTX is sufficient to promote EMT in a ROS dependent manner, supporting earlier reports suggesting EMT onset in context of pulmonary fibrosis using high doses of MTX[46,47]. Such moderate increase in cellular ROS levels after MTX might contribute to a pro-migratory stimulus that subsequently results in the observed sustained migration.

MTX-treated cells sustain high metabolic rates and enhance de novo serine synthesis. In addition to the here reported MTX-specific effects on ROS and EMT, we wanted to take advantage of the MTX effect (sustained migration) to identify growth-independent metabolic liabilities that support cell migration.

To that end, we profiled central carbon metabolism using [U-^{13}C]glutamine and [U-^{13}C]glucose tracing to monitor glycolytic activity and glutamine- or glucose-derived carbon oxidation through the TCA cycle (Fig. 3a, d). Absolute consumption and release (CORE) rates of glutamine and glutamate were sustained in response to MTX treatment (Fig. 3b), while the relative TCA-cycle flux of [U-^{13}C]glutamine was significantly increased in response to MTX (Fig. 3c). Absolute quantification of CORE rates of glucose and lactate also revealed sustained high glycolytic rates upon MTX treatment (Fig. 3e). This came as a surprise, as lactate release rates were previously shown to correlate with cell growth rates[48]. In MDA-MB-468 cells, the maintained glycolytic rate and the associated lactate release at constant high levels (Fig. 3e) indicate a constant generation of glycolysis-derived ATP even in the presence of reduced energetic demand for anabolic reactions in growth-arresting MTX conditions. Consequently, [U-^{13}C] glucose distribution within the TCA-cycle was sustained by MTX treatment in MDA-MB-468 cells (Fig. 3f) as well as in 4T1 and LN229 cells (Fig. S3A, B). It has previously been shown that MTX inhibits oxygen consumption rates (OCR) in HCT116 cells[18]. We could replicate this finding and observed a ~30 % reduction of OCR in HCT116 cells upon MTX (Fig, S3C), while OCR in MDA-MB-468, LN229, and 4T1 cells was sustained (Fig. 3g). This indicates cell line specific effects of MTX on OCR. Furthermore, MTX treatment significantly increased the relative flux of glucose to serine despite decreased anabolic demands for nucleotide synthesis (Fig. 3h, S3D). Protein levels of PHGDH, PSPH, and PSAT1 that catalyze the serine de novo synthesis pathway from glucose were unaltered in response to MTX treatment in multiple cell lines (Fig. S3E–H). In agreement with Diehl et al[49]. who showed that changes in NAD^+/NADH ratio can increase PHGDH activity and in consequence serine de novo synthesis rates, we observed an increased NAD^+/NADH ratio upon MTX (Fig. 3i). As MTX is well characterized as an inhibitor of DHFR and thus 1C metabolism, it came to our surprise that MTX treatment did also increase the abundance of extracellular formate M + 1 isotopologues derived from [U-^{13}C]glucose through serine and the mitochondrial 1C metabolism (Fig. 3j, S3I).

In summary, the metabolic profiling demonstrates that, despite decreased metabolic demand for biomass production, MTX-treated cells sustain high metabolic rates that are comparable to fully proliferating cells. Additionally, and in contrast to general assumptions, cytosolic DHFR inhibition results in increased rates of serine synthesis and downstream mitochondrial formate excretion suggesting an uncoupling of mitochondrial 1C metabolism from cytosolic 1C metabolism.

Mitochondria protect 1C metabolism-dependent serine catabolism upon cytosolic 1C pathway inhibition. Our finding of

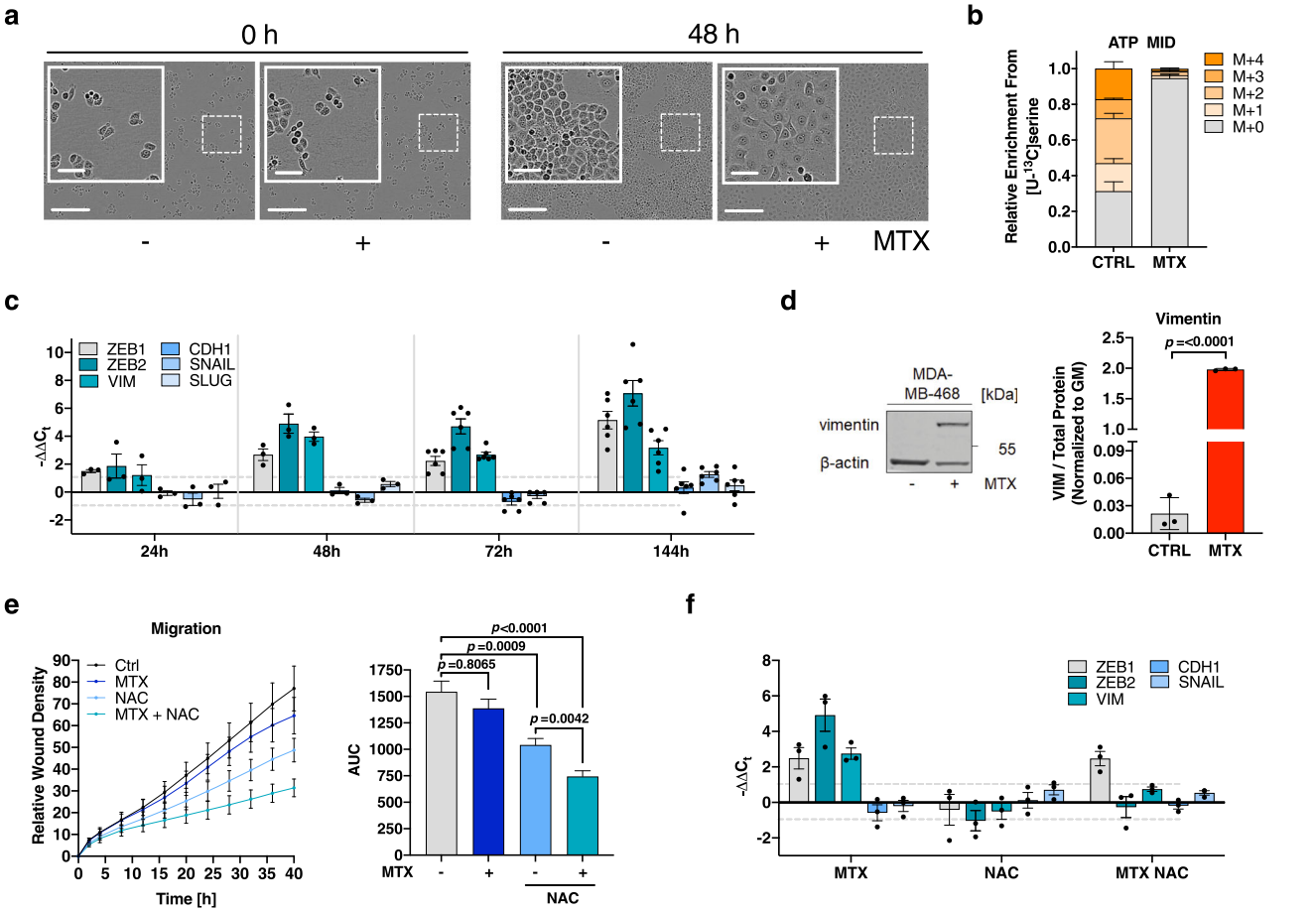

Fig. 2 Enhanced motility under MTX is supported by a ROS-driven EMT phenotype. a Morphology of MDA-MB-468 cells after 48 h 50 nM MTX. Bright-field images are representative of 3 independent experiments. Scale bars correspond to 60 and 300 µm. **b** Mass isotopomere distribution (MID) of intracellular ATP upon [U-^{13}C]serine tracer in response to 24 h 50 nM MTX in MDA-MB-468 cells. Mean ± SEM of 5 independent experiments each measured in triplicate wells. **c** mRNA expression from the indicated target genes in MDA-MB-468 cells upon 50 nM MTX at the indicated time points measured by real-time RT-qPCR. Mean ± SEM ($n = 3$ (24 h, 48 h), 6 (72 h, 144 h)). No data measured for SLUG expression at 72 h. **d** Protein levels of vimentin in MDA-MB-468 cells after 240 h 50 nM MTX; β-actin as loading control. Quantification of vimentin signal relative to total protein stain. Mean ± SD ($n = 3$); unpaired, two-tailed *t*-test with Welch's correction. **e** Migratory potential of MDA-MB-468 cells in response to 10 mM N-acetylcysteine (NAC) and 50 nM MTX as quantification of relative wound density in IncuCyte and respective AUC. Graph shows mean ± SEM of independent experiments ($n = 3$); Brown-Forsythe and Welch ANOVA test with Games-Howell's multiple comparisons test. **f** mRNA expression from the indicated target genes in MDA-MB-468 cells upon 10 mM NAC and 50 nM MTX at 72 h measured by real-time RT-qPCR. Mean ± SEM ($n = 3$). Source data are provided as a Source Data file.

increased [U-^{13}C]glucose-derived M + 1 formate excretion under MTX (Fig. 3j, S3I), allows the hypothesis that mitochondrial 1C metabolism can function in an autarkic manner when cytosolic 1C metabolism is inactivated (Fig. 4a). To corroborate this hypothesis, we employed [U-^{13}C]serine tracing to monitor serine flux through 1C metabolism. We observed that cytosolic block of 1C metabolism via MTX did not reduce the exchange rates of serine, glycine and formate in MDA-MB-468 or LN229 cells (Fig. 4b, C, S4A, C). In contrast, the formate release rate was significantly increased and the increased fraction of labeled formate proved that most of the released formate is derived from [U-^{13}C]serine and not from other carbon sources that could alternatively generate formate in presence of MTX. Of note, sustained serine consumption and formate overflow via 1C metabolism upon DHFR inhibition could also be confirmed in Plasmax medium[50], which is a culture medium closer to human physiology (Fig. S4D). Since cell dry mass composition is constituted by around 60% of proteins[51], growth arresting conditions generally result in decreased consumption rates of proteinogenic amino acids. In fact, a general trend for decreased consumption of essential amino acids was observed (Fig. S4b). Hence, sustained serine consumption rates upon growth arrest suggest that spared serine that is otherwise used for anabolic processes such as nucleotide synthesis, is used for alternative metabolic pathways that support cell motility and survival.

Mechanistically, 1C metabolism follows a cycle in which serine can be resynthesized in the cytoplasm and mitochondrion from glycine via serine hydroxymethyltransferase 1 and 2 (SHMT1, SHMT2) (Fig. 4a). As the SHMT reaction is highly reversible, the serine labeling pattern from [U-^{13}C]serine is composed of a mix of M + 1, M + 2 and M + 3 isotopologues, which represents the different recombination events with labeled and unlabeled glycine and formate[16,21,52]. Consequently, M + 1 and M + 2 serine isotopologues are expected to be absent upon complete 1C metabolism inhibition. Intriguingly, cytosolic DHFR inhibition with MTX neither completely abrogated serine M + 1 and M + 2 isotopologues upon [U-^{13}C]serine nor did it significantly affect the serine to glycine level ratio in MDA-MB-468 or LN229 cells (Fig. 4d, e, S4E, F), further supporting our hypothesis of a persistent mitochondrial 1C metabolism upon DHFR inhibition.

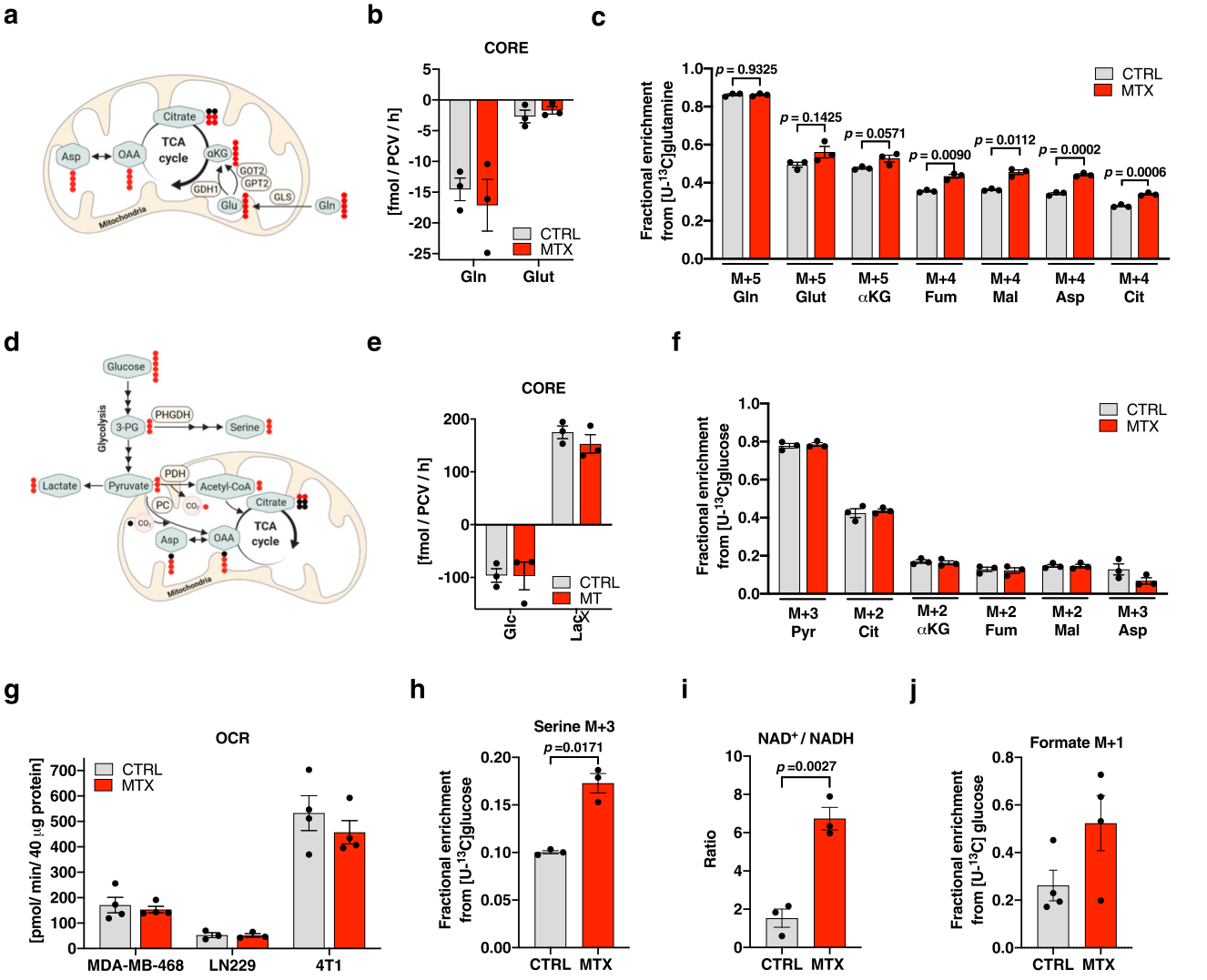

Fig. 3 MTX-treated cells sustain high metabolic rates and enhance de novo serine synthesis. a Interdependence of glycolysis and tricarboxylic acid (TCA) cycle and metabolic ^{13}C label pattern from [U-^{13}C]glutamine. **b** Absolute consumption and release (CORE) rates of glutamine (Gln) and glutamate (Glut) in the culture medium of MDA-MB-468 cells after 24 h 50 nM MTX. Dots represent the mean of an individual experiments composed of triplicate wells; mean ± SEM ($n = 3$). **c** Enrichment of selected isotopologues of Gln, Glut, α-ketoglutarate (αKG), fumarate (Fum), malate (Mal), aspartate (Asp), and citrate (Cit) upon [U-^{13}C]glutamine tracer in response to 24 h 50 nM MTX in MDA-MB-468 cells. Dots represent the mean of an independent experiments in triplicate wells; mean ± SEM; unpaired, two-tailed *t*-test with Welch's correction ($n = 3$). **d** Interdependence of glycolysis and TCA cycle and metabolic ^{13}C label pattern from [U-^{13}C]glucose. **e** Absolute CORE rates of lactate and glucose in the culture medium of MDA-MB-468 cells after 24 h 50 nM MTX. Dots represent the mean of an individual experiments composed of triplicate wells; mean ± SEM ($n = 3$). **f** Enrichment of selcted isotopologues of pyruvate (Pyr), Cit, αKG, Fum, Mal, and Asp upon [U-^{13}C]glucose tracer in response to 24 h 50 nM MTX in MDA-MB-468 cells. Dots represent the mean of an individual experiments composed of triplicate wells; mean ± SEM; unpaired *t*-test with Welch's correction ($n = 3$). **g** Basal cellular respiration upon 24 h 50 nM MTX in MDA-MB-468, LN229, and 4T1 cells as quantification of mitochondrial oxygen consumption rate (OCR). Dots represent the mean of an individual experiments composed of six technical replicates; mean ± SEM ($n = 3$ (LN229), 4 (MDA-MB-468, 4T1)). **h** Enrichment of M + 3 isotopologue of serine upon [U-^{13}C]glucose upon 24 h 50 nM MTX in MDA-MB-468 cells. Dots represent the mean of an independent experiments in triplicate wells; mean ± SEM; unpaired, two-tailed *t*-test with Welch's correction ($n = 3$). **i** Ratio of absolute intracellular NAD^+ to NADH in MDA-MB-468 cells upon 24 h 50 nM MTX. Dots represents the mean of an individual experiments composed of triplicate wells; mean ± SEM; unpaired *t*-test with Welch's correction ($n = 3$). **j** M + 1 isotopologue of extracellular formate in MDA-MB-468 cells from [U-^{13}C]glucose upon 24 h 50 nM MTX. Dots indicate the mean of an independent experiments measured in triplicate wells; mean ± SEM ($n = 4$). Source data are provided as a Source Data file.

To mechanistically disentangle cytosolic from mitochondrial 1C metabolism, we analyzed a panel of CRISPR knockouts in HAP1 cells in which either the cytosolic (SHMT1), the mitochondrial (MFT, SHMT2), or both compartments (FPGS, MFT + SHMT1) of 1C metabolism were abrogated[53]. Here, cytosolic *SHMT1* KO did not eliminate intermediary M + 1 and M + 2 serine isotopologues from [U-^{13}C]serine comparable to MTX treatment, whereas mitochondrial or combined cytosolic and mitochondrial inhibition of 1C metabolism upon *MFT* KO, *SHMT2* KO, *FPGS* KO and *MFT* + *SHMT1* KO resulted in a complete loss of M + 1 and M + 2 serine isotopologues (Fig. 4f). In mutants harboring a full inhibition of 1C metabolism or mitochondrial 1C metabolism alone, we additionally observed an increase in the ratio of serine to glycine levels, whereas MTX treatment and *SHMT1* KO did not substantially increase serine to glycine ratio (Fig. 4g).

Of note the protein abundance of mitochondrial serine catabolism enzymes was not increased upon MTX. MTHFD2

abundance even decreased upon MTX, however, this did apparently not affect the rate of serine catabolism (Fig. S4G, H).

To test if knock-out of mitochondrial serine catabolism stops formate overflow, we monitored formate release flux upon MTX in HAP1 cells deficient for SHMT1 or SHMT2. As expected, loss of SHMT2 completely abolished formate overflow, while SHMT1 KO increased formate overflow (Fig. 4h). This experiment was then validated in MDA-MB-468 cells harboring *MTHFD1L* KO[20]

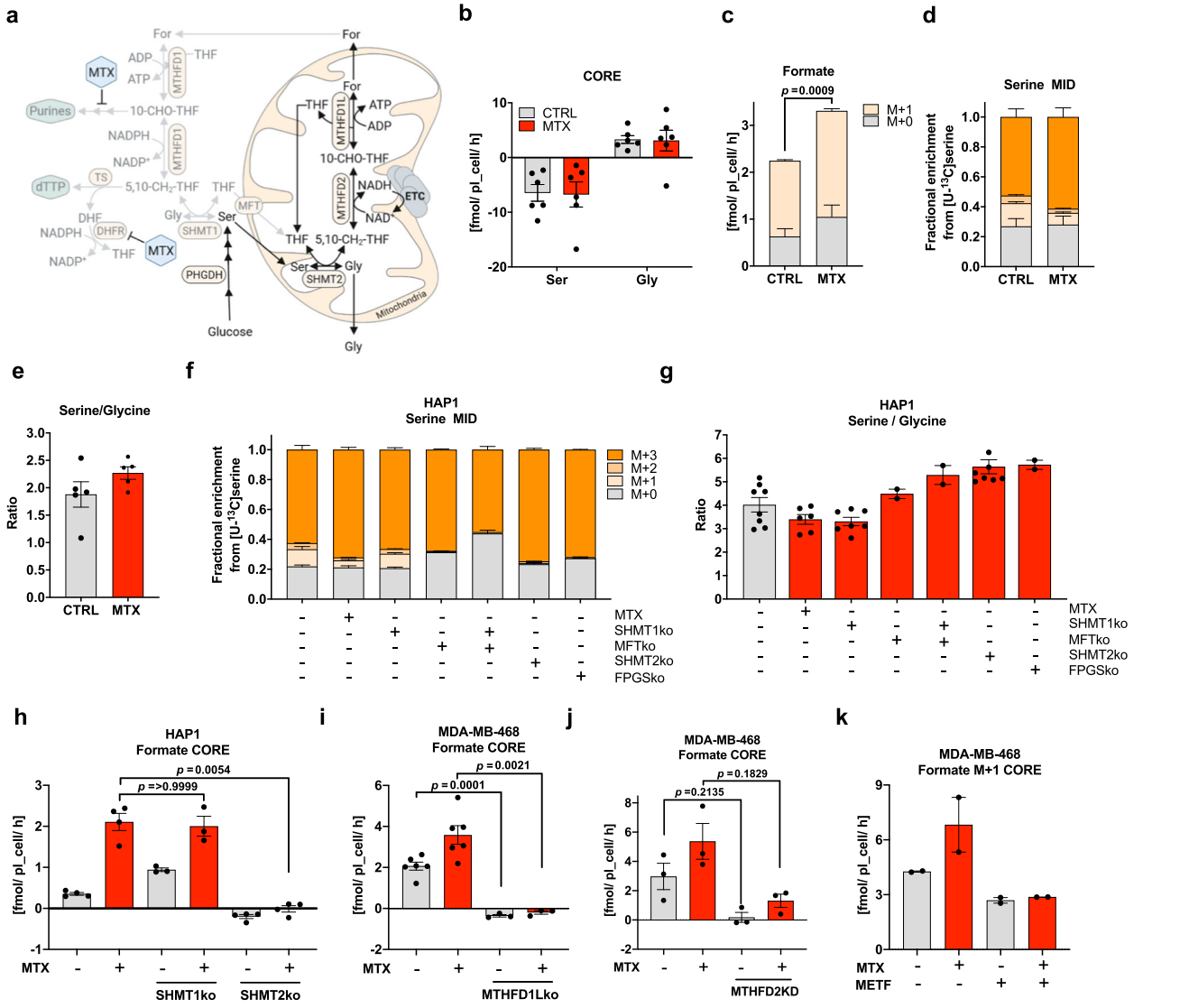

Fig. 4 Mitochondria protect 1C metabolism-dependent serine catabolism upon cytosolic 1C pathway inhibition. a Cytosolic and mitochondrial 1C metabolism and the pharmacologic intervention points of MTX. **b** Absolute consumption and release (CORE) rates of serine (Ser) and glycine (Gly) from MDA-MB-468 cells upon 24 h 50 nM MTX. Dots represent the mean of an individual experiment each measured in triplicate wells; mean ± SEM ($n = 6$). **c** Formate release rate upon [U-^{13}C]serine in MDA-MB-468 cells after 24 h 50 nM MTX; mean ± SEM of three independent experiments each measured in triplicate wells; unpaired *t*-test with Welch's correction for M + 1 isotopologue ($n = 3$). **d** MID of intracellular serine upon [U-^{13}C]serine in MDA-MB-468 cells upon 24 h 50 nM MTX; mean ± SEM of four independent experiments each measured in triplicate wells. **e** Ratio of absolute intracellular serine and glycine after 24 h 50 nM MTX in MDA-MB-468 cells. Dots represent the mean of an independent experiment in triplicate wells; mean ± SEM ($n = 5$). **f** MID of intracellular serine upon [U-^{13}C]serine in SHMT1, MFT, SHMT2, and FPGS-depleted HAP1 cells; mean ± SEM of independent experiments each measured in triplicate wells ($n = 8$ for CTRL, SHMT1ko, and SHMT2ko; $n = 5$ for MTX; $n = 2$ for FPGSko, MFTko and MFT/SHMT1ko). **g** Ratio of absolute intracellular serine and glycine levels in SHMT1, MFT, SHMT2, and FPGS depleted HAP1 cells. Dots represent the mean of an independent experiment in triplicate wells; mean ± SEM ($n = 8$ for CTRL and SHMT2ko, $n = 7$ for SHMT1ko, $n = 6$ for MTX, $n = 2$ for FPGSko, MFTko and MFT/SHMT1ko). **h** Absolute CORE rates of formate from WT and SHMT1- or SHMT2-depleted HAP1 cells upon 24 h 50 nM MTX. Each dot indicates the mean of an individual experiment measured in triplicate wells; Brown-Forsythe and Welch ANOVA test with Dunnetts multiple comparisons test. Mean ± SEM ($n = 4$ for CTRL, MTX, SHMT2ko, SHMT2ko MTX; $n = 3$ for SHMT1ko and SHMT1ko MTX) **i** Absolute CORE rates of formate from WT and MTHFD1L-depleted MDA-MB-468 cells upon 24 h 50 nM MTX. Mean ± SEM ($n = 6$ for CTRL and MTX; $n = 3$ for MTHFD1Lko + /- MTX) of an individual experiment measured in triplicate wells; Brown-Forsythe and Welch ANOVA test with Dunnetts multiple comparisons test. **j** Absolute CORE rates of formate from SCR and MTHFD2 KD MDA-MB-468 cells upon 24 h 50 nM MTX. Dots represent mean of an individual experiment measured in triplicate wells; mean ± SEM; ($n = 3$) Brown-Forsythe and Welch ANOVA test with Dunnetts multiple comparisons test. **k** Absolute CORE rates of formate from MDA-MB-468 cells upon 24 h treatment with 2.5 mM Metformin and 50 nM MTX. Dots represent mean of an individual experiment measured in triplicate wells; mean ± SEM ($n = 2$). Source data are provided as a Source Data file.

or shRNA mediated *MTHFD2* knock-down and *MTHFD2* KO (Fig. 4i, j, S4I-M). All genetic interventions resulted in a strong suppression of formate overflow during MTX treatment, further suggesting that increased formate overflow upon MTX depends on mitochondrial serine catabolism via the folate pathway (Fig. 4i, j, S4J, M).

As an alternative approach to genetic silencing we used Metformin to target complex 1 of the electron transport chain (ETC). We have previously shown that mitochondrial formate production depends on active ETC[21,22]. Here, we demonstrate that targeting of complex 1 with Metformin strongly suppresses mitochondrial formate production both at baseline and in presence of MTX, further supporting our finding that formate production in presence of MTX depends on mitochondrial 1C metabolism (Fig. 4k). To proof that Metformin indeed inhibits respiration under the applied conditions, we performed Seahorse experiments to measure the expected drop in oxygen consumption rate (Fig. S4N). We also monitored a reduction in proliferation (Fig. S4O) and we performed [U-^{13}C]glutamine tracing to monitor the expected strong increase in reductive carboxylation (Fig. S4P, Q), a well-known phenomenon upon ETC inhibition[54,55].

In summary, these results show that mitochondria provide a protected cellular environment that permits autarkic folate-mediated serine catabolism independent of the cytosolic folate metabolism.

Limiting serine availability decreases formate overflow and cancer cell migration. As we observed increased glucose derived serine synthesis and subsequent downstream catabolism of serine via mitochondrial 1C metabolism, we investigated if interfering with serine synthesis is effective to reduce sustained cell migration upon pharmacologic inhibition of cytosolic 1C metabolism. First, to identify an effective inhibitor of serine de novo synthesis, we tested multiple available allosteric and one competitive inhibitor of PHGDH. Indicated by the strong abrogation of labeled serine, we observed that the competitive inhibitor BI-4916 (BI)[12] had superior efficacy compared to the allosteric inhibitors WQ-2101 (WQ)[11], NCT-502 (NCT)[9], and CBR-5884 (CBR)[15] (Fig. 5a). Released M + 1 formate from [U-^{13}C]glucose was also effectively inhibited after BI treatment alone or in combination with MTX (Fig. 5b). Additionally, routine screening for metabolic side effects revealed that treatment with the allosteric inhibitors WQ, NCT, and CBR did result in a significant reduction of mitochondrial OCR (Fig. 5c), which was not observed with the competitive inhibitor BI (Fig. 5c). WQ and NCT also negatively affected TCA cycle activity as characterized by a reduction of M + 2 isotopologue abundance of TCA cycle associated metabolites (Fig. 5d). In contrast to the other inhibitors, BI had no adverse effect on TCA cycle activity and proliferation rate and thus emerged as the preferred PHGDH inhibitor in all subsequent experiments (Fig. 5d, S5A–D). Combined treatment with the specific PHGDH inhibitor BI significantly reduced MTX-mediated cell migration (Fig. 5e). This inhibitory effect was further enhanced upon combined PHGDH inhibition and serine and glycine (S/G) starvation (Fig. 5f). While S/G starvation alone resulted only in moderate inhibitory effects on migration of MTX-treated cells, combined treatment with PHGDH inhibition fully blunted cell migration (Fig. 5f). Similar results were observed in 4T1 cells (Fig. S5F). As all MTX conditions resulted in full growth arrest (Fig. S5E), this finding indicates a role for mitochondrial 1C metabolism in cell motility that is independent of serine's anabolic function to support biosynthetic processes.

While neither BI treatment alone nor S/G starvation alone were sufficient to prevent the induction of the observed EMT-phenotype, combined inhibition and starvation did minimize *ZEB1*, *ZEB2*, and *VIM* upregulation upon DHFR inhibition (Fig. 5g). This indicates that serine represents an underlying requirement for EMT onset upon DHFR inhibition. Importantly, S/G starvation did not further increase cell death after combined MTX and BI treatment (Fig. 5h). Of note, we also found that BI treatment was effective to reduce the migratory capacity of MTX-resistant, pro-migratory MDA-MB-468 cells (Fig. 5i). In summary, using MTX as a tool compound to study cell migration in absence of proliferation revealed that serine is essential to sustain full cancer cell migratory capacity (Fig. 5j).

Mitochondrial 1C metabolism supports cell motility and depends on mitochondrial THF availability. As withdrawal of serine can affect different aspects of cell physiology, we aimed to investigate more specifically the role of mitochondrial 1C metabolism in promoting cell migration. Analogue to the interventions presented in Fig. 4i–k, we used Metformin to target the ETC and genetic interventions to target *MTHFD2* or *MTHFD1L* both in MDA-MB-468 and 4T1 cells.

Metformin treatment of MTX exposed (growth arrested) cells reduced the migration of MDA-MB-468 cells (Fig. 6A), suggesting that one function of the ETC is to support cell migration.

Next, we investigated the role of mitochondrial serine catabolism in context of migration directly, by monitoring the migration of MTX treated *MTHFD2* or *MTHFD1L* silenced MDA-MB-468 and 4T1 cells. Of note, neither *MTHFD2* nor *MTHFD1L* silencing reduced cell proliferation or sensitivity to the growth-arresting effects of MTX (Fig. S6A–D). Also, cell death rates upon MTX were not affected by *MTHFD2* or *MTHFD1L* silencing (Fig. S6E–H). Scratch assay analysis showed that *MTHFD2* silencing markedly reduced MTX-mediated cell motility both in MDA-MB-468 and 4T1 cells (Fig. 6b, c). As shRNA used to silence human and murine *MTHFD2* were different, we do not expect shRNA specific off-target effects. Nevertheless, we confirmed the shMTHFD2 KD results in MDA-MB-468 cells with *MTHFD2* knock-out cells (Fig. S6I).

Mthfd1l silencing of MTX treated 4T1 cells also resulted in decreased migration (Fig. 6d). Somewhat surprisingly, loss of *MTHFD1L* in MDA-MB-468 cells had no negative effect on the migration of MTX treated cells (Fig. 6e). By following different hypotheses and various experiments, we realized that there is a striking difference in ALDH1L2 expression in 4T1 versus MDA-MB-468 cells, while MTHFD1L expression was comparable between these two cell lines (Fig. 6f, g).

This observation reminded us that in MDA-MB-468 cells, ALDH1L2 can act as an alternative outlet to oxidize formyl-THF to CO_2 thereby regenerating mitochondrial THF (in contrast to 4T1). That said, in MTHFD1L deficient cells, the ALDH1L2 status can be decisive whether THF can be regenerated or if THF will be trapped as 10-CHO-THF in the mitochondrion. Loss of free THF will potentially inhibit the autarkic mitochondrial cycle that can otherwise act in presence of MTX (Fig. 6h). In support of this hypothesis, we also measured increased formate release flux in 4T1 cells compared to MDA-MB468 (Fig. S6J), suggesting that in 4T1 cells less 10-CHO-THF is oxidized via Aldh1l2 and instead catabolized through Mthfd1l.

To test this hypothesis, we targeted *ALDH1L2* in MTHFD1L KO cells and monitored migration. We found that combinatorial depletion of *MTHFD1L* and *ALDH1L2* in MDA-MB-468 cells resulted at least in a reduction of migration upon MTX compared to single depletion of *MTHFD1L* alone. This was observed both for shRNA as well as for siRNA mediated knockdown of *ALDH1L2* (Fig. 6i, S6K).

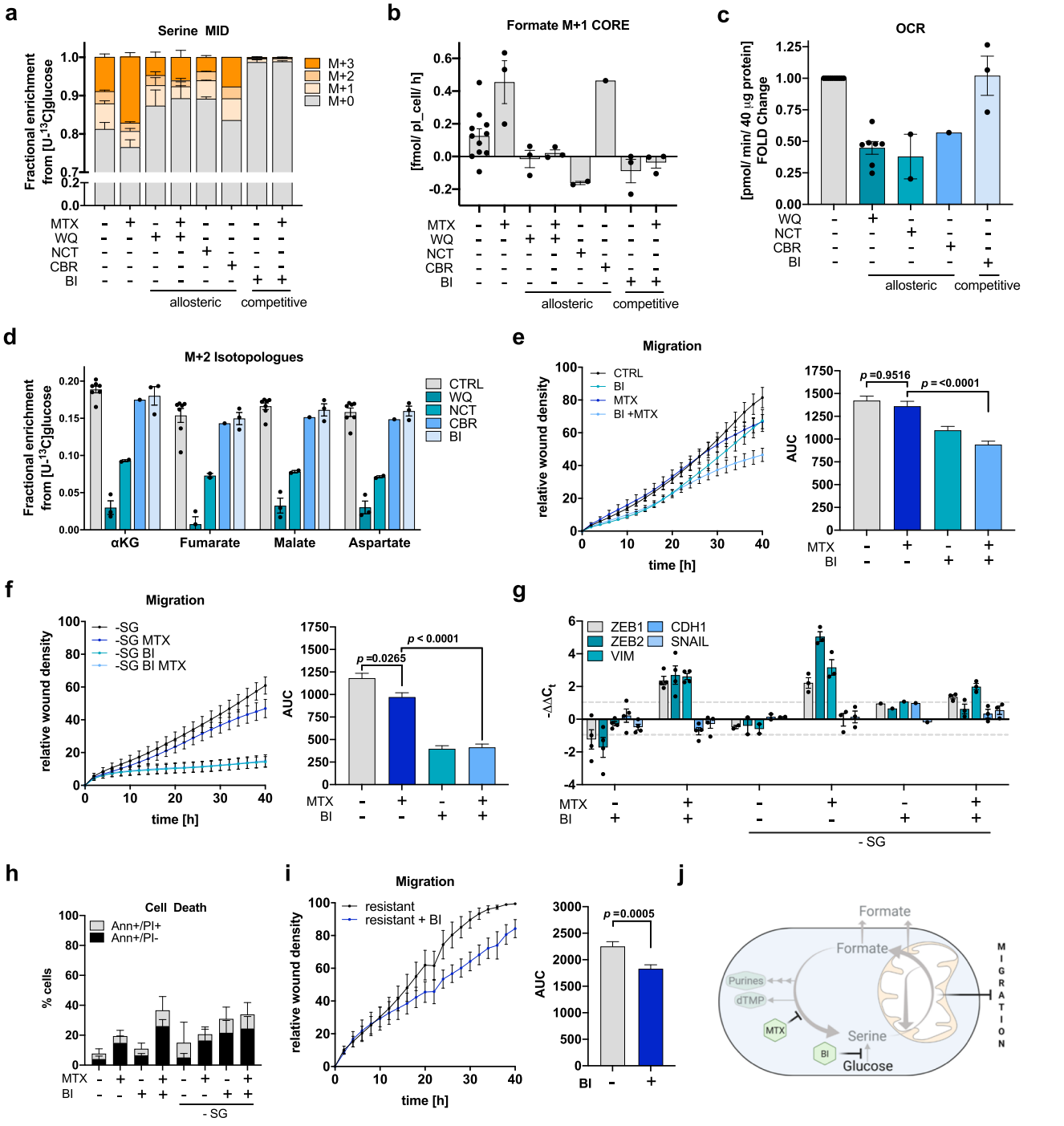

In conclusion, these results reveal a growth-independent role of mitochondrial 1C metabolism for cancer cell motility. Interestingly, the pool of free THF might be relevant for the functionality of the autarkic mitochondrial 1C cycle and ALDH1L2 can serve as an alternative outlet to regenerate THF when MTHFD1L is missing (summarized in Fig. 6J).

Genetic targeting of mitochondrial 1C metabolism reduces metastasis formation in vivo. According to our model, we predict that sole inhibition of mitochondrial 1C metabolism might be sufficient and effective to reduce cancer cell escape from the primary tumor and subsequent metastasis formation. To test this hypothesis, we employed the 4T1 cells with *Mthfd1l* KD to study the metastatic cascade in orthotopic tumors in vivo.

To evaluate first if Mthfd1l KD cells are more prone to oxidative stress, which could impact metastatic dissemination in vivo[56], we measured ROS levels in MTHFD1L silenced MDA-MB-468 and 4T1 cells at baseline and after MTX treatment. At baseline, ROS levels between MTHDF1L silenced and control cells were unchanged. MTX treatment induced ROS levels to comparable extends and 500 µM of H_2O_2 treatment did induce cell death rate comparable to Ctrl cells (Fig. S7A–C). In summary, these experiments do not indicate that loss of MTHFD1L results in increased cellular ROS levels or increased susceptibility to oxidative insults.

We then injected 4T1 cells with or without silenced *Mthfd1l* into the mammary fat pad of immunocompetent BALB/c mice to form orthotopic tumors (Fig. 7a). Primary tumor growth was

Fig. 5 Limiting serine availability decreases formate overflow and cancer cell migration. a MID of intracellular serine in MDA-MB-468 cells upon [U-^{13}C]glucose and 24 h 10 μM WQ-2101, 10 μM NCT-502, 30 μM CBR-5884, 15 μM BI-4916, and 50 nM MTX; mean ± SEM ($n = 10$ for CTRL; $n = 3$ for WQ, MTX, WQ MTX, BI, BI MTX; $n = 2$ for NCT; $n = 1$ for CBR) of independent experiments each measured in triplicate wells. **b** Formate M + 1 isotopologue exchange rate in MDA-MB-468 cells using [U-^{13}C]glucose and treatment as in (**a**). Dots indicate independent experiments measured in triplicate wells; mean ± SEM ($n = 10$ for CTRL; $n = 3$ for WQ, MTX, WQ MTX, BI, BI MTX; $n = 2$ for NCT; $n = 1$ for CBR). **c** Basal cellular respiration upon 24 h 10 μM WQ-2101, 10 μM NCT-502, 30 μM CBR-5884, and 15 μM BI-4916 in MDA-MB-468 cells as fold mitochondrial OCR compared to control. Dots represent individual experiments composed of six technical replicates; mean ± SEM ($n = 10$ for CTRL, $n = 7$ for WQ, $n = 3$ for BI, $n = 2$ for NCT, $n = 1$ for CBR). **d** M + 2 isotopologues of selected TCA-metabolites in MDA-MB-468 cells upon [U-^{13}C]glucose and treatment as in (**b**). Dots indicate independent experiments measured in triplicate wells; mean ± SEM ($n = 7$ for CTRL, $n = 3$ for WQ, BI, $n = 2$ for NCT, $n = 1$ for CBR). **e** Migration of MDA-MB-468 cells upon 50 nM MTX, 15 μM BI-4916 and **f** serine- and glycine starvation and respective AUC; mean ± SEM of independent experiments ($n = 5$ for (**e**), $n = 4$ for (**f**)); Brown-Forsythe and Welch one-way ANOVA with Dunnett's multiple comparisons test. **g** mRNA expression from indicated genes in MDA-MB-468 cells upon 72 h 50 nM MTX, 15 μM BI-4916, and serine- and glycine starvation measured by real-time RT-qPCR. Mean ± SEM ($n = 4$ for BI, BI + MTX, $n = 3$ for MTX-SG, MTX-SG + BI, $n = 2$ for -SG, $n = 1$ for BI-SG). **h** Cell death induction in MDA-MB-468 cells upon 48 h 50 nM MTX, 15 μM BI-4916 and serine- and glycine starvation was assessed by flow cytometry and AnnexinV-FITC/PI-staining; mean ± SD of independent experiments ($n = 3$). Two-way ANOVA with Dunnett's multiple comparisons test. **i** Migration of MTX-resistant MDA-MB-468 cells upon 50 nM MTX and 15 μM BI-4916 and respective AUC; mean ± SEM of independent experiments ($n = 4$); Brown-Forsythe and Welch one-way ANOVA with Dunnett's multiple comparisons test. **j** Cytosolic and mitochondrial compartments of 1C metabolism and the pharmacologic intervention points of MTX and inhibitors of PHGDH. Source data are provided as a Source Data file.

monitored over 6 weeks. In concordance with the in vitro data, primary tumor growth was not affected and tumor weight at endpoint was not different compared to Ctrl conditions (Fig. 7b, c). Knock-down of Mthfd1l in the primary tumors was confirmed by Western Blot (Fig. 7d, S7D–F). In line with our hypothesis, the number of macroscopic lung metastases was significantly reduced in mice that were carrying tumors deficient in Mthfd1l (Fig. 7e). While all mice that were injected with Mthfd1l-expressing 4T1 cells exhibited lung metastases, over 50% of mice injected with *Mthfd1l* KD cells did not show macroscopic metastatic lesions. Of note, expression of EMT related genes in the primary tumor was unchanged between the two groups (Fig. S7G). H&E staining of lungs and quantification of the metastatic area per lung confirmed reduced metastasis in Mthfd1l deficient tumors (Fig. 7f, g).

These in vivo findings further strengthen the key relevance of mitochondrial 1C metabolism as a cornerstone to support cancer cell migration independent of primary tumor growth and cancer cell proliferation rates.

Discussion

In this study, we uncover a growth-independent function of mitochondrial serine catabolism to drive cancer cell motility. Importantly, by using MTX as a tool compound to study migration independent of proliferation, we observed that upon inhibition of cytosolic 1C metabolism, mitochondria sustain an autarkic 1C metabolism that is sufficient to sustain full migratory capacity.

Such compartmentalization of 1C metabolism during MTX treatment is feasible because release of the 1C unit from THF in the mitochondrial MTHFD1L reaction is, in contrast to cytosolic thymidylate synthetase reaction, not oxidizing THF to DHF. Therefore, the mitochondrial THF pool is sustained to allow SHMT2-dependent mitochondrial serine catabolism, while cytosolic 1C metabolism enzymes are inhibited due to accumulating DHF species. Our finding that ALDH1L2 can serve as an alternative source for THF regeneration in MTHFD1L deficient cells, supports the notion that mitochondria can maintain an independent THF pool that is required for an autarkic mitochondrial 1C metabolism as long as there is THF available that can accept the hydroxymethyl group in the first (SHMT2 dependent) step of serine catabolism.

An autarkic mitochondrial 1C metabolism is further supported by a chemical modification of folate species that alters their transport activities across the mitochondrial membrane. For maximal biologic activity, folate species need to be polyglutamated by folylpolyglutamate synthase (FPGS) and the resulting polyglutamate species were shown to be only poorly transported across the mitochondrial membrane[57,58]. Consequently, polyglutamated folate species can be chemically trapped within the mitochondria to sustain the mitochondrial 1C cycle. Especially, upon growth arrest when cells can retain their mitochondrial content and don't need to amplify their content as it is required during proliferation. Additionally, there is evidence that transport activity of the mitochondrial folate transporter is limited to reduced folates[59]. This indicates a limited transport of MTX and folic acid itself across the mitochondrial membrane. Taken together, such compartmentalization of 1C metabolism and autarkic function of mitochondrial 1C metabolism emerges as a selective advantage in cells upon perturbation of cytosolic 1C metabolism and indicates a function of the mitochondrial 1C metabolism pathway to support cell motility.

While our data demonstrate that mitochondrial serine catabolism is needed to allow full migratory capacity, the specific biochemical output conferring this function still needs to be determined in more detail. Mitochondrial serine catabolism can generate NADH, NADPH, ATP, glycine, CO_2, methylene- and formyl-THF and formate. The plasticity of this pathway allows tailoring the catabolism towards current cellular needs[38]. Therefore, it can be possible that serine is differentially catabolized along the metastatic cascade in a context dependent manner. We have previously shown that exogenous formate promotes cancer cell invasion[22] and various cellular stress situations such as energy stress[21] or MTX treatment (this study) can increase the rate of formate overflow which results in increased extracellular formate concentrations. It is therefore tempting to speculate that increasing formate concentrations in the tumor microenvironment promote a more invasive phenotype of stressed cancer cells. In more general terms, it could be possible that mitochondrial serine catabolism can selectively promote cell motility in response to extrinsic or intrinsic stress stimuli such as growth inhibition or nutrient deprivation. On the other hand, MDA-MB-468 MTHFD1L KO cells are also formate overflow negative but do not show reduced migration. As ROS levels are neither increased in MDA-MB-468 nor in 4T1 MTHFD1L deficient cells, we do not think that the observed migration effects in this study are ROS dependent. Given previous work[22] and the current study, there might also be differences when comparing migration with invasion.

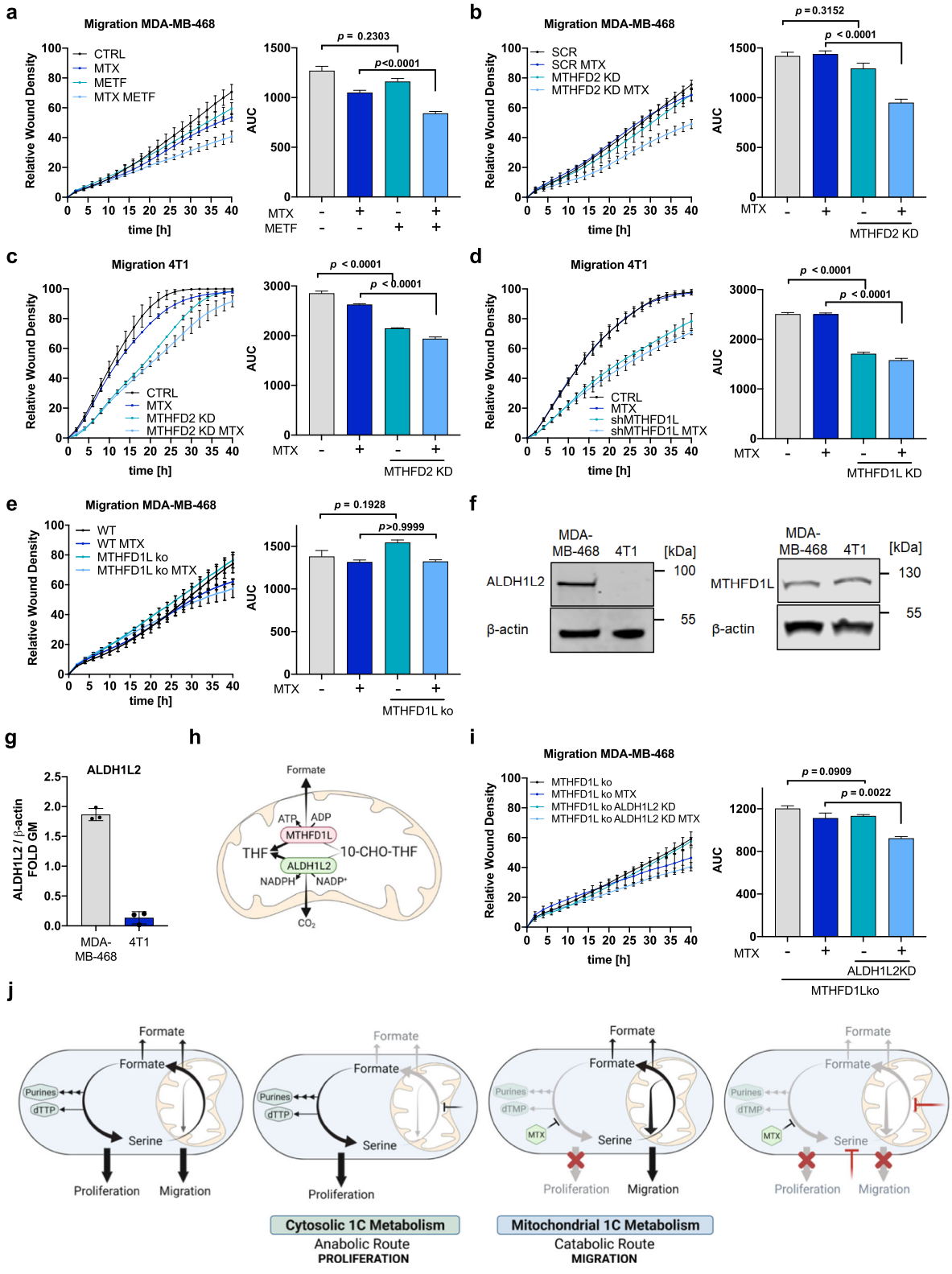

Ongoing work in our lab will help clarifying these questions in the future. To do so, it will be of particular importance to further disentangle effects arising from exogenous formate from effects depending on endogenous serine catabolism. Independent of these yet unknown details, we remain with the conclusion that mitochondrial serine catabolism contributes to cancer cell migration and metastasis independent of its known anabolic functions.

Finally, we would like to note that although we mainly use MTX as a tool compound to separate proliferative from migratory processes and to inhibit cytosolic 1C metabolism, our results have also some implications in regard to MTX as an anchor drug in chronic treatment of autoimmune diseases. Intracellular erythrocyte and mean plasma concentration of MTX were reported to be in a comparable, even slightly higher, nM range to our chosen drug concentration[60,61]. Finally, we also

Fig. 6 Mitochondrial 1C metabolism supports cell motility and depends on mitochondrial THF availability. a Migration of MDA-MB-468 cells upon 2.5 mM Metformin and 50 nM MTX and respective AUC; mean ± SEM of independent experiments ($n = 3$); Brown-Forsythe and Welch one-way ANOVA with Dunnett's multiple comparisons test. **b** Migration of MDA-MB-468 cells upon MTHFD2 knockdown and 50 nM MTX and respective AUC; mean ± SEM of independent experiments ($n = 4$); Brown-Forsythe and Welch one-way ANOVA with Dunnett's multiple comparisons test. **c** Migration of 4T1 cells upon Mthfd2 knockdown and 75 nM MTX and respective AUC; mean ± SEM of independent experiments ($n = 3$); Brown-Forsythe and Welch one-way ANOVA with Dunnett's multiple comparisons test. **d** Migration of 4T1 cells upon Mthfd1l knockdown and 75 nM MTX and respective AUC; mean ± SEM of independent experiments ($n = 3$); Brown-Forsythe and Welch one-way ANOVA with Dunnett's multiple comparisons test. **e** Migration of MDA-MB-468 cells upon MTHFD1L knockout and 50 nM MTX and respective AUC; mean ± SEM of independent experiments ($n = 3$); Brown-Forsythe and Welch one-way ANOVA with Dunnett's multiple comparisons test. **f** ALDH1L2 and MTHFD1L protein expression in MDA-MB-468 and 4T1 cells. **g** Signal intensity of ALDH1L2 on Western Blot was quantified relative to β-actin as loading control. Mean ± SEM ($n = 3$); unpaired *t*-test with Welch's correction. **h** MTHFD1L- and ALDH1L2-dependent reactions in mitochondrial 1C metabolism. **i** Migration of MDA-MB-468 cells upon MTHFD1L knockout, ALDH1L2 knockdown and 50 nM MTX and respective AUC; mean ± SEM of independent experiments ($n = 3$); Brown-Forsythe and Welch one-way ANOVA with Dunnett's multiple comparisons test. **j** Model summarizing the autarkic activity of mitochondrial and cytosolic 1C metabolism and their respective relevance for cell migration and cell proliferation. Source data are provided as a Source Data file.

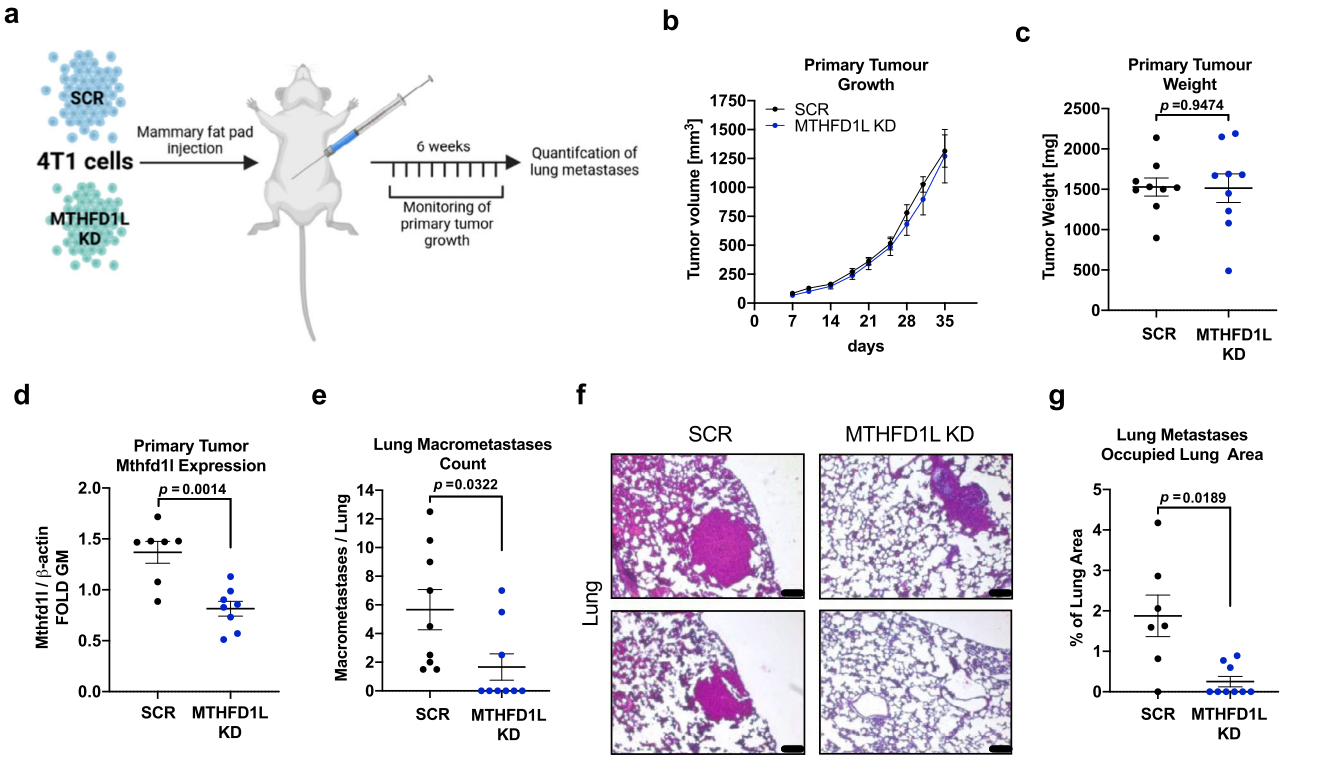

Fig. 7 Genetic targeting of mitochondrial 1C metabolism reduces metastasis formation in vivo. a 4T1 breast cancer cells transfected with non-targeting control (SCR, $n = 9$) and 4T1 cells with KD of *Mthfd1l* ($n = 9$) were injected into the mammary fat pads of immunocompetent female Balb/c mice. Primary tumor growth was monitored and lung metastasis formation was evaluated at end-point. **b** Primary tumor size was measured and mean tumor volume for each group was calculated; mean ± SEM ($n = 8$ (Scr) and 9 (Mthfd1l KD)). **c** Primary tumor weight was measured at the end-point. Dots indicate individual animals; mean ± SEM ($n = 9$); unpaired, two-tailed *t*-test with Welch's correction. **d** Primary tumor tissue was analyzed for Mthfd1l protein expression by Western Blot and quantified relative to β-actin as loading control. Dots indicate individual animals; mean ± SEM ($n = 7$ (Scr) and 8 (Mthfd1l KD)); unpaired, two-tailed *t*-test with Welch's correction. Protein lysates from tumors with significantly low Mthfd1l and β-actin expression relative to total protein were judged to be not pure tumor lysate and discarded from analysis (see Figure S7D–F for details). **e** Macroscopic lung metastases were counted and are depicted as number of metastases per lung. Dots indicate individual animals; mean ± SEM ($n = 9$); unpaired, two-tailed t-test with Welch's correction. **f** Lung tissue was embedded in paraffin and stained with H&E. 2 representative images per group are presented to show microscopic lung metastasis; scale bar corresponds to 100 µm. **g** Metastatic area per lung was quantified and is expressed as % area of lung tissue. Dots indicate individual animals; mean ± SEM ($n = 7$ (Scr) and 9 (Mthf1l KD)); unpaired, two-tailed *t*-test with Welch's correction. Source data are provided as a Source Data file.

would like to refer to a parallel and independent (back-to-back) publication that provides additional evidence that purine depletion promotes serine de novo synthesis and cell migration[62]. Interestingly, in this parallel work, the authors provide data that MTX also promotes the metastatic potential of melanoma cells in vivo. Hence, our findings on mitochondrial 1C metabolism might justify future investigations in cancer patients and patients that undergo chronic MTX therapy for an arthritic comorbidity.

Methods

Chemicals. Methotrexate, rotenone, PKUMDL-WQ-2101, galactose, hydroxyurea, NAC, metformin and fluorouracil were purchased from Sigma Aldrich. Clofarabine, pemetrexed disodium hydrate, sirolimus were purchased from Bio Connect. Simvastatin was purchased from Sanbio. CBR-5884 and BI-4916 were purchased from MedChemExpress. NCT-502 was purchased from ApeXBio.

Cell culture. All cell lines (except HAP1 cells) were cultured in Dulbecco's modified Eagle's medium (DMEM) without phenol red, glucose, and glutamine (Thermo Fisher Scientific) and supplemented with 2 mM glutamine, 17 mM

glucose, and 10% fetal bovine serum (FBS) at 37 °C and 5% CO_2. HAP1 cells were cultured in IMDM medium supplemented with 10% FBS. For galactose treatment, supplemented glucose was replaced by 17 mM galactose at the beginning of the experiment. For serine/glycine starvation experiments cells were kept in MEM (Thermo Fisher Scientific) supplemented with or without 400 µM glycine and serine, 2 mM glutamine, 17 mM glucose and 10% dialyzed FBS.

MDA-MB-468 and MTHFD1L CRISPR/Cas9 KO cells were obtained from Lewis Cantley lab, Weill Cornell Medical College, USA[20]. MDA-MB-468 were authenticated by STR profiling in our lab in 2021 (originally from ATCC); LN229 cells obtained from Alexei Vazquez lab Beatson Institute for Cancer Research (authenticated by STR profiling in our lab in 2021) (originally from ATCC); 4T1 cells from Luxembourg Institute of Health, Clement Thomas lab (authenticated by Clement lab in 2018) (originally from ATCC). HCT-116 cells from University of Luxembourg, Elisabeth Letellier lab (originally from ATCC), HEK293T: NorLux Lab, Luxembourg Institute of Health (originally from ATCC). HAP1 cells were obtained from Patel's laboratory[53] (originally from Horizon Discovery). MTX-resistant MDA-MB-468 cells were generated through prolonged culturing of MDA-MB-468 cells with 50 nM MTX for 2 months until cells started to regrowth under MTX. All cell lines were routinely tested for mycoplasma contamination.

Metabolic characterization. For metabolic characterization of cell lines, previously established protocols for absolute quantification of exchange fluxes and intracellular fluxes of one-carbon metabolism were applied[21].

Stable isotope tracing and metabolite extraction. Stable isotope tracing experiments with [U-^{13}C]-glucose tracer or [U-^{13}C]-glutamine tracer (Cambridge Isotope Laboratories, CLM-1396) were performed in DMEM supplemented with 2 mM glutamine, 17 mM glucose, and 10 % FBS. Stable isotope tracing experiments with [U-^{13}C]-serine tracer (Cambridge Isotope Laboratories) were performed in MEM (Thermo Fisher Scientific) supplemented with 400 µM glycine, 2 mM glutamine, 17 mM glucose, 400 µM serine tracer, and 10% FBS. To allow for adaptation, cells were cultivated in MEM for at least one passage prior to [U-^{13}C]-serine tracer experiments. 150,000 to 200,000 cells were seeded in 12-well plates in triplicates for each experimental condition. Identical triplicate wells were seeded to allow for cell count and cell volume determination (to calculate the packed cell volume (PCV)) at the start and end of each tracing experiment. The day after seeding, growth medium was replaced by tracer medium and cells were cultured for 24 h. In parallel, 3 wells per condition were counted to assess starting PCV. After 24 h, triplicate wells were counted to assess PCV at the end of the experiment and one set of triplicates was used for subsequent metabolite extraction. Medium of these triplicates were collected and analyzed for exchange rates. To determine the basal medium composition for the subsequent calculation of exchange rates, identical medium was incubated in triplicates in empty 12 wells throughout the experiment and analyzed in parallel to the medium samples. Collected medium samples were centrifuged at 300 g for 5 min. Supernatant was collected and stored at −20°C until extraction of metabolites. Formate extraction, derivatization, and quantification as well as metabolite extraction for LC-MS analysis was performed as described in[21]. For metabolite extraction for GC-MS analysis after [U-^{13}C]-glucose tracing and [U-^{13}C]-glutamine tracing, cells were washed with cold 0.9% NaCl solution. 400 µl ice-cold MeOH/H_2O_{MQ} [(ratio, 1:1) containing the internal standards pentanedioc-d6 acid and [U-^{13}C]-ribitol at a final concentration of 1 µg/ml and Tridecanoid-d25 acid at a final concentration of 5 µg/ml] was added to each well. Plates were incubated for 5 min at 4°C on a rocking shaker. Supernatant was collected, mixed with 200 µl $CHCl_3$, and centrifuged for 5 min at 13,000 g at 4°C. Upper polar phase was collected and stored at −20°C for subsequent MS analysis of polar metabolites.

GC-MS measurements

Analysis of formate release rates. Formate derivatization in the culture medium was performed using MCF derivatization as described in[21]. GC-MS analysis was performed using an Agilent 7890 A GC coupled to an Agilent 5975 C inert XL Mass Selective Detector (Agilent Technologies). A sample volume of 1 µl was injected into a Split/Splitless inlet, operating in split mode (20:1) at 270 °C. The gas chromatograph was equipped with a 30 m (I.D. 250 µm, film 0.25 µm) DB-5MS capillary column (Agilent J&W GC Column, 122-5532 G). Helium was used as carrier gas with a constant flow rate of 1.4 ml/min. GC oven temperature was held at 80 °C for 1 min and increased to 130 °C at 10 °C/min followed by a post run time of 4 min at 280 °C. Total run time was 15 min. Transfer line temperature was set to 280 °C. Mass selective detector (MSD) was operating under electron ionization at 70 eV. MS source was held at 230 °C and the quadrupole at 150 °C. For precise quantification, measurements were performed in selected ion monitoring mode. Target ions (*m/z*) and dwell times are shown in Table S1. GC-MS chromatograms were processed using Agilent MassHunter Quantitative Analysis for GC-MS, Version B.08.00. Final determination of release rates was performed as described in[21].

Determination of mass isotopomere distribution (MID) of Intracellular TCA Cycle Metabolites following Stable Isotope Tracing. First, polar metabolites were derivatized for 90 min at 55 °C with 20 µl of methoxyamine (c = 20 mg/ml) in pyridine under continuous shaking and subsequently for 60 min at 55 °C with additional 20 µl of MTBSTFA w/ 1% TBDMCS. GC-MS analysis was performed using an Agilent 7890B GC coupled to an Agilent 5977 A Mass Selective Detector (Agilent Technologies). A sample volume of 1 µl was injected into a Split/Splitless inlet, operating in splitless mode at 270 °C. Gas chromatograph was equipped with a 30 m (I.D. 250 µm, film 0.25 µm) ZB-35MS capillary column with 5 m guard column (Phenomenex). Helium was used as carrier gas with a constant flow rate of 1.2 ml/min. GC oven temperature was held at 100°C for 2 min and increased to 300°C at 10°C/min and held for 4 min. Total run time was 26 min. Transfer line temperature was set to 280°C. Mass selective detector (MSD) was operating under electron ionization at 70 eV. MS source was held at 230°C and the quadrupole at 150 °C. For precise quantification of the MID, measurements were performed in selected ion monitoring mode. Target ions (*m/z*) and dwell times are shown in Table S2.

The MetaboliteDetector software package (Version 3.220180913) was used for mass spectrometric data post processing, quantification, MID calculations, correction of natural isotope abundance, and determinations of fractional carbon contributions[63].

Analysis of medium exchange rates. Polar metabolites of the culture medium were derivatized for 90 min at 45°C with 20 µl of methoxyamine (c = 20 mg/ml) in pyridine under continuous shaking and subsequently for 30 min at 45 °C with 20 µl of MSTFA. GC-MS analysis was performed using an Agilent 7890B GC coupled to an Agilent 5977 A Mass Selective Detector (Agilent Technologies). A sample volume of 1 µl was injected into a Split/Splitless inlet, operating in split mode (10:1) at 270°C. Gas chromatograph was equipped with a 30 m (I.D. 250 µm, film 0.25 µm) ZB-35MS capillary column with 5 m guard column (Phenomenex). Helium was used as carrier gas with a constant flow rate of 1.2 ml/min. GC oven temperature program: 90°C for 1 min, 9°C/min to 270°C, 25°C/min to 320°C and held for 7 min. Total run time was 30 min. Transfer line temperature was set to 280°C. MSD was operated under electron ionization at 70 eV. MS source was held at 230°C and the quadrupole at 150°C. Full scan mass spectra were acquired between m/z 70 and 700.

The MetaboliteDetector software package (Version 3.220180913) was used for quantification. Briefly, peak areas of all isotopologues of defined quantification ions were summed up and divided by the peak area of the internal standard for normalization. In addition, a calibration curve was prepared to calculate absolute concentrations. Absolute uptake and release rates were calculated as described in[21]

LC-MS measurements. Untargeted LC-MS analysis was carried out as previously described in[21].

Nucleotide and NAD/NADH analysis. The following analytical conditions are based on a protocol from[21]. Metabolite analyses were performed using a Thermo Vanquish Flex Quaternary LC coupled to a Thermo Q Exactive HF mass spectrometer. Chromatography was carried out with a SeQuant ZIC-pHILIC 5 µm polymer (150 × 2.1 mm) column connected to the corresponding SeQuant ZIC-pHILIC Guard (20 × 2.1 mm) pre-column. Column temperature was maintained at 45 °C. The flow rate was set to 0.2 mL/min and the mobile phases consisted of 20 mmol/L ammonium carbonate in water, pH 9.2 (Eluent A) and Acetonitrile (Eluent B). The gradient was: 0 min, 80% B; 2 min, 80% B; 17 min, 20% B; 18 min 20% B; 19 min 80 % B; 20 min 80% B (0.4 mL/min); 24 min 80% B (0.4 mL/min); 24.5 min 80% B. The injection volume was 5 µL. All MS experiments were performed using electrospray ionization with polarity switching enabled (+ESI/-ESI). The source parameters were applied as follows: sheath gas flow rate, 25; aux gas flow rate, 15; sweep gas flow rate, 0; spray voltage, 4.5 kV (+) / 3.5 kV (–); capillary temperature, 325°C; S-lense RF level, 50; aux gas heater temperature, 50°C. The Orbitrap mass analyzer was operated at a resolving power of 30,000 in full-scan mode (scan range: *m/z* 75…1000; automatic gain control target: 1e6; maximum injection time: 250 ms). Data were acquired with Thermo Xcalibur software (Version 4.3.73.11) and analyzed with TraceFinder (Version 4.1). Subsequent data analysis for normalization and natural isotope subtraction were performed using in house scripts as in[21].

Western blot. Total cell lysates from cells cultured in vitro were prepared by 30 min incubation of cell pellets on ice in cell lysis buffer (150 mM NaCl, 1 mM EDTA, 50 mM Tris-HCl, 1% NP-40). Protein lysates from tumor tissue were obtained by lysing 10 mg tumor tissue pieces in 150 µl cell lysis buffer. Homogenization of tumor tissue lysates was achieved with TissueLyser II (Quiagen) using 5 mm metal beads. Lysis efficiency was maximized by sonification. Lysis solution was centrifuged at 13,000 g for 15 min at 4°C and supernatant was collected and stored at −80°C. Protein concentration was determined by Bradford assay. 15 – 30 µg of total protein were loaded on NuPAGE 4–12% Bis-Tris gels (Life Technologies) or RunBlue 4–12% Bis-Tris gels (Westburg) using 4x NuPage LDS Sample buffer (Thermo Fisher Scientific) supplemented with 10 mM DTT (Sigma Aldrich) and blotted on nitrocellulose membrane according to standard protocols. Membranes were stained with REVERT staining solution (LI-COR) and analyzed for total protein abundance. Subsequently, membranes were blocked with Odyssey TBS blocking buffer (LI-COR) or 5% milk-powder in TBST and incubated with the

indicated primary antibodies over night at 4°C. Incubation with secondary antibody occurred for 2 h at RT. Detection was performed with the Odyssey CLx Infrared Imaging System (LI-COR). ImageStudioLite Software Vers.5.2 (LI-COR) was used for image analysis. All uncropped and unprocessed scans are available in the source data file. Antibodies used for Western blot analysis in this study:

MTHFD1L (16113-1-AP, LOT: 00024322, RRID: AB_2250974) from Proteintech; Vimentin (3390, clone 5G3F10, LOT:2, RRID: AB_2216128), β-actin (3700, clone 8H10D10, LOT: 18, RRID: AB_2242334), NRF2 XP(R) (12721, clone D179C, LOT: 8, RRID: AB_2715528) and MTHFD2 (41377, D8W9U, LOT: 1, RRID: AB_2799200) from Cell Signaling Technology (CST); PHGDH (HPA021241, LOT: B115626, RRID: AB_1855299), PSAT1 (HPA042924, LOT: R40839, RRID: AB_2678223), PSPH (HPA020376, LOT: B115600, RRID: AB_1855867), SHMT1 (HPA023314, LOT: A78402, RRID: AB_1856830), and SHMT2 (HPA020549, LOT: A96534, RRID: AB_1856834) from Sigma Aldrich; LaminB (ab16048, LOT: GR32836742, RRID: AB_443298) from Abcam; IRDye 680RD Goat Anti-Mouse IgG (H + L) (926-68070, LOT: C90910-21, RRID: RRID AB_10956588) and IRDye 800CW Donkey Anti-Rabbit IgG (H + L) (926-32213, LOT: 926-32213, RRID: RRID AB_621848) from LI-COR (used in a 1:10,000 dilution). All antibodies were used in a 1:1,000 dilution unless stated otherwise.

Poly-L-Lysine coating. Poly-L-lysine (P1274) was purchased from Sigma-Aldrich and reconstituted at 500 µg/ml in H_2O_{MQ}. Wells were coated with PLL prior to Seahorse measurement and Scratch assay. To this end, PLL solution was diluted 1:20 in H_2O_{MQ} and added to the plates at least 1 h prior to seeding. Following incubation with PLL at 37°C and prior to cell seeding, plates were washed twice with H_2O_{MQ} and allowed to air-dry.

Seahorse measurements. The day prior to measurement, 40,000 cells were seeded on poly-L-lysine coated plates and treated the subsequent day as indicated. XF96 Extracellular Flux Analyzer (Seahorse Bioscience) was used to measure basal OCR following manufacturer's instructions using WAVE software. OCR was normalized to the protein concentration or cell number in the wells following the protocol described in[64] using Bradford assay.

Flow cytometric analysis of cell cycle distribution and cell death. 200,000 cells were seeded in 2 ml DMEM and treated the subsequent day as indicated. After incubation, medium was collected and cells were washed with PBS. PBS fraction was collected and cells were detached with trypsin. Detached cells were collected in DMEM. The combined, collected solutions were centrifuged and pellet was washed with PBS.

Cell cycle distribution. Centrifugation yielded a pellet that was resuspended in 100 µl PBS and fixed with ice-cold 80% EtOH. Fixed cells were stored at −20°C for at least 1 h and maximum 5 days prior to measurement. Cells were centrifuged, pellet was incubated for 1 h in 200 µl RNAse A in PBS (30 µg/ml) at RT. Immediately prior to measurement, 98 µl propidium iodide (PI) in PBS (50 µg/ml) was added. Flow cytometric analysis was performed using BD FACSCanto and BD FACSDiva software (version 8.0.1). Analysis was performed in FlowJo Version 10.6.2.

Cell death analysis. Pellet following centrifugation was resuspended in 50 µl AnnexinV-FITC staining solution (5% AnnexinV-FITC in AnnexinV binding buffer (10 mM HEPES pH 7.4, 140 mM NaCl, 2.5 mM $CaCl_2$, 0.1% BSA in $_{dd}H_2O$)) and incubated for 15 min on ice in the dark. 450 µl PI-staining solution (1.1 µg/ml PI in AnnexinV binding buffer) was added immediately prior to measurement using BD FACSCanto and BD FACSDiva software (version 8.0.1) (for wild-type cells) or NovoCyte Quanteon and software NovoExpress (version 1.5.0) (for GFP-positive transfected cells). Analysis was performed in FlowJo Version 10.6.2.

Flow cytometric analysis of ROS levels. 250,000 MDA-MB-468 cells were seeded in 2 ml medium and treated the subsequent day as indicated. Following incubation, cells were detached with trypsin, centrifuged at 350 *g* for 5 min and washed with warm DMEM. Cells were stained in 100 µl DMEM supplemented with 1:2,000 DAPI and 1:500 DCFDA for 30 min at 37°C. Following incubation, samples were centrifuged at 350 *g* for 5 min and washed with PBS. Following centrifugation at 350 *g* for 5 min, cells were resuspended in 100 µl PBS and measured using the BD LSRFortessa™ system and BD FACSDiva software (version 8.0.1). Data analysis was performed using FlowJo software Version 10.6.2.

Cell proliferation. Cell proliferation was determined using the IncuCyte® Live-Cell Analysis system (Essen Bioscience). Cell proliferation was either determined as measurement of cell density (confluence) or by quantification of red nuclei using the IncuCyte® NucLight Rapid Red Reagent (Essen Bioscience). Staining was performed according to manufacturer's instructions. Alternatively, viable cell number was determined by trypan blue staining and automatic counting using a Countess™ Cell Counting Chamber Slide (Thermo Fisher).

Migration assay (wound closure). Cell migration was determined using the IncuCyte® Scratch Wound Assay system for 96 well plates (Essen Bioscience). 96 well image lock plates (Essen Bioscience) were PLL coated prior to seeding of 40,000 cells per well. Wound application was performed 24 h post seeding using the 96-pin IncuCyte WoundMaker tool (Essen Bioscience) and indicated treatments were applied simultaneously. Measurement was performed in technical replicates ($n = 4–8$) and repeated as independent, biological experiments as stated for the respective experiment in figure legends.

Invasion and migration assay (transwell assay). Invasion and migration was analyzed by Boyden chamber assay as described in Meiser et al., 2018[22]. Transwells were coated with ECM-Collagen for invasion assays and left un-coated for migration assay. Treatment and migration/invasion was carried out for 18 h to 24 h.

RNA extraction, cDNA synthesis, and qPCR analysis. Total RNA was extracted from cell culture dishes following manufacturer instructions of RNeasy Mini Kit (Qiagen, 74104) or NucleoSpin RNA Kit (Machery&Nagel, 740955). For RNA extracts from tumor tissue, 10 mg tissue were homogenized in 350 µL RNA using 5 mm metal beads in TissueLyser II (Quiagen). RNA was transcribed to cDNA with High-capacity cDNA Reverse Transcription Kit (ThermoFisher, 4368814). qPCR was performed from 20 ng cDNA per sample using Fast SYBR™ Green Master Mix (ThermoFisher, 4385612). All samples were analyzed in technical duplicates or triplicates. qPCR using Fast SYBR Green was conducted at 95°C for 20 s, 40 cycles of 95°C for 1 s and 60°C for 20 s using the QuantStudio 5 Real-Time PCR System (Applied Biosciences, ThermoFisher Scientific). Specificity was verified by melt curve analysis. Relative quantification of each mRNA was done by QuantStudio Design&Analysis v1.5.1 software (Applied Biosciences, ThermoFisher Scientific) and comparative Ct method. All expression data was normalized to two housekeeping genes (*GAPDH* and *CycloA*). All primers used in this study are listed in Table S3.

shRNA-mediated gene silencing. Knockdown with shRNA was performed in MDA-MB-468 and 4T1 cells using lentiviral particles expressing two different shRNAs targeting the gene of interest and one non-silencing control vector (pGIPZ-shSCR: TTACTCTCGCCCAAGCGAG (Code: RHS4346). For silencing of the *MTHFD2* gene in MDA-MB-468 cells, pGIPZ shMTHFD2-2: ATTG-CATTTCTATTGGCCT (V2LHS_90968) purchased from Horizon Discovery was used. For silencing of the *ALDH1L2* gene in MDA-MB-468 cells, pGIPZ shALDH1L2: ACTGCTTTATCAACATCCG (Code: V3LHS_385780) purchased from Horizon Discovery was used. For silencing of the *Mthfd1l* gene in 4T1 cells, pGIPZ shMTHFD1L-2: TAGATTTCAATTTCATCTG (Code: V2LHS_96542) purchased from Horizon Discovery was used. For silencing Mthfd2 gene in 4T1 cells, pGIPZ shMthfd2-2: ATGACAACGGCTTCATTTC (Code: V2LMM_23800) purchased from Horizon Discovery was used. Plasmids used for generation of lentivirus were amplified from glycerol stocks, isolated (Machery&Nagel plasmid isolation kit), and used for transfection of HEK293T cells. Lentivirus was produced for 24 h in HEK293T cells co-transfected with the viral core packaging construct pCMVR8.74, the VSV-G envelope protein vector pMD2.G and the respective pGIPZ-shRNA-target plasmid using lipofectamine 3000 (Invitrogen #L3000008). Filtered virus supernatant was used to transduce MDA-MB-468 and 4T1 cells in DMEM supplemented with 2% FBS. After 24 h incubation at 37 °C, virus was removed and cells were cultured in DMEM supplemented with 10 % FBS for 48 h. 96 h post transduction, cells were cultured in selection media containing 2 µg/mL of puromycin (Sigma #P8833) for five passages to obtain stably transduced GFP-positive cells.

Generation of KO cells. Gene knock-out (KO) using the CRISPR-Cas9 system was performed in MDA-MB-468 using a vector expressing hCas9 and the respective guideRNA to target the gene of interest. For silencing of the *MTHFD2* gene in MDA-MB-468 cells, two different gRNA sequences (gRNA#918: CGCCAAC-CAGGATCACACTC (Vector ID: VB190718-1104ncn); gRNA1.Ex: GCTCGCGGCAGTTCGGTAAGA (Vector ID: VB190719-1026vzh) purchased from VectorBuilder were used. A control vector was used scramble_gRNA (GTGTAGTTCGACCATTCGTG (Vector ID: VB190718-1103vja) together with both constructs. To generate a *MTHFD2*-KO cell line, 300.000 cells were seeded the day prior to transfection into a 6 well plate in DMEM supplemented with 10% FBS. 24 h later, the culture medium was replaced with 2 mL of DMEM-F12 (LONZA #12-719 F) supplemented with 10 % FBS, Glucose (17 mM final concentration), Glutamine (2 mM final concentration), and 1 mM Sodium Formate and the cells were transfected using Opti-MEM, Lipofectamine, P3000 and 2 µg of plasmid DNA. Post incubation for 24 h, the transfection mix was removed and cells were replaced with fresh DMEM-F12. 72 h post transfection, cells were sorted into single cells by FACS based on their GFP fluorescence. Single cells were grown in DMEM-F12 supplemented with 1% Pen-Strep (Sigma, # P4333) until the formation of single colonies. These were further expanded and characterised by means of Western Blot.

siRNA-mediated gene silencing. 500.000 MDA-MB-468 cells were transfected with 40 pmol siRNA upon seeding in 6 well-plates using Lipofectamine 3000 (ThermoFisher) according to the manufacturer's instructions. Non-silencing control siRNA (siRNA ON-TARGETplus Human non-targeting (1810-10-05) siRNA SMARTpool) and siRNA directed against human *ALDH1L2* mRNA (siRNA ON-TARGETplus Human ALDH1L2 (160428; 26918-01-0005) siRNA SMARTpool) were purchased from Dharmacon.

Animal model. Animal experiments were performed according to all applicable laws and regulations, after receiving approval by the institution's Animal Experimentation Ethics Committee at UL (AEEC) and the veterinarian service of the Ministry of Agriculture, Viniculture & Rural Development (TumorMetab LUPA 2020/01). They ensure that care and use of animals for research purposes was conducted according to the EU Directive 2010/63/EU, as well as the Grand-Ducal Regulation of January 11, 2013 on the protection of animals used for scientific purposes. These included the justification of the use of animals, their welfare and the incorporation of the principles of the 3 R's (Replacement, Reduction and Refinement). A biostatistician reviewed all animal protocols. Mice were housed in a specific pathogen free (SPF) facility at a relative humidity of 40–70%, at 22 °C, and in 12 h dark/light cycles. Syngeneic 4T1 mammary carcinoma cells were orthotopically implanted into the left mammary fat pads (1 injection/mouse) of immune competent female Balb/c mice (8-10 month old) according to established protocols[65]. Briefly, each injection contained 2000 cells in a mixture of 25 µL PBS and 25 µL matrigel. 9 mice per group were injected with either 4T1 SCR or 4T1 *Mthfd1l* KD cells. Primary tumor growth was monitored between day 7 and day 35 of the experiment. Weight was monitored and no weight loss was observed. Experiment was terminated after 6 weeks and lung and liver were prepared for examination of metastatic outgrowth. No metastases were found in the liver. Macroscopic lung metastases were blindly counted under a microscope and microscopic lung metastases were visualized by H&E staining.

H&E staining. H&E staining was performed on 10 µm sections of paraffin embedded lung tissue. Staining was performed according to established protocols. Briefly, selected sections were dehydrated with MeOH and stained with Gill 2 hematoxylin. Sections were neutralized with successive washes of tap water, hard water (10 g $MgSO_4$ and 0.7 g $NaHCO_3$ per L), and distilled water. Subsequently, sections were stained with Eosin-solution and dehydrated through successive washes with 80%, 95%, 100% EtOH and Xylol prior to mounting. Images for quantification were acquired using BioTek Cytation 5 Cell Imaging Multimode Reader. Area of lung and metastasis were measured in ImageJ. Representative images for publication were acquired using Olympus IX83 microscope. Collapsed lungs were excluded from quantitative analysis.

Proteomics. SILAC (Stable Isotope Labeling with Amino acids in Cell culture) strategy was used for proteomic analysis. In general, MDA-MB-468 cells were cultivated in DMEM-F12 SILAC medium supplemented either with Lys^0 and Arg^0 (light channel) or Lys^8 and Arg^{10} (heavy channel). After 6 passages, labeling efficiency of heavy channel was confirmed using LC-MS/MS. Cells in light channel were treated with 50 nM MTX for 24 h and 72 h, while heavy channel was used as control. Cell pellets of biological duplicates were collected. Proteins were extracted in lysis buffer (50 mM ammonium bicarbonate, 6 M Urea, 2 M Thio-urea, pH 8) following a 30 min incubation at 4°C in the presence of protease inhibitors (cOmplete™ EDTA-free Protease Inhibitor Cocktail, Roche). Following centrifugation at 16,000 *g* for 10 min, supernatants were taken for protein quantification. Samples from light channel (50 µg protein) were mixed with control heavy channel (50 µg protein) for protein reduction (5 mM DTT, 1 h incubation at 37°C) and alkylation (10 mM IAA, 45 min in dark at room temperature). Protein digestion was performed with Lys-C (FUJIFILM Wako, 125-05061) at 1:30 ratio (enzyme/protein substances) for 4 h at 37 °C, then samples were diluted 4 times with 50 mM ammonium bicarbonate and digested overnight with 1 µg of trypsin at 37°C. Digestion was terminated through addition of formic acid (1% final concentration). Digested peptides were cleaned up with reverse phase Sep-Pak C18 1 cc Vac Cartridge (Waters, WAT054955) and eluted with 1 mL 50% ACN. Eluted peptides were dried by Speedvac (Thermo Fisher Scientific) and re-suspended in 0.1% formic acid. Peptide concentration was measured with Nanodrop. Peptides were measured by LC-MS/MS on Q-Exactive HF mass spectrometer (Thermo Fisher) connected to a Dionex Ultimate 3000 (Thermo Fisher). 500 ng of peptides were loaded onto a trap column (Acclaim PepMap 75 µm x 2 cm, C18, 3 µm) and separated on a 25 cm Acclaim pepmap RSLC column (75 µm x 25 cm, C18, 2 µm) using a 150 min gradient (2% to 90% acetonitrile) with a flow rate of 0.3 µL/min. MS data were acquired in data-dependent mode. Survey scans of peptide precursors from 375 to 1500 m/z were performed at 70,000 resolution with a 3×10^6 ion count target and the top 12 abundant peaks from survey scan were selected for fragmentation. Tandem MS was performed by isolation at 1.4 m/z with the quadrupole, HCD fragmentation with a normalized collision energy of 28. The MS2 ion count target was set to 1×10^5 and the max injection time was 45 ms. Only precursors with a charge state of 2–7 were sampled for MS2. The dynamic exclusion duration was set to 20 s with a 10 ppm mass tolerance around the selected precursor and its isotopes. Each sample was analyzed twice as technical replicates. All raw data was analyzed with MaxQuant (version 1.6.7.0) and searched with Andromeda against the Homo sapiens database from Uniprot. The minimal peptide length was set to 7 amino acids and the maximum of 3 missed cleavages were allowed. The search included variable modifications of methionine oxidation and N-terminal acetylation, deamidation (N and Q) and fixed modification of carbamidomethyl cysteine. The "Match between run" was checked within 1 min retention time window. Mass tolerance for peptide precursor and fragments were set as 10 ppm and 20 ppm, respectively. The FDR was set to 0.01 for peptide and protein identifications. SILAC based protein quantification (MaxQuant built-in) was used for quantitative evaluation of identified proteins. ProTIGY (https://github.com/broadinstitute/protigy), an R based tool, was used for differential analysis of MaxQuant output.

Statistics. Unpaired *t*-test with Welch's correction was applied for pairwise comparison (two-sided) using GraphPad Software Vers.8. For comparison of multiple groups ordinary Brown Forsythe & Welch one-way or two-way ANOVA with Dunnett's multiple comparison or Games-Howell's multiple comparisons test was performed using GraphPad Software Vers.8. Resulting *p*-values for comparisons of interest are given as numerical values within the respective graphs. For normalization, data points of one experiment were either normalized to the untreated control or divided by the global mean of the individual experiment. We define one *n* as one independent biological experiment (in some cases further consisting of several wells, e.g. triplicate wells for all stable isotope tracing experiments). The technical mean of one biological experiment was considered as one *n*. The mean values of several independent, biological experiments (as indicated in figure legends) were plotted and used for statistical analysis as indicated.

Reporting summary. Further information on research design is available in the Nature Research Reporting Summary linked to this article.

Data availability

Source data are provided with this paper. Proteomics data is available at the proteomics identification database (PRIDE) under the id: PXD027175 (INSERT URL here, once available). The remaining metabolomics data from targeted analysis are available within the article and the supplementary information files (source data file). Source data are provided with this paper.

Received: 24 January 2022; Accepted: 22 April 2022;
Published online: 16 May 2022

References

1. Siegel, R. L., Miller, K. D. & Jemal, A. Cancer statistics, 2019. *CA Cancer J. Clin.* **69**, 7–34 (2019).
2. Luengo, A., Gui, D. Y. & Vander, M. G. Heiden, targeting metabolism for cancer therapy. *Cell Chem. Biol.* **24**, 1161–1180 (2017).
3. Counihan, J. L., Grossman, E. A. & Nomura, D. K. Cancer metabolism: current understanding and therapies. *Chem. Rev.* **118**, 6893–6923 (2018).
4. Bergers, G. and S. M. Fendt, The metabolism of cancer cells during metastasis. *Nat. Rev. Cancer* **21**(3),162–180 (2021).
5. Locasale, J. W. Serine, glycine and one-carbon units: cancer metabolism in full circle. *Nat. Rev. Cancer* **13**, 572–583 (2013).
6. Locasale, J. W. et al. Phosphoglycerate dehydrogenase diverts glycolytic flux and contributes to oncogenesis. *Nat. Genet* **43**, 869–874 (2011).
7. Pollari, S. et al. Enhanced serine production by bone metastatic breast cancer cells stimulates osteoclastogenesis. *Breast Cancer Res Treat.* **125**, 421–430 (2011).
8. Possemato, R. et al. Functional genomics reveal that the serine synthesis pathway is essential in breast cancer. *Nature* **476**, 346–350 (2011).
9. Pacold, M. E. et al. A PHGDH inhibitor reveals coordination of serine synthesis and one-carbon unit fate. *Nat. Chem. Biol.* **12**, 452–458 (2016).
10. Tajan, M. et al. Serine synthesis pathway inhibition cooperates with dietary serine and glycine limitation for cancer therapy. *Nat. Commun.* **12**, 366 (2021).
11. Wang, Q. et al. Rational design of selective allosteric inhibitors of PHGDH and serine synthesis with anti-tumor activity. *Cell Chem. Biol.* **24**, 55–65 (2017).
12. Weinstabl, H. et al. Intracellular trapping of the selective phosphoglycerate dehydrogenase (PHGDH) inhibitor bi-4924 disrupts serine biosynthesis. *J. Med Chem.* **62**, 7976–7997 (2019).
13. Maddocks, O. D. K. et al. Modulating the therapeutic response of tumours to dietary serine and glycine starvation. *Nature* **544**, 372–376 (2017).
14. Ngo, B. et al. Limited environmental serine and glycine confer brain metastasis sensitivity to PHGDH inhibition. *Cancer Disco.* **10**, 1352–1373 (2020).

15. Mullarky, E. et al. Identification of a small molecule inhibitor of 3-phosphoglycerate dehydrogenase to target serine biosynthesis in cancers. *Proc. Natl Acad. Sci. USA* **113**, 1778–1783 (2016).
16. Ducker, G. S. et al. Reversal of cytosolic one-carbon flux compensates for loss of the mitochondrial folate pathway. *Cell Metab.* **24**, 640–641 (2016).
17. Lee, W. D. et al. Tumor reliance on cytosolic versus mitochondrial one-carbon flux depends on folate availability. *Cell Metab.* **33**, 190–198.e6 (2021).
18. Morscher, R. J. et al. Mitochondrial translation requires folate-dependent tRNA methylation. *Nature* **554**, 128–132 (2018).
19. Minton, D. R. et al. Serine catabolism by SHMT2 is required for proper mitochondrial translation initiation and maintenance of formylmethionyl-tRNAs. *Mol. Cell* **69**(4), 610–621.e5 (2018).
20. Zheng, Y. et al. Mitochondrial one-carbon pathway supports cytosolic folate integrity in cancer cells. *Cell* **175**(6), 1546–1560.e17 (2018).
21. Meiser, J. et al. Serine one-carbon catabolism with formate overflow. *Sci. Adv.* **2**(10), e1601273 (2016).
22. Meiser, J. et al. Increased formate overflow is a hallmark of oxidative cancer. *Nat. Commun.* **9**(1), 1368 (2018).
23. Rossi, M., et al., Heterogeneity in PHGDH protein expression potentiates cancer cell dissemination and metastasis. https://doi.org/10.1101/2021.01.24.427949 (2021).
24. Samanta, D. et al. PHGDH expression is required for mitochondrial redox homeostasis, breast cancer stem cell maintenance, and lung metastasis. *Cancer Res* **76**, 4430–4442 (2016).
25. Rinaldi, G. et al. In vivo evidence for serine biosynthesis-defined sensitivity of lung metastasis, but not of primary breast tumors, to mTORC1 inhibition. *Mol. Cell* **81**, 386–397.e7 (2021).
26. Stoller, R. G. et al. Use of plasma pharmacokinetics to predict and prevent methotrexate toxicity. *N. Engl. J. Med* **297**, 630–634 (1977).
27. Chabner, B. A. & Young, R. C. Threshold methotrexate concentration for in vivo inhibition of DNA synthesis in normal and tumorous target tissues. *J. Clin. Invest* **52**, 1804–1811 (1973).
28. Huang, S. et al. Study on relationships of tumor status and gene polymorphism with blood concentration of MTX and toxicities in 63 pediatric mature B cell lymphoma in chinese population. *Technol. Cancer Res Treat.* **20**, 1533033821995288 (2021).
29. Kawakatsu, S. et al. Population pharmacokinetic analysis of high-dose methotrexate in pediatric and adult oncology patients. *Cancer Chemother. Pharm.* **84**, 1339–1348 (2019).
30. Phillips, D. C., Woollard, K. J. & Griffiths, H. R. *T*he anti-inflammatory actions of methotrexate are critically dependent upon the production of reactive oxygen species. *Br. J. Pharm.* **138**, 501–511 (2003).
31. Soula, M. et al. Metabolic determinants of cancer cell sensitivity to canonical ferroptosis inducers. *Nat. Chem. Biol.* **16**, 1351–1360 (2020).
32. Wu, S. et al. Activation of RSK2 upregulates SOX8 to promote methotrexate resistance in gestational trophoblastic neoplasia. Lab Invest. 2021.
33. AlBasher, G. et al. Methotrexate-induced apoptosis in human ovarian adenocarcinoma SKOV-3 cells via ROS-mediated bax/bcl-2-cyt-c release cascading. *Onco Targets Ther.* **12**, 21–30 (2019).
34. Garcia-Sanchez, A., Miranda-Diaz, A. G. & Cardona-Munoz, E. G. The role of oxidative stress in physiopathology and pharmacological treatment with pro- and antioxidant properties in chronic diseases. *Oxid. Med Cell Longev.* **2020**, 2082145 (2020).
35. Babiak, R. M. et al. Methotrexate: pentose cycle and oxidative stress. *Cell Biochem Funct.* **16**, 283–293 (1998).
36. Lignitto, L. et al. Nrf2 activation promotes lung cancer metastasis by inhibiting the degradation of Bach1. *Cell* **178**, 316–329 e18 (2019).
37. Wiel, C. et al. BACH1 stabilization by antioxidants stimulates lung cancer metastasis. *Cell* **178**, 330–345 e22 (2019).
38. Benzarti, M. et al. Metabolic potential of cancer cells in context of the metastatic cascade. *Cells* **9**, 2035 (2020)
39. Nguyen, H. L. et al. Oxidative stress and prostate cancer progression are elicited by membrane-type 1 matrix metalloproteinase. *Mol. Cancer Res* **9**, 1305–1318 (2011).
40. Rhyu, D. Y. et al. Role of reactive oxygen species in TGF-beta1-induced mitogen-activated protein kinase activation and epithelial-mesenchymal transition in renal tubular epithelial cells. *J. Am. Soc. Nephrol.* **16**, 667–675 (2005).
41. Chen, D. et al. MiR-373 drives the epithelial-to-mesenchymal transition and metastasis via the miR-373-TXNIP-HIF1alpha-TWIST signaling axis in breast cancer. *Oncotarget* **6**, 32701–32712 (2015).
42. Reczek, C. R. & Chandel, N. S. ROS-dependent signal transduction. *Curr. Opin. Cell Biol.* **33**, 8–13 (2015).
43. Hunter, M. V. et al. Oxidative stress orchestrates cell polarity to promote embryonic wound healing. *Dev. Cell* **47**, 377–387 e4 (2018).
44. Porporato, P. E. et al. A mitochondrial switch promotes tumor metastasis. *Cell Rep.* **8**, 754–766 (2014).
45. Piperigkou, Z. et al. Key matrix remodeling enzymes: functions and targeting in cancer. *Cancers (Basel)*, **13**(6):1441 (2021)
46. Kawami, M. et al. Methotrexate-induced epithelial-mesenchymal transition in the alveolar epithelial cell line A549. *Lung* **194**, 923–930 (2016).
47. Ohbayashi, M. et al. Involvement of epithelial-mesenchymal transition in methotrexate-induced pulmonary fibrosis. *J. Toxicol. Sci.* **39**, 319–330 (2014).
48. Vazquez, A. et al. Catabolic efficiency of aerobic glycolysis: The Warburg effect revisited. *BMC Syst. Biol.* **4**, 58 (2010).
49. Diehl, F. F. et al. Cellular redox state constrains serine synthesis and nucleotide production to impact cell proliferation. *Nat. Metab.* **1**, 861–867 (2019).
50. Vande Voorde, J. et al. Improving the metabolic fidelity of cancer models with a physiological cell culture medium. *Sci. Adv.* **5**, eaau7314 (2019).
51. Palm, W. & Thompson, C. B. Nutrient acquisition strategies of mammalian cells. *Nature* **546**, 234–242 (2017).
52. Tibbetts, A. S. & Appling, D. R. Compartmentalization of Mammalian folate-mediated one-carbon metabolism. *Annu Rev. Nutr.* **30**, 57–81 (2010).
53. Burgos-Barragan, G. et al. Mammals divert endogenous genotoxic formaldehyde into one-carbon metabolism. *Nature* **548**, 549–554 (2017).
54. Mullen, A. R. et al. Reductive carboxylation supports growth in tumour cells with defective mitochondria. *Nature* **481**, 385–U171 (2012).
55. Metallo, C. M. et al. *Reductive glutamine metabolism by IDH1 mediates lipogenesis under hypoxia*. *Nature* **481**(7381), 380–384 (2011).
56. Piskounova, E. et al. Oxidative stress inhibits distant metastasis by human melanoma cells. *Nature* **527**, 186–191 (2015).
57. Lawrence, S. A. et al. Mammalian mitochondrial and cytosolic folylpolyglutamate synthetase maintain the subcellular compartmentalization of folates. *J. Biol. Chem.* **289**, 29386–29396 (2014).
58. Lowe, K. E. et al. Regulation of folate and one-carbon metabolism in mammalian cells. II. Effect of folylpoly-gamma-glutamate synthetase substrate specificity and level on folate metabolism and folylpoly-gamma-glutamate specificity of metabolic cycles of one-carbon metabolism. *J. Biol. Chem.* **268**, 21665–21673 (1993).
59. Horne, D. W., Holloway, R. S. & Said, H. M. Uptake of 5-formyltetrahydrofolate in isolated rat liver mitochondria is carrier-mediated. *J. Nutr.* **122**, 2204–2209 (1992).
60. den Boer, E. et al. Determinants of erythrocyte methotrexate polyglutamate levels in rheumatoid arthritis. *J. Rheumatol.* **41**, 2167–2178 (2014).
61. Zhu, T. et al. Investigation of potential drug-drug interactions between peficitinib (ASP015K) and methotrexate in patients with rheumatoid arthritis. *Clin. Drug Investig.* **40**, 827–838 (2020).
62. Soflaee, M. H. et al. Purine nucleotide depletion prompts cell migration by stimulating the serine synthesis pathway. *Nat. Commun.* https://doi.org/10.1038/s41467-022-30362-z (2022).
63. Hiller, K. et al. MetaboliteDetector: comprehensive analysis tool for targeted and nontargeted GC/MS based metabolome analysis. *Anal. Chem.* **81**, 3429–3439 (2009).
64. Dranka, B. P. et al. Assessing bioenergetic function in response to oxidative stress by metabolic profiling. *Free Radic. Biol. Med* **51**, 1621–1635 (2011).
65. Kocaturk, B. & Versteeg, H. H. Orthotopic injection of breast cancer cells into the mammary fat pad of mice to study tumor growth. *J. Vis. Exp.* 8(96), 51967 (2015).

Acknowledgements

We thank Fabien Rodriguez (Letellier lab) for technical support during the tissue analysis of the in vivo experiment. We are grateful to Lewis Cantley (Weill Cornell Medical College) for providing MDA-MB-468 cells with MTHFD1L KO[20] and to Patel's laboratory (Cambridge, UK) for providing various HAP1 KO cells[53] We thank Clément Thomas (LIH, Luxembourg) for providing 4T1 cells and Saverio Tardito (Cancer Research UK Beatson Institute, Glasgow, UK) for providing Plasmax medium.

We would like to thank: the LCSB Metabolomics Platform, especially Xiangyi Dong and Floriane Vanhalle, for providing technical and analytical support; the National Cytometry Platform (Quantitative Biology Unit, LIH) and especially Thomas Cerutti for support with flow cytometric analyses; Magretta Adiamah for her diligent proofreading of the manuscript; all our collaboration partners for fruitful discussions and constructive feedback. All graphical figures were produced with BioRender.com (Agreement Number *OJ23O9J9QD*).

J.M. is supported by the FNR-ATTRACT program (A18/BM/11809970), J.M. and L.H. are supported by the FNR-PRIDE NEXTIMMUNE (PRIDE/11012546) and J.M. and K.E. by the FNR-PRIDE i2Tron (PRIDE19/14254520) program. N.K. is supported by the LIH Career Launchpad program (Legs Baertz) and by a DFG fellowship (KI 2508/1-1). D.B. is supported by the FNR-ATTRACT program (A14/BM/7632103), the FNR-CORE program (C18/BM/12691266 and C21/BM/15796788) and the i2Tron (PRIDE19/14254520) grant. D.B. and L.S.B. are funded by the FNR-PRIDE (PRIDE/11012546/NEXTIMMUNE) scheme. E.L. is supported by the FNR-CORE program (C16/BM/11282028 and C20/BM/14591557), by a Proof of Concept FNR grant (PoC/18/12554295), a PRIDE17/11823097 and by i2Tron (PRIDE19/14254520). G.D. and F.X. are supported by FNR-

CORE (C17/BM/11642138). B.J. and M.Z.N. are supported by Luxembourg National Research Fund (C18/BM/12670304/COMBATIC) and FNRS Televie grant (7.4579.20).

Author contributions

Conceptualization, J.M., N.K.; Methodology, J.M., N.K., C.J., M.Z.N., B.J., E.L., D.B., G.D., V.I.P.; Software, A.V., F.X.; Validation, N.K., J.M., L.N., C.D., K.E., L.H.; Formal Analysis, N.K., C.D., L.N., M.B., L.S.B., F.X., V.I.P., M.S., C.J., K.E., E.K., L.H.; Investigation, N.K., C.D., L.N., M.B., L.S.B., F.X., V.I.P., M.S., E.L., K.E., L.H.; Resources, C.J., A.V., J.M., E.L.; Data Curation, N.K., J.M., F.X., A.V.; Writing – Original Draft, N.K., J.M.; Writing – Review & Editing, All Authors; Visualization, N.K., J.M., L.S.B., F.X., V.I.P.; Supervision, J.M., D.B., A.V., E.L., G.D.; Project Administration, J.M., Funding Acquisition, J.M., D.B., E.L., A.V., G.D.

Competing interests

The authors declare no competing interests.

Additional information

Supplementary information The online version contains supplementary material available at https://doi.org/10.1038/s41467-022-30363-y.

Correspondence and requests for materials should be addressed to Johannes Meiser.

Peer review information *Nature Communications* thanks the anonymous reviewer(s) for their contribution to the peer review of this work.

Reprints and permission information is available at http://www.nature.com/reprints

Publisher's note Springer Nature remains neutral with regard to jurisdictional claims in published maps and institutional affiliations.

APPENDIX 6

Research Publication

(Co-author)

YANG, W., DENGER, A., DIENER, C., KÜPPERS, F., SORIANO-BAGUET, L., SCHÄFER, G., YANAMANDRA, A.K., ZHAO, R., KNÖRCK, A., SCHWARZ, E.C., HART, M., LAMMERT, F., ROMA, L.P., BRENNER, D., CHRISTIDIS, G., HELMS, V., MEESE, E., HOTH, M., QU, B., 2022. **Unspecific CTL Killing Is Enhanced by High Glucose via TNF-Related Apoptosis-Inducing Ligand.** *Front. Immunol.* 13, 831680.

frontiers in Immunology

ORIGINAL RESEARCH
published: 21 February 2022
doi: 10.3389/fimmu.2022.831680

Unspecific CTL Killing Is Enhanced by High Glucose *via* TNF-Related Apoptosis-Inducing Ligand

*Wenjuan Yang[1], Andreas Denger[2], Caroline Diener[3], Frederic Küppers[4], Leticia Soriano-Baguet[5,6,7], Gertrud Schäfer[1], Archana K. Yanamandra[1,8], Renping Zhao[1], Arne Knörck[1], Eva C. Schwarz[1], Martin Hart[3], Frank Lammert[4,9], Leticia Prates Roma[1], Dirk Brenner[5,6,10], Grigorios Christidis[4], Volkhard Helms[2], Eckart Meese[3], Markus Hoth[1] and Bin Qu[1,8]**

[1] Biophysics, Center for Integrative Physiology and Molecular Medicine (CIPMM), School of Medicine, Saarland University, Homburg, Germany, [2] Center for Bioinformatics, Saarland University, Saarbrücken, Germany, [3] Institute of Human Genetics, School of Medicine, Saarland University, Homburg, Germany, [4] Internal Medicine II, University Hospital Saarland, Homburg, Germany, [5] Experimental and Molecular Immunology, Department of Infection and Immunity, Luxembourg Institute of Health, Esch-sur-Alzette, Luxembourg, [6] Immunology and Genetics, Luxembourg Centre for Systems Biomedicine (LCSB), University of Luxembourg, Belvaux, Luxembourg, [7] Faculty of Science, Technology and Medicine, University of Luxembourg, Esch-sur-Alzette, Luxembourg, [8] INM-Leibniz Institute for New Materials, Saarbrücken, Germany, [9] Hannover Medical School (MHH), Hannover, Germany, [10] Odense Research Center for Anaphylaxis, Department of Dermatology and Allergy Center, Odense University Hospital University of Southern Denmark, Odense, Denmark

OPEN ACCESS

Edited by:
Hu Zeng,
Mayo Clinic, United States

Reviewed by:
Xingrong Du,
Fudan University, China
Katayoun Ayasoufi,
Mayo Clinic, United States

***Correspondence:**
Bin Qu
bin.qu@uks.eu

Specialty section:
This article was submitted to T Cell Biology, a section of the journal Frontiers in Immunology

Received: *08 December 2021*
Accepted: *24 January 2022*
Published: *21 February 2022*

Citation:
Yang W, Denger A, Diener C, Küppers F, Soriano-Baguet L, Schäfer G, Yanamandra AK, Zhao R, Knörck A, Schwarz EC, Hart M, Lammert F, Roma LP, Brenner D, Christidis G, Helms V, Meese E, Hoth M and Qu B (2022) Unspecific CTL Killing Is Enhanced by High Glucose via TNF-Related Apoptosis-Inducing Ligand. Front. Immunol. 13:831680. doi: 10.3389/fimmu.2022.831680

TNF-related apoptosis inducing ligand (TRAIL) is expressed on cytotoxic T lymphocytes (CTLs) and TRAIL is linked to progression of diabetes. However, the impact of high glucose on TRAIL expression and its related killing function in CTLs still remains largely elusive. Here, we report that TRAIL is substantially up-regulated in CTLs in environments with high glucose (HG) both *in vitro* and *in vivo*. Non-mitochondrial reactive oxygen species, NFκB and PI3K/Akt are essential in HG-induced TRAIL upregulation in CTLs. $TRAIL^{high}$ CTLs induce apoptosis of pancreatic beta cell line 1.4E7. Treatment with metformin and vitamin D reduces HG-enhanced expression of TRAIL in CTLs and coherently protects 1.4E7 cells from TRAIL-mediated apoptosis. Our work suggests that HG-induced $TRAIL^{high}$ CTLs might contribute to the destruction of pancreatic beta cells in a hyperglycemia condition.

Keywords: High glucose, CTLs, TRAIL, ROS, PI3K-Akt, NFκB

INTRODUCTION

An elevated level of blood glucose is a typical symptom for diabetes, a metabolic disease. Diabetes affects 422 million people globally and has become the seventh leading cause of death worldwide (1). Diabetes is mainly categorized into two groups, type 1 diabetes and type 2 diabetes. Type 1 diabetes has been identified as an autoimmune disease, for which Cytotoxic T lymphocytes (CTLs) play an important role in destroying the insulin-producing pancreatic beta-cells in an antigen specific manner (2). For type 2 diabetes, CTLs, along with other factors, are reported to be associated with its initiation and progression (3).

CTLs are the key players in the adaptive immune system to destroy pathogen-infected or tumorigenic cells (4). Usually, CTLs employ two major killing mechanisms: lytic granules (LGs) and

the Fas/Fas ligand (FasL) pathway. LGs contain cytotoxic proteins, such as the pore-forming protein perforin and the serine proteases termed granzymes. Upon target recognition, LGs are reoriented towards the CTL-target contact site, termed the immunological synapse (IS), and their cytotoxic content will be specifically released into the cleft, resulting in direct lysis or apoptosis of target cells (5). FasL, a member of tumor necrosis factor (TNF) family, is expressed on the surface of CTLs. Engagement of FasL with its Fas receptor, which spans on the target cell surface, initiates apoptotic cascades in target cells (5, 6). Emerging evidence shows that the effector functions of CTLs are highly dependent on their metabolic status (7). Glucose metabolism and the proper access to glucose are essential to maintain CTL effector functions, especially their killing function (8). It is reported that with excessive glucose, calcium influx elicited upon conjugation with target cells is reduced (9) and CTL killing efficiency is elevated partially regulated by Ca^{2+} without affecting lytic granule pathway and FasL expression (10).

TNF-related apoptosis-inducing ligand (TRAIL), similar as FasL, also belongs to the TNF super family. A rich body of studies suggests that TRAIL and/or TRAIL receptors are correlated with progression of diabetes and diabetes-related complications (11, 12). Interestingly, TRAIL is expressed in CTLs (13) to clear viral-infected cells and down-size the effector population to terminate immune responses in an antigen-independent manner (14). TRAIL and TRAIL receptors are linked to both type 1 and type 2 diabetes (15, 16). In humans, four TRAIL receptors are expressed, TRAIL-R1, -R2, -R3 and -R4 (17). The former two (TRAIL-R1 and -R2) are activating receptors, which contain functional death domains to trigger the caspase-8-dependent apoptotic pathway. TRAIL-R3 and -R4 function as decoy receptors, lacking the capability to initiate the death signaling pathway. TRAIL-R1 and/or -R2 are expressed in many normal tissues including pancreas and especially pancreatic beta cells (18, 19).

In this work, we show that TRAIL is substantially up-regulated in high glucose-cultured CTLs and in CTLs from diabetic patients or diabetic mouse models. This high glucose-enhanced TRAIL expression could be diminished by removal of reactive oxygen species (ROS), blockade of NFκB or PI3K/Akt. Pancreatic beta-cells can be killed by $TRAIL^{high}$ CTLs in a TRAIL-dependent manner. Furthermore, we found that treatment of two drugs, metformin and vitamin D, could individually or additively abolish the enhanced TRAIL expression induced by high glucose in CTLs to protect pancreatic beta cells from TRAIL-mediated apoptosis.

MATERIALS AND METHODS

Antibodies and Reagents

All chemicals are from Sigma-Aldrich (highest grade) if not mentioned otherwise. The following antibodies and reagents were purchased from Biolegend: APC/Cy7 anti-human CD3 antibody, BV421 anti-human CD3 antibody, BV421 anti-human CD8 antibody, APC anti-human CD253 (TRAIL) antibody, APC anti-mouse CD253 (TRAIL) Antibody, BV421 anti-mouse CD8a Antibody, PE anti-mouse CD3 Antibody, PerCP anti-human CD25 antibody, APC anti-human CD62L antibody, APC anti-human CD262 (TRAIL-R2), and 7-AAD viability staining solution. The following antibodies were also used: FITC anti-human CD69 (eBiosciences), FITC anti-human CD44 (DAKO), Purified NA/LE mouse anti-human CD253 (BD Biosciences), BV421 mouse anti-human CD263 (TRAIL-R3) (BD Biosciences), Alexa647 mouse anti-human GLUT1 (BD Biosciences), human TRAIL R1/TNFRSF 10A PerCP-conjugated antibody (R&D Systems), and human TRAIL R4/TNFRSF 10D PE-conjugated antibody (R&D Systems). In addition, the following reagents were used: NucView Caspase-3 enzyme substrates (Biotium), Idelalisib (Selleckchem), MK-2206 (Selleckchem), Rapamycin (Selleckchem), Caffeic acid phenethyl ester (CAPE) (R&D Systems), Mitoquinone (MitoQ) (Biotrend), N-acetyl-L-cysteine (NAC) (Merck), vitamin 1,25D3 (Merck), Calcipotriol (TOCRIS), DMSO (Merck), Cellular ROS Assay Kit (Abcam), metformin hydrochloride (Merck), H_2O_2 (Merck), and Streptozotocin (Merck).

Cell Culture

Peripheral blood mononuclear cells (PBMCs) were obtained from healthy donors as described elsewhere (20). Primary human $CD8^+$ T cells were negatively isolated from PBMCs using Human $CD8^+$ T Cell isolation Kits (Miltenyi Biotec). Human $CD8^+$ T cells were stimulated with CD3/CD28 activator beads (Thermo Fisher Scientific) and cultured in DMEM medium (Thermo Fisher Scientific) containing normal (5.6 mM) or high glucose (25 mM) for up to three days if not otherwise mentioned. Levels of glucose in medium was examined every day using "Contour Next Sensoren" test strips (SMS Medipool) and consumed glucose was compensated accordingly. If CTLs were cultured longer than three days, human recombinant IL-2 (Miltenyi Biotec) was added to the medium every two days from day 2 on (100 U/ml). All cells were cultured at 37°C with 5% CO_2. Human pancreatic beta cell line 1.4E7 was purchased from Merck and cultured in RPMI-1640 medium (Thermo Fisher Scientific) supplemented with 2 mM glutamine, 1% Penicillin-Streptomycin plus 10% FCS (ThermoFisher Scientific).

Flow Cytometry Analysis

For cell surface staining, cells were washed twice with PBS/0.5% BSA and stained for 30 minutes at 4°C in dark using corresponding antibodies mentioned in the figure legends. For intracellular staining, cells were fixed in pre-chilled 4% PFA and permeabilized with 0.1% saponin in PBS containing 5% FCS and 0.5% BSA, followed by the immunostaining as described above. Flow cytometry data were acquired using a FACSVerse flow cytometer (BD Biosciences) and were analyzed with FlowJo v10 (FLOWOJO, LLC).

Assays for Apoptosis and Viability

To assess cell apoptosis, 1.4E7 cell were co-cultured with primary human $CD8^+$ T cells and incubated at 37°C with 5% CO_2. Cells were harvested at various time points as indicated in the text and stained with BV421-CD3, and then incubated with NucView Caspase-3 Substrates at room temperature for 30 minutes,

followed with analysis using flow cytometry. To determine the viability of CTLs, cells were stained with 7-AAD.

Diabetic Mouse Model

C57BL/6N mice were injected with streptozotocin intraperitoneally for five days consecutively (50 mg/kg per day) and were sacrificed at day 21. Blood samples were taken from the tail vein and glucose level was tested by standard test strips every day after injection. Mice with blood glucose level more than 250 mg/dL one week after the first injection were considered as diabetic.

Microarray and Analysis

For transcriptome analyses, total RNA of $CD8^+$ human T cells was extracted by miRNeasy Mini Kit (Qiagen), following the manufacturers' instructions, and quantified using NanoDrop 2000c Spectrophotometer (Thermo Fisher Scientific). The quality of the RNA samples was assessed by determining the corresponding RIN (RNA integrity number) values. For this purpose, an Agilent 2100 Bioanalyzer instrument was used together with the RNA 6000 Nano assay from Agilent Technologies (Santa Clara). An excellent quality of the analyzed total RNA was verified by RIN values of 10 for all samples. To determine the cellular transcriptomes, 100 ng of the total RNA was analysed by microarray. The microarray analyses were performed as previously described (21). Differential expression analysis of the Agilent microarray data was performed with the Linear Models for Microarray Data (limma) R package (22). First, samples were corrected for background (NormExp) and quantile normalized, respectively. Control probes used for background correction, probes without associated gene symbols, and genes classified as not expressed in at least 6 out of 12 arrays by the Agilent feature extraction software were removed from the dataset. After the filtering step, the dataset contained a total of 29,037 transcripts, corresponding to 19,834 genes. For differential expression analysis, a linear model was fitted to each individual sample. Then, a linear model was calculated between samples in high glucose (HG) or normal glucose (NG) conditions. Differentially expressed genes were identified with a t-test. The associated p-values were calculated for each gene with an empirical Bayes method and adjusted for multiple testing with the Benjamini-Hochberg method (23). A gene was classified as differentially expressed (DE) for a given contrast if its adjusted p-value was below 0.05. Among the DE genes, an enrichment analysis for gene annotations was performed with the limma package. Also, an enrichment analysis based on protein interaction subnetworks was carried out by the pathfindR package (24).

Seahorse Assay

Primary human $CD8^+$ T cells were stimulated either in normal (5.6 mM) or high glucose (25 mM) for three days. At day 3, CTLs were counted and seeded in 96-well XF Cell Culture Microplate in XF Seahorse DMEM medium at a cell concentration of 3×10^5 cells/well. Following the manufacturer's instructions (Agilent), the extracellular acidification rate (ECAR) and oxygen consumption rate (OCR) were measured using the XF Glycolytic Stress Test and XF Cell Mitochondrial Stress Test kits, respectively.

Patient Materials

Blood samples were collected from patients with diabetes type 1 and 2 (using the current diagnostic criteria from the American Diabetes Association-ADA) and healthy control subjects (all with normal glycated haemoglobin level (HbA1c < 5,7%) at the day of the blood sample collection). Both patients and healthy controls were recruited in the Department of Internal Medicine II in the Saarland University Medical Center, Homburg, Saarland, Germany. Written informed consent was obtained from all subjects before blood sampling, strictly following the procedure described in the ethical approval of the ethic committee of the medical association of Saarland (Ethic Vote Nr: Ha 84/19). PBMCs were obtained from the blood samples and were stimulated with CD3/CD28 activator beads (Thermo Fisher Scientific) and cultured in DMEM containing normal (5.6 mM) or high glucose (25 mM) for three days, supplemented with recombinant IL-2 (100 U/ml, Miltenyi).

Intracellular ROS Detection

Cellular ROS Assay Kit (Abcam) was used to determine intracellular ROS. Briefly, at 6 hours after activation of CD3/CD28 activator beads, the CTLs were stained with BV421-CD8 for 30 minutes at 4°C in dark, and then incubated with dichlorofluorescein diacetate (DCFDA, 20 μM) at 37°C for 30 minutes, followed by analysis using flow cytometry.

Quantitative RT-PCR

The mRNA expression analysis was carried out as described before (25). Briefly, total RNA was isolated from CTLs using TRIzol reagent (ThermoFisher Scientific). Then the isolated RNA was reversely transcribed into complementary DNA (cDNA) and relative gene expression was performed by qRT-PCR using CFX96Real-TimeSystemC1000 Thermal Cycler (Bio-Rad Laboratories). TATA box-binding protein (TBP) was used as the housekeeping gene for the normalization of the target genes. Primer sequences are as follows (forward/reverse): TBP (5'-CGGAGAGTTCTGGGATTGT-3'/5'-GGTTCGTGGCT CTCTTATC-3'). Pre-designed primers were purchased for TRAIL (QT00068957) and Glut1 (QT00079212).

Statistical Analysis

Data are presented as mean ± SD. GraphPad Prism Software (San Diego, CA, USA) was used for statistical analysis. The differences between two groups were analyzed by the Student's t-test. For multiple comparisons, two-way ANOVA or one-way ANOVA was performed followed by Bonferroni test.

RESULTS

Expression of TRAIL Is Up-Regulated in CTLs by High Glucose and $TRAIL^{high}$ CTLs Induces Destruction of Pancreatic Beta Cells

Our previous work shows that culturing CTLs in high glucose-containing medium does not alter their expression of perforin, granzymes, FasL, and degranulation (10). Thus, in this study we

analyzed the impact of high glucose on expression of TRAIL in CTLs. We used negatively isolated primary human $CD8^+$ T cells from healthy donors and stimulated the cells with CD3/CD28 antibody-coated beads in presence of normal (5.6 mM, NG) or high glucose (25 mM, HG) for three days (hereafter referred to as NG or HG-CTLs). At mRNA level, TRAIL was substantially up-regulated in HG-CTLs compared to NG-CTLs (**Figure 1A**). Concomitantly, at protein level, not only the total expression of TRAIL was considerably enhanced (**Figure 1B**), but also the expression of TRAIL on the surface was significantly elevated in HG-CTLs compared to NG-CTLs (**Figures 1C, D**). To test the *in vivo* relevance of this finding, we used a streptozotocin-induced diabetic mouse model. Compared to CTLs from the control group, CTLs from diabetic mice exhibited significantly elevated levels of TRAIL (**Figure 1E**). The level of blood glucose was positively correlated with expression of TRAIL (**Figure 1F**). Furthermore, we examined TRAIL expression in freshly isolated $CD8^+$ T cells from diabetic patients, which was also positively correlated with the level of blood glucose (**Figure 1G**). These findings suggest that TRAIL expression in CTLs is up-regulated by HG and that glucose levels correlate with TRAIL expression *in vivo* in the context of diabetes.

Given the fact that treatment of soluble TRAIL can induce apoptosis of human pancreatic beta cells (19), we then examined whether CTLs expressing TRAIL could have a similar effect. We used the human pancreatic beta cell line 1.4E7, which is a hybrid cell line derived from electrofusion of primary human pancreatic islets with a human pancreatic ductal carcinoma cell line PANC-1. We incubated 1.4E7 cells with CTLs and used activity of caspase-3 in 1.4E7 cells as a readout for CTL-induced apoptosis. The results show that HG-cultured CTLs exhibited significantly higher killing capacity compared to their counterparts in NG (**Figures 2A–D** and **Figures S1A, B**). Of note, apoptosis of beta cells is positively correlated with TRAIL expression (**Figures 2E, F** and **Figure S1C**). To test a potential causal relation between TRAIL expression and CTL cytotoxicity against beta cells, we blocked TRAIL function with its neutralizing antibody. The analysis of caspase-3 activity shows that TRAIL blockade diminished CTL-mediated killing against 1.4E7 beta cells to a large extent for HG-CTLs (**Figures 2G, H**). Next, we examined the expression of TRAIL receptors on 1.4E7 cell surface. We found that out of four TRAIL receptors, TRAIL-R2 was predominantly expressed (**Figure S1D**), which likely mediates $TRAIL^{high}$ CTL-induced apoptosis of 1.4E7 cells. Taken together, our results indicate that

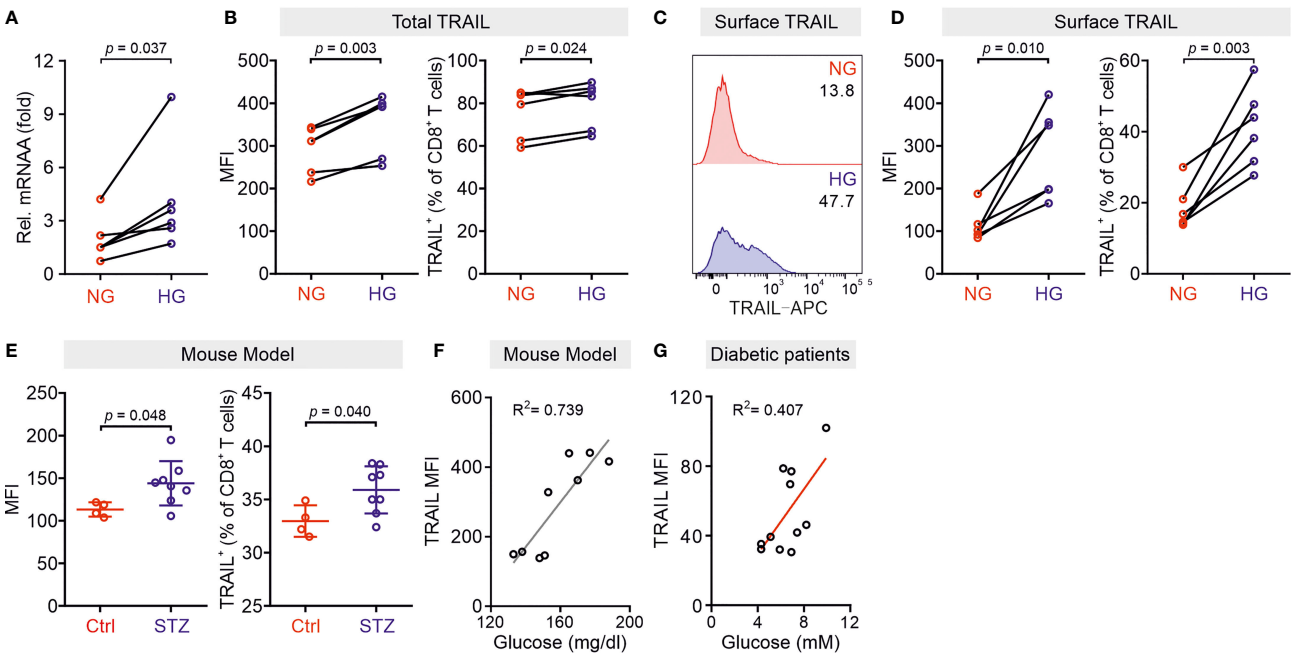

FIGURE 1 | TRAIL is up-regulated in CTLs in environments with high glucose. Primary human $CD8^+$ T cells were stimulated with CD3/CD28 beads for 3 days in NG (5.6 mM) or HG (25 mM) medium. **(A)** Relative mRNA expression levels of TRAIL in CTLs were quantified by qRT-PCR (n = 6 donors from three independent experiments). **(B–D)** Expression of TRAIL in CTLs was detected by flow cytometry. CTLs were stained with the antibodies against CD8 and TRAIL following permeabilization **(B)** or without permeabilization **(C, D)** for total or surface protein level of TRAIL (n = 6 donors from three independent experiments). **(E, F)** TRAIL is up-regulated in diabetic mice. Mouse splenocytes were isolated and stained with PE-mCD3, BV421-mCD8, and APC-mTRAIL for analysis using flow cytometry (Ctrl = 4, STZ mice = 8). Data are represented as Mean ± SD. Correlation of TRAIL expression in $CD8^+$ T cells and blood glucose is shown in **(F, G)** Positive correlation of TRAIL expression in freshly isolated $CD8^+$ T cells from 11 diabetic patients with the blood glucose levels from ten independent experiments. MFI, mean fluorescent intensity. Data were analyzed by two-tailed paired Student's *t* test **(A, B, D)**, two-tailed unpaired Student's *t* test **(E)**, trendline analysis **(F)**, or Pearson's correlation coefficient analysis **(G)**. Connected lines are the data from the same donor.

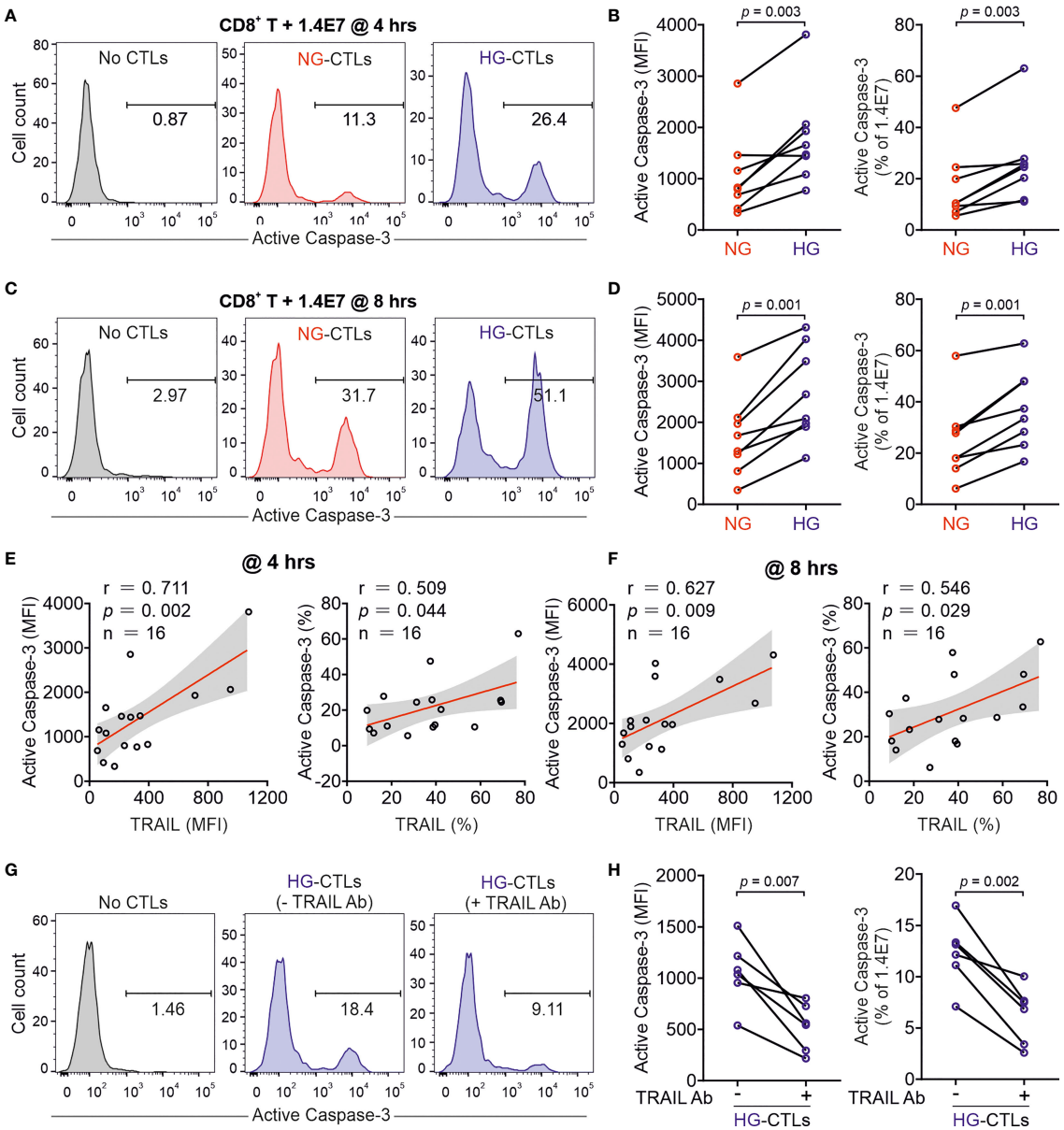

FIGURE 2 | Up-regulation of TRAIL in HG-CTLs enhances apoptosis of pancreatic beta cells. Primary human CD8$^+$ T cells were stimulated with CD3/CD28 beads for 3 days in NG (5.6 mM) or HG (25 mM) medium. **(A–D)** Apoptosis of pancreatic beta cells induced by CTLs were measured by staining active Caspase-3 using flow cytometry. Human pancreatic beta cells 1.4E7 were incubated with CTLs with an effector to target (E:T) ratio of 20:1 for 4 hours **(A, B)** or 8 hours **(C, D)** (n = 8 donors from five independent experiments). One representative donor out of eight is shown in **(A, C)** respectively. **(E, F)** Correlation of expression of TRAIL in CD8$^+$ T cells with apoptosis of 1.4E7 cells (Caspase-3 activity) (n = 16 donors from five independent experiments). **(G, H)** CD8$^+$ T cells-induced beta cell apoptosis is TRAIL dependent. Caspase-3 activity was analyzed in co-culture of 1.4E7 cells and CTLs in the presence or absence of anti-human TRAIL antibody (50 μg/ml) for 4 hours. One representative donor is shown in **(G)** and the quantification is shown in **(H)** (n = 6 donors from two independent experiments). MFI, mean fluorescent intensity. Data were analyzed by two-tailed paired Student's *t* test **(B, D, H)** or Pearson's correlation coefficients **(E, F)**. Connected lines are the data from the same donor.

HG-CTLs are able to destroy TRAIL-R2^{high} pancreatic beta cells in a TRAIL-mediated manner.

Glucose Metabolic Processes in CTLs Are Enhanced by High Glucose

Glucose metabolism encompasses the intracellular biochemical processes to breakdown and utilize glucose to generate energy, including oxidative phosphorylation and glycolysis. Using the Seahorse assay, we evaluated the oxygen consumption rate (OCR) and the extracellular acidification rate (ECAR). We found that HG-cultured CTLs exhibited significantly elevated OCR and ECAR compared to their counterparts cultured in NG (**Figures 3A–D**).

Given the essential role of mTOR in regulating glycolysis in T cells (26), we next examined the possible involvement of mTOR

in HG-induced metabolic reprogramming in CTLs. To our surprise, no difference was identified between NG- and HG-CTLs regarding mTOR activation (**Figure S2A**). Since glucose uptake and transport play an essential role for overall glucose metabolism, we examined the expression of glucose transporter 1 (Glut1) and found that although its expression was down-regulated at mRNA level in HG-CTLs (**Figure S2B**), at the protein level it remained unchanged (**Figures S2C, D**). In addition, the fraction of Glut1 transported to the plasma membrane was also not altered by HG (**Figures S2E, F**). Together, our results suggest that neither mTOR nor glucose transport are likely to be responsible for HG-reprogrammed glucose metabolic processes in CTLs.

To gain deeper insights into the genes affected by HG for glucose metabolic reprogramming, we compared transcriptomes of NG-CTLs and HG-CTLs (**Figure 3E** and **Table S1**). First, we examined the expression of all glucose transporters. We found that three glucose transporters (Glut1/SLC2A1, Glut3/SLC2A3, and Glut14/SLC2A14) were predominantly expressed in CTLs, and moderate downregulation in Glut1 was observed in HG-CTLs compared to their NG counterparts (**Figure 3F**), which is in a good agreement with our data from quantitative PCR (**Figure S2B**). No further difference in expression of glucose transporters was identified between NG- and HG-CTLs (**Figure 3F**), further supporting our conclusion that glucose transport is unlikely to be responsible for HG-reprogrammed metabolic processes in CTLs. With regards to enriched GO terms, the most significant change happened in the cellular metabolism. When comparing HG- to NG-CTL samples, many genes involved in metabolic processes are significantly changed with a total of 58 being significantly up-regulated and 47 genes being significantly down-regulated (**Table S2**, Row 2), which are associated with a total of 265 GO annotations describing various metabolic processes (**Table S2**). Furthermore, 6 genes annotated with the metabolism of ROS were significantly deregulated (**Table S3**).

We then examined whether ROS was involved in HG-enhanced TRAIL expression. We first determined ROS production in CTLs using DCFDA, a fluorescent probe used to detect ROS in living cells (27). We found that upon activation, ROS produced in HG-CTLs was higher than that in their NG counterparts (**Figures 3G, H**). To explore whether ROS is involved in HG-enhanced TRAIL expression, we first added H_2O_2, a relatively stable form of ROS, during NG- and HG-culture. We found that in NG condition, compared to the control group, with 1 μM H_2O_2, the fraction of TRAIL$^+$ CTLs was enhanced (p=0.031) and the mean of MFI is also higher but statistically not significant (p=0.218); with 3 μM H_2O_2, both the fraction of TRAIL$^+$ CTLs and MFI were enhanced (p=0.001/0.012); whereas with 10 μM H_2O_2, the mean of the fraction of TRAIL$^+$ CTLs and MFI were enhanced but statistically not significant (p=0.176/0.331) (**Figures 3I, J**). While in HG-CTLs, neither MFI nor the fraction of TRAIL$^+$ CTLs were altered by addition of H_2O_2 (**Figures 3I, J**). This implies that the elevation in TRAIL expression by HG is likely *via* enhanced ROS in HG-CTLs. To test this hypothesis, we used ROS scavengers either with a general inhibition effect [N-acetyl-L-cysteine (NAC)] or specifically targeted to mitochondrial ROS (MitoQ). We found that when ROS production in cytosol was removed by NAC, the expression of TRAIL was drastically decreased in HG-CTLs to a comparable level as in NG-CTLs (**Figures 3K, L**). In contrast, removal of mitochondria-produced ROS by MitoQ in HG-CTLs did not significantly alter TRAIL expression (**Figures 3M, N**). Thus, our results suggest that in CTLs, ROS, especially cytosolic ROS, plays a key role in HG-enhanced TRAIL expression.

HG-Enhanced TRAIL Expression on CTLs Is Regulated by PI3K/Akt and NFκB

We then analyzed KEGG pathways based on the transcriptomics data (**Figure 4A**). This analysis also revealed a statistically significant up-regulation of 11 genes including TRAIL (synonym name TNFSF10) annotated with the KEGG pathway *apoptosis* in HG samples (**Table S4**). Among the top 10 GO terms affected by HG, TRAIL is linked both to "positive regulation of IκB kinase/NFκB signaling" and to "positive regulation of apoptotic process" (**Figure 4B**).

We then focused on the involvement of NFκB in HG-enhanced TRAIL expression and tested the effect of the NFκB specific inhibitor CAPE. Notably, the expression of TRAIL on HG-cultured CTLs treated with CAPE was substantially reduced compared to untreated control cells (**Figures 4C, D**). This indicates that NFκB is indispensable for expression of TRAIL in CTLs. NFκB function can be regulated by the PI3K-Akt pathway, which was among the deregulated KEGG pathways (**Figure 4A**). We therefore used the PI3Kδ inhibitor idelalisib to block the activity of PI3K. We found that in HG-CTLs, abruption of PI3K function with the corresponding inhibitor reduced the expression of TRAIL to the level of NG (**Figures 4E, F**). We further examined Akt, a molecule downstream of PI3K and upstream of NFκB. We found that disruption of Akt function by MK-2206 abolished HG-enhanced TRAIL expression (**Figures 4G, H**). Apart from NFκB, mTOR is also regulated by Akt (28). To examine whether mTOR is involved in HG-enhanced TRAIL expression, we used rapamycin, a specific inhibitor for mTOR, to functionally block mTOR activity. We found that in HG-CTLs even with the highest concentration (600 nM) of rapamycin, the change in TRAIL expression was not statistically significant, and the fraction of TRAIL$^+$ CTLs in rapamycin-treated HG-CTLs remained significantly higher than the level in NG-CTLs (**Figures 4I, J**). Taken together, these findings suggest that NFκB and PI3K/Akt play essential roles in enhancement of TRAIL expression in CTLs by HG.

Metformin and Vitamin D Protect Pancreatic Beta Cells From HG-CTL-Mediated Apoptosis

Since the enhancement of TRAIL levels on CTLs induced by HG leads to apoptosis of pancreatic beta cells as shown above (**Figure 2**), a decrease of TRAIL expression to normal levels should protect beta cells. We sought for possible therapeutical approaches to achieve this purpose. We first examined metformin, which is a widely applied first-line medication to

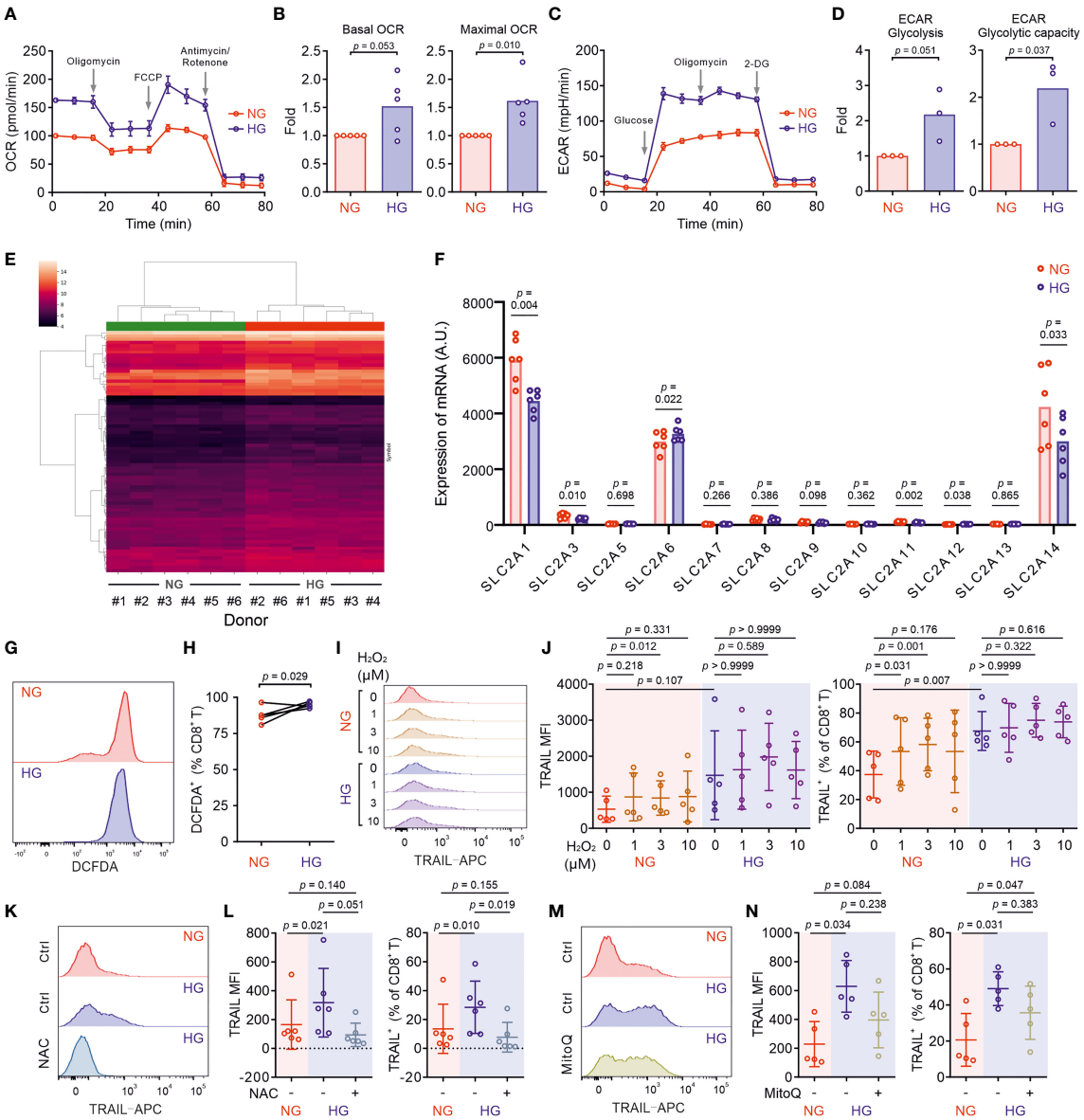

FIGURE 3 | Metabolic processes in CTLs are reprogrammed by high glucose. Primary human $CD8^+$ T cells were stimulated with CD3/CD28 beads for 3 days in NG (5.6 mM) or HG (25 mM) medium. **(A–D)** Oxidative phosphorylation (n = 5 donors) and glycolysis (n = 3 donors) of CTLs from two independent experiments were determined with seahorse assay. One representative donor for oxidative phosphorylation and glycolysis is shown in **(A, C)**, respectively. **(E)** Heatmap of log2-transformed gene expression data. The microarray data was normalized using quantile normalization. Duplicate probes for genes were aggregated by taking the median intensity. Genes were filtered for those with an absolute fold change > 1.5, and a Benjamini-Hochberg adjusted *p*-value < 0.05. **(F)** Expression of glucose transporters at mRNA level from the transcriptomics data (**Table S1**) of 6 donors collected from five independent stimulations and two independent microarray analyses. A.U. stands for arbitrary units. **(G, H)** ROS production in $CD8^+$ T cells was determined at 6 hours after CD3/CD28 bead stimulation by DCFDA (n = 5 donors from three independent experiments). One representative donor is shown in **(G)** Connected lines in **(H)** are the data from the same donor. **(I, J)** H_2O_2 enhances TRAIL expression in CTLs in NG. $CD8^+$ T cells were stimulated with CD3/CD28 beads in presence or absence of H_2O_2 for 3 days (n = 5 from three independent experiments). One representative donor is shown in **(I, K–N)** Inhibition of ROS production abolishes HG-enhanced TRAIL expression in CTLs. NAC (**K**, **L**, 10 mM, n = 6 donors) or MitoQ (**M, N**, 0.4 μM, n = 5 donors) from three independent experiments was added during the activation for 3 days. One representative donor for NAC and MitoQ is shown in **(K, M)**, respectively. Results are represented as Mean ± SD. Data were analyzed by two-tailed unpaired Student's *t* test **(B, D)**, two-tailed paired Student's *t* test **(H)** or one-way ANOVA with Bonferroni's multiple comparison test **(J, L, N)**.

treat type 2 diabetes. We stimulated primary human CD8$^+$ T cells from healthy donors in medium containing NG or HG in presence or absence of metformin for three days. We found that TRAIL expression in HG-CTLs was significantly reduced by metformin in a dose-dependent manner (**Figures 5A, B**), down to the level of NG-CTLs at 1 mM (compare NG/vehicle and HG/Met 1 mM). These results suggest a putative protective role of metformin on TRAIL-mediated apoptosis of pancreatic beta cells.

Apart from metformin, vitamin D has been also linked to diabetes (29, 30), glucose metabolism (31, 32), protection of pancreatic beta cells (33), as well as HG-regulated cell functions (34). Therefore, we used 1,25-dihydroxy-vitamin D3 (1,25D3), the active form of vitamin D, and analyzed its impact on TRAIL expression. We found that HG-induced enhancement of TRAIL expression on CTLs was reduced by 1,25D3 in a dose-dependent manner (**Figures 5C, D**). Beside the naturally existing active form 1,25D3, the vitamin D analogue calcipotriol is widely used topically to treat psoriasis. Our results show that nanomolar concentrations of calcipotriol were sufficient to abolish HG-induced enhancement in TRAIL expression (**Figures 5E, F**). Our data suggest that activation of the vitamin D pathway can diminish HG-enhanced TRAIL expression on CTLs.

Since both metformin and vitamin D down-regulate HG-enhanced TRAIL expression, we tested whether they may

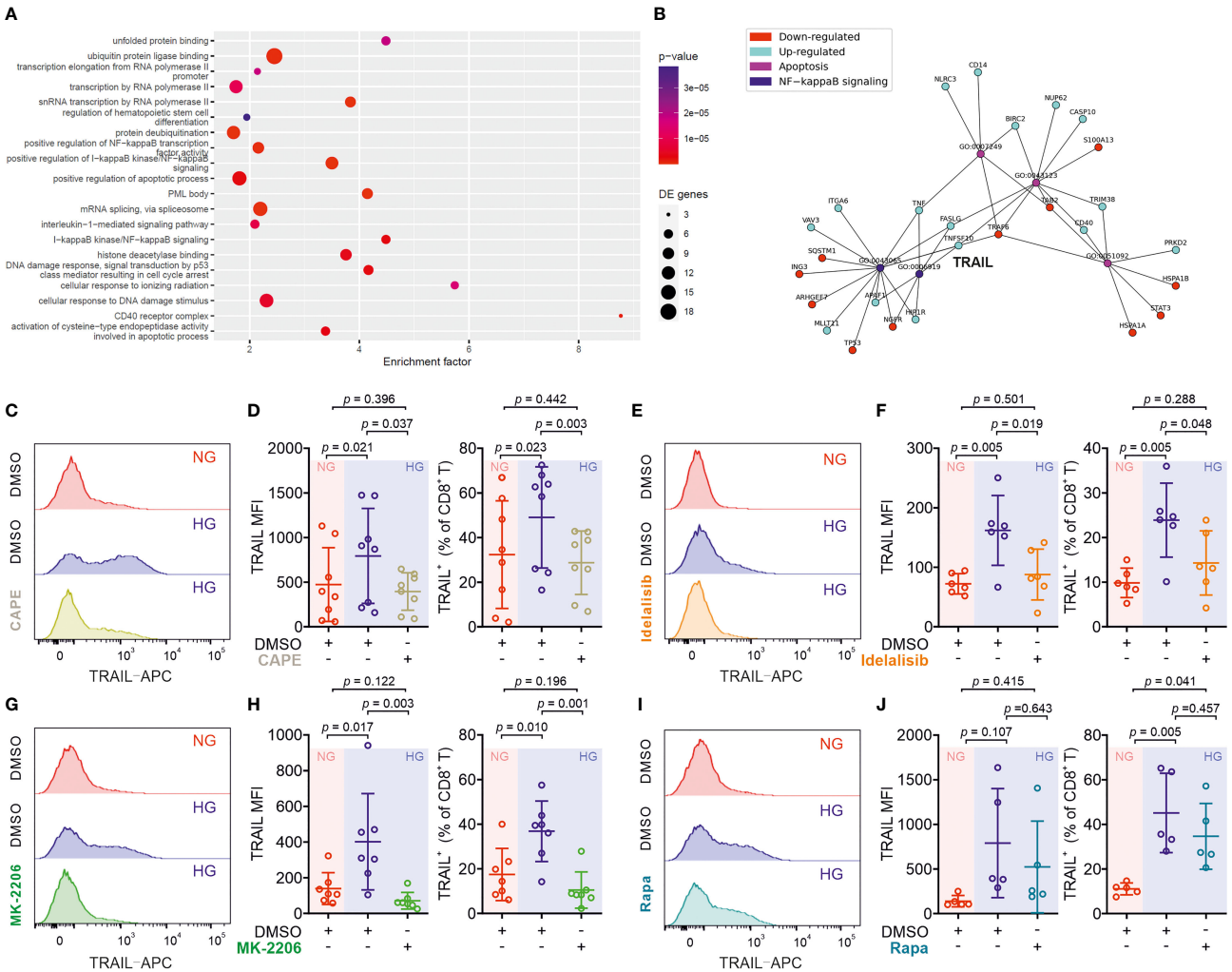

FIGURE 4 | Up-regulation of TRAIL in CTLs is regulated by the PI3K/Akt/NFκB axis. **(A)** Enriched KEGG pathways for the comparison between HG and NG conditions. **(B)** Ten most significantly enriched/depleted Gene ontology terms in HG vs NG conditions. Enrichment analysis was performed with the *pathfindR* package, which creates a sub-network of the human protein-protein interaction network that only contains genes with significant differential expression. The enrichment factor of an annotation is calculated as the fraction of proteins having this annotation in the sub-network, relative to the entire network. **(C–J)** Primary human CD8$^+$ T cells were stimulated with CD3/CD28 beads for 3 days in presence or absence of NF-κB specific inhibitor CAPE (**C, D**, 5 µM, n = 8 donors from three independent experiments), PI3K inhibitor Idelalisib (**E**, **F**, 300 nM, n = 6 donors from three independent experiments), Akt inhibitor MK-2206 (**G, H**, 200 nM, n = 7 donors from four independent experiments), or mTOR inhibitor Rapamycin (**I, J,** 600 nM, n = 5 donors from three independent experiments). CD8$^+$ T cells were stained with antibody against CD8 and TRAIL and were analyzed by flow cytometry. Representative donors are shown in **(C, E, G, I)**. Data are represented as Mean ± SD and *p* values were assessed by one-way ANOVA with Bonferroni's multiple comparison test.

function in a synergistic manner. We chose intermediate concentrations for metformin (0.3 mM) and 1,25D3 (4 μM), at which the down-regulation of TRAIL was modest in both cases (**Figures 5B, D**). Under this condition, we observed that metformin and 1,25D3 together further down-regulated TRAIL expression enhanced by HG (**Figures 5G, H**). Importantly, treatment with metformin or 1,25D3 did not affect T cell activation (**Figures S3A–D**) or viability (**Figure S3E**). These results indicate that metformin and vitamin D function in an additive manner to down-regulate HG-enhanced TRAIL expression on CTLs.

Our findings raise the important question whether metformin and/or vitamin D could protect pancreatic beta cells from HG-

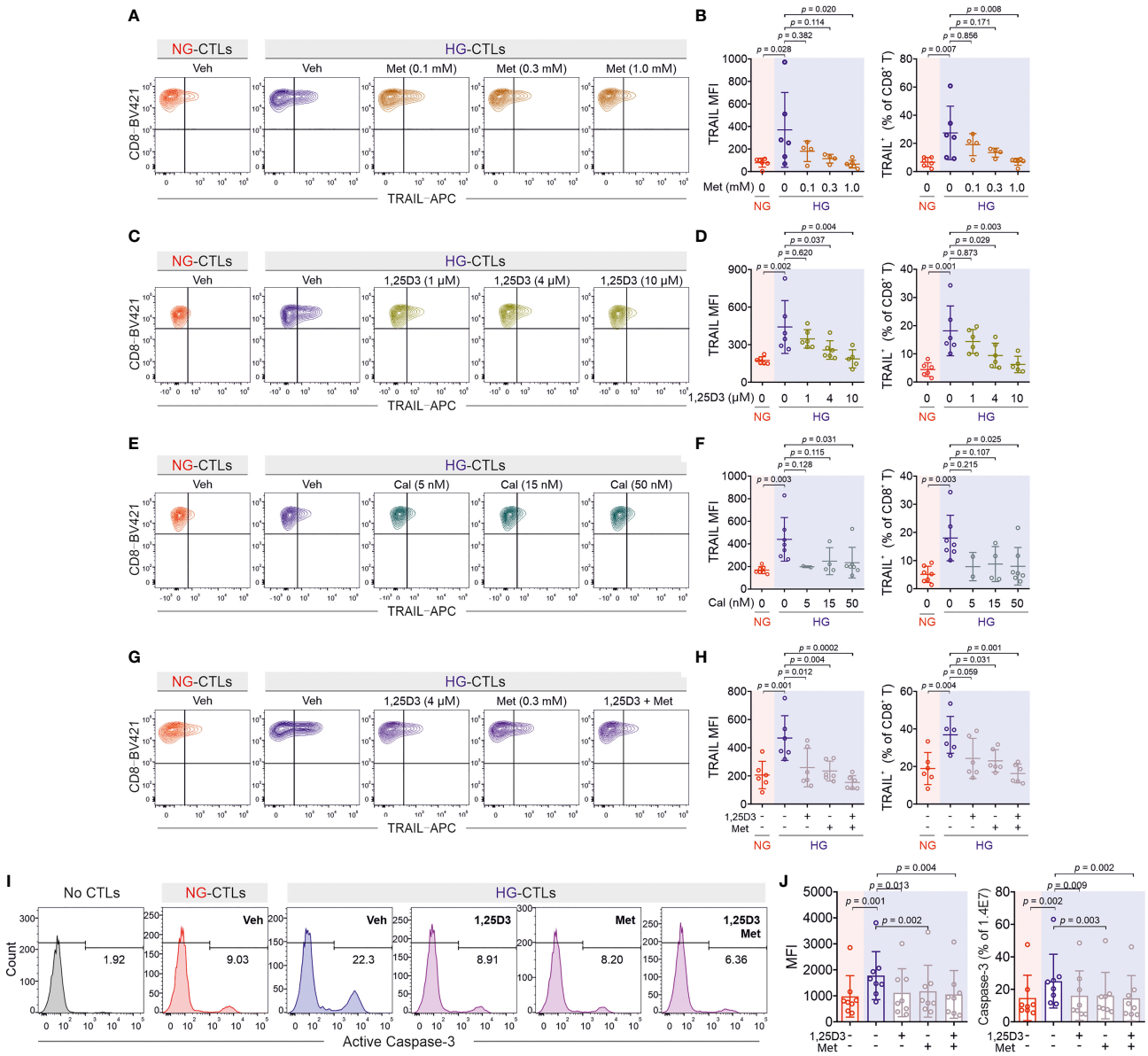

FIGURE 5 | Treatment of metformin and vitamin D rescues TRAIL-mediated pancreatic beta cell destruction. Primary human CD8$^+$ T cells were stimulated with CD3/CD28 beads for 3 days in presence of metformin (Met), 1,25D3, or calcipotriol (Cal) with indicated concentrations. TRAIL expression was analyzed by flow cytometry. **(A, B)** Treatment of metformin reduces HG-enhanced TRAIL expression in CD8$^+$ T cells (n = 4-6 donors from four independent experiments). **(C, D)** Vitamin D regulates TRAIL expression (n = 5-6 donors from four independent experiments). **(E, F)** Enhancement of TRAIL expression by HG could be downregulated by calcipotriol (n = 2-7 donors from four independent experiments). **(G, H)** The combination of metformin and vitamin D synergistically inhibits HG-enhanced TRAIL expression (n = 6 donors from three independent experiments). **(I, J)** Metformin and vitamin D can rescue HG-enhanced CTL-mediated beta cell apoptosis. Primary human CD8$^+$ T cells were stimulated with CD3/CD28 beads for 3 days in presence of metformin (Met, 300 μM) and/or Vitamin D (1,25D3, 4 μM). 1.4E7 beta cells were co-incubated with CTLs for 4 hours. Results are from 8 donors from six independent experiments. Data are shown as means ± SD. One-way ANOVA with Bonferroni's multiple comparison test was applied for statistical analysis.

cultured CTLs by reducing their TRAIL expression. To address this question, we stimulated primary human $CD8^+$ T cells in presence of metformin and/or 1,25D3. Subsequently CTLs were added to 1.4E7 beta cells without metformin and 1,25D3 to avoid the possible effect on beta cells per se. Analysis of 1.4E7 apoptosis at various time points shows that metformin, 1,25D3, or the combination of both reduced TRAIL-mediated beta cell apoptosis to the level of NG control cells (**Figures 5I, J**; **Figures S3F, G**). In summary, our results suggest that apoptosis of beta cells mediated by HG-induced $TRAIL^{high}$ CTLs from healthy donors can be protected by metformin and/or vitamin D *in vitro*.

To test the clinical relevance of metformin and vitamin D protection against TRAIL-induced beta cell apoptosis, we analyzed CTLs from patients diagnosed with diabetes. We found that after stimulation, the expression of TRAIL on diabetic CTLs was significantly higher compared to that of CTLs from healthy individuals, for both NG and HG conditions (**Figures 6A, B**). Remarkably, TRAIL expression of diabetic CTLs under the NG condition was already comparable to that of healthy CTLs in the HG condition (**Figure 6B**). TRAIL expression in diabetic CTLs did not differ between type 1 and type 2 diabetes (**Figures S4A, B**), or between males and females (**Figures S4C, D**), and did not correlate with the age (**Figures S4E, F**).

The correlations between TRAIL expression and diabetes prompted us to examine whether metformin and 1,25D3 can also regulate TRAIL expression in CTLs from diabetic patients. We found that TRAIL expression in diabetic CTLs was down-regulated by 1,25D3 (**Figure S5A**), calcipotriol (**Figure S5B**) or metformin (**Figure S5C**) in a dose-dependent manner. Together, metformin and 1,25D3 could even further suppress TRAIL expression in diabetic CTLs (**Figure 6C**). Interestingly, CTLs from patients who did not take metformin or vitamin D showed clear TRAIL enhancement in HG (**Figure 6D**), whereas CTLs from patients who took metformin did not show any difference between NG and HG (**Figure 6E**). CTLs from patients who took vitamin D exhibited only a moderate increase in TRAIL expression under HG condition (**Figure 6F**). For both the control group (no metformin and no vitamin D) and the metformin group, culturing CTLs from diabetic patients in presence of metformin in HG further down-regulated TRAIL expression (**Figure 6G**). Similarly, for the vitamin D group and the control group, culturing the diabetic CTLs with vitamin D in HG decreased TRAIL expression (**Figure 6H**). These findings suggest that HG-enhanced TRAIL expression on diabetic CTLs can be also down-regulated by metformin and vitamin D.

DISCUSSION

TRAIL is involved in the development of obesity and diabetes (11). In humans, the TRAIL family consists of four membrane receptors, TRAIL-R1, -R2, -R3 and -R4. Among them, TRAIL-R1 and -R2, also known as death receptor 4 (DR4) and 5 (DR5), are responsible for inducing TRAIL-mediated cell apoptosis, whereas TRAIL-R3 and -R4 are decoy receptors, which lack the cytoplasmic death domain. Thus, the ratio of death receptors over decoy receptors determines the sensitivity or efficacy of TRAIL-mediated cell apoptosis. TRAIL-R1 and -R2 are highly expressed in many tissues including kidney, heart, adipose tissue, and pancreas; in comparison, decoy receptors TRAIL-R3 and -R4 are not detectable in most of the tissues except for immune function-related organs/tissues (e.g. spleen, bone marrow, and lymph nodes) and pancreas (35). Infiltration of immune cells, especially $CD8^+$ T cells, is positively correlated with the progression of diabetes and related complications (11). Therefore, it is likely that $TRAIL^{high}$ CTLs induced by diabetic conditions not only contribute to destruction of pancreatic beta-cells in an antigen-independent manner but are also involved in attacking TRAIL-R1/-$R2^{high}$ cells in different tissues resulting in undesirable complications. Our findings indicate that harnessing TRAIL expression in CTLs can therefore protect insulin-producing beta cells.

If down-regulation of TRAIL expression on CTLs could protect beta-cells, is progression of diabetes ameliorated by TRAIL deficiency? Feeding high-fat diet to a TRAIL/ApoE double knock-out strain significantly enhanced their fasting glucose compared to ApoE-/- or TRAIL-/- mice (36). Along this line, intraperitoneal injection of soluble TRAIL in mice fed with high-fat diet reduces beta-cell loss (37). An obvious question is why systemic blockade of TRAIL exacerbates diabetes? Compelling evidence show that TRAIL is an essential regulator to suppress the function of diabetogenic T cells, which recognize autoantigens on pancreatic beta-cells leading to their destruction. For example, injection of soluble DR5 (TRAIL-R2) in NOD mice elevates proliferation of GAD65-specific T cells (15). Along this line, blockade of TRAIL enhances proliferation of transferred diabetogenic T cells in NOD mice (37). Therefore, systematic blockade of TRAIL cannot protect pancreatic beta-cells.

In many cell types, glucose transporters (Gluts), especially Glut1, are up-regulated upon activation. For example, expression of Glut1 is elevated upon activation in murine $CD4^+$ T cells and macrophages to favor glucose glycolysis over oxidative phosphorylation (38). In human T cells, expression of Glut1 is reported to be enhanced in CD3/CD28 bead-stimulated T cells compared to naive T cells (38). In comparison, our results how that the expression of Glut1 at the protein level is not altered by HG and even marginally down-regulated at the mRNA level. Our microarray data suggest that the expression levels of other Gluts are not influenced by HG, at least at the mRNA level. This indicates that in CTLs, glucose transporters are unlikely the target proteins responsive to HG to mediate HG-induced metabolic reprogramming.

Type I interferons (IFNs, e.g., IFN-α and IFN-β) can induce TRAIL expression on T cells (39). However, we could not detect differences in IFN-α and IFN-β expression by microarray analysis between CTLs cultured in NG and HG. This indicates that type I IFNs produced by CTLs are very unlikely to be involved in HG-enhanced TRAIL expression in CTLs. Interestingly, compelling evidence show that IFN-α plays a critical role in initiation of type 1 diabetes (40–42). In a mouse model, blockade of IFN-α signaling at prediabetic stage prevents beta-cells from destruction by CTLs (43). Therefore, we postulate that prior to clinical disease-resulted elevation of blood glucose, TRAIL expression on CTLs could be induced by IFN-α, which could also contribute to development of diabetes.

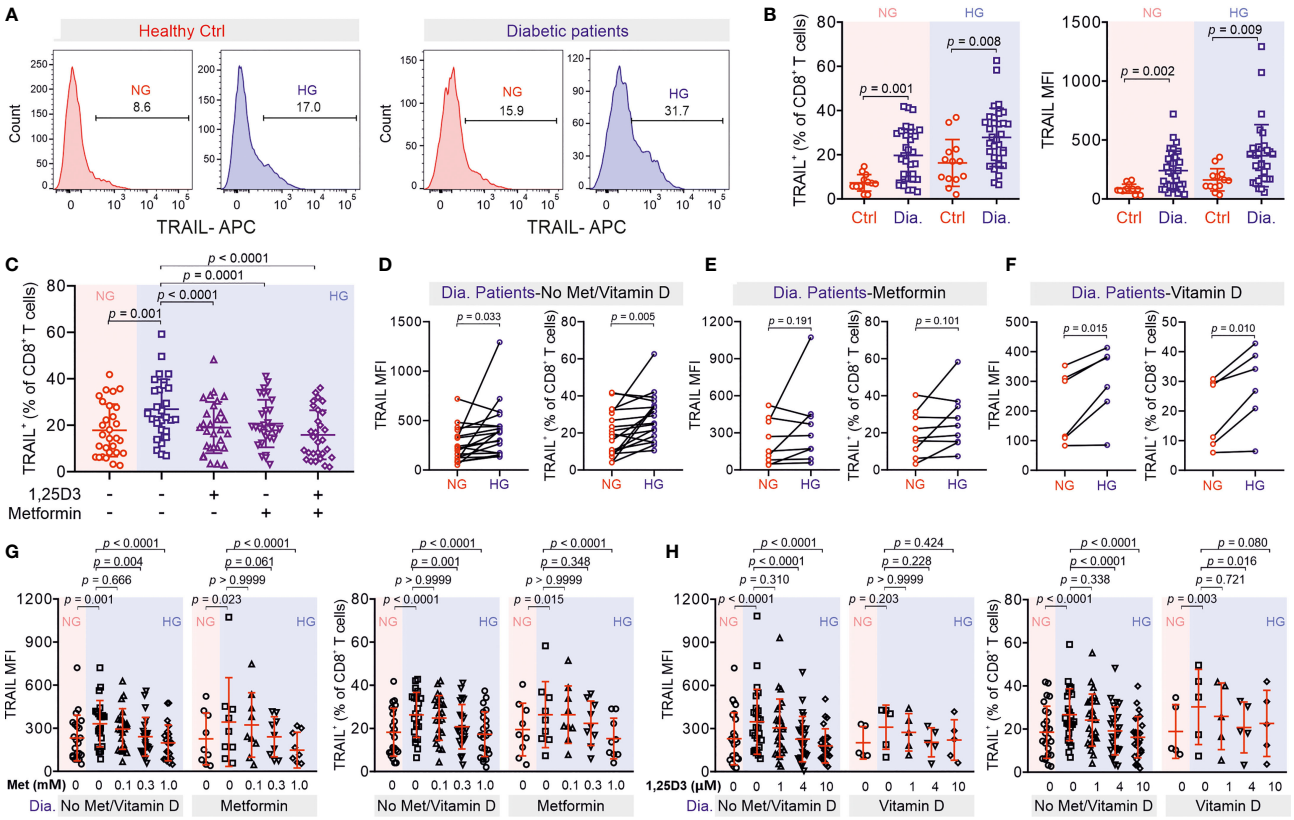

FIGURE 6 | Treatment of metformin and vitamin D decreases TRAIL-expression in CTLs from diabetic patients. **(A, B)** TRAIL expression in CTLs from control and diabetic patients. PBMCs isolated from healthy individuals or diabetic patients were stimulated with CD3/CD28 beads in NG (5.6 mM, pink shade) or HG (25 mM, blue shade) medium for 3 days. Then the samples were stained with CD3, CD8 and TRAIL and analyzed by flow cytometry (Ctrl, n = 13 from thirteen independent experiments; diabetic patients, n = 33 from twenty-four independent experiments). One representative donor from either group is shown in **(A, C)** Metformin and vitamin D diminish enhanced TRAIL expression in diabetic CTLs. Diabetic CTLs from **(B)** were treated with met (300 μM) and/or 1,25D3 (4 μM) during bead-activation for 3 days (n = 29 from twenty-one independent experiments). **(D–H)** Diabetic patients from **(B)** were categorized into three groups based on whether metformin or vitamin D was taken. Data are represented as Mean ± SD and *p* values were assessed by two-tailed unpaired Student's *t* test **(B)**, two-tailed paired Student's *t* test **(D–F)**, one-way ANOVA **(C)**, or two-way ANOVA with Bonferroni's multiple comparison test **(G, H)**.

ROS is a byproduct of cellular metabolic redox reactions, which is closely related to progression of diabetes and its complications (44). In Th17 cells, a high glucose-induced autoimmune reaction is mediated by ROS originated from mitochondria (45). Our results show that for human CTLs, ROS is indeed involved in regulating HG-enhanced TRAIL expression, but cytosolic rather than mitochondrial ROS appears to be decisive. This suggests that Th17 cells and CTLs may differ in their regulatory mechanisms in response to HG. Interestingly, ROS can activate the PI3K/Akt pathway as well as the NFκB pathway (46, 47), which we also found to be essential for HG-enhanced TRAIL expression. Thus, in CTLs, ROS could act upstream of the PI3K/Akt/NFκB axis to regulate HG-enhanced TRAIL expression.

Vitamin D is closely related to insulin resistance and onset of diabetes (48). Vitamin D also has a profound impact on the immune system (49). In particular, expression of the vitamin D receptor induced by initial TCR signaling *via* p38 is essential for upregulation of phospholipase C gamma 1, which plays a pivotal role in T cell activation and Treg/Th17 differentiation (50, 51). In addition, vitamin D could also accelerate the transition of Th1 cells from pro-inflammatory to anti-inflammatory phase by epigenetic remodeling (52). Interestingly, vitamin D is involved in maintaining mitochondrial functions to optimize cellular redox conditions, thus protecting cells from oxidative stress-related damages (53). We postulate that vitamin D could diminish HG-enhanced TRAIL expression through reducing intracellular ROS production.

The impact of combined use of vitamin D and metformin has been investigated in various pathological scenarios. For example, combination of vitamin D and metformin shows a positive chemopreventive effect on colorectal cancer in rat and mouse models (12) and could be potentially effective to treat patients with polycystic ovary syndrome based on its effect on menstrual cycle (54). A recent study reported that in a type 2 diabetes mouse model, which cannot be controlled by metformin alone, additional vitamin D therapy improved insulin sensitivity in skeletal muscles (55). This finding supports our findings that combination of

metformin and vitamin D could be beneficial to diabetic patients by reducing HG-enhanced expression of TRAIL in CTLs to protect beta cells from TRAIL-mediated apoptosis. In summary, we suggest a novel mechanism of CTL involvement in progression of diabetes, which establishes CTLs as a possible target for combined metformin and vitamin D therapy to protect pancreatic beta cells of diabetic patients, especially for the patients who still have sufficient numbers of beta-cells stay undestroyed.

DATA AVAILABILITY STATEMENT

The original contributions presented in the study are included in the article/**Supplementary Material**. Microarray data have been deposited in the ArrayExpress database at EMBL-EBI (www.ebi.ac.uk/arrayexpress) under accession number E-MTAB-11441. Further inquiries can be directed to the corresponding author.

ETHICS STATEMENT

Research carried out for this study with material from healthy donors (leukocyte reduction system chambers from human blood donors), from diabetic patients and the healthy individuals is authorized by the local ethic committee (declaration from Ha 84/15, Prof. Dr. Rettig-Stürmer/Amendment M Hoth and Ha 84/19, GC, respectively). Protocols for the STZ-induced diabetes mouse model for this study is approved by the local regulatory authorities (Animal experiment approval 49/2019, LP). The animal experiments were performed according to local, national, and European Union ethical guidelines.

AUTHOR CONTRIBUTIONS

WY designed and performed most experiments and all the corresponding analyses if not mentioned otherwise. AD and VH analyzed microarray data. CD and MHa carried out microarray and EM helped interpret the results. FK, GC, and FL collected blood samples from diabetic patients and controls, and supervised the treatment of the patients. LS-B and DB performed seahorse assay and the analysis. GS carried out qRT-PCR. AY, RZ, and AK helped with flow cytometry. LP provided diabetic mice. MHo helped with data interpretation and provided critical feedback on all aspects of the project. BQ generated concepts, designed experiments, and wrote the manuscript. All authors contributed to the article and approved the submitted version.

FUNDING

This project was funded by the Deutsche Forschungsgemeinschaft (SFB 1027 A2 to BQ, A11 to MHo, C3 and ZX to VH, TRR219 (M04) to LP), and HOMFOR2019 (to BQ). The flow cytometer was funded by DFG (GZ: INST 256/423-1 FUGG). LS-B and DB are funded by the FNR, respectively by the PRIDE program (PRIDE/11012546/NEXTIMMUNE) and the ATTRACT program (A14/BM/7632103).

ACKNOWLEDGMENTS

We thank the Institute for Clinical Hemostaseology and Transfusion Medicine for providing donor blood; Carmen Hässig, Cora Hoxha, and Susanne Renno for excellent technical help; Xiangda Zhou for the support in HG-culture.

SUPPLEMENTARY MATERIAL

The Supplementary Material for this article can be found online at: https://www.frontiersin.org/articles/10.3389/fimmu.2022.831680/full#supplementary-material

REFERENCES

1. World Health Organization. *Global Report on Diabetes*. Geneva, Switzerland: World Health Organization (2016).
2. Pugliese A. Autoreactive T Cells in Type 1 Diabetes. *J Clin Invest* (2017) 127:2881–91. doi: 10.1172/JCI94549
3. Kumar NP, Sridhar R, Nair D, Banurekha VV, Nutman TB, Babu S. Type 2 Diabetes Mellitus is Associated With Altered CD8(+) T and Natural Killer Cell Function in Pulmonary Tuberculosis. *Immunology* (2015) 144:677–86. doi: 10.1111/imm.12421
4. Halle S, Halle O, Forster R. Mechanisms and Dynamics of T Cell-Mediated Cytotoxicity In Vivo. *Trends Immunol* (2017) 38:432–43. doi: 10.1016/j.it.2017.04.002
5. Dieckmann NM, Frazer GL, Asano Y, Stinchcombe JC, Griffiths GM. The Cytotoxic T Lymphocyte Immune Synapse at a Glance. *J Cell Sci* (2016) 129:2881–6. doi: 10.1242/jcs.186205
6. Hassin D, Garber OG, Meiraz A, Schiffenbauer YS, Berke G. Cytotoxic T Lymphocyte Perforin and Fas Ligand Working in Concert Even When Fas Ligand Lytic Action is Still Not Detectable. *Immunology* (2011) 133:190–6. doi: 10.1111/j.1365-2567.2011.03426.x
7. Geltink RIK, Kyle RL, Pearce EL. Unraveling the Complex Interplay Between T Cell Metabolism and Function. *Annu Rev Immunol* (2018) 36:461–88. doi: 10.1146/annurev-immunol-042617-053019
8. Sugiura A, Rathmell JC. Metabolic Barriers to T Cell Function in Tumors. *J Immunol* (2018) 200:400–7. doi: 10.4049/jimmunol.1701041
9. Zou H, Yang W, Schwar G, Zhao R, Alansary D, Yin D, et al. High Glucose Distinctively Regulates Ca(2+) Influx in Cytotoxic T Lymphocytes Upon Target Recognition and Thapsigargin Stimulation. *Eur J Immunol* (2020) 50:2095–8. doi: 10.1002/eji.202048577
10. Zhu J, Yang W, Zhou X, Zöphel D, Soriano-Baguet L, Dolgener D, et al. High Glucose Enhances Cytotoxic T Lymphocyte-Mediated Cytotoxicity. *Front Immunol* (2021) 12:689337. doi: 10.3389/fimmu.2021.689337
11. Harith HH, Morris MJ, Kavurma MM. On the TRAIL of Obesity and Diabetes. *Trends Endocrinol Metab* (2013) 24:578–87. doi: 10.1016/j.tem.2013.07.001
12. Bossi F, Bernardi S, Zauli G, Secchiero P, Fabris B. TRAIL Modulates the Immune System and Protects Against the Development of Diabetes. *J Immunol Res* (2015) 2015:680749. doi: 10.1155/2015/680749
13. Mirandola P, Ponti C, Gobbi G, Sponzilli I, Vaccarezza M, Cocco L, et al. Activated Human NK and CD8+ T Cells Express Both TNF-Related Apoptosis-Inducing Ligand (TRAIL) and TRAIL Receptors But are Resistant to TRAIL-Mediated Cytotoxicity. *Blood* (2004) 104:2418–24. doi: 10.1182/blood-2004-04-1294

14. Falschlehner C, Schaefer U, Walczak H. Following TRAIL's Path in the Immune System. *Immunology* (2009) 127:145–54. doi: 10.1111/j.1365-2567.2009.03058.x
15. Lamhamedi-Cherradi SE, Zheng S, Tisch RM, Chen YH. Critical Roles of Tumor Necrosis Factor-Related Apoptosis-Inducing Ligand in Type 1 Diabetes. *Diabetes* (2003) 52:2274–8. doi: 10.2337/diabetes.52.9.2274
16. Mattisson IY, Bjorkbacka H, Wigren M, Edsfeldt A, Melander O, Fredrikson GN, et al. Elevated Markers of Death Receptor-Activated Apoptosis are Associated With Increased Risk for Development of Diabetes and Cardiovascular Disease. *EBioMedicine* (2017) 26:187–97. doi: 10.1016/j.ebiom.2017.11.023
17. Shirley S, Morizot A, Micheau O. Regulating TRAIL Receptor-Induced Cell Death at the Membrane : A Deadly Discussion. *Recent Pat Anticancer Drug Discovery* (2011) 6:311–23. doi: 10.2174/157489211796957757
18. Daniels RA, Turley H, Kimberley FC, Liu XS, Mongkolsapaya J, Ch'En P, et al. Expression of TRAIL and TRAIL Receptors in Normal and Malignant Tissues. *Cell Res* (2005) 15:430–8. doi: 10.1038/sj.cr.7290311
19. Ou D, Metzger DL, Wang X, Huang J, Pozzilli P, Tingle AJ. TNF-Related Apoptosis-Inducing Ligand Death Pathway-Mediated Human Beta-Cell Destruction. *Diabetologia* (2002) 45:1678–88. doi: 10.1007/s00125-002-0926-2
20. Kummerow C, Schwarz EC, Bufe B, Zufall F, Hoth M, Qu B. A Simple, Economic, Time-Resolved Killing Assay. *Eur J Immunol* (2014) 44:1870–2. doi: 10.1002/eji.201444518
21. Diener C, Hart M, Kehl T, Rheinheimer S, Ludwig N, Krammes L, et al. Quantitative and Time-Resolved miRNA Pattern of Early Human T Cell Activation. *Nucleic Acids Res* (2020) 48:10164–83. doi: 10.1093/nar/gkaa788
22. Ritchie ME, Phipson B, Wu D, Hu Y, Law CW, Shi W, et al. Limma Powers Differential Expression Analyses for RNA-Sequencing and Microarray Studies. *Nucleic Acids Res* (2015) 43:e47. doi: 10.1093/nar/gkv007
23. Benjamini Y, Hochberg Y. Controlling the False Discovery Rate: A Practical and Powerful Approach to Multiple Testing. *J R Stat Soc Ser B* (1995) 57:289–300. doi: 10.1111/j.2517-6161.1995.tb02031.x
24. Ulgen E, Ozisik O, Sezerman OU. Pathfindr: An R Package for Comprehensive Identification of Enriched Pathways in Omics Data Through Active Subnetworks. *Front Genet* (2019) 10:858:858. doi: 10.3389/fgene.2019.00858
25. Qu B, Pattu V, Junker C, Schwarz EC, Bhat SS, Kummerow C, et al. Docking of Lytic Granules at the Immunological Synapse in Human CTL Requires Vti1b-Dependent Pairing With CD3 Endosomes. *J Immunol* (2011) 186:6894–904. doi: 10.4049/jimmunol.1003471
26. Salmond RJ. mTOR Regulation of Glycolytic Metabolism in T Cells. *Front Cell Dev Biol* (2018) 6:122:122. doi: 10.3389/fcell.2018.00122
27. Kristiansen KA, Jensen PE, Moller IM, Schulz A. Monitoring Reactive Oxygen Species Formation and Localisation in Living Cells by Use of the Fluorescent Probe CM-H(2)DCFDA and Confocal Laser Microscopy. *Physiol Plant* (2009) 136:369–83. doi: 10.1111/j.1399-3054.2009.01243.x
28. Xu F, Na L, Li Y, Chen L. Roles of the PI3K/AKT/mTOR Signalling Pathways in Neurodegenerative Diseases and Tumours. *Cell Biosci* (2020) 10:54. doi: 10.1186/s13578-020-00416-0
29. Mitri J, Muraru MD, Pittas AG. Vitamin D and Type 2 Diabetes: A Systematic Review. *Eur J Clin Nutr* (2011) 65:1005–15. doi: 10.1038/ejcn.2011.118
30. Maddaloni E, Cavallari I, Napoli N, Conte C. Vitamin D and Diabetes Mellitus. *Front Horm Res* (2018) 50:161–76. doi: 10.1159/000486083
31. Jamka M, Wozniewicz M, Jeszka J, Mardas M, Bogdanski P, Stelmach-Mardas M. The Effect of Vitamin D Supplementation on Insulin and Glucose Metabolism in Overweight and Obese Individuals: Systematic Review With Meta-Analysis. *Sci Rep* (2015) 5:16142. doi: 10.1038/srep16142
32. H P, O C, Da U, O G, Ng D. The Impact of Vitamin D Replacement on Glucose Metabolism. *Pak J Med Sci* (2013) 29:1311–4. doi: 10.12669/pjms.296.3891
33. Wei Z, Yoshihara E, He N, Hah N, Fan W, Pinto AFM, et al. Vitamin D Switches BAF Complexes to Protect Beta Cells. *Cell* (2018) 173:1135–49.e1115. doi: 10.1016/j.cell.2018.04.013
34. Ferreira GB, Vanherwegen AS, Eelen G, Gutierrez ACF, Van Lommel L, Marchal K, et al. Vitamin D3 Induces Tolerance in Human Dendritic Cells by Activation of Intracellular Metabolic Pathways. *Cell Rep* (2015) 10:711–25. doi: 10.1016/j.celrep.2015.01.013
35. Uhlen M, Fagerberg L, Hallstrom BM, Lindskog C, Oksvold P, Mardinoglu A, et al. Proteomics. Tissue-Based Map of the Human Proteome. *Science* (2015) 347:1260419. doi: 10.1126/science.1260419
36. Di Bartolo BA, Chan J, Bennett MR, Cartland S, Bao S, Tuch BE, et al. TNF-Related Apoptosis-Inducing Ligand (TRAIL) Protects Against Diabetes and Atherosclerosis in Apoe (-)/(-) Mice. *Diabetologia* (2011) 54:3157–67. doi: 10.1007/s00125-011-2308-0
37. Mi QS, Ly D, Lamhamedi-Cherradi SE, Salojin KV, Zhou L, Grattan M, et al. Blockade of Tumor Necrosis Factor-Related Apoptosis-Inducing Ligand Exacerbates Type 1 Diabetes in NOD Mice. *Diabetes* (2003) 52:1967–75. doi: 10.2337/diabetes.52.8.1967
38. Freemerman AJ, Johnson AR, Sacks GN, Milner JJ, Kirk EL, Troester MA, et al. Metabolic Reprogramming of Macrophages: Glucose Transporter 1 (GLUT1)-Mediated Glucose Metabolism Drives a Proinflammatory Phenotype. *J Biol Chem* (2014) 289:7884–96. doi: 10.1074/jbc.M113.522037
39. Kayagaki N, Yamaguchi N, Nakayama M, Eto H, Okumura K, Yagita H. Type I Interferons (IFNs) Regulate Tumor Necrosis Factor-Related Apoptosis-Inducing Ligand (TRAIL) Expression on Human T Cells: A Novel Mechanism for the Antitumor Effects of Type I IFNs. *J Exp Med* (1999) 189:1451–60. doi: 10.1084/jem.189.9.1451
40. Stewart TA, Hultgren B, Huang X, Pitts-Meek S, Hully J, MacLachlan NJ. Induction of Type I Diabetes by Interferon-Alpha in Transgenic Mice. *Science* (1993) 260:1942–6. doi: 10.1126/science.8100367
41. Lombardi A, Tsomos E, Hammerstad SS, Tomer Y. Interferon Alpha: The Key Trigger of Type 1 Diabetes. *J Autoimmun* (2018) 94:7–15. doi: 10.1016/j.jaut.2018.08.003
42. Qaisar N, Jurczyk A, Wang JP. Potential Role of Type I Interferon in the Pathogenic Process Leading to Type 1 Diabetes. *Curr Opin Endocrinol Diabetes Obes* (2018) 25:94–100. doi: 10.1097/MED.0000000000000399
43. Marro BS, Ware BC, Zak J, de la Torre JC, Rosen H, Oldstone MB. Progression of Type 1 Diabetes From the Prediabetic Stage Is Controlled by Interferon-Alpha Signaling. *Proc Natl Acad Sci USA* (2017) 114:3708–13. doi: 10.1073/pnas.1700878114
44. Volpe CMO, Villar-Delfino PH, Dos Anjos PMF, Nogueira-Machado JA. Cellular Death, Reactive Oxygen Species (ROS) and Diabetic Complications. *Cell Death Dis* (2018) 9:119. doi: 10.1038/s41419-017-0135-z
45. Zhang D, Jin W, Wu R, Li J, Park SA, Tu E, et al. High Glucose Intake Exacerbates Autoimmunity Through Reactive-Oxygen-Species-Mediated TGF-Beta Cytokine Activation. *Immunity* (2019) 51:671–81.e675. doi: 10.1016/j.immuni.2019.08.001
46. Koundouros N, Poulogiannis G. Phosphoinositide 3-Kinase/Akt Signaling and Redox Metabolism in Cancer. *Front Oncol* (2018) 8:160:160. doi: 10.3389/fonc.2018.00160
47. Morgan MJ, Liu ZG. Crosstalk of Reactive Oxygen Species and NF-kappaB Signaling. *Cell Res* (2011) 21:103–15. doi: 10.1038/cr.2010.178
48. Berridge MJ. Vitamin D Deficiency and Diabetes. *Biochem J* (2017) 474:1321–32. doi: 10.1042/BCJ20170042
49. Aranow C. Vitamin D and the Immune System. *J Investig Med* (2011) 59:881–6. doi: 10.2310/JIM.0b013e31821b8755
50. von Essen MR, Kongsbak M, Schjerling P, Olgaard K, Odum N, Geisler C. Vitamin D Controls T Cell Antigen Receptor Signaling and Activation of Human T Cells. *Nat Immunol* (2010) 11:344–9. doi: 10.1038/ni.1851
51. Zhou Q, Qin S, Zhang J, Zhon L, Pen Z, Xing T. 1,25(OH)2D3 Induces Regulatory T Cell Differentiation by Influencing the VDR/PLC-Gamma1/TGF-Beta1/Pathway. *Mol Immunol* (2017) 91:156–64. doi: 10.1016/j.molimm.2017.09.006
52. Chauss D, Freiwald T, McGregor R, Yan B, Wang L, Nova-Lamperti E, et al. Autocrine Vitamin D Signaling Switches Off Pro-Inflammatory Programs of TH1 Cells. *Nat Immunol* (2021) 23:62–74. doi: 10.1038/s41590-021-01080-3
53. Wimalawansa SJ. Vitamin D Deficiency: Effects on Oxidative Stress, Epigenetics, Gene Regulation, and Aging. *Biol (Basel)* (2019) 8:30. doi: 10.3390/biology8020030
54. Rashidi B, Haghollahi F, Shariat M, Zayerii F. The Effects of Calcium-Vitamin D and Metformin on Polycystic Ovary Syndrome: A Pilot Study. *Taiwan J Obstet Gynecol* (2009) 48:142–7. doi: 10.1016/S1028-4559(09)60275-8

55. Amin SN, Hussein UK, Yassa HD, Hassan SS, Rashed LA. Synergistic Actions of Vitamin D and Metformin on Skeletal Muscles and Insulin Resistance of Type 2 Diabetic Rats. *J Cell Physiol* (2018) 233:5768–79. doi: 10.1002/jcp.26300

Conflict of Interest: The authors declare that the research was conducted in the absence of any commercial or financial relationships that could be construed as a potential conflict of interest.

Publisher's Note: All claims expressed in this article are solely those of the authors and do not necessarily represent those of their affiliated organizations, or those of the publisher, the editors and the reviewers. Any product that may be evaluated in this article, or claim that may be made by its manufacturer, is not guaranteed or endorsed by the publisher.

APPENDIX 7

Research Publication

(Co-author)

ZHU, J., YANG, W., ZHOU, X., ZÖPHEL, D., SORIANO-BAGUET, L., DOLGENER, D., CARLEIN, C., HOF, C., ZHAO, R., YE, S., SCHWARZ, E.C., BRENNER, D., PRATES ROMA, L., QU, B., 2021. **High Glucose Enhances Cytotoxic T Lymphocyte-Mediated Cytotoxicity.** *Front. Immunol*. 12, 689337.

frontiers in Immunology

ORIGINAL RESEARCH
published: 25 June 2021
doi: 10.3389/fimmu.2021.689337

High Glucose Enhances Cytotoxic T Lymphocyte-Mediated Cytotoxicity

Jie Zhu[1,2†], Wenjuan Yang[2†], Xiangda Zhou[2], Dorina Zöphel[2], Leticia Soriano-Baguet[3,4,5], Denise Dolgener[2], Christopher Carlein[2], Chantal Hof[2], Renping Zhao[2], Shandong Ye[1], Eva C. Schwarz[2], Dirk Brenner[3,4,6], Leticia Prates Roma[2] and Bin Qu[2,7]*

[1] Department of Endocrinology, The First Affiliated Hospital of USTC, Division of Life Sciences and Medicine, University of Science and Technology of China, Hefei, China, [2] Biophysics, Center for Integrative Physiology and Molecular Medicine (CIPMM), School of Medicine, Saarland University, Homburg, Germany, [3] Experimental and Molecular Immunology, Department of Infection and Immunity, Luxembourg Institute of Health, Esch-sur-Alzette, Luxembourg, [4] Immunology and Genetics, Luxembourg Centre for Systems Biomedicine (LCSB), University of Luxembourg, Belvaux, Luxembourg, [5] Faculty of Science, Technology and Medicine, University of Luxembourg, Esch-sur-Alzette, Luxembourg, [6] Odense Research Center for Anaphylaxis, Department of Dermatology and Allergy Center, Odense University Hospital University of Southern Denmark, Odense, Denmark, [7] INM – Leibniz Institute for New Materials, Saarbrücken, Germany

OPEN ACCESS

Edited by:
Hu Zeng,
Mayo Clinic, United States

Reviewed by:
Henrique Borges da Silva,
Mayo Clinic Arizona, United States
Kai Yang,
Indiana University School of Medicine - Lafayette, United States

***Correspondence:**
Bin Qu
bin.qu@uks.eu

[†]These authors have contributed equally to this work

Specialty section:
This article was submitted to T Cell Biology, a section of the journal Frontiers in Immunology

Received: *31 March 2021*
Accepted: *10 June 2021*
Published: *25 June 2021*

Citation:
Zhu J, Yang W, Zhou X, Zöphel D, Soriano-Baguet L, Dolgener D, Carlein C, Hof C, Zhao R, Ye S, Schwarz EC, Brenner D, Prates Roma L and Qu B (2021) High Glucose Enhances Cytotoxic T Lymphocyte-Mediated Cytotoxicity. Front. Immunol. 12:689337. doi: 10.3389/fimmu.2021.689337

Cytotoxic T lymphocytes (CTLs) are key players to eliminate tumorigenic or pathogen-infected cells using lytic granules (LG) and Fas ligand (FasL) pathways. Depletion of glucose leads to severely impaired cytotoxic function of CTLs. However, the impact of excessive glucose on CTL functions still remains largely unknown. Here we used primary human $CD8^+$ T cells, which were stimulated by CD3/CD28 beads and cultured in medium either containing high glucose (HG, 25 mM) or normal glucose (NG, 5.6 mM). We found that in HG-CTLs, glucose uptake and glycolysis were enhanced, whereas proliferation remained unaltered. Furthermore, CTLs cultured in HG exhibited an enhanced CTL killing efficiency compared to their counterparts in NG. Unexpectedly, expression of cytotoxic proteins (perforin, granzyme A, granzyme B and FasL), LG release, cytokine/cytotoxic protein release and CTL migration remained unchanged in HG-cultured CTLs. Interestingly, additional extracellular Ca^{2+} diminished HG-enhanced CTL killing function. Our findings suggest that in an environment with excessive glucose, CTLs could eliminate target cells more efficiently, at least for a certain period of time, in a Ca^{2+}-dependent manner.

Keywords: high glucose, cytotoxic T lymphocytes, cytotoxicity, glycolysis, glucose uptake, migration, proliferation, Ca^{2+}

INTRODUCTION

Cytotoxic T lymphocytes (CTLs) are the key players to eliminate tumorigenic or pathogen-infected cells (1, 2). CTLs patrol tissues to search for cognate target cells (3–6). Once the targets are identified, killer cells form an intimate contact with the target cells, which is termed immunological synapse (IS) (7–9). To execute their effector functions, CTLs employ mainly two common killing pathways: lytic granules and Fas/Fas ligand (FasL) pathway. Lytic granules contain cytotoxic proteins, such as perforin and granzymes, which can be released at the interface between CTLs and target cells to induce destruction of target cells (10–12). FasL on CTL surface engages with the Fas receptor on target cells to trigger the apoptosis cascades in target cells (13–15).

Glucose metabolism has a central role in regulating effector killing functions of CTLs (16–18). It is known that in absence of glucose, CTLs are not able to exert their effector functions (17). Aerobic glycolysis induced by early T-cell receptor is required for cytokine production in CTLs (19). The availability of glucose modulates IFN-γ production in CTLs (20). Under pathological conditions such as leukemia, glucose metabolism of $CD8^+$ T cells is impaired leading to jeopardized cytolytic function of CTLs (21). Notably, enhancement of this impaired glycolysis in CTLs by either checkpoint block or inhibition of autophagy is beneficial for tumor rejection (22, 23). The impact of high glucose on functionality of CTLs remains, however, poorly characterized.

In this work, we investigated the regulation of effector killing function of CTLs by high glucose. We show that stimulating $CD8^+$ T cells in high glucose significantly enhances killing efficiency of CTLs without affecting cell proliferation, expression of cytotoxic proteins (perforin, granzyme A, granzyme B and FasL), LG release, or CTL migration. Increase in extracellular Ca^{2+} can diminish this HG-enhanced CTL-mediated cytotoxicity.

MATERIALS AND METHODS

Antibodies and Reagents

The following antibodies or reagents were used: Alexa 488 anti-human CD107a antibody (H4A3, Biolegend), APC-Cy7 anti-human CD3 antibody (HIT3a, Biolegend), BV421 anti-human CD8 antibody (SK1, Biolegend), Alexa 488 anti-human Granzyme A antibody (CB9, Biolegend), Alexa 647 anti-human perforin antibody (dG9, Biolegend), PE anti-human Fas-L antibody (NOK-1, Biolegend), PerCP anti-human CD3 (HIT3a, Biolegend) antibody, Carboxyfluorescein succinimidyl ester (CFSE, Thermo Fisher Scientific), 2-NBDG (ThermoFisher Scientific), Calcein-AM (ThermoFisher Scientific), Protein transport inhibitor (BD), neutralized bovine collagen type I solution (Advanced Biomatrix), Staphylococcal enterotoxin A and B (SEA and SEB, Sigma), $CaCl_2{\cdot}2H_2O$ (Biomol), Paraformaldehyde (PFA, Polysciences), Saponin (Sigma), and streptozotocin (Sigma).

Cell Culture

Raji cells were cultured in RPMI-1640 medium (ThermoFisher Scientific) containing 10% FCS and 1% Penicillin-Streptomycin. Peripheral blood mononuclear cells (PBMCs) were obtained from healthy donors as described before (24). Primary human $CD8^+$ T cells were negatively isolated from PBMCs using Human $CD8^+$ T Cell isolation Kits (Miltenyi Biotec) according to the manufacturer's instruction. Human $CD8^+$ T cells were stimulated with CD3/CD28 activator beads (ThermoFisher Scientific) and cultured in DMEM containing normal (5.6 mM, NG) or high glucose (25 mM, HG) (ThermoFisher Scientific) for 3 days if not otherwise mentioned. Since day 2, additional glucose was added into the medium every two days to compensate the consumed glucose along with recombinant human IL-2 (50 ng/ml, ThermoFisher Scientific). All cells were cultured at 37°C with 5% CO_2. EG7 mouse lymphoma cell line was stably transfected with 4 μg of pCasper-pMax plasmid (25) using SF Cell Line 4D-NucleofectorTM X Kit (Lonza). 48h after transfection, cells were treated with 0.4 mg/ml G418 and 4 μg/ml puromycin in RPMI-1640 (ThermoFisher Scientific) with 10% FCS. Monoclonally expanded EG7-pCasper cells were cultured in selection medium, supplemented with 1% Penicillin/Streptomycin. Flow cytometry analysis revealed 98% of EG7-pCasper cells were fluorescent.

2-NBDG Uptake Assay

On day 3 after bead-stimulation, CTLs were loaded with 2-NBDG (120 μM, 5% FCS in PBS) at 37°C for 30 min. Subsequently, loaded CTLs were washed twice in PBS (0.5% BSA) and analyzed immediately by flow cytometry (ex. 465 nm, em. 540 nm).

Seahorse Assay

Primary human $CD8^+$ T cells were stimulated with human CD3/CD28 Activator beads (ThermoFisher Scientific) for 3 days in DMEM containing 5.6 mM or 25 mM glucose (ThermoFisher Scientific). At day 3, CTLs were plated in 96-well XF Cell Culture Microplate in XF Seahorse DMEM medium at a cell density of 3×10^5 cells/well. Following the manufacturer's instructions (Agilent), the extracellular acidification rate (ECAR) were measured using the XF Glycolytic Stress Test kit.

Real-Time Killing Assay

The real-time killing assay was carried out as previously described (26). Briefly, Raji cells were pulsed with staphylococcal enterotoxin A (SEA; 1 μg/ml) and SEB (1 μg/ml) at 37°C for 30 min, followed by calcein-AM loading (500 nM, ThermoFisher Scientific) for 15 min at room temperature. Primary $CD8^+$ T cells were co-incubated with the target cells with indicated effector to target (E:T) ratios in AIMV medium (glucose 16.09 mM) supplemented with 10 mM HEPES. With addition of $CaCl_2$ (1 mM), the respective AIMV medium was pre-equilibrated in the incubator for 24 hours. The fluorescence was measured with a GENiosPro micro-plate reader (TECAN) using bottom reading mode at 37°C every 10 minutes for 4 hours.

Diabetic CTL Preparation

Male C57BL/6J mice were injected with streptozotocin (STZ) intraperitoneally using a single high dose injection protocol (27). STZ was administered in a concentration of 150 mg/kg body weight diluted in a 0.1 M sodium citrate buffer. Blood samples were taken from the tail vein and glucose levels were tested by standard test strips (Accu-Chek) twice a week. Additionally, overall health status and body weight was monitored and evaluated using a score sheet over the whole observation period. One week after injection, the blood sugar levels were evaluated. Mice with a blood glucose level of more than 280 mg/dL one week after the injection were considered as diabetic and were sacrificed at day 29 after injection. Spleens were removed from mice and kept in sterile PBS on ice until isolation. Splenocytes were isolated with a 40 μm cell strainer (Corning)

and erythrocytes were lysed using a hypo-osmolar solution. $CD8^+$ T cells were isolated with the Dynabeads™ Untouched™ Mouse CD8 Cells Kit (ThermoFisher Scientific). Purity of isolated cells was evaluated by flow cytometry. Isolated $CD8^+$ T cells were stimulated with Dynabeads Mouse T-Activator CD3/CD28 (ThermoFischer Scientific) for 3 days and cultured in AIM V medium (ThermoFisher Scientific) containing 10% FCS, 50 µM ß-Mercaptoethanol and 100 U/ml recombinant human IL-2 (Miltenyi Biotec).

3D Killing Assay

For 3D killing assay, the EG7-pCasper cells was used as target cells, which were embedded into collagen (type I bovine, 2 mg/ml) in a 96-well plate. After consolidation of collagen, stimulated mouse $CD8^+$ cells were loaded on the top of the collagen as effector cells. The E:T ratio was 10: 1 and all conditions were done in duplicate. The killing was measured by a high-content imaging system (ImageXpress, Molecular Devices) at 37°C with 5% CO_2 every 10 min for 24 hours. Signal of FRET and GFP channels were analyzed with ImageJ.

Degranulation Assay

To assess degranulation, SEA/SEB-pulsed Raji cell were settled with CTLs in the presence of Alexa 488 conjugated anti-human CD107a antibody and protein transport inhibitor (GolgiStop, BD). Cells were incubated at 37°C with 5% CO_2 for 4 hours. Afterwards, the cells were stained with BV421 anti-human CD8 antibody to distinguish target cells from $CD8^+$ T cells prior to analysis using flow cytometry.

Flow Cytometry

To determine proliferation, freshly isolated primary human $CD8^+$ T cells were stained with CFSE (1 µM) at room temperature for 10 min prior to CD3/CD28 bead stimulation. To stain perforin and granzyme B, cells were fixed in pre-chilled 4% PFA and permeablized with 0.1% saponin in PBS/0.5% BSA and 5% FCS. Flow cytometry data were acquired using a FACSVerse™ flow cytometer (BD Biosciences) and were analyzed with FlowJo v10 (FLOWJO, LLC).

RNA Isolation and qRT-PCR

The analysis of mRNA expression was carried out as previously reported (28). Briefly, total RNA was extracted from primary human $CD8^+$ T cells after stimulation for 3 days using TRIzol reagent (ThermoFisher Scientific). Subsequently, total RNA was reversely transcribed and the cDNA was used for quantitative Real-time PCR (qRT-PCR). Real-time PCR was performed in a CFX96Real-TimeSystemC1000 Thermal Cycler (Bio-Rad Laboratories) (software: Bio-Rad CFX Manager, Version 3.0). As internal controls, TBP (TATA box-binding protein) and RNA polymerase were used. The mRNA level from the genes of interest is normalized to TBP and RNA polymerase as described elsewhere (29). Primer sequences for the two reference genes *RNAPol* and *TBP* are listed in (29) and for perforin (*PRF1*) in (30). Primer sequences for *GZMA* (NM_006144) are *GZMA*_forw. 5' TTGGGGCTCACTCAATAACC 3' and *GZMA*_rev. 5' TGGTT CCTGGTTTCACATCA 3', for *GZMB* (NM_00413) *GZMB*_forw. 5' GAGACGACTTCGTGCTGACA 3' and *GZMB*_rev. 5' CTGGGCCTTGTT GCTAGGTA 3' and for *FASLG* (NM_000639) *FASLG*_forw. 5' GCACACAGCATCATCT TTGG 3' and *FASLG*_rev. 5' CAAGATTGAC CCCGGAAGTA 3'.

Multiplex Cytokine Assay

Supernatant was harvested at day 3 after bead-activation and kept at -80°C until use. The preset CD8/NK panel (Biolegend) was used. Concentration of each analyte was determined according to manufacturer's instructions.

Light-Sheet Microscopy

Visualization of CTL migration using light-sheet microscopy was conducted as previous described (31). Briefly, day 2 after stimulation, the CD3/CD28 beads were removed and the CTLs were loaded with CFSE according to the manufacturer instruction and further cultured in NG- or HG-medium for 24 hours. Then CFSE-loaded CTLs were resuspended in chilled neutralized collagen type I solution (2 mg/ml, Advanced Biomatrix) and polymerized at 37°C with 5% CO_2 for 40 min followed by 1 hour-recovery in AIMV medium. Migration of CTLs was visualized at 37°C with 5% CO_2 for 1 hour with an interval of 30 sec using the Z.1 light-sheet microscope (Zeiss). Z-stepsize was 1 µm and 201 slices were obtained for each stack. Using Imaris 8.1.2 (Bitplane), cell trajectories were automatically tracked, the velocity and persistence were analyzed. The CTLs with a track duration less than 10 min were excluded from the quantification.

Ethical Considerations

Protocols of research carried out for this study with human material (leukocyte reduction system chambers from human blood donors) is authorized by the local ethic committee [declaration from 16.4.2015 (84/15; Prof. Dr. Rettig-Stürmer)]. All individuals fulfilled the donor criteria of the German regulations (32). Informed consent was obtained from all subjects or, if subjects are under 18, from a parent and/or legal guardian. Protocols for the STZ-induced diabetes mouse model for this study is approved by the local regulatory authorities (Animal experiment approval 49/2019, Prof. Leticia Prates Roma). The animal experiments were performed according to local, national, and European Union ethical guidelines.

Statistical Analysis

GraphPad Prism Software (San Diego, CA, USA) was used for statistical analysis. The differences between two groups were analyzed by paired t-test. For multiple comparisons, two-way ANOVA were performed, followed by Bonferroni test. *P < 0.05; **P < 0.01; ***P < 0.001; ns, not significant. Data are presented as mean or mean ± S.E.M.

RESULTS

Glycolysis Is Enhanced in CTLs Cultured in High Glucose

To analyze whether high glucose affects CTL functions, we used 5.6 mM as normal glucose level (NG) and 25 mM as high glucose

(HG), which imitates a severe hyperglycemia condition (33). Primary human CD8$^+$ T cells were activated with anti-CD3/CD28 antibody-coated beads in NG- or HG-medium. Given the fact that stimulated CD8$^+$ T cells consume significant amount of glucose (34), glucose was added every day to compensate the consumed glucose (**Supplementary Figure 1**). First, we examined the glucose uptake using 2-NBDG, a fluorescent analog of glucose, which cannot be metabolized by glycolytic enzymes. The uptake of 2-NBDG was substantially enhanced in stimulated CD8$^+$ T cells compared to their unstimulated counterparts both in NG and HG conditions (**Figures 1A, B**). Although no difference was identified in fraction of 2-NBDG$^+$ stimulated CD8$^+$ T cells between NG and HG conditions, the mean fluorescence intensity (MFI) of 2-NBDG in HG-CTLs is higher than that in NG-CTLs (**Figures 1A, B**). Since 2-NBDG uptake does not reflect functional change in Glucose transporter 1 (35), we also determined the consumption of glucose on each day after stimulation. We found that although no significant difference was identified for day 1 between HG- and NG-CTLs, for the second day, NG-CTLs consumed more glucose, whereas for the third day HG-CTLs consumed more glucose (**Figure 1C**), which is in good agreement with MFI of 2-NBDG (**Figure 1B**, right panel). Of note, the overall consumption of glucose within 3 days was slightly higher in HG-CTLs than in NG-CTLs (**Figure 1D**).

Next, we examined the impact of HG on glycolysis in CTLs. We used Seahorse Extracellular Flux Analyzer to determine the extracellular acidification rate (ECAR) of NG- and HG-CTLs at day 3 after stimulation. The results show that both glycolysis (between glucose and oligomycin) and glycolytic capacity (between oligomycin and 2-DG) was elevated in HG-CTLs relative to NG-CTLs for both donors examined (**Figure 1E**). This result is in good agreement with our observation that the color of HG medium was more yellowish than NG medium on day 3. Thus, we conclude that glycolysis of fully activated CTLs is enhanced in an environment with excessive glucose.

Compelling evidence shows that deficiency in glycolysis leads to impaired T cell proliferation (36). Here we examined the impact of enhanced glycolysis in CTLs by HG on CTL proliferation. Freshly isolated primary human CD8$^+$ T cells were stained with CFSE and then stimulated by anti-CD3/anti-CD28 antibody-coated beads in NG- or HG-medium. The results

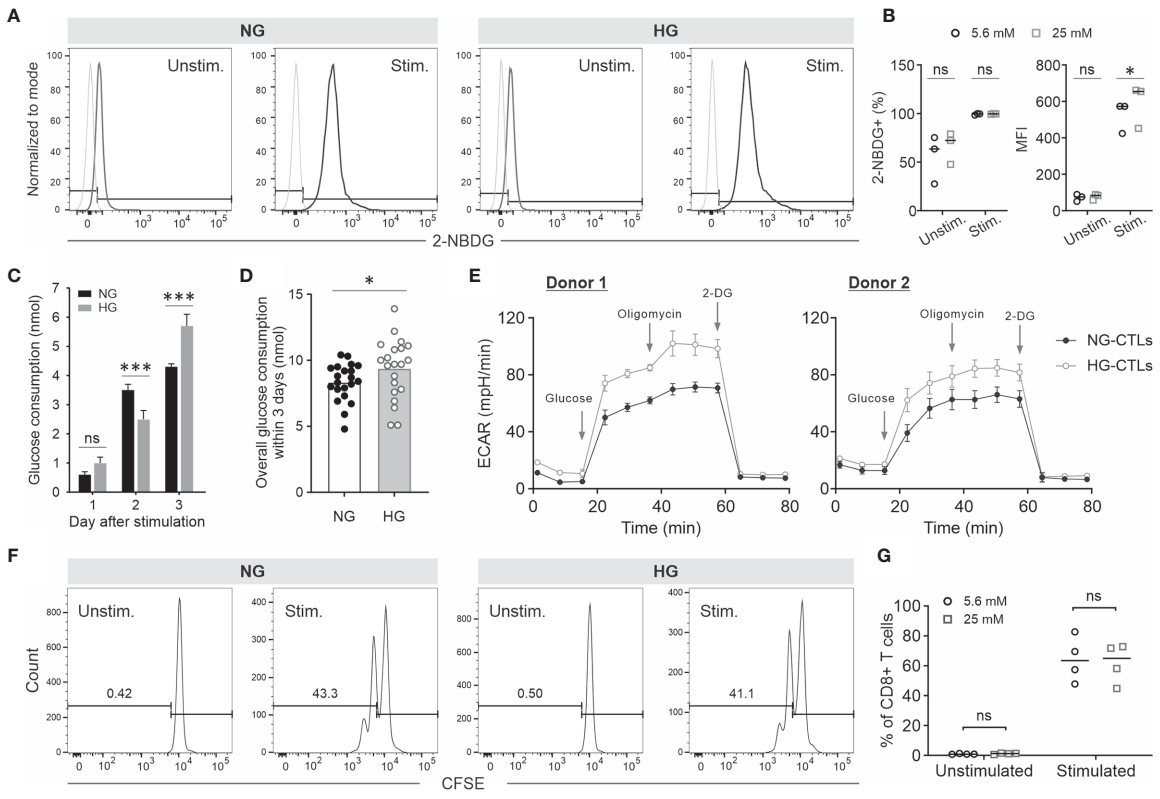

FIGURE 1 | Impact of HG culture on glycolysis and proliferation of CTLs. Primary human CD8+ T cells were stimulated with anti-CD3/CD28-antibody coated beads in medium containing NG (5.6 mM) or HG (25 mM) for 3 days. **(A, B)** Glucose uptake in NG- and HG-cultured CTLs. On day 3, bead-stimulated (stim.) or unstimulated CD8+ T cells (Unstim.) were loaded with 2-NBDG at 37°C for 30 min and analyzed with flow cytometry. FMO for gating is shown in light grey in **(A)**. Fraction of 2-NBDG+ cells and mean fluorescence intensity (MFI) is shown in **(B)**. **(C, D)** Glucose concentration was measured at indicated time points using blood glucose meter (Bayer). Glucose consumption was calculated for 1.5 × 106 CTLs. **(E)** Extracellular acidification rate (ECAR) of CTLs. **(F, G)** Proliferation of CTLs cultured in NG- or HG-medium. Primary human CD8+ cells were stained with CFSE prior to CD3/CD28 bead-activation. The fluorescence was determined with flow cytometry. Results are from three **(A, B)**, twenty-two **(C, D)**, two **(E)** or four donors **(F, G)**. * $p < 0.05$; *** $p < 0.001$; ns, not significant.

show that without bead-stimulation, $CD8^+$ T cells did not proliferate; with bead-stimulation, proliferation of $CD8^+$ T cells cultured in HG stayed in a comparable range as their counterparts in NG (**Figures 1F, G**). This result indicates that HG-enhanced glycolysis in CTLs does not further promote their proliferation.

CTL-Mediated Cytotoxicity Is Enhanced in an Environment With Excessive Glucose

We further investigated the impact of HG on CTL-mediated cytotoxicity. The killing kinetics was determined using the real-time killing assay (26). We observed that cytotoxicity of CTLs is significantly enhanced when cultivated in HG, in comparison with their counterpart in NG on day 3 (**Figures 2A, B**) and day 6 (**Figure 2C**) after CD3/CD28 bead-stimulation. In addition, we also examined cytotoxicity of CTLs from a diabetes mouse model. We visualized CTL-mediated cytotoxicity using a 3D killing assay established in our lab, where the target cells were embedded in 3D collagen matrices and CTLs were added from top. The target cells (EG7-pCasper) stably express an apoptosis reporter pCasper, a GFP-RFP FRET pair, allowing us to distinguish live targets (yellow-colored) from apoptotic (green-colored) or dead (complete loss of fluorescence) targets (**Figure 3A**). In collagen matrices, target cells proliferated during the period of visualization and only a few target cells went apoptotic (**Figure 3A**, Target only, **Movie 1**), indicating that photocytotoxicity of this long-term measurement is negligible. Analyses of conditions with effector cells show that both the control CTLs and the diabetic CTLs induced apoptosis (determined by a drop in FRET signal followed by an increase in GFP signal) and complete destruction of target cells (indicated by an abrupt drop in GFP signal) (**Figures 3A, B**, **Movies 2–3***). Remarkably, the CTLs from all three diabetic mice exhibited faster killing kinetics compared to their control counterparts (**Figure 3B**). Together, these results suggest that cytotoxicity of CTLs is enhanced in an environment with excessive glucose.

HG-Enhanced CTL Is Regulated By $Ca2^+$

Next, we investigated potential mechanisms how HG could regulate CTL killing efficiency. The lytic granule (LG) pathway is considered as one of the main mechanisms to mediate elimination of target cells by CTLs. Therefore, we investigated the possible impact of HG on release of LG using a CD107a degranulation assay. We found that release of LG upon target-

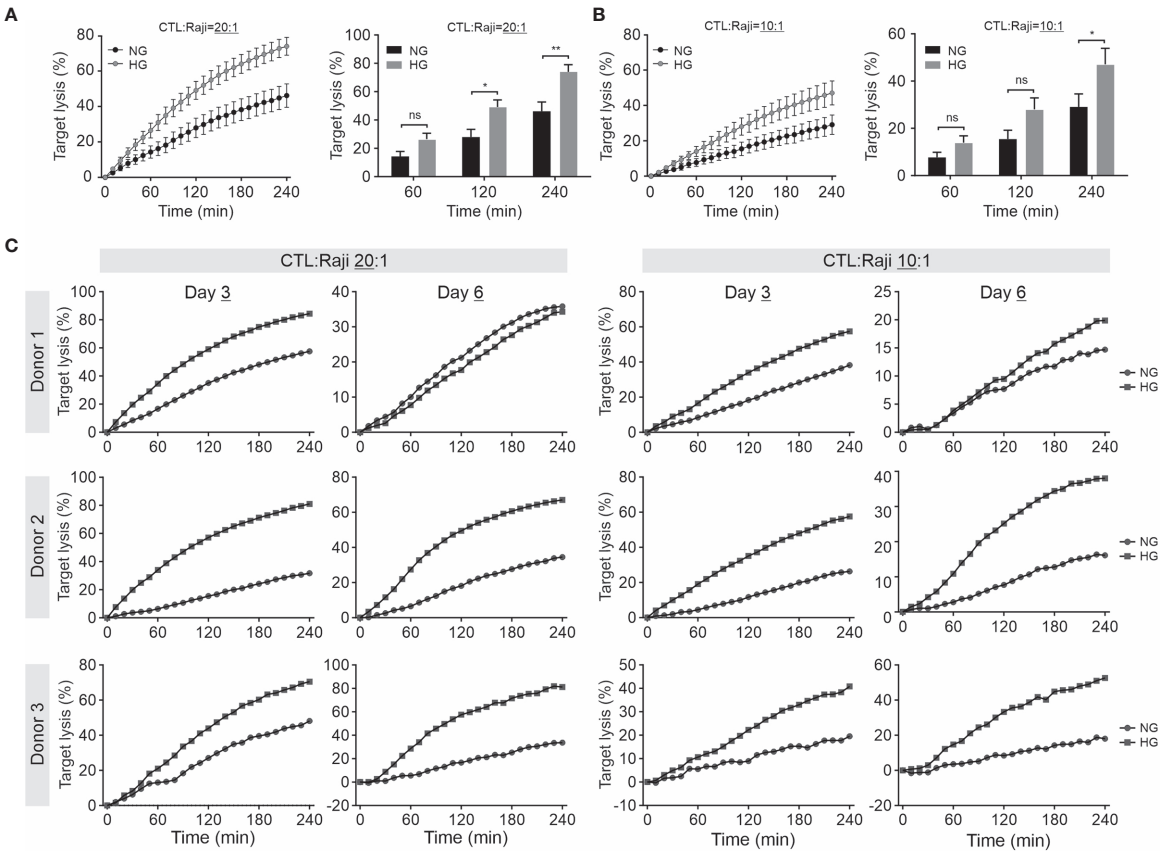

FIGURE 2 | Culture in HG enhances CTL-mediated cytotoxicity. Primary human CD8+ T cells were stimulated with anti-CD3/CD28-antibody coated beads in medium containing NG (5.6 mM) or HG (25 mM) for 3 days **(A-C)** or 6 days **(C)** as indicated. Killing kinetics was determined with the real-time killing assay. SEA/SEA pulsed Raji cells were used as target cells at an effector to target (E:T) ratio of 20:1 or 10:1. Results are from five **(A, B)** or three donors **(C)**. * $p < 0.05$; ** $p < 0.01$; ns, not significant.

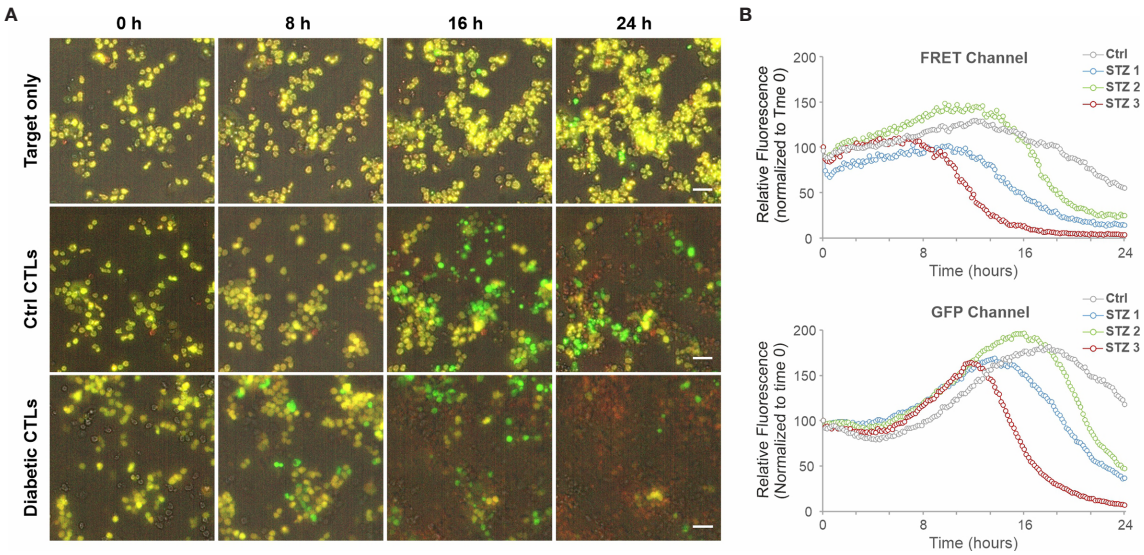

FIGURE 3 | CTLs from diabetic exhibit faster killing kinetics. 3D killing assay was carried out to determine killing kinetics at 37°C with 5% CO_2 every 10 minutes for 24 hours. EG7-pCasper cells were used as target cells, which were embedded in collagen (2 mg/ml). CTLs were added from top. CTLs from STZ-3 mouse is shown in **(A)**. The quantification of the signal from FRET or GFP channel is shown in **(B)**. Scale bars are 40 μm.

recognition in HG-cultured CTLs is in a comparable range as their counterparts in NG (**Figures 4A, B**). Subsequently, we examined the expression of LG-containing cytotoxic proteins, such as perforin, granzyme A (GzmA) and granzyme B (GzmB) using quantitative PCR and flow cytometry. We found that at mRNA level the expression of perforin and GzmB was not altered, whereas GzmA was even slightly down-regulated by HG (**Figure 4C**). Concomitantly, at protein level, there is no difference identified in perforin but a slight reduction in GzmA in HG-cultured CTLs (**Figures 4D, E**). Since GzmA and GzmB are serine proteases and contribute to target lysis, HG-enhanced CTL killing capacity cannot be attributed to this slight reduction in GzmA expression. The slight GzmA reduction should, if at all, decrease the cytotoxic capacity of CTL but certainly not enhance it. Next, we examined Fas/FasL pathway, another key mechanism employed by CTLs to destroy target cells. Our results show that in HG-cultured CTLs, the expression of FasL was moderately up-regulated at mRNA level (**Figure 4F**), but did not differ at protein level compared to their counterparts in NG (**Figure 4G**). Taken together, our data suggest that both LG machinery and FasL pathway do not contribute to the enhancement of CTL-mediated cytotoxicity by HG.

Although expression of these cytotoxic proteins was not altered by HG, the release could still differ. To examine this hypothesis, we carried out a bead-based multiplex cytokine assay, which enabled us to simultaneously determine up to 13 analytes from same samples. The panel includes six key cytotoxic proteins (perforin, GzmA, GzmB, granulysin, soluble Fas, and soluble FasL) and seven main cytokines produced by CD8/NK cells (IFNγ, TNFα, IL-2, IL-4, IL-6, IL-10 and IL-17A). As shown in **Figure 4H**, no difference was identified in the above-mentioned cytotoxic proteins or cytokines between NG- and HG-CTLs (**Figure 4H**), indicating that the vesicle release machinery in CTLs is not affected by HG. This result suggests that HG-enhanced cytotoxicity of CTLs is not due to change in release of cytokine or cytotoxic proteins.

Migration also plays an essential role in CTL-mediated killing. Generally speaking, higher speed would allow CTLs to find their target cells more quickly, hence increasing the number of killing events in a limited period of time. Therefore, using light-sheet microscopy, we visualized CTL migration in a 3D collagen matrix. The quantification of velocity and persistence shows that there is no significant difference between NG- and HG-treated CTLs (**Figures 4I, J**). These results imply that HG does not alter the motility of CTLs.

Our previous work shows that intracellular calcium in HG-cultured CTLs was decreased upon contact with target cells compared to their counterparts cultured in NG (37). We thus postulated that the enhanced CTL cytotoxicity by HG-culture could be linked to decreased Ca^{2+} influx. To test this postulation, we added extra Ca^{2+} in the medium during the killing assay to elevate the decreased Ca^{2+} influx in HG-cultured CTLs upon target recognition. The real-time killing results show that addition of Ca^{2+} could indeed abolish (Donor1) or diminish (Donor2&3) the difference in killing efficiency between NG- and HG-cultured CTLs (**Figure 4K**). Moreover, we compared the target lysis of HG-CTLs between Ctrl and addition of Ca^{2+} at three time points (60, 120, and 240 min). The statistics show that target lysis of HG-CTLs was significantly diminished with addition of Ca^{2+} (**Figure 4L**). These data suggest intracellular Ca^{2+} as a potential target manipulated by HG to modulate TCR-dependent CTL killing functions.

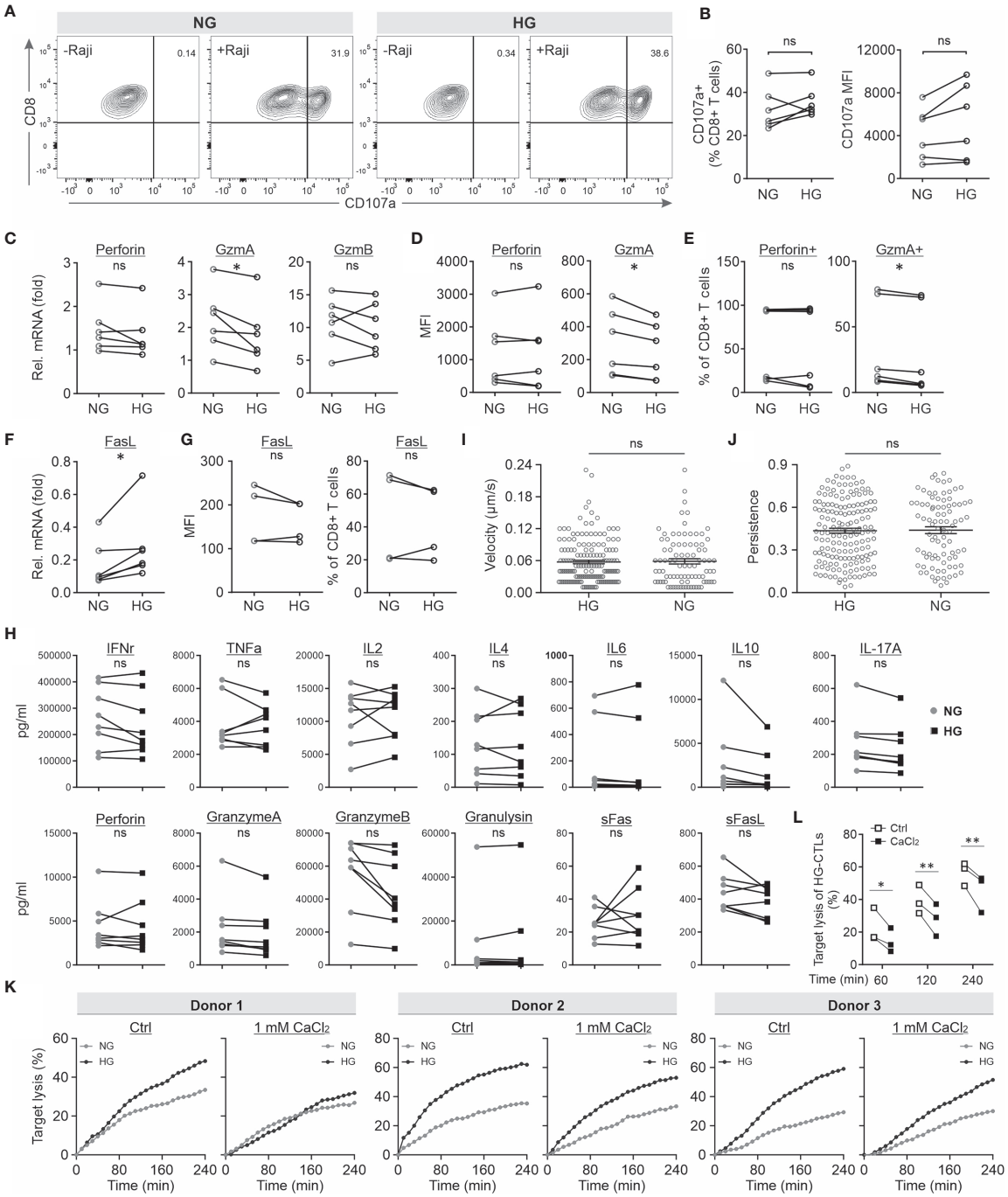

FIGURE 4 | HG-enhanced CTL killing function is regulated by extracellular Ca^{2+}. **(A, B)** Degranulation of lytic granules is not influenced by HG. CD 107a degranulation assay was conducted. Raji cells pulsed with SEA/SEB were used as target cells. Results are from six donors. **(C)** The mRNA level was determined by quantitative PCR using TBP and RNA polymerase as internal controls. Results are from six donors. **(D, E)** The protein level was determined using flow cytometry. Mean fluorescence intensity (MFI, **D**) and the positive fraction of CTLs **(E)** are shown. Results are from six donors. **(F, G)** Expression level of FasL at mRNA level **(F)** and at protein level **(G)**. **(H)** Release of cytokines and cytotoxic proteins. Multiplex cytokine assay was performed to determine the concentration of the analytes. Results are from eight donors. **(I, J)** Migration of CTLs is not altered in HG-cultured CTLs. Migration of CTLs was visualized using light-sheet microscopy. Velocity **(I)** and persistence **(J)** were analyzed using Imaris. Results are from two independent experiments and from two donors (88 cells for HG and 162 cells for NG). **(K, L)** Addition of extracellular Ca^{2+} diminishes HG-enhanced CTL killing efficiency. Bead-stimulated primary $CD8^+$ T cells and SEA/SEB-pulsed Raji cells were used for the real-time killing assay with addition of $CaCl_2$ (1 mM). Target lysis of HG-CTLs at 60, 120 and 240 min were extracted from the kinetics and shown in **(L)**. Results are from two independent experiments and from three donors. * $p < 0.05$; ** $p < 0.01$; ns, not significant.

DISCUSSION

An increasing number of studies have demonstrated that glycolysis is indispensable for proper killing function of CTLs (38, 39). Up-to-date, most studies investigate functional changes in CTLs in a scenario of abrogation of glycolysis, for example by using the glucose analog 2-Deoxy-D-glucose (2DG) or by excluding glucose in the medium. A recent study also shows that functionally-impaired T cell senescence is correlated with prediabetes and transfer of senescent T cells leads to a deterioration of glucose homeostasis in human and mice (40). Targeting T cell metabolism has been suggested recently as a promising strategy to enhance their anti-tumor function (41, 42). In this work, we investigated the impact of excessive glucose on killing efficiency of CTLs. We found that CTL-mediated killing is enhanced when stimulated and cultured in medium containing HG. Our findings are in good agreement with the previous reports that enhancement of glycolysis in CTLs is beneficial for tumor rejection (22, 23). A recent study has revealed that glucose supplementation substantially improves the survival of virus-infected mice *via* CHOP-mediated tissue tolerance (43). Under this circumstance, enhanced CTL killing capability could also contribute to the ameliorated viral clearance. In addition, we observed that activated $CD8^+$ T cells consumed large amount of glucose, supporting the evidence that T cells contribute to glucose homeostasis (44).

High blood glucose level is a typical symptom for diabetes mellitus, which is a major cause of blindness, kidney failure, heart attacks, stroke and lower limb amputation and is the seventh leading cause of death worldwide (45). Type 1 diabetes (T1D) has been identified to be an autoimmune disease for which CTLs play an important role by destroying the insulin-producing pancreatic beta-cells (46). Our findings suggest that high level of blood glucose caused by T1D could potentially further enhance CTL-mediated destruction of pancreatic beta-cells, thus accelerating the progression of the disease. On the other hand, a rich body of literature shows that diabetic patients are more prone to cancer and chronic infections (47–50). In this work, we have examined CTL functions only up to 6 days. Our previous work shows that when co-incubated with the cognate target cells, viability of HG-CTLs did not differ from NG-CTLs at 2 hours, and then fraction of apoptotic CTLs was slightly enhanced in HG condition compared to their NG counterparts (17.8% *vs* 15.1%) (37). It indicates that although cytotoxicity of HG-CTLs is enhanced, but after killing more HG-CTLs undergo apoptosis, which may lead to a decreased number of CTLs in a long run.

In this work, we tried to identify the mechanism upregulating CTL cytotoxicity by HG. We examined CTL proliferation, cytotoxic protein expression, degranulation, migration and cytokine release. None of these factors are altered by HG culture, and they are thus unlikely to be involved in HG-enhanced CTL killing capacity. Viability of HG-CTLs does not explain how cytotoxicity is up-regulated, as our previous work shows that the viability of HG-CTLs did not differ from NG-CTLs at 2 hours after killing, and slightly more HG-CTLs were apoptotic 16 hours after killing compared to their NG counterparts (37). Compelling evidence shows that CTL-mediated cytotoxicity is calcium dependent. More particularly, reduced calcium influx in CTLs upon target recognition by decreasing extracellular Ca^{2+} concentration or down-regulation of Ca^{2+} channel Orai1 leads to an enhancement in CTL-mediated cytotoxicity (28). Hallmarks of IS formation, for example reorientation of microtubule-organizing center, are linked to sustained Ca^{2+} influx (51). In this work, we identified that Ca^{2+} is involved in elevation of CTL killing capacity by HG. Our previous work shows that decreased Ca^{2+} influx upon target recognition was correlated with enhanced CTL-mediated cytotoxicity, and additional extracellular Ca^{2+} led to elevated calcium influx upon target recognition (28). Of note, target recognition-induced calcium influx is decreased in HG-CTLs (37). Concerning the key components of SOCE (store-operated calcium entry) channels (ORAI1, ORAI2, ORAI3, STIM1, and STIM2), in HG-CTLs, ORAI2 and ORAI3 were upregulated, whereas STIM1 and STIM2 were down-regulated at the mRNA level. However, no statistically significant difference of these proteins (ORAI1, STIM1 and STIM2) was identified at the protein level (37). Taken together, the reduced difference in killing between NG- and HG-CTLs by addition of extracellular Ca^{2+} can be explained by the decreased difference in Ca^{2+} influx upon target recognition.

Glycolysis is required for cytotoxic function of CTLs. Inhibition of glycolysis by its inhibitor 2-DG (2-deoxyglucose) reduces cytotoxic capacity of T cells and the expression of key effector molecules such as IFNγ and granzymes (52). It is reported that T cell activation induces rapid aerobic glycolysis *via* PDHK1; and deficiency of PDHK1 leads to decrease in cytokine production but does not affect $CD8^+$ T cell-induced target lysis (19). Our results provide the first evidence from the other direction that enhanced glycolysis in HG-CTLs is correlated with increased cytotoxicity.

It is reported previously that cytolytic killing by mouse CTLs is not affected *in vivo* by hyperglycaemia (53). More specifically, the authors used either stimulated OT-I $CD8^+$ T cells *in vitro* in medium containing 5.5, 10, or 25 mM glucose or STZ-induced diabetic mouse model (C57BL/6 mice), and the ones with blood glucose > 13.3 mM were considered diabetic. The authors found that glucose levels did not affect glycolysis, proliferation or cytokine release in stimulated OT-I $CD8^+$ T cells. Similarly, proliferation, cytokine production, and cytotoxicity of $CD8^+$ T cells did not differ between control and diabetic mice. Our work has the same conclusion about the impact of high glucose on proliferation and cytokine production in CTLs as reported by Recino et al. (53). However, there is a contradiction in the results about glycolysis and cytotoxicity in these two studies, which can be well explained by the differences in experiment design between these two studies. In our STZ mouse model, the criterion for diabetes is > 280 mg/dL (corresponding to 15.5 mM) and the mice were sacrificed at day 29. In comparison, Recino et al. used > 13.3 mM and likely sacrificed the mice not later than day 14. Considering the basal level of blood glucose in mice is around 10 mM (the blood glucose of the four mice used

in our experiments before injection: 168, 180, 157, and 192 mg/dL, mean = 174.3 mg/dL, corresponding to 9.7 mM), the functional changes in diabetic mouse CTLs can likely be enhanced or become more prominent by more elevated glucose level and longer incubation time like in our case. In addition, the difference between human and mouse CTLs in response to high glucose also cannot be excluded. Of note, the C57BL/6N strain carries a mutation in the nicotinamide nucleotide transhydrogenase (Nnt) gene. This gene encodes a mitochondrial protein and is involved in T cell function (54). We used C57BL/6J strain to avoid this problem.

DATA AVAILABILITY STATEMENT

The raw data supporting the conclusions of this article will be made available by the authors, without undue reservation.

AUTHOR CONTRIBUTIONS

JZ initiated the project and performed glucose measurement in **Figure 1** and **Supplementary Figure 1**, real-time killing assay in **Figure 2**. WY performed degranulation assay, flow cytometry analysis, and multiplex cytokine assay in **Figure 4** and did the quantification analyses for all experiments if not otherwise mentioned. XZ carried out migration experiments, real-time killing assay in **Figure 4**, 3D killing assay in **Figure 3**, and the corresponding analysis. DZ established the EG7-pCasper cell line. DZ and CH isolated and stimulated mouse $CD8^+$ T cells. LS-B performed the seahorse assay and the analysis. DD performed 2-NBDG and CFSE experiments in **Figure 1**. CC and LP established the STZ diabetic mouse model. RZ helped with degranulation assay. SY provided expertise in diabetes. ES was involved in qRT-PCR. DB provided expertise in glycolysis and experiment design of seahorse assay. BQ generated concepts, designed experiments, and wrote the manuscript. All authors contributed to the article and approved the submitted version.

FUNDING

This project was funded by the Deutsche Forschungsgemeinschaft (Sonderforschungsbereich 1027 project A2 to BQ, TRR219 (M04) to LP), INM Fellow, and HOMFOR2019 (to BQ) and Forschungsgroßgeräte (GZ: INST 256/423-1 FUGG and GZ: INST 256/419-1 FUGG) for flow cytometer and light-sheet microscope, respectively. LS-B and DB are funded by the FNR, respectively by the PRIDE (PRIDE/11012546/NEXTIMMUNE) and the ATTRACT program (A14/BM/7632103).

ACKNOWLEDGMENTS

We thank the Institute for Clinical Hemostaseology and Transfusion Medicine for providing donor blood; Annette Lis for mouse $CD8^+$ T cell preparation and EG7-pCasper cells, Carmen Hässig, Cora Hoxha and Gertrud Schäfer for excellent technical help; Sandra Janku for her careful and critical reading; We are grateful to Markus Hoth for constant support, inspiring discussions and advice regarding writing of the manuscript. All the experiments except seahorse assay were conducted in Saarland University.

SUPPLEMENTARY MATERIAL

The Supplementary Material for this article can be found online at: https://www.frontiersin.org/articles/10.3389/fimmu.2021.689337/full#supplementary-material

REFERENCES

1. Zhang N, Bevan MJ. Cd8(+) T Cells: Foot Soldiers of the Immune System. *Immunity* (2011) 35:161–8. doi: 10.1016/j.immuni.2011.07.010
2. Barry M, Bleackley RC. Cytotoxic T Lymphocytes: All Roads Lead to Death. *Nat Rev Immunol* (2002) 2:401–9. doi: 10.1038/nri819
3. Dupre L, Houmadi R, Tang C, Rey-Barroso J. T Lymphocyte Migration: An Action Movie Starring the Actin and Associated Actors. *Front Immunol* (2015) 6:586. doi: 10.3389/fimmu.2015.00586
4. Weigelin B, Krause M, Friedl P. Cytotoxic T Lymphocyte Migration and Effector Function in the Tumor Microenvironment. *Immunol Lett* (2011) 138:19–21. doi: 10.1016/j.imlet.2011.02.016
5. Finlay D, Cantrell DA. Metabolism, Migration and Memory in Cytotoxic T Cells. *Nat Rev Immunol* (2011) 11:109–17. doi: 10.1038/nri2888
6. Halle S, Halle O, Forster R. Mechanisms and Dynamics of T Cell-Mediated Cytotoxicity *In Vivo*. *Trends Immunol* (2017) 38:432–43. doi: 10.1016/j.it.2017.04.002
7. Bromley SK, Burack WR, Johnson KG, Somersalo K, Sims TN, Sumen C, et al. The Immunological Synapse. *Annu Rev Immunol* (2001) 19:375–96. doi: 10.1146/annurev.immunol.19.1.375
8. Dieckmann NM, Frazer GL, Asano Y, Stinchcombe JC, Griffiths GM. The Cytotoxic T Lymphocyte Immune Synapse at a Glance. *J Cell Sci* (2016) 129:2881–6. doi: 10.1242/jcs.186205
9. Dustin ML, Chakraborty AK, Shaw AS. Understanding the Structure and Function of the Immunological Synapse. *Cold Spring Harbor Perspect Biol* (2010) 2:a002311. doi: 10.1101/cshperspect.a002311
10. Stinchcombe JC, Bossi G, Booth S, Griffiths GM. The Immunological Synapse of CTL Contains a Secretory Domain and Membrane Bridges. *Immunity* (2001) 15:751–61. doi: 10.1016/S1074-7613(01)00234-5
11. Peters PJ, Borst J, Oorschot V, Fukuda M, Krahenbuhl O, Tschopp J, et al. Cytotoxic T Lymphocyte Granules Are Secretory Lysosomes, Containing Both Perforin and Granzymes. *J Exp Med* (1991) 173:1099–109. doi: 10.1084/jem.173.5.1099
12. Qu B, Pattu V, Junker C, Schwarz EC, Bhat SS, Kummerow C, et al. Docking of Lytic Granules at the Immunological Synapse in Human CTL Requires Vti1b-dependent Pairing With CD3 Endosomes. *J Immunol* (2011) 186:6894–904. doi: 10.4049/jimmunol.1003471
13. Hassin D, Garber OG, Meiraz A, Schiffenbauer YS, Berke G. Cytotoxic T Lymphocyte Perforin and Fas Ligand Working in Concert Even When Fas Ligand Lytic Action Is Still Not Detectable. *Immunology* (2011) 133:190–6. doi: 10.1111/j.1365-2567.2011.03426.x
14. He JS, Gong DE, Ostergaard HL. Stored Fas Ligand, A Mediator of Rapid CTL-Mediated Killing, Has a Lower Threshold for Response Than Degranulation or Newly Synthesized Fas Ligand. *J Immunol* (2010) 184:555–63. doi: 10.4049/jimmunol.0902465
15. Caldwell SA, Ryan MH, McDuffie E, Abrams SI. The Fas/Fas Ligand Pathway Is Important for Optimal Tumor Regression in a Mouse Model of CTL

Adoptive Immunotherapy of Experimental CMS4 Lung Metastases. *J Immunol* (2003) 171:2402–12. doi: 10.4049/jimmunol.171.5.2402
16. MacIver NJ, Michalek RD, Rathmell JC. Metabolic Regulation of T Lymphocytes. *Annu Rev Immunol* (2013) 31:259–83. doi: 10.1146/annurev-immunol-032712-095956
17. Buck MD, O'Sullivan D, Pearce EL. T Cell Metabolism Drives Immunity. *J Exp Med* (2015) 212:1345–60. doi: 10.1084/jem.20151159
18. Geltink RIK, Kyle RL, Pearce EL. Unraveling the Complex Interplay Between T Cell Metabolism and Function. *Annu Rev Immunol* (2018) 36:461–88. doi: 10.1146/annurev-immunol-042617-053019
19. Menk AV, Scharping NE, Moreci RS, Zeng X, Guy C, Salvatore S, et al. Early TCR Signaling Induces Rapid Aerobic Glycolysis Enabling Distinct Acute T Cell Effector Functions. *Cell Rep* (2018) 22:1509–21. doi: 10.1016/j.celrep.2018.01.040
20. Cham CM, Gajewski TF. Glucose Availability Regulates IFN-Gamma Production and p70S6 Kinase Activation in CD8+ Effector T Cells. *J Immunol* (2005) 174:4670–7. doi: 10.4049/jimmunol.174.8.4670
21. van Bruggen JAC, Martens AWJ, Fraietta JA, Hofland T, Tonino SH, Eldering E, et al. Chronic Lymphocytic Leukemia Cells Impair Mitochondrial Fitness in CD8(+) T Cells and Impede CAR T-Cell Efficacy. *Blood* (2019) 134:44–58. doi: 10.1182/blood.2018885863
22. Chang CH, Qiu J, O'Sullivan D, Buck MD, Noguchi T, Curtis JD, et al. Metabolic Competition in the Tumor Microenvironment Is a Driver of Cancer Progression. *Cell* (2015) 162:1229–41. doi: 10.1016/j.cell.2015.08.016
23. DeVorkin L, Pavey N, Carleton G, Comber A, Ho C, Lim J, et al. Autophagy Regulation of Metabolism Is Required for CD8(+) T Cell Anti-Tumor Immunity. *Cell Rep* (2019) 27(2):502-13:e505. doi: 10.1016/j.celrep.2019.03.037
24. Knorck A, Marx S, Friedmann KS, Zophel S, Lieblang L, Hassig C, et al. Quantity, Quality, and Functionality of Peripheral Blood Cells Derived From Residual Blood of Different Apheresis Kits. *Transfusion* (2018) 58:1516–26. doi: 10.1111/trf.14616
25. Backes CS, Friedmann KS, Mang S, Knorck A, Hoth M, Kummerow C. Natural Killer Cells Induce Distinct Modes of Cancer Cell Death: Discrimination, Quantification, and Modulation of Apoptosis, Necrosis, and Mixed Forms. *J Biol Chem* (2018) 293:16348–63. doi: 10.1074/jbc.RA118.004549
26. Kummerow C, Schwarz EC, Bufe B, Zufall F, Hoth M, Qu B. A Simple, Economic, Time-Resolved Killing Assay. *Eur J Immunol* (2014) 44:1870–2. doi: 10.1002/eji.201444518
27. Nalbach L, Roma LP, Schmitt BM, Becker V, Korbel C, Wrublewsky S, et al. Improvement of Islet Transplantation by the Fusion of Islet Cells With Functional Blood Vessels. *EMBO Mol Med* (2021) 13:e12616. doi: 10.15252/emmm.202012616
28. Zhou X, Friedmann KS, Lyrmann H, Zhou Y, Schoppmeyer R, Knorck A, et al. A Calcium Optimum for Cytotoxic T Lymphocyte and Natural Killer Cell Cytotoxicity. *J Physiol* (2018) 596:2681–98. doi: 10.1113/JP274964
29. Wenning AS, Neblung K, Strauss B, Wolfs MJ, Sappok A, Hoth M, et al. TRP Expression Pattern and the Functional Importance of TRPC3 in Primary Human T-Cells. *Biochim Et Biophys Acta* (2011) 1813:412–23. doi: 10.1016/j.bbamcr.2010.12.022
30. Bhat SS, Friedmann KS, Knorck A, Hoxha C, Leidinger P, Backes C, et al. Syntaxin 8 Is Required for Efficient Lytic Granule Trafficking in Cytotoxic T Lymphocytes. *Biochim Et Biophys Acta* (2016) 1863:1653–64. doi: 10.1016/j.bbamcr.2016.04.014
31. Schoppmeyer R, Zhao R, Hoth M, Qu B. Light-Sheet Microscopy for Three-Dimensional Visualization of Human Immune Cells. *J visualized experiments: JoVE* (2018) (136):e57651. doi: 10.3791/57651
32. Bundesärztekammer. Richtlinie Zur Gewinnung Von Blut Und Blutbestandteilen Und Zur Anwendung Von Blutprodukten (Hämotherapie). Bundesärztekammer (2017).
33. Atkinson MA. Chapter 32 - Type 1 Diabetes Mellitus. In: *Williams Textbook of Endocrinology*, *Thirteenth Edition*. Elsevier (2016). p. 1451–83.
34. Jones N, Cronin JG, Dolton G, Panetti S, Schauenburg AJ, Galloway SAE, et al. Metabolic Adaptation of Human CD4(+) and CD8(+) T-Cells to T-Cell Receptor-Mediated Stimulation. *Front Immunol* (2017) 8:1516. doi: 10.3389/fimmu.2017.01516
35. Sinclair LV, Barthelemy C, Cantrell DA. Single Cell Glucose Uptake Assays: A Cautionary Tale. *Immunometabolism* (2020) 2:e200029. doi: 10.20900/immunometab20200029
36. Shyer JA, Flavell RA, Bailis W. Metabolic Signaling in T Cells. *Cell Res* (2020) 30:649–59. doi: 10.1038/s41422-020-0379-5
37. Zou H, Schwaer G, Zhao R, Alansary D, Yin D, Schwarz EC, et al. High Glucose Attenuates Ca2+ Influx in Cytotoxic T Lymphocytes Upon Target Recognition. *Eur J Immunol* (2020) 50:2095–8. doi: 10.1002/eji.202048577. online ahead of print.
38. Zhang L, Romero P. Metabolic Control of CD8(+) T Cell Fate Decisions and Antitumor Immunity. *Trends Mol Med* (2018) 24:30–48. doi: 10.1016/j.molmed.2017.11.005
39. Konjar S, Veldhoen M. Dynamic Metabolic State of Tissue Resident Cd8 T Cells. *Front Immunol* (2019) 10:1683. doi: 10.3389/fimmu.2019.01683
40. Yi HS, Kim SY, Kim JT, Lee YS, Moon JS, Kim M, et al. T-Cell Senescence Contributes to Abnormal FFGlucose Homeostasis in Humans and Mice. *Cell Death Dis* (2019) 10:249. doi: 10.1038/s41419-019-1494-4
41. Yin Z, Bai L, Li W, Zeng T, Tian H, Cui J. Targeting T Cell Metabolism in the Tumor Microenvironment: An Anti-Cancer Therapeutic Strategy. *J Exp Clin Cancer Research: CR* (2019) 38:403. doi: 10.1186/s13046-019-1409-3
42. Renner K, Bruss C, Schnell A, Koehl G, Becker HM, Fante M, et al. Restricting Glycolysis Preserves T Cell Effector Functions and Augments Checkpoint Therapy. *Cell Rep* (2019) 29:135–150 e139. doi: 10.1016/j.celrep.2019.08.068
43. Wang A, Huen SC, Luan HH, Yu S, Zhang C, Gallezot JD, et al. Opposing Effects of Fasting Metabolism on Tissue Tolerance in Bacterial and Viral Inflammation. *Cell* (2016) 166:1512–25.e1512. doi: 10.1016/j.cell.2016.07.026
44. Newsholme EA, Dimitriadis G. The Role of the Lymphoid System in the Regulation of the Blood Glucose Level. *Hormone Metab Res = Hormon- Und Stoffwechselforschung = Hormones Et Metabolisme* (2007) 39:730–3. doi: 10.1055/s-2007-990272
45. Organization, W. H. *Global Report on Diabetes*. WHO Press (2016).
46. Skowera A, Ellis RJ, Varela-Calvino R, Arif S, Huang GC, Van-Krinks C, et al. Ctls are Targeted to Kill Beta Cells in Patients With Type 1 Diabetes Through Recognition of a Glucose-Regulated Preproinsulin Epitope. *J Clin Invest* (2008) 118:3390–402. doi: 10.1172/JCI35449
47. Abudawood M. Diabetes and Cancer: A Comprehensive Review. *J Res Med Sciences: Off J Isfahan Univ Med Sci* (2019) 24:94. doi: 10.4103/jrms.JRMS_242_19
48. Habib SL, Rojna M. Diabetes and Risk of Cancer. *ISRN Oncol* (2013) 2013:583786. doi: 10.1155/2013/583786
49. Casqueiro J, Casqueiro J, Alves C. Infections in Patients With Diabetes Mellitus: A Review of Pathogenesis. *Indian J Endocrinol Metab* (2012) 16 (Suppl 1):S27–36. doi: 10.4103/2230-8210.94253
50. Dunachie S, Chamnan P. The Double Burden of Diabetes and Global Infection in Low and Middle-Income Countries. *Trans R Soc Trop Med Hygiene* (2019) 113:56–64. doi: 10.1093/trstmh/try124
51. Maccari I, Zhao R, Peglow M, Schwarz K, Hornak I, Pasche M, et al. Cytoskeleton Rotation Relocates Mitochondria to the Immunological Synapse and Increases Calcium Signals. *Cell Calcium* (2016) 60:309–21. doi: 10.1016/j.ceca.2016.06.007
52. Salmond RJ. Mtor Regulation of Glycolytic Metabolism in T Cells. *Front Cell Dev Biol* (2018) 6:122. doi: 10.3389/fcell.2018.00122
53. Recino A, Barkan K, Wong FS, Ladds G, Cooke A, Wallberg M. Hyperglycaemia Does Not Affect Antigen-Specific Activation and Cytolytic Killing by CD8(+) T Cells *In Vivo*. *Biosci Rep* (2017) 37:BSR20171079. doi: 10.1042/BSR20171079
54. McCambridge G, Agrawal M, Keady A, Kern PA, Hasturk H, Nikolajczyk BS, et al. Saturated Fatty Acid Activates T Cell Inflammation Through a Nicotinamide Nucleotide Transhydrogenase (Nnt)-Dependent Mechanism. *Biomolecules* (2019) 9:79. doi: 10.3390/biom9020079

Conflict of Interest: The authors declare that the research was conducted in the absence of any commercial or financial relationships that could be construed as a potential conflict of interest.